A NUMERICAL STUDY OF VORTEX DYNAMICS
OVER RIGID RIPPLES

by

K T Shum

Submitted to the Department of Civil Engineering
in partial fulfillment
of the requirements for the degree of

Doctor of Science

at the

Massachusetts Institute of Technology

January 1988

© Massachusetts Institute of Technology 1988
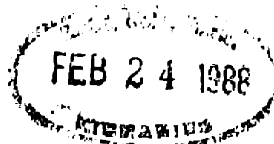
Signature of Author _____

Department of Civil Engineering
January 15, 1987

Certified by _____

Prof. Chiang C. Mei
Thesis Supervisor

Accepted by _____

Prof. Ole S. Madsen
Chairman, Department Committee

A NUMERICAL STUDY OF VORTEX DYNAMICS
OVER RIGID RIPPLES

by

K T Shum

Submitted to the Department of Civil Engineering
in partial fulfillment
of the requirements for the degree of

Doctor of Science

at the

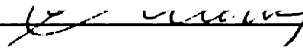Massachusetts Institute of Technology

January 1988

Signature of Author _____
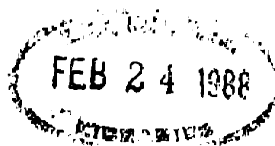Department of Civil Engineering
January 15, 1987

Certified by _____
Prof. Chiang C. Mei
Thesis Supervisor

Accepted by _____
Prof. Ole S. Madsen
Chairman, Department Committee

A NUMERICAL STUDY OF VORTEX DYNAMICS OVER RIGID RIPPLES

by

K T Shum

In this thesis we shall study the separated flow over fixed periodic ripples due to an oscillatory far field velocity. In terms of the length L and amplitude a of the ripple, amplitude U and period T of the ambient flow, and kinematic viscosity ν, three parameters can be defined: the Reynolds number $R=U2a/\nu$, the Keulegan-Carpenter number $K=UT/L$, and the ripple slope $2a/L$. While their practical range is wide, there are situations in which they can be small enough such that the flow is laminar while vortical motion is prominent during a significant part of the wave period.

Two-dimensional Navier-Stokes equations are solved numerically for a semi-infinite fluid over a ripple bed. Grid spacings are chosen to be sufficiently small such that the flow field can be resolved in detail. The accuracy of the numerical scheme is examined by comparing with the analytical solution for the oscillatory flow over a plane bed and established numerical results for the flow around an impulsively started circular cylinder. Tests on the numerical convergence of the solutions and the conservation of energy are also performed in the computations for the flow over ripples.

Ripples with an approximately sinusoidal profile and a mild slope of 0.1 are used in all computations. A systematic study is made over a range of Reynolds number ($15 \leq R \leq 500$) and Keulegan-Carpenter number ($2.5 \leq K \leq 12$). Vortices are generated during the deceleration of the ambient velocity even at the lowest values of these dimensionless parameters.

The pressure distribution along the ripple surface is found to be very close to that from the potential flow solution except at the ripple crests and under the vortices, where the amplitudes of the local shear stress are also highest. These amplitudes can be up to three times that on a plane bed under an ambient flow of the same magnitude.

The horizontal force on a ripple length of the bed depends on the exact ripple profile used in the computation, for example, that calculated from a crest to crest profile F_c or from a trough to trough profile F_t. Both F_c and F_t vary sinusoidally with time at low Reynolds numbers (≤ 50) or Keulegan-Carpenter numbers (≤ 3), and F_t is in phase with the ambient velocity. At higher values of R and K the ambient velocity leads F_c and lags F_t in phase. The amplitudes of these forces are up to more than five times that in the corresponding flow over a plane bed.

2

Values of the friction factor are deduced using two different definitions: from the energy dissipation in the flow domain, and from the magnitude of the horizontal force on a ripple length of the bed. Both friction factors decrease when R or K increases, with the dependence on K appearing to be stronger. The variation of the computed values of the friction factor based on the horizontal force follows closely that of the theoretical values for rough turbulent flows proposed by Kajiura (1968), while that based on energy dissipation appears to follow the same bilinear relationship deduced from the laboratory data of Bagnold (1946).

The flow field due to a steady ambient current is also studied. At large time, both the velocity profile and the hydrodynamic stresses are very nearly the same as those in the impulsively started current over a plane bed. In the final case, an oscillatory component is superimposed onto an ambient current. Both the viscous dissipation and the forces on the ripple increase dramatically even when the oscillatory component is much smaller in magnitude than the current.

Thesis Supervisor: Chiang C. Mei
          Title: Professor of Civil Engineering

Table of Contents

Acknowledgment

List of Figures

Chapter VI.   Numerical aspects of results

List of Tables

Chapter I. Introduction

Vortex ripples, typically between 20 to 60 cm in length, 1 to 10 cm in height, and with a slope of 0.05 to 0.2, are one of the major bed forms in coastal water where bed materials are no coarser than medium sand. The flow immediately above ripple beds, be it oscillatory due to wave actions or unidirectional due to currents, induces separations on the leesides of crests which develop into vortical flows.[1] The high velocity gradients associated with these vortices excavate bed materials from the trough and redistribute them along the ripple profile. This distorts the bed geometry further, and in turn enhances further flow separations. These interactions between sediment motion and the fluid flow makes the quantitative description of the flow field and the dynamics of the ripple bed a very complicated problem indeed.

Aside from scientific curiosities, studies on the flow field immediately above a ripple bed serve important engineering needs. Solutions to this velocity field, and the associated hydrodynamic forces, are essential first steps in answering some of the fundamental problems in nearshore hydrodynamics, for example wave attenuation and sediment transport over ripple beds. Unfortunately, an accurate description of this complicated flow pattern is still lacking. Indeed, as will be discussed in Chapter II, even the solutions to the simpler problem of the flow of a sediment-free fluid above a fixed ripple bed are yet unsatisfactory. It is on the latter problem that this thesis will focus.

The flows immediately above ripples in the coastal environment are mostly turbulent in nature (Jonsson, 1963). However, turbulence theory is still in a

---

[1]An example of this vortical flow visualized using alumina is shown in Fig. I.1. It was taken during the deceleration of the ambient flow, with dimensionless parameters (to be defined in 3.1.8) R=1880, K=4.4, and s=0.21.
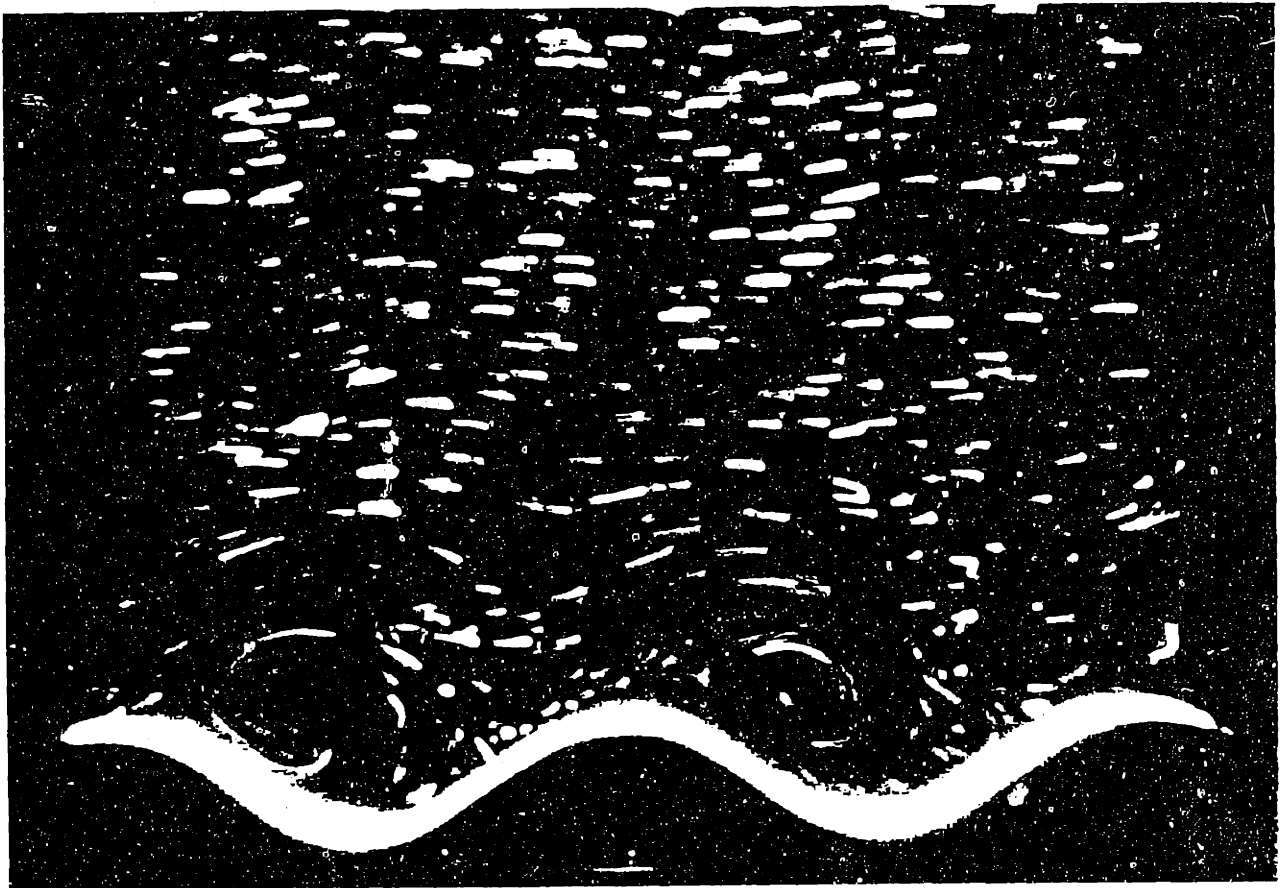
Fig. I.1. Laboratory visualization of the streak lines in the separated flow over ripples. (Courtesy of Tetsu Hara)

developing stage and is unlikely to be able to offer satisfactory solutions to the ripple flow problem in the near future. Laboratory studies, on the other hand, are in many cases laminar,[2] and a reliable solution to the laminar flow problem is therefore a valuable complement. In this thesis we shall examine the numerical solutions to the Navier-Stokes equations in two dimensions over a range of flow parameters. We shall first show that the flows we are to study in this thesis are laminar.

Based on laboratory results, Jonsson (1966) classified the flows over ripples as laminar or turbulent according to two dimensionless parameters

$$RE = \frac{u_b A_b}{\nu} = \frac{RK}{2 \cdot s} \tag{1.1}$$

and

$$\frac{A_b}{k_s} = \frac{K}{4\pi s}. \tag{1.2}$$

The variables u_b and A_b are the amplitudes of the velocity and oscillations over the ripples due to wave motion, k_s is the roughness parameter and ν is the kinematic viscosity of water. Their correspondence to the dimensionless parameters used in our study and defined in (3.1.8) is also noted, where k_s=4a is assumed as suggested in Grant and Madsen (1979). For the ranges of R and K studied in this thesis,[3] $110 \le RE \le 3600$ and $2.0 \le A_b/k_s \le 9.5$ and according to Fig. 6 in Jonsson (1966), they are all laminar flows.

The Navier-Stokes equations will be solved for a semi-infinite incompressible fluid (water) of constant density and viscosity. A far field velocity of arbitrary time dependence will be imposed. The ripples are assumed to be rigid and impermeable, and with an arbitrary periodic profile. The mobility of sediment particles and their

---

[2] Earlier discussions in the literature on the simulation of laminar and turbulent flows over ripples in the laboratory have been cited in Jonsson (1966).

[3] They are tabulated in Table VI.1.1.

effects on the flow field, and the free-surface effects due to the finite depth of the water body, will be neglected. Computation is therefore reduced to a semi-infinite strip of one ripple length in width and bounded below by the ripple bed. Spatial resolution used in our computation will not be adequate to describe fine surface roughness on the ripple profile.

Rigid, periodic ripples are assumed for expediency in the numerical computation. Neglecting the effects of bed load (and the changing shape of ripple profiles) and bottom permeability allows the far simpler 'no-slip' condition on the fixed ripple boundary. Specifically, an approximately sinusoidal profile is assumed which can be defined as a simple function of the horizontal coordinate. Du Toit and Sleath (1981) found that this is a good approximation of the actual steady state ripple profiles formed in their wave tank.[4]

The computation power and storage available on current supercomputers available for this study necessarily restricts the solution to two dimensional flows. Both two dimensional (long-crested) and three dimensional (brick pattern) ripples have been observed to form in the field and in wave tanks. In the study on ripple formations by Carsten (1966), Carstens *et al* (1969), and Lofquist (1978), the ratio of the excursion amplitude of the fluid particle to the sediment size and, to a lesser extent, Shields parameter are found to be the critical parameters in determining whether two or three dimensional bedforms are generated. By defining the grain size accordingly, we shall assume that two dimensional ripples do exist for the dimensionless flow parameters used in our study. We shall give an example in the following.

An approximate condition has been proposed in Lofquist (1978) for two cases

---

[4]Ripples with two different sizes were examined in their study: one with a slope s of 0.17 and length L of 0.14m, and the other with s=0.14 and L=0.16m, both developed over a sand bed with a mean grain size of 0.4mm.

when the mean grain size of sand are 0.18mm and 0.21mm (Figs. 27 and 28 in his paper). From extensive laboratory measurements of ripples under oscillatory flows, he found that two dimensional ripples (that is, ripples with a long crest normal to the direction of the oscillatory velocity) are formed if

$$\frac{U_0 T}{0.46\pi} < 10T$$

or

$$K < 4.6\pi \frac{T}{L}, \tag{1.3}$$

where T is the wave period and L the ripple length. The parameter K is no greater than 12 in our study, and therefore (1.3) is satisfied for most combinations of T and L under laboratory conditions.

The assumption of a fluid of constant density and viscosity overlooks the effects of suspension load which may be prominent in the immediate vicinity of the ripple bed. Significant variations in sediment concentration are observed in the vicinity of the ripple bed in experimental studies. However, viscous and inertial effects of the sand suspension in two phase flows pose too complicated a problem and will not be attempted here. Nevertheless, Raudkivi (1963) observed in his experiments on steady flows that bed load alone was sufficient for the formation of ripples from a flat bed.

Since the water depths under consideration are orders of magnitude that of a ripple length, it is expected that the free–surface will have negligible influence on the flow field near the bottom.

One of the original intents of this study was to relate the results to sediment transport. It was found that, due to limitations on computer time, our computations can be carried only to flows in which only very fine grains can be moved according to the modified Shields' criterion (Grant and Madsen, 1982). Based on the magnitude of the shear stress on the bottom $\hat{\tau}_0$ related to the

amplitude of velocity U_0 using the friction factor f_w in (7.6.1), the Shield's parameter can be written as

$$\Psi_s = \frac{\tau_0}{(\rho_s - \rho)gD} = \frac{\rho}{2g(\rho_s - \rho)} f_w \frac{U_0^2}{D}$$

where ρ_s and ρ are the densities of sand and water, g the acceleration due to gravity, and D the mean grain size of the sand. The first fraction on the right hand side $\rho/2g(\rho_s - \rho) \approx 0.02$.

For the flow under an ambient current of magnitude c, we can write

$$\Psi_s = 0.02 \, f_w \frac{c^2}{D} = 0.02 \, f_w \, R_c^2 \frac{\nu^2}{4Da^2} \qquad (1.4)$$

where R_c is defined in §VIII.1, $\nu = 10^{-6} m/s^2$ is the kinematic viscosity of water, and 2a is the ripple height. From Table IX.6.4, $f_w \approx 0.5 \times 10^{-3}$ for $R_c = 1000$, the highest R_c examined, and therefore Ψ_s in this case is of the order of $0.25 \times 10^{-11}/Da^2$. No sediment motion is expected in this case.

For the oscillatory flow, we can write

$$\Psi_s = 0.02 \, f_w \frac{RK}{s} \frac{\nu}{T} \frac{1}{D} \qquad (1.5)$$

where R, K, and s are defined in (3.1.8). For $\nu RK/sT = o(10^{-2})$ and $f_w = o(0.1)$, there will be sediment transport only for $D < 10^{-4} m = 1 mm$ for $\Psi_s \approx 0.1$ (see for example Fig. 6.3 of Sleath, 1984). Therefore sediment transport occurs in the flows we study only for very fine sand.

Previous studies on the flow over ripples will be reviewed in Chapter II. Details of the mathematical formulation and numerical solution will be given in Chapters III and IV. Verification of the numerical code will be made in Chapter V by comparisons with available solutions in closely related flow problems. The accuracy of the numerical results will be discussed in Chapter VI. Results for the flow over ripples for three cases of ambient flows: oscillatory, steady, and a combination of

the two, will be presented in Chapters VII, VIII, and IX. These results will be summarized and discussed in Chapter X.

In §II.1 we list some of the experimental investigations on the formation of ripples and the flow fields above them. In §II.2 we shall examine theoretical studies of the flow fields based on semi-empirical models, potential flow models, or the Navier-Stokes equations.

§II.1 Experiments

Experiments on the formation of ripples in steady currents have been performed by Yalin (1964) and Williams and Kemp (1971). The growth of ripples under wave action was studied by Hunt (1882), Darwin (1883), Ayrton (1910), Kennedy and Falcon (1965), and Logquist (1978) in wave tanks and Raudkivi (1963) in oscillatory flow tunnels, and by Bagnold (1946) who oscillated a tray of sand in a wave tank of otherwise still water.[1] Bagnold classified three types of wave induced ripples: rolling-grain, vortex, and brick-pattern, corresponding to different grain sizes of sediment and flow velocities. We shall limit ourselves to vortex ripples in this study.

Laboratory visualizations of the vortical flow field were reported in Bagnold (1946), Honji and Matsunaga (1979), and Honji et al (1980). The magnitudes of velocity fluctuations immediately above fixed ripples were measured by Sleath (1970). More detailed time histories of velocity profiles were reported in Du Toit and Sleath (1981), Sato et al (1984), and Tanaka and Shuto (1987).

Sediment concentration in suspension was measured in the laboratory by Nakato et al (1977) and Ikeda and Asaeda (1983) for oscillatory flow over ripples.

---

[1]It should be noted, however, that there are basic differences between the simple harmonic motion of a tray of sediment through still water and wave motion over a sand bed. The more important ones are fluid accelerations, turbulence intensities, and pressure fluctuations. A detailed discussion can be found in Vincent (1958).

20

It was shown that horizontal gradients of sediment concentration in suspension may not be negligible and they can alter flow characteristics significantly. However, this concentration decreases rapidly with the distance from the bed.

Other quantities of engineering interests include the rate of energy dissipation which was measured in the laboratory by Carstens *et al* (1969). Their data was further studied by Vitale (1979) and Sleath (1985). The bottom shear and the associated friction factor were experimentally determined by Bagnold (1946), Bayazit (1969), Kamphius (1975), and Lofquist (1980).

Dingler and Inman (1976) performed a field study at La Jolla, California, a location that "included all nearshore ripple regimes". Characteristic dimensions of ripples under various flow conditions were measured using a high resolution sonar.

Surveys on earlier experimental results can be found in Kennedy and Falcon (1965), Kobayashi (1979), and Hedegaard (1985).

§II.2. Theoretical studies

Aside from a handful of papers which sought solutions to the Navier-Stokes equations, theoretical studies are mostly based on semi-empirical approaches.

§II.2.1. Semi-empirical models

In most turbulent flow models the flow field is solved using an eddy viscosity, and the ripple amplitude appears as an equivalent roughness parameter in the formulation. Vertical profiles of the mean horizontal velocity were derived independently by Nikuradse, von Karman, and Prandtl for steady flows, Jonsson (1963) and Kajiura (1968) for oscillatory flows, and Grant and Madsen (1979) for combined oscillatory flows and currents.

§II.2.2. Analytic solutions

Analytic solutions to the full Navier-Stokes equation for flows over ripple beds have been based on asymptotic methods such that the nonlinear convective terms can be linearized at each order. Series expansions for various limiting cases of ripple slope s, Reynolds number R, and Keulegan-Carpenter number K defined in (3.1.8) have been proposed. Benjamin (1959) obtained leading order asymptotic solution for large R for a steady shear flow over an approximately sinusoidal bed.

Lyne (1971) derived a series solution for the streamfunction in orders of $\sqrt{sR/K}$ for oscillatory flows over the same bed profile. This smallness parameter used is also the square root of the ratio of the time scale of viscous diffusion to the period of oscillations in the ambient flow. Sleath (1974) obtained series expansion for the streamfunction in orders of πs, and Kaneko and Honji (1979) expressed the same function as a series in K. Unfortunately, the complexity of these asymptotic solutions increases drastically beyond the first couple of orders, thus limiting their applications to weak ambient flows and gentle ripple profiles. As a consequence, their results do not describe vortical flows.

Separated flows are typically high Reynolds number phenomena and therefore potential flow models appear attractive. Based on the ideas of von Karman (1911) and Rosenhead (1931), in which the high shear layer in the separation was treated mathematically as an infinitesimally thin vortex sheet and approximated by a string of discrete point vortices, Longuet-Higgins (1981) proposed a potential flow model for the description of oscillatory flow over periodic ripples with sharp crests. The strengths of vortices used in simulating the vortex sheet were determined from the potential flow velocities at a certain distance from the crest. However, this distance was chosen somewhat arbitrarily and was not related to the thickness of the boundary layer. The vortex strengths thus determined could therefore vary considerably. Furthermore, the Kutta condition was not satisfied at the crests (see

Crighton, 1985 for its significance). Subsequent motions of these vortices were traced with a numerical scheme which had been demonstrated (for example Birkhoff and Fisher, 1959 and Takami, 1964) to fail to reproduce the rollup of a simple vortex sheet in an infinite fluid, and this problem was also found in oscillatory flows (Craik, 1982). In the flow over ripples, these point vortices moved into close vicinity of each other and induced high velocity gradients, thereby violating the basic assumption of an inviscid flow. This crowding of vortices led to a chaotic picture, and further *ad hoc* remedies were introduced. In addition, the rapidly increasing number of vortices in the flow domain had to be artificially decreased by amalgamations to reduce comptutation time.[2] But this procedure lacks physical justifications. It was not apparent that his results described large scale vortical motions observed in visualization experiments (for example, in Honji *et al*, 1980).

§II.2.3. Numerical solutions

It is apparent from the previous section that neither convective inertia nor viscous dissipation can be neglected in the modeling of separated flows. Since analytical solutions to the full Navier-Stokes equations are unavailable for general flow cases, numerical methods appear to be the appropriate approach.

Numerical simulations of separated flows over boundaries with periodic variations have been presented in Gillani and Swanson (1976) for an unsteady flow through spherical cavities, Sobey (1980, 1982, 1983) for both steady and unsteady flows in two-dimensional symmetric and asymmetric furrowed channels, Ralph (1986) for oscillatory flows in wavy-walled tubes, and Ghaddar *et al* (1986a,b) on flows in two-dimensional grooved channels. All these results were in good agreement with laboratory visualizations. Of special interest is the observation in

---

[2]The amount of computation is proportional to the third power of the number of point vortices in the flow field.

Ralph (1986) that, for oscillatory flows starting from a quiescent fluid, solution at large times cease to be symmetrical in the two halves of the wave period as the Reynods number and Keulegan–Carpenter number increase.

Numerical solutions to the full Navier-Stokes equations to the flow over ripples with an approximately sinusoidal profile was first reported by Sleath (1973). Navier-Stokes equations were solved in terms of streamfunction and vorticity function. For the vorticity equation, the viscous terms were treated with a Dufort-Frankel (Dufort and Frankel, 1953) type scheme and convective terms were treated with a scheme first suggested by Arakawa (1966), both being leap-frog type explicit schemes. The streamfunction (Poisson) equation was solved by an alternating-direction implicit scheme or successive over-relaxation according to the ratio of the estimate of the thickness of viscous boundary layer to the ripple length. Centered finite-differencing was used for spatial derivatives in the truncated transformed plane. Unfortunately, limitations on computation time restricted spatial resolution to eight grid points per ripple length and nine grid points in the vertical direction, and such a coarse grid spacing was, for the range of Reynolds numbers considered, insufficient to resolve the viscous boundary sublayer immediately next to the ripple surface.[3] Even though the formal spatial accuracy of the scheme is fourth order for convective terms and second order for the viscous terms and the Poisson equation, the lack of resolution due to the coarse grids raised doubts on the convergence of the numerical solution to the exact solution of the original Navier-Stokes equations. Small scale variations in the flow field, especially at instants when separation first occurs, were not resolved and a detailed picture of the flow field is therefore still lacking.

---

[3]Grid spacing is decided by the length scale of the vortices and the thickness of the viscous boundary layer immediately above the ripple surface, and will be discussed in detail in §IV.3 and §IV.4. The resolution used by Sleath in relation to the Reynolds number in his studies will be examined in §VII.6.

The same numerical procedure was later used to derive other quantities of interest for the oscillatory flow over ripples, for example the velocity profile (Sleath, 1974), mean drift (Sleath, 1975), drag and shear forces on ripple (Sleath, 1976), and the energy dissipation factor and friction coefficients (Sleath, 1982). The uncertainty in the numerical accuracy discussed above renders the results open to questions. Quantitative variations with various flow parameters of the variables conducive to wave attenuation and sediment transport, for example the rate of energy dissipation and the stresses on the ripple, remain unresolved.

Sato *et al* (1984) applied the same implicit finite difference scheme to oscillatory flows over asymmetric ripples. Details of the finite-differencing scheme and boundary conditions was not given in that paper. Approximately the same resolution as in Sleath (1973) was used. In their results, the rate of energy dissipation over the flow domain was negative during part of the wave cycle. Since the formulation was strictly for a laminar flow model, the explanation that this was due to "a part of turbulence energy is transfered back to the mean flow" is unacceptable. This in fact is more likely to be due to numerical errors from a lack of resolution rather than an accurate simulation of the actual physical flow.

An access to supercomputers allows a more accurate simulation of the flow field over a ripple bed. In the study to be described in the following chapters, a different numerical scheme than the one used by Sleath is introduced. The flow over ripples under an oscillatory flow, a current, and a combination of the two, will be studied. The resolution of the flow field and the accuracy of the numerical solution will be examined carefully to ensure an accurate description of all salient features of the flow field. This in turn gives confidence on the computed rates of energy dissipation, surface stresses on the ripple, and the friction factors.

Chapter III. Formulation

We shall study the velocity field of an initially quiescent, incompressible Newtonian fluid over a ripple bed and driven by an imposed unsteady far field velocity. Navier-Stokes equations in two dimensions will be solved numerically in a transformed plane such that the flow domain, spanning one ripple length and truncated sufficiently high above the bed, is reduced to a rectangle.

The following notations will be used: physical variables are denoted by subscript p (e.g. x_p), nondimensional variables in the physical plane are denoted by over-head tilde (e.g. $\tilde{x}$), and variables in the mapped plane are denoted by plain letters (e.g. x).

§III.1. Governing equations in transformed coordinates and dimensionless variables

In terms of streamfunction ψ_p and vorticity function ω_p, Navier-Stokes equations in two dimensions take the form

$$\frac{\partial \omega_p}{\partial t_p} + \frac{\partial \psi_p}{\partial y_p}\frac{\partial \omega_p}{\partial x_p} - \frac{\partial \psi_p}{\partial x_p}\frac{\partial \omega_p}{\partial y_p} = \nu\left(\frac{\partial^2 \omega_p}{\partial x_p^2} + \frac{\partial^2 \omega_p}{\partial y_p^2}\right) \tag{3.1.1}$$

and

$$\frac{\partial^2 \psi_p}{\partial x_p^2} + \frac{\partial^2 \psi_p}{\partial y_p^2} = -\omega_p . \tag{3.1.2}$$

The velocity components are defined as

$$u_p = \frac{\partial \psi_p}{\partial y_p} \quad \text{and} \quad v_p = -\frac{\partial \psi_p}{\partial x_p} . \tag{3.1.3}$$

A detailed derivation can be found in, for example, Batchelor (1967).

Introduce nondimensional variables such that

$$x_p = L\,\tilde{x}\,, \quad u_p = U_0\,\tilde{u}\,,$$

$$y_p = L\,\tilde{y}\,, \quad v_p = U_0\,\tilde{v}\,, \quad t_p = T\,t\,,$$

$$\psi_p = U_0 L\,\psi\,, \quad \omega_p = \frac{U_0}{L}\,\omega\,,$$

$$\tau_p = \rho U_0^2\,\tau\,, \quad p_p = \rho U_0^2\,p\,, \quad \text{and} \quad F_p = \rho U_0^2 L\,F\,, \tag{3.1.4}$$

where

L = ripple length,

U_0 = amplitude of ambient velocity, and

T = wave period of ambient oscillatory flow,

and τ_p, p_p, and F_p are respectively the shear stress, pressure, and hydrodynamic force. Equations (3.1.1) to (3.1.3) become

$$\frac{\partial \omega}{\partial t} + K\left(\frac{\partial \psi}{\partial \tilde{y}}\frac{\partial \omega}{\partial \tilde{x}} - \frac{\partial \psi}{\partial \tilde{x}}\frac{\partial \omega}{\partial \tilde{y}}\right) = s\frac{K}{R}\left(\frac{\partial^2 \omega}{\partial \tilde{x}^2} + \frac{\partial^2 \omega}{\partial \tilde{y}^2}\right), \tag{3.1.5}$$

$$\frac{\partial^2 \psi}{\partial \tilde{x}^2} + \frac{\partial^2 \psi}{\partial \tilde{y}^2} = -\omega\,, \tag{3.1.6}$$

$$\tilde{u} = \frac{\partial \psi}{\partial \tilde{y}} \quad \text{and} \quad \tilde{v} = -\frac{\partial \psi}{\partial \tilde{x}}\,, \tag{3.1.7}$$

where

$$K = \frac{U_0 T}{L} = \text{Keulegan--Carpenter number,}$$

$$R = \frac{U_0 2a}{\nu} = \text{Reynolds number, and}$$

$$s = 2\frac{a}{L} = \text{ripple slope} \tag{3.1.8}$$

are the dimensionless parameters, and a is the amplitude of ripple.

We next introduce a conformal mapping $(\tilde{x},\tilde{y}) \to (x,y)$ such that the flow domain above one ripple length of the bottom boundary is transformed onto a semi-infinite rectangular strip in the (x,y) plane (Fig. III.1.1). Let the Jacobian of the transformation $J(x,y)$ be

physical plane

mapped plane
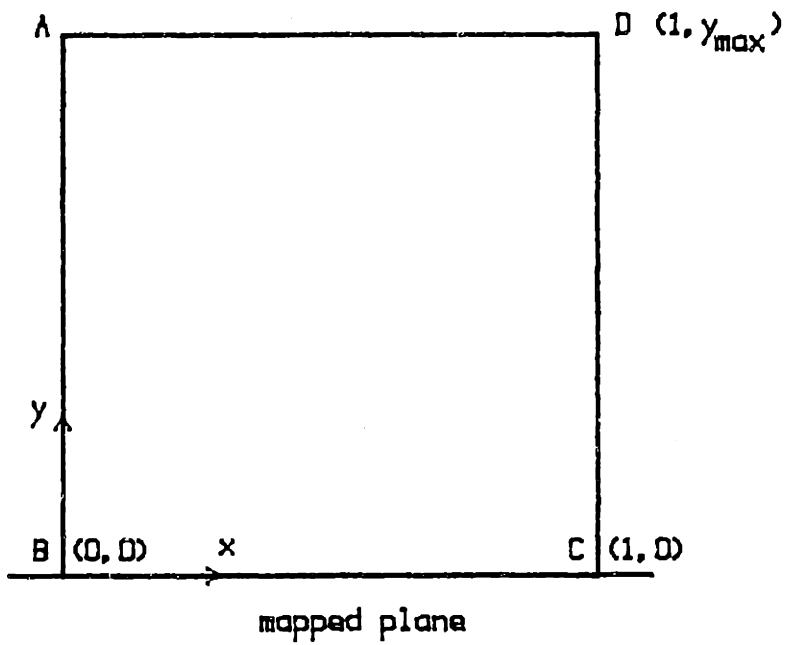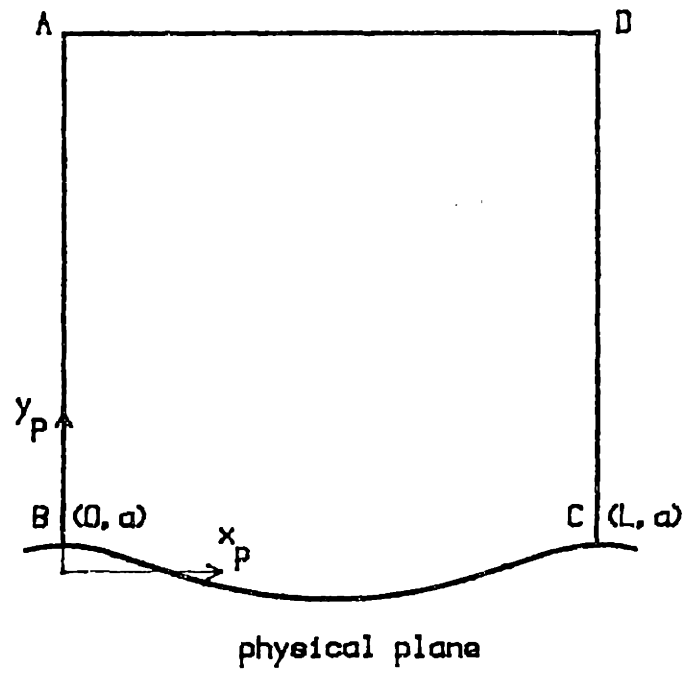
Fig. III.1.1. Conformal mapping

$s = 0.1, \quad y_{max} = 1.0$

$$J(x, y) = \begin{vmatrix} \dfrac{\partial \tilde{x}}{\partial x} & \dfrac{\partial \tilde{x}}{\partial y} \\[2ex] \dfrac{\partial \tilde{y}}{\partial x} & \dfrac{\partial \tilde{y}}{\partial y} \end{vmatrix} = \dfrac{1}{L^2} \begin{vmatrix} \dfrac{\partial x_p}{\partial x} & \dfrac{\partial x_p}{\partial y} \\[2ex] \dfrac{\partial y_p}{\partial x} & \dfrac{\partial y_p}{\partial y} \end{vmatrix}. \tag{3.1.9}$$

For any analytic functions f and g defined in $(\tilde{x}, \tilde{y})$, the equalities

$$\frac{\partial f}{\partial \tilde{x}} \frac{\partial g}{\partial \tilde{y}} - \frac{\partial f}{\partial \tilde{y}} \frac{\partial g}{\partial \tilde{x}} = \frac{1}{J}\left(\frac{\partial f}{\partial x} \frac{\partial g}{\partial y} - \frac{\partial f}{\partial y} \frac{\partial g}{\partial x}\right) \tag{3.1.9.a}$$

and

$$\frac{\partial^2 f}{\partial \tilde{x}^2} + \frac{\partial^2 f}{\partial \tilde{y}^2} = \frac{1}{J}\left(\frac{\partial^2 f}{\partial x^2} + \frac{\partial^2 f}{\partial y^2}\right) \tag{3.1.9.b}$$

hold, as are derived in the Appendices, §AI.2 and §AI.3 respectively. Equations (3.1.5) to (3.1.6) can then be written as

$$J \frac{\partial \omega}{\partial t} + K\left(\frac{\partial \psi}{\partial y} \frac{\partial \omega}{\partial x} - \frac{\partial \psi}{\partial x} \frac{\partial \omega}{\partial y}\right) = s\frac{K}{R}\left(\frac{\partial^2 \omega}{\partial x^2} + \frac{\partial^2 \omega}{\partial y^2}\right), \tag{3.1.10}$$

$$\frac{\partial^2 \psi}{\partial x^2} + \frac{\partial^2 \psi}{\partial y^2} = -J\omega. \tag{3.1.11}$$

From (A1.1.6) and (A1.1.5), (3.1.7) can be written as

$$\tilde{u} = \frac{1}{J}\left(\frac{\partial \tilde{x}}{\partial x} \frac{\partial \psi}{\partial y} + \frac{\partial \tilde{y}}{\partial x} \frac{\partial \psi}{\partial x}\right) \quad \text{and} \quad \tilde{v} = -\frac{1}{J}\left(\frac{\partial \tilde{x}}{\partial x} \frac{\partial \psi}{\partial x} - \frac{\partial \tilde{y}}{\partial x} \frac{\partial \psi}{\partial y}\right). \tag{3.1.12}$$

Physical boundary conditions are as follows. There can be 'no-slip' on the surface of ripple, that is,

$$u_p = v_p = 0 \quad \text{on the ripple surface} \quad y = 0. \tag{3.1.13a}$$

The ambient velocity must be approached in the far field,

$$u_p = U_0 U_\infty(t), \quad v_p = 0 \quad \text{as} \quad y_p \to \infty, \tag{3.1.13b}$$

where $U_\infty(t)$ is dimensionless. The flow must be periodic such that

$$u_p(x_p=0, y_p, t_p) = u_p(x_p=L, y_p, t_p) \tag{3.1.13c}$$

and

$$v_p(x_p=0, y_p, t_p) = v_p(x_p=L, y_p, t_p) .$$ (3.1.13d)

The ambient velocity can in general be a uniform current c superimposed on a sinusoidal oscillation $U_0 \sin(2\pi t_p/T)$, where $0<c<1$, and therefore

$$U_\infty(t) = \frac{c}{U_0} + \sin(2\pi \frac{t_p}{T}) .$$ (3.1.14)

By choosing a conformal mapping such that $x \to \tilde{x}$ and $y \to \tilde{y}$ as $y \to \infty$, (3.1.13) and (3.1.14) can be written as

$$\psi = \frac{\partial \psi}{\partial y} = 0 \quad \text{at} \quad y = 0$$ (3.1.15)

and

$$\psi = \text{constant} , \quad \frac{\partial \psi}{\partial y} = U_\infty(t) \quad \text{as} \quad y \to \infty .$$ (3.1.16)

Note that ψ=constant as $y \to \infty$ corresponds directly to the potential flow solution, and is identical to (3.1.13b) since $v_p=0$ implies $\partial \psi/\partial x=0$ for all x, or $\partial^r \psi/\partial x^r$ for all $r \geq 1$.

§III.2. Hydrodynamic forces on ripple

Expressions for the pressure, shear stress, and lift and drag forces acting on the ripple surface will be derived in transformed coordinates in this section.

§III.2.1. Pressure at the surface of ripple

In nondimensional variables and transformed coordinates, the momentum equations in two dimensions can be written as

$$\frac{\partial p}{\partial x} = -\frac{1}{K} \frac{\partial}{\partial t} \frac{\partial \psi}{\partial y} + \frac{s}{R} \frac{\partial}{\partial y} [\frac{1}{J} (\frac{\partial^2 \psi}{\partial x^2} + \frac{\partial^2 \psi}{\partial y^2})]$$

$$+ \frac{1}{J} \{ \frac{\partial \psi}{\partial x} \frac{\partial^2 \psi}{\partial y^2} - \frac{\partial \psi}{\partial y} \frac{\partial^2 \psi}{\partial x \partial y} + \frac{1}{2J} \frac{\partial J}{\partial x} [(\frac{\partial \psi}{\partial x})^2 + (\frac{\partial \psi}{\partial y})^2] \}$$ (3.2.1)

and

$$\frac{\partial p}{\partial y} = \frac{1}{K}\frac{\partial}{\partial t}\frac{\partial \psi}{\partial x} - \frac{s}{R}\frac{\partial}{\partial x}[\frac{1}{J}(\frac{\partial^2 \psi}{\partial x^2} + \frac{\partial^2 \psi}{\partial y^2})]$$

$$+ \frac{1}{J}\{\frac{\partial \psi}{\partial y}\frac{\partial^2 \psi}{\partial x^2} - \frac{\partial \psi}{\partial x}\frac{\partial^2 \psi}{\partial x \partial y} + \frac{1}{2J}\frac{\partial J}{\partial y}[(\frac{\partial \psi}{\partial x})^2 + (\frac{\partial \psi}{\partial y})^2]\} \; . \qquad (3.2.2)$$

Details of derivation is given in §AI.7.

From (3.2.2), the pressure at any point can be written as

$$p(x, y, t) - p(x, y=\infty, t) = -\int_y^\infty dy \; \{\frac{1}{K}\frac{\partial}{\partial t}\frac{\partial \psi}{\partial x} - \frac{s}{R}\frac{\partial}{\partial x}[\frac{1}{J}(\frac{\partial^2 \psi}{\partial x^2} + \frac{\partial^2 \psi}{\partial y^2})]$$

$$+ \frac{1}{J}\{\frac{\partial \psi}{\partial y}\frac{\partial^2 \psi}{\partial x^2} - \frac{\partial \psi}{\partial x}\frac{\partial^2 \psi}{\partial x \partial y} + \frac{1}{2J}\frac{\partial J}{\partial y}[(\frac{\partial \psi}{\partial x})^2 + (\frac{\partial \psi}{\partial y})^2]\}\} \; . \qquad (3.2.3)$$

The integral

$$-\int_y^\infty dy \; \frac{1}{2J^2}\frac{\partial J}{\partial y}[(\frac{\partial \psi}{\partial x})^2 + (\frac{\partial \psi}{\partial y})^2]$$

can be integrated by parts to give

$$\frac{1}{2J}[(\frac{\partial \psi}{\partial x})^2 + (\frac{\partial \psi}{\partial y})^2]\; \Big|_y^{y=\alpha} - \int_y^\infty dy \; [\frac{1}{J}(\frac{\partial \psi}{\partial y}\frac{\partial^2 \psi}{\partial y^2} + \frac{\partial \psi}{\partial x}\frac{\partial^2 \psi}{\partial x \partial y})] \; .$$

From boundary condition (3.1.16), this can be rewritten as

$$\frac{1}{2}U_\infty^2 - \frac{1}{2}U^2(x,y,t) - \int_y^\infty dy \; [\frac{1}{J}(\frac{\partial \psi}{\partial y}\frac{\partial^2 \psi}{\partial y^2} + \frac{\partial \psi}{\partial x}\frac{\partial^2 \psi}{\partial x \partial y})] \; ,$$

where

$$U^2(x, y, t) \equiv \frac{1}{J}[(\frac{\partial \psi}{\partial x})^2 + (\frac{\partial \psi}{\partial y})^2] \; .$$

Substitution into (3.2.2) gives

$$p(x, y, t) - p(x, y=\infty, t) = \frac{1}{2}U_\infty^2 - \frac{1}{2}U^2(x,y,t)$$

$$-\int_y^\infty dy \; \{\frac{1}{K}\frac{\partial}{\partial t}\frac{\partial \psi}{\partial x} - \frac{s}{R}\frac{\partial}{\partial x}[\frac{1}{J}(\frac{\partial^2 \psi}{\partial x^2} + \frac{\partial^2 \psi}{\partial y^2})] + \frac{1}{J}\frac{\partial \psi}{\partial y}(\frac{\partial^2 \psi}{\partial x^2} + \frac{\partial^2 \psi}{\partial y^2})\} \; . \qquad (3.2.4)$$

Far above the ripples, boundary conditions (3.1.16) reduce (3.2.1) to

$$\frac{\partial p}{\partial x} = -\frac{1}{K}\frac{\partial}{\partial t}\frac{\partial \psi}{\partial y} = -\frac{1}{K}\frac{dU_\infty}{dt} \quad \text{as} \quad y \to \infty \qquad (3.2.5.a)$$

and therefore

$$p(x, y=\infty; t) = p_\infty(t) - \int_0^x dx \, \frac{1}{K}\frac{\partial}{\partial t}\frac{\partial \psi_\infty}{\partial y} = p_\infty(t) - \frac{x}{K}\frac{dU_\infty}{dt}, \qquad (3.2.5.b)$$

where $p_\infty(t)$ is the far field (as $y \to \infty$) pressure at $x=0$ and ψ_∞ is the streamfunction as $y \to \infty$ (and is constant along x).

Upon applying governing equation (3.1.11) and boundary conditions (3.1.16) and (3.2.5.b), equation (3.2.4) can be reduced to

$$p(x, y, t) - [p_\infty(t) - \frac{x}{K}\frac{dU_\infty}{dt}]$$

$$= \frac{1}{2}U_\infty^2 - \frac{1}{2}U^2(x, y, t) - \int_y^\infty dy \, (\frac{1}{K}\frac{\partial}{\partial t}\frac{\partial \psi}{\partial x} + \frac{s}{R}\frac{\partial \omega}{\partial x} - \omega\frac{\partial \psi}{\partial y}) ,$$

and, finally, to the form

$$p(x, y, t) - p_\infty(t)$$

$$= -\frac{x}{K}\frac{dU_\infty}{dt} + \frac{U_\infty^2}{2} - \frac{U^2(x,y,t)}{2} - \int_y^\infty dy \, (\frac{1}{K}\frac{\partial}{\partial t}\frac{\partial \psi}{\partial x} + \frac{s}{R}\frac{\partial \omega}{\partial x} - \omega\frac{\partial \psi}{\partial y}) . \qquad (3.2.6)$$

The pressure along the ripple surface is of particular interest. From (3.2.6) and boundary conditions (3.1.15), we have

$$p_r(x, t) = p(x, y=0, t)$$

$$= p_\infty(t) - \frac{x}{K}\frac{dU_\infty}{dt} + \frac{1}{2}U_\infty^2 - \int_0^\infty dy \, (\frac{1}{K}\frac{\partial}{\partial t}\frac{\partial \psi}{\partial x} + \frac{s}{R}\frac{\partial \omega}{\partial x} - \omega\frac{\partial \psi}{\partial y}) . \qquad (3.2.7)$$

While the pressure term is absent in the governing equations (3.1.10) and (3.1.11), the far field pressure (3.2.5) is implied, although not imposed as a boundary condition. As will be discussed in Chapter IV, the flow field is truncated at a finite height from the ripple bed, and the pressure at this boundary can be estimated from (3.2.1) and boundary conditions (3.1.16), which give

$$\frac{\partial p}{\partial x} = -\frac{1}{K}\frac{dU_\infty}{dt} - \frac{s}{R}\frac{\partial \omega}{\partial y} + \frac{U_\infty^2}{2}\frac{\partial J}{\partial x} \quad \text{at} \quad y = y_{max} .$$ (3.2.5.c)

Its difference from that of the far field pressure in a semi-infinite fluid given by (3.2.5.a) can therefore be estimated from the magnitudes of the last two terms on the right hand side, which should assume very small values for y_{max} chosen sufficiently large.

§III.2.2. Drag and lift forces on ripple

Consider a surface element ds_p with components of its unit normal vector (Fig. III.2.1) given by

$$n_x = -\frac{dy_p}{ds_p} \quad \text{and} \quad n_y = \frac{dx_p}{ds_p}$$

where

$$ds_p = (dx_p^2 + dy_p^2)^{\frac{1}{2}} .$$

The drag and lift forces per unit arc length on the ripple are given by

$$f_{p_x} = \tau_{p_{xx}} n_x + \tau_{p_{yx}} n_y \quad \text{and} \quad f_{p_y} = \tau_{p_{xy}} n_x + \tau_{p_{yy}} n_y$$ (3.2.8)

respectively, and the sign convention is defined in Fig. III.2.2. Since

$$\tau_{p_{xx}} = -p_p + 2\mu \frac{\partial u_p}{\partial x_p}, \quad \tau_{p_{yy}} = -p_p + 2\mu \frac{\partial v_p}{\partial y_p},$$

and

$$\tau_{p_{xy}} = \tau_{p_{yx}} = \mu \left(\frac{\partial u_p}{\partial y_p} + \frac{\partial v_p}{\partial x_p}\right)$$ (3.2.9)

where $\mu = \rho\nu$, (3.2.8) gives

$$dF_{p_x} = f_{p_x} ds_p = \mu \left(\frac{\partial u_p}{\partial y_p} + \frac{\partial v_p}{\partial x_p}\right) dx_p + \left(p_p - 2\mu \frac{\partial u_p}{\partial x_p}\right) dy_p$$

and

$$dF_{p_y} = f_{p_y} ds_p = -\mu \left(\frac{\partial u_p}{\partial y_p} + \frac{\partial v_p}{\partial x_p}\right) dy_p - \left(p_p - 2\mu \frac{\partial v_p}{\partial y_p}\right) dx_p .$$ (3.2.10)
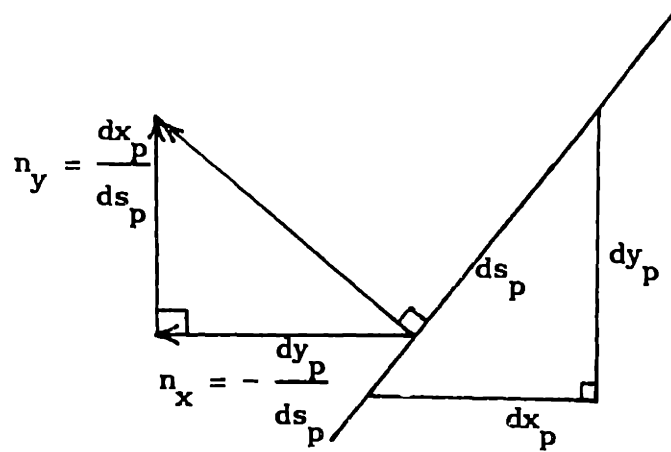
Fig. III.2.1.　Normal vector of surface element ds_p
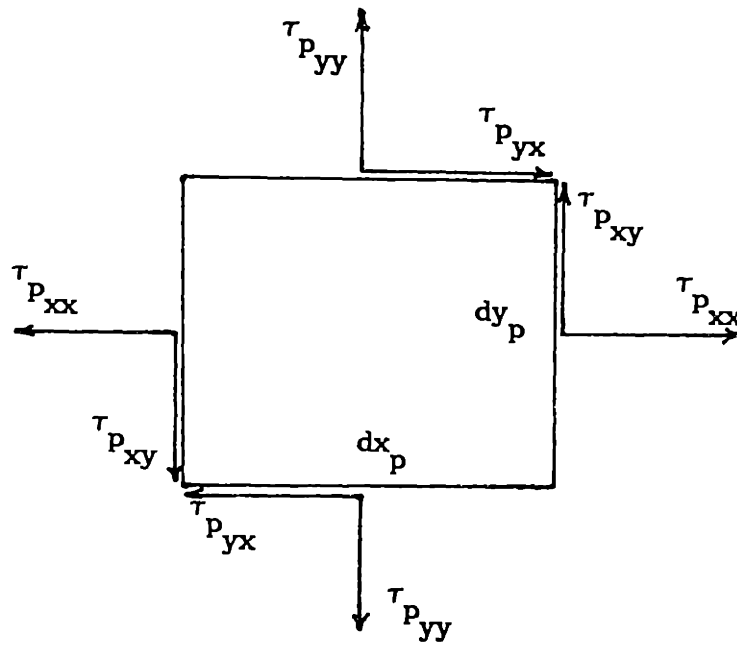
Fig. III.2.2.　Sign convention of stress vector

In terms of the streamfunction, they are

$$
dF_{P_x} = \mu \left(\frac{\partial^2 \psi_p}{\partial y_p^2} - \frac{\partial^2 \psi_p}{\partial x_p^2} \right) dx_p + \left(p_p - 2\mu \frac{\partial^2 \psi_p}{\partial x_p \partial y_p} \right) dy_p
$$

and

$$
dF_{P_y} = -\mu \left(\frac{\partial^2 \psi_p}{\partial y_p^2} - \frac{\partial^2 \psi_p}{\partial x_p^2} \right) dy_p - \left(p_p + 2\mu \frac{\partial^2 \psi_p}{\partial x_p \partial y_p} \right) dx_p . \qquad (3.2.11)
$$

If the force components are normalized as

$$
dF_p = \rho U_0^2 L \, dF ,
$$

(3.2.11) becomes

$$
dF_x = \frac{s}{R} \left(\frac{\partial^2 \psi}{\partial \tilde{y}^2} - \frac{\partial^2 \psi}{\partial \tilde{x}^2} \right) d\tilde{x} + \left(p - 2 \frac{s}{R} \frac{\partial^2 \psi}{\partial \tilde{x} \partial \tilde{y}} \right) d\tilde{y}
$$

and

$$
dF_y = -\frac{s}{R} \left(\frac{\partial^2 \psi}{\partial \tilde{y}^2} - \frac{\partial^2 \psi}{\partial \tilde{x}^2} \right) d\tilde{y} - \left(p + 2 \frac{s}{R} \frac{\partial^2 \psi}{\partial \tilde{x} \partial \tilde{y}} \right) d\tilde{x} . \qquad (3.2.12)
$$

To express (3.2.12) in terms of transformed coordinates, we make use of (A1.4.1) and (A1.5.1) derived in Appendix I. The relationship between the differential operators are

$$
\frac{\partial^2}{\partial \tilde{y}^2} - \frac{\partial^2}{\partial \tilde{x}^2} = A \left(\frac{\partial^2}{\partial y^2} - \frac{\partial^2}{\partial x^2} \right) + 4B \frac{\partial^2}{\partial x \partial y} + 2C \frac{\partial}{\partial x} + 2D \frac{\partial}{\partial y} \qquad (3.2.13.a)
$$

and

$$
\frac{\partial^2}{\partial \tilde{x} \partial \tilde{y}} = -B \left(\frac{\partial^2}{\partial y^2} - \frac{\partial^2}{\partial x^2} \right) + A \frac{\partial^2}{\partial x \partial y} + D \frac{\partial}{\partial x} - C \frac{\partial}{\partial y} , \qquad (3.2.13.b)
$$

where

$$
A \equiv A(x, y) \equiv \frac{1}{J^2} \left[\left(\frac{\partial \tilde{x}}{\partial x} \right)^2 - \left(\frac{\partial \tilde{y}}{\partial x} \right)^2 \right] ,
$$

35

$$B \equiv B(x, y) \equiv \frac{1}{J^2} \frac{\partial \tilde{x}}{\partial x} \frac{\partial \tilde{y}}{\partial x},$$

$$C \equiv C(x, y) \equiv \frac{1}{J^3} \left\{ \frac{\partial \tilde{x}}{\partial x} \frac{\partial^2 \tilde{x}}{\partial x^2} \left[\left(\frac{\partial \tilde{x}}{\partial x}\right)^2 - 3 \left(\frac{\partial \tilde{y}}{\partial x}\right)^2 \right] - \frac{\partial \tilde{y}}{\partial x} \frac{\partial^2 \tilde{y}}{\partial x^2} \left[\left(\frac{\partial \tilde{y}}{\partial x}\right)^2 - 3 \left(\frac{\partial \tilde{x}}{\partial x}\right)^2 \right] \right\},$$

and

$$D \equiv D(x, y) \equiv \frac{1}{J^3} \left\{ \frac{\partial \tilde{y}}{\partial x} \frac{\partial^2 \tilde{x}}{\partial x^2} \left[\left(\frac{\partial \tilde{x}}{\partial x}\right)^2 - 3 \left(\frac{\partial \tilde{x}}{\partial x}\right)^2 \right] - \frac{\partial \tilde{y}}{\partial x} \frac{\partial^2 \tilde{y}}{\partial x^2} \left[\left(\frac{\partial \tilde{x}}{\partial x}\right)^2 - 3 \left(\frac{\partial \tilde{y}}{\partial x}\right)^2 \right] \right\}.$$

$$(3.2.14)$$

Along the ripple surface, dy=0 and therefore

$$d\tilde{x} = \frac{\partial \tilde{x}}{\partial x} dx \quad \text{and} \quad d\tilde{y} = \frac{\partial \tilde{y}}{\partial x} dx.$$

Boundary conditions (3.1.15) reduce (3.2.13) to

$$\left(\frac{\partial^2}{\partial \tilde{y}^2} - \frac{\partial^2}{\partial \tilde{x}^2} \right) \psi = A(x, 0) \frac{\partial^2 \psi}{\partial y^2}$$

and

$$\frac{\partial^2 \psi}{\partial \tilde{x} \partial \tilde{y}} = -B(x, 0) \frac{\partial^2 \psi}{\partial y^2}.$$

$$(3.2.15)$$

Upon substitution of (3.2.15) and Cauchy-Riemann relations, (3.2.12) becomes

$$\frac{\partial \tilde{x}}{\partial x} = \frac{\partial \tilde{y}}{\partial y} \quad \text{and} \quad \frac{\partial \tilde{x}}{\partial y} = -\frac{\partial \tilde{y}}{\partial x},$$

$$dF_x = \left\{ \frac{s}{R} A(x,0) \frac{\partial^2 \psi}{\partial y^2} \frac{\partial \tilde{x}}{\partial x} + \left[p_r + 2 \frac{s}{R} B(x,0) \frac{\partial^2 \psi}{\partial y^2} \right] \frac{\partial \tilde{y}}{\partial x} \right\} dx$$

$$= \left\{ p_r \frac{\partial \tilde{y}}{\partial x} + \frac{s}{R} \left[A(x,0) \frac{\partial \tilde{x}}{\partial x} + 2 B(x,0) \frac{\partial \tilde{y}}{\partial x} \right] \frac{\partial^2 \psi}{\partial y^2} \right\} dx$$

$$= \left\{ p_r \frac{\partial \tilde{y}}{\partial x} - \tau \left[A(x,0) \frac{\partial \tilde{x}}{\partial x} + 2 B(x,0) \frac{\partial \tilde{y}}{\partial x} \right] \right\} dx$$

and

$$dF_y = \{ -\frac{s}{R} A(x,0) \frac{\partial^2 \psi}{\partial y^2} \frac{\partial \tilde{y}}{\partial x} - [p_r - 2\frac{s}{R} B(x,0) \frac{\partial^2 \psi}{\partial y^2}] \frac{\partial \tilde{x}}{\partial x} \} \, dx$$

$$= \{ -p_r \frac{\partial \tilde{x}}{\partial x} - \frac{s}{R} [A(x,0) \frac{\partial \tilde{y}}{\partial x} - 2 B(x,0) \frac{\partial \tilde{x}}{\partial x}] \frac{\partial^2 \psi}{\partial y^2} \} \, dx$$

$$= \{ -p_r \frac{\partial \tilde{x}}{\partial x} + \tau [A(x,0) \frac{\partial \tilde{y}}{\partial x} - 2 B(x,0) \frac{\partial \tilde{x}}{\partial x}] \} \, dx \qquad (3.2.16)$$

where τ is the shear stress on the ripple surface and will defined in (3.2.17).

The total drag or lift force acting on a ripple length of the bottom boundary can therefore be computed by integrating (3.2.16) between $x=x_0$ and $x=x_0+1$. However, the integral for the horizontal force varies with the choice of x_0. Physically, this is due to the pressure gradient associated with the acceleration of the ambient velocity, which is the term linearly proportional to x, $-\frac{x}{K}\frac{dU_\infty}{dt}$, in the expression for p_r in (3.2.7). The horizontal component of this force on surfaces with the same slope therefore varies with the location along x. Therefore, when multiplied by $\partial \tilde{y}/\partial x$ in (3.2.16) and integrated over a ripple length, the integral involving this term depends on the particular choice of ripple profile defined by the value of x_0. Such non-uniqueness leads to uncertainties in comparisons of computed forces with laboratory measurements, since most reports do not specify the exact ripple profile used in the experiments. This problem is discussed in detail in Appendix IV.

§III.2.3. Shear stress on ripple surface

Local shear stress on the ripple surface can be computed from the difference between the total hydrodynamic stress (3.2.16) and pressure force (3.2.7) acting on the ripple,

$$\tau \frac{ds_p}{L} = \{ [dF_x - p_r \frac{\partial \tilde{y}}{\partial x} dx]^2 + [dF_y + p_r \frac{\partial \tilde{x}}{\partial x} dx]^2 \}^{\frac{1}{2}}$$

$$= dx \frac{s}{R} \frac{\partial^2 \psi}{\partial y^2} \{ [A(x,0) \frac{\partial \tilde{x}}{\partial x} + 2 B(x,0) \frac{\partial \tilde{y}}{\partial x}]^2 + [A(x,0) \frac{\partial \tilde{y}}{\partial x} - 2 B(x,0) \frac{\partial \tilde{x}}{\partial x}]^2 \}^{\frac{1}{2}}$$

$$= dx \frac{s}{R} \frac{\partial^2 \psi}{\partial y^2} \{ A^2(x,0) [(\frac{\partial \tilde{x}}{\partial x})^2 + (\frac{\partial \tilde{y}}{\partial x})^2] + 4B^2(x,0) [(\frac{\partial \tilde{x}}{\partial x})^2 + (\frac{\partial \tilde{y}}{\partial x})^2] \}^{\frac{1}{2}}$$

$$= dx \frac{s}{R} \frac{\partial^2 \psi}{\partial y^2} \frac{1}{J^2} \{ [(\frac{\partial \tilde{x}}{\partial x})^2 - (\frac{\partial \tilde{y}}{\partial x})^2]^2 [(\frac{\partial \tilde{x}}{\partial x})^2 + (\frac{\partial \tilde{y}}{\partial x})^2] + 4 (\frac{\partial \tilde{x}}{\partial x} \frac{\partial \tilde{y}}{\partial x})^2 [(\frac{\partial \tilde{x}}{\partial x})^2 + (\frac{\partial \tilde{y}}{\partial x})^2] \}^{\frac{1}{2}}$$

$$= dx \frac{s}{R} \frac{\partial^2 \psi}{\partial y^2} \frac{1}{J} J^{\frac{1}{2}} = - dx J^{\frac{1}{2}} \frac{s}{R} \omega = \frac{ds_p}{L} (-\frac{s}{R} \omega)$$

or,

$$\tau = - \frac{s}{R} \omega \qquad (3.2.17)$$

where the shear stress τ is nondimensionalized by ρU_0^2, and (3.2.14) and (3.1.9) are used for $A(x, 0)$, $B(x, 0)$, and J. The final equality is obtained from (3.1.11), (3.1.15), and the identity $ds_p/L = dx \sqrt{J}$.

As a check, note that the slope of this stress is given by

$$[df_y + p \frac{\partial \tilde{x}}{\partial x} dx] / [df_x - p \frac{\partial \tilde{y}}{\partial x} dx]$$

$$= - [A(x, 0) \frac{\partial \tilde{y}}{\partial x} - 2B(x, 0) \frac{\partial \tilde{x}}{\partial x}] / [A(x, 0) \frac{\partial \tilde{x}}{\partial x} + 2B(x, 0) \frac{\partial \tilde{y}}{\partial x}]$$

$$= \frac{\partial \tilde{y}}{\partial x} / \frac{\partial \tilde{x}}{\partial x} = \frac{d\tilde{y}}{d\tilde{x}} \qquad (3.2.18)$$

since dy=0 along the ripple surface. This stress is therefore tangential to the ripple surface, as expected.

§III.3. Rate of energy dissipation and energy balance

We shall consider the fluid above two successive ripple crests as defined by the control volume ABCD in Fig. III.1.1. This corresponds to a fixed control

volume defined by $0<x<1$, $0<y<y_{max}$ in the mapped plane.

Energy balance for an incompressible Newtonian fluid in two dimensions can be expressed in vector notation as ((15.2), (16.2), and (16.3), Landau and Lifshitz, 1959)

$$\frac{\partial}{\partial t_p} \int ds_p \frac{1}{2} \rho |\vec{v}_p|^2 = -\oint dl_p \hat{n} \cdot [\frac{1}{2} \rho \vec{v}_p |\vec{v}_p|^2 - \vec{v}_p \cdot \bar{\bar{\tau}}_p]$$

$$- \rho \nu \int ds_p \left\{ (\frac{\partial u_p}{\partial y_p} + \frac{\partial v_p}{\partial x_p})^2 + 2[(\frac{\partial u_p}{\partial x_p})^2 + (\frac{\partial v_p}{\partial y_p})^2] \right\}, \qquad (3.3.1)$$

where

$\vec{v}_p \equiv$ velocity vector of fluid element,

$\hat{n} \equiv$ unit outward normal of control volume,

$\bar{\bar{\tau}}_p \equiv$ two dimensional stress tensor with components defined in (3.2.9), and

ds_p and dl_p are surface and line elements.

For the control volume defined in Fig. III.1.1, (3.3.1) becomes

$$\frac{\partial}{\partial t_p} \int dx_p \int dy_p \frac{\rho}{2} (u_p^2 + v_p^2) + \rho \nu \int dx_p \int dy_p \left\{ (\frac{\partial u_p}{\partial y_p} + \frac{\partial v_p}{\partial x_p})^2 + 2[(\frac{\partial u_p}{\partial x_p})^2 + (\frac{\partial v_p}{\partial y_p})^2] \right\}$$

$$= -(\int_{BC} + \int_{DA}) dl_p \hat{n} \cdot [\frac{1}{2} \rho \vec{v}_p |\vec{v}_p|^2 - \vec{v}_p \cdot \bar{\bar{\tau}}_p]$$

$$-(\int_{AB} + \int_{CD}) dl_p \hat{n} \cdot [\frac{1}{2} \rho \vec{v}_p |\vec{v}_p|^2 - \vec{v}_p \cdot \bar{\bar{\tau}}_p] . \qquad (3.3.2)$$

§III.3.1. Energy flux from pressure work done on the boundaries

On the right hand side of (3.3.2), the line integral $\int_{BC}$ vanishes since $\vec{v}_p \equiv 0$ along the bottom boundary. The integral $\int_{DA}$ is also zero since, from boundary condition (3.1.13b), $\hat{n} \cdot \vec{v}_p \equiv 0$, $\vec{v}_p \cdot \bar{\bar{\tau}}_p = p_p \hat{n} \cdot \vec{v}_p \equiv 0$ along DA. The integral $\int_{AB} + \int_{CD}$ can be reduced using periodicity conditions (3.1.13c) and (3.1.13d) to

$$\int_a^{y_{Pmax}} dy_p \left(u_p P_p \Big|_{@\, x_p=0} - u_p P_p \Big|_{@\, x_p=L} \right),$$

and is the rate of pressure work done on the fluid in the control volume. From (3.2.6) and periodicity conditions (3.1.13c) and (3.1.13d), we have

$$u_p P_p \Big|_{@\, x_p=0} - u_p P_p \Big|_{@\, x_p=L} = \rho U_0^3 \, \tilde{u} \, \frac{1}{K} \frac{dU_\infty}{dt}.$$

For a ripple profile defined in parametric form by (3.4.2), along with the conformal mapping defined by (3.4.1), the increment dx equals zero along both AB and CD. Equations (3.4.1) and (3.4.3) give

$$d\tilde{y} = \frac{\partial \tilde{y}}{\partial y} dy, \quad \frac{\partial \tilde{y}}{\partial x} = 0, \quad \text{and} \quad \left(\frac{\partial \tilde{x}}{\partial x}\right)^2 = J$$

at x=0 and x=1. The rate of energy flux through pressure work done on the boundaries can therefore be normalized to give,

$$-\oint dl_p \, \hat{n} \cdot \left[\frac{1}{2} \rho \vec{v}_p |\vec{v}_p|^2 - \vec{v}_p \cdot \tau_p \right] = \rho L U_0^3 \, \frac{1}{K} \int_{\frac{1}{2}s}^{\infty} d\tilde{y} \left(\tilde{u} \frac{dU_\infty}{dt} \right) \Big|_{@\, x=0}$$

$$= \rho L U_0^3 \, \frac{1}{K} \int_0^{\infty} dy \, \frac{\partial \tilde{y}}{\partial y} \left(\frac{1}{J} \frac{\partial \tilde{x}}{\partial x} \frac{\partial \psi}{\partial y} \frac{dU_\infty}{dt} \right) \Big|_{@\, x=0} = \rho L U_0^3 \, \frac{1}{K} \int_0^{\infty} dy \left(\frac{\partial \psi}{\partial y} \frac{dU_\infty}{dt} \right) \Big|_{@\, x=0}$$

$$= \rho L U_0^3 \, \frac{1}{K} \, \psi_\infty \frac{dU_\infty}{dt}. \tag{3.3.3}$$

The last equality is deduced from boundary conditions (3.1.15).

§III.3.2. Rate of energy dissipation

The second integral on the left hand side of (3.3.2) is the rate of energy dissipation and can be written in terms of the streamfunction as

$$\mathscr{D}_p = \rho \int dy_p \int dx_p \, \nu \left[\left(\frac{\partial^2 \psi_p}{\partial x_p^2} + \frac{\partial^2 \psi_p}{\partial y_p^2} \right)^2 + 4 \left(\frac{\partial u_p}{\partial y_p} \frac{\partial v_p}{\partial x_p} - \frac{\partial u_p}{\partial x_p} \frac{\partial v_p}{\partial y_p} \right) \right] \tag{3.3.4}$$

by using the continuity equation. In terms of nondimensionalized variables and transformed coordinates, this can be written as

$$\mathscr{D}_p = \rho\nu U_0^2 \int_0^\infty dy \int_0^1 dx\, J\left\{\left[\frac{1}{J}\left(\frac{\partial^2\psi}{\partial x^2} + \frac{\partial^2\psi}{\partial y^2}\right)\right]^2 + \frac{4}{J}\left(\frac{\partial\tilde{u}}{\partial y}\frac{\partial\tilde{v}}{\partial x} - \frac{\partial\tilde{u}}{\partial x}\frac{\partial\tilde{v}}{\partial y}\right)\right\} \quad (3.3.5)$$

by applying (A1.3.1) and (A1.4.1). Upon substitution of (3.1.11) into the first term in (3.3.5), we get

$$\mathscr{D}_p = \rho\nu U_0^2 \left\{\int_0^\infty dy \int_0^1 dx\, J\omega^2 + 4\int_0^\infty dy \int_0^1 dx\left(\frac{\partial\tilde{u}}{\partial y}\frac{\partial\tilde{v}}{\partial x} - \frac{\partial\tilde{u}}{\partial x}\frac{\partial\tilde{v}}{\partial y}\right)\right\} \quad .(3.3.6)$$

By using boundary conditions (3.1.13a) and (3.1.13b) and periodicity conditions (3.1.13c) and (3.1.13d), the second term can be integrated by parts to give

$$4\rho\nu U_0^2\left\{\int_0^1 dx\left[\tilde{u}\frac{\partial\tilde{v}}{\partial x}\Big|_{@\,y=0}^{@\,y=\infty} - \int_0^\infty dy\,\tilde{u}\frac{\partial^2\tilde{v}}{\partial x\partial y}\right] - \int_0^\infty dy\left[\tilde{u}\frac{\partial\tilde{v}}{\partial y}\Big|_{@\,x=0}^{@\,x=1}\right.\right.$$

$$\left.\left. - \int_0^1 dx\,\tilde{u}\frac{\partial^2\tilde{v}}{\partial x\partial y}\right]\right\} = 0. \quad (3.3.7)$$

Finally, we define the nondimensional rate of energy dissipation as

$$\mathscr{D} = \frac{1}{\rho L U_0^3}\mathscr{D}_p \quad (3.3.8)$$

such that

$$\mathscr{D} = \frac{s}{R}\int_0^\infty dy \int_0^1 dx\, J\omega^2 . \quad (3.3.9)$$

§III.3.3. Rate of change in kinetic energy

The first term on the left hand side of (3.3.2) represents the time rate of change in kinetic energy. The integral under the partial time derivative can be expressed in transformed coordinates by using (3.1.12),

$$\frac{\rho}{2}\int dy_p \int dx_p\,(u_p^2 + v_p^2)$$

$$= \frac{\rho}{2}U_0^2 L^2 \int_0^\infty dy \int_0^1 dx\, J\left\{\left[\frac{1}{J}\left(\frac{\partial\tilde{x}}{\partial x}\frac{\partial\psi}{\partial y} + \frac{\partial\tilde{y}}{\partial x}\frac{\partial\psi}{\partial x}\right)\right]^2 + \left[\frac{1}{J}\left(\frac{\partial\tilde{x}}{\partial x}\frac{\partial\psi}{\partial x} - \frac{\partial\tilde{y}}{\partial x}\frac{\partial\psi}{\partial y}\right)\right]^2\right\}$$

$$= \frac{\rho}{2}U_0^2 L^2 \int_0^\infty dy \int_0^1 dx\left[\left(\frac{\partial\psi}{\partial x}\right)^2 + \left(\frac{\partial\psi}{\partial y}\right)^2\right] .$$

If we integrate this last expression by parts and apply governing equation (3.1.11), boundary conditions (3.1.15) and (3.1.16), and periodicity, we obtain

$$\frac{\rho}{2} U_0^2 L^2 \left\{ -\int_0^\infty dy \int_0^1 dx\ \psi \left(\frac{\partial^2 \psi}{\partial x^2} + \frac{\partial^2 \psi}{\partial y^2} \right) + \int_0^1 dx\ \left(\psi \frac{\partial \psi}{\partial y}\right) \Big|_{@\ y=0}^{@\ y=\infty} \right. $$
$$\left. + \int_0^\infty dy\ \left(\psi \frac{\partial \psi}{\partial x}\right) \Big|_{@\ x=0}^{@\ x=1} \right\} = \frac{\rho}{2} U_0^2 L^2 \left[\psi_\infty U_\infty + \int_0^\infty dy \int_0^1 dx\ J\psi\omega \right] .$$

The rate of change in kinetic energy is therefore given by

$$\frac{\rho}{2} U_0^2 L^2 \frac{1}{T} \frac{\partial}{\partial t} \left[\psi_\infty U_\infty + \int_0^\infty dy \int_0^1 dx\ J\psi\omega \right] . \tag{3.3.10}$$

Combining (3.3.2), (3.3.3), (3.3.9), and (3.3.10), we finally obtain the dimensionless equation for energy balance over one ripple length,

$$\frac{1}{K} \psi_\infty \frac{dU_\infty}{dt} - \frac{1}{2K} \frac{\partial}{\partial t} \left[\psi_\infty U_\infty + \int_0^\infty dy \int_0^1 dx\ J\psi\omega \right] - \frac{S}{R} \int_0^\infty dy \int_0^1 dx\ J\omega^2$$
$$= 0 . \tag{3.3.11}$$

This provides a check on the conservative property of the numerical scheme.

§III.4. Conformal Mapping

The transformation (Benjamin, 1959)

$$\begin{Bmatrix} x_p \\ y_p \end{Bmatrix} = L \begin{Bmatrix} \tilde{x} \\ \tilde{y} \end{Bmatrix} = L \begin{Bmatrix} x - \frac{1}{2}se^{-2\pi y}\sin 2\pi x \\ y - \frac{1}{2}se^{-2\pi y}\cos 2\pi x \end{Bmatrix} \tag{3.4.1}$$

maps the ripple profile

$$(x_p, y_p) = (Lx - a \sin 2\pi x, a \cos 2\pi x) \tag{3.4.2}$$

onto (x, 0) in the transformed plane. The Jacobian is given by

$$J = \frac{1}{L^2} \begin{vmatrix} \dfrac{\partial x_p}{\partial x} & \dfrac{\partial x_p}{\partial y} \\[2ex] \dfrac{\partial y_p}{\partial x} & \dfrac{\partial y_p}{\partial y} \end{vmatrix} = (1 - \pi s\, e^{-2\pi y}\cos 2\pi x)^2 + (\pi s\, e^{-2\pi y}\sin 2\pi x)^2$$

$$= 1 + \pi^2 s^2 e^{-4\pi y} - 2\pi s\, e^{-2\pi y}\cos 2\pi x \,. \qquad (3.4.3)$$

For later use in the evaluation of the stresses on the ripple surface, (3.2.7) and (3.2.16), we note that,

$$\frac{\partial \tilde{x}}{\partial x} = \frac{\partial \tilde{y}}{\partial y} = 1 - \pi s \cos 2\pi x \,, \qquad \frac{\partial \tilde{x}}{\partial y} = -\frac{\partial \tilde{y}}{\partial x} = \pi s \sin 2\pi x \,,$$

and

$$J = 1 + \pi^2 s^2 - 2\pi s \cos 2\pi x \qquad (3.4.4)$$

at y=0. Substitution into equation (3.2.14) gives

$$A(x, 0) = \frac{1}{(1 + \pi^2 s^2 - 2\pi s \cos 2\pi x)^2}(1 + \pi^2 s^2 \cos 4\pi x - 2\pi s \cos 2\pi x)$$

and

$$B(x, 0) = \frac{\pi s}{(1 + \pi^2 s^2 - 2\pi s \cos 2\pi x)^2}\left(\frac{1}{2}\pi s \sin 4\pi x - \sin 2\pi x\right) . \qquad (3.4.5)$$

Note that the value of s has to be less than $\pi^{-1}\approx 0.318$, at which $\partial y_p / \partial x_p$ is singular at x = 0, L, 2L, ... Some ripple profiles (3.4.2) corresponding to the values of s used in previous experiments or numerical computations are plotted in Fig. III.4.1. The mapping (3.4.1) with s=0.1 will be used exclusively in our study.

This mapping can be extended to periodic ripples with arbitrary profiles (Sato *et al*, 1984). Consider Fast Fourier Transform pair

$$-i(\tilde{z}_k - z_k) = \sum_{m=1}^{M} (a_m + ib_m) \exp(i2m\pi z_k) \qquad (3.4.6)$$

and

$$a_m + ib_m = -\frac{i}{M} \sum_{k=1}^{M} (\tilde{z}_k - z_k) \exp(-i2m\pi z_k) \,. \qquad (3.4.7)$$

s = 0.318

s = 0.200

s = 0.170

s = 0.145

s = 0.100

s = 0.050
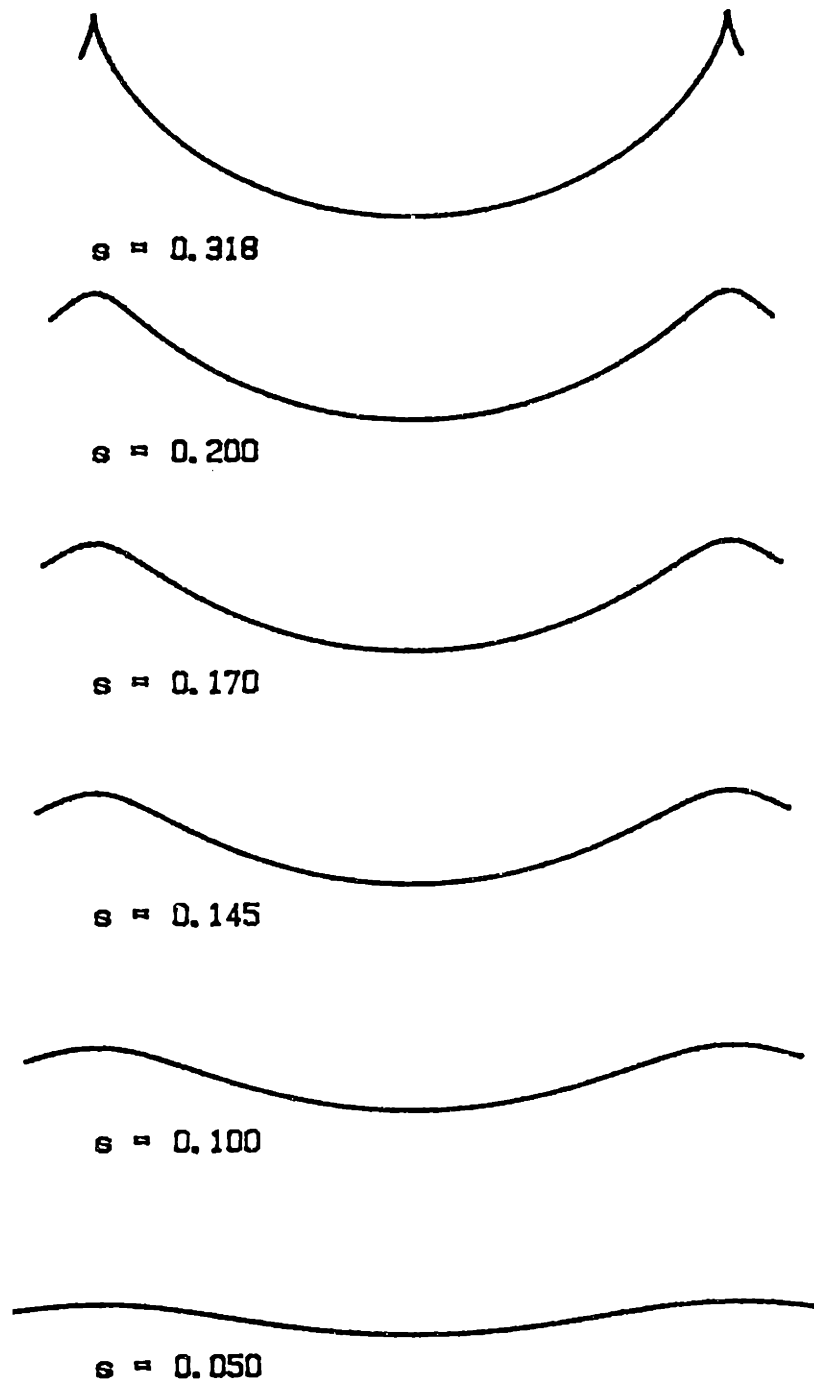
Fig. III. 4. 1.　Ripple profiles defined by conformal mapping (3. 4. 2)

Let

$$z_k = x_k + iy_k \, , \tag{3.4.8}$$

$$\tilde{z}_k = \tilde{x}_k + i\tilde{y}_k \, , \tag{3.4.9}$$

and require that the points in the mapped plane

$$z_{r_k} = (k-1)\,\Delta x \, , \quad k = 1, \, ..., \, M \tag{3.4.10}$$

correspond to points on the given ripple profile

$$\tilde{z}_{r_k} = (k-1)\Delta x + i\tilde{y}_{r_k} \, , \quad k = 1, \, ..., \, M \, . \tag{3.4.11}$$

For a domain of computation spanning r ripple lengths, we have

$$\Delta x = \frac{r}{M} \, . \tag{3.4.12}$$

Substitution into (3.4.7) gives

$$a_m + ib_m = \frac{1}{M} \sum_{k=1}^{M} \tilde{y}_{r_k} \exp[-i2m\pi(k-1)\Delta x] \, , \quad m = 1, \, ..., \, M \, . \tag{3.4.13}$$

The choice of $r=1$, $a_1=s/2=a/L$, $b_1=0$, and $a_m=b_m=0$ for all $m\neq1$ yields the mapping (3.4.1).

It has been shown in §III.1 that the streamfunction/vorticity formulation of two-dimensional laminar flows takes the form of two coupled second-order, homogeneous, nonlinear partial differential equations in three variables, (3.1.10) and (3.1.11). The forcing in this initial/boundary-value problem comes solely from the far field boundary condition (3.1.16), which implies an ambient pressure gradient given by (3.2.5.c). We shall now describe the numerical scheme for solving the system of equations inside the rectangular domain $(0<x<1, 0<y<y_{max})$ that results from truncating the flow field at a certain height above the ripple bed.

§IV.1. Numerical scheme

The periodicity in x_p, and thus x, suggests spectral decomposition in the horizontal direction, which has the advantage of convergence to an infinite order for an infinitely differentiable periodic function. Specifically, a pseudo-spectral (collocation) method in terms of a Fourier series is used, that is, x derivatives at the grid points are computed in the Fourier space while the nonlinear terms in (3.1.10) are evaluated in the physical space. Derivatives in the y direction are computed using second-order center-differencing given by (A2.2.1) and (A2.2.2).

Let the grid points in the rectangular computational domain be denoted by

$$x_k = (k\text{-}1)\,\Delta x, \quad k = 1, ..., M; \quad \Delta x = \frac{1}{M} \tag{4.1.1}$$

and

$$y_1 = 0 \, , \, y_2 \, , \, y_3, \, ..., \, y_N = y_{max} \tag{4.1.2}$$

with grid-spacings

$$\Delta_j = y_{j+1} - y_j \, . \tag{4.1.3}$$

A typical grid with M=32 and N=57 is shown in Fig. IV.1.1.
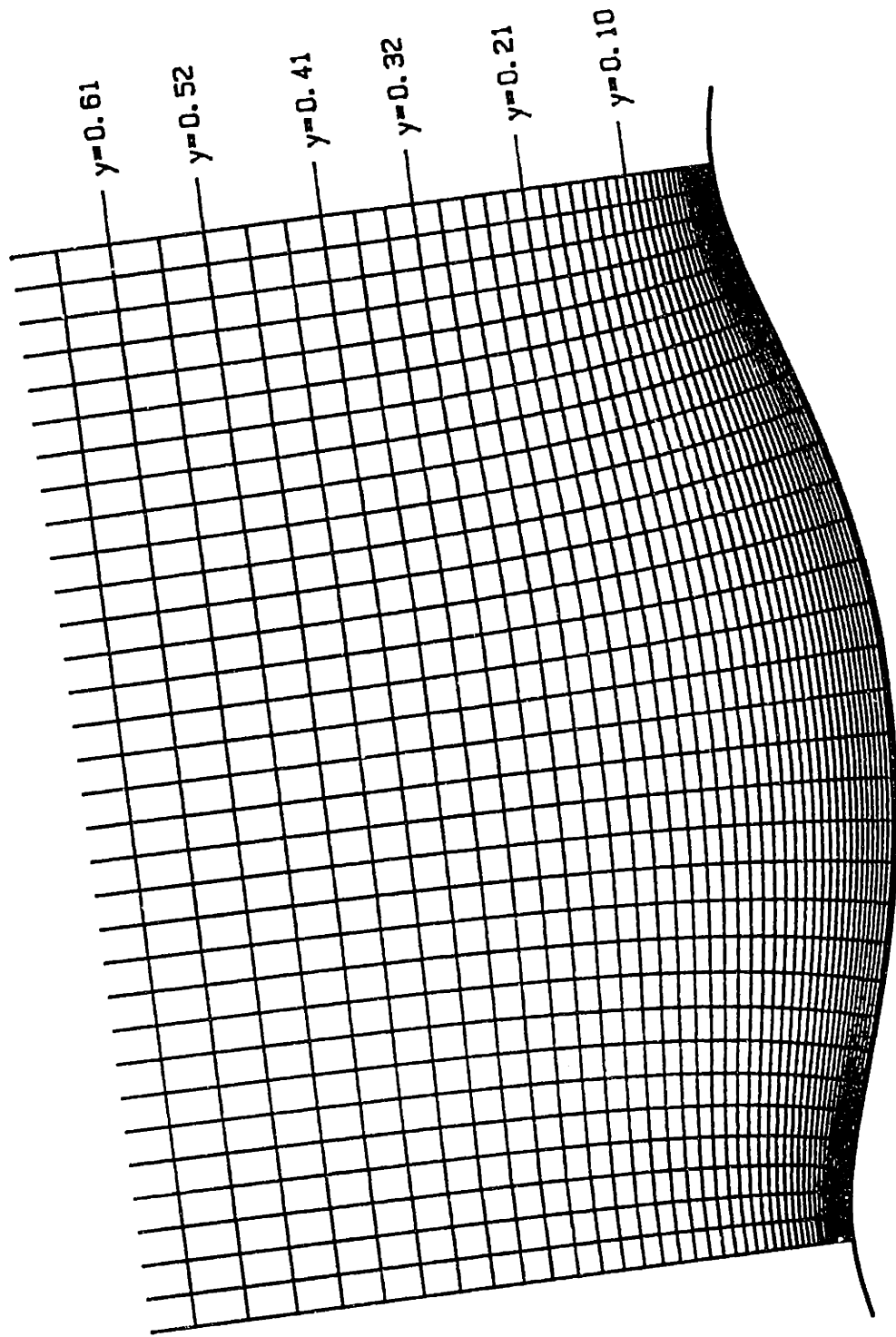
Fig. IV.1.1. Computational grid.
M=32   N=57   s=0.1

y=0.61

y=0.52

y=0.41

y=0.32

y=0.21

y=0.10

47

Let the unknown functions ψ and ω be defined as

$$\psi(x_k, y_j, t_n) \equiv \psi_{kj}^n = \sum_{m=0}^{M-1} \Psi_{mj}^n \exp(im2\pi x_k) \tag{4.1.4}$$

and

$$\omega(x_k, y_j, t_n) \equiv \omega_{kj}^n = \sum_{m=0}^{M-1} \Omega_{mj}^n \exp(im2\pi x_k) . \tag{4.1.5}$$

The r-th derivative of the streamfunction with respect to x is defined as

$$\frac{\partial^r \psi}{\partial x^r}(x_k, y_j, t_n) = \sum_{m=0}^{M-1} {}^r\Psi_{mj}^n \exp(im2\pi x_k)$$

in which

$${}^r\Psi_{mj}^n = \begin{cases} (im2\pi)^r \Psi_{mj}^n \\ ({}^r\Psi_{nx-m,j}^n)^* \end{cases} \quad \text{for} \quad m \begin{array}{c} \leq \\ > \end{array} \tfrac{1}{2}M$$

and

$${}^r\Psi_{\frac{1}{2}M,j}^n = \begin{cases} (iM\pi)^r \Psi_{\frac{1}{2}M,j}^n \\ 0 \end{cases} \quad \text{for} \quad r \begin{cases} \text{even} \\ \text{odd} \end{cases} , \tag{4.1.6}$$

and superscript * denotes complex conjugation. Derivatives in x for ω are similarly defined.

At each time-step, the vorticity equation (3.1.10) is solved in mapped coordinates. A 'split-step' treatment is used in which the nonlinear convective term is accounted for using a third-order Adams-Bashforth scheme and the viscous term using an Euler forward scheme. The expression takes the form

$$(\overline{J\omega})_{kj}^{n+1} = (J\omega)_{kj}^n - \Delta t \left[\frac{23}{12} \varphi_{kj}^n - \frac{4}{3} \varphi_{kj}^{n-1} + \frac{5}{12} \varphi_{kj}^{n-2} \right] , \tag{4.1.7}$$

$$(J\omega)_{kj}^{n+1} = (\overline{J\omega})_{kj}^{n+1} + \Delta t \, \vartheta_{kj}^n ; \tag{4.1.8}$$

$k = 1, ..., M$, $j = 2, ..., N-1$; and

$$\varphi_{kj}^n = K \left(\frac{\partial \psi}{\partial y} \frac{\partial \omega}{\partial x} - \frac{\partial \psi}{\partial x} \frac{\partial \omega}{\partial y} \right)_{kj}^n \quad \text{and} \quad \vartheta_{kj}^n = s \frac{K}{R} \left(\frac{\partial^2 \omega}{\partial x^2} + \frac{\partial^2 \omega}{\partial y^2} \right)_{kj}^n \qquad (4.1.9)$$

are respectively the convective and viscous terms.[1] Since this is an explicit time-ste in which only values at interior grid-points are updated, no boundary conditions are necessary.

Equation (3.1.11) is solved for the streamfunction in the Fourier space by compact differencing. The Poisson equation is discretized as

$$[12 - (2\pi m)^2 (\Delta_j^2 + \Delta_j \Delta_{j-1} - \Delta_{j-1}^2)] \, \Delta_{j-1} \, \Psi_{m,j+1}^{n+1}$$

$$- [12 + (2\pi m)^2 (\Delta_j^2 + 3 \Delta_j \Delta_{j-1} + \Delta_{j-1}^2)] \, (\Delta_j + \Delta_{j-1}) \, \Psi_{m,j}^{n+1}$$

$$+ [12 + (2\pi m)^2 (\Delta_j^2 - \Delta_j \Delta_{j-1} - \Delta_{j-1}^2)] \, \Delta_j \, \Psi_{m,j-1}^{n+1}$$

$$= - (\Delta_j^2 + \Delta_j \Delta_{j-1} - \Delta_{j-1}^2)] \, \Delta_{j-1} \, (J\Omega)_{m,j+1}^{n+1}$$

$$- (\Delta_j^2 + 3 \Delta_j \Delta_{j-1} + \Delta_{j-1}^2) \, (\Delta_j + \Delta_{j-1}) \, (J\Omega)_{m,j}^{n+1}$$

$$+ (\Delta_j^2 - \Delta_j \Delta_{j-1} - \Delta_{j-1}^2)] \, \Delta_j \, (J\Omega)_{m,j-1}^{n+1} ; \qquad (4.1.10)$$

where $m = 0, ..., \frac{1}{2}M$; $j = 2, ..., N-1$; and $(J\Omega)_{mj}^n$ is the m-th Fourier coefficient in the transform of $J\omega$ at $t=t_n$ and $y=y_j$. A derivation of (4.1.10) is given in §AII.3. The tridiagonal matrix from the Poisson solver is inverted by LU–decomposition. Updated values of ω evaluated in (4.1.8) are substituted into (4.1.10) and the streamfunction solved by forward and back substitution in compact form (Ralston and Rabinowitz, 1978). Note, however, that since the values for $J\omega$ at the boundaries $y=0$ and $y=y_{max}$ have not been updated in (4.1.7) and (4.1.8), the old values $(J\Omega)_{m,1}^{n+1}$ and $(J\Omega)_{m,N}^{n+1}$ are used in (4.1.10) for j=2 and N-1, respectively, such that the algorithm remains explicit.

---

[1]The third–order Adams-Bashforth scheme for the convective terms is replaced by Euler forward and second-order Adams-Bashforth schemes at the beginning of computation and immediately after a change in the time-step.

The decoupling in x (by Fourier Transform) and y and the use of Fast Fourier Transform allow the amount of computation required to be competitive with explicit iterative schemes using finite differencing.

One–sided derivatives of second order are used in evaluating boundary values, namely,

$$\psi_{k,1}^{n+1} = \Psi_{m,1}^{n+1} = 0 , \qquad (4.1.11)$$

$$\omega_{k,1}^{n+1} = \frac{2}{\Delta_2 J_{k,1}} \left[\frac{\Delta_1}{(\Delta_1+\Delta_2)^2} \psi_{k,3}^{n+1} - \frac{\Delta_1+\Delta_2}{\Delta_1^2} \psi_{k,2}^{n+1} \right] , \qquad (4.1.12)$$

$$\psi_{k,N}^{n+1} = \frac{1}{2\Delta_{N-1}+\Delta_{N-2}} \{ (\Delta_{N-1}+\Delta_{N-2}) \Delta_{N-1} U_\infty^{n+1}$$

$$+ \frac{1}{\Delta_{N-2}} [(\Delta_{N-1}+\Delta_{N-2})^2 \psi_{k,N-1}^{n+1} - \Delta_{N-1}^2 \psi_{k,N-2}^{n+1}] \} , \qquad (4.1.13)$$

$$\Psi_{m,N}^{n+1} = \frac{1}{2\Delta_{N-1}+\Delta_{N-2}} \{ (\Delta_{N-1}+\Delta_{N-2}) \Delta_{N-1} U_\infty^{n+1} \delta_{0m}$$

$$+ \frac{1}{\Delta_{N-2}} [(\Delta_{N-1}+\Delta_{N-2})^2 \Psi_{m,N-1}^{n+1} - \Delta_{N-1}^2 \Psi_{m,N-2}^{n+1}] \} , \qquad (4.1.14)$$

and

$$\omega_{k,N}^n = -\frac{1}{J_{k,N}} \left\{ \frac{\partial^2 \psi_{k,N}}{\partial x^2} + \frac{2}{\Delta_{N-2}\Delta_{N-1}^2(\Delta_{N-2}+\Delta_{N-1})^2} [-\Delta_{N-1}^3 \psi_{k,N-2}^n \right.$$

$$+ (\Delta_{N-2}+\Delta_{N-1})^3 \psi_{k,N-1}^n - \Delta_{N-2}(\Delta_{N-2}^2+3\Delta_{N-2}\Delta_{N-1}+3\Delta_{N-1}^2)\psi_{k,N}^n$$

$$+ \Delta_{N-2}\Delta_{N-1}(\Delta_{N-2}+\Delta_{N-1})(2\Delta_{N-1}+\Delta_{N-2})U_\infty] \left. \right\}, \qquad (4.1.15)$$

$k = 1, ..., M$; $m = 0, ..., M-1$, and can be derived from boundary conditions (3.1.15) and (3.1.16). The details of derivation and their truncation errors are given in §AII.2, where (4.1.12) can be deduced from (A2.2.3), (4.1.13) and (4.1.14) from (A2.2.5), and (4.1.15) from (A2.2.6).

The truncation error is $o(\Delta t^3, s/R \, \Delta t, \Delta y^2)$ in the vorticity equation, $o(\Delta y^4)$

in the compact differencing in the streamfunction equation, and $o(\Delta y^2)$ in the boundary conditions (4.1.12) through (4.1.14). The overall accuracy of the scheme is therefore expected to be $o(s/R\ \Delta t, \Delta y^2)$ for moderate Reynolds numbers. Exact expressions for these errors will be discussed in the next section.

A formal proof of the convergence of the numerical solution to the analytical solution will not be attempted here. For a linear problem, Lax Equivalence Theorem (see for example Richtmyer and Morton, 1967) states that a numerical algorithm that is stable and consistent converges to the exact solution in the limit of vanishing grid sizes and time-steps. In our system of equations, there are no apparent mathematical singularities and it is therefore expected that a stable numerical solution will converge to the exact solution up to the order of truncation errors.

At regular time intervals, computed values of vorticity and streamfunction values are used to evaluate the hydrodynamic forces: the shear stress, pressure, and force components on the ripple, and the rate of energy dissipation in the domain of computation. One-dimensional integrations are evaluated using IMSL subroutines ICSICU and DCSQDU, which is based on a cubic spline quadrature. Since the integrands are known only at regular (3.2.16) or irregular (3.2.7) intervals (at the grid points), a series of cubic polynomials, each defined within adjacent grid-points such that their values and first two derivatives at these points are continuous across the grid-points, are therefore used to intrapolate the integrand. Details of its derivation can be found, for example, in Ralston and Rabinowitz (1978). Since the spline coefficients are underdetermined with four free parameters, we define the splines only to the last interior grid-point in the range and specify the values of the four parameters using values of the integrand at the two boundary points. Two-dimensional integrations in (3.3.13) are computed using IMSL subroutine DBCQDU. Time derivatives in (3.3.13) are estimated using a one-sided third-order

finite–differencing formula.

Further details on the implementation of the numerical scheme are discussed in the following subsections. Detailed derivations of some of the results are given in the Appendices.

§IV.2. Truncation error

For uniform grids, local truncation error per unit time in the vorticity equation is given by

$$\frac{1}{6} K \, \Delta y^2 \left(\frac{\partial \omega}{\partial x} \frac{\partial^3 \psi}{\partial y^3} - \frac{\partial \psi}{\partial x} \frac{\partial^3 \omega}{\partial y^3} \right) - \frac{3}{8} K \, \Delta t^3 \frac{\partial^3}{\partial t^3} \left(\frac{\partial \omega}{\partial x} \frac{\partial \psi}{\partial y} - \frac{\partial \psi}{\partial x} \frac{\partial \omega}{\partial y} \right) -$$

$$s \, \frac{\Delta y^2}{12} \frac{K}{R} \frac{\partial^4 \omega}{\partial y^4} + \frac{s}{2} \frac{K}{R} \Delta t \frac{\partial}{\partial t} \left(\frac{\partial^2 \omega}{\partial x^2} + \frac{\partial^2 \omega}{\partial y^2} \right) + O(\Delta y^4, \Delta t^4, \Delta y^2 \Delta t, \frac{1}{R} \Delta t^2) ,$$

$$(4.2.1)$$

and can be obtained from Taylor series expansions of equations (4.1.7) to (4.1.9), with exact values of the grid–spacings Δ_j's replaced by a mean value Δy in the error terms for simplicity. Details of the derivation are given in §AIII.2. The first two terms in (4.2.1) are errors due to the temporal and spatial (in y) discretization in the convective terms and the next two are those in the viscous terms. Error estimates for discretization in the x–direction are less straightforward and will be discussed in the next section. Even though the Euler forward scheme is first–order in time while the Adams–Bashforth scheme is third order, the leading order error is associated with spatial discretization in the convective terms, and is dissipative in nature. This will be demonstrated using the time–step defined in §IV.5. An immediate consequence is the requirement

$$\Delta y^2 \ll \frac{s}{R} \left(\frac{\partial \psi}{\partial x} \right)^{-1} \equiv \Delta_{max}^2 \qquad (4.2.2)$$

such that numerical viscosity from the treatment of convective terms is smaller

than the actual physical viscosity at all y. This is satisfied using the values of Δy defined in §IV.4.

Local truncation error in the compact differencing scheme (4.1.10) for the Poisson equation is, from (A2.3.8),

$$\frac{\Delta y^4}{180} \frac{\partial^6 \psi}{\partial y^6} . \tag{4.2.3}$$

Truncation errors in boundary conditions are, from (A2.2.4) to (A2.2.6),

$$-\frac{2}{9} \Delta y^3 \frac{\partial^3 \psi}{\partial y^3}\Big|_{@\ y=y_{max}} \tag{4.2.4}$$

for the boundary value of streamfunction given by (4.1.13),

$$-\frac{1}{6} \Delta y^2 \frac{1}{J} \frac{\partial^4 \psi}{\partial y^4}\Big|_{@\ y=0} \tag{4.2.5}$$

for the value of vorticity on the ripple surface given by (4.1.12), and

$$-\frac{1}{6} \Delta y^2 \frac{1}{J} \frac{\partial^4 \psi}{\partial y^4}\Big|_{@\ y=y_{max}} \tag{4.2.6}$$

for the value of vorticity at the upper boundary given by (4.1.15). The exact expressions for these errors are given in §AII.2 and AII.3.

§IV.3. Grid spacing in the x direction

The grid spacing in the x direction is determined from the length scale of variation in the flow field and aliasing considerations. As seen by substituting (4.1.4) and (4.1.5) into (4.1.9) and (4.1.7), the quadratic terms in the vorticity equation give components with wavenumbers up to twice that of the Nyquist frequency $Q \equiv \pi M$, and the components with frequencies in the range $(Q, 2Q)$ are aliased in the primary wavenumber range $(0, Q)$. This error is further magnified since these nonlinear terms involve derivatives in the x direction in which the higher wavenumber components are accentuated according to (4.1.6).

To limit this aliasing error, the amplitudes of the Fourier coefficients at high wavenumbers therefore have to be much smaller than those at low wavenumbers. During the course of computation the magnitudes of the Fourier coefficients are examined at regular time intervals. We have observed that when the resolution is adequate according to convergence tests (i) for fixed n and j, the maximum of $|(im2\pi)^2\Psi_{mj}^n|$ for wavenumbers $2\pi m$ in the range $(\frac{1}{2}Q,Q)$ is less than 30% of that in $(0,\frac{1}{2}Q)$, and the amplitude at the Nyquist frequency $|(iQ)^2\Psi_{\frac{1}{2}M,j}^n|$ is less than 10% of the maximum of $|(im2\pi)^2\Psi_{mj}^n|$ in $0\leq 2\pi m\leq\frac{1}{2}Q$, and (ii) the amplitudes $|\Psi_{mj}^n|$ near the Nyquist frequency do not grow further as computation progresses.

The amplitudes $|(im2\pi)^2\Psi_{mj}^n|$ in (i) are estimates of $|\Omega_{mj}^n|$ (from 3.1.11 and 4.1.6) and the criterion is obtained empirically from convergence tests. Specifically, flows with the same dimensionless parameters are computed twice, one using twice the number of grids in the x direction as the other. For the case R=250, K=4.5 and s=0.1 good agreement in all physical quantities when the number of grid points is increased from 32 to 64. The results using 32 grid points are therefore accurate.

For R=500, K=4.5, and s=0.1, M=32 is insufficient and we only record the results using M=64. Comparisons are made with the number of grid points increased to 128 and computed up to t=2 only because of the large expense. The agreement is satisfactory within 0<t<2. No convergence is established for t>2 however. With 64 grid points, we also observe (i) and (ii) described previously for t≤22, suggesting that convergence may be acceptable for large t. This is speculative, of course. Details of these results will be presented in §VI.2.

Continuous growth in the components $|\Psi_{mj}^n|$ at high wavenumbers over successive periods suggests possible aliasing problems. It is found that a lack of resolution can indeed lead to breakdowns in the computation when the components at high wavenumbers in the Fourier spectrum of streamfunction become of comparable magnitudes with those at low wavenumbers. On the other hand, there

may be significant aliasing (discretization) errors even if the computation progresses without any apparent numerical instabilities. This is found in the case with R=500 and K=4.5 using M=32 and 64 discussed above.

§IV.4. Grid spacing in the y direction

Grid spacing of variable sizes are used in the y direction to increase computational efficiency. In principle, grid points should be chosen to achieve a uniform spatial discretization error estimated from velocity gradients. However, since the velocity field is not known *a priori*, grid sizes are made to increase exponentially away from the viscous boundary layer. Their values are determined as follows.

To ensure adequate resolution for the velocity profile inside the viscous boundary layer immediately above the ripple surface, we require that the dimensionless grid spacing in the y direction near the ripple surface to be much less than the boundary thickness. Since the thickness of this oscillatory viscous boundary layer δ_p is expected to be of the same order as that of oscillatory flow over a plane bed at steady state[2], we have

$$\tilde{\delta} = \frac{\delta_p}{L} \approx \frac{(\nu T/\pi)^{\frac{1}{2}}}{L} = (\frac{s}{\pi}\frac{K}{R})^{\frac{1}{2}} \equiv \sqrt{J_{r_{max}}}\, \delta$$

or

$$\delta \equiv (\frac{1}{J_{r_{max}}}\frac{s}{\pi}\frac{K}{R})^{\frac{1}{2}}. \tag{4.4.1}$$

The value δ is the boundary layer thickness in the mapped plane and the parameter $J_{r_{max}}$ is the maximum value of Jacobian on the ripple surface y=0. By comparing

---

[2]Our computations are started with a quiescent fluid, and the initial boundary layer thickness in the oscillatory flow over a plane bed starting from rest is infinitesimally small. Therefore our numerical solution is less accurate near t=0 but improves as t increases.

results obtained from our numerical scheme with exact solutions in the Stokes second problem, it is found that as few as five grid points equally spaced within this boundary layer are adequate to resolve accurately the velocity profile (§V.1, Figs. V.1.1 and V.1.2). If we denote the number of grid points in this layer by h, the ratio of δ to Δ_{max}, the critical value in the estimate of the maximum allowable Δy defined in (4.2.2), equals

$$\frac{\delta}{\Delta_{max}} = \frac{1}{h} \left(\frac{1}{J_{r_{max}}} \frac{K}{\pi} \frac{\partial \psi}{\partial x} \right)^{\frac{1}{2}} \qquad (4.4.2)$$

inside the boundary layer. This ratio is of an order smaller than unity since $\partial \psi / \partial x$, which is a measure of the velocity normal to the ripple profile, is much smaller thant one there. The grid size is allowed to be greater than δ at a height far enough away from this boundary layer such that $\partial \psi / \partial x$ is small again.

The exact variation of grid spacing

$$y_1 = 0, \ y_2, \ y_3, \ \dots, \ y_N = y_{max}$$

is determined from two parameters: y_{max}, the vertical extent of computation (the criteria for its magnitude will be discussed in §IV.6); and H, the ratio of the maximum grid size to the grid spacing inside the viscous boundary layer. We divide the vertical domain $0 < y < y_{max}$ into two regions. Inside the boundary layer, we define h identical spacings

$$y_1 = 0, \ y_2 = \frac{\delta}{h}, \ y_3 = \frac{2}{h} \delta, \ y_4 = \frac{3}{h} \delta, \ \dots, \ y_{h+1} = \delta.$$

Outside the boundary layer, the grid points are defined by

$$y_j = \delta + \frac{1}{b} \{ e^{a(j-h-1)\Delta z} - 1 \} , \ j = h+2, \dots, N \qquad (4.4.3)$$

where

$$a = \frac{\ln H}{1 - \Delta z}, \qquad (4.4.4)$$

$$b = \frac{h}{\delta} (H^{\Delta z / (1-\Delta z)} - 1), \qquad (4.4.5)$$

$$\Delta z = 1 - \frac{\ln H}{\ln H + \ln (1-\theta) - \ln (1-H\theta)}, \tag{4.4.6}$$

and

$$\theta = \frac{\delta}{h} \frac{1}{y_{max} - \delta}. \tag{4.4.7}$$

In actual implementation, the vertical extent is defined in the physical plane, that is, y_{max} is defined from $y_{p_{max}}$ using the criterion discussed in §IV.6. From (3.4.1), we require that

$$y_{p_{max}} = L \left[y_{max} + \frac{s}{2} \exp(-2\pi y_{max}) \cos 2\pi x \right], \tag{4.4.8}$$

and y_{max} is then solved from

$$y_{max} + \exp(-2\pi y_{max}) \cos 2\pi x - \frac{1}{L} y_{p_{max}} = 0 \tag{4.4.9}$$

using Newton's method.

§IV.5. Size of time-step : Numerical stability

The critical value of the time-step for numerical stability will be estimated by considering the viscous equation and the linearized convective equation independently. Owing to the linearization and approximation, these estimates may be off by a factor of around two.

From the von Neumann stability criterion, a third-order Adams-Bashforth scheme is conditionally stable for a hyperbolic equation with constant coefficients, the critical time-step being

$$\Delta t_{critical, convective} < 0.72 \frac{\Delta y}{K} \frac{J_0}{V_0 + \pi U_0 \Delta y / \Delta x} \tag{4.5.1}$$

where J_0, U_0 and V_0 are the maximum values of Jacobian function and x and y velocities respectively. This is in general more restrictive than the 'physical' criterion of $K\Delta t < \Delta y$, the requirement that disturbances propagate less than a grid

size per time step.

The Euler forward scheme is conditionally stable, subjected to

$$\Delta t_{critical, viscous} < \Delta y^2 \frac{R}{K} \frac{J_0}{2s} \frac{1}{1+(\frac{1}{2}\pi\Delta y/\Delta x)^2}. \tag{4.5.2}$$

Detailed derivations of (4.5.1) and (4.5.2) are given in §AIII.1.

The ratio of the two time-steps is given by

$$\frac{\Delta t_{critical,convective}}{\Delta t_{critical,viscous}} = \frac{1.4s}{R \Delta y} \frac{1+(\frac{1}{2}\pi\Delta y/\Delta x)^2}{V_0+\pi U_0 \Delta y/\Delta x}. $$

The upperbound for this ratio can be obtained by substituting the minimum grid size (Δy) discussed in the last section,

$$\Delta y = \frac{1}{h} (\frac{1}{J_{r_{max}}} \frac{s}{\pi} \frac{K}{R})^{\frac{1}{2}}, \tag{4.5.3}$$

defined in (4.4.3). Based on this minimum grid size, the time step defined in (4.5.1) can be approximated as

$$\Delta t \cong 0.72 \frac{\Delta y}{K} \cong \frac{0.72}{h} (\frac{s}{J_{r_{max}} \pi RK})^{\frac{1}{2}}. \tag{4.5.4}$$

This gives

$$\frac{\Delta t_{critical,convective}}{\Delta t_{critical,viscous}} \cong 1.4h (\frac{\pi s}{J_{r_{max}} KR})^{\frac{1}{2}} \frac{1+(\frac{1}{2}\pi\Delta y/\Delta x)^2}{V_0+\pi U_0 \Delta y/\Delta x}. $$

This ratio is generally much smaller than one.

The critical size of time-step determined from (4.5.1) varies inversely with the maximum velocity in the flow field and fluctuates within the wave cycle. The size of time-step is therefore varied at regular intervals according to the maximum of the instantaneous values of the velocity field. During the computations, we obtain at regular time intervals the maximum values of $|\partial\psi/\partial y|$ and $|\partial\psi/\partial x|$ from their vertical profiles at eight different values of x equally spaced along the ripple. These values are used for U_0 and V_0 in the determination of time-steps in (4.5.4). At the

beginning of each change in time-step (and at the start of computation), lower order numerical schemes are used for the convective term in the vorticity equation. Specifically, an Euler forward scheme, and then a second-order Adams-Bashforth scheme are used in the first two time-steps.

All our computations progress without breakdowns when time steps defined in (4.5.4) are used. Numerical experiments have also been performed to allow the size of time-step both to (i) decrease only and to (ii) fluctuate according to the instantaneous maximum flow velocity. It is found that the ratio of the number of time-steps used for the same duration of computation in the two cases is less than 1.5. To avoid introducing unnecessary numerical disturbances due to the lower order time-stepping scheme used at the beginning of each change in time-step, the time-step is allowed only to decrease in all runs.

We shall now show that spatial discretization error of the convective term is dominant in (4.2.1) if we choose the size of time-step on the basis of numerical stability rather than temporal discretization error. Based on the vertical grid spacings defined in §IV.4, substitution of (4.4.1) and (4.5.4) into the first four terms in (4.2.1) gives

$$\mathscr{E}_{\text{convective, spatial}} \cong \frac{sK^2}{6\pi R}\left(\frac{\partial\omega}{\partial x}\frac{\partial^3\psi}{\partial y^3} - \frac{\partial\psi}{\partial x}\frac{\partial^3\omega}{\partial y^3}\right), \quad (4.5.5)$$

$$\mathscr{E}_{\text{convective, temporal}} \cong -\frac{0.2}{h^3}\frac{1}{\sqrt{K}}\left(\frac{s}{\pi R}\right)^{1.5}\frac{\partial^3}{\partial t^3}\left(\frac{\partial\omega}{\partial x}\frac{\partial\psi}{\partial y} - \frac{\partial\psi}{\partial x}\frac{\partial\omega}{\partial y}\right), \quad (4.5.6)$$

$$\mathscr{E}_{\text{viscous, spatial}} \cong -\frac{1}{12\pi}\left(s\frac{K}{R}\right)^2\frac{\partial^4\omega}{\partial y^4}, \quad (4.5.7)$$

and

$$\mathscr{E}_{\text{viscous, temporal}} \cong \frac{0.4}{h}\left(\frac{K}{\pi}\right)^{\frac{1}{2}}\left(\frac{s}{R}\right)^{1.5}\frac{\partial}{\partial t}\left(\frac{\partial^2\omega}{\partial x^2} + \frac{\partial^2\omega}{\partial y^2}\right). \quad (4.5.8)$$

The ratios of the error terms (4.5.6), (4.5.7), and (4.5.8) to the error in the spatial discretization in the convective term are

$$\frac{\mathscr{E}_{convective,temporal}}{\mathscr{E}_{convective,spatial}} \cong \frac{1}{h^3}\frac{1}{K^2}\left(\frac{s}{\pi RK}\right)^{\frac{1}{2}},$$ (4.5.9)

$$\frac{\mathscr{E}_{viscous,spatial}}{\mathscr{E}_{convective,spatial}} \cong \frac{s}{2R},$$ (4.5.10)

and

$$\frac{\mathscr{E}_{viscous,temporal}}{\mathscr{E}_{convective,spatial}} \cong \frac{2}{h}\frac{1}{K}\left(\frac{s\pi}{RK}\right)^{\frac{1}{2}}$$ (4.5.11)

where all derivatives are assumed to be of order unity. All three ratios are much less than unity for the range of dimensionless parameters used in our computations, and therefore spatial discretization error in the convective term is the dominant error. The size of time-step is therefore determined from the numerical stability criterion.

It should also be noted that the time-step used in our scheme is smaller than the time scales for both viscous diffusion and convection. The ratio of time scales for viscous diffusion to convection can be estimated as

$$\frac{1}{\nu}(2a\Delta y)^2 / \left(L\frac{\Delta x}{U_0}\right) \cong \frac{s^2 K}{\pi\Delta x} < 1$$ (4.5.12)

and the ratio of the time-step to viscous diffusion is

$$T\Delta t / \frac{1}{\nu}(2a\Delta y)^2 \cong 0.72\frac{h}{s}\left(\frac{\pi}{sRK}\right)^{\frac{1}{2}} < 1$$ (4.5.13)

for the range of dimensionless parameters in our calculations.

§IV.6. Domain of computation

The horizontal extent of computations is one ripple length. Computations over multiples of a ripple length will lead to identical flow patterns over individual ripples unless irregularities are introduced either in the ripple profiles or in the

60

initial conditions.

The vertical extent of computation has to be large enough such that both viscous effects and the velocity induced from vortical motion become negligible at the upper boundary. This boundary is chosen to be between one and two ripple lengths above the bed, and increases with the Reynolds number of the flow. The first requirement is easily satisfied since the thickness of the viscous boundary layer immediately above the ripple surface is only a small fraction of a ripple height. That the second requirement, that the vortical motion at the upper boundary is much smaller than that near the ripple surface, is satisfied can be established in two steps. Firstly, we shall show that (i) for the range of dimensionless parameters used in our study, the velocity field at $t_p = o(T)$ due to the viscous decay of a point vortex can be approximated by that in an equivalent potential flow field; and secondly, that (ii) this potential velocity field induced by a point vortex near a plane bed decays to a small fraction of its maximum at the upper boundary in our computation.

(i) The viscous decay of the velocity field of an initial point vortex in an infinite fluid is given by Oseen's solution,

$$u_p(r_p, t_p) = \frac{\Gamma_P}{2\pi r_p} [1 - \exp(-\frac{r_p{}^2}{4\nu t_p})] , \tag{4.6.1}$$

where r_p is the radial distance from the point vortex and u_p is the tangential veloctiy in radial coordinates. In nondimensional variables this can be written as

$$u(r, t) = \frac{\Gamma}{2\pi r} [1 - \exp(-\frac{1}{4s}\frac{R}{K}\frac{r^2}{t})] \tag{4.6.2}$$

in which the velocity (u_p), radial coordinate (r_p), time (t_p), and vorticity potential (Γ_p) are nondimensionalized with U_0, L, T, and $U_0 L^3$ respectively. Dimensionless

---

[3]The minimum value of y_{max} needed to meet the requirements (i) and (ii) increases with the vortex strength Γ_P, and therefore the scaling of Γ_P with $U_0 L$ instead of

parameters s, K, and R are as defined in (3.1.8). From (4.6.2), u increases from zero to a maximum and decays exponentially as r increases from zero to infinity. In our parameters range of interest, $R/4Ks >> 1$, and therefore the difference between the velocity fields of a viscous and a potential vortex, the term $\exp(- Rr^2/4sKt)$ in (4.6.2), decays rapidly with r for finite values of t. The maximum velocity is given by

$$\frac{0.16}{\pi} \Gamma \left(\frac{R}{tsK}\right)^{\frac{1}{2}} = 0.051\Gamma \left(\frac{R}{tsK}\right)^{\frac{1}{2}}$$

at

$$r_{max} \approx \left(5st \frac{K}{R}\right)^{\frac{1}{2}} . \tag{4.6.3}$$

For R=250, K=4.5, and s=0.1, $r_{max} \approx 0.1 \sim o(s)$ for $t \sim o(1)$, that is, r_{max} is of the order of a ripple height. The velocity field at more than a few ripple heights away from the vortex is therefore well represented by the potential flow velocity represented by the first term in (4.6.1).

(ii) We next show that the magnitude of the velocity induced by a potential vortex placed at a distance $\alpha_p \sim o(a)$ from a plane bed has diminished substantially at a distance of a ripple length L from the bed, and therefore the requirement that the vortical motion at the upper boundary is negligible will be satisfied if the boundary is over a ripple length from the bed.

The velocity field along the y-axis induced by a potential vortex on the y-axis at a distance α_p from a plane wall defined by $y_p=0$ is given by

$$u_p(y_p, t_p) = \frac{\Gamma_P}{2\pi} \left(\frac{1}{y_P + \alpha_P} - \frac{1}{y_P - \alpha_P}\right)$$

$$= -\frac{\alpha_P \Gamma_P}{\pi y_P^2} [1 + \varepsilon^2 + \varepsilon^4 + o(\varepsilon^6)] ; \quad \varepsilon = \frac{\alpha_P}{y_P} . \tag{4.6.4}$$

U_02a gives a more conservative estimate on y_{max}.

In nondimensional variables with

$$y_p = Ly \quad \text{and} \quad \alpha_p = L\alpha \,,$$

Γ and u as defined above, and $\alpha_p \approx o(a)$ such that $\alpha \approx o(\frac{a}{L}) = \frac{s}{2} << 1,$

$$u(y,t) = -\frac{\alpha}{2\pi}\frac{\Gamma}{y^2}[1 + \epsilon^2 + o(\epsilon^4)] \,; \quad \epsilon = \frac{\alpha}{y} \,. \tag{4.6.5}$$

For both Γ and y to be of order 1, $\alpha/2\pi \approx s/4\pi$ is much less than one and the velocity induced by the vortex is negligible at $y \approx 1$ or $y_p \approx L$ for moderate Reynolds numbers.

As an example, at R=250, K=4.5, and s=0.1, $R/4sK \approx 140$ in (4.6.2) and the potential velocity can therefore very well approximate the velocity in an infinite viscous fluid. The ratio of vortex induced velocity u(y,t) given by (4.6.5) to the maximum velocity given by (4.6.3) is

$$0.5 \, \alpha \frac{\Gamma}{y^2} (st \frac{K}{R})^{\frac{1}{2}} \approx 0.002 << 1 \tag{4.6.6}$$

for $\alpha \approx o(s)$ and $y \approx t \approx 1$. Any $y_{max} > 1$ (approximately one ripple length above mean bed in the physical plane) can be chosen as the upper boundary in the computation.

In §V.3 we shall show that $y_{max} \approx 1$ gives the same results as $y_{max} \approx 3$ for the flow with R=63, K=4, and s=0.1. Further numerical confirmation of this estimate on y_{max} will be given in §VI.1 for the flow with R=500, K=4.5, and s=0.1..

§IV.7. Initial conditions and termination of computation

The fluid is inititally at rest and therefore

$$\omega \equiv \psi \equiv 0 \quad \text{for all x, y at t=0.} \tag{4.7.1}$$

The boundary condition at y_{max} is therefore discontinuous in its time-derivatives (and itself discontinuous if an impulsive start or a current is imposed).

Time-periodic solutions are of particular interest in our present study since they

can be readily applied to sediment transport[4] and other engineering problems. However, in nonlinear problems, periodic forcings do not guarantee periodic responses. In the separated flow over ripples, vortices shed in previous wave cycles modify the velocity and pressure field, and thus change the conditions near the ripple surface under which new vortices are formed. Since the mutual interactions between new and old vortices depend on their exact strengths and locations, the flow field may remain different from period to period as computation proceeds.

We therefore introduce a measure of the departure from periodicity of the solution by examining the sum of the differences in the values of the streamfunction at the same instants exactly one period apart, and define

$$\mathscr{E}_r(t) \;=\; \left\{ \frac{1}{M}\,\frac{1}{N-1}\,\sum_{k=1}^{M}\,\sum_{j=2}^{N}\,\left| \psi(x_k, y_j, t) - \psi(x_k, y_j, t-1) \right|^r \right\}^{1/r} \qquad (4.7.2)$$

in which r is an integer parameter. Thus $\mathscr{E}_1(t)$ is the mean of the absolute values of fluctuation in streamfunction values at all grid points, and $\mathscr{E}_\infty(t)$ is its maximum over the entire mesh. Linear intrapolation is used in (4.7.2) when streamfunction values exactly one wave period later are not available due to the finite size of time-steps.

An estimate of the number of periods t_c required to obtain this periodic or steady state can be obtained from that in the impulsively started oscillatory flow discussed in the next chapter. In dimensionless parameters this is given, from (5.1.14), by

$$t_c \;=\; \frac{1}{\pi}\left(\frac{1}{c^2}\,\frac{y_{max}^{\,2}\,R}{16sK} \right)^{1/3} \qquad (4.7.3)$$

where c is the deviation in the horizontal velocity from the periodic solution. For

---

[4]Recall from Chapter I that an empirical criterion for the initiation of bed load transport can be deduced from the Shields parameter in (I.4) and (I.5) for steady flows and oscillatory flows respectively. The conditions for suspended load transport, unfortunately, are not as well understood.

example, when R=250, K=4.5, and s=0.1, (4.7.3) gives $t_c \approx 22$ for c=0.01.

It will be seen in Chapter VI that, when the Reynolds number and Keulegan–Carpenter number are both high, the variables δ_1 and δ_∞ defined in (4.7.2) do not decrease monotonously but remain above some finite values. For example, we have, after twenty periods of computation, $\delta_\infty \approx 0.07$ and $\delta_1 \approx 0.015$ when R=500, K=4.5, and s=0.1, and $\delta_\infty \approx 0.06$ and $\delta_1 \approx 0.01$ when R=250, K=6, and s=0.1. A more detailed discussion will be presented in §VI.1.3. However, even under these circumstances, global quantities such as the energy dissipation or the magnitudes of the horizontal force on a ripple over a wave period do not fluctuate by more than 5% of their mean values.

§IV.8. Estimate of Central Processing Unit (CPU) time

The number of floating point operations per time–step is of the order of ϱMN where M and N are the numbber of grid points in the x and y direction respectively. The multiple ϱ is obtained by counting the number of operations in the FORTRAN code and estimating the number of operations in the FFT subroutine (Cooley and Tukey, 1965). In the computer code COMPUTE listed in Appendix V, ϱ is approximately $40+12\log_2 M$. For M=64 and N=72 (the maximum number of grid points used in our study), the operation count is around 0.5 million floating point operations (MFLOP) per time–step, a typical size of which is around 0.0005.

The bulk of computation is performed on a Cray-2 machine at the Minnesota Supercomputing Center in Minneapolis, MN and a Cray X-MP/24 at the Naval Research Laboratory in Washington, D.C. Computation time can be estimated from the speed of Cray–supercomputers, conservatively estimated at 50 MFLOP per second. The efficiency of computation may be increased by optimizing vectorizations and using library subroutines (used in FFT and one and two dimensional integrations) specifically designed for optimal efficiency on the Cray

machines.

§IV.9. Further comments

To conclude this chapter we shall discuss two variations on the numerical scheme discussed above. The first was designed to improve the numerical stability in the Poisson solver and was found to be unnecessary. The second was intended to accelerate the approach to a periodic solution and was found to be ineffective. They are not implemented in the computations reported in the rest of the thesis.

§IV.9.1. Iteration scheme for Poisson equation

The boundary values of ω are not updated in the time–stepping scheme of the vorticity equation (4.1.7) to (4.1.9) so as to keep the computation fully explicit. The values of $(J\Omega)^n_{m,1}$ and $(J\Omega)^n_{m,N}$, instead of $(J\Omega)^{n+1}_{m,1}$ and $(J\Omega)^{n+1}_{m,N}$ are therefore used in solving for the streamfunction equation with compact differencing, (4.1.10). To assure that such a lagging in time in the boundary values does not incur inaccuracies or numerical instabilities, an iterative procedure was therefore tried: after the streamfunction values had been solved in (4.1.10), the boundary values of ω obtained from (4.1.12) and (4.1.15) were substituted back into (4.1.10) and the streamfunction values were solved again. This was iterated to convergence. It was found that this procedure did not result in any noticeable differences in streamfunction values, and no more than one iteration was needed for convergence up to 10^{-4} at all times after the initial start. With a time–step defined in (4.5.1), computations without iterations remained stable provided that the aliasing error remained small.

§IV.9.2. Acceleration scheme for convergence of the solution to symmetry in the two half periods

If the solution is symmetric in the two halves of the wave period, the following relationships for the nondimensional streamfunction and vorticity function must hold: identical y-velocities requires that

$$\frac{\partial \psi}{\partial x}(x, y, t) = \frac{\partial \psi}{\partial x}(-x, y, t+\tfrac{1}{2}) \tag{4.9.1}$$

and

$$\frac{\partial \psi}{\partial y}(x, y, t) = -\frac{\partial \psi}{\partial y}(-x, y, t+\tfrac{1}{2}) \tag{4.9.2}$$

where $t+\tfrac{1}{2}$ is one-half period after t.

With streamfunction expressed in terms of Fourier series (4.1.4), (4.9.1) and (4.9.2) require that

$$\Psi_{mj}^{n1} = -(\Psi_{mj}^{n2})^* \quad \text{for} \quad t_{n1} = t_{n2} + \frac{1}{2}. \tag{4.9.3}$$

Alternatively, this can be written as

$$\psi(1-x, y, t+\tfrac{1}{2}) = -\psi(x, y, t), \tag{4.9.4}$$

$$\frac{\partial \psi}{\partial x}(1-x, y, t+\tfrac{1}{2}) = \frac{\partial \psi}{\partial x}(x, y, t), \tag{4.9.5}$$

$$\frac{\partial^2 \psi}{\partial x^2}(1-x, y, t+\tfrac{1}{2}) = -\frac{\partial^2 \psi}{\partial x^2}(x, y, t), \tag{4.9.6}$$

$$\frac{\partial \psi}{\partial y}(1-x, y, t+\tfrac{1}{2}) = -\frac{\partial \psi}{\partial y}(x, y, t), \tag{4.9.7}$$

and

$$\frac{\partial^2 \psi}{\partial y^2}(1-x, y, t+\tfrac{1}{2}) = -\frac{\partial^2 \psi}{\partial y^2}(x, y, t). \tag{4.9.8}$$

The vorticity function is, from (3.1.11), governed by

$$\omega(1-x, y, t+\tfrac{1}{2}) = -\omega(x, y, t), \tag{4.9.9}$$

$$\frac{\partial \omega}{\partial x}(1-x, y, t+\tfrac{1}{2}) = \frac{\partial \omega}{\partial x}(x, y, t), \tag{4.9.10}$$

$$\frac{\partial^2 \omega}{\partial x^2}(1\text{-}x, y, t+\tfrac{1}{2}) = -\frac{\partial^2 \omega}{\partial x^2}(x, y, t) , \qquad (4.9.11)$$

$$\frac{\partial \omega}{\partial y}(1\text{-}x, y, t+\tfrac{1}{2}) = -\frac{\partial \omega}{\partial y}(x, y, t) , \qquad (4.9.12)$$

and

$$\frac{\partial^2 \omega}{\partial y^2}(1\text{-}x, y, t+\tfrac{1}{2}) = -\frac{\partial^2 \omega}{\partial y^2}(x, y, t) . \qquad (4.9.13)$$

The relationships (4.9.1) and (4.9.2) are attained after a few periods of computation for flows at low Reynolds numbers or Keulegan–Carpenter numbers. At higher dimensionless numbers, for example, when R=250, K=4.5, and s=0.1, the solution remains asymmetric after thirty-five periods of computation. A numerical experiment was therefore performed, in an attempt to speed up convergence to a symmetric solution, such that current values of ψ, $\partial \psi / \partial y$, ω, $\partial \omega / \partial y$, $\partial^2 \omega / \partial x^2$, and $\partial^2 \omega / \partial y^2$ at (x,y,t) were replaced with half their differences with corresponding values at (1-x,y,t-$\tfrac{1}{2}$), and current values of $\partial \psi / \partial x$ and $\partial \omega / \partial x$ at (x,y,t) were replaced with their means with corresponding values at (1-x,y,t-$\tfrac{1}{2}$). It was found that, for the case of R=250, K=4.5, and s=0.1, the solution remains asymmetric in the two half periods after fifteen periods of computation, starting at the twenty-first period, and an averaging procedure every two periods. This averaging procedure was therefore discarded and is not used in any of the computations.

Chaper V. Verification of Numerical Scheme

The validity of the numerical scheme discussed previously will be demonstrated in this chapter. Various criteria used in determing the time–step, grid–size, and domain of computation proposed in Chapter IV will be verified for the test cases studied. Except for the comparison with an asymptotic solution to the flow over a ripple bed at a low Reynolds number, the verification procedure is based on well known solutions to closely related flow cases in which the exact formulations vary from that described in Chapter III. These differences will be discussed in detail.

§V.1. Oscillatory flow over a plane bed

An exact solution to the Navier–Stokes equations exists for the two–dimensional flow over a plane bed in an initially quiescent semi–infinite fluid due to an impulsively started simple harmonic flow

$$u_p = U_0 \, H(t_p) \, \sin(2\pi \frac{t_p}{T}) \tag{5.1.1}$$

in the far field, where $H(t_p)$ is the Heaviside step function. The solution takes the form (Carslaw and Jaeger, 1947)

$$\frac{1}{U_0} u_p(y_p, t_p) = \sin(2\pi \frac{t_p}{T}) - \exp(-\frac{y_p}{\delta_p}) \sin(2\pi \frac{t_p}{T} - \frac{y_p}{\delta_p})$$
$$- \frac{2}{T} \int_0^\infty d\theta \, \frac{\exp(-\theta t_p)}{\theta^2 + (2\pi/T)^2} \sin[y_p \sqrt{\theta/\nu}] . \tag{5.1.2}$$

The boundary layer thickness $\delta_p = \sqrt{\nu T/\pi}$ has been defined in (4.4.1). Alternatively, the nondimensional streamfunction can be written as

$$\psi(y,t) = y \sin 2\pi t - \frac{1}{\alpha\sqrt{2}} \exp(-\alpha y) \, [\cos(2\pi t - \alpha y + \tfrac{1}{4}\pi) - \cos(2\pi t + \tfrac{1}{4}\pi)]$$
$$+ 2 \int_0^\infty d\theta \, \frac{\exp(-\theta t)}{\theta^2 + 4\pi^2} \, \frac{\cos(\alpha y \sqrt{\pi\theta})}{\alpha\sqrt{\pi\theta}}$$

$$= \psi_s + 2 \int_0^\infty d\theta \frac{\exp(-\theta t)}{\theta^2 + 4\pi^2} \frac{\cos(\alpha y \sqrt{\pi\theta})}{\alpha\sqrt{\pi\theta}} \tag{5.1.3}$$

where $\alpha = L/\delta_p$ and ψ_s denotes the steady state solution.

A numerical solution to this problem is computed using the numerical scheme discussed in Chapter IV by choosing the Jacobian in the mapping (3.1.9) to be identically one in the entire flow domain, that is, s=0 in (3.4.1). Equations (3.1.10) and (3.1.11) become

$$\frac{\partial \omega}{\partial t} + \pi \left(\frac{\partial \psi}{\partial y} \frac{\partial \omega}{\partial x} - \frac{\partial \psi}{\partial x} \frac{\partial \omega}{\partial y} \right) - \frac{\pi}{R_s} \left(\frac{\partial^2 \omega}{\partial x^2} + \frac{\partial^2 \omega}{\partial y^2} \right) = 0 \tag{5.1.4}$$

and

$$\frac{\partial^2 \psi}{\partial x^2} + \frac{\partial^2 \psi}{\partial y^2} = -\omega \tag{5.1.5}$$

where R_s is defined in (5.1.10). Equations (5.1.4) and (5.1.5) are the forms used in the numerical computation. The boundary conditions are

$$\psi = \frac{\partial \psi}{\partial y} = 0 \quad \text{at} \quad y=0 \tag{5.1.6}$$

and

$$\frac{\partial \psi}{\partial y} = \sin 2\pi t \quad \text{and} \quad \psi = \text{constant} \quad \text{at} \quad y = y_{max} \quad \text{and} \quad t > 0. \tag{5.1.7}$$

The initial condition is

$$\psi = \omega = 0 \quad \text{for all x, y at t=0.} \tag{5.1.8}$$

The following points should be noted:

i. There are no intrinsic length scales in the boundary profile, and we define L in (3.1.4) and (3.1.8) as the excursion length L_s of a fluid particle in the ambient flow. This gives

$$L_s = \int_0^{\frac{1}{2}T} dt_p \, U_0 \sin(2\pi \frac{t_p}{T}) = \frac{U_0 T}{\pi}. \tag{5.1.9}$$

70

The dimensionless parameters then become

$$K_s = \frac{U_0 T}{L_s} = \iota \quad \text{and} \quad R_s = \frac{U_0 L_s}{\nu} = (\frac{L_s}{\delta_p})^2, \qquad (5.1.10)$$

where δ_p is the oscillatory boundary layer thickness. If we replace L by L_s in (4.4.1), the ratio

$$\delta_s = \frac{1}{L_s}\delta_p = \frac{1}{L_s}(\frac{\nu T}{\pi})^{\frac{1}{2}} = (\frac{1}{\pi}\frac{K_s}{R_s})^{\frac{1}{2}} = \frac{1}{\sqrt{R_s}}. \qquad (5.1.11)$$

ii.   The exact solution corresponding to the truncated flow domain defined by (5.1.4) to (5.1.7) can also be easily obtained. However, its difference with (5.1.3) is negligible.

iii.   For an initially quiescent semi–infinite fluid, the transient solution due to an impulsively started oscillatory ambient flow differs from the periodic solution by the last term in (5.1.2). In nondimensional variables, this equals

$$\mathscr{I}(y,t) = -2\int_0^\infty d\theta \frac{e^{-\theta t}}{\theta^2 + 4\pi^2} \sin(L_s y\sqrt{\theta/\nu T}). \qquad (5.1.12)$$

The rate of convergence can therefore be found from the asymptotic behavior of $\mathscr{I}(y,t)$ at large t. From Watson's Lemma (Bender and Orszag, 1978), we get

$$\lim_{t\to\infty} \mathscr{I}(y,t) \cong \frac{1}{4\pi}\frac{y}{t^{3/2}}\frac{L_s}{\sqrt{\pi\nu T}}[1 - \frac{y^2 L_s^2}{4t\,\nu T} + o(\frac{1}{t^2})]. \qquad (5.1.13)$$

The time t_c it takes for convergence to $\mathscr{C}$, i.e. $|\mathscr{I}(y,t)| < \mathscr{C}$ for all $t > t_c$, is therefore given by

$$t_c = (\frac{1}{\mathscr{C}^2}\frac{y^2 L_s^2}{16\pi^3 \nu T})^{1/3} = (\frac{1}{\mathscr{C}^2}\frac{y^2}{16\pi^4}R_s)^{1/3} \qquad (5.1.14)$$

for $\mathscr{C} < \frac{2\nu T}{\sqrt{\pi^3}y^2 L_s^2} = \frac{2}{\sqrt{\pi}\,y^2 R_s}$. For $R_s = 100$, $y = 1.23$, and $\mathscr{C} = 0.005$, $t_c \approx 16$.

71

The velocity profile obtained from the numerial solution (with R_s=100 and y_{max}=1.23) is compared with the exact solution (5.1.2) at equal time intervals from t=0.13 to 1 and from t=1.13 to 2 in Figs. V.1.1 and V.1.2 respectively. There is some discrepancy at small t due to the insufficient grid spacing near the bottom boundary,[1] but the agreement for t>0.5 is excellent.

Further details on the parameters used in the computation will be given below:

i.   The nondimensionalized boundary layer thickness is, from (5.1.11), $\delta = 1/\sqrt{R_s}$. It is shown in Fig. V.1.2 that $y_{max}/\delta = y_{max}\sqrt{R_s} \approx 12$ is large enough to simulate a semi-infinite flow domain. The spacing of grid points in the y-direction follows an exponential type increase from the bottom boundary, as defined by equations (4.3.3) to (4.3.7). Only five grid points within the thickness of boundary layer δ are sufficient to resolve the velocity profile, as claimed in §IV.4.ii.

ii.   Despite the absence of convective terms, the critical time-step is still chosen to be the minimum of $\Delta t_{critical,convecitve}$ and $\Delta t_{critical,viscous}$ defined in (4.5.1) and (4.5.2). This is to keep roundoff errors in the convective terms from destabilizing the computation.

iii.   The flow is uniform in the x direction. The system is therefore a function of two independent variables y and t only and the nonlinear convective terms are identically zero in the vorticity equation. In the numerical solution, variations in the x coordinate may be caused by roundoff and subsequent aliasing errors.It is found that the amplitudes of the Fourier coefficients with nonzero wavenumber is no more than 10^{-12}. Since these computations are carried out on

---

[1]The boundary layer thickness is infinitesimally small at the beginning of computation.
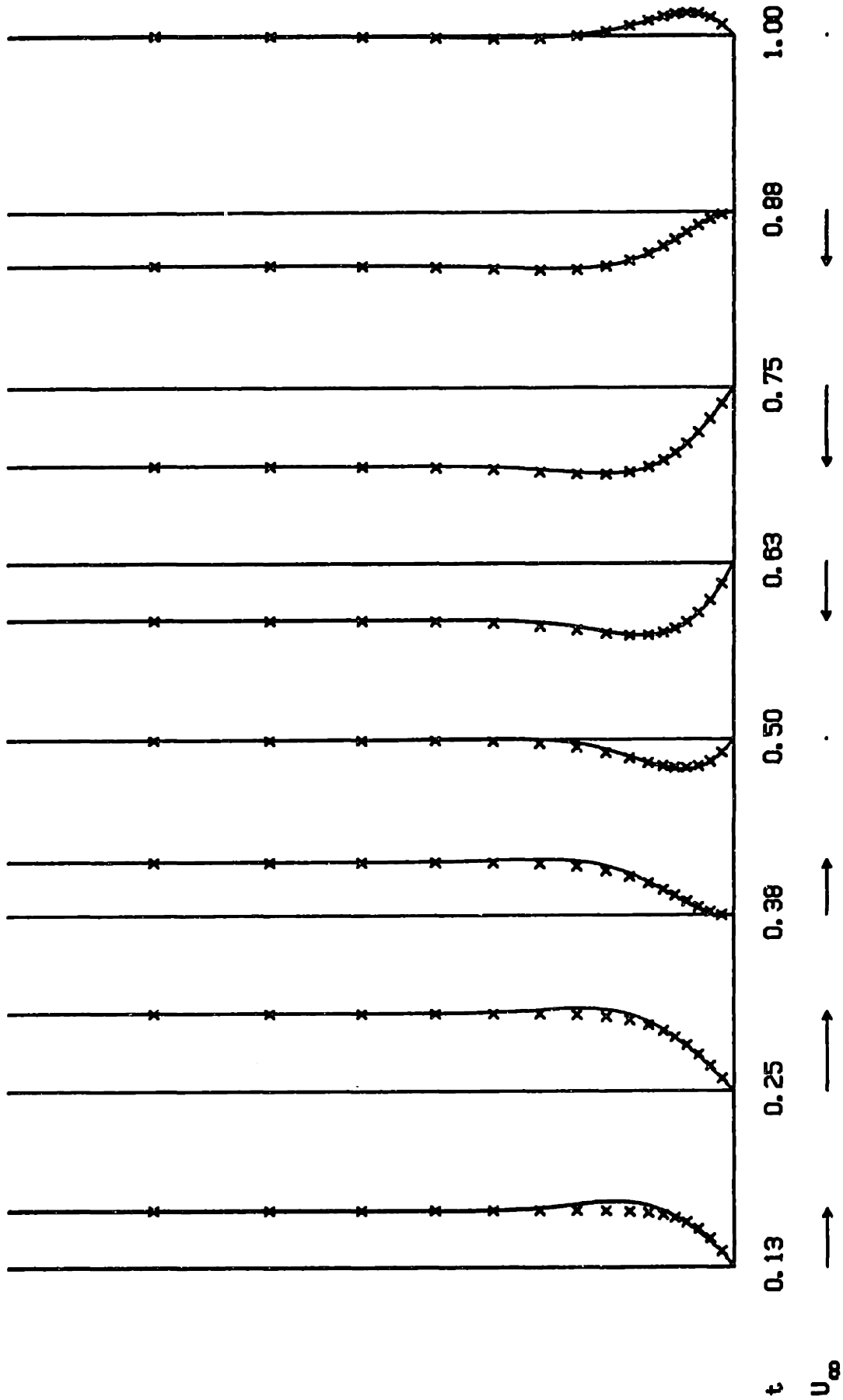
Fig. V.1.1. Velocity profile above a plane bed under oscillatory ambient flow   R = 100

Computed   M = 8   N = 18 y_{max} =1.23

x

— Exact solution for a semi-infinite fluid (5.1.2).

73

Fig. V.1.2. Velocity profile above a plane bed under oscillatory ambient flow   R = 100
           x   Computed   M = 8   N = 18 y_{max} = 1.23
           ———   Exact solution for a semi-infinite fluid, (5.1.2).

74

CRAY supercomputers with 14 significant figures for single precision computations and that the streamfunction is of unit magnitude, aliasing error in this case is therefore negligible.

§V.2. Impulsively started flow around a circular cylinder

The comparison with the exact solution of Stokes second problem presented in the previous section offers validation of the numerical scheme for a simple case in which nonlinear convective terms are absent in the vorticity equation. Since the estimate on time-step (based on numerical stability criterion) is based on linear analysis, the performance of the numerical scheme when nonlinear terms are of comparable magnitudes with unsteady and viscous terms need to be further vindicated. Unfortunately, no exact transient solutions to the fully nonlinear Navier-Stokes equations are available. We therefore turn to a flow problem in which well established numerical solutions to the full nonlinear Navier-Stokes equations exist, namely, the flow around circular cylinders.

Many papers have appeared in the last thirty years on the numerical solution to the two-dimensional laminar flow around circular cylinders. More recent ones include Fornberg (1985) (for the case of steady translation of cylinder), Ta Phuoc Loc and Bouard (1985) (for transient unsteady translation from rest), and Badr and Dennis (1985) (for impulsively started translation and rotation). A review of the more current work can be found in Lecointe and Piquet (1985).

The numerical scheme discussed in the previous chapter can be modified to solve for the flow around circular cylinders by choosing a conformal mapping such that the circumference of the circle is mapped onto the x-axis. Let z_p and z be complex coordinates in the physical and the mapped plane such that

$$z_p = x_p + i\, y_p \qquad\qquad (5.2.1)$$

and

$$z = x + i y,$$ (5.2.2)

and let a be the radius of the circular cylinder. The mapping

$$\frac{1}{a} z_p = e^{-i2\pi z}$$ (5.2.3)

used in conjunction with Fourier decomposition in x (with period 1) guarantees periodicity for any principle arguments with a range of 2π in cylindrical coordinates in the physical plane. With physical variables nondimensionalized as

$$t_p = \frac{a}{U_0} t,$$ (5.2.4)

$$\psi_p = U_0 a \, \psi,$$ (5.2.5)

and

$$\omega_p = \frac{U_0}{a} \omega,$$ (5.2.6)

and dimensionless parameters defined as

$$R_c = \frac{U_0 a}{\nu},$$ (5.2.7)

$$K_c = 1,$$ (5.2.8)

and

$$s = 2,$$ (5.2.9)

the governing equations (3.1.10) and (3.1.11) become

$$J \frac{\partial \omega}{\partial t} + \frac{\partial \psi}{\partial y} \frac{\partial \omega}{\partial x} - \frac{\partial \psi}{\partial x} \frac{\partial \omega}{\partial y} = \frac{2}{R_c} (\frac{\partial^2 \omega}{\partial x^2} + \frac{\partial^2 \omega}{\partial y^2})$$ (5.2.10)

and

$$\frac{\partial^2 \psi}{\partial x^2} + \frac{\partial^2 \psi}{\partial y^2} = - J \omega.$$ (5.2.11)

The Jacobian of the mapping defined in (5.2.3) is given by

$$J(x, y) = 4\pi^2 \exp(4\pi y).$$ (5.2.12)

The far field boundary conditions at $y=y_{max}$ are

$$\frac{\partial \psi}{\partial x} = 4\pi \cos 2\pi x \sinh 2\pi y_{max} \qquad (5.2.13)$$

and

$$\frac{\partial \psi}{\partial y} = 4\pi \sin 2\pi x \cosh 2\pi y_{max} , \qquad (5.2.14)$$

which is the potential flow solution at (x, y_{max}). No-slip condition (3.1.15) on y=0 remains unchanged.

Our quantitative results for the case of impulsively started translation of a circular cylinder is compared with the numerical results in Ta Phuoc Loc (1980) and the laboratory measurements of Bouard and Coutanceau (1980). In the numerical computation by Ta Phuoc Loc (1980), symmetry about the diameter in the direction of translation motion was assumed. Fourth order compact differencing was used in the streamfunction equation and a second order alternating direction implicit scheme was used in the time-stepping in the vorticity equation. The overall accuracy is therefore second-order in space and first-order in time. Further details in the numerical scheme can be found in Ta Phuoc Loc and Daube (1977). Note that our numerical scheme may have a higher accuracy since the time-stepping scheme in Ta Phuoc Loc (1980) is first order while that in our present one is third order. Furthermore, the time-step used in Ta Phuoc Loc (1980) is 0.033 while that in ours is around 0.0004.

Visualizations of the flow field in Bouard and Coutanceau (1980) was accomplished using magnesium cuttings in suspension and illuminated with a sheet of intense light in a meridian section of the wave tank. Velocity estimates were based on the lengths of trajectories of individual particles over the duration of exposure. Further details of the experimental techniques can be found in Coutanceau and Bouard (1977a, b).

Comparisons are made at a Reynolds number of 550 for the time range 0<t<5. The radial velocity along the downstream line of symmetry is plotted from t=1 to 5

77

at time intervals of one. Results from our computation are plotted as broken lines and compared with the laboratory measurements of Bouard and Coutanceau (1980) in Fig. V.2.1.i, and with the numerical solutions of Ta Phuoc Loc (1980) in Fig. V.2.1.ii. All three results are very much the same at t=1. For $2 \leq t \leq 5$ they also show the same qualitative behavior but the actual values vary slightly. The numerical solution of Ta Phuoc Loc, for example, are consistently higher than our results for x_p/a beyond the value at which the velocity in the negative direction are. The measurements of this radial velocity by Bouard and Coutanceau, on the other hand, show a steeper rate of increase with x_p/a, from less than the values we obtained to above. Since no two data sets are found to agree better than with the third, and all three results are very close, we shall not investigate the finite but small discrepancies any further.

The vorticity distribution on the surface of the cylinder is shown in Fig. V.2.2. Note that the vorticity function defined in (5.2.11) is opposite in sign to that in Ta Phuoc Loc (1980). We plot the two sets of results separately for clarity, noting that there are finite differences between them. The qualitative features are similar, and the maximum discrepancy is less than 5% of the range of total variation.

The computed flow field around the cylinder (Fig. V.2.3) is compared with the streak lines of Bouard and Coutanceau (1980) (Fig. V.2.4). Note that their time unit is nondimensionalized with $2a/U_0$ instead of a/U_0 as in (5.2.4) and therefore their time of 2.5 corresponds to t=5 in our formulation. It is seen that the locations of separation, the extent of separation zones and the directions of velocity at all locations are in very good agreement.

§V.3. Asymptotic solution to oscillatory flow over ripple bed

Further vindication of the numerical scheme presented in Chapter IV is accomplished by comparing with an asymptotic solution to the oscillatory flow over
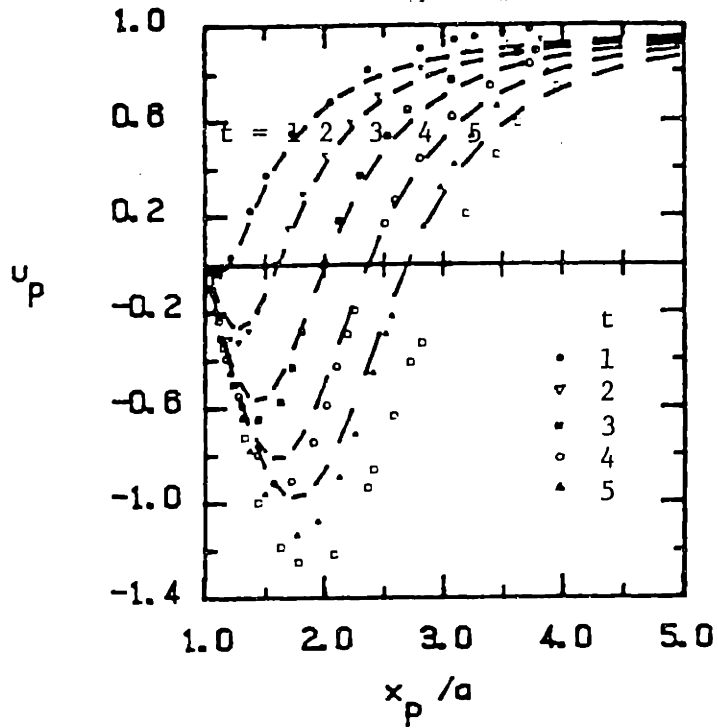
i. Comparison with the laboratory
measurements of Bouard and Coutanceau (1980)
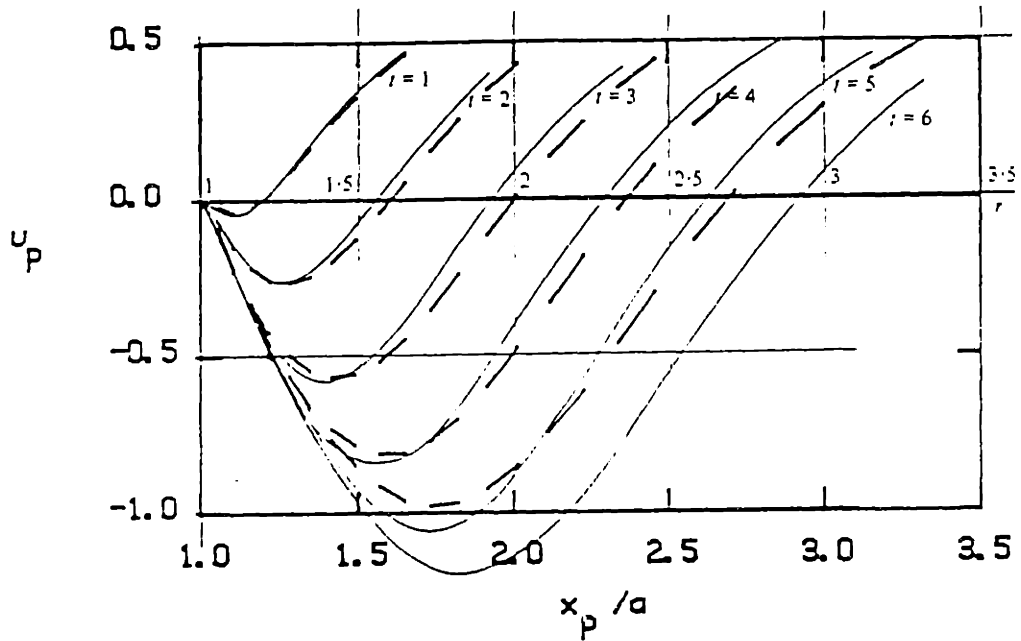
ii. Comparison with the numerical results
of Ta Phuoc Loc (1980)   M=N=61

Fig. V.2.1.   Evolution with time of the radial velocity on
the symmetry axis behind the cylinder for R=550

- - - -   Current computation   M=128   N=61

79

current computation   M = 128   N = 61

Ta Phuoc Loc (1980)   M = N = 61
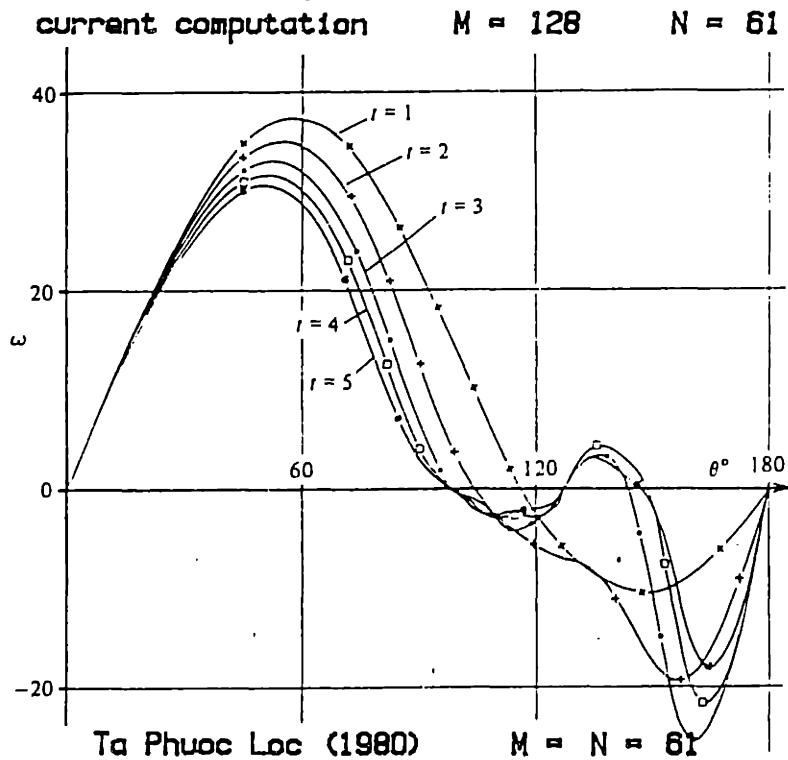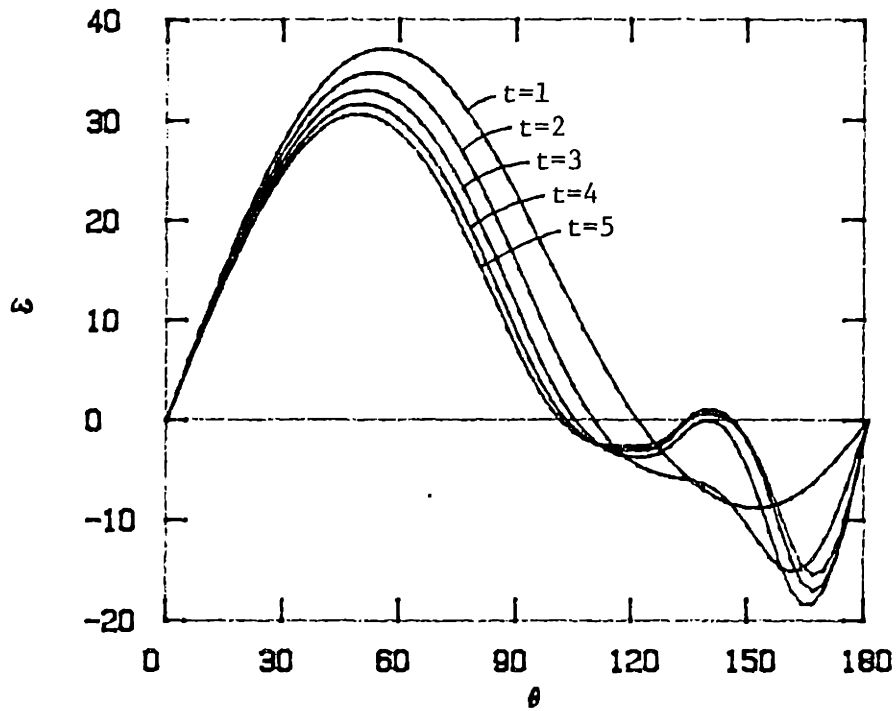
Fig. V.2.2.   Evolution with time of the vorticity
               distribution at the cylinder surface
               at R=550
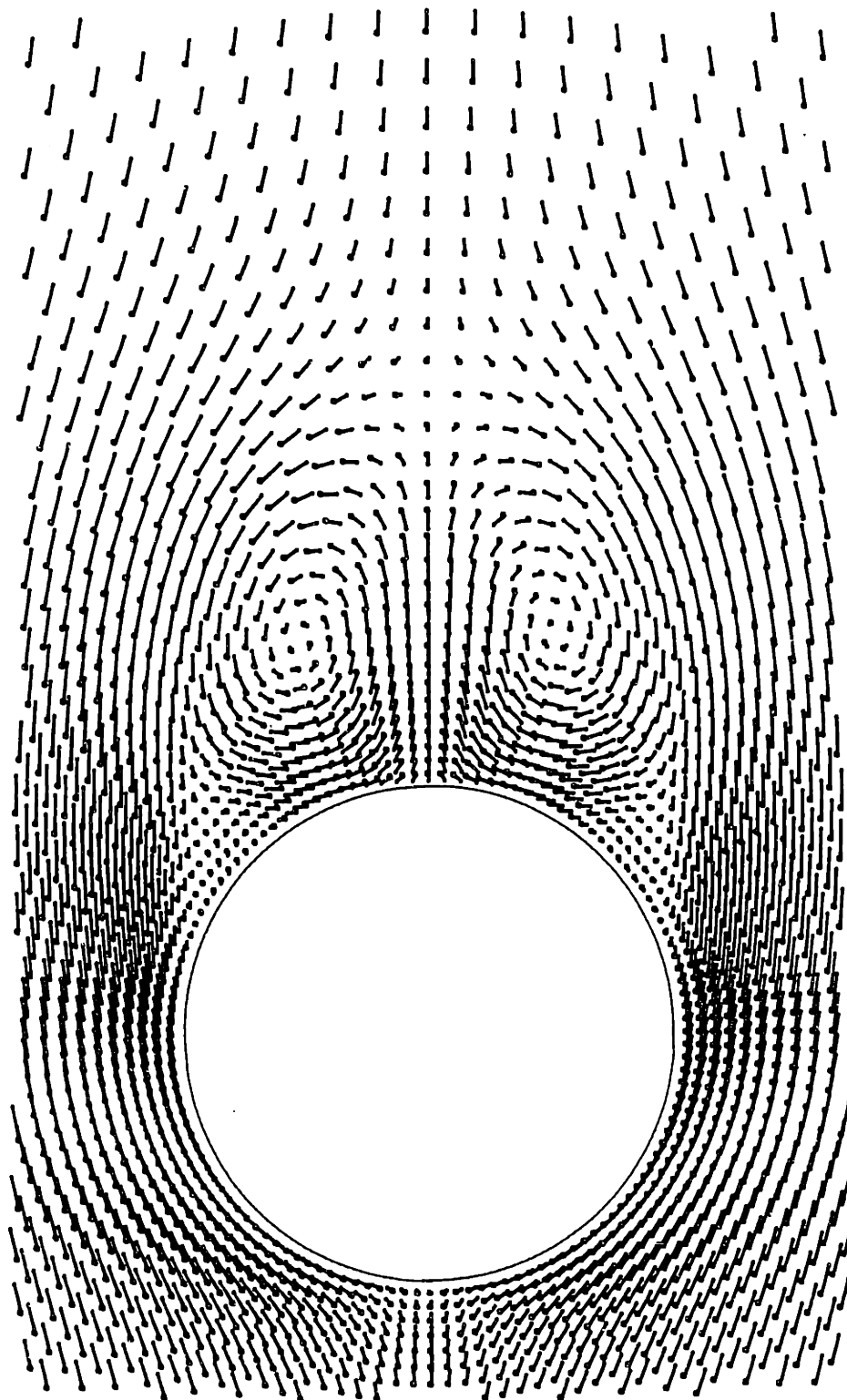
Fig. V.2.3.   Velocity field around an impulsively started cylinder
              t = 5.0   R = 550   M = 128   N = 61
              y_{max} = 1.05 U_{∞} : →

Fig. V.2.4.   Velocity field around an impulsively started cylinder
Bouard and Coutanceau (1980)   t = 5.0   R = 550

rippled bed.

It has been discussed in Chapter II that asymptotic solutions of Lyne (1971) and Kaneko and Honji (1979), valid in the limit of very small $(\pi s R/4K)^{\frac{1}{2}}$ and s respectively, do not depict separated flows. A different approach was made by Mei and Hara (1987, personal communication) which extends the convergence of the asymptotic solution to higher values of s, K, and R. Identical governing equations and boundary conditions to those in §III.1 are solved by using a perturbation approach for the same periodic ripples profiles defined in (3.4.2). The streamfunction was written as an asymptotic series in orders of the ripple slope,

$$\psi = \psi_0 + \varepsilon\psi_1 + \varepsilon^2\psi_2 + ... + \varepsilon^m\psi_m + ... , \qquad (5.3.1)$$

where $\varepsilon=\pi s$.

Substituting (5.3.1) into the governing vorticity equation and sorting out the orders, they solved the increasing orders of streamfunction in succession. Each term in the series is written in the form

$$\psi_m (x, y, t) = \sum_{n=-\infty}^{\infty} e^{in2\pi t} \sum_{k=0}^{m} {}_m\Psi_{nk}(y) \, e^{i2\pi(2k-m)x} . \qquad (5.3.2)$$

The infinite series in n is truncated and the complex functions ${}_m\Psi_{nk}(y)$, $n = -M_m$, $-(M_m-1)$, ..., M_m; $k = 0, ..., m$; are then solved simultaneously with finite differencing. The number of harmonics used was chosen such that further increase in M_m will not change the solution significantly. Note that writing the streamfunction as (5.3.2) presumes a periodicity in time with the same period as ambient flow.

This offers a direct comparison of numerical results with the semi-analytical solution to the Navier-Stokes equation specifically for the flow over ripple beds. Comparisons were made for the case of s=0.1, R=20π=63, and K=4.[2] The

---

[2]At K=4 and s=0.1, R=63 is near the upper limit at which (5.3.1) is found to converge when computed up to m=6.

asymptotic solution (5.3.1) was computed up to sixth order (m=6) and twenty-four time harmonics were used in (5.3.2) (M_m=24). Variations with y at the two lowest orders, ψ_0 and ψ_1, are compared with the Fourier coefficients of the corresponding wavenumbers at two time instants: when the magnitude of ambient velocity is at its maximum or minimum. The results are shown in Figs. V.3.1 and V.3.2 for the zeroth harmonic and Figs. V.3.3 and V.3.4 for the first harmonic. The solid curves in the plots for the m-th harmonic are the coefficients for cos $2m\pi x$ of $\psi_0+\psi_1$, and the broken curves are for the coefficients for sin $2m\pi x$. They correspond to $Re\,\{\Psi_{0j}^n\}$ for m=0 and 2 $Re\,\{\Psi_{mj}^n\}$ and -2 $Im\,\{\Psi_{mj}^n\}$ for m=1,2, or 3; where Ψ_{mj}^n are the Fourier coefficients of the streamfunction in our computation, and is discussed in detail in §VI.1. Excellent agreement for the two cases is found.

Furthermore, it should be noted that both the vertical extent of computation ($y_{max}\approx3$) and the density of grid points used in y (min$\{\Delta y\}$=0.001) are larger in the asymptotic solution (5.3.1) than those used in our numerical computation, which are $y_{max}\approx1$ and min$\{\Delta y\}$=0.007. The fact that our solution yield the same result as a computation using a larger and more detailed grid lends further support to the estimates proposed in §IV.6 and §IV.4 are adequate for an accurate simulation of the flow field.

In view of the good performance of our numerical scheme for the three different flow cases compared in this chapter, we shall move on to examine the solutions for the flow over ripples at different dimensionless flow parameters.
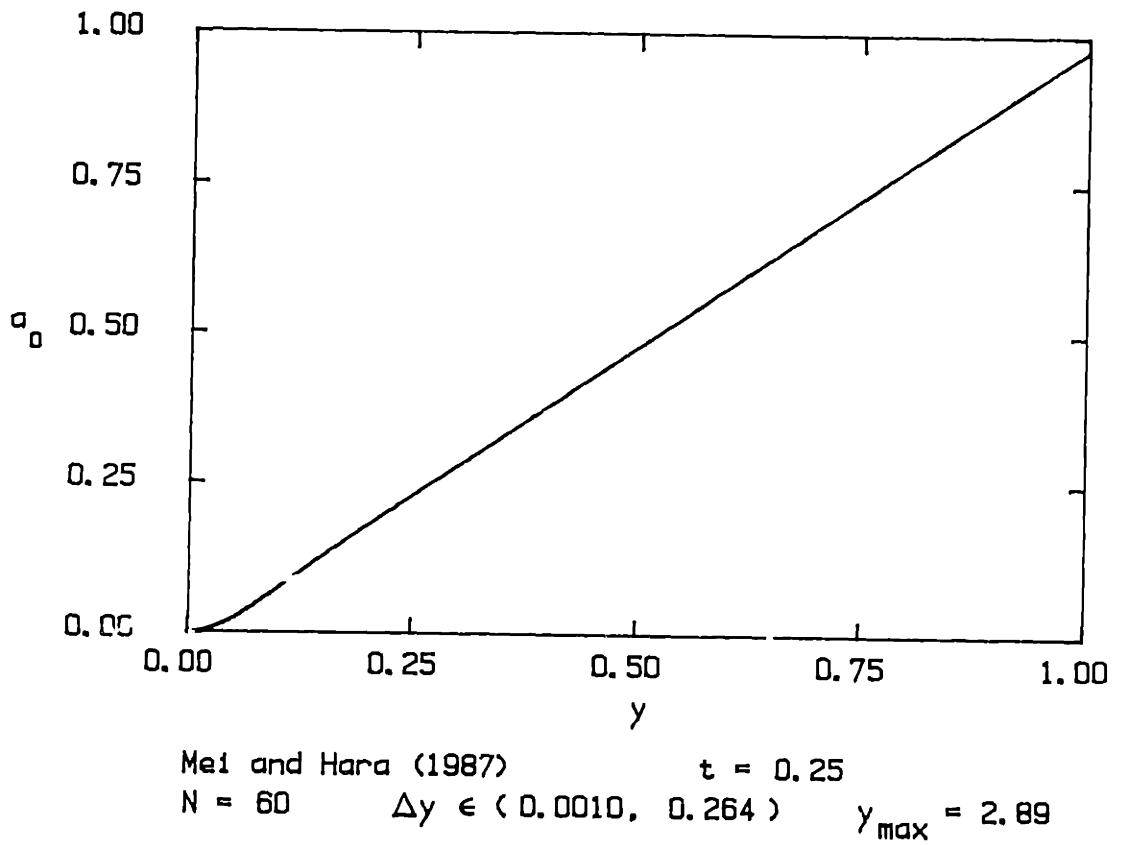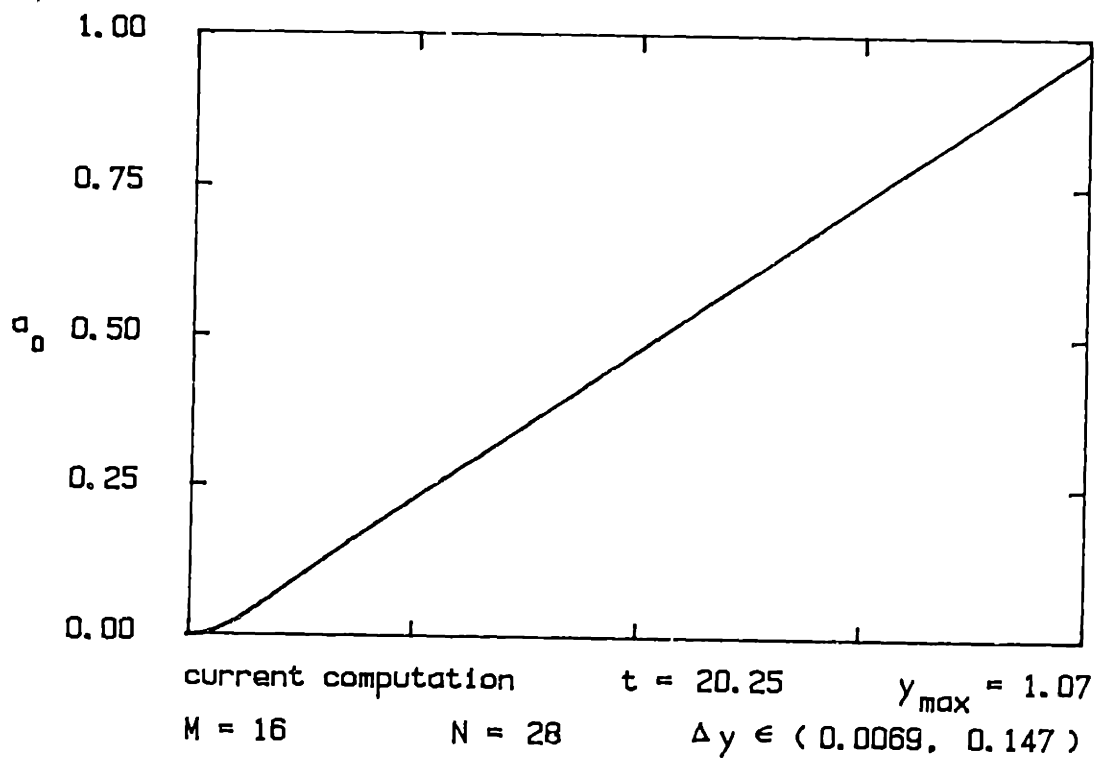
current computation　　　t = 20.25　　　y_{max} = 1.07

M = 16　　　　　N = 28　　　　$\Delta y \in$ (0.0069, 0.147)

Mei and Hara (1987)　　　t = 0.25

N = 60　　　$\Delta y \in$ (0.0010, 0.264)　　y_{max} = 2.89

Fig. V.3.1.　　Fourier coefficients of stream function

　　　　　　　R = 63　　　K = 4.0　　　e = 0.1

　　　a_0 defined in (6.1.3)

current computation   t = 20.50 y_{max} = 1.07

M = 16   N = 28 $\Delta y \in$ (0.0069, 0.147)

Mei and Hara (1987)   t = 0.50

N = 60 $\Delta y \in$ (0.0010, 0.264) y_{max} = 2.89

Fig. V.3.2.   Fourier coefficients of stream function

R = 63   K = 4.0   s = 0.1

a_0 defined in (6.1.3)

current computation   t = 20.25 y_{max} = 1.07

M = 16   N = 28 $\Delta y \in (\ 0.0069,\ 0.147\ )$

Mei and Hara (1987)   t = 0.25

N = 60 $\Delta y \in (\ 0.0010,\ 0.264\ )$ y_{max} = 2.89

Fig. V.3.3.   Fourier coefficients of stream function

R = 63   K = 4.0   s = 0.1

——— $2a_1$ — — — $2b_1$ defined in (6.1.3)

current computation   t = 20.50 y_{max} = 1.07

M = 16   N = 28 $\Delta y \in$ (0.0069, 0.147)

Mei and Hara (1987)   t = 0.50
N = 60 $\Delta y \in$ (0.0010, 0.264) y_{max} = 2.89
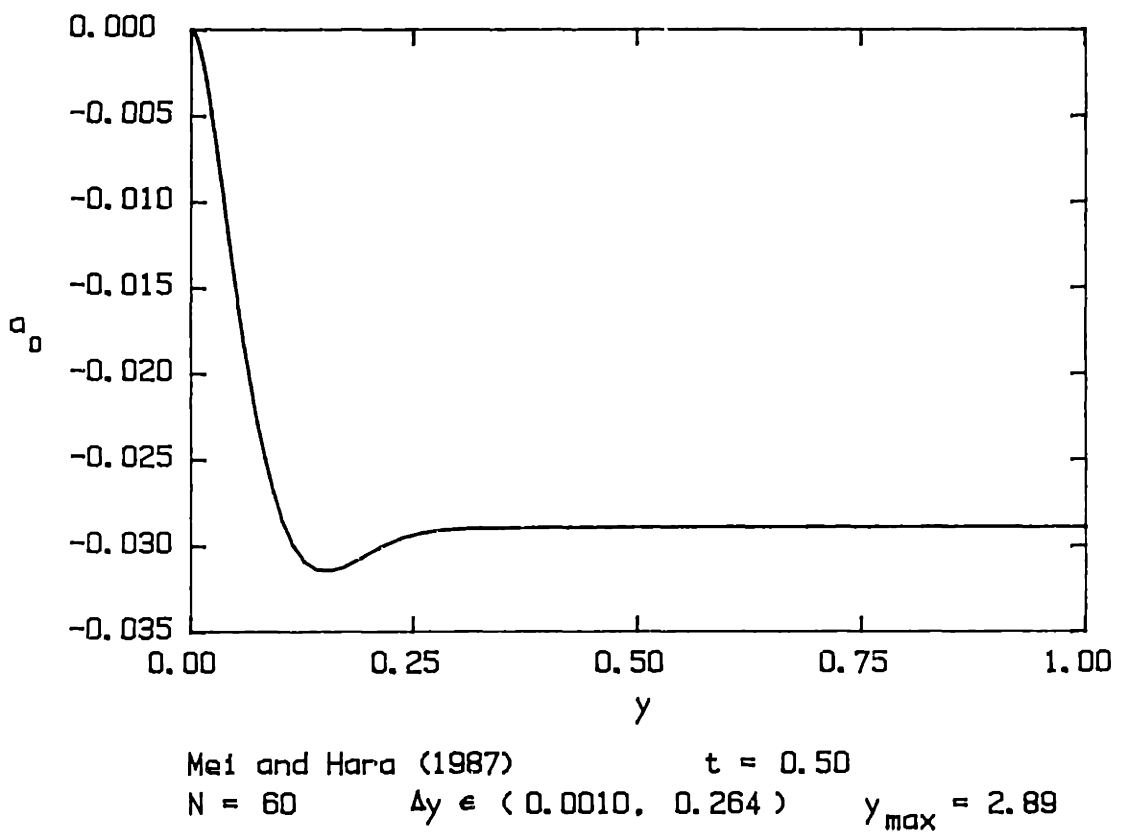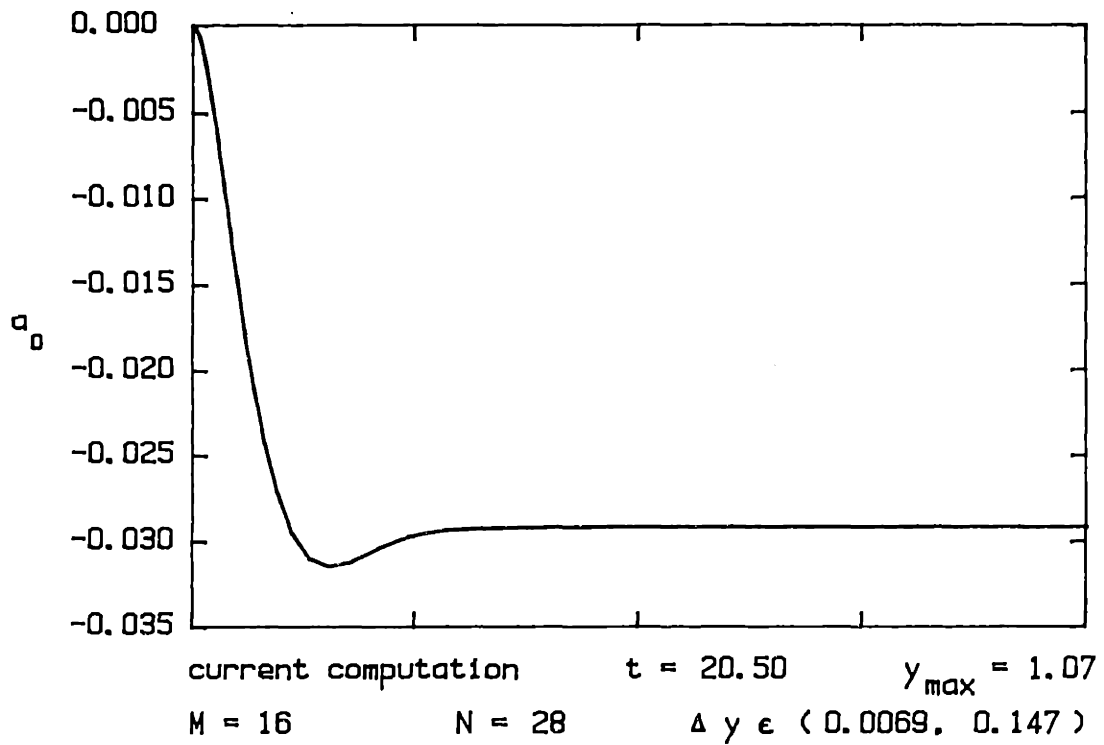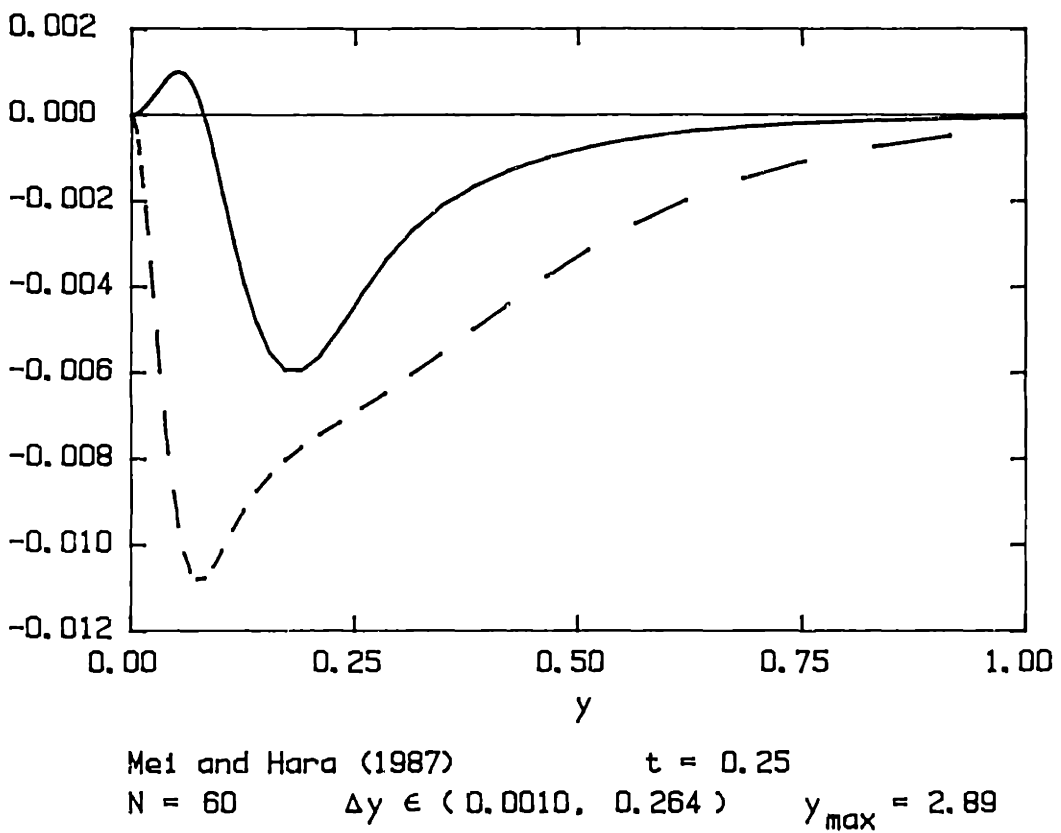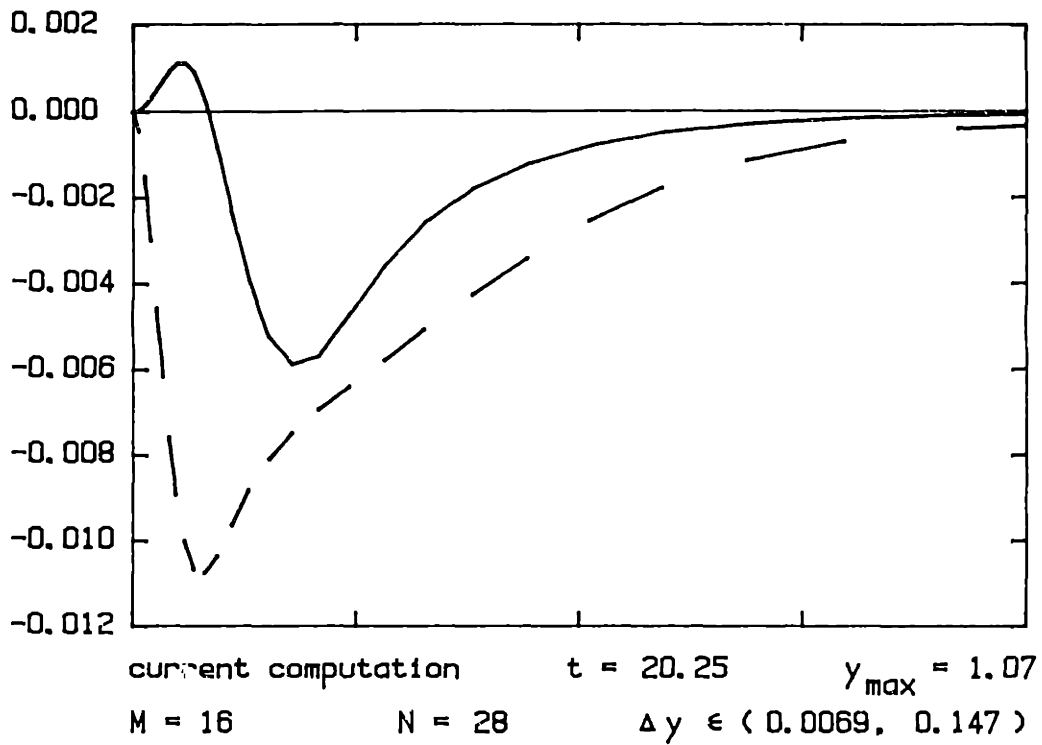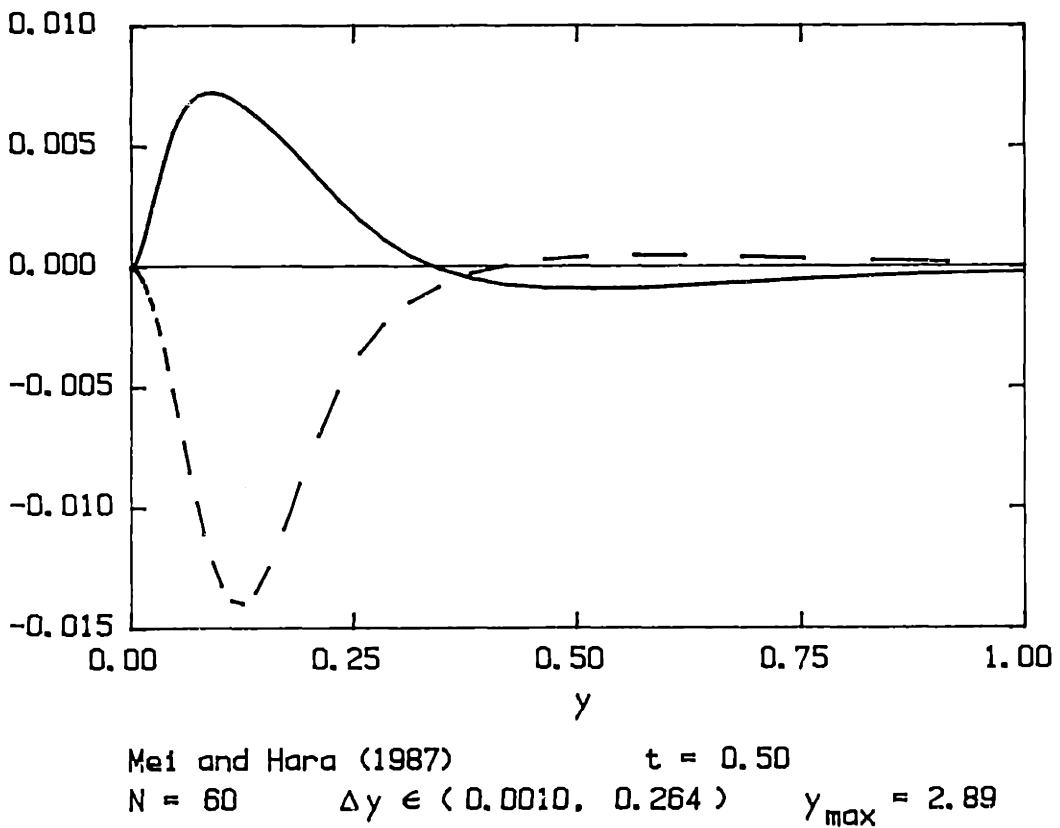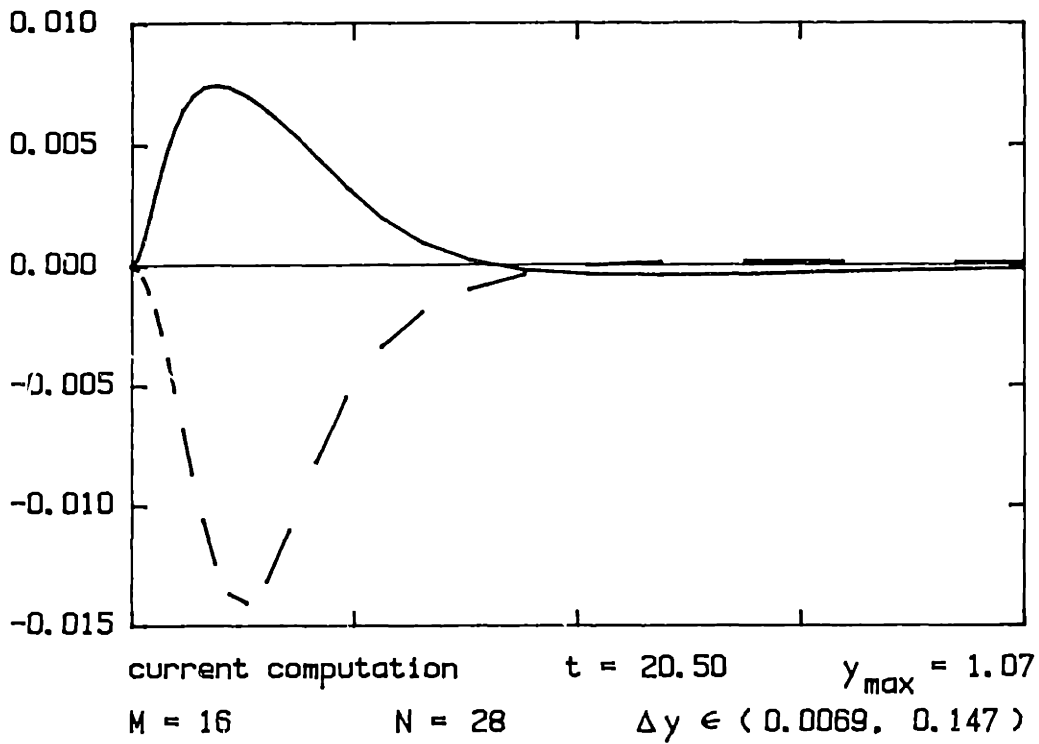
Fig. V.3.4.   Fourier coefficients of stream function
                R = 63   K = 4.0   s = 0.1
                ———— $2a_1$ — — — $2b_1$ defined in (6.1.3)

Chapter VI. Numerical Aspects of Results

Calculations were performed on a Cray-2 supercomputer at the Minnesota Supercomputing Center in Minneapolis, Minnesota, and a Cray X-MP/24 at the Naval Research Laboratory in Washington, District of Columbia, both with a single precision accuracy of 48 binary digits (approximately 14 decimal digits).

A ripple profile defined by (3.4.2) with s=2a/L=0.1 was studied. Three types of ambient flow were considered: (i) purely sinusoidal oscillation, (ii) steady current, and (iii) combination of sinusoidal oscillation and current. Their results will be discussed in Chapters VII, VIII, and IX, respectively. In this chapter we shall examine the numerical aspects of the results for the case of a purely sinusoidal ambient oscillation.

All computations were started at t=0 when both the streamfunction and the vorticity function were defined to be zero at all grid points. The far field velocities for the three types of ambient flow introduced above are defined as

$$\text{(i)} \quad U_\infty(t) = H(t) \sin 2\pi t, \tag{6.0.1}$$

$$\text{(ii)} \quad U_\infty(t) = \begin{cases} \sin t/r, & 0 < t \leq \tfrac{1}{2}r\pi \\ 1, & \tfrac{1}{2}r\pi < t \end{cases} \tag{6.0.2}$$

and

$$\text{(iii)} \quad U_\infty(t) = H(t) \sin 2\pi t + \begin{cases} c/U_0 \sin t, & 0 < t < \pi/2 \\ c/U_0, & \pi/2 \leq t \end{cases} \tag{6.0.3}$$

where H(t) is the Heaviside step function and r is a constant. Throughout this chapter, the acceleration (deceleration) phase of the wave cycle refers to the time when the magnitude of the ambient velocity is increasing (decreasing).

All runs were performed over one ripple length. Increasing the horizontal extent of computation to several ripples should not alter the spatial periodicity of the solution unless asymmetries in the initial condition or in adjacent ripple profiles

were introduced. This was confirmed in the purely oscillatory flow with R=250 and K=4.5, where the flow fields above each ripple were found to remain the same when computation was extended over two ripple lengths. Comparisons of these two flow fields will be omitted here.

Since an increase in the Reynolds number increases the complexity of the flow field, finer grids and smaller time–steps are also required. To limit computational expense, the Reynolds numbers studied were limited to 500 and below. A series of runs were then performed by varying either the Reynolds number or the Keulegan–Carpenter number while keeping one of the parameters constant. These dimensionless parameters are within the ranges $2.5 \leq K \leq 12$ and $15 \leq R \leq 500$, and are listed in Table VI.1.1. The entries in parentheses are computations for flows with identical dimensionless parameters but different grids, and serve as tests for convergence. The case of R=500 and K=4.5 with M=128 is computed only up to t=2 due to the huge computer cost required.

Further computational aspects of the numerical results will be discussed for the case defined by (6.0.1). Specifically, the vertical extent of computation, the extent of aliasing errors, the convergence to periodic solution, and energy balance will be discussed. The discussion for the flows defined by (6.0.2) and (6.0.3) are very similar and will be included in the corresponding chapters on the results.

§VI.1. Vertical extent of computation

As discussed in §IV.6, the vertical extent of computation has to be large enough such that both viscous effects and the velocity induced by vortical motion become negligible at the top boundary. The upper boundary in our runs were chosen to be approximately one ripple length above the mean bed elevation ($y_{max} \approx 1$), except for the two extremes of Reynolds number (R=15, 250, and 500) in which y_{max} chosen to be two.

Numerical confirmation that our choice is indeed sufficient will be demonstrated by examining the spectra of Fourier coefficients Ψ_{mj}^n of the streamfunction ψ defined in (4.1.4) as a function of y, and write

$$\Psi_{mj}^n = a_{mj}^n + ib_{mj}^n .$$
(6.1.1)

Since the streamfunction is real, the relationship

$$\Psi_{M-m,j}^n = \Psi_{mj}^{n\ *}$$
(6.1.2)

holds and (4.1.4) can be written as

$$\psi_{kj}^n = a_{0j}^n + \sum_{m=1}^{\frac{1}{2}M-1} (2a_{mj}^n\cos 2\pi mx_k - 2b_{mj}^n\sin 2\pi mx_k) + (-1)^{k-1}a_{\frac{1}{2}M,j}^n .$$
(6.1.3)

The grid points x_k and y_j have been defined in (4.1.1) and (4.1.2).

We plot the variables a_{0j}^n and $2a_{mj}^n$ and $-2b_{mj}^n$, m=1,2, and 3 as functions of y, and refer to them as the cosine and sine coefficients of the m-th harmonic at time t_n.[1] Coefficients of the zeroth harmonic a_{0j}^n are plotted in Fig. VI.1.0.i at a time when U_∞=1 and Fig. VI.1.0.ii when U_∞=0 for the flow with R=250 and K=4.5. Similarly the first to third harmonics are presented in Figs. VI.1.1.i,ii to VI.1.3.i,ii. All harmonics except the zeroth indeed decay to zero at less than one ripple length above the bed. At large y, the zeroth harmonic increases linearly with y when U_∞=1 and approaches a constant when U_∞=0, which corresponds respectively to a constant velocity and a zero velocity. The vertical velocity near the upper boundary therefore vanishes and the horizontal velocity is uniform in both directions. The choice of y_{max} is therefore adequate.

---

[1]These coefficients have also been plotted in §V.3 for the flow with R=63 and K=4.5 in the verification of our numerical scheme with semi–analytical asymptotic solutions.

§VI.2. Aliasing error

It is discussed in §IV.3 that grid spacing in the x direction has to be small enough such that the aliasing error is small. Since the flow field becomes more complex at higher Reynolds numbers, the amplitudes of the Fourier coefficients at high wavenumbers increase accordingly. The number of grid points used therefore increases from 16 for $R \leq 100$ to 32 for $125 \leq R \leq 250$ and 64 at $R = 500$. This growth of the Fourier coefficients at high wavenumbers is demonstrated in Fig VI.2.1 and VI.2.2 for $R = 15$ and 250 respectively, both with $K = 4.5$. The Fourier spectra of the streamfunctions $|\Psi^n_{mj}|$ defined in (4.1.4) at various values of y are plotted at two instants: when the ambient velocity is at its peak and when it is instantaneously at rest. The decay of $|\Psi^n_{mj}|$ with wavenumber is much slower at the higher Reynolds number.

It was stated in §IV.3 that, when convergence is achieved, then, for fixed n and j, the maximum of $|(im2\pi)^2\Psi^n_{mj}|$ for wavenumbers $2\pi m$ in the range $(\frac{1}{2}Q, Q)$ is less than 30% of that in $(0, \frac{1}{2}Q)$, and that $|Q^2\Psi^n_{\frac{1}{2}M,j}|$ is less than 10% of the maximum of $|(im2\pi)^2\Psi^n_{mj}|$ for $2\pi m$ in the range $(0, \frac{1}{2}Q)$, where Q is the Nyquist frequency (wavenumber). We now show the evidence. The magnitudes $|m^2\Psi^n_{mj}|$ are used because they correspond to $|\Omega^n_{mj}|$ and are plotted in Fig. VI.2.3 for the flow with $R = 250$ and $K = 4.5$ with $M = 32$ ($m = 16$). This observation is found to be common for the five different values of y examined. As an evidence that aliasing error is indeed small, we plot the new values of $|m^2\Psi^n_{mj}|$ for $M = 64$ at the same instants $t = 19.75$ and 20 and at approximately the same elevations y_j in Fig. VI.2.4. The magnitudes with m in the range (8,16), which corresponds to $(\frac{1}{2}Q, Q)$ in the previous case of $M = 32$, are not any smaller than the results computed using $M = 64$. As a further demonstration, the shear stress on the ripple surface deduced from the two results (with $M = 32$, 64) is plotted in Figs. VI.2.5 and VI.2.6. The agreement is excellent. The resolution using thirty-two grid points is therefore adequate for the

flow with R=250 and K=4.5.

On the other hand, considerable differences are found between the results with M=32 and 64 for the flow with R=500 and K=4.5, and the amplitudes of $|m^2 \Psi_{mj}^n|$ are found to be of the same order of magnitude over the entire range $0 < m \leq \frac{1}{2}M$ in the computation with the coarser grid. An accurate numerical solution for this flow therefore requires at least 64 grid points in the x direction. The test on convergence is carried only up to t=2 due to the huge computer cost in the computations with M=128.[2] Nevertheless, observations (i) and (ii) described in §IV.3 are found to hold up to the end of computation at t=20 with M=64, and is shown in Fig. VI.2.7. Although definite proof is lacking, this may suggest that the accuracy of the results in this case is acceptable with M=64.

As an aside, Figs. VI.2.1 and VI.2.2 also serve as an estimate of the convergence of the perturbation solution of oscillatory flow over ripple beds. Although different smallness parameters have been used by earlier authors: $a\sqrt{(\pi/\nu T)}$ by Lyne (1971), $2\pi a/L$ by Sleath (1974), and $U_0 T/L\pi$ by Kaneko and Honji (1979), the m-th order solution always introduces a new m-th harmonic in x of the form $\cos 2m\pi x$ and $\sin 2m\pi x$, which corresponds to the m-th Fourier coefficients of the streamfunction in (4.1.4). At a Reynolds number of 250, the amplitude of the fifth harmonic is roughly one-tenth that of the first harmonic, and therefore at least a fifth order solution is needed in the asymptotic solution such that the first truncated term in the asymptotic expansion is less than one-tenth of the zeroth-order term. At R=15, on the other hand, only a first-order solution is needed for the same accuracy.

---

[2]For M=128 and N=96, over one CPU–hour is required per wave period of computation.

§VI.3. Convergence to periodic solution

Before we examine the convergence to periodic solutions in the flows studied, it should be noted that the dimensionless amplitude of fluctuation of the streamfunction approximately equals the vertical extent y_{max} of computation, which varies between one and two in our runs. It can be deduced from the flow rate across any vertical cross section along the ripple profile, and a rough estimate can be obtained from the potential flow solution which gives $\psi_\infty \approx U_\infty y_{max}$. This gives the datum for judging the departure from periodicity using the variation in the streamfunction from one wave period to the next discussed in §4.7. Since $y_{max} > 1$ and thus $\|\psi_\infty\| > 1$ in all our computations, difference in the streamfunction values one wave period apart are insignificant if they are of a magnitude less than 0.001. This suggests that the solutions can be considered periodic if $\mathscr{E}_\infty$ is smaller than 0.001.

The variables $\mathscr{E}_1$ and $\mathscr{E}_\infty$ defined in (4.7.2), the mean and maximum of this departure, are plotted in Figs. VI.3.1 and VI.3.2 for the cases R=63, K=4 and R=250, K=4.5. As the Reynolds number increases, the computation has to be extended to a larger t before convergence to a periodic solution is achieved. The variable $\mathscr{E}_\infty$ has dropped below 10^{-3} after less than ten periods of computation for the flow with R=63 and K=4, while thirty periods have elapsed before the same convergence is reached in the flow with R=250 and K=4.5. This increase in the time for convergence is considerably higher than the estimate of (4.7.3).

We have also compared the rates of energy dissipation and the shear stress on the ripple for R=250 and K=4.5 in the intervals $19 < t < 20$ and $29 < t < 30$. They are found to agree to within 1% of the magnitude of the functions. The rate of energy dissipation between t=20 and 30 has been examined and found to be periodic. From Fig. VI.3.2, the values of $\mathscr{E}_\infty$ in these two time intervals are approximately 0.01 and 0.001 respectively. This suggests that solutions at a time when $\mathscr{E}_\infty < 0.01$

are representative of the final periodic solutions. This condition is less restrictive than the requirement of $\mathscr{E}_\infty < 0.001$ proposed at the beginning of this section.

For the flow at R=500, the difference in the streamfunction at two instants exactly one period apart no longer decrease monotonously with time but remain at some finite values. This departure is evident from Fig. VI.3.3, in which $\mathscr{E}_1$ and $\mathscr{E}_\infty$ remain above 0.01 after twenty periods of computation and show no tendency of decreasing. Aside from an earlier report by Sleath (1982) for an oscillatory flow over a ripple bed,[3] we are not aware of other reports of aperiodic solutions in oscillatory flows. This phenomenon is therefore of much interest if it can be proved beyond doubts. Unfortunately, the most reliable test of numerical accuracy, that of convergence with decreasing grid size, has been performed for only two periods due to the limitation on computer time for the case aperiodicity is observed. This, together with the high frequency oscillations found in the rate of change in kinetic energy in the test on the conservation of energy to be discussed in the next section, force us to view this result with reservations.

In the results reported in Chapter VII, solutions at a time when $\mathscr{E}_\infty < 0.01$ are accepted as final for cases in which $\mathscr{E}_\infty$ decreases monotonously. Otherwise we shall present solutions after a time when $\mathscr{E}_\infty$ decreases no further. At R=500 and K=4.5, this finite value of $\mathscr{E}_\infty$ does not exceed 0.1. The variations of various integrated values, for example the rate of energy dissipation and the pressure distribution along the ripple surface, do not change by more than 5% of its mean value.

It is possible that $\mathscr{E}_\infty$ will increase further with R, leading ultimately to chaos or turbulence. This agrees with the views expressed in some experimental studies on flow over ripple beds, where turbulence is defined as variabilities in the flow fields

---

[3]Our reservations on the accuracy of the numerical solution reported by Sleath has been discussed in §II.3 and §VII.6.2.1. The aperiodic behavior may therefore not be a true characteristic of the flows he examined.

from one wave period to the next (for example Sleath, 1974 and Kemp and Simons, 1982). Since a great amount of computer time would be needed to explore these possibilities, flows at higher Reynolds numbers will not be pursued here.

§VI.4. Energy balance

The numerical accuracy of the solution is checked by considering energy conservation in the flow field. For an incompressible Newtonian fluid in the absence of net changes in potential energy and net work done through shear stresses at the boundaries, the rate of pressure work done $\mathscr{P}$ on a material volume equals the sum of the rate of change in kinetic energy $\mathscr{K}$ and the rate of energy dissipation $\mathscr{D}$. In a spatially periodic flow, the material volume can be replaced by a fixed control volume spanning one ripple length, and the mathematical expression of these quantities in terms of the streamfunction and vorticity function have been derived in §III.3. From (3.3.11), the equation for energy budget can be written as

$$\frac{1}{K}\psi_\infty \frac{dU_\infty}{dt} - \frac{1}{2K}\frac{d}{dt}[\psi_\infty U_\infty + \int_0^{y_{max}}dy \int_0^1 dx\, J\psi\omega] - \frac{s}{R}\int_0^{y_{max}}dy\int_0^1 dx\, J\omega^2$$
$$= 0 \qquad\qquad (6.4.1)$$

in which the first, second, and third term correspond to $\mathscr{P}$, $\mathscr{K}$, and $\mathscr{D}$ respectively.

Since the values of $\mathscr{P}$ and $\mathscr{K}$ are an order of magnitude larger than $\mathscr{D}$ and increase monotonously with the vertical extent of the control volume, the differences $\mathscr{P}_1 = \mathscr{P} - \mathscr{P}_p$ and $\mathscr{K}_1 = \mathscr{K} - \mathscr{K}_p$, where $\mathscr{P}_p$ and $\mathscr{K}_p$ are the values of $\mathscr{P}$ and $\mathscr{K}$ in the corresponding potential flow, will be studied instead. The values of $\mathscr{P}$ and $\mathscr{K}$ in potential flows are given by

$$\mathscr{P}_p = \mathscr{K}_p = \frac{1}{K}\psi_\infty \frac{dU_\infty}{dt} = \frac{\pi}{K}y_{max}\sin 4\pi t \qquad\qquad (6.4.2)$$

for $U_\infty = \sin 2\pi t$.

The functions $\mathscr{P}_1$, $\mathscr{K}_1$, $\mathscr{D}$, and

$$\Delta = \mathscr{P}_1 - \mathscr{K}_1 - \mathscr{D} \tag{6.4.3}$$

are plotted for three flow cases with K=4.5 and R=50, 125, and 500 in Figs. VI.4.1 to VI.4.3. The vertical scale is in units of $\overline{\mathscr{D}_s}=\frac{1}{2}\sqrt{(\pi s/KR)}$, which is the mean rate of energy dissipation of the corresponding flow over a plane bed.

The agreement on energy balance is excellent for the case with the lowest Reynolds numbers of 50, Fig. VI.4.1. When R is increased to 125, Fig. VI.4.2, however, the value of Δ assumes finite values and varies from zero to up to 15% of the amplitude of energy dissipation. The disagreement gets worse when R=500, Fig. VI.4.3, in which the magnitude of the error Δ is comprable to the amplitude of $\mathscr{D}$. This discrepancy is large at the same instants as high frequency oscillations in $\mathscr{K}_1$, and since the magnitudes of the individual 'bursts' of finite Δ approximately equal the "jaggedness" of $\mathscr{K}_1$, the latter appears to be the cause of the discrepancy.[4]

There are two likely reasons for the inaccuracy in computed values of $\mathscr{K}_1$, or $\mathscr{K}$: (i) error in taking the time derivative, and/or (ii) error in the two-dimensional integration of the function $J\psi\omega$ in (3.3.10). A third-order one-sided difference scheme has been used to approximate the time-derivative, and comparisons with second-order and fourth-order time-derivatives show negligible differnces which are much less than the magnitude of the discepancy. The first possibility is therefore ruled out.

The integral of function $J\psi\omega$ is computed with a numerical quadrature scheme based on a bicubic spline intrapolation, implemented with an International Mathematics and Statistics Library (IMSL) subroutine DBCQDU. For a natural

---

[4]The other possibility, of course, is that the computed values of ψ, and thus ω, are inaccurate. This is unlikely for two counts. Firstly, erratic behavior is limited only to the computed values of $\mathscr{K}_1$ but not the other two functions $\mathscr{A}$ and $\mathscr{D}$, even though all three functions are computed from the values of ψ and ω. Secondly, numerical instabilities and aliasing error and, to a lesser degree, truncation and roundoff errors, usually grow in time. It is found, however, that the error Δ in the very first period of computation is roughly of the same magnitude as that after twenty periods of computation.

one-dimensional cubic spline, the error in $\int_{x_1}^{x_2} dx\, f(x)$ is bounded by

$(x_2-x_1)\Delta x \{\Delta x \int_{x_1}^{x_2} dx\, [\frac{d^2 f}{dx^2}]^2\}^{\frac{1}{2}}$ (Ralston & Rabinowitz, 1978). A sizable error is

therefore possible if high frequency fluctuations are present in the integrand.

To demonstrate that the inaccuracy in the numerical quadrature in (3.3.10) is indeed the cause of the discrepancy, we will show that a reduction in the grid size leads to a smoother function $\mathcal{K}_1$ and decreases the error Δ, while leaving the other hydrodynamic quantities unchanged. The error Δ for the flow with R=500 is therefore computed from the values of $\mathcal{P}_1$, $\mathcal{K}_1$, and $\mathcal{D}$ obtained, at a great expense of computer time, and for $0<t<2$ only using grid spacings in x one half of the original. It is shown in Fig. VI.4.4 and the magnitude of the error estimate Δ indeed diminishes considerably to under 8% of the amplitude of $\mathcal{D}$. Note that the curves of $\mathcal{P}_1$ and $\mathcal{D}$ remain unchanged.

To confirm that this improvement is due to better accuracy in the computed values of $\mathcal{K}$ (or $\mathcal{K}_1$) but not different streamfunction values, the shear stresses on the ripple surface from computations using grids of M=64, N=72 and M=128, N=96 are plotted in Figs. VI.4.5 and VI.4.6, and the agreement is excellent. This comparison also serves to demonstrate the convergence of the numerical solutions.

As a further demonstration that the error in the computed values of the time rate of change in the kinetic energy is not due to numerical inaccuracies in ψ and ω, the results from using M=64 are plotted in Fig. VI.4.7 after twenty periods of computation. The amplitudes of these high frequency oscillations are found to be no larger than those at the beginning of computation shown in Fig. VI.4.3.

As a matter of fact, this problem is also found in the flow with R=250 and K=4.5 using M=32, which has shown to be accurate in §VI.3. Similar oscillations in $\mathcal{K}_1$ are found (Fig. VI.4.8) at a time when the solution has become periodic in time. Further proofs that the solutions for R=250 and K=4.5 using M=32 is in

order here. The rates of pressure work $\mathscr{P}_1$, change in kinetic energy $\mathscr{K}_1$, and viscous dissipation $\mathscr{D}$ at $18 \leq t \leq 20$ from the two results, using M=32 and M=64, are plotted in Figs. VI.4.9 and VI.4.10. Once again, both $\mathscr{P}_1$ and $\mathscr{D}$ in the two computations are the same, and the high frequency oscillations in $\mathscr{K}_1$ from the results using M=32 are smoothed out at the corresponding instants in the results using M=64.

That energy balance is not satisfied at high R is therefore due to inaccuracies in the numerical quadrature of $\mathscr{K}$ but not errors in ψ or ω and does not seem fatal. Since $\mathscr{K}$ can be obtained from the difference between $\mathscr{P}$ and $\mathscr{D}$, and that both functions can be computed accurately by considering energy balance, no further attempts will be made to improve the estimate of $\mathscr{K}$ at higher Reynolds numbers using (3.3.10).

Table VI.1.1. Computational data   s = 0.1

(1) Purely oscillatory ambient flow

K	R	M	N	y_{max}	Δy_{min}	Δy_{max}
4.5	15	16	31	2.05	0.0124	0.254
4.5	50	16	29	1.11	0.0081	0.135
4.0	63	16	28	1.07	0.0069	0.147
4.5	100	16	29	1.11	0.0081	0.135
↓	↓	32	39	1.09	0.0058	0.094
4.5	125	32	39	1.08	0.0052	0.097
6.0	↓	↓	41	1.06	0.0050	0.092
4.5	150	32	39	1.10	0.0047	0.103
3.0	175	32	49	1.01	0.0036	0.072
4.5			38	1.02	0.0044	0.100
6.5			43	1.34	0.0052	0.112
9.0			37	1.31	0.0062	0.129
12.0	↓	↓	45	1.33	0.0071	0.091
2.5	250	32	51	1.06	0.0034	0.072
4.5		↓	57	2.08	0.0036	0.151
↓		64	62	2.00	0.0036	0.128
6.0		32	50	2.08	0.0042	0.175
9.0	↓	↓	42	2.16	0.0052	0.223
4.5	500	64	72	2.03	0.0026	0.118
↓	↓	128	96	2.03	0.0026	0.078

(2) Purely oscillatory ambient flow $R_c = 250, 1000$

M	N	y_{max}	Δy_{min}	Δy_{max}
32	57	2.08	0.0036	0.151

(3) Combination of wave and current

K	R	M	N	y_{max}	Δy_{min}	Δy_{max}	c/U_0
4.5	250	32	57	2.08	0.0036	0.151	1,2,4
9.0	↓	↓	42	2.16	0.0052	0.223	1
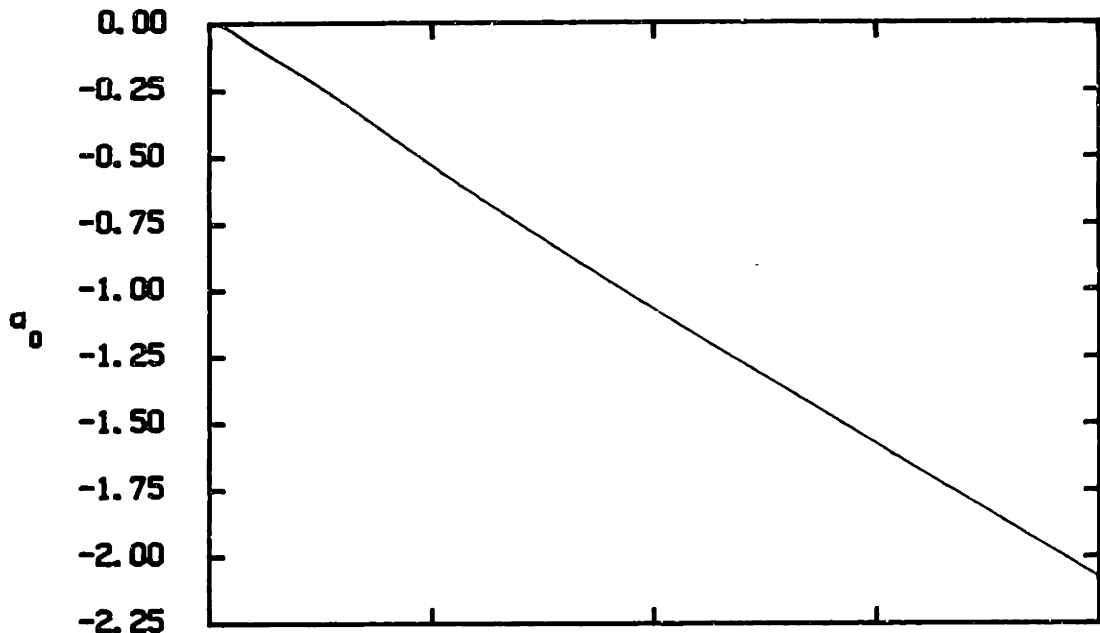
i.   t = P+0.75
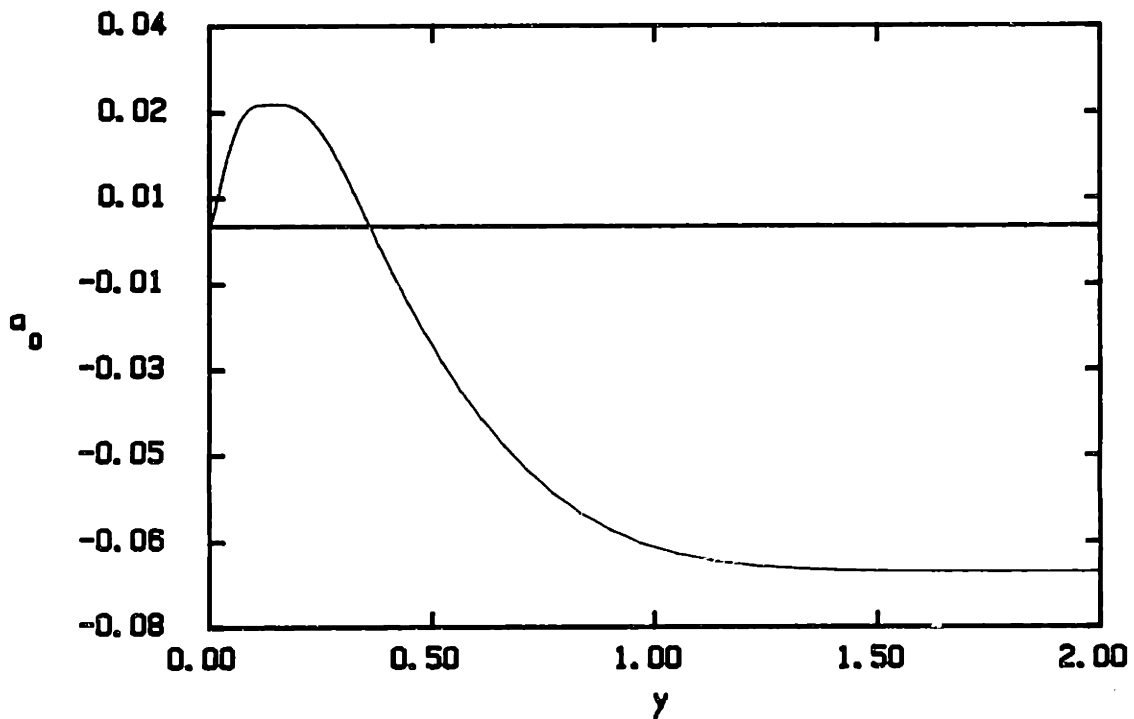
ii.   t = P+1.00

Fig. VI.1.0.   Fourier coefficients of stream function
R = 250   K = 4.5   e = 0.1
M = 32   N = 57   P = 34
dy = (0.0036, 0.151) y_{max} = 2.08

a_0 defined in (6.1.3)
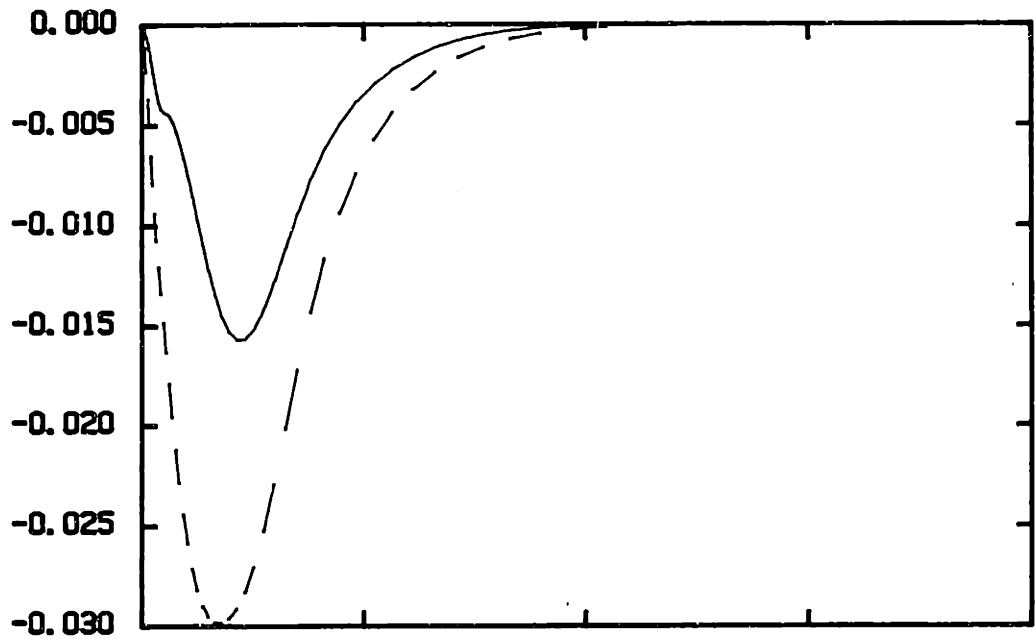
i.   t = P+0.75
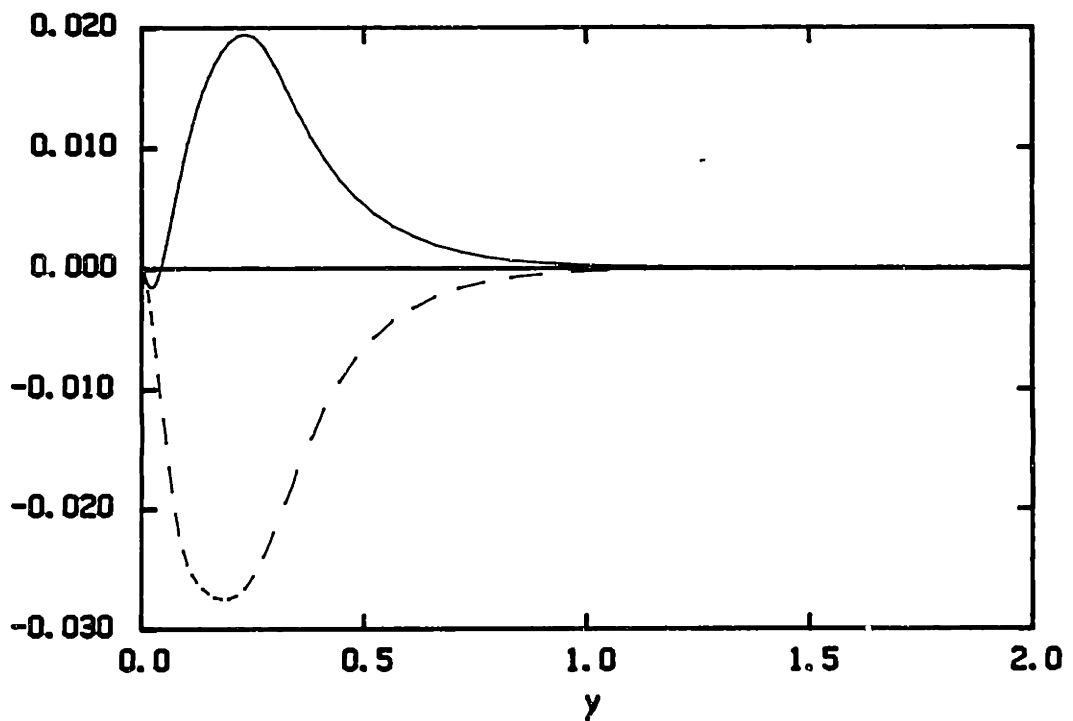
ii.   t = P+1.00

Fig. VI.1.1.   Fourier coefficients of stream function

R = 250   K = 4.5   e = 0.1
M = 32   N = 57   P = 34
dy = (0.0036, 0.151) y_{max} = 2.08
———— $2a_1$ — — — $2b_1$ defined in (6.1.3)
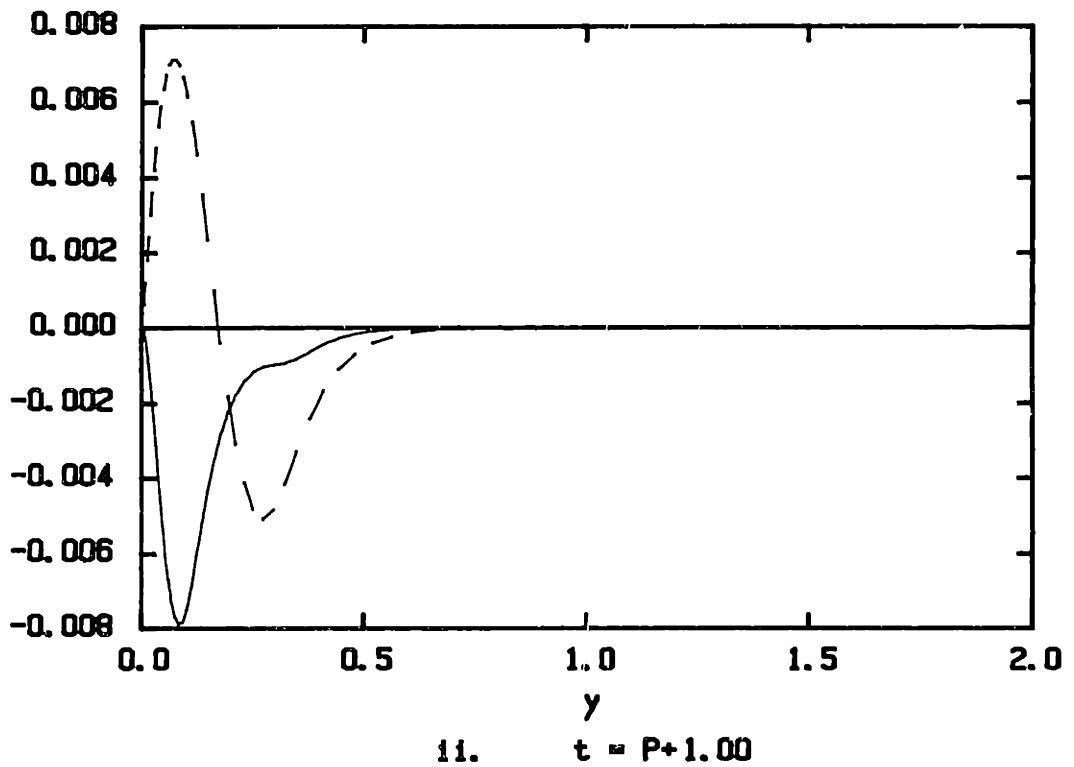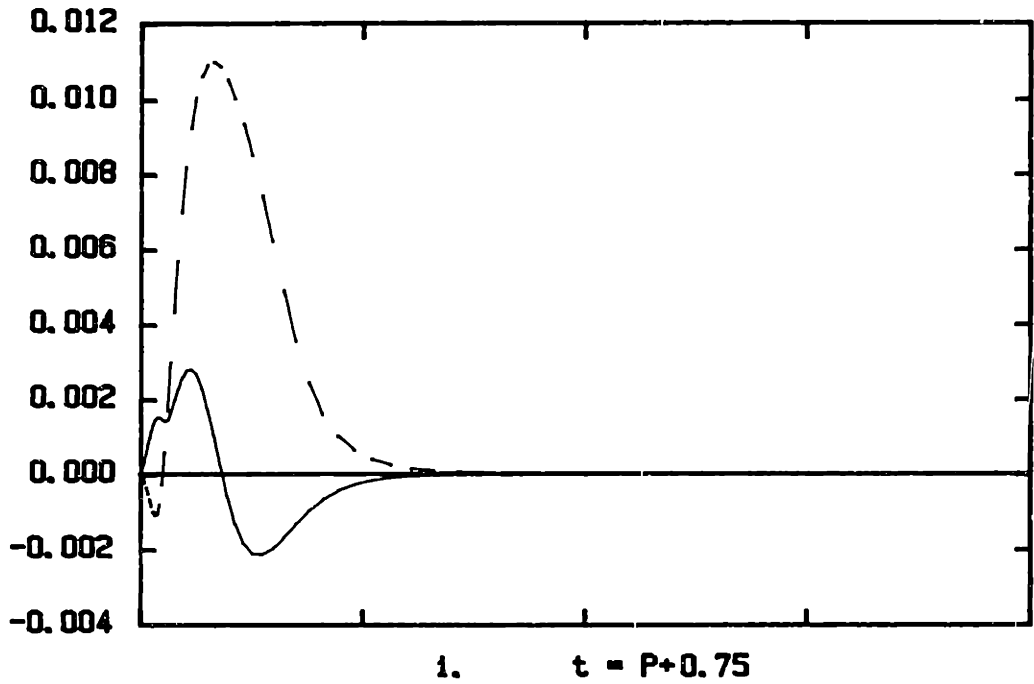
1.   t = P+0.75

ii.   t = P+1.00

Fig. VI.1.2.   Fourier coefficients of stream function

R = 250   K = 4.5   e = 0.1
M = 32   N = 57   P = 34
dy = (0.0036, 0.151) y_{max} = 2.08
———— $2a_2$ — — — $2b_2$ defined in (6.1.3)

103
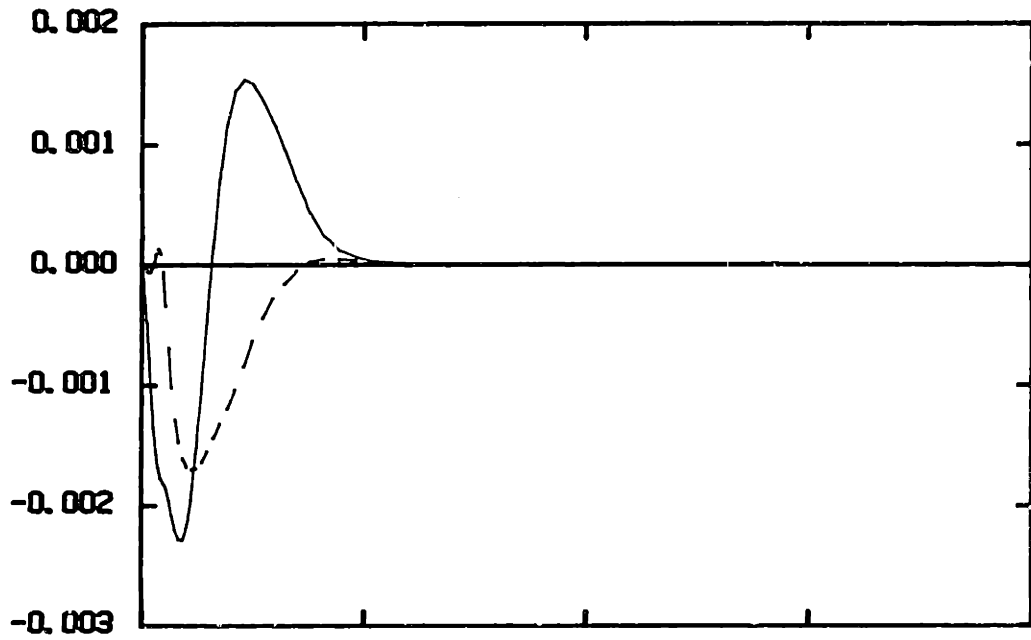
i.   t = P+0.75
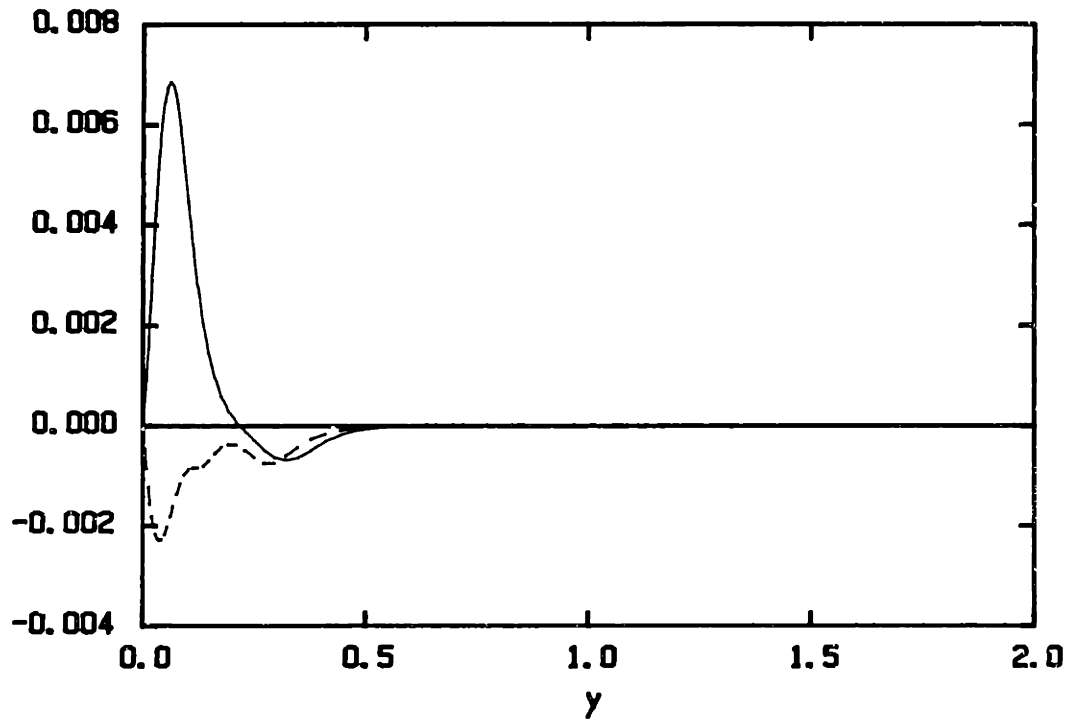
ii.   t = P+1.00

Fig. VI.1.3.   Fourier coefficients of stream function

R = 250   K = 4.5   e = 0.1

M = 32   N = 57   P = 34

dy = (0.0036, 0.151) y_{max} = 2.08

———— $2a_3$ — — — - $2b_3$ defined in (6.1.3)
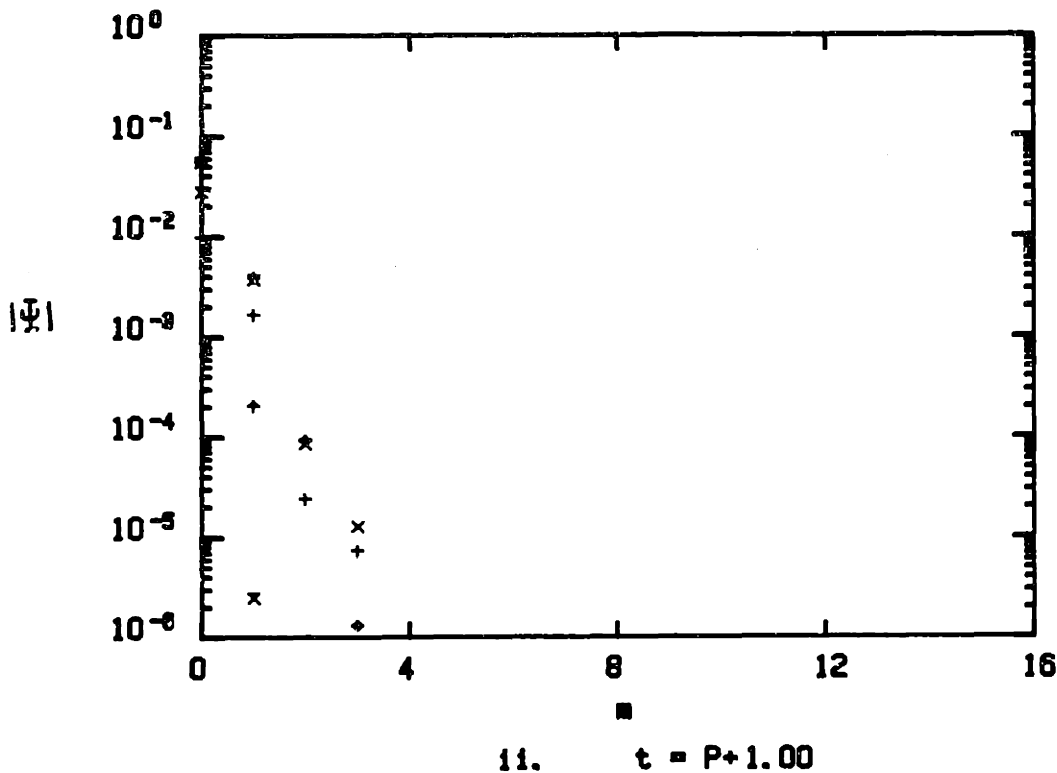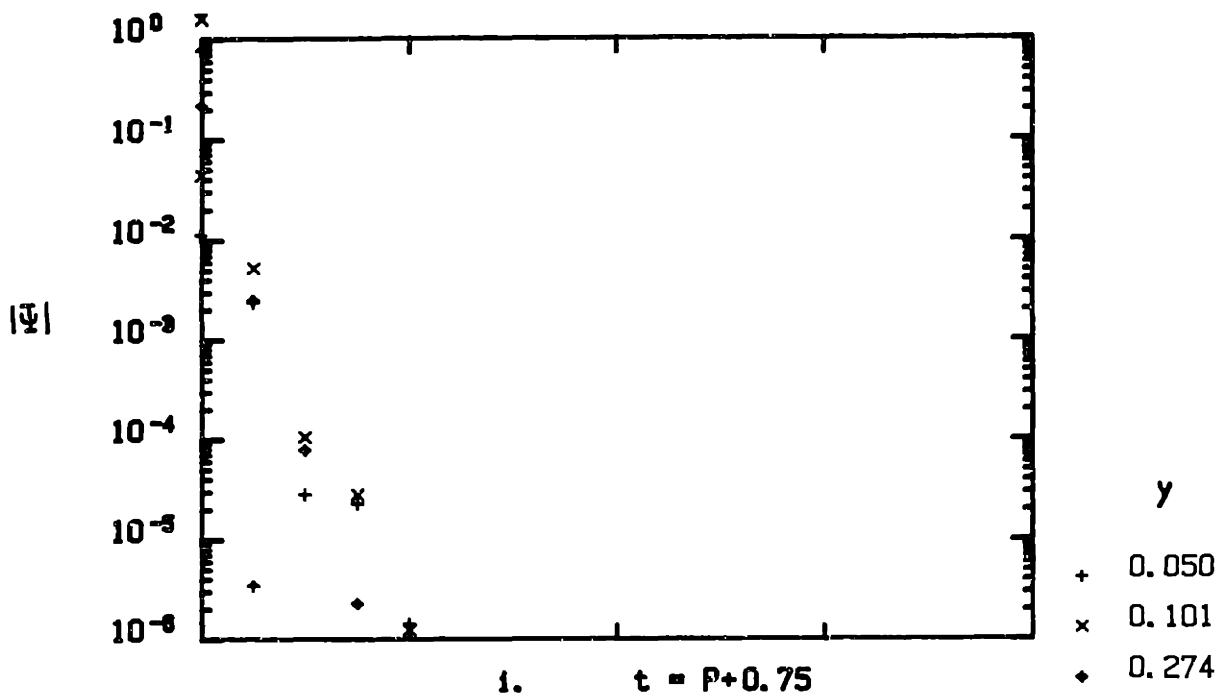
Fig. VI.2.1. Magnitudes of Fourier coefficients of streamfunction

R = 15   K = 4.5   e = 0.1
M = 16   N = 31   P = 29
dy = (0.0124, 0.254) y_{max} = 2.05
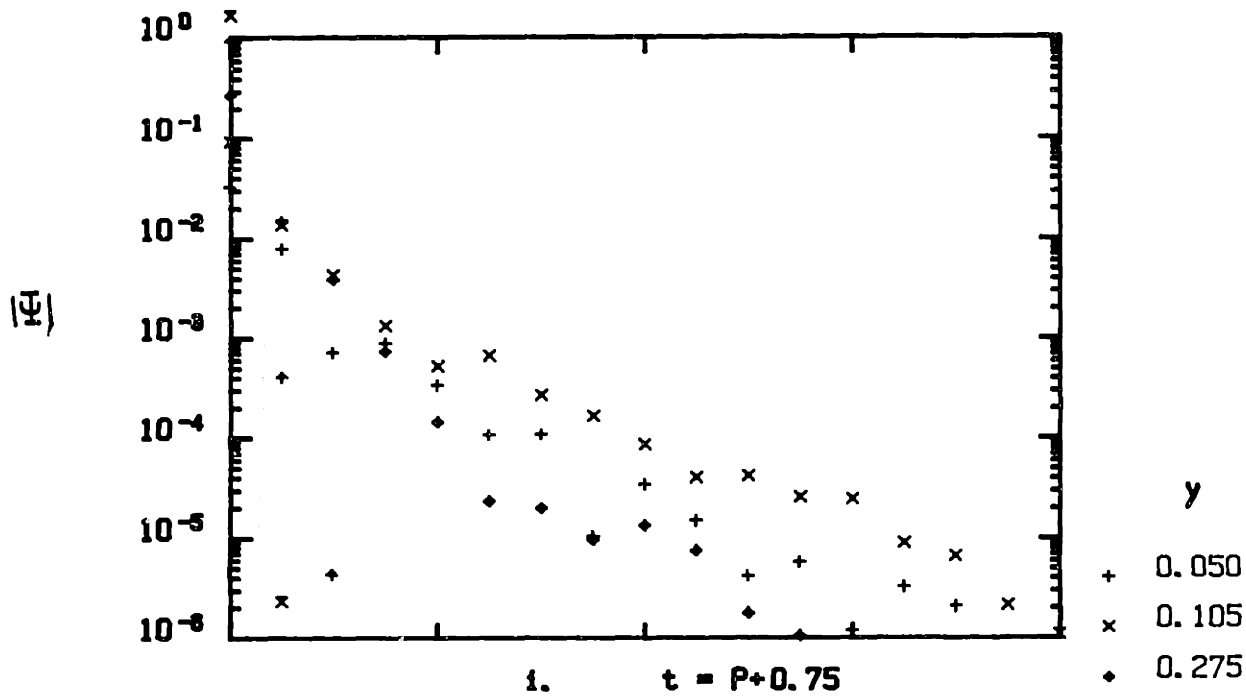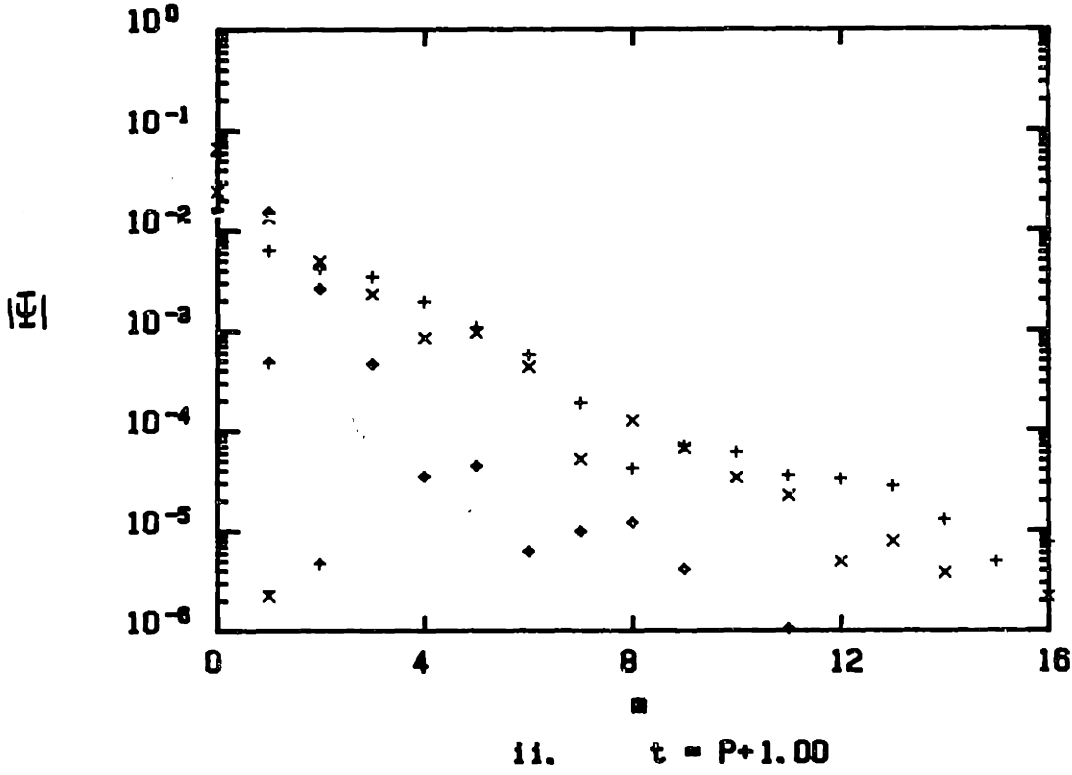
Fig. VI.2.2. Magnitudes of Fourier coefficients of streamfunction

R = 250   K = 4.5   e = 0.1
M = 32   N = 57   P = 29
dy = (0.0036, 0.151) y_{max} = 2.08
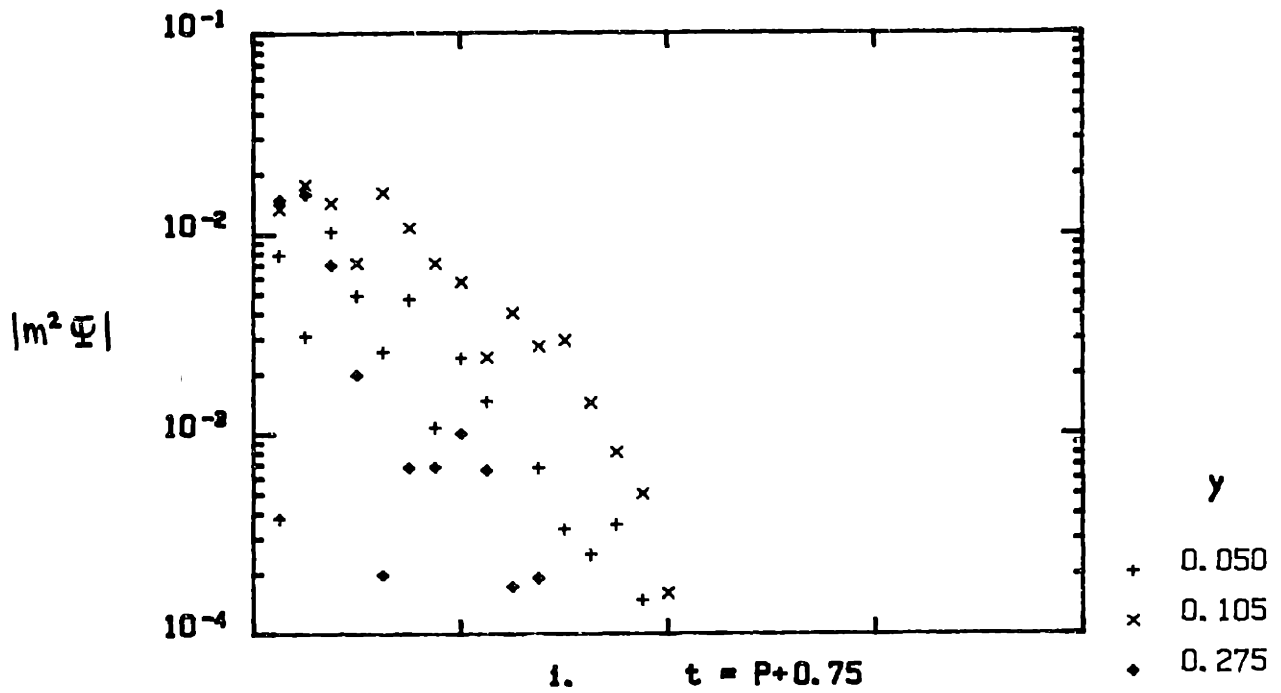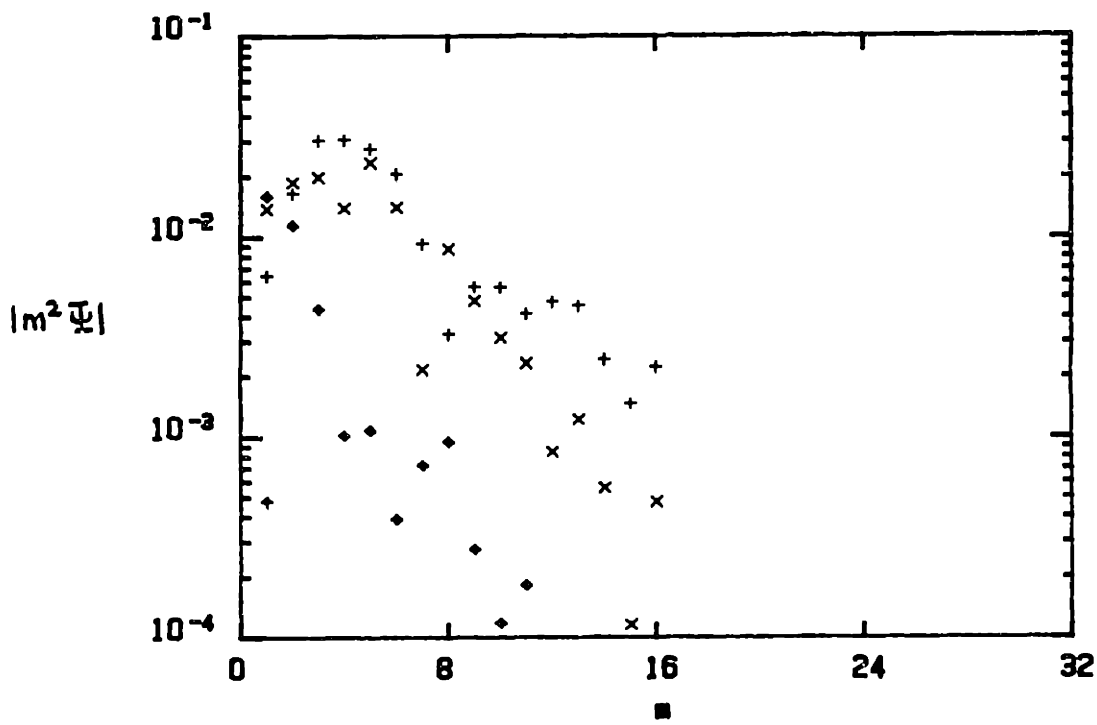
Fig. VI.2.3. Magnitudes of Fourier coefficients of
streamfunction multiplied by m**2
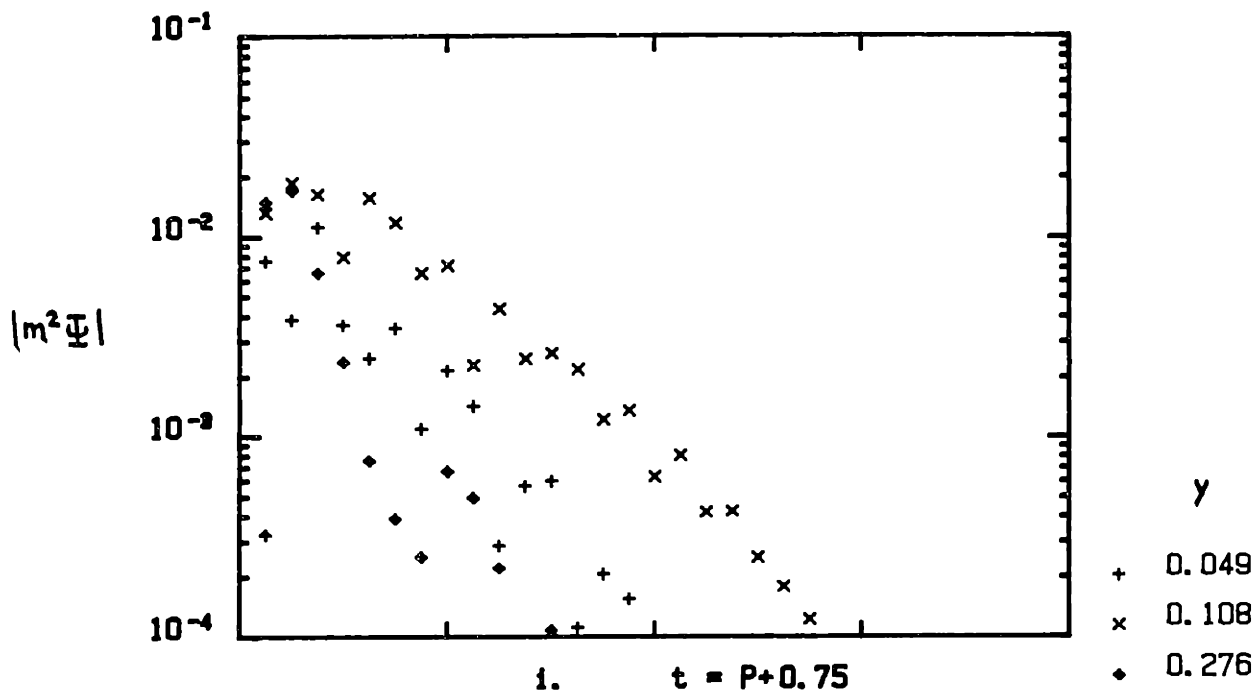
R = 250   K = 4.5   s = 0.1
M = 32   N = 57   P = 19
dy = (0.0036, 0.151) y_{max} = 2.08
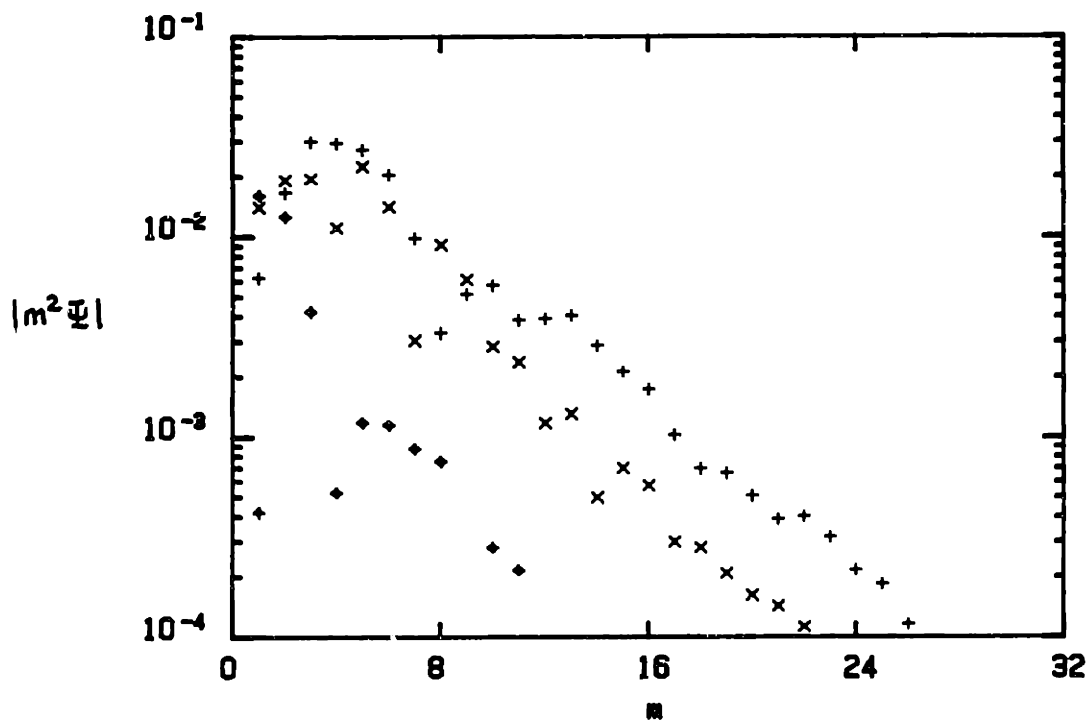
Fig. VI.2.4.   Magnitudes of Fourier coefficients of
streamfunction multiplied by m**2

R = 250   K = 4.5   e = 0.1
M = 64   N = 62   P = 19
dy = (0.0036, 0.128)   y_max = 2.00
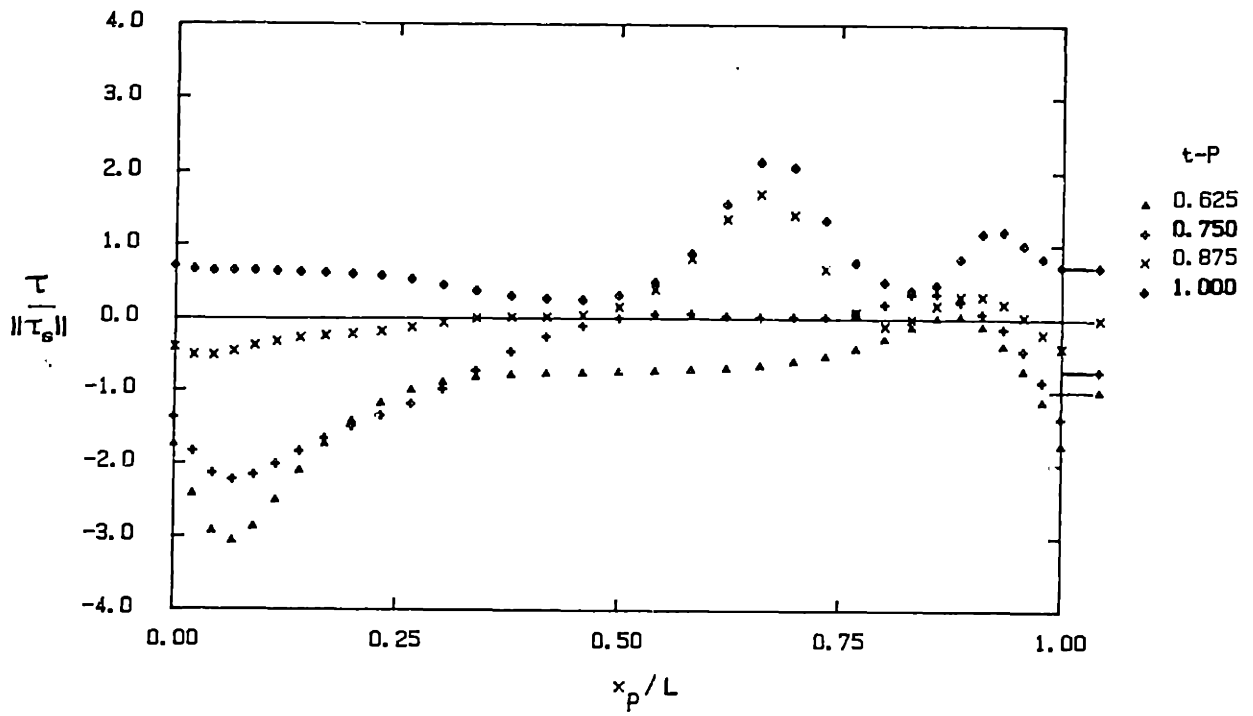
Fig. VI.2.5.　　Shear stress on ripple surface

R = 250　　K = 4.5　　s = 0.1　　　　M = 32　　N = 57　　　P = 19
dy : (0.0036 , 0.151)　　　　y_{max} = 2.08　　　$\|\tau_s\|$= 0.024
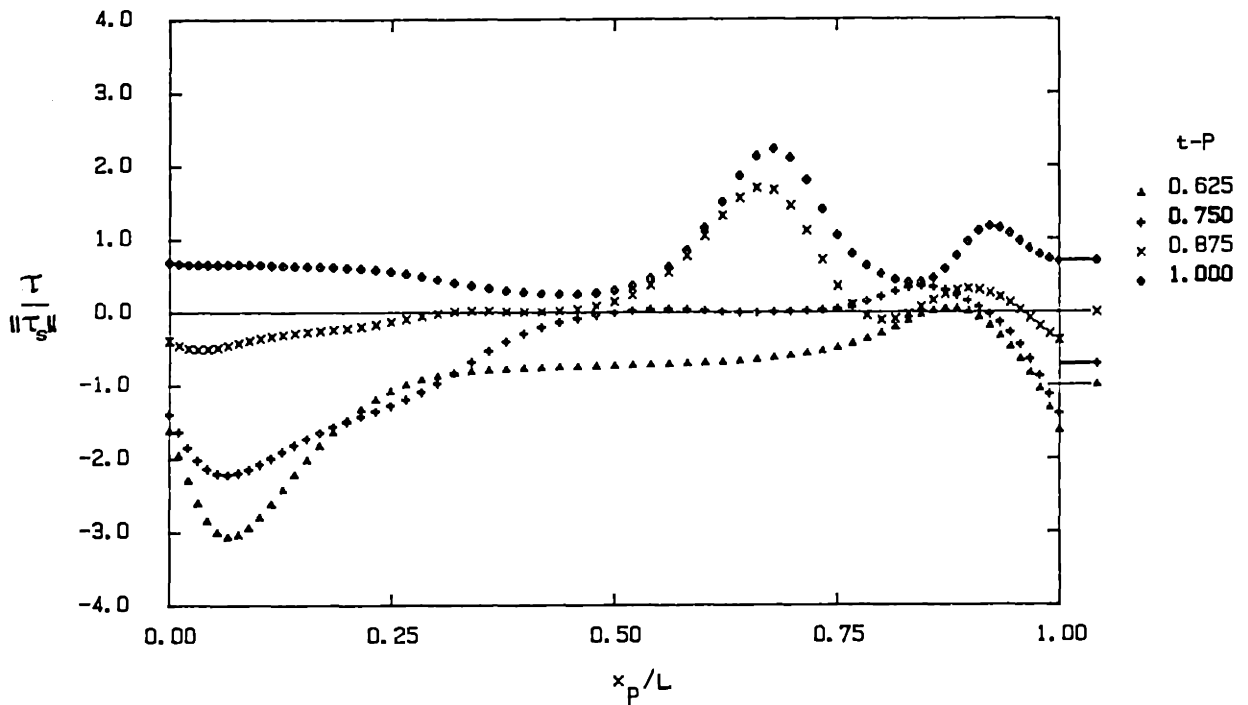
Fig. VI.2.6.　　Shear stress on ripple surface

R = 250　　K = 4.5　　s = 0.1　　　　M = 64　　N = 62　　　P = 19
dy : (0.0036 , 0.128)　　　　y_{max} = 2.00　　　$\|\tau_s\|$= 0.024

109
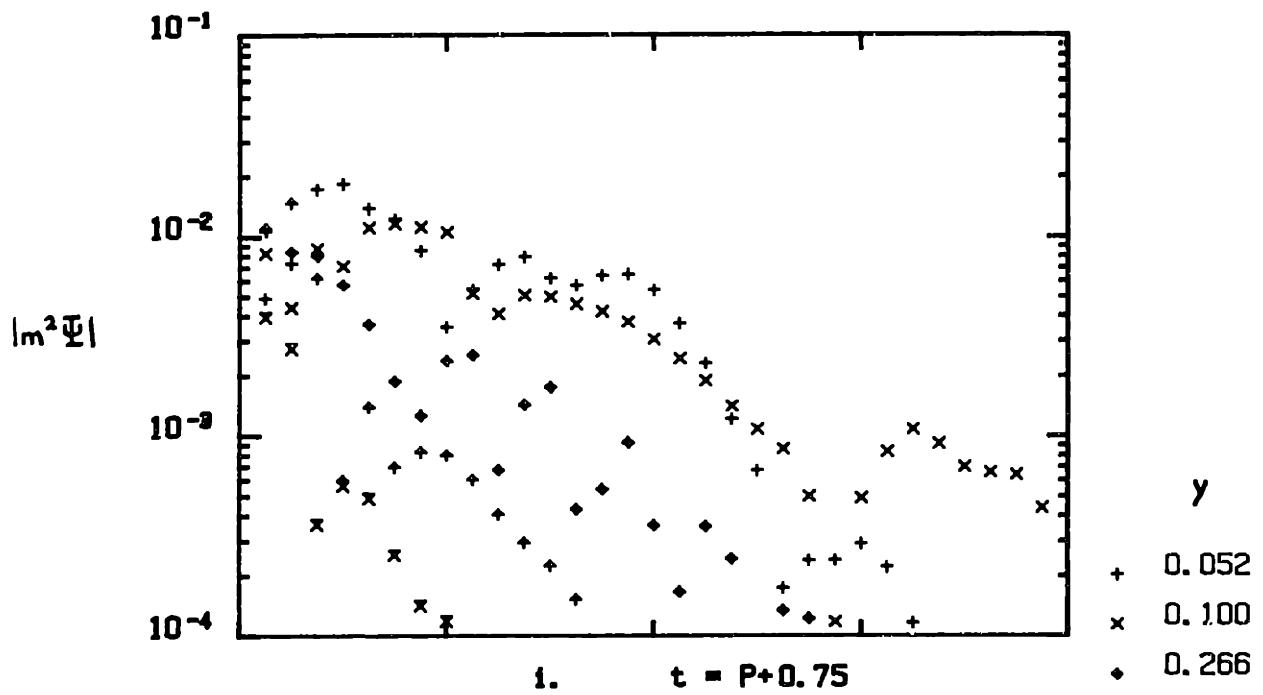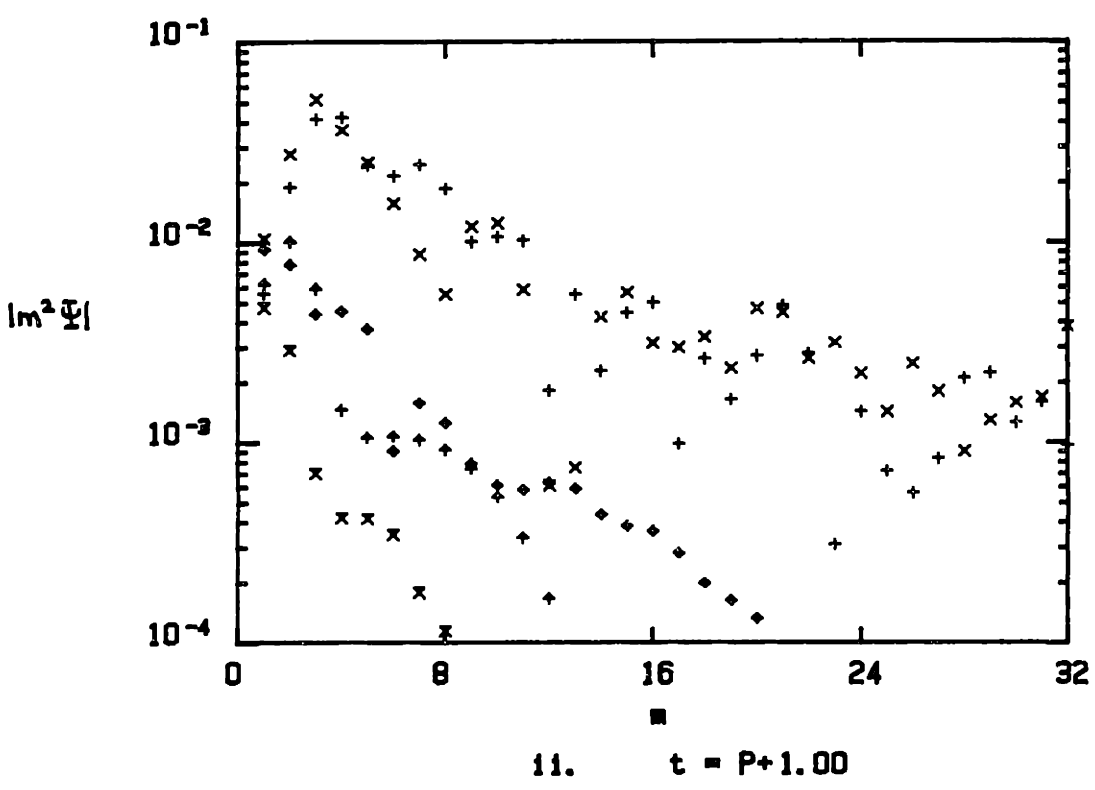
Fig. VI.2.7. Magnitudes of Fourier coefficients of
streamfunction multiplied by m**2

R = 500   K = 4.5   e = 0.1
M = 64   N = 72   P = 19
dy = (0.0026, 0.118) y_{max} = 2.03
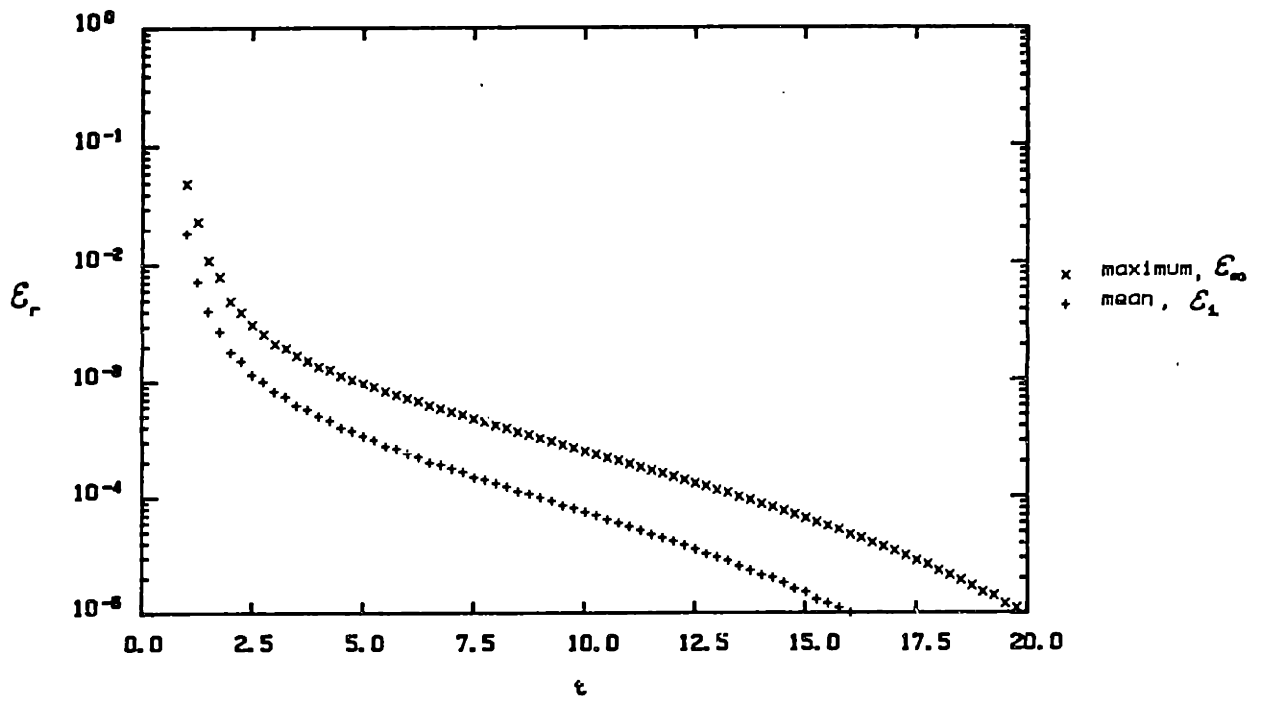
Fig. VI.3.1.   Variation of streamfunction values one wave period apart as
defined in (4.7.2)
R = 63   K = 4.0   s = 0.1   M = 16   N = 28
dy = (0.0069, 0.147) y_{max} = 1.07
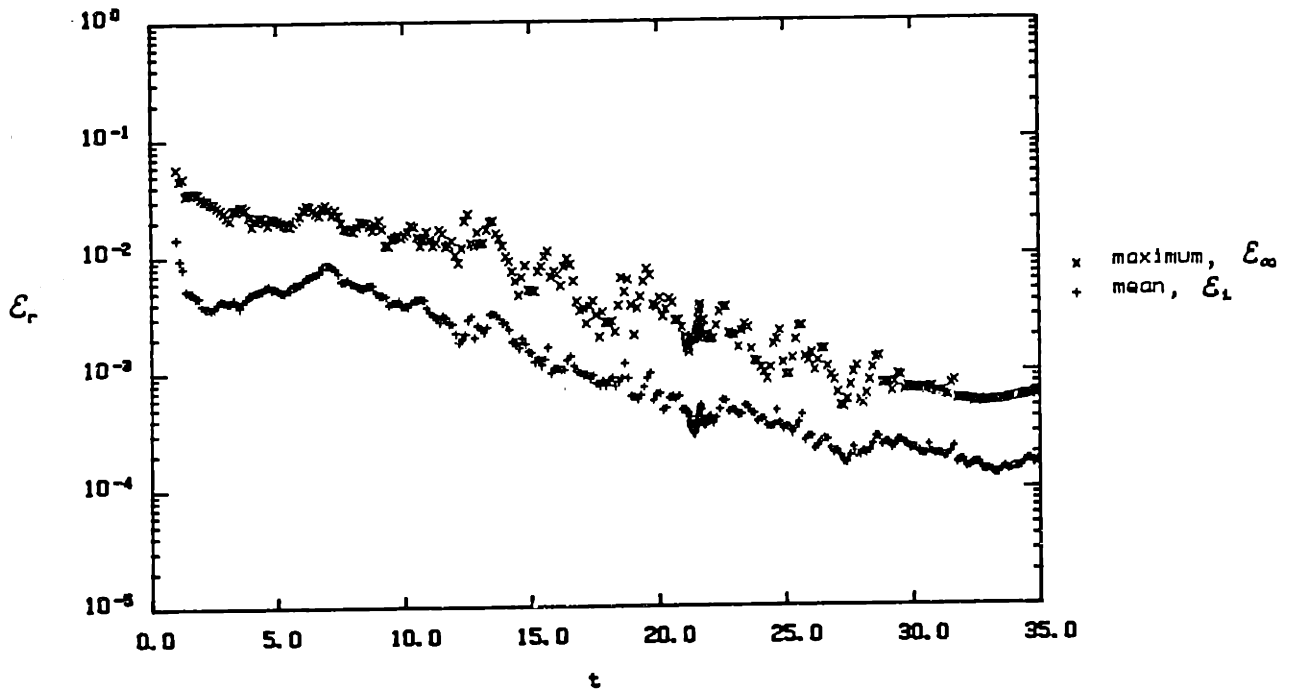
Fig. VI.3.2.   Variation of streamfunction values one wave period apart as
defined in (4.7.2)
R = 250   K = 4.5   s = 0.1   M = 32   N = 57
dy = (0.0036, 0.151) y_{max} = 2.08
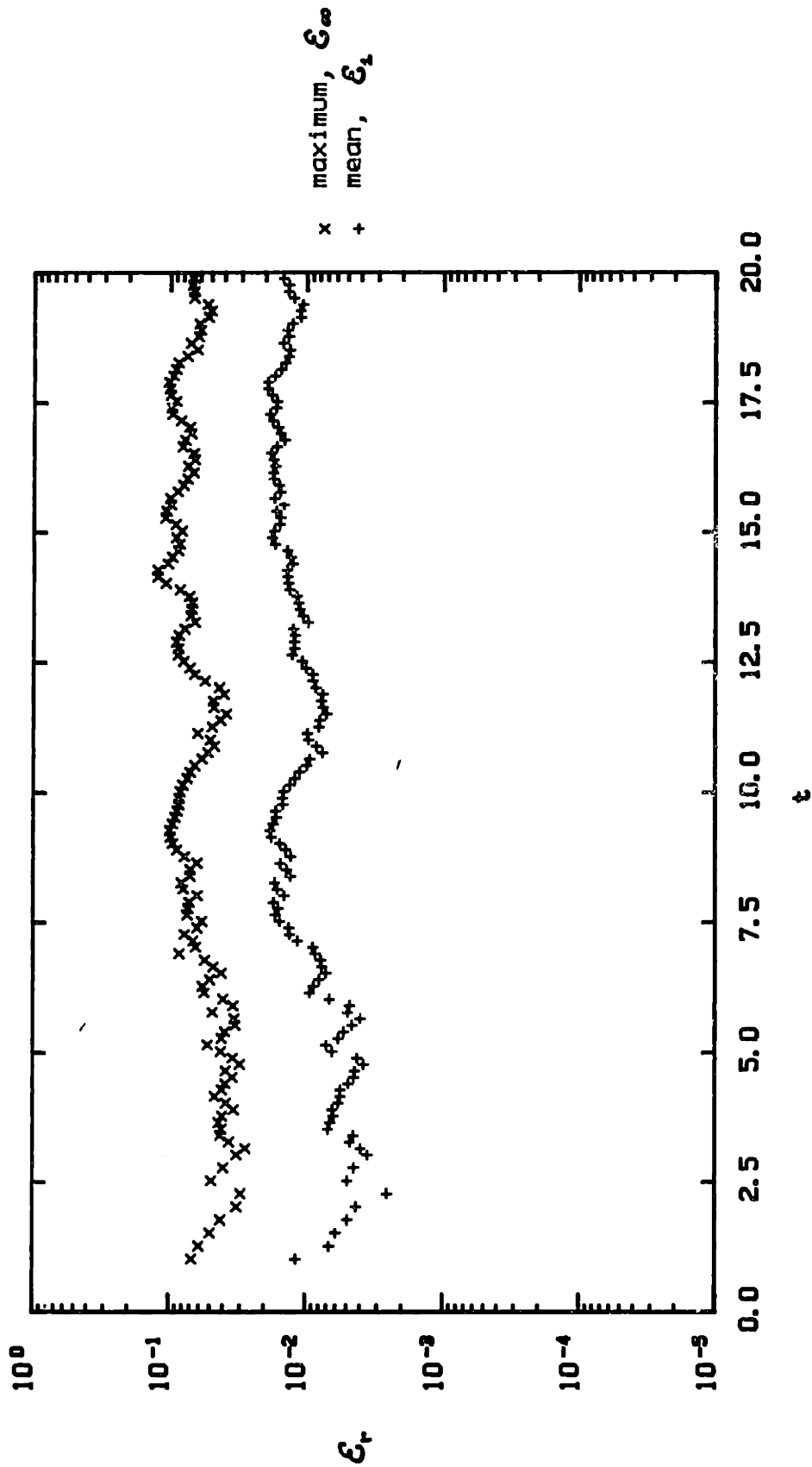
Fig. VI.3.3. Variation of streamfunction values one wave period apart as
defined in (4.7.2)

R = 500   K = 4.5   s = 0.1   M = 84   N = 72

dy = (0.0026 , 0.118) y_{max} = 2.03

× maximum, $\mathcal{E}_{\infty}$

+ mean, $\mathcal{E}_{2}$
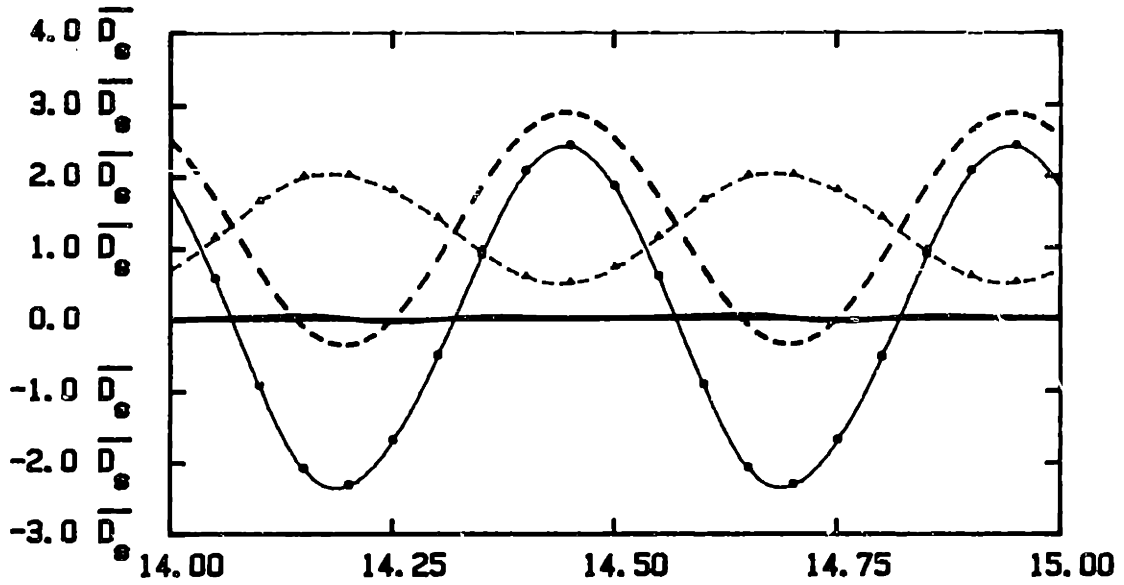
Fig. VI. 4. 1.   Conservation of energy inside the domain of computation

R = 50   K = 4.5   e = 0.1   M = 16   N = 29

dy = (0.0081, 0.135) y_{max} = 1.11 $\overline{D_e}$ = 0.0187

rate of change in
kinetic energy

rate of energy
dissipation

rate of pressure work

pressure work
- energy dissipation
- change in kinetic energy
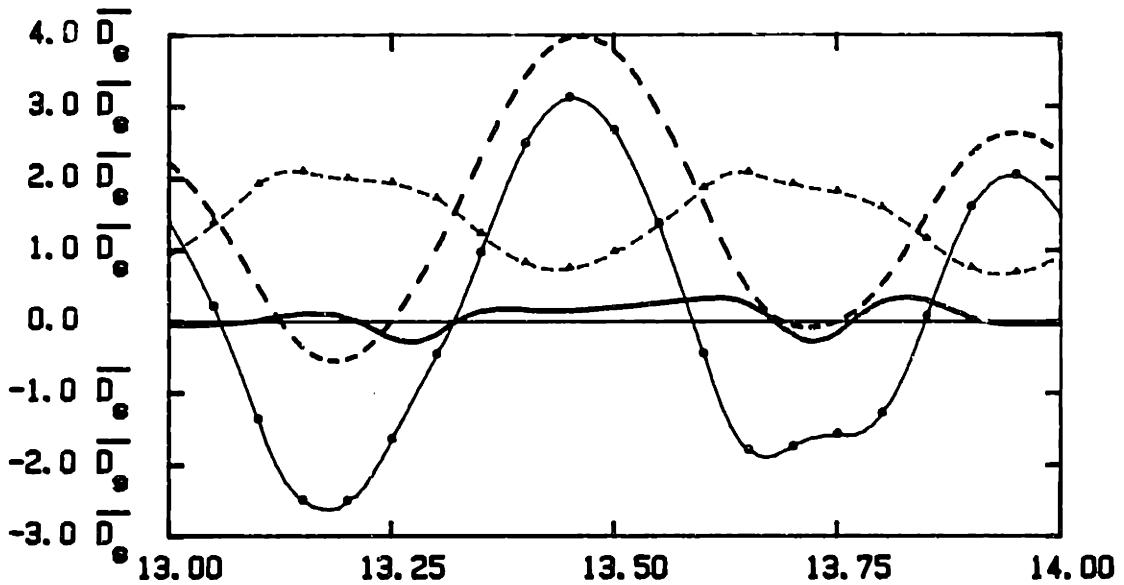
Fig. VI. 4. 2.   Conservation of energy inside the domain of computation

R = 125   K = 4.5   e = 0.1   M = 32   N = 39

dy = (0.0052, 0.097) y_{max} = 1.08 $\overline{D_e}$ = 0.0118

113
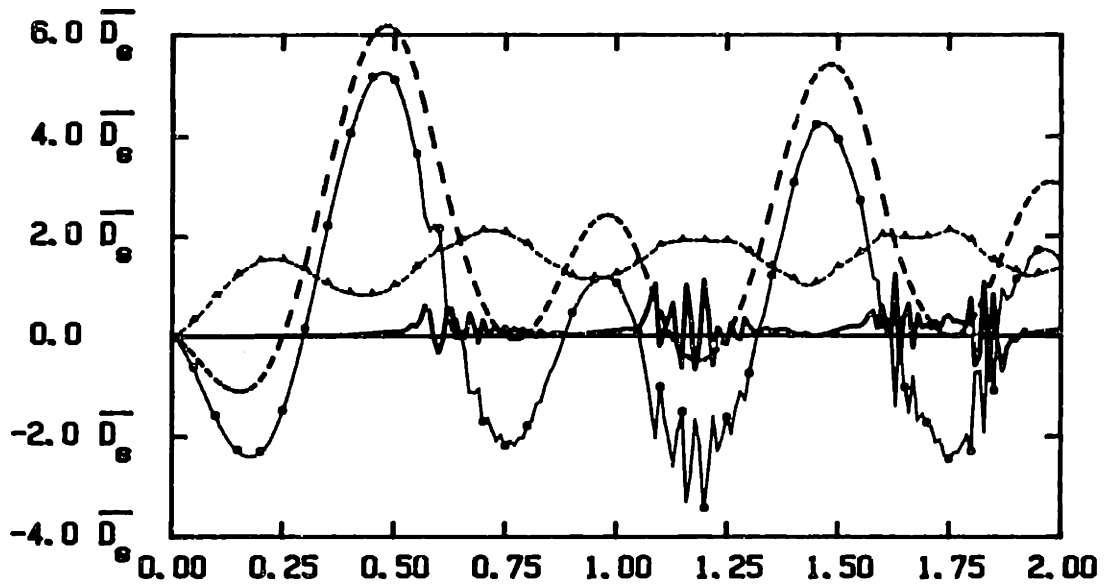
Fig. VI.4.3. Conservation of energy inside the domain of computation

R = 500   K = 4.5   e = 0.1   M = 64   N = 72
dy = (0.0026, 0.118) y_{max} = 2.03 $\overline{D}_e$ = 0.0059

─────•──────•──────
rate of change in kinetic energy

- - - - - - - - - - - -
rate of energy dissipation

- - - - - - - -
rate of pressure work

──────────────
pressure work
- energy dissipation
- change in kinetic energy
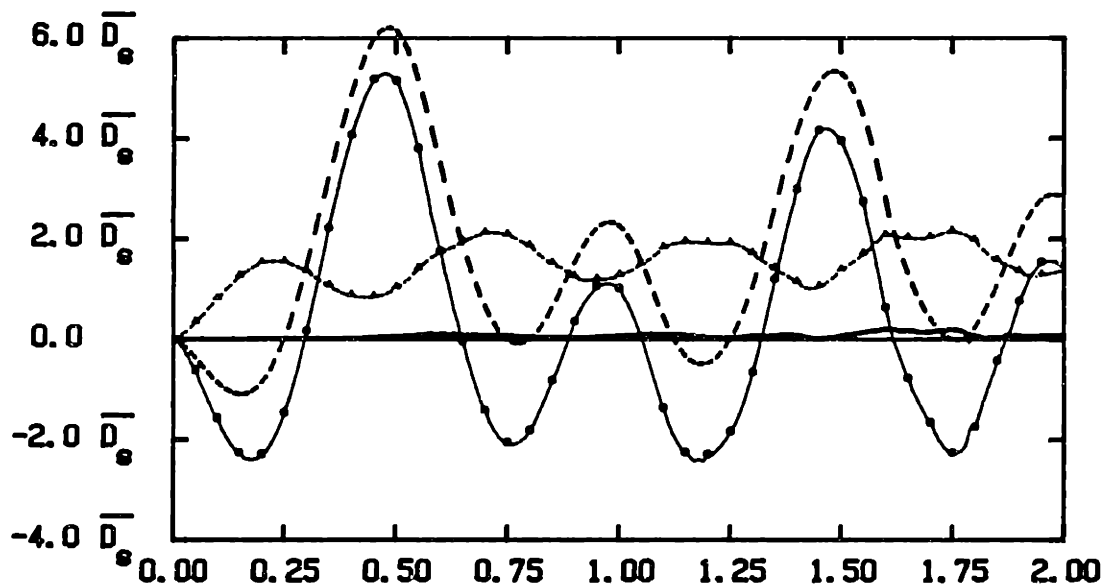
Fig. VI.4.4. Conservation of energy inside the domain of computation.

R = 500   K = 4.5   e = 0.1   M = 128   N = 96
dy = (0.0026, 0.078) y_{max} = 2.03 $\overline{D}_e$ = 0.0059

114
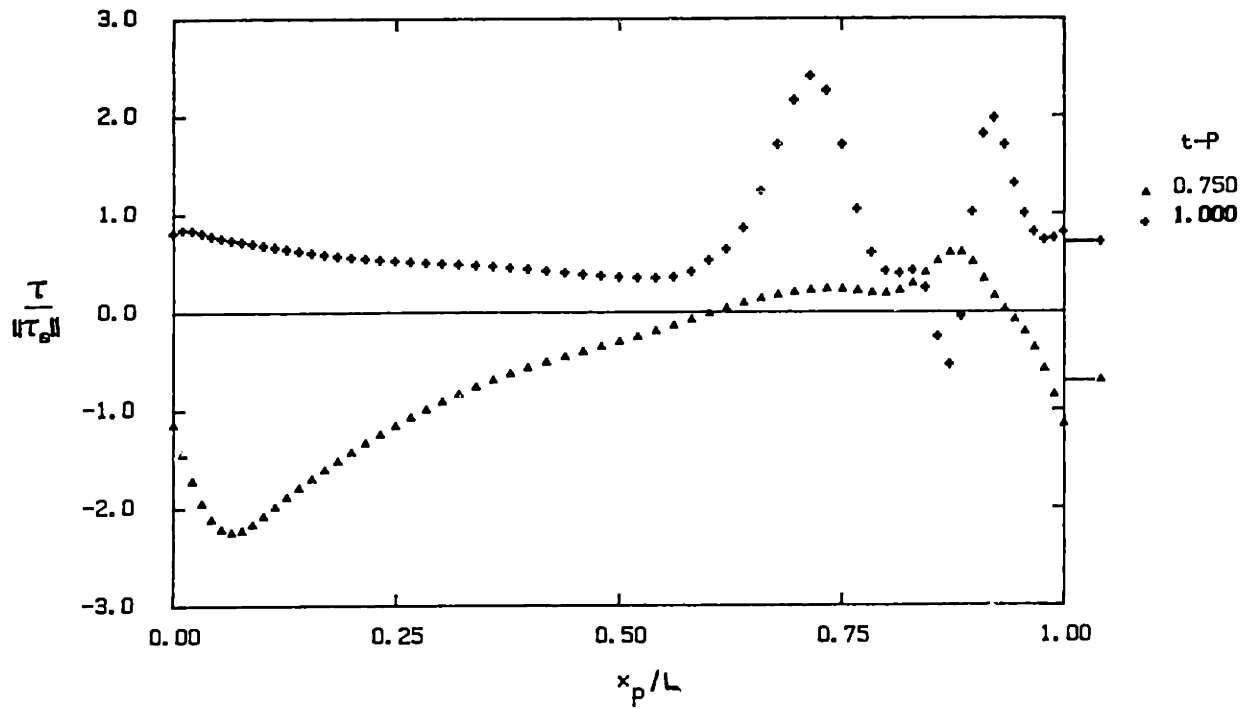
Fig. VI. 4. 5.   Shear stress on ripple surface

R = 500   K = 4.5   s = 0.1   M = 64   N = 72   P = 1
dy : (0.0026 , 0.118) y_{max} = 2.03 $\|\tau_6\|$ = 0.017
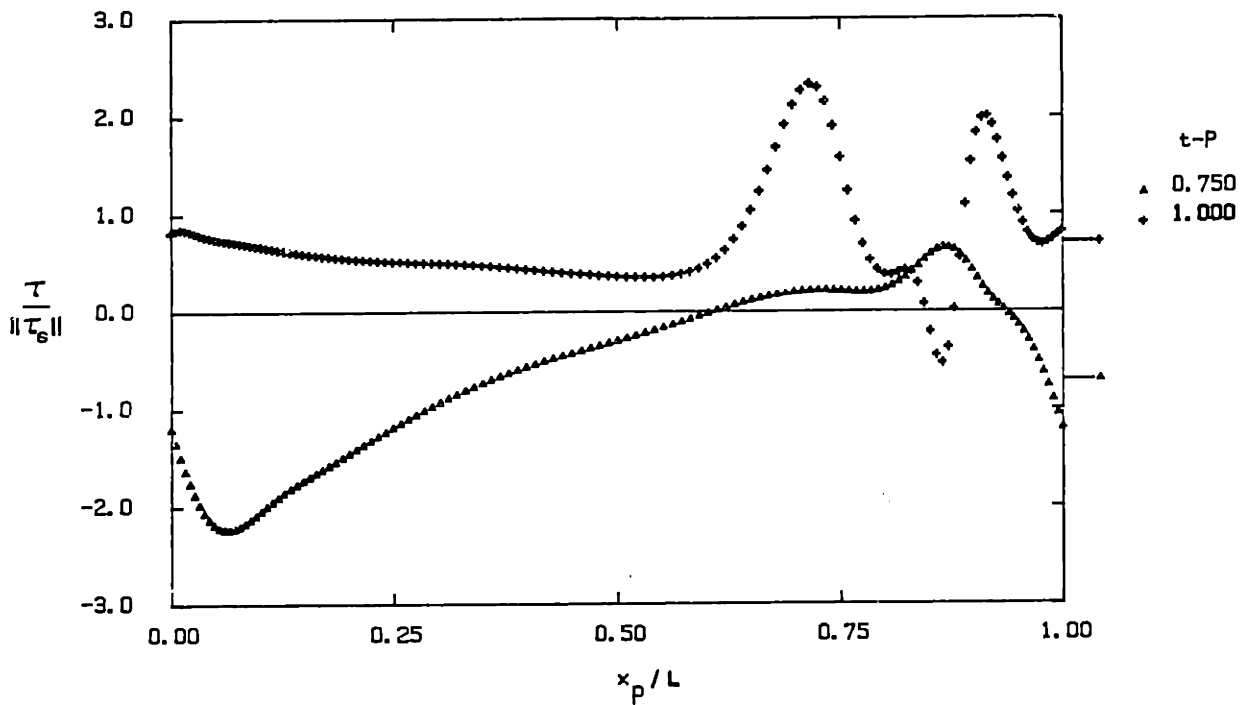
Fig. VI. 4. 6.   Shear stress on ripple surface

R = 500   K = 4.5   s = 0.1   M = 128   N = 96   P = 1
dy : (0.0026 , 0.078) y_{max} = 2.03 $\|\tau_6\|$ = 0.017

115
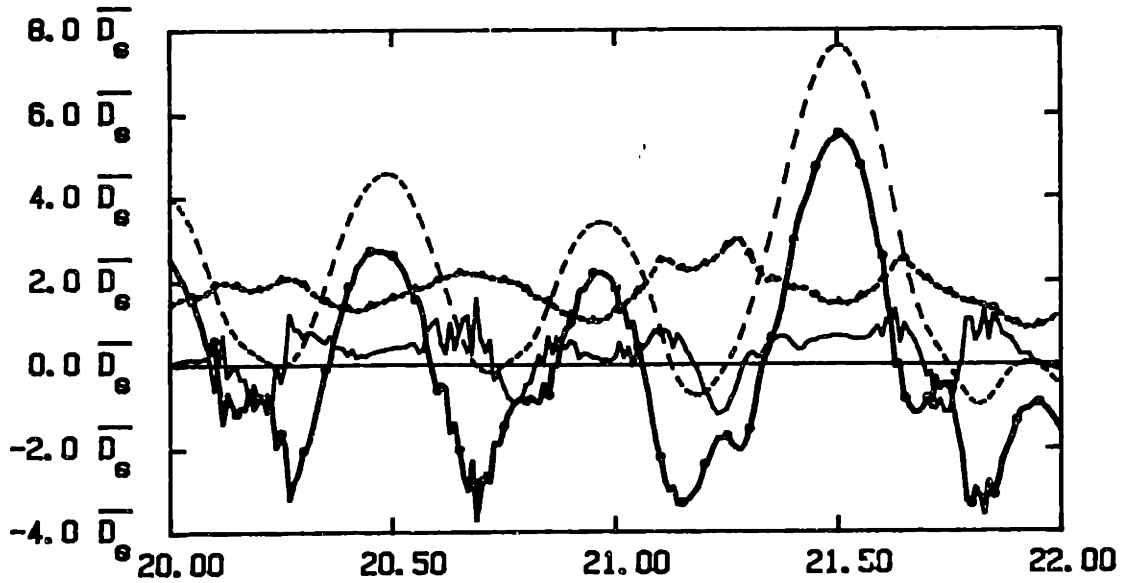
Fig. VI. 4. 7. Conservation of energy inside the domain of computation.

R = 500   K = 4.5   s = 0.1   M = 64   N = 72

dy = (0.0026, 0.118) y_{max} = 2.03 $\overline{D_s}$ = 0.0059

rate of change in kinetic energy	rate of pressure work
rate of energy dissipation	pressure work - energy dissipation - change in kinetic energy

Fig. VI. 4. 8. Conservation of energy inside the domain of computation.

R = 250   K = 4.5   s = 0.1   M = 32   N = 57

dy = (0.0036, 0.151) y_{max} = 2.08 $\overline{D_s}$ = 0.0084

116
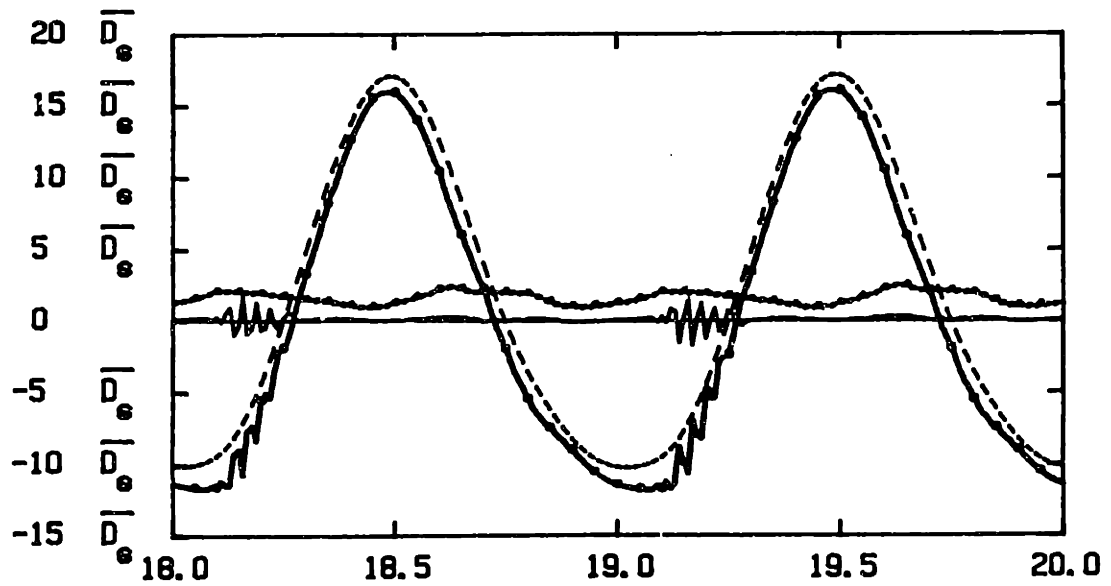
Fig. VI. 4. 9.   Conservation of energy inside the domain of computation.

R = 250   K = 4.5   s = 0.1   M = 32   N = 57
dy = (0.0036, 0.151) y_{max} = 2.08 $\overline{D_e}$ = 0.0084

rate of change in kinetic energy	rate of pressure work
rate of energy dissipation	pressure work − energy dissipation − change in kinetic energy
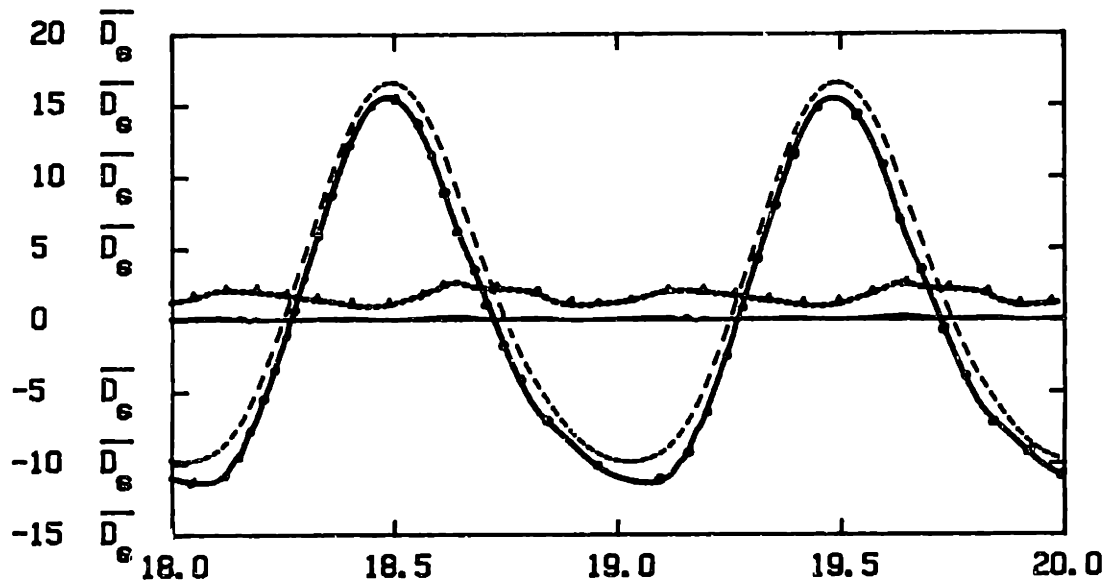
Fig. VI. 4. 10.   Conservation of energy inside the domain of computation.

R = 250   K = 4.5   s = 0.1   M = 64   N = 62
dy = (0.0036, 0.128) y_{max} = 2.00 $\overline{D_e}$ = 0.0084

117

Chapter VII. Results for a Purely Oscillatory Ambient Flow

In this chapter we shall examine the results for a purely oscillatory ambient flow over a ripple bed. A list of the flows studied has been given in Table VI.1, from which only representative cases will be presented.

The solutions examined are chosen at a time after they have become periodic for low Reynolds number flows, or after the transient effects of the impulsive start have subsided for flows at high Reynolds numbers or Keulegan-Carpenter numbers. Quantitatively, this criterion corresponds to when δ_∞ defined in (4.7.2) has decreased to less than 0.01 or has ceased to decrease, and has been discussed in detail in §IV.7 and §VI.3. We should emphasize at this point that the results for R=500 and K=4.5 are only tentative. This has been discussed at length in Chapter VI.

In §VII.1 and §VII.2 we shall discuss the variations of the velocity field and the rate of energy dissipation with dimensionless parameters R and K. In §VII.3 to §VII.5 the variations of hydrodynamic stresses on the ripple: the shear stress, the pressure force, and the horizontal force will be examined. In §VII.6 the computed rate of energy dissipation and horizontal force will be used to deduce the friction factor and compared with values in the literature.

Even though periodic solutions, if they do exist, have not been attained in flows at high dimensionless numbers, the maximum variations of these hydrodynamic stresses and energy dissipation are within 5% of their mean values. An example of this fluctuation will be presented for the energy dissipation in a wave period in §VII.2.

§VII.1. The velocity field

Flow visualizations of separated flow over ripples have been reported in

Bagnold (1946), Honji and Matsunaga (1979), and Honji *et al* (1980). Prominent vortices of a size comparable to the length scale of the ripples are found during part of the wave cycle in all three cases.

Velocity measurements in turbulent flows immediately above the ripple bed have been made by Du Toit and Sleath (1981) for waves and Tanaka and Shuto (1987) for combined wave and current over asymmetric ripples.

The velocity fields over a wave period have also been obtained from the numerical solutions of Sleath (1973) *et seq* and Sato *et al* (1984) using finite differencing schemes and Aydin and Shuto (1985) using a 'cloud-in-cell' formulation based on a potential flow model. However, aside from a qualitative description on the effects of varying the Keulegan–Carpenter number on vortex shedding in Bagnold (1946), a systematic study on how the flow characteristics vary with the dimensionless parameters K and R does not appear to have been presented.

In our computations, the velocity components at the grid points are calculated from streamfunction values in the mapped plane using (3.1.12) and second–order finite–differencing in both x and y derivatives. The beginning of all velocity vectors (at the grid points) are marked by a dot.

Two different scales are used for the velocity vectors, and the magnitude of the instantaneous far field velocity is drawn in the caption. Only the flow field immediately above the ripples where there are noticeable differences from the potential flow is plotted. The velocity fields above adjacent ripples are identical due to periodicity.

In all velocity plots in this thesis, the domain is defined horizontally by two adjacent crests, and vertically from the ripple surface to $y_p \approx 0.4L$. From the periodicity in x, the right of the ripple crest on the left of the plot is the same as that of the ripple crest on the right, and so on. Therefore, when we refer to 'the crest', we mean any crest.

As a reference, the sinusoidal ambient veloctiy $U_\infty(t)=\sin 2\pi t$ is 0, 1, 0, -1 at $t=P$, $P+\frac{1}{4}$, $P+\frac{1}{2}$, and $P+3/4$ respectively, where P is the number of wave periods since the start of computation. At low Reynolds numbers the solutions are periodic, that is,

$$u_p(x_p,y_p,t_p+T) = u_p(x_p,y_p,t_p)$$

and

$$v_p(x_p,y_p,t_p+T) = v_p(x_p,y_p,t_p) , \qquad (7.1.1)$$

and except at the highest R's studied, the flow pictures in the two half periods are symmetric, that is,

$$u_p(L\text{-}x_p,y_p,t_p+\tfrac{1}{2}T) = -u_p(x_p,y_p,t_p)$$

and

$$v_p(L\text{-}x_p,y_p,t_p+\tfrac{1}{2}T) = v_p(x_p,y_p,t_p) . \qquad (7.1.2)$$

Hence we present only the velocity fields in the second half of the wave period when the flow is from right to left (in the negative x_p direction).

We first examine the effects of increasing the Reynolds number at a constant Keulegan-Carpenter number. Specifically, the flows at R=15 and 175 with K=4.5 will be discussed. Two other Keulegan–Carpenter numbers, at K=2.5 and 12, will also be presented.

For later reference, we recall the flow field over a plane bed under an oscillatory far field velocity discussed in §V.1. The periodic horizontal velocity profile immediately above the plane bed can be approximated from (5.1.1) to give

$$u(y, t) \approx \beta y \sin(2\pi t + \frac{\pi}{4}) \qquad (7.1.3)$$

for

$$0 < \beta y = (\frac{2\pi R}{sK})^{\frac{1}{2}} y << \frac{\pi}{2} .$$

This near-bed velocity leads the phase of ambient flow by one–eighth of a wave period, as is apparent in the velocity plots in Figs. V.1.1 and V.1.2.

§VII.1.1. Flow field at R=15, K=4.5

This case serves to demonstrate that vortices are present at a very low Reynolds number. The velocity field in the second half of the thirtieth wave period from the start of computation, that is, from t=P+0.5 to t=P+1 with P=29 are plotted at time intervals of 0.1 in Fig. VII.1.1. The ambient flow is from right to left during this period.

At the beginning of the half period (t=P+0.5), a single weak residual vortex is found over the trough and two ripple heights above the ripple crest. The velocity profiles immediately above the bed are to the left and are similar along the ripple profile and vanish as y increases, reminiscent of the phase lead in the oscillatory flow over a plane bed (Fig. VII.1.1.i). As the ambient flow $U_\infty(t)$ increases, the residual vortex is overwhelmed by the ambient flow and disappears. Throughout this accelerating phase, the velocity profiles extending away from the ripple bed consist of three sections: a linear, a parabolic, and a uniform region (t=P+0.6 and P+0.7, Figs. VII.1.1.ii, iii). When the far field velocity starts to decreases from its peak, a reverse flow immediately downstream of the ripple crest appears close to the bottom boundary (t=P+0.8, Fig. VII.1.1.iv) and develops into a distinct vortex spanning three-quarters of the length of the ripple (t=P+0.9, Fig. VII.1.1.v), and by t=P+1 this vortex has climbed above the ripple crests (Fig. VII.1.1.vi). The velocity field is now exactly symmetric to the instant half a wave period earlier (Fig. VII.1.1.i), and the flow picture continues to evolve in the same manner as in the previous half period.

§VII.1.2. Flow field at R=175, K=4.5

The flow field becomes more complex when the Reynolds number is increased to 175. The velocity field in the second half of the nineteenth period from the start of computation is shown in Fig. VII.1.2 at one-twentieth of a wave period intervals.

When the far field velocity is zero at t=P+0.5, where P=18, two distinct vortices are present over the ripple (Fig. VII.1.2.i). The stronger and lower of the two, with a clockwise rotation, was generated in the preceeding half period when the ambient flow was from left to right, and is one-third of a ripple length to the right of the ripple crest. A high velocity gradient is found between its center and the ripple surface. The weaker vortex with a counter-clockwise rotation is further away from the bed above the trough. A phase lead in the velocity immediately above the ripple surface similar to that of the oscillatory flow over a plane bed described in §VII.1.1 is found.

As the ambient flow increases leftward, the vortices become embedded in the ambient flow, distorting the streamlines in their vicinity (Fig. VII.1.2.ii). As in the previous case, the entire flow field has become unidirectional by t=P+0.6 (Fig. VII.1.2.iii). At t=P+0.65, sharp velocity gradients appear immediately downstream of the crest indicating the beginning of a new vortex (Fig. VII.1.2.iv). The flow picture remains unchanged until past the peak in the ambient velocity at t=P+0.75 (Figs. VII.1.2.v, vi).

As the ambient flow decelerates, a distinct vortex appears at t=P+0.8 on the downstream side of the ripple crest (Fig. VII.1.2.vii) which grows in size and moves further downstream (Figs. VII.1.2.viii, ix). At around t=P+0.95 it has reversed its movement back towards the crest while rising slightly from the ripple bed (Fig. VII.1.2.x). This new vortex has so far been the only vortex visible since the beginning of the half cycle. The near bed velocity profiles away from the vortex have also reversed in direction, leading the ambient velocity in phase reminiscent of oscillatory flow over plane beds.

As the far field velocity diminishes to zero, this new vortex has risen above but is still downstream of the ripple crest. A weaker counter-clockwise vortex appears directly above the ripple crest (Fig. VII.1.2.xi). The asymmetry of the flow field in

the two half periods is now most visible when the ambient flow is at rest, at t-P=0.5 and 1. In each case the vortex generated in that half period is at about one-third of a ripple length from the crest at which it develops, but the locations of the 'free-vortices' are different. At t=P+0.5 it is above the ripple trough while at t=P+1 it is above the crest. The flow picture during the rest of the wave period, however, are very much symmetrical.

The flow field becomes increasingly asymmetric when the Reynolds number is increased to 250 due to the increased strengths of the vortices generated. The evolution of the velocity field, however, remains qualitatively the same and therefore will not be presented here.

Velocity difference from potential flow

It is clear from Fig. VII.1.2 that, during most of the wave period, the velocity gradient is high only in a thin boundary layer immediately above the ripple surface where viscous diffusion is important. The vortices in the flow field, on the other hand, are well above the ripple bed subsequent to the half periods they are generated. Their dynamics are therefore essentially inviscid and dominated by convection. Since the vortices induce velocities of a smaller magnitude than the ambient flow, they are overwhelmed during most of the wave period. To help visualize these vortices, we plot in Fig. VII.1.3 the difference between the computed and the potential flow velocity, $(\tilde{u}-\tilde{u}_{potential}, \tilde{v}-\tilde{v}_{potential})$, for the same instants as in Fig. VII.1.2.

The potential flow velocity is given by

$$\tilde{u}_{potential} - i\,\tilde{v}_{potential} = U_\infty(t)\frac{d(x+iy)}{d(\tilde{x}+i\tilde{y})}$$

$$= \frac{U_\infty(t)}{1+\pi^2 s^2 e^{-4\pi y}-2\pi s e^{-2\pi y}\cos 2\pi x}[(1-\pi s e^{-2\pi y}\cos 2\pi x) + i(\pi s e^{-2\pi y}\sin 2\pi x)]$$

for x, y, x̃, and ȳ defined in (3.4.1). This velocity difference will therefore display the rotational part of the flow field as vortices with closed streamlines. However, the vortices seen in the original velocity field will be distorted and displaced but the sense of rotation, and hence the qualitative features, should not be altered.

The scale of velocity vectors in Fig. VII.1.3 is twice that in Fig. VII.1.2. The vortex with an anti-clockwise rotation (labeled 1) above the ripple trough at t=P+0.5, while subsequently obscured by the ambient flow in the original plots of velocity vectors in Figs. VII.1.2.ii to x, can now be seen in Fig. VII.1.3 throughout the entire half period. It moves steadily in the direction of the ambient flow, and is at the next trough downstream by t=P+0.8 (Figs. VII.1.3.i to vii). By the end of the half period it has travelled to the left by over one and a half ripple length to the far crest of the ripple downstream.

Also present at the start of the half period, vortex 2 has a clockwise circulation, is closer to the ripple bed, and exhibits a similar type of movement downstream. It appears distorted and displaced because of the removal of the corresponding potential velocity. Between t=P+0.6 and t=P+0.65 (Figs. VII.1.3.iii and iv) it climbs over the ripple crest where it developed and continues to move horizontally downstream.

A third vortex (labeled 3) is generated immediately downstream of the ripple crest at t=P+0.8 when the ambient velocity starts to decrease (Fig. VII.1.3.vii). This vortex can also be found in Fig. VII.1.2.vii. By t=P+0.85 this new vortex has grown considerably in size while moving away from the crest. Vortex 2 has now disappeared. The newly generated vortex is found furthest away from the crest at t=P+0.9 (Fig. VII.1.3.ix), and drifts back towards the crest as the ambient flow decreases to zero (Figs. VII.1.3.x and xi). This backward drift is analogous to the velocity induced by a clockwise image vortex on the other side of the solid

boundary.

§VII.1.3. Flow field at R=500, K=4.5 (tentative)

At R=500 the velocity field is both asymmetric and aperiodic.[1] Despite that the detailed flow field increases in complexity as the Reynolds number increases, the evolution of vortices remains qualitatively similar to the flow at R=175. Therefore, only six snapshots of the flow picture, two each at the same instants during deceleration of the ambient flow over three consecutive half periods, are presented for R=500 and K=4.5 in Fig. VII.1.4.

Figures. VII.1.4.i and VII.1.4.v are both taken at the same phase of two successive wave periods, at t-P=0.875 in which P=18 and 19 respectively. The shapes of the vortices generated downstream of the ripple crests are noticeably different, and the one in Fig. VII.1.4.i is flatter and further away from the crest. The distortions in the streamlines further away from the ripple surface are also found at different locations.[2]

The aperiodicity is most significant when the ambient velocity is instantaneously at rest, and are plotted in Figs. VII.1.4.ii and vi at t-P=1, P=18 and 19 respectively. The locations of the two vortices immediately above the ripple bed are further away from the crest on the right in Fig. VII.1.4.vi. In addition, a third vortex is found about one-fifth a ripple length to the right and three ripple heights above the ripple crest on the left in Fig. VII.1.4.ii, while none is found in VII.1.4.vi. There are indications in both figures that there are more vortices further away from the bed, but they are considerably weaker.

Similarly, asymmetries in the flow field are apparent when we compare

---

[1]The definitions for a periodic and a symmetric flow field are given in (7.1.1) and (7.1.2) respectively.

[2]These distortions are, from the discussion of Fig. VII.1.3, due to the presence of vortices generated earlier.

Figs. VII.1.4.iii and VII.1.4.iv with Figs. VII.1.4.v and VII.1.4.vi. The first two are in the first half of the twentieth period and the last two are at exactly half a wave period later. In particular, the flow picture at t-P=0.5 is drastically different from a mirror image of the one at t=1.

§VII.1.3. Flow field at R=250, K=2.5

In §VII.1.1 we showed that vortical flows are present even at a very low Reynolds number. We shall now show that the same is true when the Keulegan–Carpenter number is small. Two snapshots of the flow field at t=P+0.9 and P+1, where P=10, with K=2.5 and R=250 are plotted in Fig. VII.1.5. The vortex, even though much smaller and weaker than the ones generated in flows at higher K's, is clearly visible.

§VII.1.4. Flow field at R=175, K=12

The vortices in flows with higher Keulegan–Carpenter numbers develop earlier in the wave period and moves further downstream away from the crest during its generation. This is shown in Fig. VII.1.6 for t=P+0.7 and t=P+0.9, P=9. As a comparison, recall from §VII.1.2 that reverse flows at the lee of the ripple crests do not appear until t=P+0.8, and the vortices do not drift further than one-third of a ripple length from the crest. In the present case, on the other hand, a vortex has appeared by t=P+0.7 and is found at about two-thirds of a ripple length downstream from the crest at t=P+0.9 before it moves back towards the crest upstream.

Summary

We have shown that vortical flows are present during part of the period in all the flow cases discussed, even at the very low Reynolds number of 15 and

Keulegan–Carpenter number of 2.5 for ripples with a mild slope of 0.1. The velocity immediately above the bed leads the ambient velocity in phase along the entire ripple profile, and this phase lead becomes especially prominent when the far field velocity is near zero, when the flow immediately above the ripple has reversed.

At a moderately large Reynolds number, new vortices are generated on the lees of the ripple crests during the deceleration of the ambient velocity. These vortices are then convected horizontally by the ambient flow and rise above the ripple surface. The horizontal excursions can be greater than a ripple length in subsequent wave periods before they eventually dissipate.

Only one vortex is generated per half period, and for $K \leq 6$, this vortex first appears during the deceleration of the ambient flow. The flow pattern reported as vortex-pairing in visualization experiments (Bagnold, 1946; Tunstall and Inman, 1975), in which two vortices generated in succeeding half periods get into close vicinity and moves away from the bed together, is not observed for the range of R and K studied. Instead, vortices already present at the beginning of the half periods (at $t=P$ or $t=P+\frac{1}{2}$ where P is an integer) are overwhelmed by the ambient flow as the latter increases from rest. Embedded in the ambient flow, they can move horizontally over a considerable distance over a half period and dissipate within a couple of wave periods. The newly created vortices are confined to immediately downstream of the crest during their development stages.

As R increases, the flow increases in complexity and the vortices generated increase in strengths. At the highest Reynolds numbers studied, the flow appears both aperiodic and asymmetric over succeeding half periods. If confirmed by more refined calculations, we envision that these fluctuations would increase further with Reynolds number, leading eventually to turbulent flows.

As K increases, the vortices generated at the ripple crest move further downstream and occupy a bigger portion of the trough, and the new vortices appear

earlier in the wave period. These observations are expected, since increasing K while keeping R constant can be viewed as increasing the wave period alone.

§VII.2. Energy dissipation

The sharp velocity gradient associated with vortical flow fields increases the rate of viscous dissipation, and an estimate of this energy loss is essential in the study of wave attenuation over ripples in water of finite depth. Experimental measurements of this energy dissipation have also been used to estimate the friction factor, an empirical parameter widely used in the study of flows over rough bottoms and will be discussed in §VII.6.

The rate of energy dissipation over one ripple length of the flow domain is, from (3.3.9), given by

$$\mathscr{D} = \frac{s}{R} \int_0^{y_{max}} dy \int_0^1 dx \, J\omega^2 \, , \tag{7.2.1}$$

and the double integral is calculated using an IMSL bicubic spline quadrature subroutine, DBCQDU. The variations in the rate of energy dissipation for R=15, 100, 175, 250, and 500 at K=4.5, and the variation of $\mathscr{D}$ for K=4.5 and 9 at R=250 are presented below.

As a comparison, the rate of energy dissipation in the oscillatory flow over a plane bed, given by

$$\mathscr{D}_s = \frac{1}{2} \left(\frac{\pi s}{RK} \right)^{\frac{1}{2}} \left\{ 1 + \frac{1}{\sqrt{2}} \sin \left[2\pi(2t) - \frac{\pi}{4} \right] \right\}$$

$$= \overline{\mathscr{D}_s} \left\{ 1 + \frac{1}{\sqrt{2}} \sin \left[2\pi(2t) - \frac{\pi}{4} \right] \right\} \, , \tag{7.2.2}$$

is plotted as a broken curve in plots of the computed rate of energy dissipation. Equation (7.2.2) is obtained by substituting $\omega_p^2 = (\partial u_p / \partial y_p)^2$ from (5.1.2) into the integral

128

$$\mathscr{D}_s = \frac{1}{\rho U_0{}^3} \int_0^\infty dy_p \, \rho\nu \, \omega_p{}^2 \, . \qquad\qquad (7.2.3)$$

The maxima and minima of $\mathscr{D}_s$ lead the maxima and the minima in the magnitude of ambient velocity by one-sixteenth of a wave period, and fluctuates up to $\pm 71\%$ of its mean value of $\overline{\mathscr{D}_s} = \frac{1}{2}\sqrt{\pi s/RK}$.

When the Reynolds number is low (R=15 and K=4.5. Fig. VII.2.1), the rate of energy dissipation $\mathscr{D}$ varies very nearly sinusoidally, with its maxima and minima occuring at the same instants but with a magnitude 10% (at the maxima) to 21% (at the minima) higher than the maxima and minima in flows over a plane bed. As can be seen from the velocity field discussed in §VII.1, the higher rate of energy dissipation of flow over ripples during the accelerating phase of the ambient flow is due to the higher velocity gradient above the ripple crests (Fig. VII.1.1.ii). When the ambient flow is small, $\mathscr{D}$ is higher than $\mathscr{D}_s$ due to the vortical flow (Fig. VII.1.1.iv). The rate of energy dissipation at low Keulegan–Carpenter numbers, for example at K=2.5 and R=250, is very much similar, with the ratios of the magnitudes of $\mathscr{D}$ and $\mathscr{D}_s$ higher at 1.15 and 1.79 at their maxima and minima.

As the Reynolds number increases, the rate of energy dissipation begins to deviate from a sinusoidal variation with time. At R=100 and K=4.5 (Fig.VII.2.2), the phase lead between the maxima in $\mathscr{D}$ and the maxima in the ambient velocity has increased to one-eighth of a wave period, while the minima in $\mathscr{D}$ occur one-sixteenth of a period before the instants of zero ambient velocity as in the case of $\mathscr{D}_s$. The magnitude of $\mathscr{D}$ also increases to from 21% (at their maxima) to 113% (at their minima) larger than $\mathscr{D}_s$. This difference is due to the stronger vortices generated with increasing Reynolds number and will be examined further at the end of this section.

The rate of energy dissipation in the two half periods becomes different with further increase in Reynolds number to 175 (and K=4.5, Fig. VII.2.3), and the

asymmetry increases when R=250 and K=4.5 (Fig. VII.2.4). Nevertheless, $\mathscr{D}$ is periodic in both cases. The difference between $\mathscr{D}$ and $\mathscr{D}_s$ increases especially at their minima, where $\mathscr{D}$ is three times that of $\mathscr{D}_s$ in both cases. Even though this difference in $\mathscr{D}$ between the two half periods depends on the initial condition imposed in our calculation, a qualitative prediction of this asymmetry is not apparent. For example, the total dissipation in the second half period $0.5 < t-P < 1$ is slightly lower than the first half period for R=175 while it is noticeably higher for R=250.

At still higher Reynolds numbers (R=500 and K=4.5, Fig. VII.2.5) or Keulegan–Carpenter numbers (R=250 and K=9, Fig. VII.2.6), the rate of energy dissipation is no longer periodic and becomes very irregular.[3] Multiple maxima in are found in the same half period. The difference between $\mathscr{D}$ and $\mathscr{D}_s$ is directly related to the strengths of the vortices in the separated flow field.[4] We have seen in §VII.1 that the strengths and trajectories of the vortices vary from period to period at high Reynolds number, and the flow field they induce therefore varies accordingly, leading to a highly irregular behavior in the rate of energy dissipation. The difference between $\mathscr{D}$ and $\mathscr{D}_s$ also becomes more pronounced.

To demonstrate further the aperiodicity at high R or K, the mean energy dissipation over one wave period is plotted as a function of time. The value of

---

[3] Both figures are for values after only twenty periods of computation, which is even less than the thirty periods it takes for the flow at R=250 to reach a periodic solution. The reason for not extending the computation has been explained in length in §VI.3. Furthermore, the results for R=500 and K=4.5 have to be taken with reservation since the convergence test using a finer grid has not been performed to a long time, and the tests on the energy balance for this case suggests a possibility of inaccuracy. The discussion in §VI.4, however, shows evidences that the results are accurate.

[4] The ratio of the two energy dissipations over a wave period, $\overline{\mathscr{D}}/\overline{\mathscr{D}_s}$, which equals f_e/f_e^S as discussed in §VII.6, is listed in Table VII.6.2.

$$\overline{\mathscr{D}}(P+\tfrac{1}{2}) = \int_{P}^{P+1} dt \, \mathscr{D}, \tag{7.2.4}$$

where P is the number of periods from the beginning of computation, for flows with K=4.5 and R increasing from 100 to 500 is shown in Fig. VII.2.7, and those for flows with R=250 and K increasing from 2.5 to 9 is presented in Fig. VII.2.8. The fluctuation of $\overline{\mathscr{D}}$ with time increase with R and K, up to nearly 10% of their mean values at the highest Reynolds number studied.

§VII.3. Shear stress on ripple surface

In the following three sections we shall examine the hydrodynamic forces acting on the ripple surface: the shear stress, the pressure (§VII.4), and the horizontal force on a ripple (§VII.5).

The distribution of tangential shear stress at the ripple surface is of primary interest in the study of sediment transport in ripple beds, and is the determining factor in the bed load transport. Furthermore, since the shear stress is proportional to the velocity gradient at the ripple surface, sign changes in the shear stress indicate the locations of separation. Despite its significance, a detailed exposition on how the shear stress distribution varies within a wave period for different combinations of dimensionless parameters does not appear to have been reported in the literature.

The nondimensional shear stress τ defined in (3.2.17) will be plotted. For comparison, the shear stress above a plane bed under an oscillatory ambient velocity can be obtained from (5.1.2),

$$\rho\nu\frac{\partial u_p}{\partial y_p} = \rho U_0^2 \, (2\frac{\pi s}{RK})^{\frac{1}{2}} \exp(-\frac{y_p}{\delta_p}) \sin(\frac{2\pi t_p}{T} - \frac{y_p}{\delta_p} + \frac{\pi}{4}) \tag{7.3.1}$$

after a periodic solution is reached, and the parameter δ_p has been defined in (5.1.11). On the plane bed $y_p=0$, we have, in nondimensional variables,

$$\tau_s = \frac{\rho\nu}{\rho U_0{}^2} \frac{\partial u_p}{2\, \partial y_p} = \left(2\frac{\pi s}{RK}\right)^{\frac{1}{2}} \sin\left(2\pi t + \frac{\pi}{4}\right) \equiv \|\tau_s\| \sin(2\pi t + \tfrac{1}{4}\pi) \qquad (7.3.2)$$

and therefore the bottom shear stress leads the ambient velocity in phase by one-eighth of a wave period.

The instantaneous distributions of τ along the ripple profile, normalized with $\|\tau_s\|$ defined in (7.3.2), are plotted at one-tenth of a wave period intervals. We shall examine the variation of τ with increasing Reynolds number at a constant Keulegan-Carpenter number of 4.5 for R=15, 175, and 500. The variation of τ with K at constant R are studied by comparing cases K=4.5 and 12 at R=175. The shear stress distribution at the lowest Keulegan-Carpenter number studied, K=2.5 and R=250, is very similar to that at the lowest Reynolds number and will not be presented. The shear stress for K=6 and R=250 will also be discussed as an example of flows at higher values of K. The data points plotted outside the right margin are the corresponding values $\tau_s = \|\tau_s\| \sin(2\pi t + \tfrac{1}{4}\pi)$ at the same instants of τ.

§VII.3.1. R=15, K=4.5

The distribution of the shear stress over one ripple length is plotted in Fig. VII.3.1.i from t=P+0.6 to t=P+1 where P=29, during which the ambient velocity is negative. The distribution of τ over the first half of the wave period (t=P to t=P+0.5) is exactly symmetric, that is, $\tau(x,t) = -\tau(1-x, t+\tfrac{1}{2})$.

Throughout the accelerating phase of the ambient flow (P+0.5<t<P+0.75), τ is of the same sign as the ambient velocity (in a direction from right to left). The magnitude of this shear stress is largest near the crest and smallest near the trough. The difference between the extrema increases during this time. At t=P+0.7 when the local maximum has reached its maximum over the wave period, the ratio between the magnitudes of the local maximum and minimum is 5.4.

The minimum in the magnitude of shear stress has decreased to zero at t=P+0.8, marking the beginning of separation. By t=P+0.9 the shear stress has reversed its sign over most of the ripple, and by t=P+1 the shear stress has changed sign across the entire ripple profile.

The variation in shear stress over the half period is significantly higher around the crest than around the trough. The amplitude of fluctuation near the crest over the half period is $2.8\|\tau_s\|$ while the variation at the trough is only $1.4\|\tau_s\|$. This sharp contrast may be of interest in the study of bedload transport.

The distribution of the local shear stress integrated over one wave period is plotted in Fig. VII.3.1.ii. This time mean corresponds to the shear stress associated with the induced streaming (for example, Kaneko and Honji, 1979), which is the zeroth harmonic in time of the asymptotic solution. This net shear is positive on the left of a ripple crest and negative on the right, indicating a net mean shear in a direction from the ripple trough to the crest. It increases or decreases linearly between its maximum and minimum values, attaining its extrema one–eighth of a ripple length to either side of the ripple crest, and is zero at both the crest and the trough. Despite that it is less than 15% of the amplitude of fluctuation of τ, this mean shear suggests that sediment will drift from ripple troughs to crests once they are mobilized.

§VII.3.2. R=175, K=4.5

As the Reynolds number increases, the shear stress distribution becomes asymmetric in the two half periods, as has already been observed in the rate of energy dissipation. The variation of τ from t=P+0.1 to P+0.5 (when $U_\infty > 0$) and from t=P+0.6 to t=P+1 (when $U_\infty < 0$), where P=18, are plotted in Figs. VII.3.2.i and VII.3.2.ii respectively. Only the magnitudes of τ in the two half periods differ (by about 19% of the larger amplitude) while the qualitative features are the same.

We shall therefore discuss only the variation between t=P+0.6 to t=P+1 when the ambient velocity is from right to left.

The absolute maximum in $|\tau|$ occurs soon after the ambient flow reverses (at t=P+0.6) with a magnitude of $2.3\|\tau_s\|$ compared with that of $2.9\|\tau_s\|$ half a period earlier at t=P+0.1. The shear stress over the entire ripple is in the direction of the ambient flow at this time, with the maximum shear stress acting in the direction of the crest. The magnitude of τ decreases as the magnitude of the ambient velocity increases between t=P+0.6 and P+0.7, and is due to the phase lead of the near bed velocity discussed in §VII.1.

Two local maxima in $|\tau|$ are found during the deceleration of the ambient flow (t=P+0.9 and t=P+1). From the flow field discussed in §VII.1.2, the absolute maximum is found to be due to the new vortex generated at the lee of the crest.

The variation along the ripple profile of the mean stress over a wave period is shown in Fig. VII.3.2.iii. As in Fig. VII.3.1.ii, this mean value is directed from the ripple trough towards the crest, with an amplitude approximately 20% that of τ.

§VII.3.3. R=175, K=12

The distribution of τ between t=9 and 10 is plotted in Figs. VII.3.3.i and VII.3.3.ii. As in the case of K=4.5, the shear stress distribution in the two half periods are very much symmetric even though their magnitudes vary (but only by less than 4% of the larger amplitude). We shall discuss only the half period between t=P+0.6 and t=P+1, where P=9.

Separation appears earlier than in the previous two cases, and by t=P+0.7 reversed flow is found over more than half of the ripple profile downstream of the crest. The local maximum during the acceleration phase of the period is upstream of the crest with a magnitude three times that of $\|\tau_s\|$.

During the deceleration of the ambient velocity, the location of the absolute

maximum in $|\tau|$ due to the new vortex is much further downstream than in the previous case, with a maximum of about $1.5\|\tau_s\|$. The other local maximum is not as pronounced as in the previous case examined. By $t=P+0.9$ the flow above more than four-fifths of the ripple is separated.

The mean value of τ over a wave period is shown in Fig. VII.3.3.iii. It is very nonlinear and with a magnitude of about a quarter of the amplitude of τ.

§VII.3.4. R=250, K=6

Due to the lack of periodicity, the shear stress distributions over two wave periods from $t=20$ to 22 are plotted in Fig. VII.3.4. Noticeable differences are found at two instants one wave period apart.

As in cases discussed earlier, the flow has already separated shortly after the ambient velocity reverses: at $t=P_1+0.1$, $P_1+0.6$, $P_2+0.1$, and $P_2+0.6$ where $P_1=20$ and $P_2=21$. The locations and strengths of the maxima in the shear stress associated with the new vortices vary in the four half periods. It appears that the vortex generated in the first half of the wave period is either stronger or closer to the ripple surface, leading to a higher local maximum in shear stress in both periods: $2.0\|\tau_s\|$ and $2.3\|\tau_s\|$ at $t=P_1+0.5$ and $t=P_2+0.5$. This is considerably higher than the ones at $t=P_1$ and $t=P_2$, which are $1.6\|\tau_s\|$ and $1.7\|\tau_s\|$ respectively. The local maxima during the acceleration of the ambient velocity, however, are approximately the same in the four half periods.

An increase in the maximum local shear is found towards the end of the second half periods (compare $t=P_1+0.9$ and $t=P_1+1$, and $t=P_2+0.9$ and $t=P_2+1$), while the values of the maximum shear towards the end of the first half period remain constant (compare $t=P_1+0.4$ and $t=P_1+0.5$, and $t=P_2+0.4$ and $t=P_2+0.5$). Furthermore, the maximum local shear are further downstream from the ripple crest in the first half of the period than the second half during deceleration of the

ambient flow.

§VII.3.5. R=500, K=4.5

The shear stress distribution over the ripple profile between t=20 and 22 is plotted in Fig. VII.3.5. Very significant differences are found both between the two halves of the same period and between succeeding wave periods. Most noticeable of all is the very high local maximum shear between $t=P_2+0.3$ and $P_2+0.5$ where $P_2=21$, which is approximately $4\|\tau_s\|$ at $t=P_2+0.4$ near the trough. This is due to the clockwise vortex developing, which induces a considerably higher shear than that $2.7\|\tau_s\|$ exactly one period before and those in the two other half periods, which are $2.4\|\tau_s\|$ and $1.0\|\tau_s\|$ at $t=P_1+0.9$ and $t=P_2+0.9$ respectively.

Summary

Large variations in the amplitudes of the shear stress, both along the ripple surface at the same instant and at different instants of the wave period for the same location, are found. In all cases examined, the maximum shear stress occurs during acceleration of the ambient flow, approximately one-tenth of a wave period after the ambient flow reverses, and is due to the phase lead of the near bed velocity discussed in §VII.1. The location of the maximum shear is about a tenth of a wavelength upstream of the ripple crest, its magnitude about two to three times that of the corresponding flow over a plane bed, and in a direction from trough to crest. The minimum shear is less than $\|\tau_s\|$ in the vicinity of the trough.

The shear stress during deceleration of the ambient flow increases as the Reynolds number increases due to the stronger vortices generated. On the other hand, the distribution of the shear stress during the acceleration phase of the wave cycle remains qualitatively the same as those at lower Reynolds numbers. The symmetry in shear stress in the two halves of the wave cycle breaks down above

136

R=175 and is expected from the earlier discussion on the velocity fields. Significant variations in the shear stress distribution in succeeding wave periods are found at higher Reynolds number, and the amplitude of τ can double from one wave period to the next.

As the Keulegan–Carpenter number increases, the location of the local maximum shear moves further away from the ripple crest.

§VII.4. Pressure on the ripple surface

The 'no-slip' condition and continuity imply that the pressure is the sole component of normal stress on the ripple surface. A knowledge of the pressure distribution along the ripple profile is therefore the first step in an estimate of the lifting of sediment particles into suspension and in bed load transport, since an adverse pressure gradient tends to inhibit sediment movement in that direction.

The computed values of pressure on the ripple surface given by (3.2.7) are plotted along with that calculated from the potential flow solution. In nondimensional variables, the potential pressure on the ripple surface is given by

$$
P_{potential} = -\frac{x}{K}\frac{dU_\infty}{dt} + \frac{1}{2}[U_\infty^2 - (\tilde{u}_{potential}^2 + \tilde{v}_{potential}^2)]
$$

$$
= -\frac{x}{K}\frac{dU_\infty}{dt} + \frac{U_\infty^2}{2}[1 - \frac{1}{1 + \pi^2 s^2 - 2\pi s \cos 2\pi x}], \tag{7.4.1}
$$

where $\tilde{u}_{potential}$ and $\tilde{v}_{potential}$ have been defined in (7.1.1), and the pressure is defined to be zero in the limit of $y\rightarrow\infty$ at x=0 (directly above a ripple crest) at all times. The potential pressure is plotted as a solid curve, and the symbol outside the right corresponds to that of the computed pressure at the same instant.

The first term on the right hand side of (7.4.1) is due to the ambient acceleration as a result of the unsteadiness in the ambient flow. It increases or decreases monotonously across the ripple profile proportional to the magnitude of

137

acceleration in the far field velocity. The second term in (7.4.1) is due to the difference between the ambient velocity and the potential velocity on the ripple surface: a reduction in the flow domain immediately above the ripple crest leads to a higher local velocity, and thus decreases the dynamic pressure, and the reverse is true over a ripple trough. This component therefore increases from the crests to a maximum at the trough.

From (3.2.7) and (7.4.1), the difference between the computed pressure on the ripple surface p_r and the potential pressure $p_{potential}$ is given by

$$p_r(x,t) - p_{potential}(x,t)$$

$$= \frac{1}{2}(\tilde{u}_{potential}{}^2 + \tilde{v}_{potential}{}^2) - \int_0^\infty dy \left(\frac{1}{K}\frac{\partial}{\partial t}\frac{\partial \psi}{\partial x} + \frac{s}{R}\frac{\partial \omega}{\partial x} - \omega \frac{\partial \psi}{\partial y}\right). \qquad (7.4.2)$$

From (7.4.1), the first term on the right is proportional to the square of the ambient velocity.

The second term on the right-hand-side of (7.4.2) can be written as

$$P_{visc} = \int_0^\infty dy \left(\frac{1}{K}\frac{\partial v}{\partial t} - \frac{s}{R}\frac{\partial \omega}{\partial x} + \omega u\right), \qquad (7.4.3)$$

and is due to viscosity effects and separation where u and v are the velocity components in the transformed plane. The first term in the integral is due to the acceleration in the y–direction. The magnitude of the second term increases with the local gradient of vorticity and is proportional to the strength of vortices generated. The last term is due to the convection of vorticity. In the viscous oscillatory flow over a plane boundary at steady state, the second term is zero and the third term is negative since u and ω have opposite signs.

The pressure distribution on the ripple surface is plotted at time intervals of 0.1 for the following cases: R=15 and K=4.5 in Fig. VII.4.1, R=175 and K=4.5 in Fig. VII.4.2, and R=175 and K=12 in Fig. VII.4.3. The variations of p_r in the other flows studied are very similar to one of these three cases, and will be pointed

out in the corresponding sections. The curves for the potential pressure are identical in all cases.

§VII.4.1. R=15, K=4.5

The computed and the potential pressure from t=29 to 30 are plotted in Fig. VII.4.1. For the potential pressure, the component due to the ambient acceleration (the first term in (7.4.1)) is the dominant component when the ambient velocity is small, and the distribution of pressure along the ripple surface increases (from t=P+0.4 to P+0.6, P=29) or decreases (at t=P+0.1, P+0.9, and P+1) monotonously. However, when the ambient velocity is near maximum, the second term in (7.4.1) is of a comparable magnitude, and the potential pressure therefore has a local maximum near the trough of the ripple.

The computed pressure is very nearly equal to the potential flow pressure when the ambient velocity is zero (at t=P+0.5 in Fig. VII.4.1.i and t=P+1 in Fig. VII.4.1.ii). In view of (7.4.1) and (7.4.2), the component of the computed pressure due to viscosity effects and separation (p_{visc} defined in (7.4.3)) is therefore much smaller than that due to the acceleration of the ambient flow when the ambient velocity is near its maximum. As the ambient flow increases in the positive x_p direction, the maximum difference between the computed and potential pressure is found just downstream of the ripple crest throughout the half period, and is at its maximum at t=P+0.3.

The relative difference between the computed pressure and the potential pressure is exactly symmetric in the second half of the wave period, that is,

$$p_r(1-x, t+\tfrac{1}{2}) = p_r(x,t) . \qquad (7.4.4)$$

This is shown in Fig. VII.4.1.ii.

The pressure distribution therefore follows closely that of the potential flow. The maximum deviations are found above the ripple crests when the ambient

velocity is near maximum. The pressure distributions in flows with low Keulegan–Carpenter numbers (for example, K=2.5, R=250 and K=3, R=175) are very similar and will not be presented.

§VII.4.2. R=175, K=4.5

The computed pressure begins to deviate from the potential pressure as the Reynolds number increases. From the flow field plotted in Fig. VII.1.2.i and the computed pressure in Fig. VII.4.2.i, the maximum deviation occurs at t=P+0.5 and is directly under the vortices. Specifically, the clockwise vortex near x=1 is above where p_r is lower than $p_{potential}$, and the counter-clockwise vortex near x=0.25 is above the part of the ripple profile at which p_r is higher than $p_{potential}$.

At t=P+0.1 when the ambient flow is increasing towards the right, p_r is lower than $p_{potential}$ at the crest. The computed pressure increases beyond the potential pressure between the ripple crests and over most of the ripple.

At t=P+0.2 and P+0.3 the computed pressure is still higher than the potential pressure at the crest, but the magnitude of this difference decreases downstream. The potential pressure is actually higher from about one-eighth of a ripple length from the crest to the trough . This pattern has also been found in the previous case.

At t=P+0.4 the minimum in the computed pressure, which is also found at the same point in the wave period in the flow at R=15, is the most prominent during this half period. The difference between computed and potential pressure decreases appreciably in magnitude at t=P+0.5 but is qualitatively the same as at t=P+0.4.

The computed pressure during the second half of the wave period (Fig. VII.4.2.ii) is very similar to that half a wave period earlier. The absolute minimum in $p_r - p_{potential}$ at t=P+0.9 and P+1, however, is not as pronounced as the corresponding minimum half a wave period earlier, at t=P+0.4 and P+0.5.

As R or K increases further, the magnitude of the difference between p_r and

$p_{potential}$ increases, but the qualitative features are the same up to the upper limits of the dimensionless parameters studied, at R=500, K=4.5 and R=250, K=6.

§VII.4.3. R=175, K=12

This case serves to show the large percentage difference between p_r and $p_{potential}$. Since the pressure gradient due to the inertial acceleration of the ambient flow, the first term in (7.4.1), is inversely proportional to K, the range of pressure variation in this case is therefore significantly smaller than the two previous cases (Fig. VII.4.3).

As in the cases discussed before, the difference between the computed and the potential pressure is positive throughout the wave period at the crest, but its magnitude is considerably larger than that at K=4.5, and the minimum of this difference is found further downstream. This is consistent with the assertion made earlier that the location of this minimum is the same as that of the new vortex generated: comparing the flow fields in Figs. VII.1.2.ix and VII.1.6.ii, the new vortex also travels much further downstream at the higher Keulegan–Carpenter number.

Summary

The computed pressure is very nearly the same as the potential pressure when the Reynolds number or the Keulegan–Carpenter number is low. Maximum deviations are found at the ripple crests due to the high stagnation pressure, the first term in (7.4.2).

At higher Reynolds numbers and Keulegan–Carpenter numbers, the computed pressure differs significantly from the potential pressure especially during the deceleration of the ambient flow. The maximum discrepancy is found directly below the newly generated vortex. The magnitude of this difference is proportional

to the vortex strength and exceeds that at the ripple crests at high Reynolds numbers.

§VII.5. Horizontal force acting on the ripple

The horizontal component of the hydrodynamic force acting on the ripple surface has been derived in §III.2.2. Its integral over a ripple length is of practical interest to the coastal engineer since it provides an estimate of the friction factor, an empirical parameter widely used in studies of wave attenuation and sediment transport over a ripple bed.

From (3.2.16), the total force acting on one ripple length and nondimensionalized with $\rho U_0^2 L$ is given by the integral

$$F_x(t) = \int dF_x$$
$$= \int_{x_0}^{x_0+1} dx \left\{ p_r \frac{\partial \tilde{y}}{\partial x} + \frac{s}{R} [A(x,0) \frac{\partial \tilde{x}}{\partial x} + 2\,B(x,0) \frac{\partial \tilde{y}}{\partial x}] \frac{\partial^2 \psi}{\partial y^2} \right\}. \qquad (7.5.1)$$

The function p_r is the pressure on the ripple surface and is given by (3.2.7). The expressions $\partial \tilde{y}/\partial x$, $\partial \tilde{x}/\partial x$, $A(x,0)$, and $B(x,0)$ are given by (3.4.4) and (3.4.5) and depends only on the geometry of the ripple profile.

Since the component due to the hydrodynamic pressure in (7.5.1) increases with the slope of the ripple profile, any asymmetry in the pressure distribution about the ripple trough or crest will lead to a net force on a ripple. In an oscillatory ambient flow, there exists a pressure component in p_r at all times which varies linearly in x, and is given by

$$P_{accel} = -\frac{x}{K} \frac{dU_\infty}{dt} = -2\pi \frac{x}{K} \cos 2\pi t \qquad (7.5.2)$$

for $U_\infty(t) = \sin 2\pi t$. Hence, the value of $F_x(t)$ is non-unique in that it depends on the value of x_0 chosen in the integral in (7.5.1), and the magnitude of the component due to P_{accel} is largest when $x_0 = 0$ or $\frac{1}{2}$, and vanishes when $x_0 = \frac{1}{4}$. This

is discussed in detail in Appendix IV.

For comparison, we shall examine the forces acting on a crest-to-crest profile, a node-to-node profile, and a trough-to-trough profile. They are denoted respectively as F_c, F_n, and F_t and are obtained by defining x_0 to be 0, $\frac{1}{4}$, and $\frac{1}{2}$. The component in the integral in (7.5.1) due to p_{accel} corresponding to these values of x_0 are $- \pi s/K \cos 2\pi t$, 0, and $\pi s/K \cos 2\pi t$.

As the Reynolds number increases, the variations of these forces over a wave period are found to increase only gradually in complexity. We shall therefore present only the cases at the two extremes of Reynolds number, R=15 and 500. As would be expected from earlier discussions in this chapter, the variation with time of the horizontal force at low Keulegan-Carpenter numbers is similar to that at low Reynolds numbers. Above K=4.5, the qualitative features of the time history of these forces do not change appreciably with K.

The vertical scale is in units of $\|\tau_s\|$ defined in (7.3.2), which is the magnitude of the shear stress on a plane bed under an oscillatory ambient flow.

§VII.5.1. R=15, K=4.5

At this low Reynolds number, all three forces F_c, F_t, and F_n vary very nearly sinusoidally in time, and F_c is very nearly in phase with the ambient velocity (Fig. VII.5.1). The forces F_n and F_t, on the other hand, leads the ambient velocity by around one-eigth and one-fifth of a wave period respectively. The amplitude of F_t is two times that of F_c. In the absence of a net contribution due to p_{accel} defined in (7.5.2), the horizontal force F_n on a ripple at low Reynolds number is very nearly identical to that over a plane bed both in magnitude and in its variation with time.

§VII.5.2. R=500, K=4.5

When the Reynolds number is increased to 500 with K=4.5, the variations of the horizontal forces are no longer sinusoidal (Fig. VII.5.2). Indeed, they are neither periodic nor symmetric in the two half periods.

The amplitude of F_n is the smallest of the three, but even in the absence of contribution from p_{accel}, it is still almost two times that of $\|\tau_s\|$. As in the flows at lower Reynolds numbers, the maxima of F_n are near instants of maximum shear in the oscillatory flow over a plane bed. A second local maximum in magnitude occurs later in each half period, and appears at a time just before the local shear stress induced by the new vortex gain in strength.

The phase differences between both F_c and F_t and the ambient velocity increase to close to a quarter of a wave period, suggesting the even more dominant role of p_{accel}. It is interesting to note that both horizontal forces vanish near a time when the far field velocity is at its peak. Their amplitudes are approximately the same and are more than $5\|\tau_s\|$.

Summary

Significant variations, up to half a wave period in their phase differences with the ambient velocity and a factor of two in their amplitudes, are found when different sections of the ripple, all of one ripple length, are considered in the computation of the horizontal force on the bottom boundary. Even in the absence of the force component due to p_{accel}, the horizontal force on a ripple can be significantly higher than that on a plane bed due to the strong vortical flows especially at high Reynolds numbers.

We now turn to an assumption widely used in the semi-empirical studies of the oscillatory flow over a rough bed (for example in Kajiura, 1968), namely, the concept of a 'phase-lag' in which the shear stress at the bottom is assumed to be sinusoidal but with a phase difference with the ambient velocity. To relate this

shear stress to the horizontal force acting on the ripple bed, however, can be questioned for two reasons. From the results discussed above, the horizontal force on a ripple deviates from a sinusoidal variation as the Reynolds number increases. Furthermore, the difference in time between the peaks of the horizontal force and the far field velocity depends on the section of the ripple profile used in the computation.[5] Since these differences increase with the Reynolds number, the concept of a phase-lag becomes ambiguous since these semi-empirical models are used in turbulent flow models at much higher Reynolds numbers.

§VII.6. Friction factor

Most experimental and analytical studies on flow over ripple beds involve empirical parameters in their formulations due to the complexity of the problem. In this section we shall examine the values of the most commonly used parameter, the friction factor, which can be deduced from our results discussed above. Since most theoretical derivations and laboratory and field measurements of its value are for turbulent flows whereas all our computations are in the laminar range, a direct comparison is inappropriate. Nevertheless, it is of interest to contrast its variation with dimensionless parameters in the two flow regimes.

---

[5]As discussed in Appendix IV, this difference is proportional to the number of ripples used in the computation, and therefore cannot be reconciled by taking the mean over a large number of ripples. Experimental determination of these values will therefore vary significantly with even a small change in the section of the bed used in the measurement.

§VII.6.1. Definitions

The friction factor f relates the resistance of the bottom boundary to the ambient flow outside the boundary layer and is most commonly defined as

$$\langle \tau_p \rangle = \frac{f}{2} \rho \, U_p \, |U_p| \, , \tag{7.6.1}$$

where U_p is the far field velocity outside the boundary layer and $\langle \tau_p \rangle$ is the (spatial) mean shear stress over the bottom boundary, and corresponds to the horizontal force F_x in our computation. In a uniform flow, the friction factor in (7.6.1) is deduced directly from measured values of ambient velocity and the time averaged value of $\langle \tau_p \rangle$ on the bed. Some modifications, however, are required to apply the same definition to unsteady ambient flows.

As discussed in the last section, the time-dependence of the horizontal force on a ripple, and thus that of $\langle \tau_p \rangle$, is different from that of U_p when the far field velocity is oscillatory. The friction factor according to (7.6.1) therefore varies with time and is ill-defined when the ambient velocity U_p is near zero. Two approaches have been used to circumvent this predicament. One may (for example in Jonsson, 1966) define the value of f either (i) by using the amplitudes of $\langle \tau_p \rangle$ and U_p, or (ii) by equating the measured rate of energy dissipation to the work done by $\langle \tau_p \rangle$. Since only the amplitude of the horizontal force is used in (i), its detailed time history need not be defined. In (ii), on the other hand, further *ad hoc* assumptions have to be made on the time dependence of $\langle \tau_p \rangle$.

The friction factors defined by (i) and (ii) will be labeled as f_w and f_e respectively. Semi-empirical expressions for f_w in turbulent flows have been proposed by Kajiura (1968) and Grant (1977) for a purely oscillatory ambient flow and by Grant and Madsen (1979) for flows under combined wave and current. The friction factor f_e for laminar flows have been computed from the numerical solutions to the Navier-Stokes equations by Sleath (1982).

We shall examine the values of friction factor according to both definitions. A brief discussion on their relationships with our results is given below.

§VII.6.1.1. Friction factor from the amplitude of horizontal force on the ripple

The friction factor f_w can be defined using the maximum value of $|\langle \tau_p \rangle|$ and $|U_p|$ over a wave period, denoted as $\|\langle \tau_p \rangle\|$ and U_0, in place of $\langle \tau_p \rangle$ and U_p in equation (7.6.1), that is,

$$\|\langle \tau_p \rangle\| = \frac{1}{2} f_w \, \rho \, U_0^2 .\tag{7.6.2}$$

The friction factor f_w can then be deduced by equating $\|\langle \tau_p \rangle\|$ with the maximum horizontal force acting on a ripple, F_x computed from (7.5.1), divided by the ripple length. Recall from (3.1.4) that $F_{x_p} = \rho U_0^2 L \, F_x$, this horizontal stress on the ripple can be equated with (7.6.2) to give

$$\|\langle \tau_p \rangle\| = \frac{1}{L} \|F_{x_p}\|$$

where $\|F_{x_p}\|$ is the amplitude of F_{x_p}. This gives

$$\frac{1}{2} f_w \rho U_0^2 = \rho U_0^2 \, \|F_x\|$$

or

$$f_w = 2 \, \|F_x\| .\tag{7.6.3}$$

As discussed in Appendix IV, the value of F_x is determinate up to the function $-\dfrac{s}{2K} \dfrac{dU_\infty}{dt} \cos 2\pi x_0$ in which x_0 defines the particular choice of the section of ripple profile used in the calculation. In §VII.5 we compute F_x using the two extreme values: F_c for a crest-to-crest profile with $x_0=0$; F_t for a trough-to-trough profile with $x_0=\frac{1}{2}$; and F_n for a node-to-node profile with $x_0=\frac{1}{4}$. These three values, F_c, F_t, and F_n, have been defined in (A4.2), (A4.3), and (A4.4), and will be used in (7.6.3). The corresponding friction factors will be denoted as f_c, f_t, and f_n,

respectively. Recall that, for a node-to-node profile, the net force due to the ambient pressure component associated with the accelerations of the far field velocity vanishes.

§VII.6.1.2. Friction factor deduced from the rate of energy dissipation

Alternatively, we can assume the boundary shear stress $\langle \tau_p \rangle$ to be of the form (7.6.1) but with a phase lag with the ambient velocity, that is,

$$\langle \tau_p \rangle = \frac{f}{2} \rho U_0^2 \sin(2\pi t + \theta) \, |\sin(2\pi t + \theta)| \, .$$

The rate of work done per ripple length is then

$$L \langle \tau_p \rangle U_p = \frac{f}{2} \rho U_0^3 L \sin(2\pi t + \theta) \, |\sin(2\pi t + \theta)| \, \sin 2\pi t \, , \qquad (7.6.4)$$

and the total work done over a wave period is therefore

$$\int_0^T dt_p \, L \langle \tau_p \rangle U_p = \frac{f}{2} \rho L T U_0^3 \int_0^1 dt \, \sin 2\pi t \, |\sin 2\pi t| \, \sin(2\pi t - \theta)$$

$$= \frac{2f}{3\pi} \rho L T U_0^3 \cos \theta \, . \qquad (7.6.5)$$

We shall denote this friction factor as f_e, and its value can be obtained by equating (7.6.5) with the total energy dissipated in one wave period, $\int_0^T dt_p \, \rho L U_0^3 \mathscr{D}$, in which $\mathscr{D}$ is computed from (3.3.9). This gives

$$f_e = \frac{1.5 \, \pi}{\cos \theta} \int_0^1 dt \, \mathscr{D} \, . \qquad (7.6.6)$$

The shortcomings of this approach, namely the assumption of (7.6.4) and a constant phase shift θ, have been discussed in Jonsson (1966).

As a comparison, the friction factor in the oscillatory flow of a semi-infinite fluid over a plane bed can be obtained from the exact solution of the horizontal velocity at steady state, (5.1.1). The horizontal shear stress at height y is given by

$$\langle \tau_p \rangle = \rho\nu \frac{\partial u_p}{\partial y_p} = \rho\nu \frac{U_0}{\delta_p} \sqrt{2} \exp(-\frac{y_p}{\delta_p}) \sin(2\pi \frac{t_p}{T} - \frac{y_p}{\delta_p} + \frac{\pi}{4})$$

where $\delta_p = \sqrt{\nu T / \pi}$. At $y_p = 0$, this becomes

$$\langle \tau_p \rangle = \rho U_0 (2\pi \frac{\nu}{T})^{\frac{1}{2}} \sin(2\pi \frac{t_p}{T} + \frac{\pi}{4}) = \rho U_0^2 (2\frac{\pi s}{RK})^{\frac{1}{2}} \sin(2\pi t + \tfrac{1}{4})$$

and therefore the magnitude of horizontal force on the bottom is given by

$$\frac{1}{L} \| F_{x_p} \| = \| \langle \tau_p \rangle \| = \rho U_0^2 (2\frac{\pi s}{RK})^{\frac{1}{2}}. \tag{7.6.7}$$

The rate of energy dissipation per unit length of bottom is given by

$$\int_0^\infty dy_p \, \tau_p \frac{\partial u_p}{\partial y_p} = \int_0^\infty dy_p \, \rho\nu \frac{\partial u_p}{\partial y_p} \frac{\partial u_p}{\partial y_p}$$

$$= \int_0^\infty dy_p \, \frac{1}{2} \rho\nu (\frac{U_0}{\delta_p})^2 \exp(-2\frac{y_p}{\delta_p}) \sin^2(2\pi \frac{t_p}{T} - \frac{y_p}{\delta_p} + \frac{\pi}{4})$$

$$= \rho U_0^3 \frac{1}{2} (\frac{\pi s}{KR})^{\frac{1}{2}} [1 + \sqrt{\tfrac{1}{2}} \sin 2(2\pi t - \frac{\pi}{8})]$$

at steady state. The nondimensional rate of energy dissipation is therefore

$$\mathcal{D}_s \equiv \frac{1}{2} (\frac{\pi s}{KR})^{\frac{1}{2}} [1 + \sqrt{\tfrac{1}{2}} \sin 2(2\pi t - \frac{\pi}{8})]$$

and the total dissipation of energy per unit length of flow field in a wave period is

$$\int_0^T dt_p \, \rho U_0^3 \, \mathcal{D}_s = \rho T U_0^3 \frac{1}{2} (\frac{\pi s}{KR})^{\frac{1}{2}}. \tag{7.6.8}$$

If we denote the friction factors corresponding to (7.6.3) and (7.6.6) as f_w^s and f_e^s respectively, we have, from (7.6.3) and (7.6.7),

$$f_w^s = 2 (2\frac{\pi s}{RK})^{\frac{1}{2}}, \tag{7.6.9}$$

and from (7.6.6) and (7.6.8),

$$f_e^s = \frac{0.75\pi}{\cos\theta} \frac{\pi s}{RK} (\frac{\pi s}{RK})^{\frac{1}{2}}. \tag{7.6.10}$$

Note that both expressions have the same dependence on s, R, and K, and the ratio

of the two friction factors is

$$\frac{f_w^s}{f_e^s} = \frac{8\sqrt{2}}{3\pi} \cos\theta \approx 1.2 \cos\theta .$$ (7.6.11)

§VII.6.2. Past work on the estimates of fricion factor

We shall briefly examine previous theoretical derivations of the values of friction factor in laminar and turbulent oscillatory flows over fixed ripple beds.

§VII.6.2.1. Laminar Flow

Theoretical values of the friction factor in the oscillatory laminar flows with separation over fixed ripple beds have been deduced from the computed rates of energy dissipation, assuming the phase lag θ in (7.6.6) to be zero.

Longuet-Higgins (1981) proposed a potential flow model in which the high shear layer assoicated with the separated flow is simulated by an array of Rankine vortices. The radii of constant vorticity of these vortices increase as $\sqrt{\epsilon t_p}$ in which ϵ is an empirical parameter and is a measure of the physical viscosity, and assumes the values of 10^{-4} or 10^{-5}. The rate of decrease in kinetic energy due to the expanding core of the vortex is then assumed to be the rate of energy dissipation in the flow domain. The value of f_e for sharp crested ripples with a slope of 0.17 is found to range in between 0.14 and 0.24 as the Keulegan-Carpenter number increases from π to 4π.

Both Sleath (1982) and Sato et al (1984) computed the rate of energy dissipation from numerical solutions to the Navier-Stokes equations. Sleath (1982) solved the same governing equations (3.1.10) and (3.1.11) using a finite differencing scheme first proposed in Sleath (1973), and the same ripple profiles as that defined in (3.4.1) with s=0.12 and s=0.17 are studied. However, instead of computing $\mathscr{D}$ from (3.3.9), the total energy dissipation over one wave period is computed from the

difference between the total pressure work done over one wave period and the change in momentum in the fluid. In our notation, this can be obtained by substituting $\mathcal{D}$ in (7.6.6) with the first two terms on the left hand side of (3.3.11),

$$f_e = \frac{1.5}{\cos\theta}\frac{\pi}{K}\left\{\int_P^{P+1} dt\ \psi_\infty\frac{dU_\infty}{dt} - \frac{1}{2}[\psi_\infty U_\infty + \int_0^\infty dy \int_0^1 dx\ J\psi\omega]\Big|_{t=P}^{t=P+1}\right\}$$

$$(7.6.12)$$

where P is the number of wave periods since the start of computation. For a strictly periodic solution such that $\psi(x,y,t=P+1) = \psi(x,y,t=P)$, the second term vanishes, and the expression for f_e can therefore be reduced to

$$f_e = \frac{1.5\pi}{K\cos\theta}\int_P^{P+1} dt\ \psi_\infty\frac{dU_\infty}{dt} = -\frac{3\pi^2}{K\cos\theta}\int_P^{P+1} dt\ \psi_\infty \sin 2\pi t \qquad (7.6.13)$$

for $U_\infty(t)=\cos 2\pi t$. If we assume $\theta=0$, (7.6.13) is equivalent to equation (14) in Sleath (1982).

Equation (7.6.13) holds only if the solution is strictly periodic. However, it has been observed in §VI.3 that the solutions become aperiodic at high Reynolds number. This aperiodicity has also been observed by Sleath (1982) in computations at high Reynolds number (in the discussion between equations 16 and 17 in that paper), and therefore estimating f_e using (7.6.13) in lieu of (7.6.12) is only an approximation. The value obtained from (7.6.13), nevertheless, may be considered as the mean value of f_e over many periods.

The resolution used in Sleath's computations deserves comment. The upper boundary y_{max} was chosen to be 1.46 for the case of $\delta_p/L=0.008$, and an eight by eight grid with a logarithmic type spacing in the y direction was used. The first grid spacing at the ripple surface is therefore around 0.12, which is much larger than the nondimensional thickness of the viscous boundary sublayer δ_p/L estimated from (4.4.1). Such a coarse grid cannot adequately describe the steep velocity gradient immediately above the ripple surface. Furthermore, from the plots of velocity

151

vectors in Fig. VII.1.4, the spatial variation in the near bottom flow field is already quite complicated at a relatively modest Reynolds number of 500, and significant variation in the flow field is found between grid points L/64 apart. The even finer flow structure expected at higher Reynolds numbers (up to 30 000) studied in that paper is therefore unlikely to be resolved in the estimate of energy dissipation by the eight by eight grid used.

Sato *et al* (1984) computed the variation of the rate of energy dissipation within a wave period using the same approach with a 13x13 grid. The plot of the instantaneous rate of energy dissipation $\mathscr{D}$ for the flow at s=0.1, K=6.4, and R=1150 shows instants at which $\mathscr{D}$ is negative (Fig. 13 in their paper) which is impossible in a laminar flow model.

For comparison, the ranges of dimensionless parameters studied in Sleath (1982), Sato *et al* (1984), and the present computation are listed in Table VII.6.1.

§VII.6.2.2. Related works on turbulent oscillatory flow

Due to the empirical nature of the analyses, the exact geometry of the bottom profile is not taken into account in the theoretical expressions for the friction factor in turbulent flows over ripple beds, and only the ripple height appears as a roughness parameter. In all cases of practical interest, the amplitudes of ripples are at least an order of magnitude larger than the thickness of the viscous laminar boundary sublayer, and the flows are therefore hydrodynamically rough. A quantitative discussion of the criterion for a smooth or rough bottom boundary specifically on flow over ripples is given in §5(c) in Kajiura (1968).

Based on a time invariant eddy viscosity, Kajiura (1968) found that the friction factor decreases when the Keulegan–Carpenter number increases in flows over fixed beds. This is confirmed in the laboratory measurements of Jonsson (1963) and Kamphuis (1975) over a rough bottom, Jonsson and Carlsen (1976) in flows over a

bottom covered with periodic wedges, and Sleath (1985) in flows over sinusoidal bed profiles.

A comparison of the variations of the friction factor with $K/4\pi s$ proposed by Jonsson (1966), Kajiura (1968), Kamphuis (1975), and Grant (1977) can be found in Fig. A.15 of Grant (1977). Since these predicted values differ by a factor of less than two over a wide range of Keulegan–Carpenter number, $K \in (2,20)$, we shall compare our results only with the values of Kajiura (1968) in the following.

Other laboratory measurements of the friction factor specifically on flow over ripples include those of Bagnold (1946), Carstens *et al* (1969), and the review of Vitale (1979) and Jonsson (1980).

§VII.6.3. Results of present computations

Our estimates of f_e are computed from (7.6.6) using numerical quadratures of the rates of energy dissipation $\mathscr{D}$ over one wave period defined in (7.2.4). The function $\mathscr{D}$ is given by (3.3.9) and are computed at constant time intervals of 0.01. As pointed out earlier, the numerical solution ceases to be periodic as R increases and the mean $\overline{\mathscr{D}}$ therefore varies over adjacent wave periods. The variation of this integral with time at various dimensionless parameters has been shown in Figs. VII.2.7 and VII.2.8, in which the fluctuations can be up to 10% at the highest dimensionless parameters studied. The averaged value over five wave periods after the solution has converged will be used in all cases. The criterion of this convergence is based on the parameters $\mathscr{E}_1$ and $\mathscr{E}_\infty$ discussed in §VI.3, namely, that their values have decreased to below 0.01 for flows at low R or K, or have ceased to decrease any further for flows at high R or K.

As discussed in §VII.6.1.i, the values of f_c are computd from (7.6.3) with $\|F_x\|$ taken as the maximum value of $|F_c|$ evaluated from (A4.2) after the transient

effects at the beginning of computation have subsided. Similarly, f_t and f_n are computed using $|F_t|$ and $|F_n|$ defined in (A4.3) and (A4.4), respectively. Numerical values of f_e, f_c, f_t, and f_n are listed in Table VII.6.2.

The computed friction factors will be plotted as a function of dimensionless parameters R, K, and R_δ defined as

$$R_\delta = \frac{1}{\sqrt{2}} \frac{U_0 \delta_p}{\nu} = \frac{U_0}{\sqrt{\omega\nu}} = \sqrt{(\frac{1}{2} \frac{RK}{\pi s})} , \qquad (7.6.14)$$

and is the Reynolds number based on the thickness of the viscous boundary sublayer estimated from that in the oscillatory flow over a plane bed. Note that K can also be written as

$$K = 2\pi \frac{U_0 T/2\pi}{\delta} = 2\pi \frac{A}{L} \qquad (7.6.15)$$

in which A is the excursion amplitude of fluid particles far from the bottom boundary under the sinusoidal ambient flow, and the ratio A/L is often used in place of K as an independent parameter in the literature.

§VII.6.3.1. Friction factor based on the amplitude of horiontal force

To illustrate the extent f_w fluctuates due to different sections of ripple profile used in its definition, the variations of f_c, f_t and f_n with R_δ at K=4.5 are plotted in Fig. VII.6.1, and the broken line is f_w defined in (7.6.9) for a flat bed. The values of f_t are higher than the corresponding values of f_c and f_n in the range $10 < R_\delta < 60$. Both f_t and f_n are larger than the corresponding friction factor for the oscillatory flow over plane beds, and vary as $R_\delta^{-0.2}$ and $R_\delta^{-0.3}$ respectively, a decrease significantly slower than R_δ^{-1} of f_w^S in the oscillatory flow over a plane bed. At higher R_δ the values of f_c are in between f_t and f_n but at $R_\delta=10$, the lowest R_δ studied, it is actually lower than f_w^S. Contrary to the decrease of f_t, f_n, and f_w^S with R_δ, f_c increases as $R_\delta^{0.3}$ in the range $20 < R_\delta < 60$, and the ratio f_c/f_w^S increases from

0.80 to 4.40 as R_δ increases from 10 to 60.

The mild slopes the values of f_w make with the R_δ axis in Fig. VII.6.1 suggest that, at a constant Keulegan–Carptenter number, f_w does not vary significantly with R. This is confirmed in Fig. VII.6.2 in which f_t at three Reynolds numbers are plotted versus K, and only a very small variation in the values of f_t is found when R increases by a factor of two at the same K. The weak dependence of f_t on R is also apparent from Table VII.6.2. For the flows at K=4.5, f_t decreases by less than a quarter of its value when the Reynolds number increases ten-folds, from 50 to 500[6]. The decrease in f_t with K, on the other hand, is more drastic, as it decreases by two-thirds when K increases from 3 to 12 at R=175.

Comparison with the theoretical expression in Kajiura (1968)

The theoretical expression proposed by Kajiura (1968) for rough turbulent flows, in which the friction factor f_w ($\tilde{C}/2$ in that paper) was found to be a function of $U_0 T/2\pi z_0$ only, is also plotted in Fig. VII.6.2. The parameter z_0 is the roughness length and equals D/30 where D is the Nikuradse's equivalent roughness, and assumed to be twice the ripple height (Grant and Madsen, 1979). For $U_0 T/2\pi z_0 < 1000$, f_w can be approximated as

$$f_w^k = 3.4 \left(\frac{U_0 T}{2\pi z_0}\right)^{-2/3} = 3.4 \left(\frac{7.5}{\pi}\frac{K}{s}\right)^{-2/3} \tag{7.6.16}$$

which is independent of the Reynolds number and is plotted as a dotted line. Both f_t and f_w^k decrease with K in similar ways, with values in our computation consistently higher by a constant. An approximate relation is $f_t \approx 1.2 f_w^k$. Since the assumption that the roughness parameter z_0 in (7.6.16) equals 4a is only an

---

[6]The thickness of the viscous boundary layer for the flow with K=4.5 and R=15 is 0.10 according to (4.4.1), which is the same as the ripple height. The bottom boundary in this case cannot therefore be considered rough.

approximation, a better agreement between f_t and f_w^k can be achieved if we assume a larger ratio of a/z_0. Indeed, Grant and Madsen (1982, equation 23) proposed that

$$z_0 = 27.7(2a)s$$

based on physical arguments and experimental results. In our case $s=0.1$ and therefore $a/z_0=5.5$ and (7.6.16) becomes

$$\tilde{f}_w^k = 3.4 \left(\frac{5.5}{\pi} \frac{K}{s}\right)^{-2/3} . \tag{7.6.17}$$

This is also plotted in Fig. VII.6.2 and f_t becomes very nearly the same as $\tilde{f}_w^k$. However, this comparison also depends on the choice of f_w we choose. From Table VII.6.2, the ratio between the friction factors f_c and f_n to f_t can be up to a factor of over four. The agreement between the results of Kajiura and ours will be less satisfactory if f_c or f_n is chosen instead,[7] and therefore the 'improvement' in the comparison is of limited significance. Afterall, we are mainly interested in a qualitatively comparison of the variations of the friction factors between the two models.

The values of f_e plotted in Fig. VII.6.2 will be discussed in the next section.

§VII.6.3.2. Friction factor based on the rate of energy dissipation

The values of f_e are plotted as functions of R_δ in Fig. VII.6.3 for $K=4.5$, 6, and 9, and the dotted line is the friction factor f_e^s for flows over a plane bed. The variables f_e, R_δ, and f_e^s have been defined in (7.6.6), (7.6.14), and (7.6.10), and the angel θ in (7.6.6) is assumed to be 0. The results in the numerical computation of

---

[7] We noted in Fig. VII.6.1 that, for $R_\delta > 20$, the relationship $f_t > f_c > f_n$ holds. If, instead, f_c or f_n is plotted in place of f_t, they are found to be smaller than Kajiura's prediction given by (7.6.16). A similar decrease, as $K^{-2/3}$, is found for f_c while the variation of f_n with K is not as uniform.

Sleath (1982) are also plotted for the case of $\dfrac{\beta}{k} = \dfrac{\sqrt{\pi/\nu T}}{2\pi/L} = \dfrac{1}{2}\left(\dfrac{1}{\pi s}\dfrac{R}{K}\right)^{\frac{1}{2}} = 5$, 12, and

20 with s=0.12. The values of f_e from the present computation and Sleath (1982) have been listed in Tables VII.6.2 and VII.6.3 respectively.

At K=4.5, f_e varies very nearly algebrically as $0.19\ R_\delta^{-0.76}$ in the range $R_\delta\epsilon(10, 60)$, or, $0.50\ R^{-0.38}$ in $R\epsilon(15, 500)$. This decrease is slower than that in the oscillatory flow over plane beds, f_e^s given in (7.6.10), and the ratio $r = f_e/f_e^s$ increases from 1.11 at R=15 to 1.68 at R=500. This suggests an increasing rate of energy dissipation associated with stronger vortical flows which has been observed in the velocity fields in §VII.1. Computed data for K=6 and 9 show a more gradual variation of f_e with R_δ, as $R_\delta^{-0.39}$ and $R_\delta^{-0.46}$, or $R^{-0.20}$ and $R^{-0.23}$, respectively. They become larger than the friction factor at K=4.5 as R_δ increases.

Comparison with the numerical results of Sleath (1982)

Owing to the differences in the dimensionless parameters used in the two studies, a direct comparison of the values of f_e in our computation with those of Sleath (1982) can be made only at a few data points. From Table VII.6.3, his data point nos. 2, 3, and 4 correspond to the Keulegan–Carpenter numbers of close to 4.5, 6, and 9 used in our study, and the Reynolds number corresponding to these three points are also in the range of our computation. At the lowest K, point no. 2 (K=3.9, R=110) in Table VII.6.3 falls onto the straight line from the intrapolation of our computed values of f_e with K=4.5. However, the friction factors at point nos. 3 (K=6.2, R=170) and 4 (K=9.4, R=250) are respectively 30% larger and 15% smaller than the values intrapolated from our results with roughly the same K. These differneces may be attributed to the inaccuracies in Sleath's numerical solution discussed in §VII.6.2.i.

Sharp increases in f_e with R_δ were reported in Sleath (1982) at various ratios of

157

A/L=K/2π defined in (7.6.15), and was attributed to the abrupt appearance of vortices in the flow field at some critical values of R_δ. The threshold value of R_δ at which this was reported to occur is higher than the range of R_δ examined in our computation. However, our results in §VII.1 show that prominent vortices are already present during part of the wave period at lower values of R_δ, and their strengths increase gradually with R_δ. Therefore, if such a steep increase does exist, the reason may be different from that suggested by Sleath. Despite of its apparent interest, we have not performed computations at these critical values of R_δ because of the limitation on computer time.

Comparison with the exact solution to the oscillatory flow over a plane bed

Since vortices are absent in the oscillatory laminar flow over a plane bed, the ratio $r = f_e/f_e^S$ gives an estimate of the energy dissipation due to separation. The variation of r with K at constant R is plotted in Fig. VII.6.4. From Fig. VII.6.3, this ratio[8] increases monotonously with R at constant K, whereas, at a constant R, r reaches a local maximum when K is between 5 and 6 both when R=175 and when R=250. This, incidentally, happens to be close to the value of K of 4.7 at which equilibrium ripples are reported to be found. An eloquent exposition of this critical value can be found in §I.3.d in Lofquist (1978).

Comparison with the theoretical expression of Kajiura (1968)

In this comparison, the values of f_e are deduced from (7.6.6) by substituting the phase lag θ between the bed shear and the ambient velocity proposed by Kajiura (1968) for rough turbulent flows (Fig. 7 in that paper). This phase lag varies only

---

[8]The logarithm of this ratio is given by the vertical distance between the computed value of f_e and the dotted line for f_e^S.

slightly between 0.24π and 0.27π in the range of K examined, and the factor $1/\cos\theta$ in (7.6.6) therefore lies within a small range, between 1.4 and 1.5. The results are plotted in Fig. VII.6.2. Contrary to the monotonous decrease deduced by Kajiura (equation 7.6.16), the friction factor f_e remains constant in the range $2.5<K<6$ at both R=175 and 250. At higher K, however, f_e decreases as $K^{-2/3}$ as suggested.

Comparison with experiments

The variation of f_e with K and R_δ are compared with laboratory measurements of Bagnold (1946) and Sleath (1985), both on fixed sinusoidal ripple beds. The friction factor in both papers were derived from the measured work done in oscillating a plate with ripple shaped surface on both sides in a tank of otherwise still water.

For ripples with a slope of 0.15, Bagnold found that the friction factor is independent of the Reynolds number and can be expressed approximately as a function of $A/L=K/2\pi$,

$$f_e = \begin{cases} 0.16 \\ 0.57\,K^{-0.75} \end{cases} \quad \text{for} \quad K \underset{>}{\overset{<}{}} 2\pi. \tag{7.6.18}$$

This is plotted as a dotted line in Fig. VII.6.5 along with our results for R=175 and 250. A similar trend is found in our computed values of f_e, but the magnitudes are smaller by a factor of more than two. This may be attributed to the smaller ripple slope used in our computation. From the values listed in Table VII.6.2, f_e varies by a factor of almost two as R increases from 100 to 500 at a constant K of 4.5. This contradicts Bagnolds' conclusion that f_e is independent of R.

Sleath (1985) also reported significant variations of f_e with R from his experiments using sinusoidal shaped ripples of slope 0.23. The values of f_e are plotted as a function of R_δ for K=4.5 and 8.9, and large differences are found from our values for s=0.1, K=4.5, and 9. For R_δ=56 and K=4.5, Sleath's result is about

three times as large, even though the values at $R_\delta=48$ and the same K=4.5 are very much the same. Sleath's f_e at $R_\delta=75$ and K=8.9 is much smaller than the corresponding value obtained from extrapolating our results at K=9. This suggests that the ripple slope is an important parameter in the dependence of f_e.

Finally, since both f_e and f_w have been widely studied in the literature, sometimes interchangably, the ratios f_c/f_e, f_t/f_e, and f_n/f_e are listed in Table VII.6.2. As a comparison, all three ratios equal the same constant 1.2 for the oscillatory flow over a plane bed assuming $\theta=0$ in (7.6.11). Both f_c/f_e and f_t/f_e increase with R at constant K. While f_c/f_e is less than 1.2 at small R's, f_t/f_e is considerably larger at all R. Both ratios decrease with increasing K at constant R. The ratio f_n/f_e, on the other and, remains slightly below 1.2 until R increases to 250 at K=4.5, beyond which it increases to 1.43 at R=500. No apparent trend is spotted on the variation of this ratio with K when R is kept constant.

Summary

The two definitions of friction factor, f_w defined by (7.6.3) and f_e defined by (7.6.6), give considerably different values over the range of dimensionless numbers studied. The ratio f_w/f_e can be up to almost four, with f_w generally higher. At constant K, the variation of friction factor with R is more drastic for f_e than f_w.

Both f_w and f_e decrease with increasing R or K. As the Reynolds number increases, the ratio between the friction factors in flows over ripples to those over a plane bed increases, suggesting the increasing vortical motion in the flow field. The Keulegan–Carpenter number, however, appears to be a more important parameter, in that a change in K leads to a bigger change in f than that from the same percentage change in R. Unlike the monotonous increase of f/f^S with R, the ratio f/f^S reaches a maximum as K increases, and this critical value of K is near five for

160

both R=175 and R=250.

No computations are performed to examine the variation of f with ripple slope because of computer cost. However, comparisons of f_e with the experimental values of Bagnold (1946) and Sleath (1985) show that a difference in the ripple slopes may lead to very different values of friction factor. Nevertheless, similar trends are found in Bagnold's results and ours.

Despite the fundamental differences between our laminar flow model and turbulent flow models, the variation of the computed values of f_w follows closely that of the theoretical values for rough turbulent flows derived in Kajiura (1968). The predictions of Kajiura lie in between the maximum and minimum values of the computed f_w, namely, f_t and f_n respectively, according to the choice of ripple profile used in the computation.

**Table VII.6.1. Dimensionless parameters used in previous studies**

	s	range of K		range of R	
Sleath (1982)	0.12	1.8	14.6	64	4300
	0.17	0.6	30.0	60	30000
Sato *et al* (1984)	0.10	6.4		1150	
Present computation	0.10	2.5	12.0	15	500

Table VII.6.3. Friction factor f_e from the computation of Sleath (1982)

No.	$\dfrac{\beta}{k} = \dfrac{1}{2}\sqrt{\dfrac{R}{\pi s K}}$	R_δ	R	K	f_e
1	5	13	50	1.88	0.137
2		28	105	3.93	0.084
3		44	166	6.22	0.072
4		66	250	9.36	0.062
5		91	343	12.88	0.045
6	12	64	581	3.79	0.056
7		91	824	5.37	0.072
8		109	988	6.44	0.062
9		154	1394	9.08	0.060
10		227	2057	13.40	0.075
11	20	56	841	1.97	0.041
12		136	2057	4.82	0.075
13		167	2518	5.90	0.072
14		244	3679	8.63	0.084

Table VII.6.2. Friction Factors from our computation

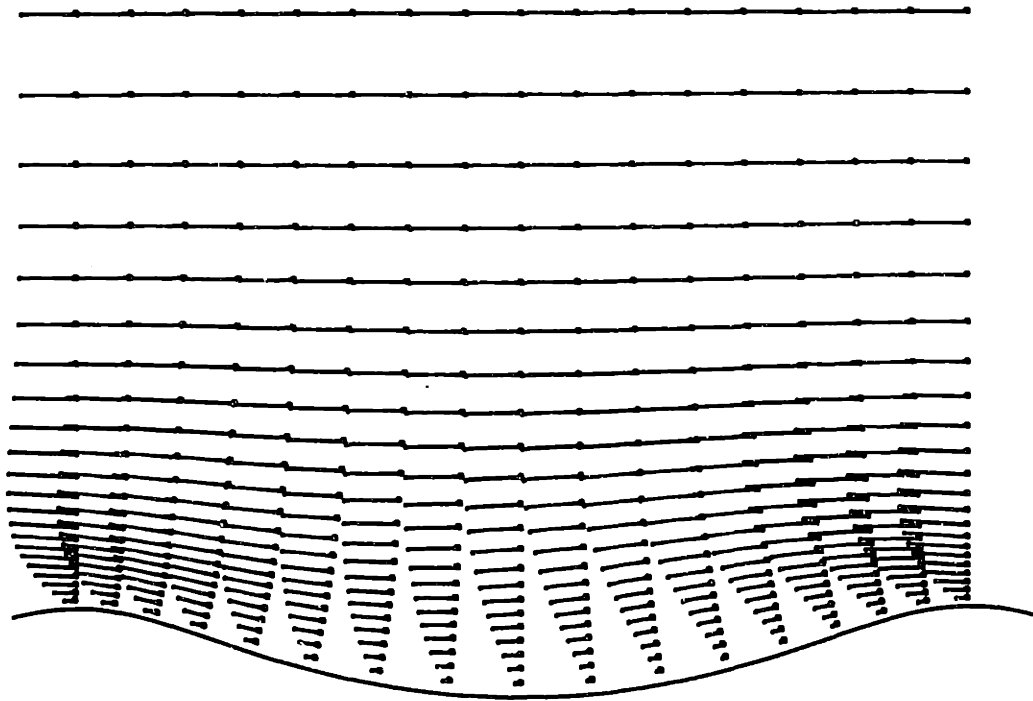| K	R	f_e	$\dfrac{f_e}{f_e^s}$	f_c	f_t	f_n	$\dfrac{f_c}{f_e}$	$\dfrac{f_t}{f_e}$	$\dfrac{f_n}{f_e}$
4.5	125	0.079	1.42	0.118	0.196	0.083	1.49	2.47	1.05
6.0	↓	0.071	1.47	0.091	0.161	0.076	1.29	2.28	1.08
3.0	175	0.074	1.28	0.172	0.250	0.077	2.34	3.41	1.04
4.5		0.070	1.48	0.126	0.192	0.079	1.81	2.75	1.13
6.5		0.063	1.60	0.098	0.144	0.066	1.56	2.30	1.05
9.0		0.051	1.53	0.064	0.114	0.057	1.20	2.23	1.12
12.0	↓	0.043	1.48	0.039	0.091	0.052	0.92	2.13	1.22
2.5	250	0.065	1.22	0.218	0.298	0.072	2.37	4.61	1.11
4.5		0.062	1.58	0.135	0.180	0.074	2.18	2.90	1.18
6.0		0.062	1.81	0.120	0.159	0.066	1.95	2.58	1.08
9.0	↓	0.047	1.69	0.082	0.122	0.064	1.72	2.59	1.36
4.5	15	0.178	1.11	0.154	0.318	0.209	0.86	1.78	1.17
	50	0.110	1.25	0.112	0.229	0.116	1.02	2.07	1.05
	100	0.086	1.38	0.114	0.201	0.088	1.34	2.35	1.03
	125	0.079	1.42	0.118	0.196	0.083	1.49	2.47	1.05
	150	0.074	1.46	0.124	0.194	0.081	1.68	2.62	1.09
	175	0.070	1.48	0.126	0.192	0.079	1.81	2.75	1.13
	250	0.062	1.58	0.135	0.180	0.074	2.18	2.90	1.18
↓	500	0.047	1.68	0.147	0.180	0.067	3.15	3.85	1.43
6.0	125	0.071	1.47	0.091	0.161	0.076	1.29	2.28	1.08
↓	250	0.062	1.81	0.120	0 160	0.066	1.95	2.58	1.08
9.0	175	0.051	1.53	0.064	0.114	0.057	1.26	2.23	1.12
↓	250	0.047	1.69	0.082	0.122	0.064	1.72	2.59	1.36
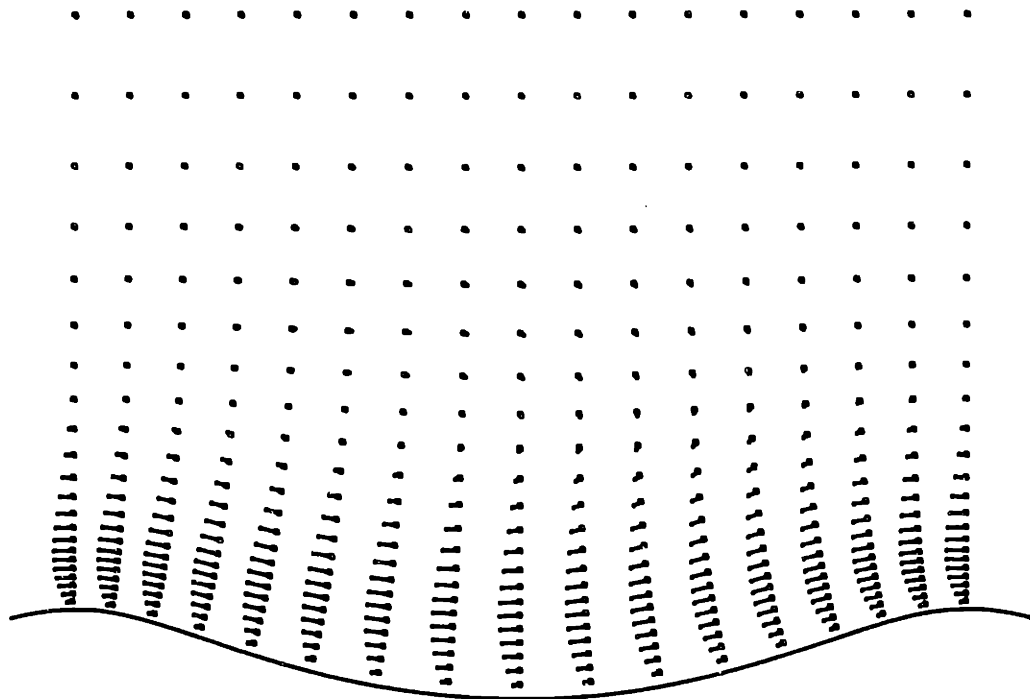
i.   t = P+.5   U∞:   .
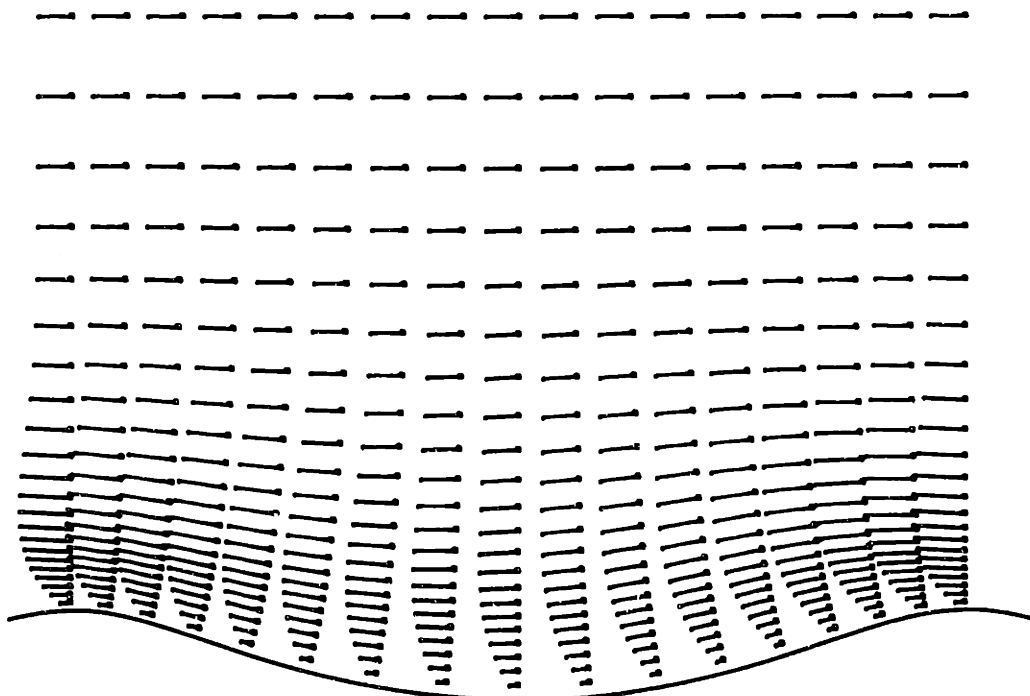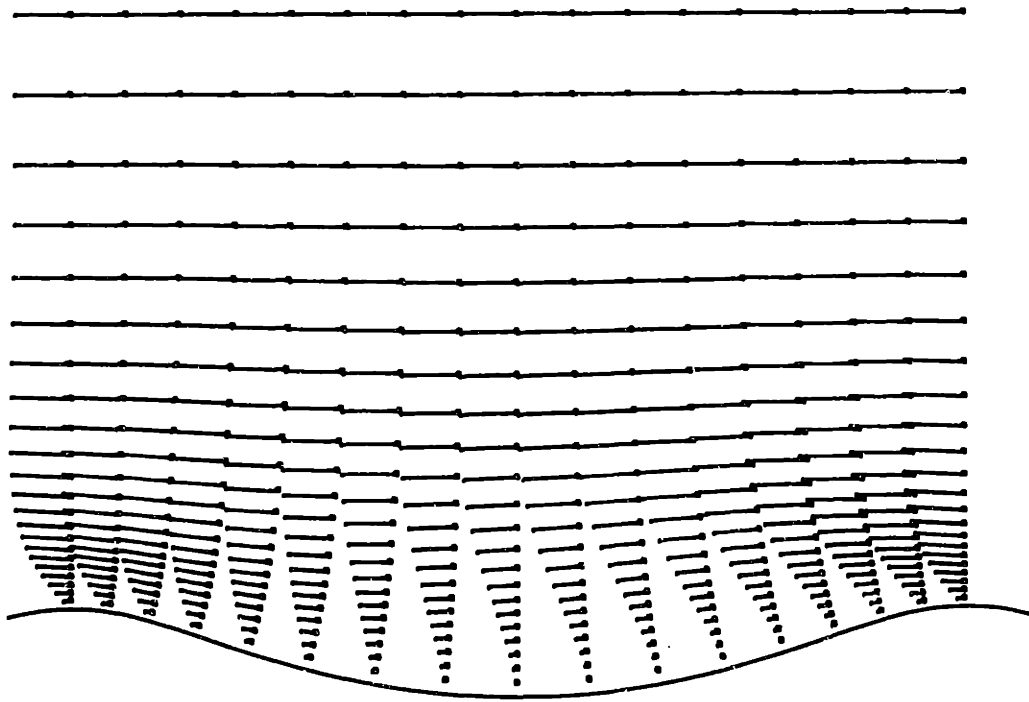

ii.   t = P+.6   U∞:   ←
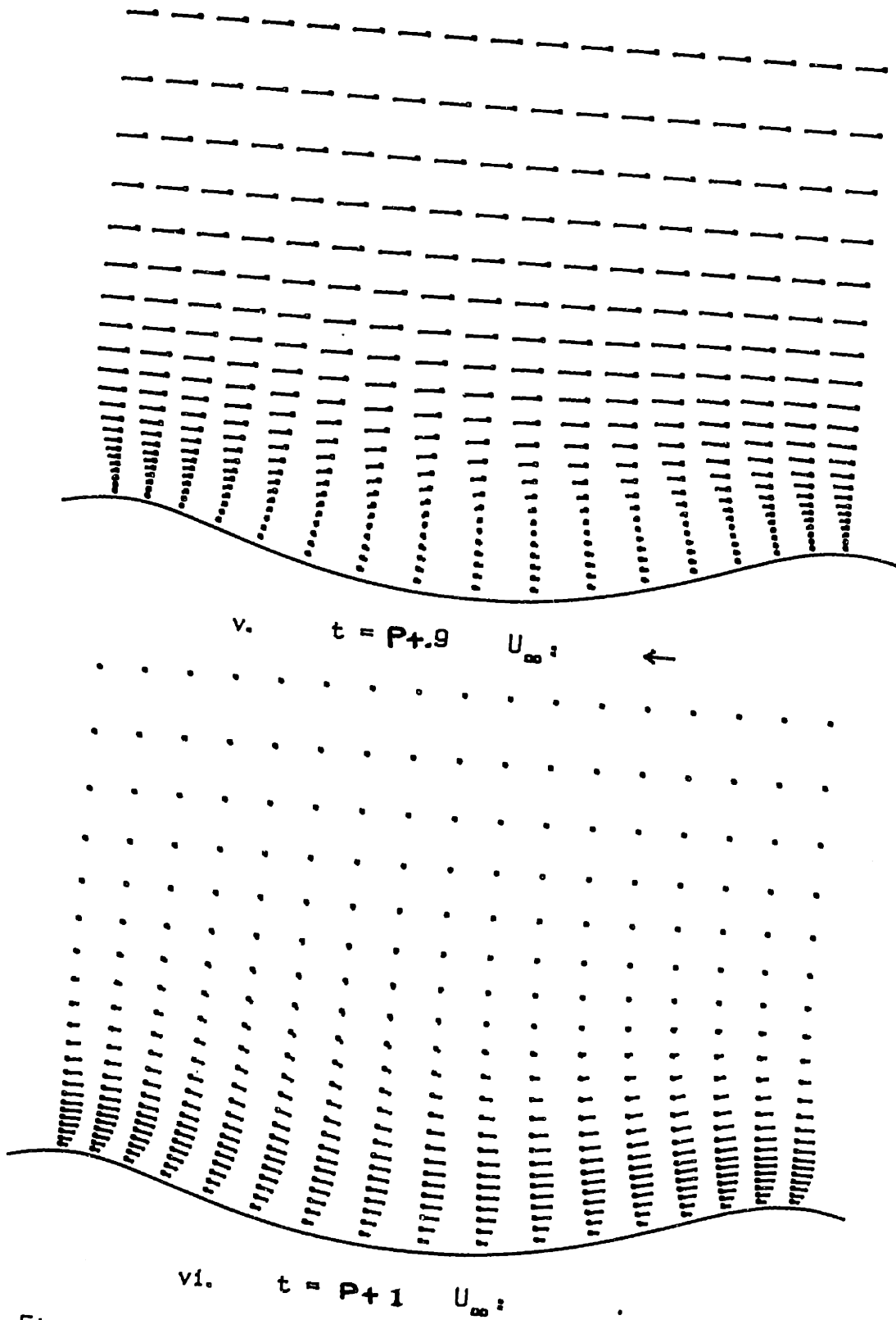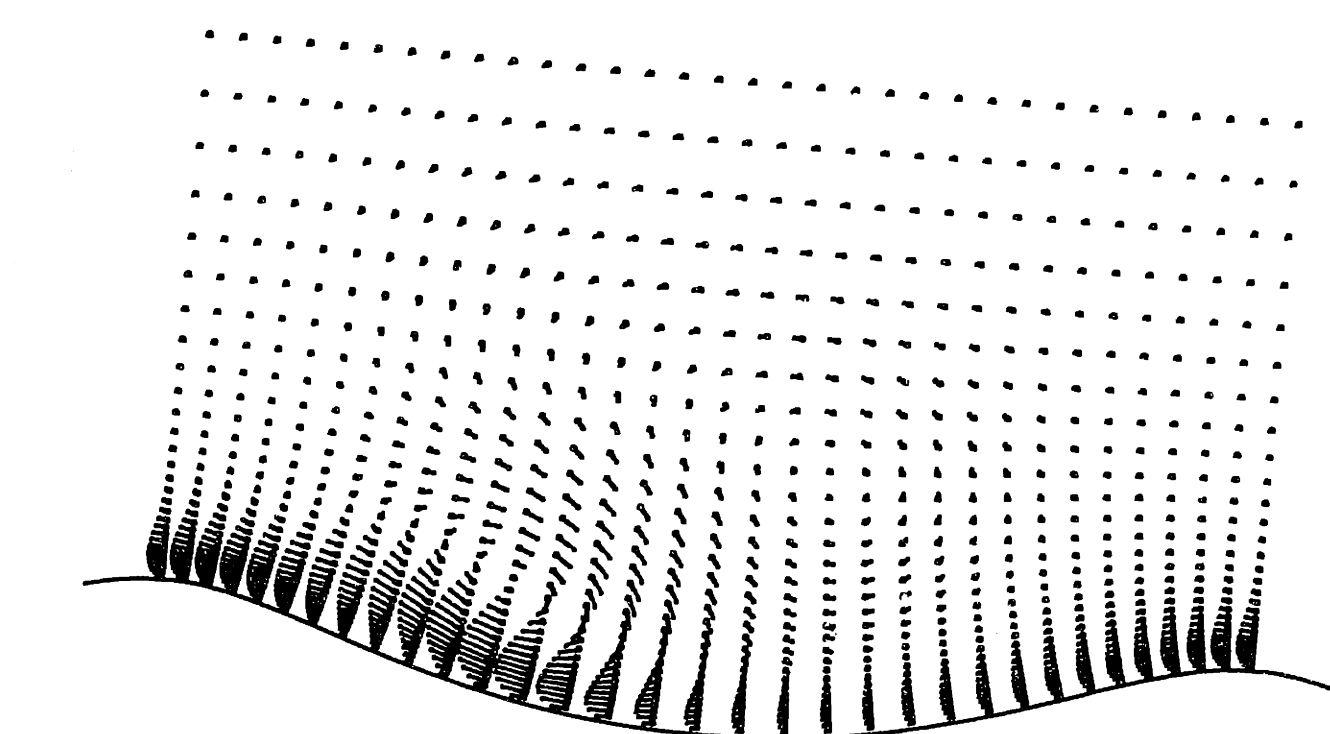
Fig. VII.1.1.   Velocity vectors

R = 15   K = 4.5   s = 0.1

$\Delta y \in (0.0124, 0.254)$ y_{max} = 2.05

M = 16   N = 31   P = 29

iii.   t = P+.7 U_∞:   ←

iv.   t = P+.8 U_∞:   ←

Fig. VII.1.1.   Velocity vectors

R = 15   K = 4.5   s = 0.1

$\Delta y \in$ (0.0124, 0.254) y_{max} = 2.05

M = 16   N = 31   P = 29

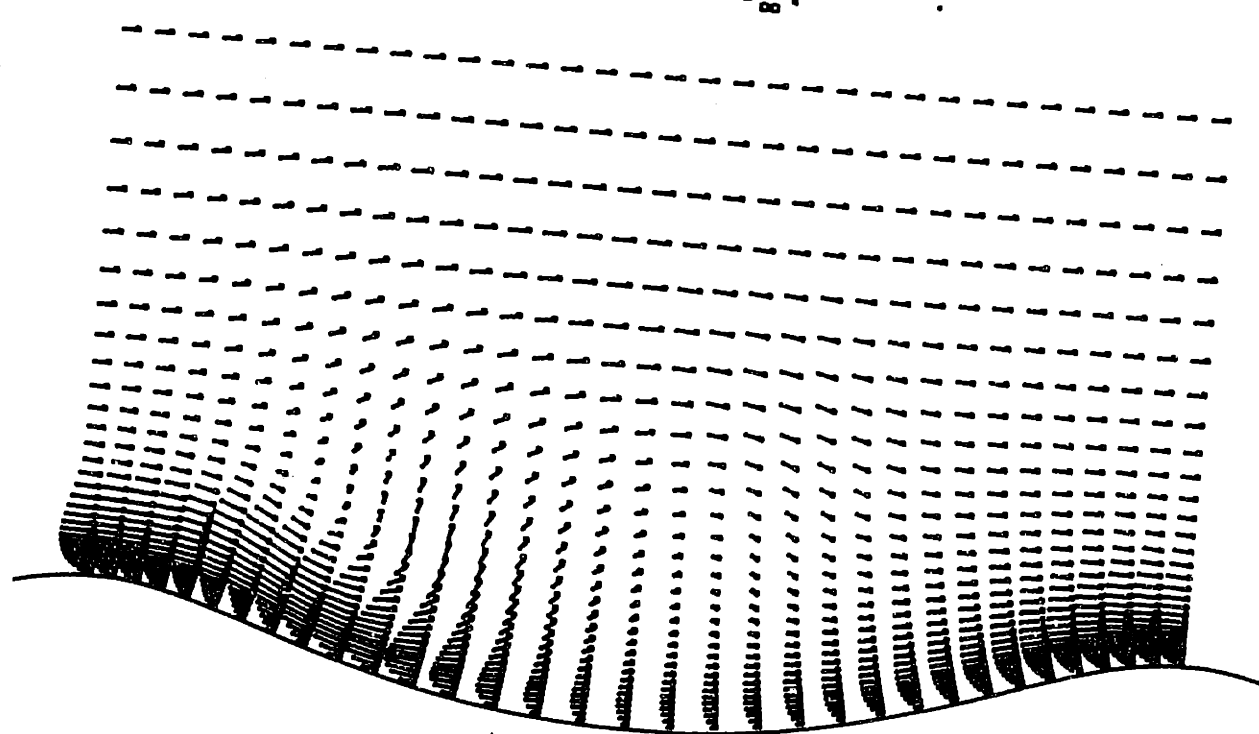165

v. t = P+.9 U∞: ←

vi. t = P+ 1 U∞:

Fig. VII.1.1. Velocity vectors

R = 15 K = 4.5 s = 0.1
Δy ∈ (0.0124, 0.254)
M = 16 N = 31 P≈29 y_max = 2.05

1.   t = P+.50 U_∞ :

11.   t = P+.55 U_∞ :

Fig. VII.1.2.   Velocity vectors

$R = 175$ $K = 4.5$ $s = 0.1$ $M = 32$ $N = 38$
$\Delta y \in (0.0044, 0.100)$ $y_{max} = 1.02$ $P = 18$

iii.   t = P+.60 U_∞ :   ←

iv.   t = P+.65 U_∞ :   ←

Fig. VII.1.2.   Velocity vectors

R = 175   K = 4.5   s = 0.1   M = 32   N = 38

$\Delta y \in$ (0.0044, 0.100) y_{max} = 1.02   P = 18

v.   t = P + .70 U_∞ :   ←

vi.   t = P + .75 U_∞ :   ←

Fig. VII.1.2.   Velocity vectors

R = 175   K = 4.5   s = 0.1   M = 32   N = 38

$\Delta y \in$ (0.0044, 0.100) y_{max} = 1.02   P = 18
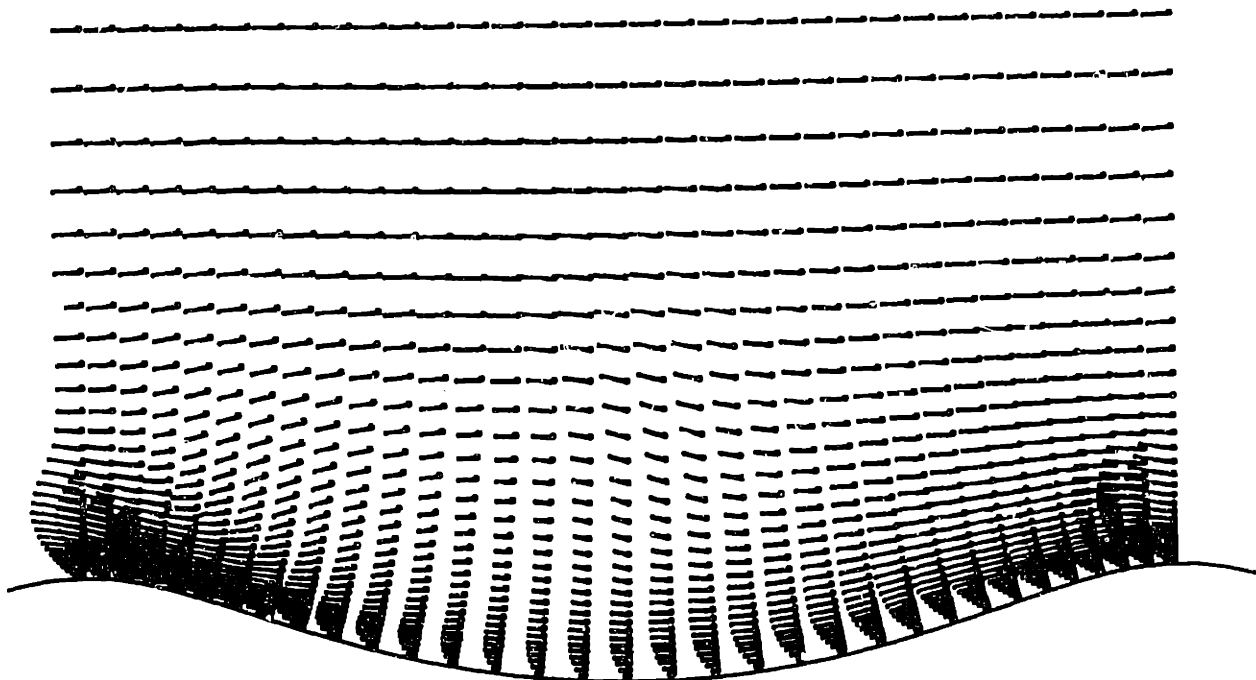
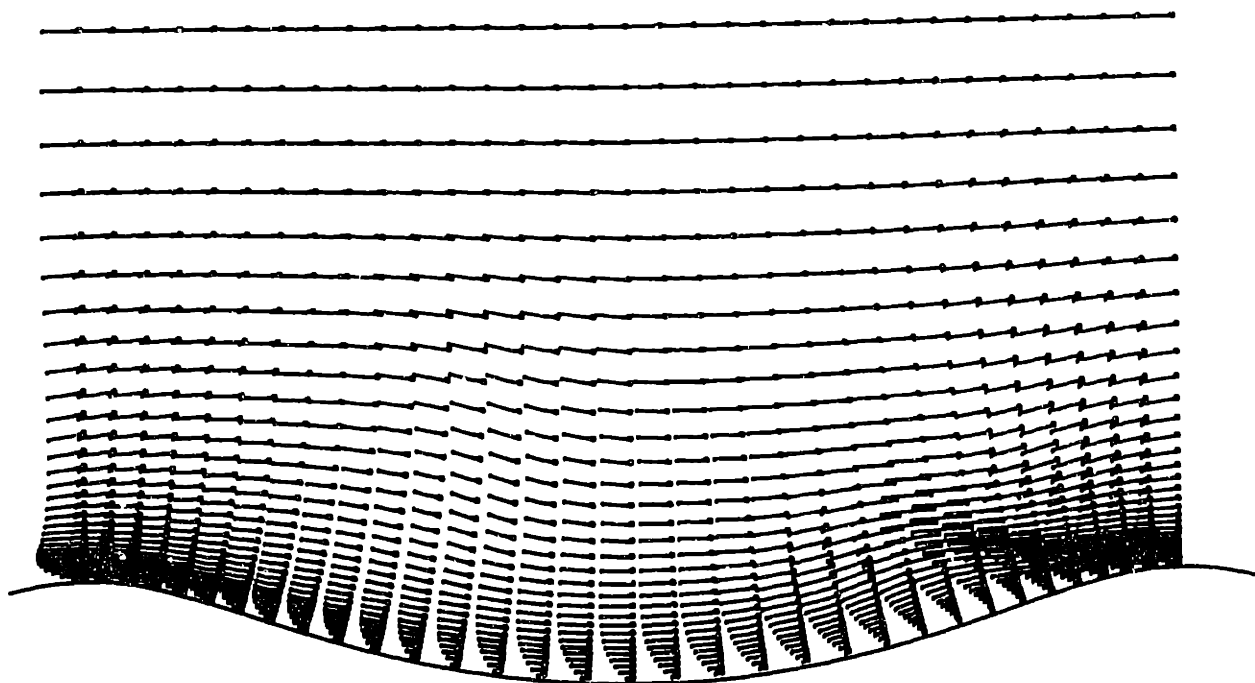vii. $t = P+.80$ U_∞: ←

viii. $t = P+.85$ U_∞: ←

Fig. VII.1.2. Velocity vectors

$R = 175$ $K = 4.5$ $s = 0.1$ $M = 32$ $N = 38$
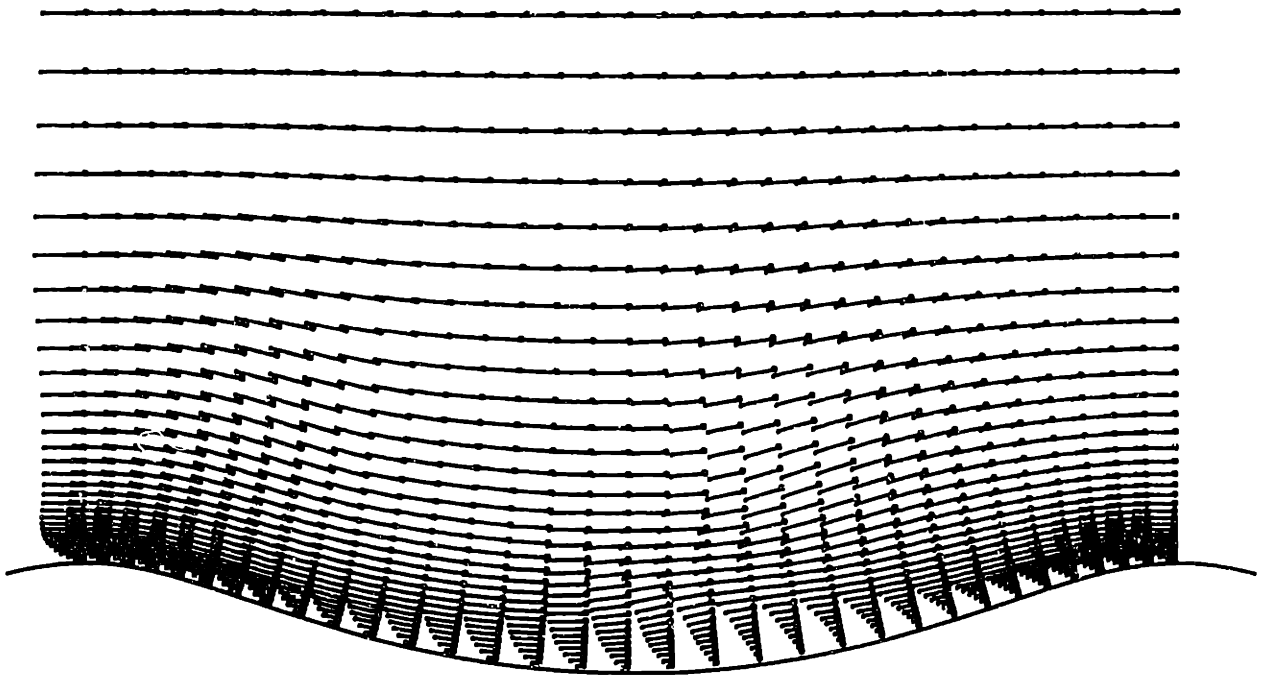
$\Delta y \in (0.0044, 0.100)$ $y_{max} = 1.02$ $P = 18$

ix.   t = P+.90   U∞ :   ←
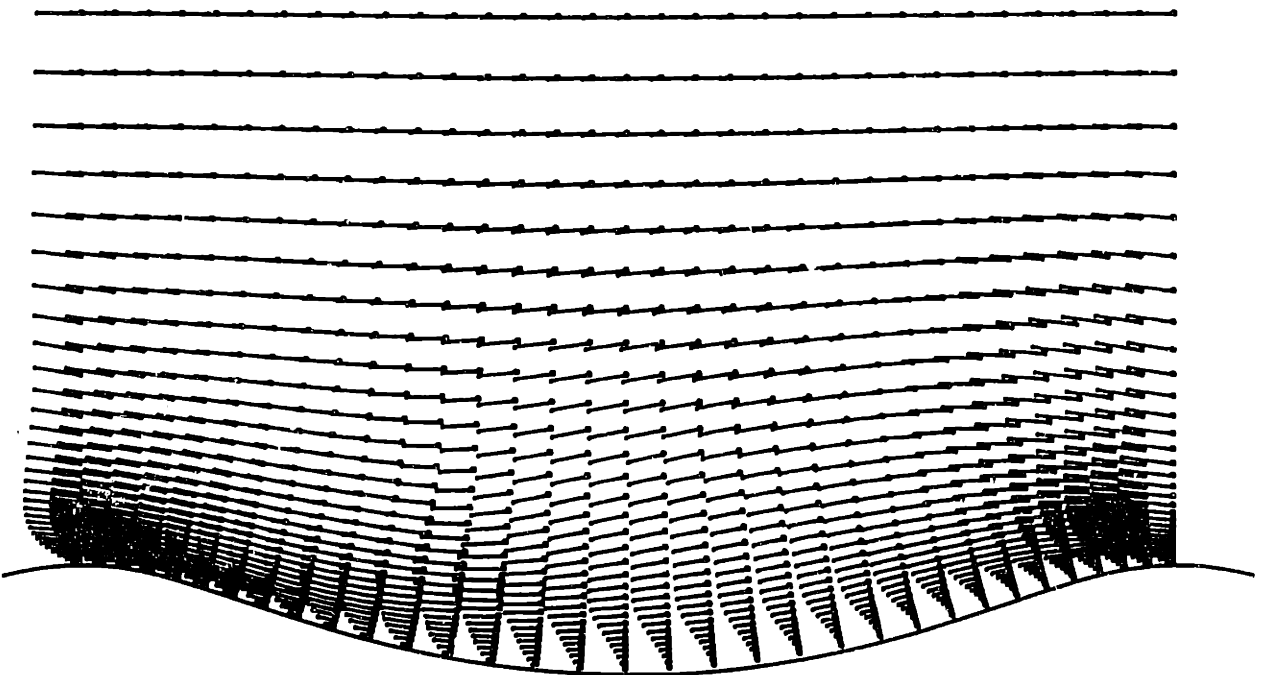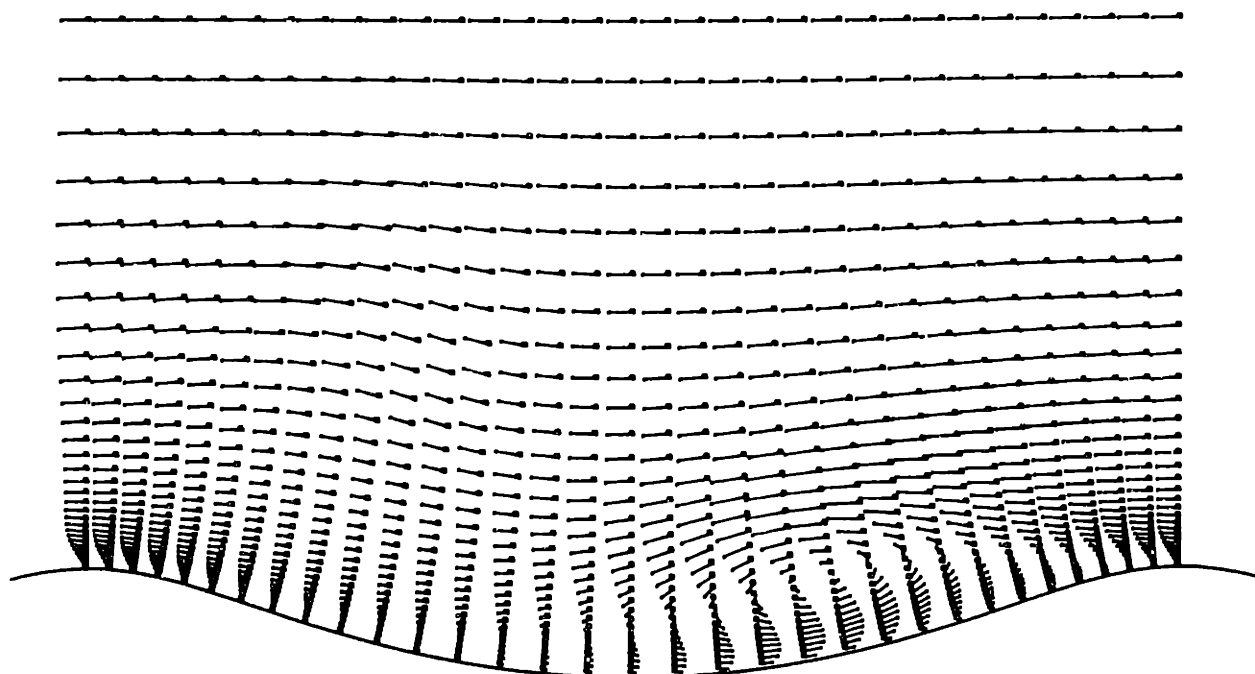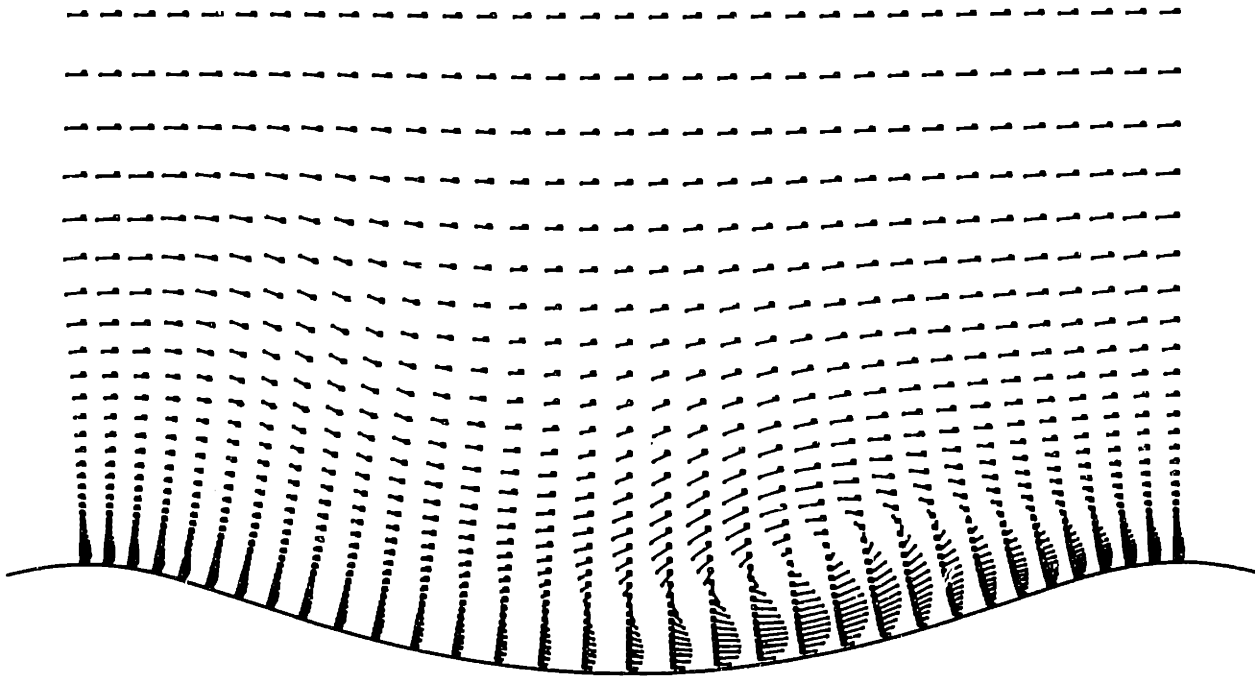

x.   t = P+.95   U∞ :   ←

Fig. VII.1.2.   Velocity vectors

R = 175   K = 4.5   s = 0.1   M = 32   N = 38
$\Delta y \in (\,0.0044,\ 0.100\,)$ $y_{max} = 1.02$ P = 18

171

xi.   t = P + 1.0 U_∞:

Fig. VII.1.2.   Velocity vectors

R = 175   K = 4.5   s = 0.1   M = 32   N = 38
$\Delta y \in (0.0044, 0.100)$ y_{max} = 1.02   P = 18
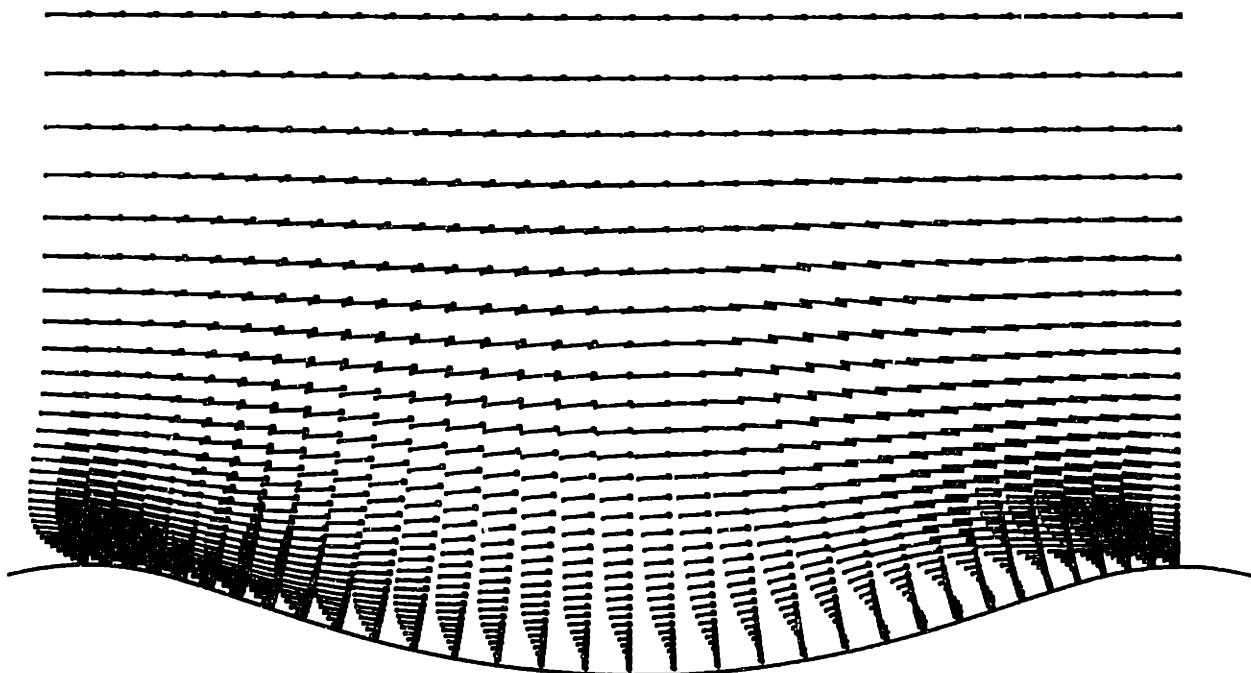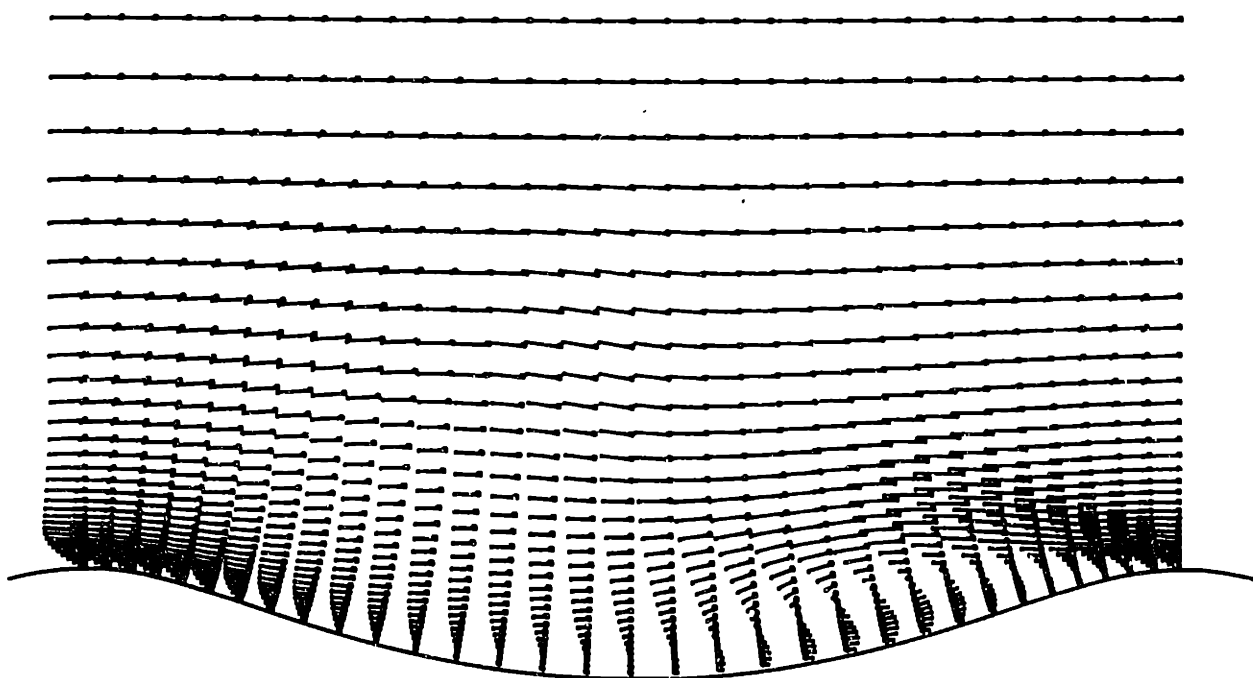
172

i.   t = P+.50 U_∞ :   ·
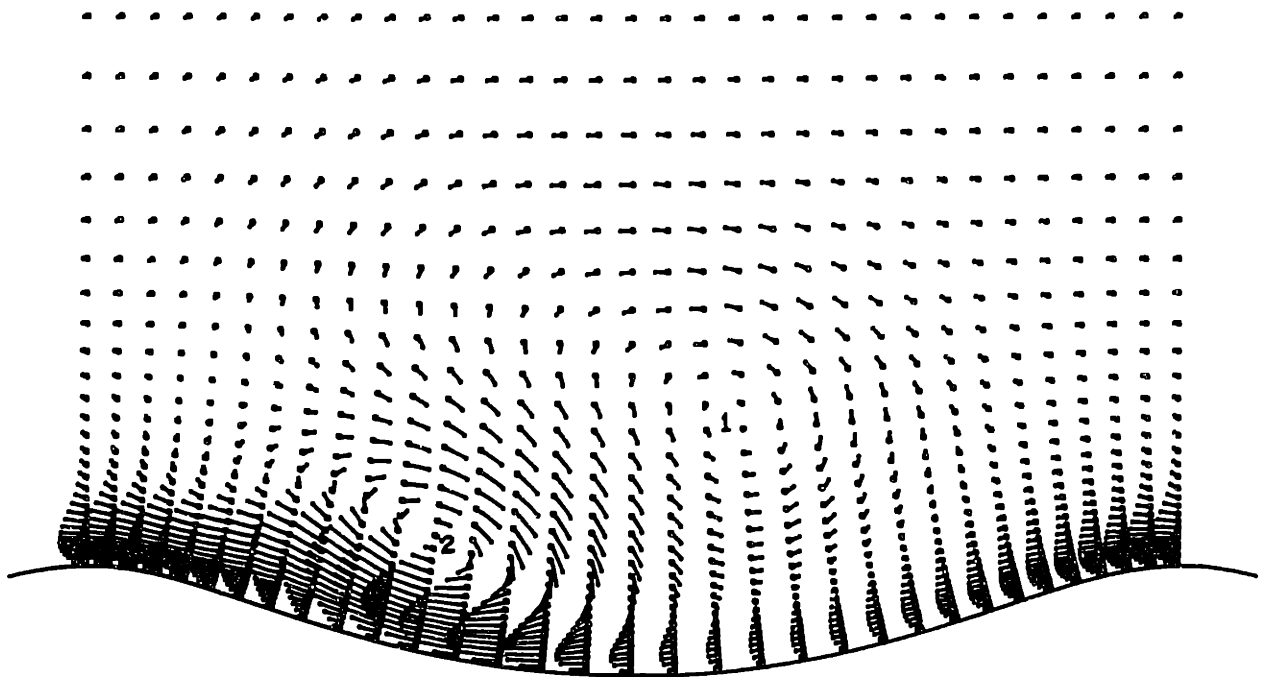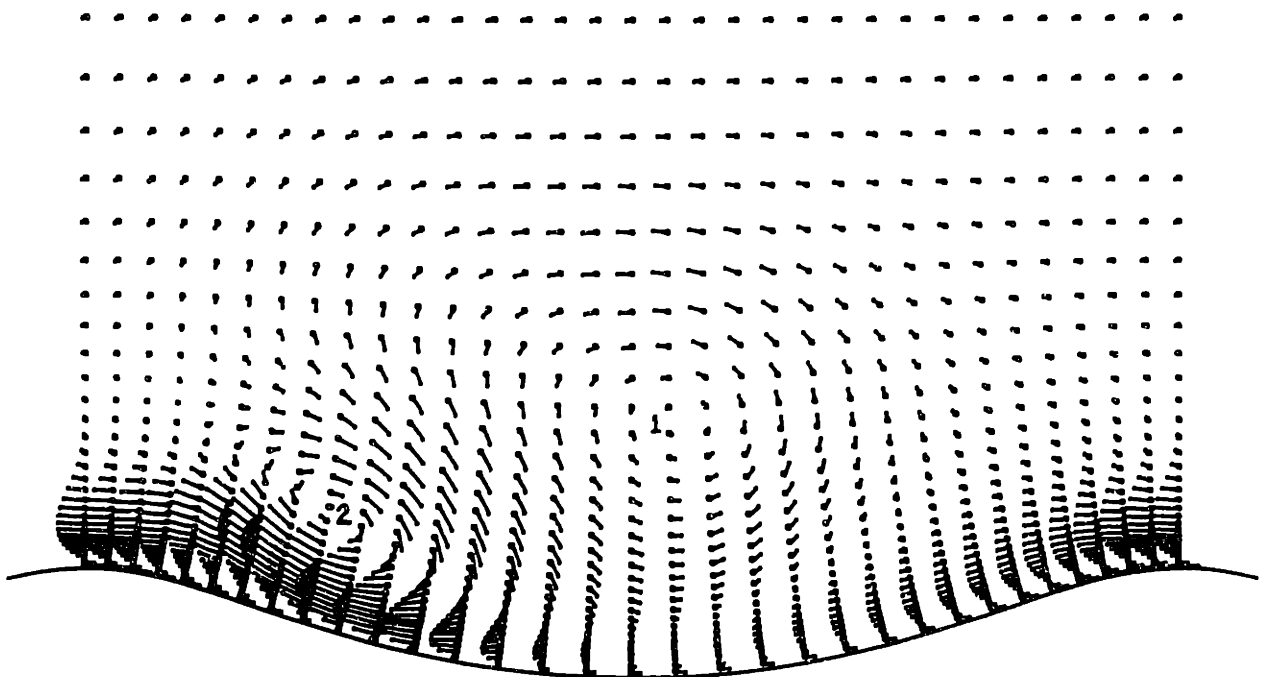
ii.   t = P+.55 U_∞ :   ←

Fig. VII.1.3.   Difference between computed and potential velocity

R = 175   K = 4.5   s = 0.1   M = 32   N = 38

$\Delta y \in$ (0.0044, 0.100) y_{max} = 1.02   P = 18
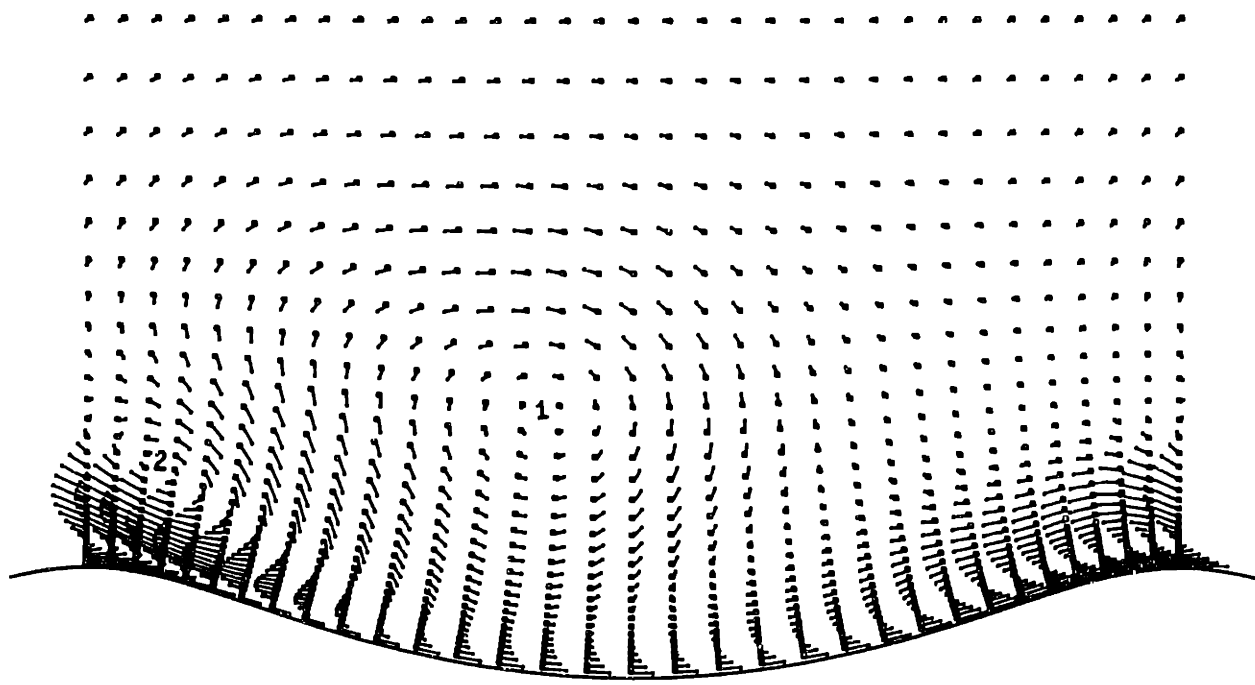
iii.   t = P+.60 U_∞:   ←
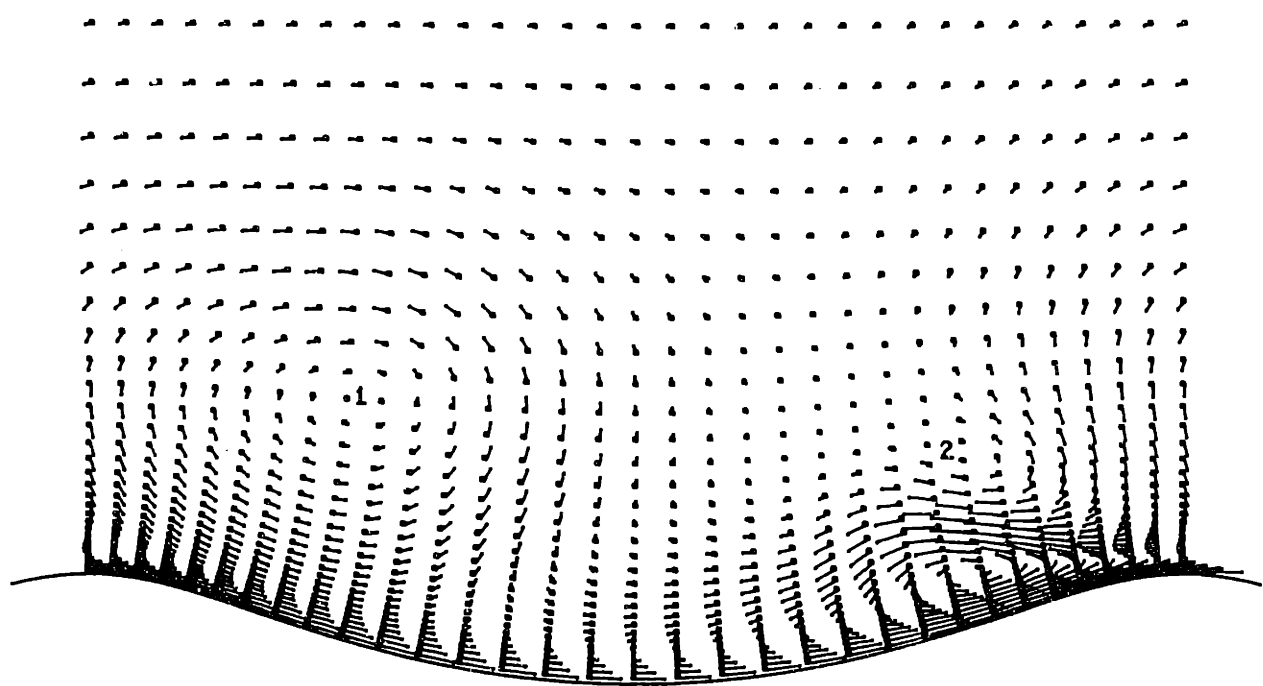
iv.   t = P+.65 U_∞:   ←

Fig. VII.1.3.   Difference between computed and potential velocity

R = 175   K = 4.5   s = 0.1   M = 32   N = 38

$\Delta y \in$ (0.0044, 0.100) y_{max} = 1.02   P = 18

v. $t = P + .70$ U_∞:   ←
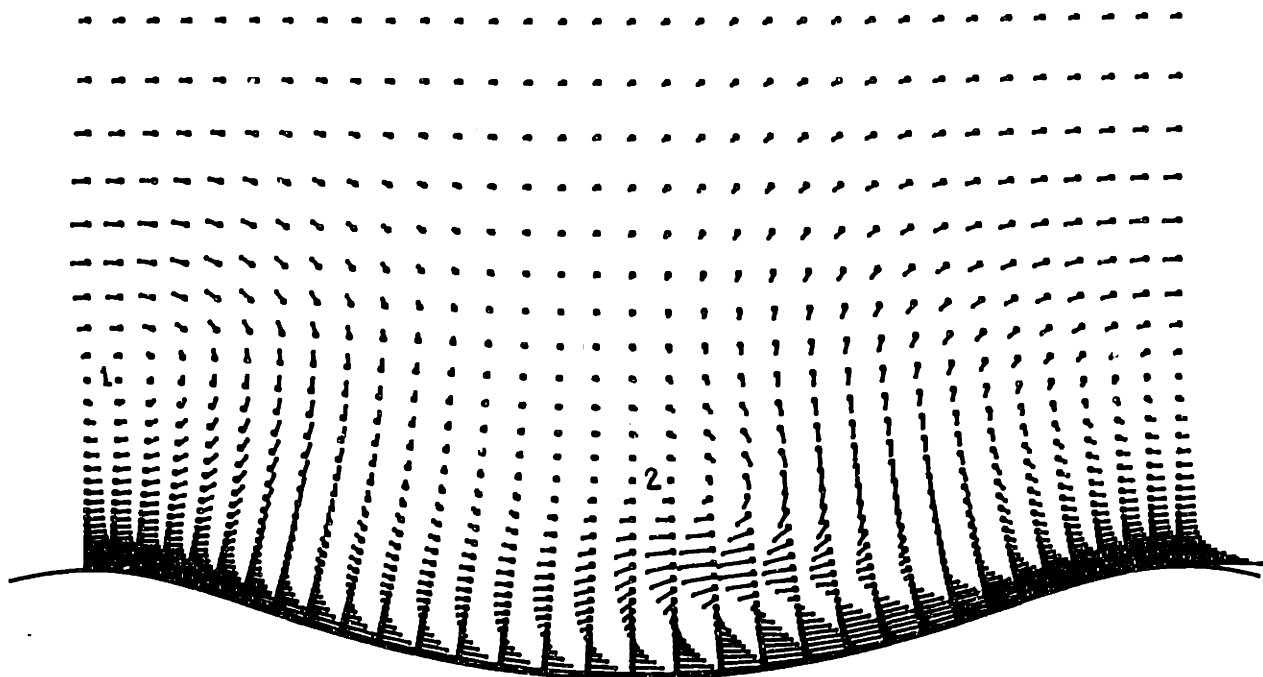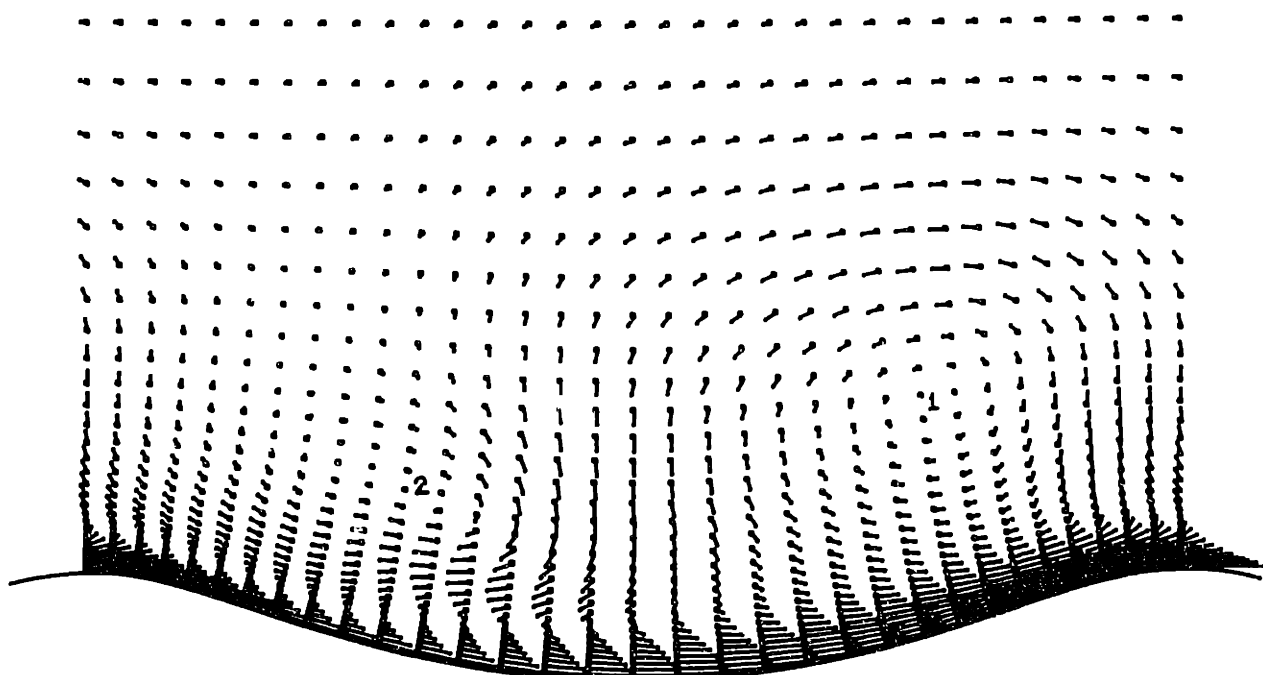
vi. $t = P + .75$ U_∞:   ←

Fig. VII.1.3.   Difference between computed and potential velocity

R = 175   K = 4.5   s = 0.1   M = 32   N = 38

$\Delta y \in (\, 0.0044, \ 0.100 \,)$ $y_{max} = 1.02$ P = 18

175

vii.   t = P+.80 U_∞:   ←
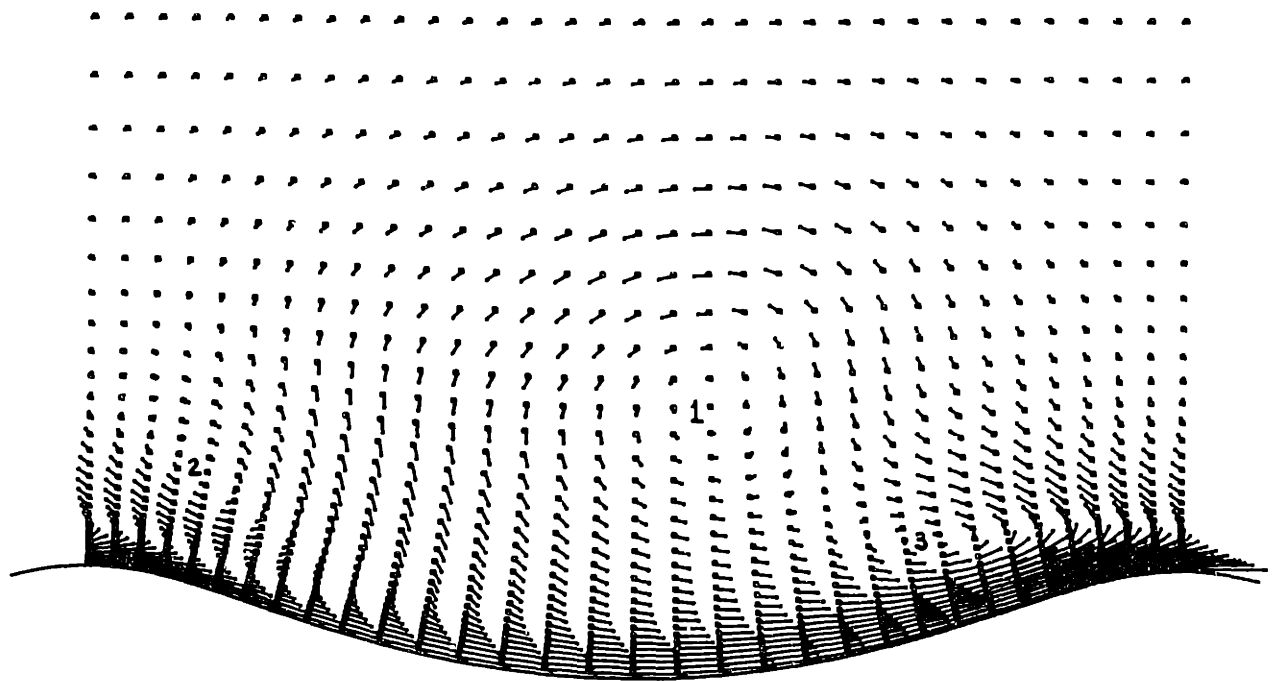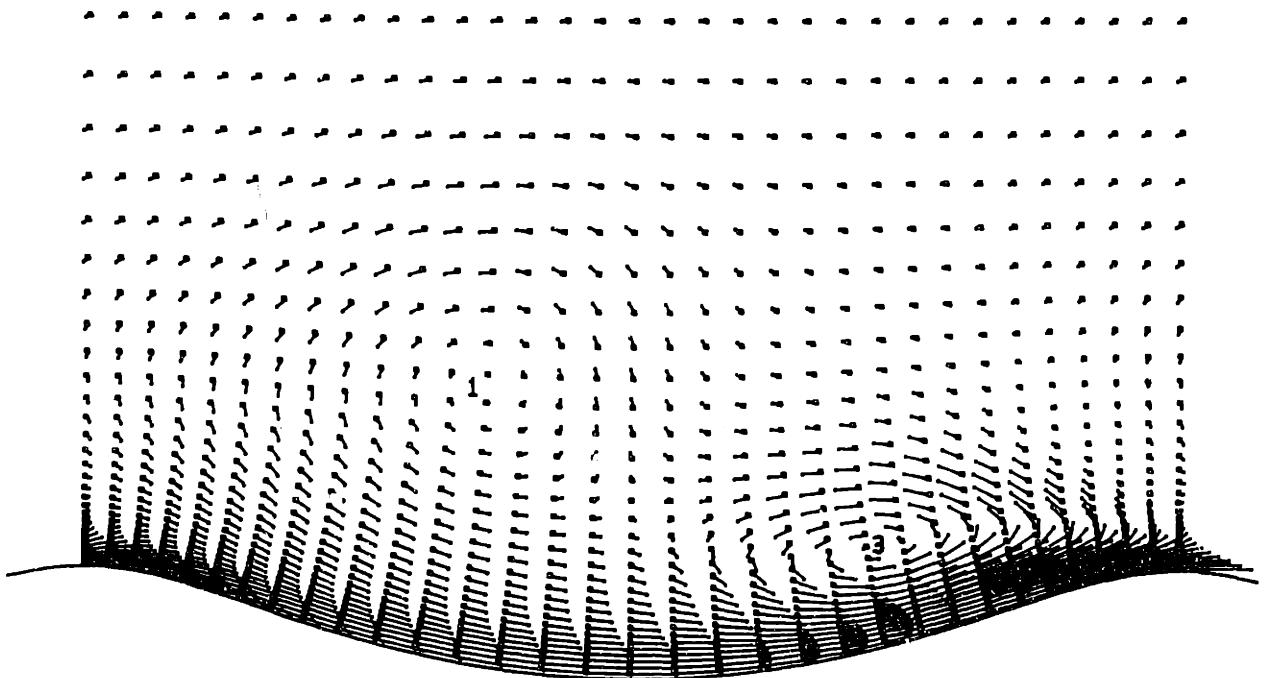
viii.   t = P+.85 U_∞:   ←

Fig. VII.1.3.   Difference between computed and potential velocity

R = 175   K = 4.5   s = 0.1   M = 32   N = 38

$\Delta y \in (\ 0.0044, \ 0.100\ )$ y_{max} = 1.02   P = 18

ix.   t = P + .90 U_∞ :   ←

x.   t = P + .95 U_∞ :   ←

Fig. VII. 1. 3.   Difference between computed and potential velocity

R = 175   K = 4.5   s = 0.1   M = 32   N = 38

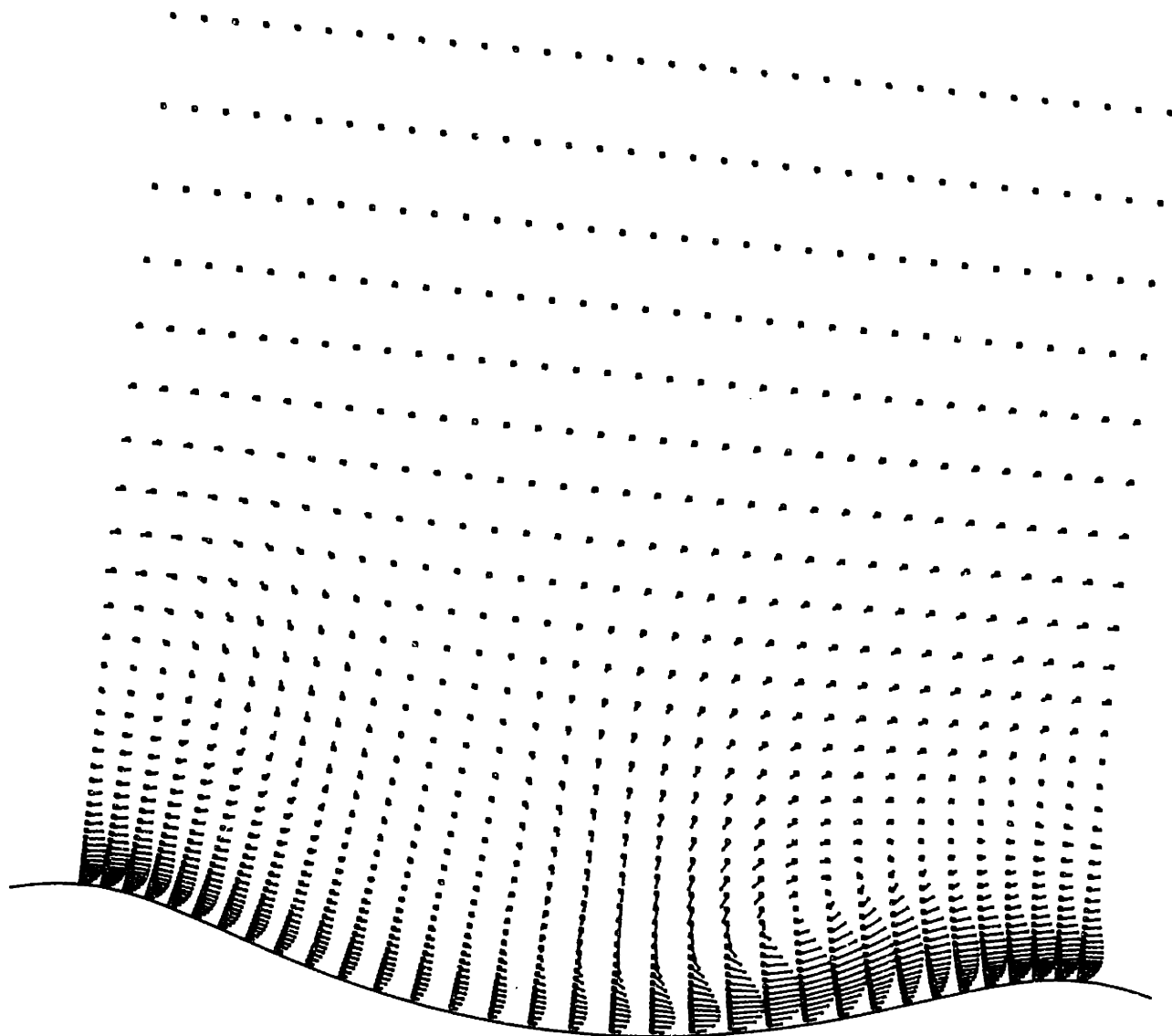$\Delta y \in$ (0.0044, 0.100) y_{max} = 1.02   P = 18
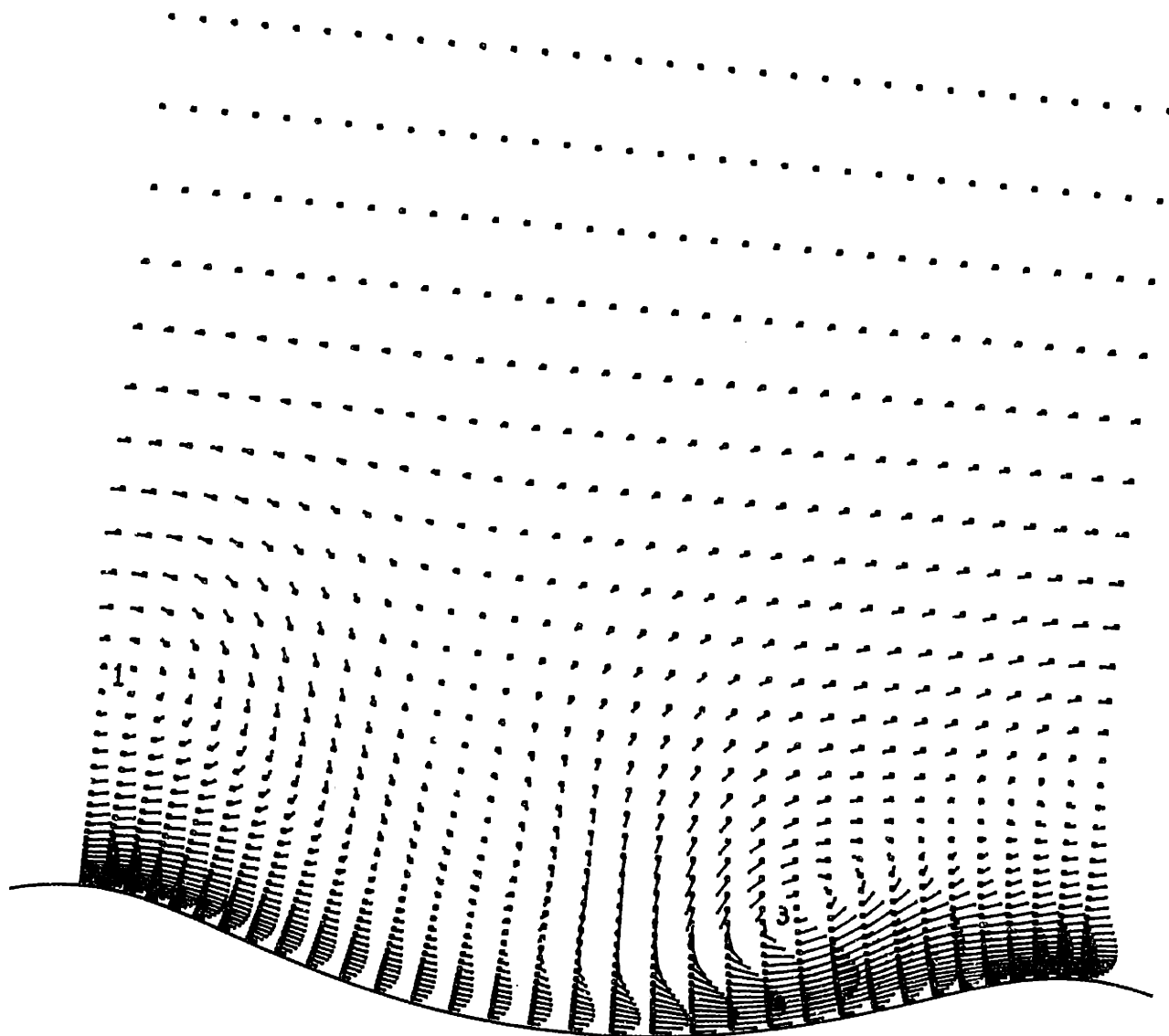
xi.   t = P + 1.0 U_∞ :

Fig. VII.1.3.   Difference between computed and potential velocity
R = 175   K = 4.5   S = 0.1   M = 32   N = 38
$\Delta y \in (0.0044, 0.100)$ y_{max} = 1.02   P = 18
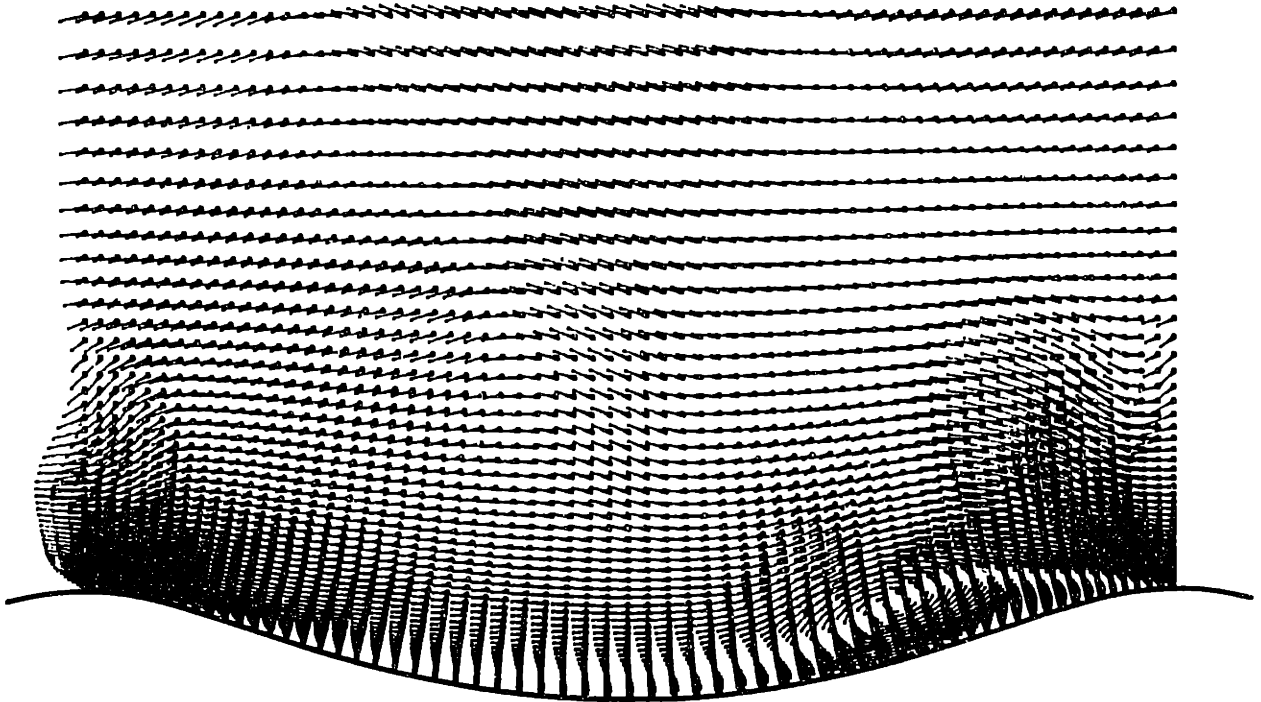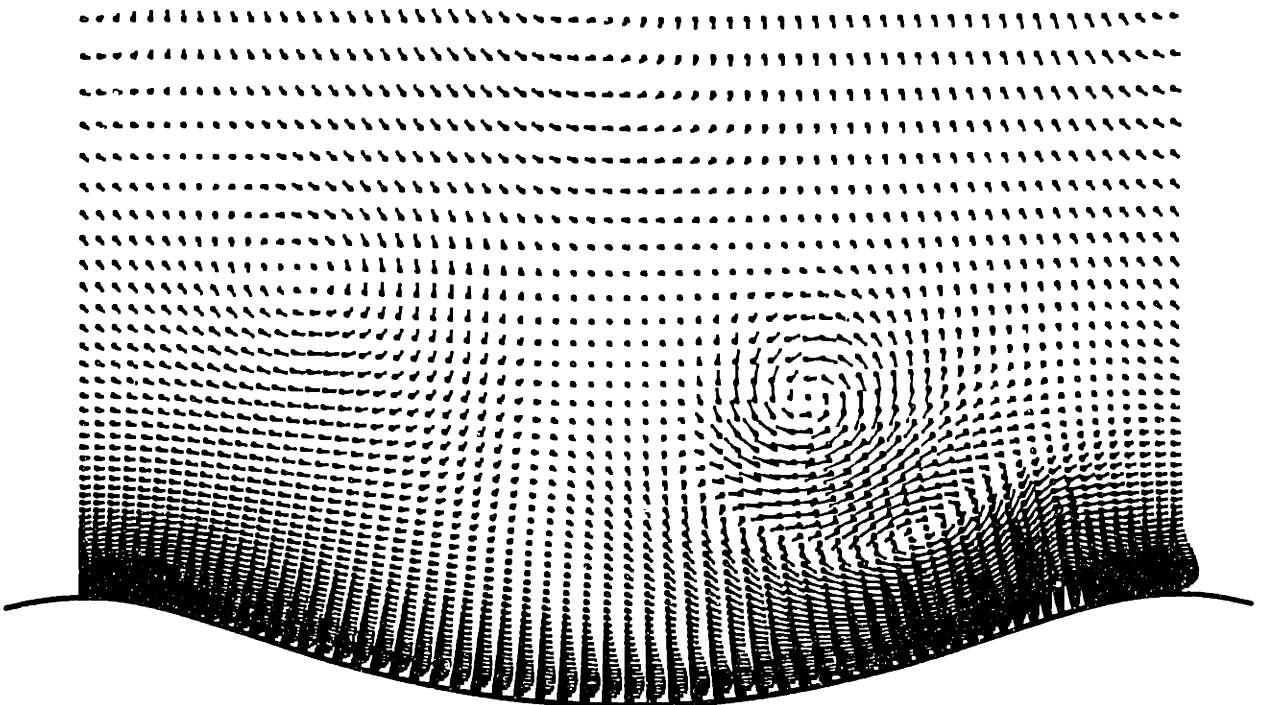
i.   t = P+0.875   U$_\infty$:   ←

ii.   t = P+1.000   U$_\infty$:   ·

Fig. VII.1.4.   Velocity vectors.

R = 500   K = 4.5   s = 0.1   M = 64   N = 72

dy = (0.0026, 0.118)   y$_{max}$ = 2.03   P = 18
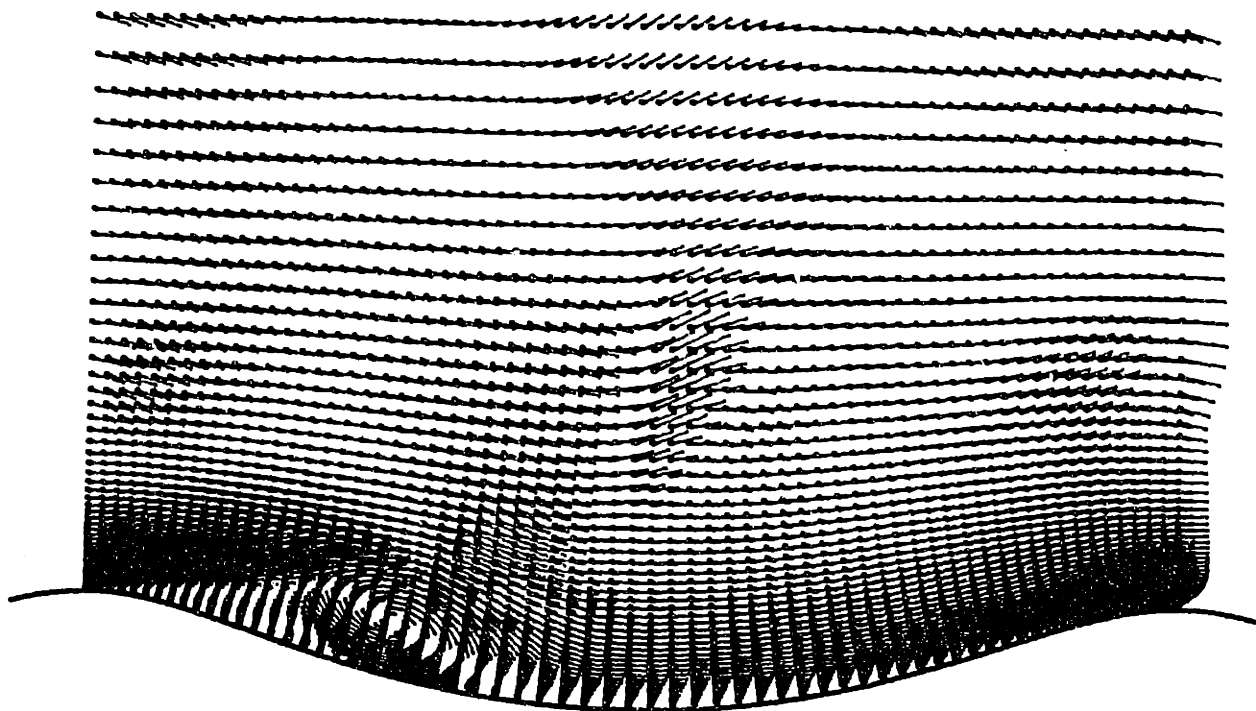
iii.   t = P+0.375   U∞ :   →
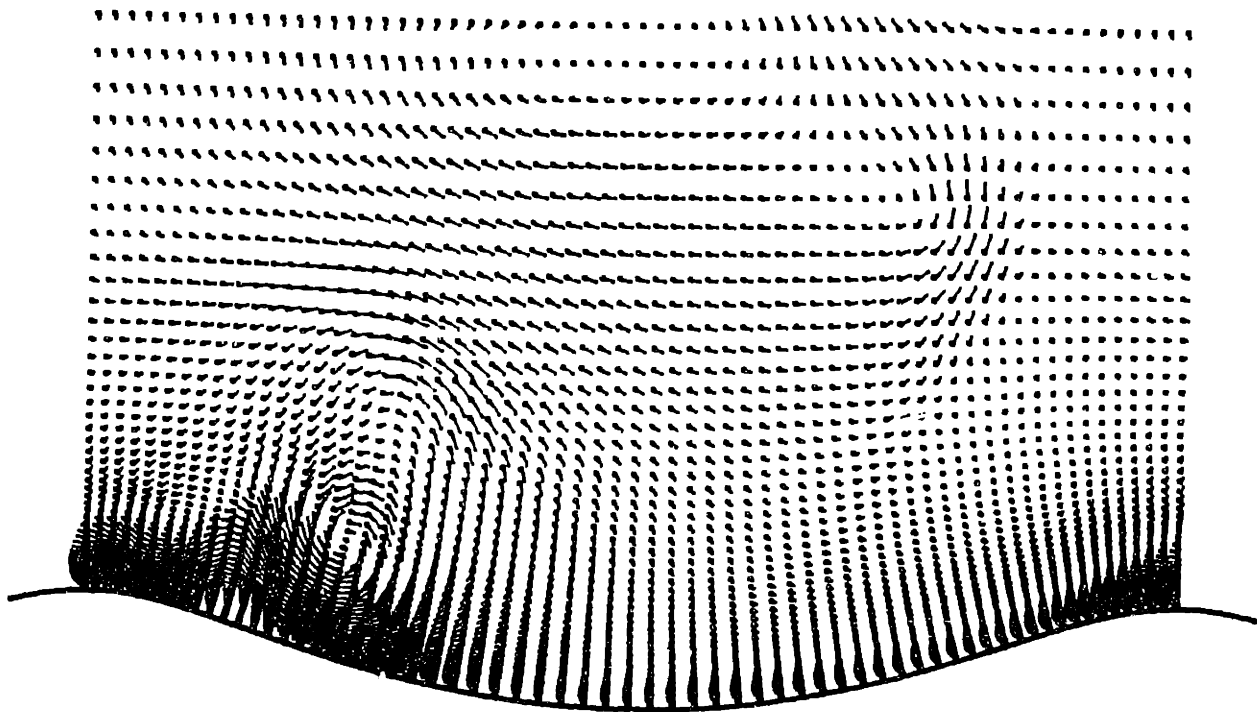
iv.   t = P+0.500   U∞ :   .

Fig. VII.1.4.   Velocity vectors.

R = 500   K = 4.5   s = 0.1   M = 64   N = 72
dy = (0.0026, 0.118) y_{max} = 2.03   P = 19
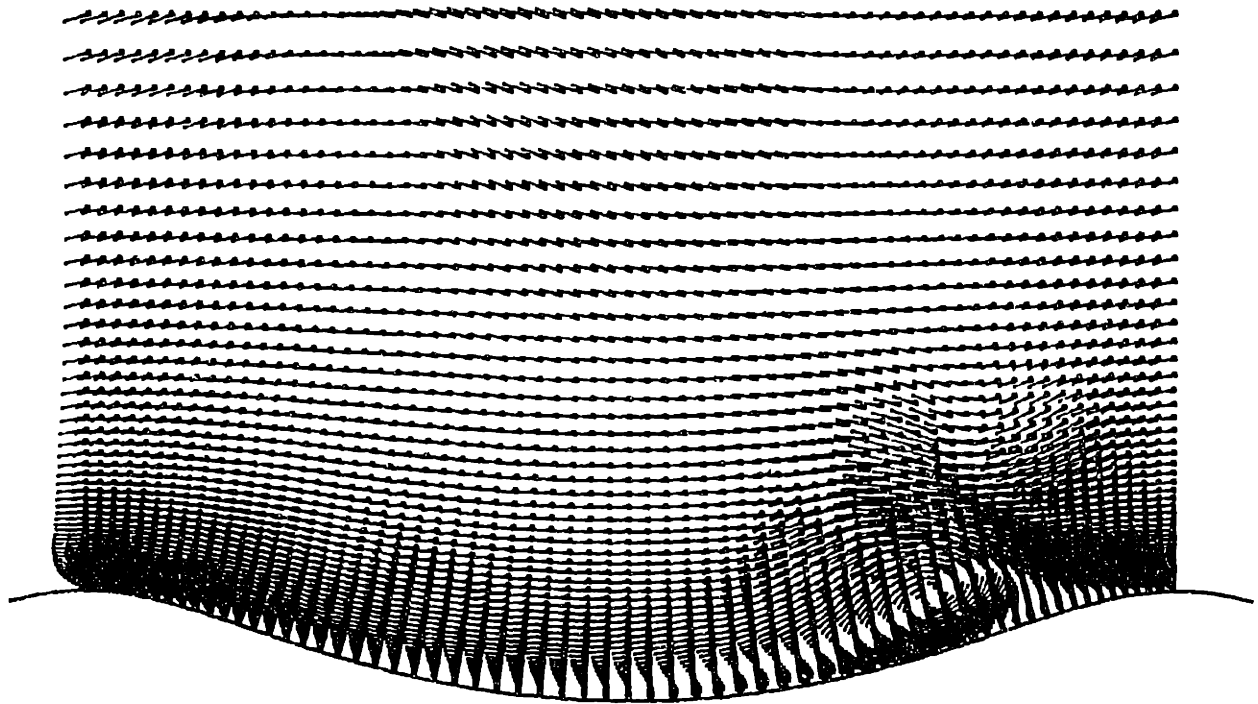
v.   t = P+0.875 U_∞ :   ←
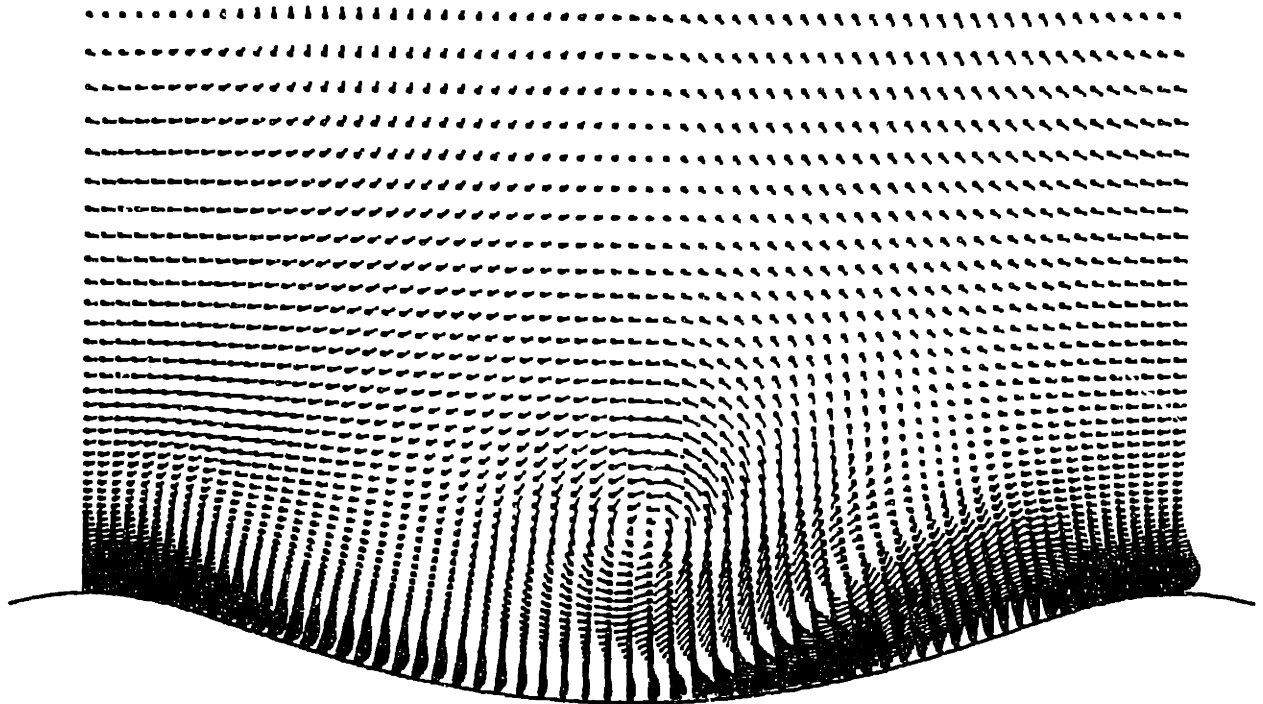
vi.   t = P+1.00 U_∞ :   ·

Fig. VII.1.4. **Velocity Vectors**

R = 500   K = 4.5   s = 0.1   M = 64   N = 72

dy = (0.0026, 0.118) y_{max} = 2.03   P = 19

i.   t = P+.90 U_∞:   ←

ii.   t = P+1.00 U_∞:
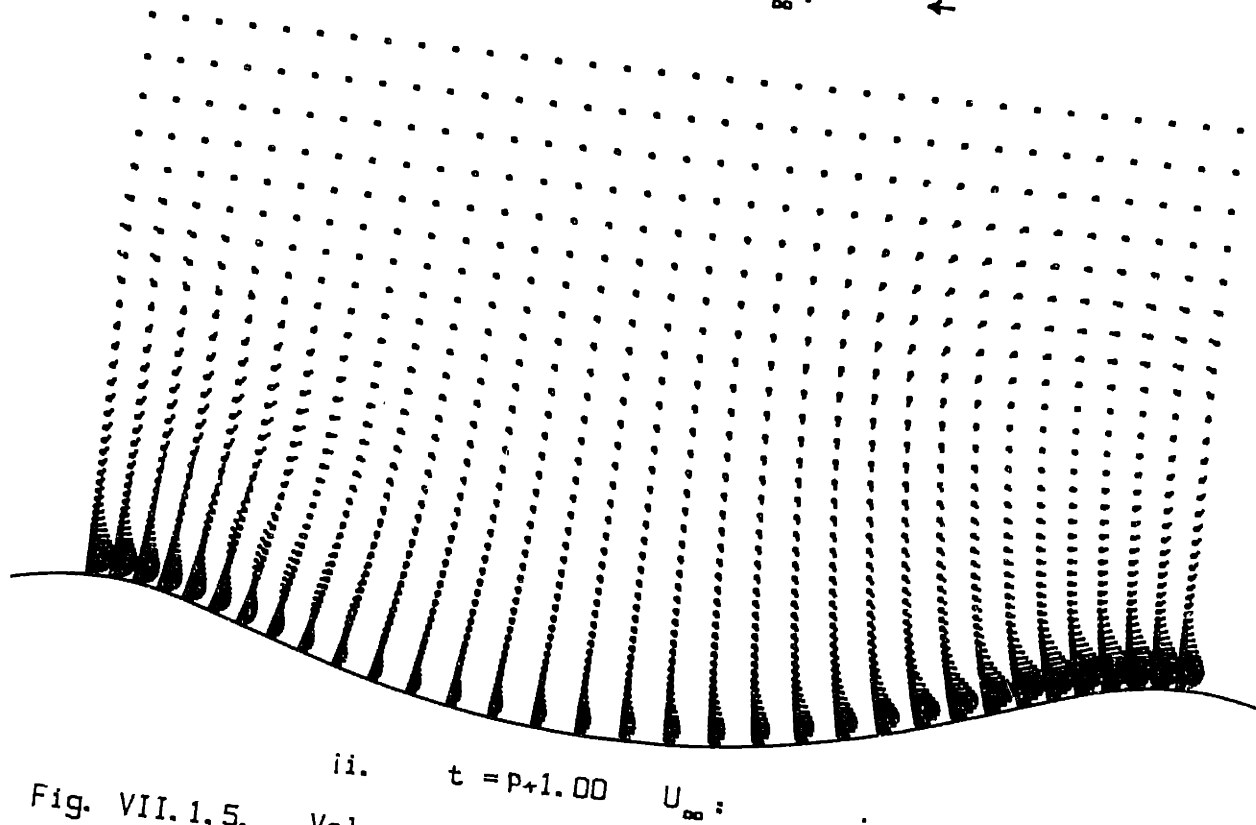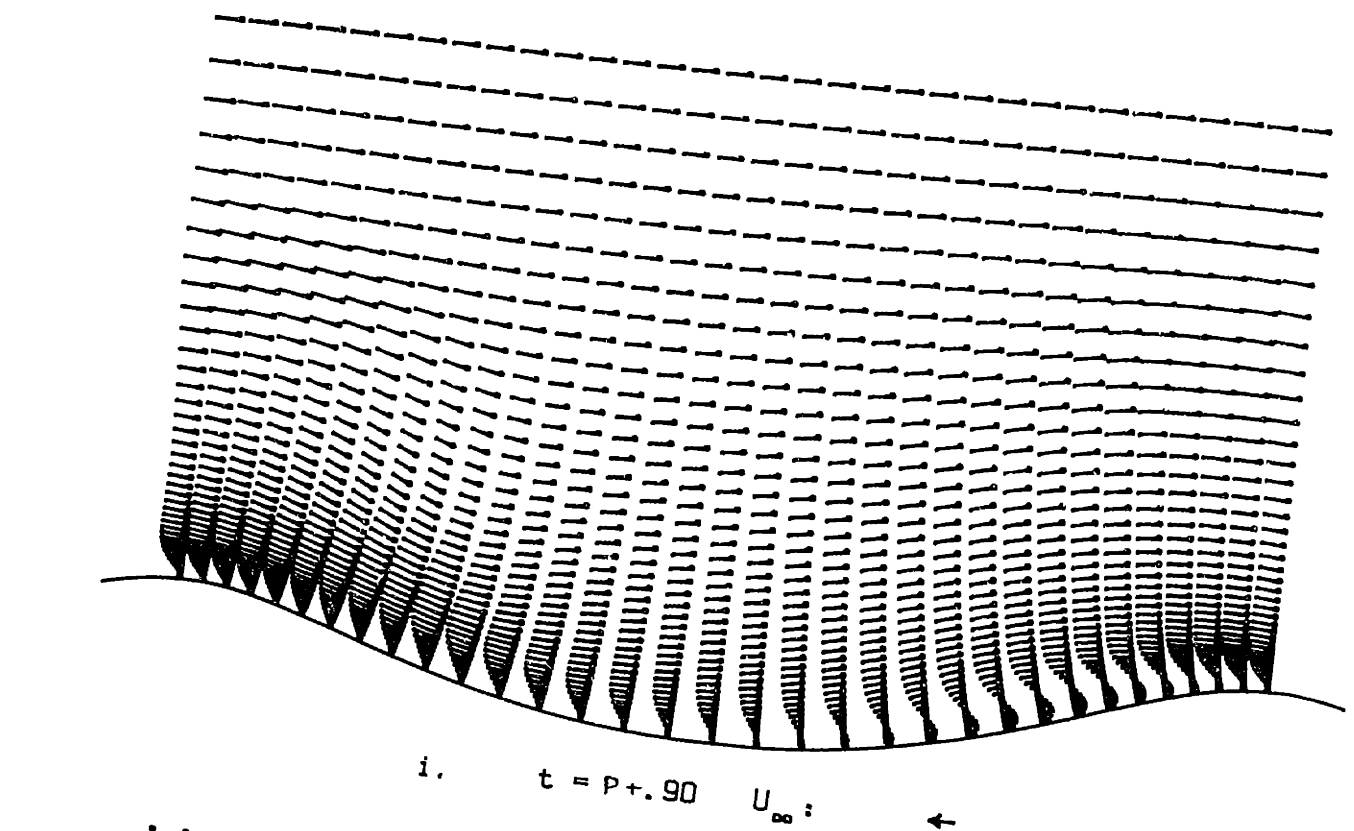
Fig. VII.1.5.   Velocity vectors

$R = 250$ $K = 2.5$ $s = 0.1$ $M = 32$ $N = 51$

$\Delta y \in (0.0034, 0.072)$ $y_{max} = 1.06$ $P = 10$

i.   t = P+.70 U_∞ :   ←
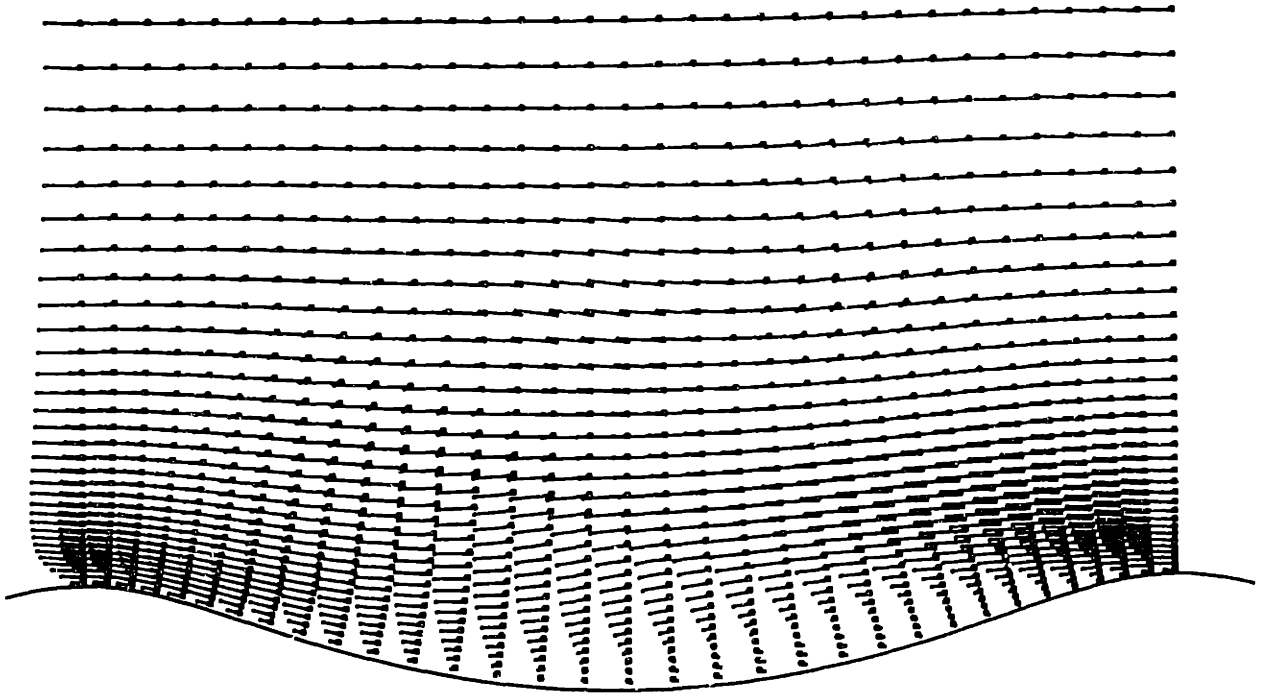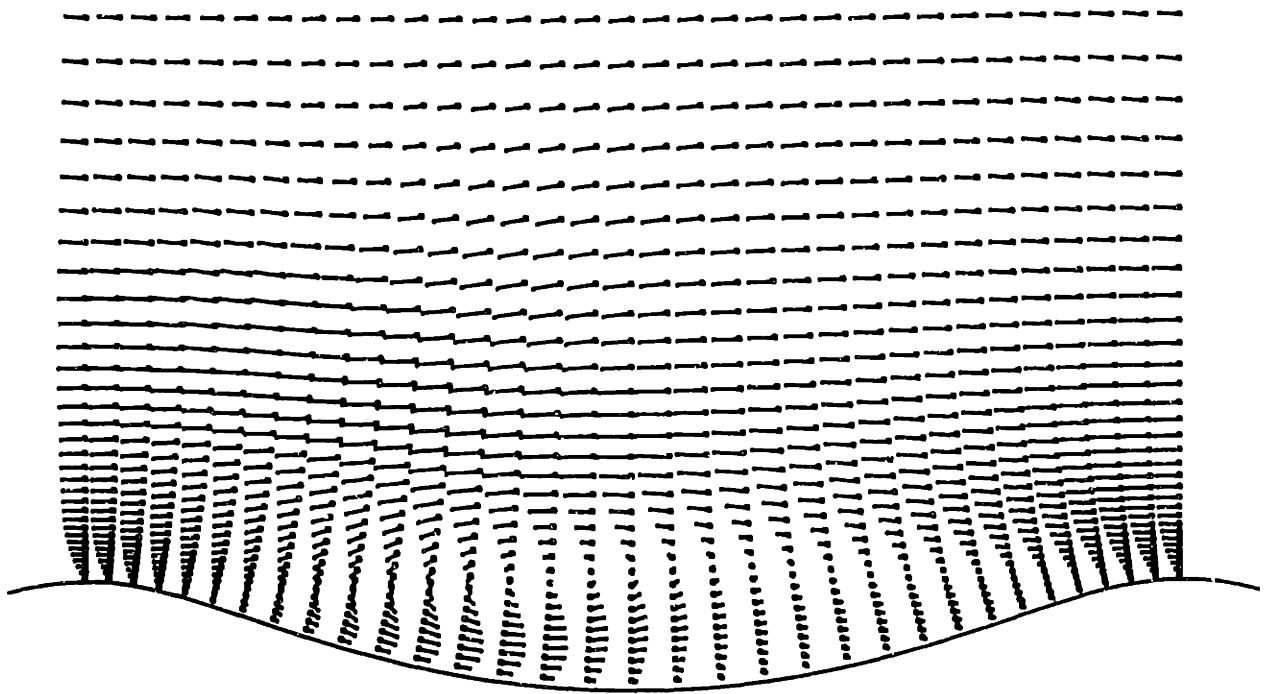
ii.   t = P+.90 U_∞ :   ←

Fig. VII.1.6.   Velocity vectors

R = 175   K = 12.0   s = 0.1   M = 32   N = 45

$\Delta y \in (0.0071, 0.091)$ y_{max} = 1.33   P = 9
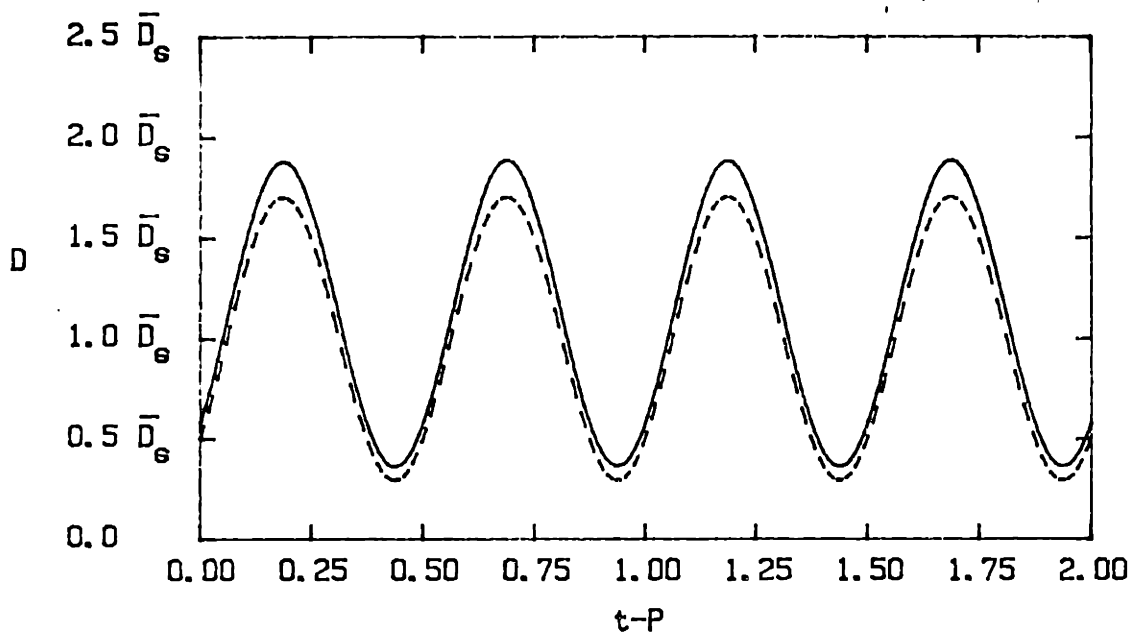
Fig. VII.2.1.   Rate of viscous dissipation   P = 8
R = 15   K = 4.5   s = 0.1
M = 16   N = 31 $\bar{D}_s$ = 0.0341
dy = (0.0124, 0.254) y_{max} = 2.05

———— over ripples, D
------- over plane bed, D_s
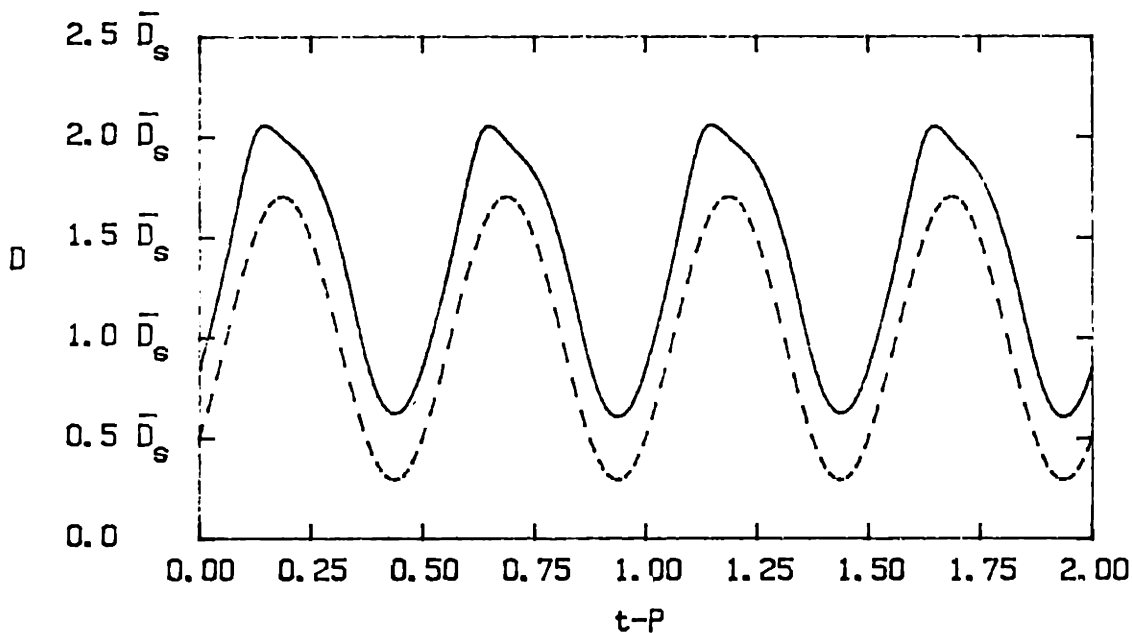
Fig. VII.2.2.   Rate of viscous dissipation   P = 8
R = 100   K = 4.5   s = 0.1
M = 16   N = 32 $\bar{D}_s$ = 0.0132
dy = (0.0058, 0.117) y_{max} = 1.01

184
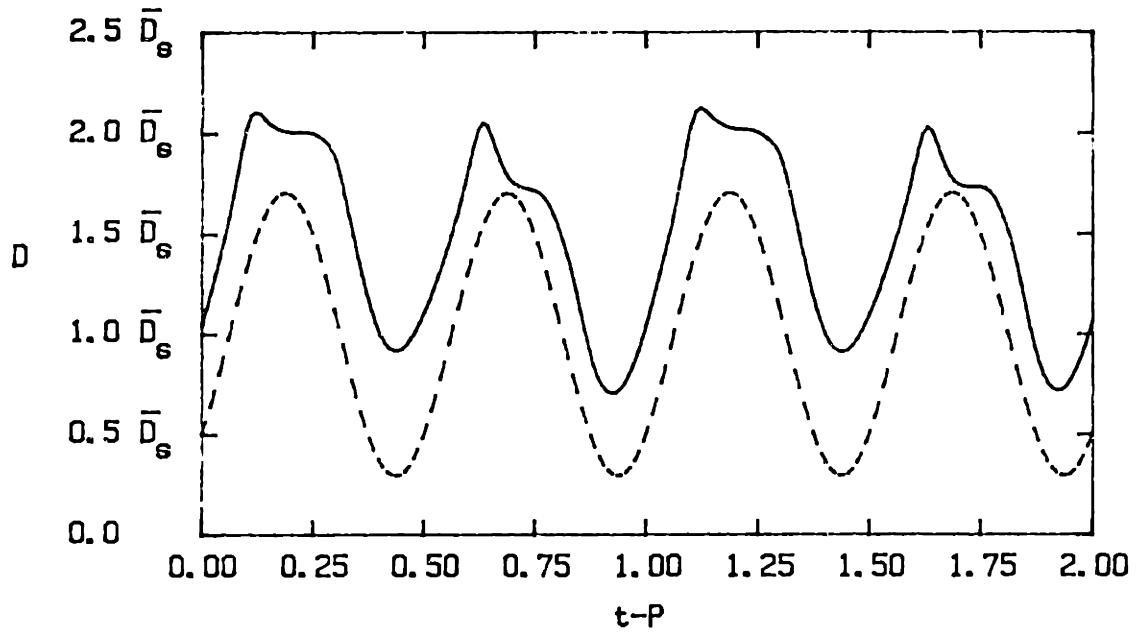
Fig. VII.2.3.   Rate of viscous dissipation   P = 16
                 R = 175   K = 4.5   s = 0.1
                 M = 32   N = 38 $\bar{D}_s$ = 0.0100
                 dy = (0.0044, 0.100) y_{max} = 1.02

——————— over ripples, D
- - - - - over plane bed, D_s
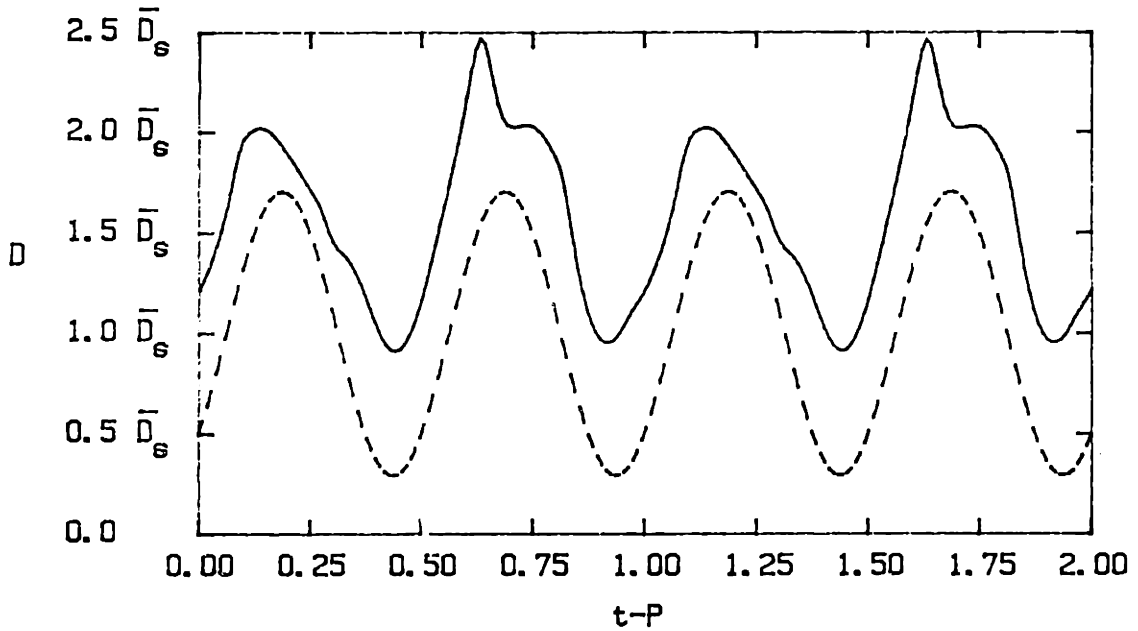
Fig. VII.2.4.   Rate of viscous dissipation   P = 33
                 R = 250   K = 4.5   s = 0.1
                 M = 32   N = 57 $\bar{D}_s$ = 0.0084
                 dy = (0.0036, 0.151) y_{max} = 2.08

185
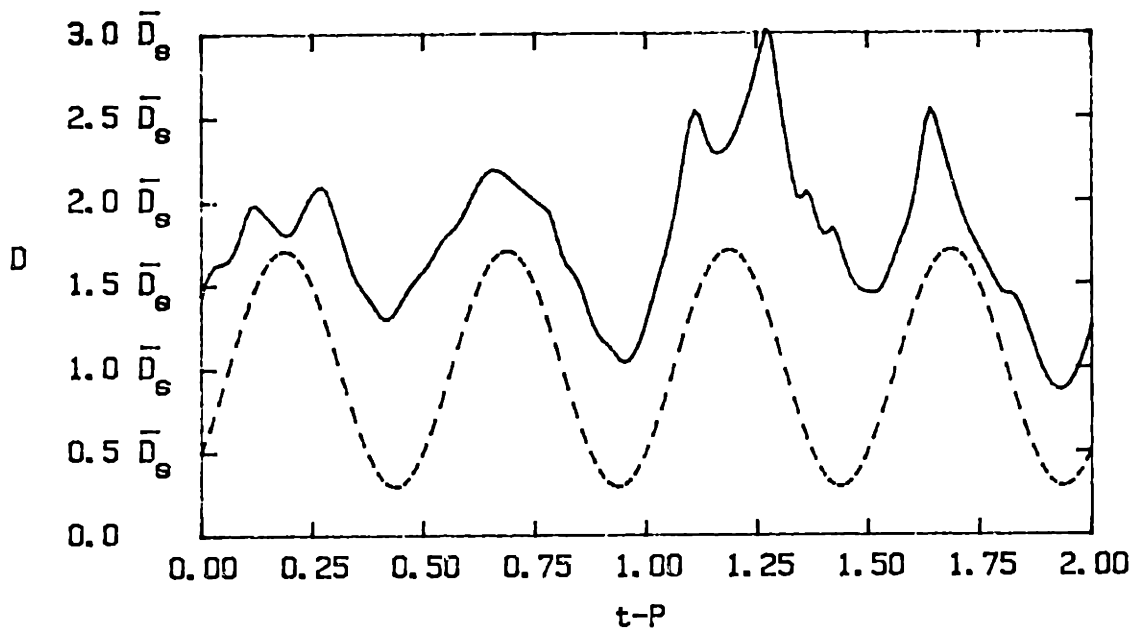
Fig. VII.2.5.   Rate of viscous dissipation   P = 20
R = 500   K = 4.5   s = 0.1
M = 64   N = 72 $\overline{D}_s$ = 0.0059
dy = (0.0026, 0.118) y_{max} = 2.03

───────   over ripples, D
─ ─ ─ ─   over plane bed, D_s
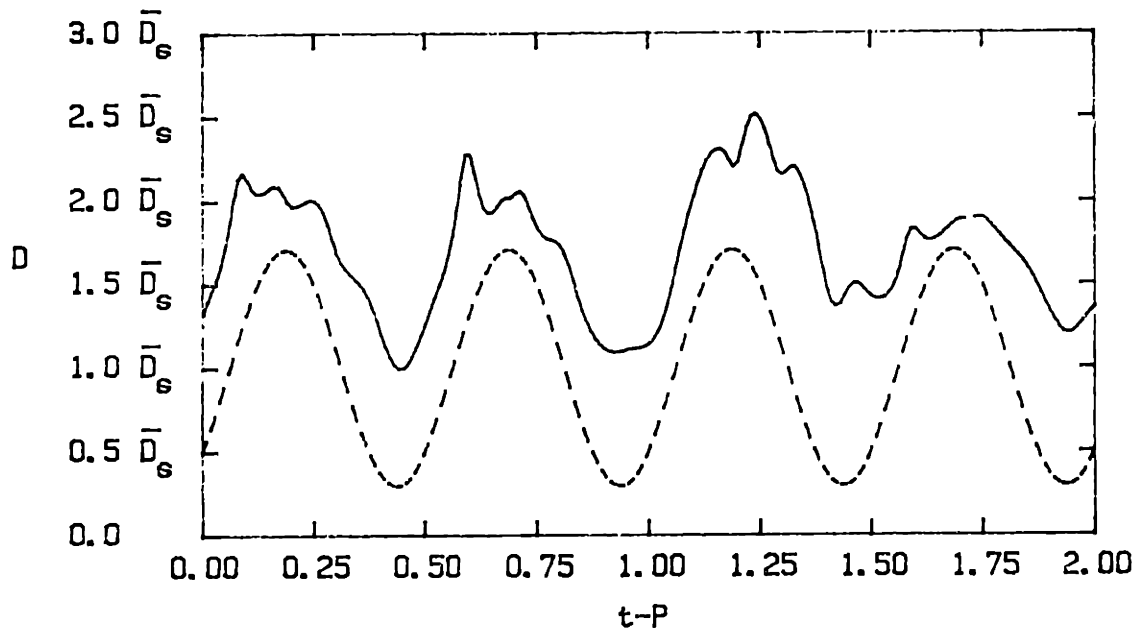
Fig. VII.2.6.   Rate of viscous dissipation   P = 20
R = 250   K = 9.0   s = 0.1
M = 32   N = 42 $\overline{D}_s$ = 0.0059
dy = (0.0052, 0.223) y_{max} = 2.16
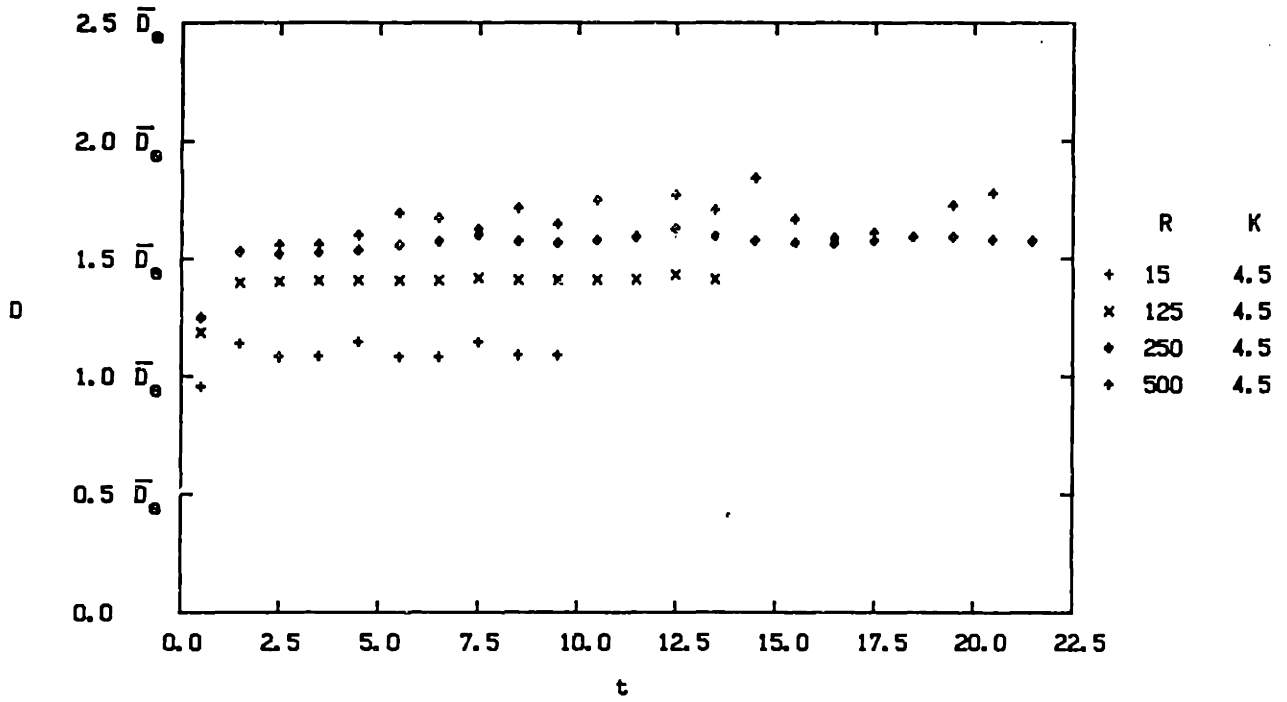
Fig. VII.2.7.   Variation of energy dissipation with time $\varepsilon = 0.1$
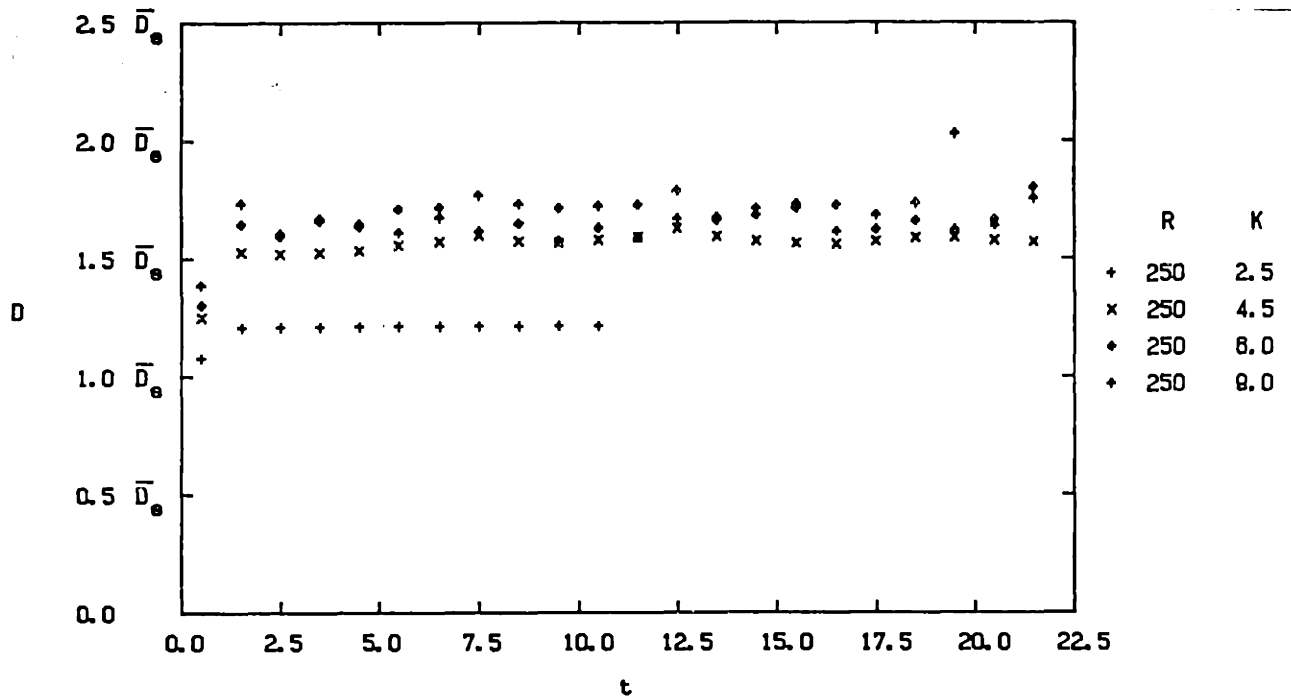
Fig. VII.2.8.   Variation of energy dissipation with time $\varepsilon = 0.1$
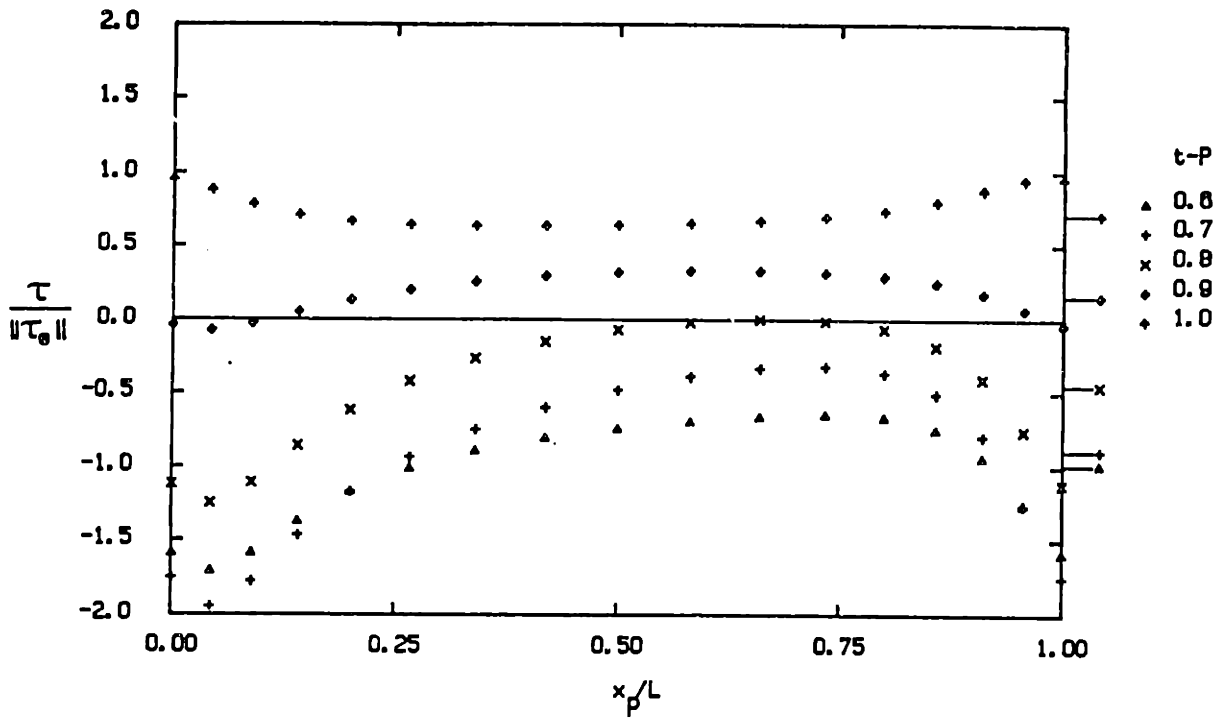
Fig. VII.3.1.i.   Shear stress on ripple surface

R = 15   K = 4.5   θ = 0.1   M = 16   N = 31   P = 29
dy = (0.0124 , 0.254) y_{max} = 2.05 $\|\tau_e\|$ = 0.0985
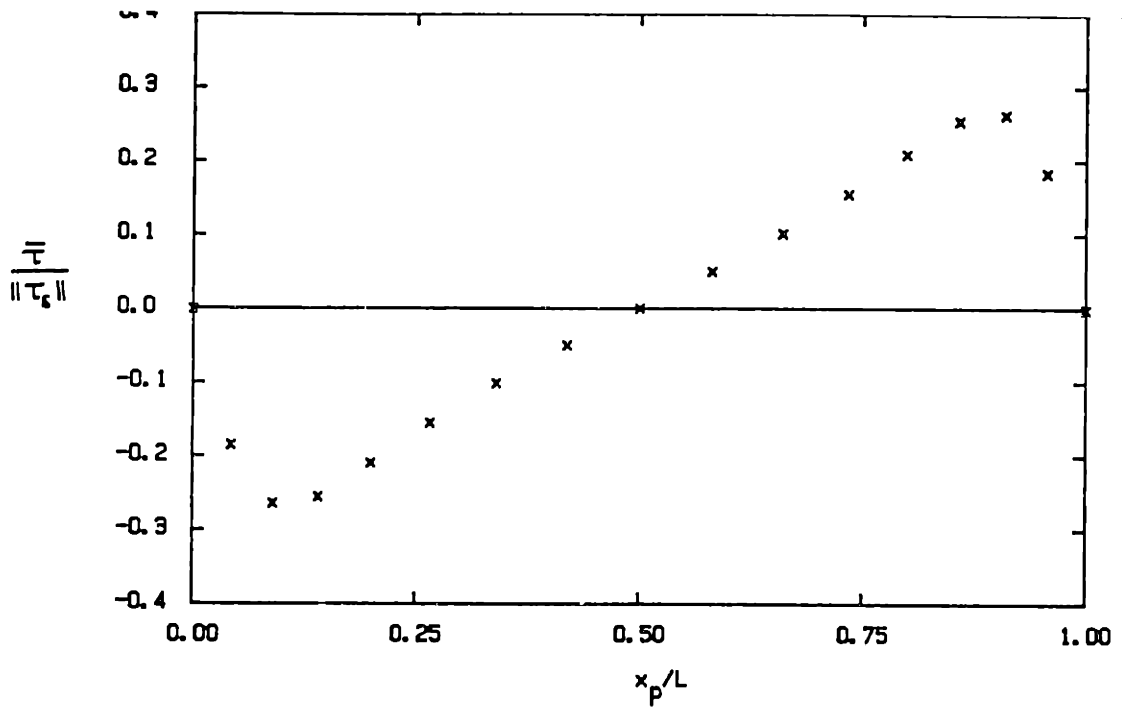
Fig. VII.3.1.ii.   Mean shear on ripple surface from t = 29 to 30

R = 15   K = 4.5   θ = 0.1   M = 16   N = 31
dy = (0.0124 , 0.254) y_{max} = 2.05 $\|\tau_e\|$ = 0.098

188
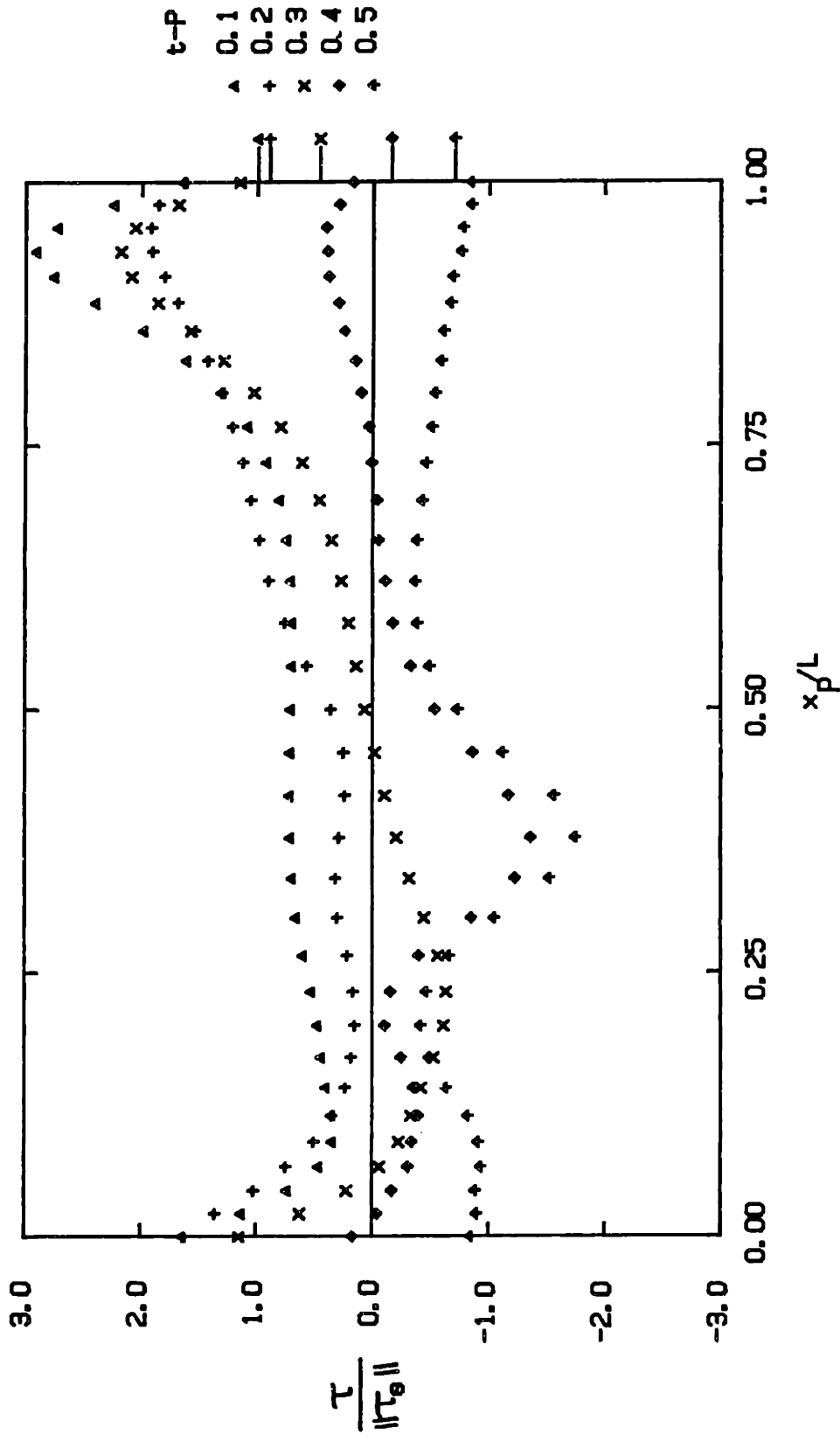
Fig. VII.3.2.1.   Shear stress on ripple surface
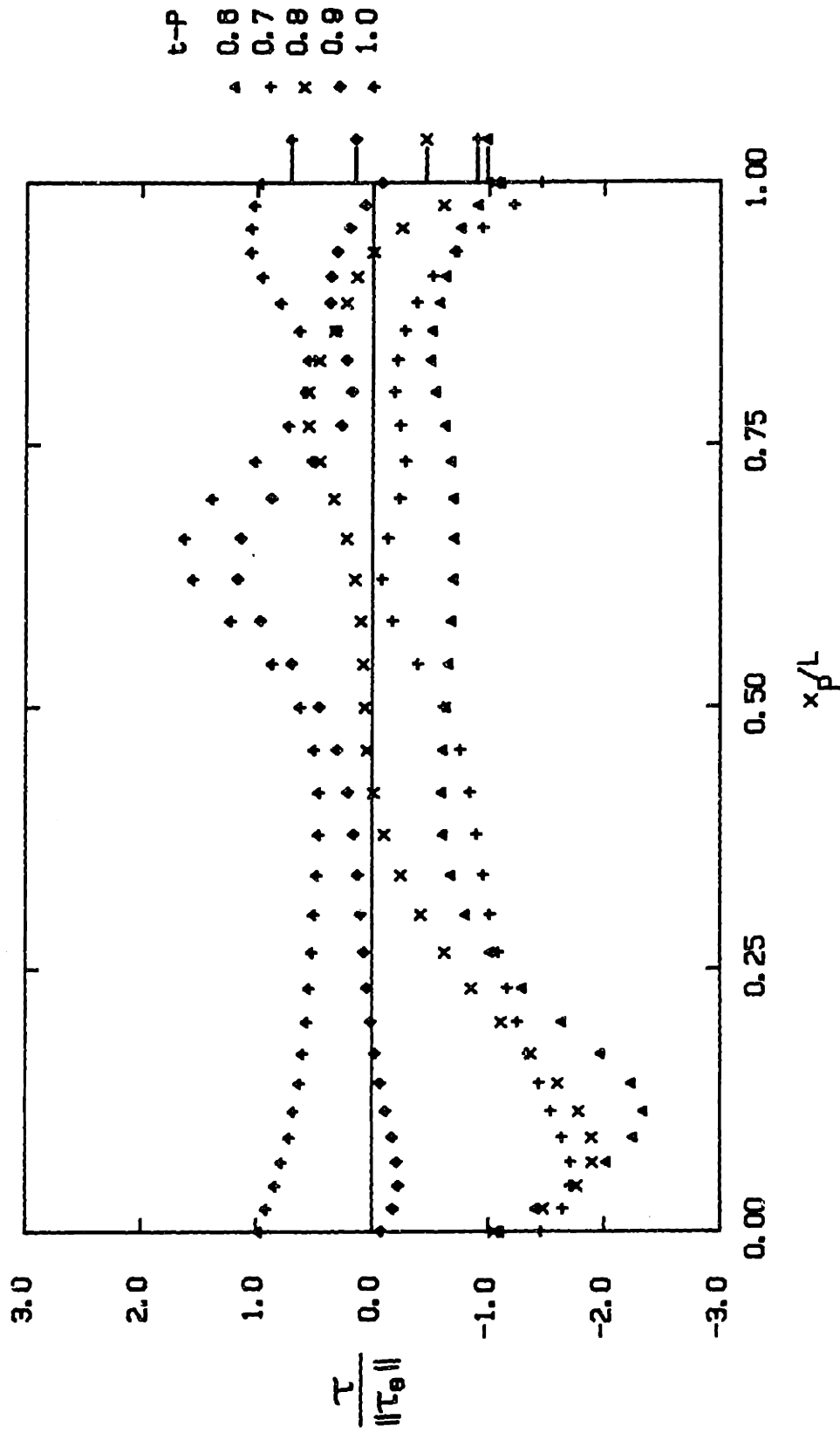
R = 175   K = 4.5   s = 0.1   M = 32   N = 38   P = 18

dy = (0.0044, 0.100) y_{max} = 1.02 $\|\tau_e\|$ = 0.0282

Fig. VII.3.2.ii. Shear stress on ripple surface

R = 175   K = 4.5   s = 0.1   M = 32   N = 38   P = 18

dy = (0.0044 , 0.100) y_{max} = 1.02 $\|\tau_{e}\|$ = 0.0282
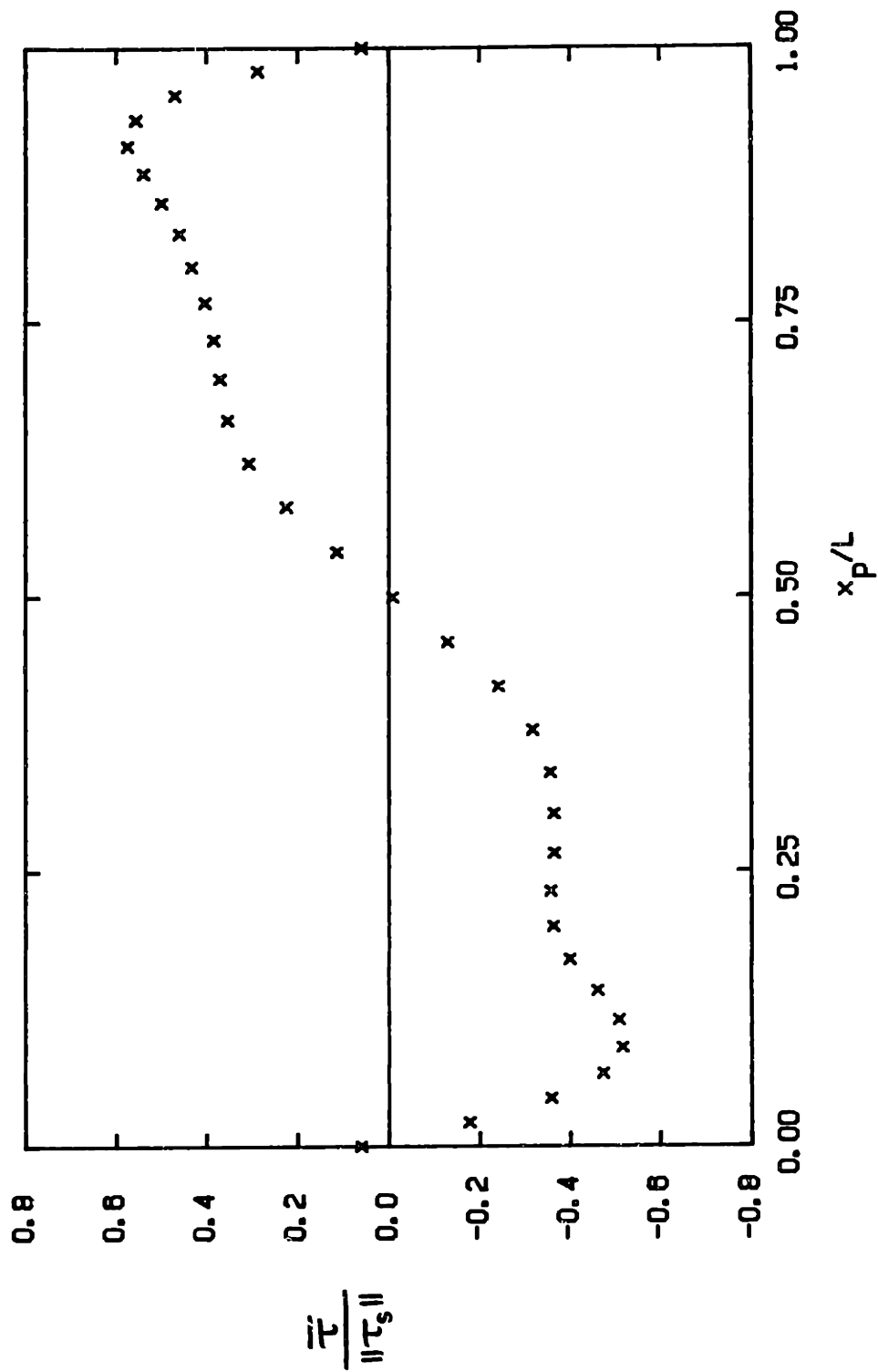
Fig. VII.3.2.iii.   Mean shear on ripple surface from t = 18 to 19

R = 175   K = 4.5   s = 0.1   M = 32   N = 38
dy = (0.0044, 0.100) y_{max} = 1.02 $\|\tau_e\|$ = 0.028
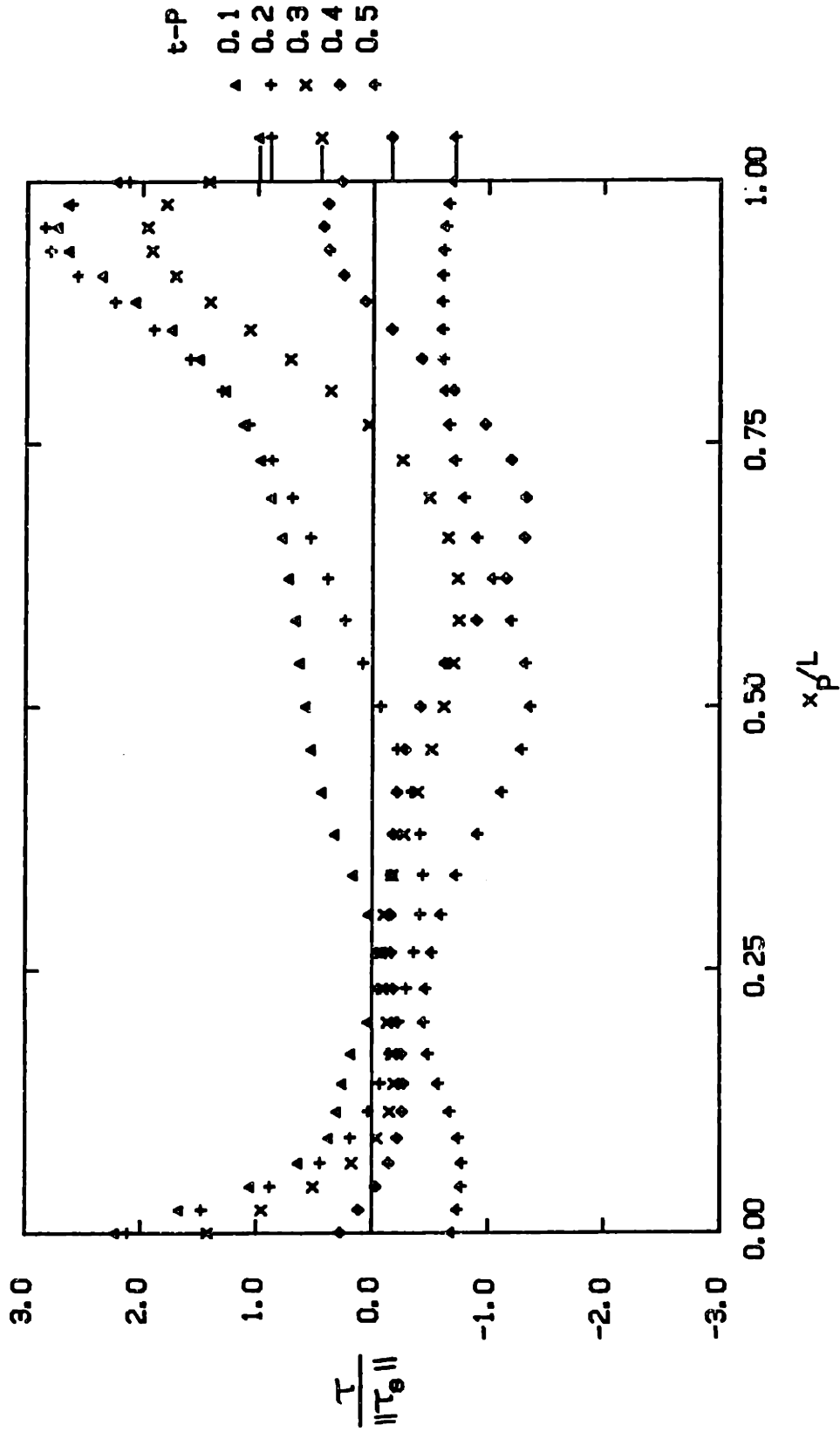
Fig. VII.3.3.1. Shear stress on ripple surface

R = 175 K = 12.0 s = 0.1 M = 32 N = 45 P = 9
dy = (0.0071, 0.091) y_{max} = 1.33 $\|\tau_e\|$ = 0.0173
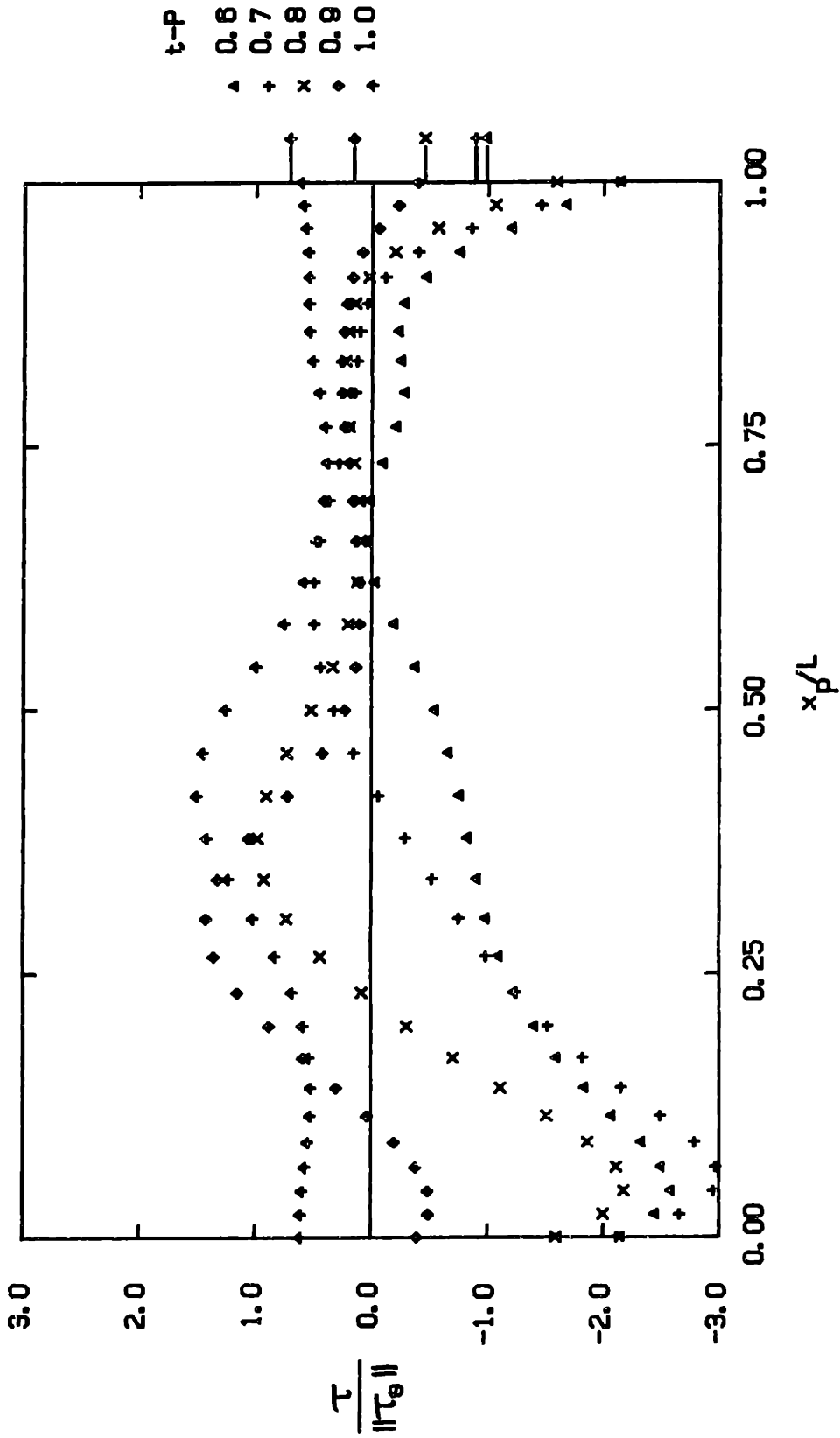
Fig. VII.3.3.ii. Shear stress on ripple surface

R = 175   K = 12.0   s = 0.1   M = 32   N = 45   P = 9

dy = (0.0071 , 0.091) y_{max} = 1.33 $\|\tau_s\|$ = 0.0173
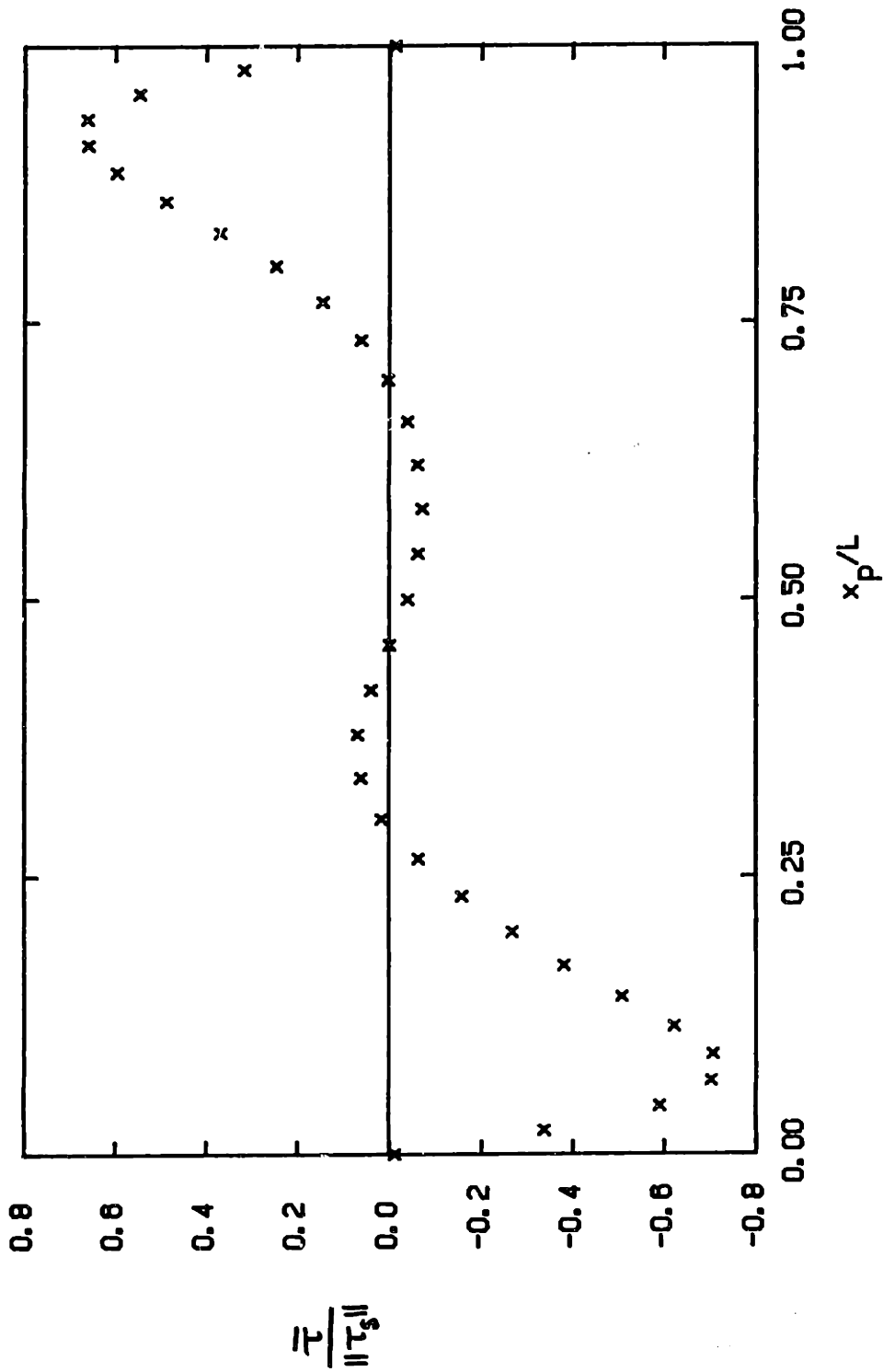
Fig. VII.3.3.iii. Mean shear on ripple surface from t = 9 to 10

R = 175   K = 12.0   θ = 0.1   M = 32   N = 45

dy = (0.0071, 0.091) y_{max} = 1.33 $\|\tau_e\|$ = 0.017
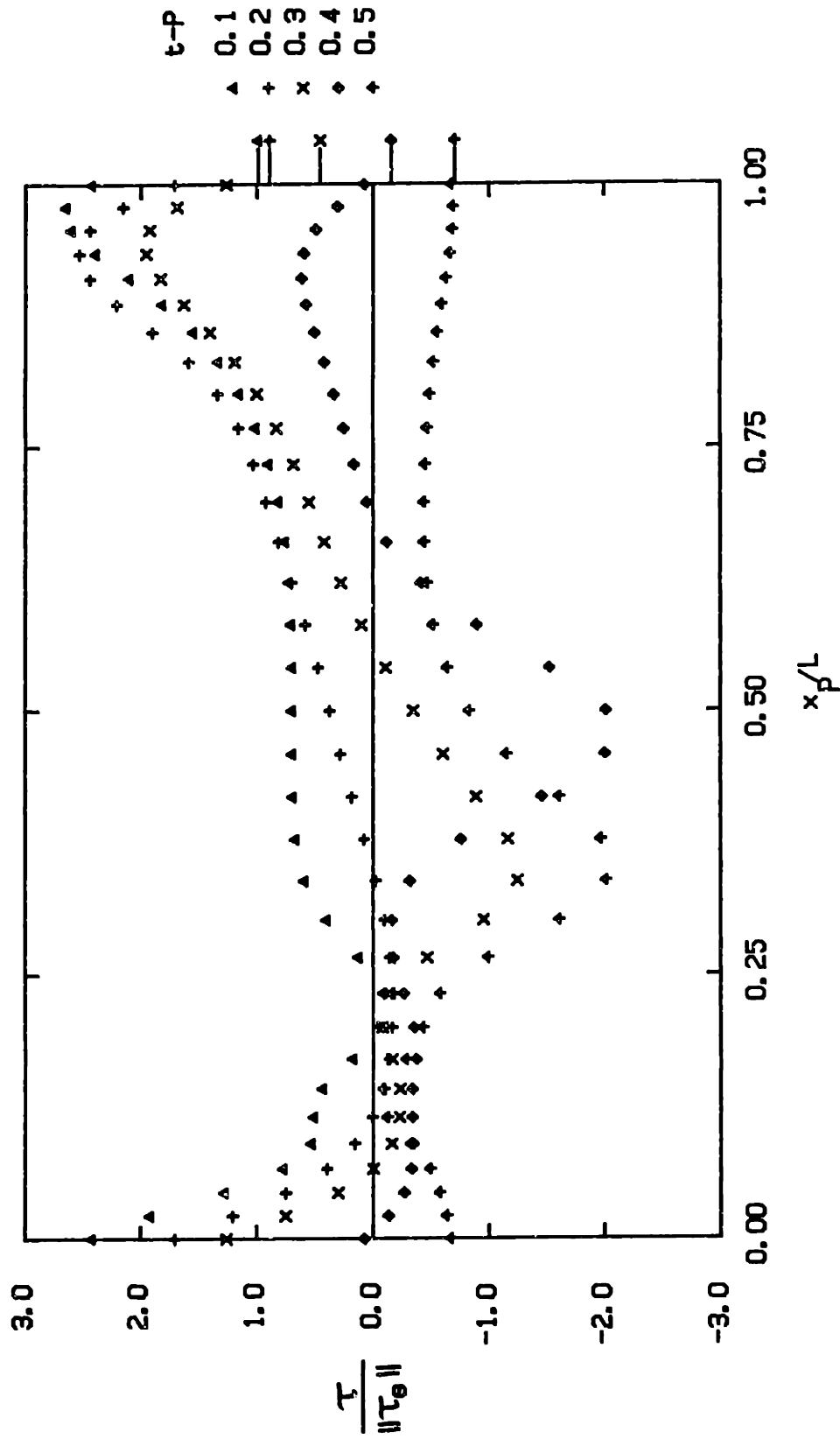
Fig. VII.3.4.1.   Shear stress on ripple surface

R = 250   K = 6.0 θ = 0.1   M = 32   N = 50   P = 20

dy = (0.0042 , 0.175) y_{max} = 2.08 $\|\tau_\theta\|$ = 0.0205
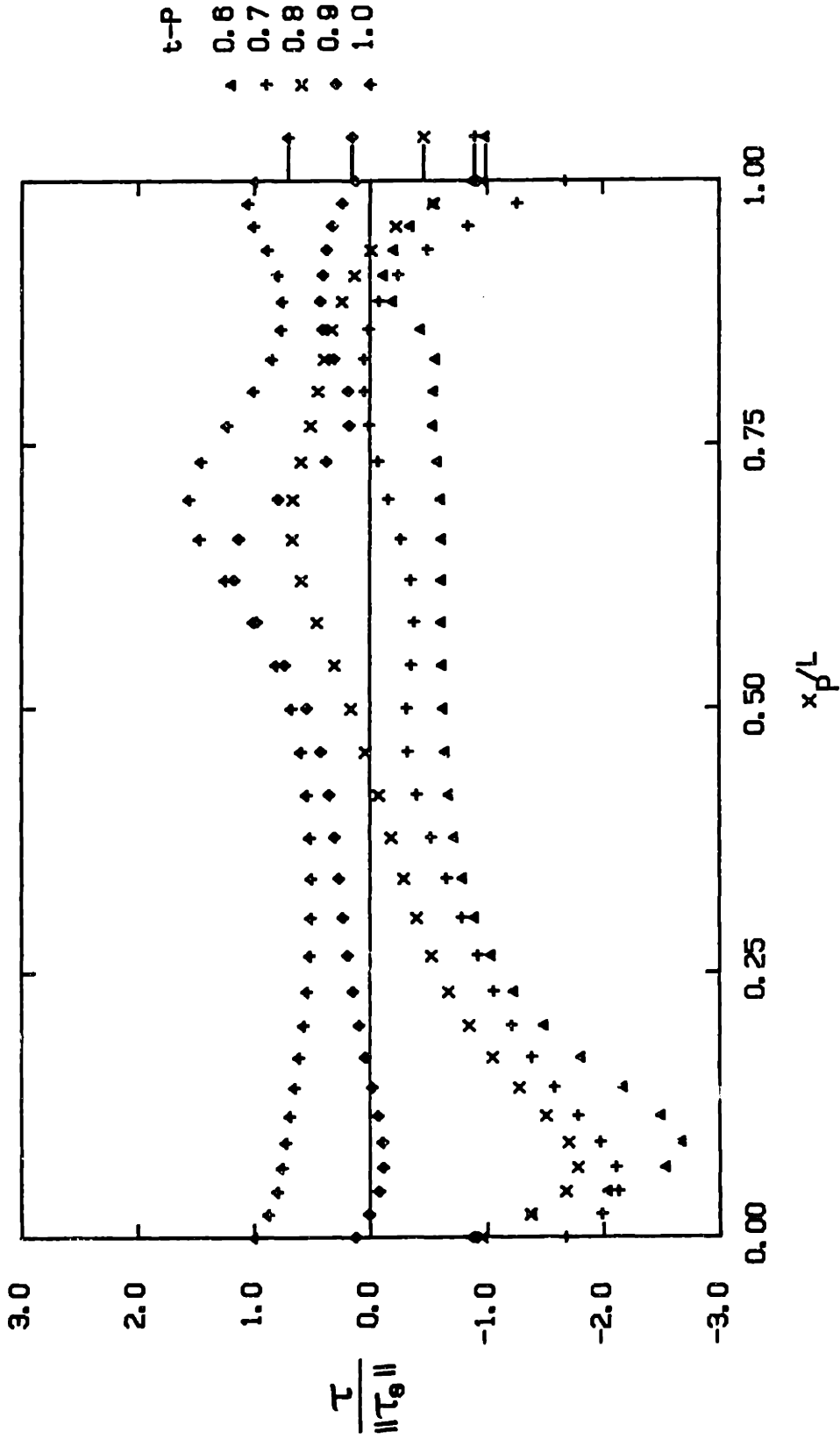
Fig. VII.3.4.ii.   Shear stress on ripple surface

R = 250   K = 6.0   s = 0.1   M = 32   N = 50   P = 20
dy = (0.0042 , 0.175) y_{max} = 2.08 $||\tau_\theta||$ = 0.0205
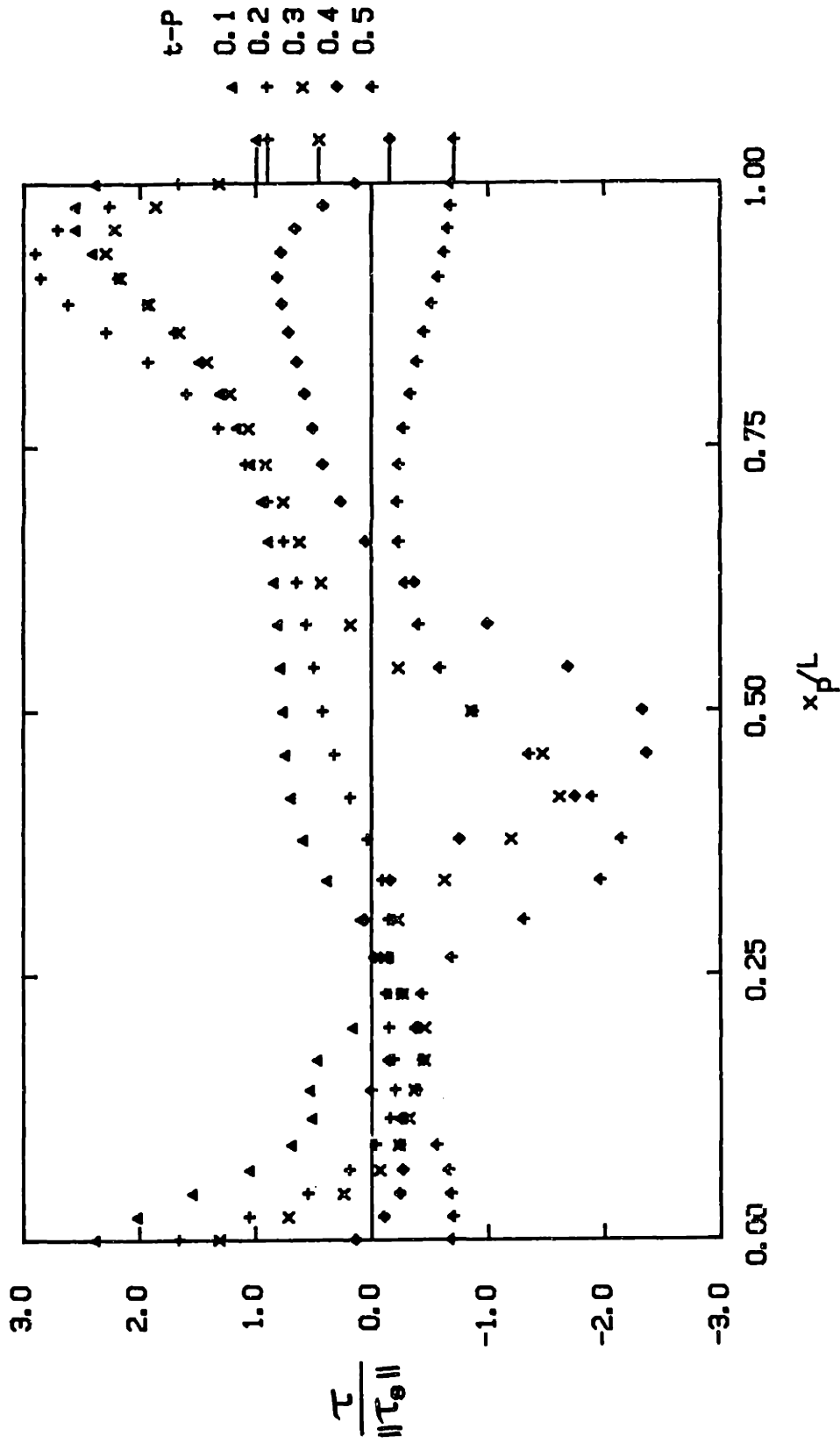
Fig. VII.3.4.iii.   Shear stress on ripple surface

R = 250   K = 6.0   s = 0.1   M = 32   N = 50   P = 21
dy = (0.0042 , 0.175) y_{max} = 2.08 $\|\tau_s\|$= 0.0205
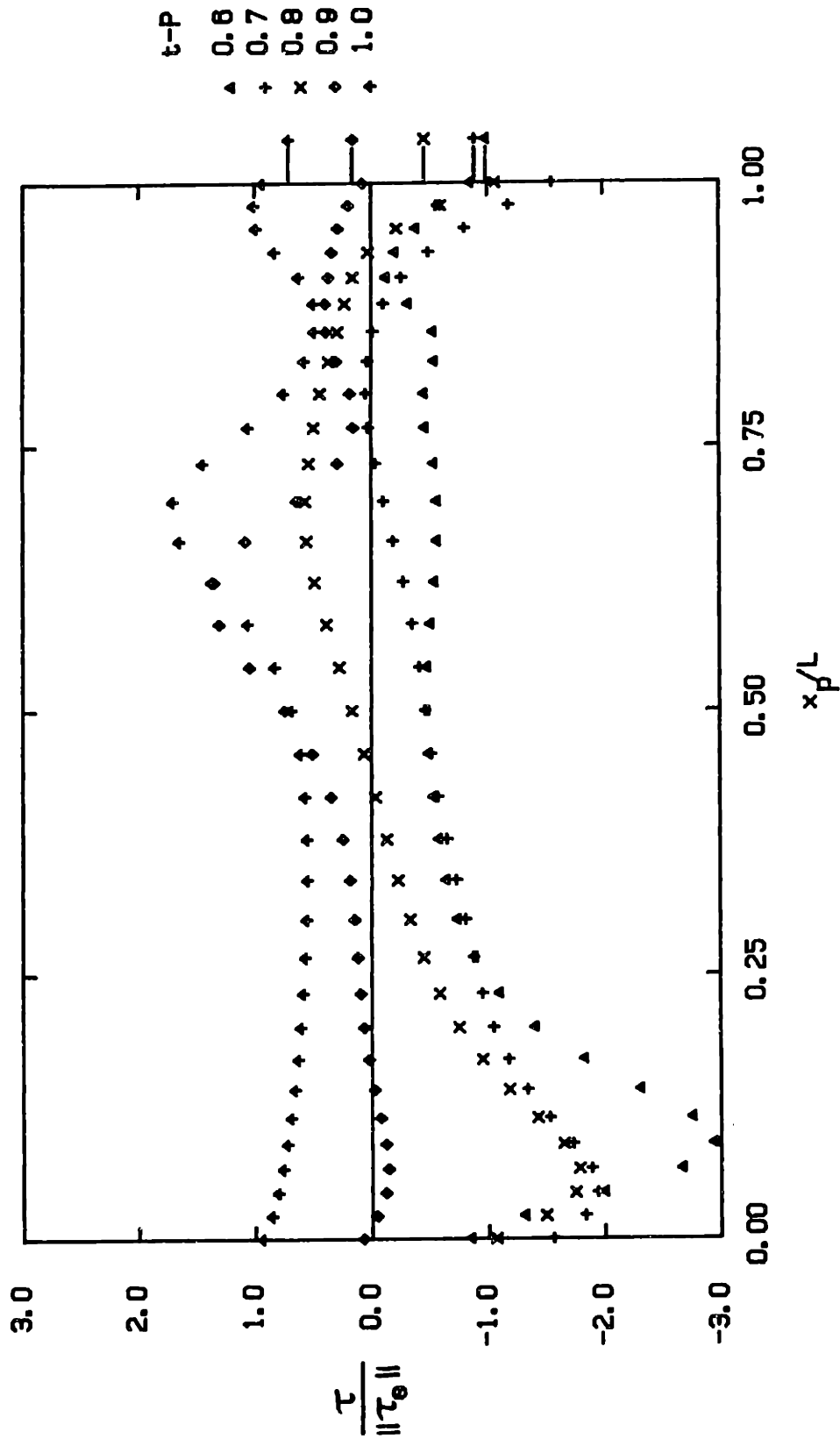
Fig. VII.3.4.iv. Shear stress on ripple surface

R = 250   K = 8.0   s = 0.1   M = 32   N = 50   P = 21
dy = (0.0042 , 0.175) y_{max} = 2.08 $\|\tau_e\|$ = 0.0205
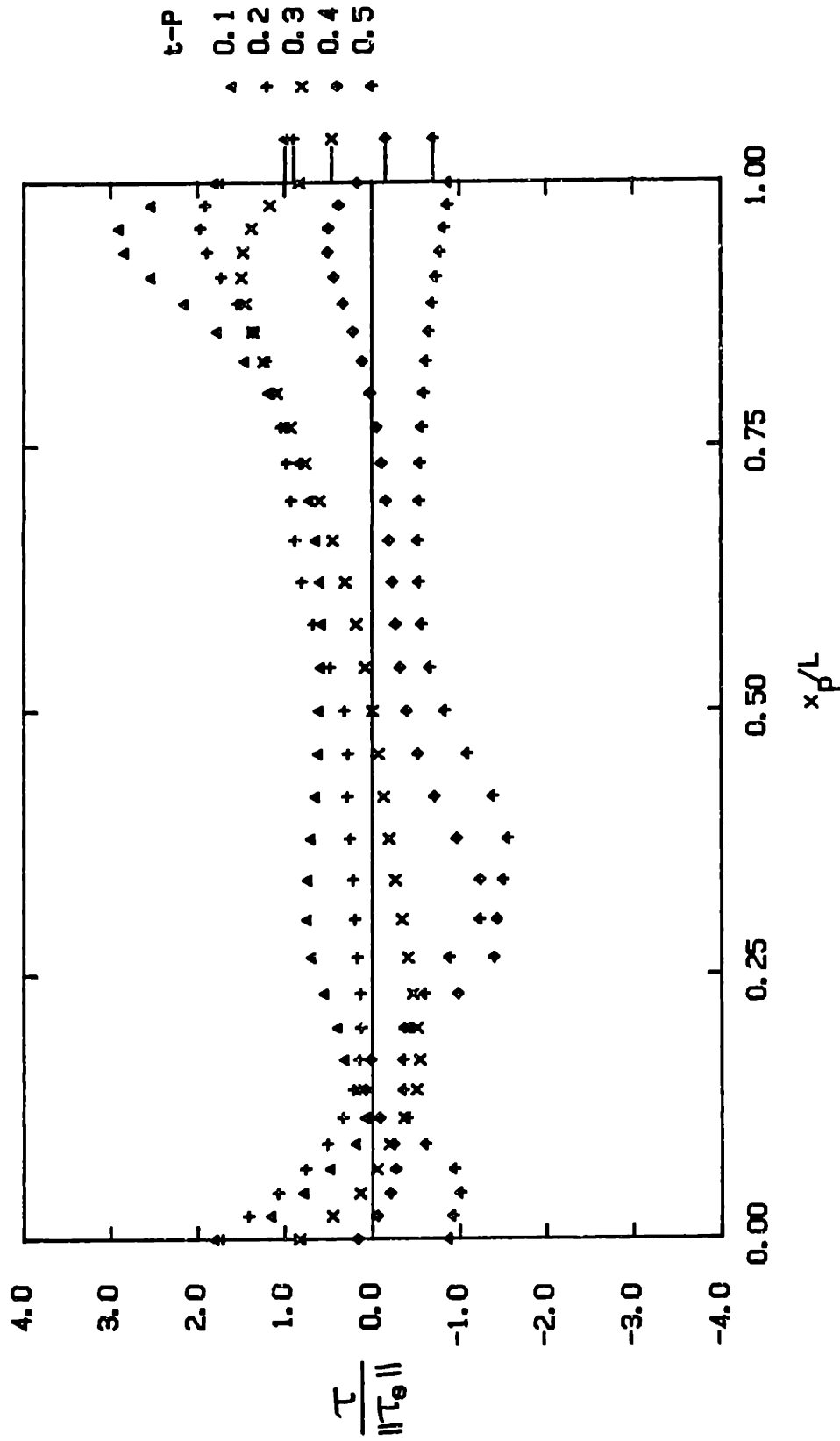
Fig. VII.3.5.i.   Shear stress on ripple surface

R = 250   K = 4.5   S = 0.1   M = 32   N = 57   P = 20

dy = (0.0036, 0.151) y_{max} = 2.08 $\|\tau_s\|$ = 0.0236
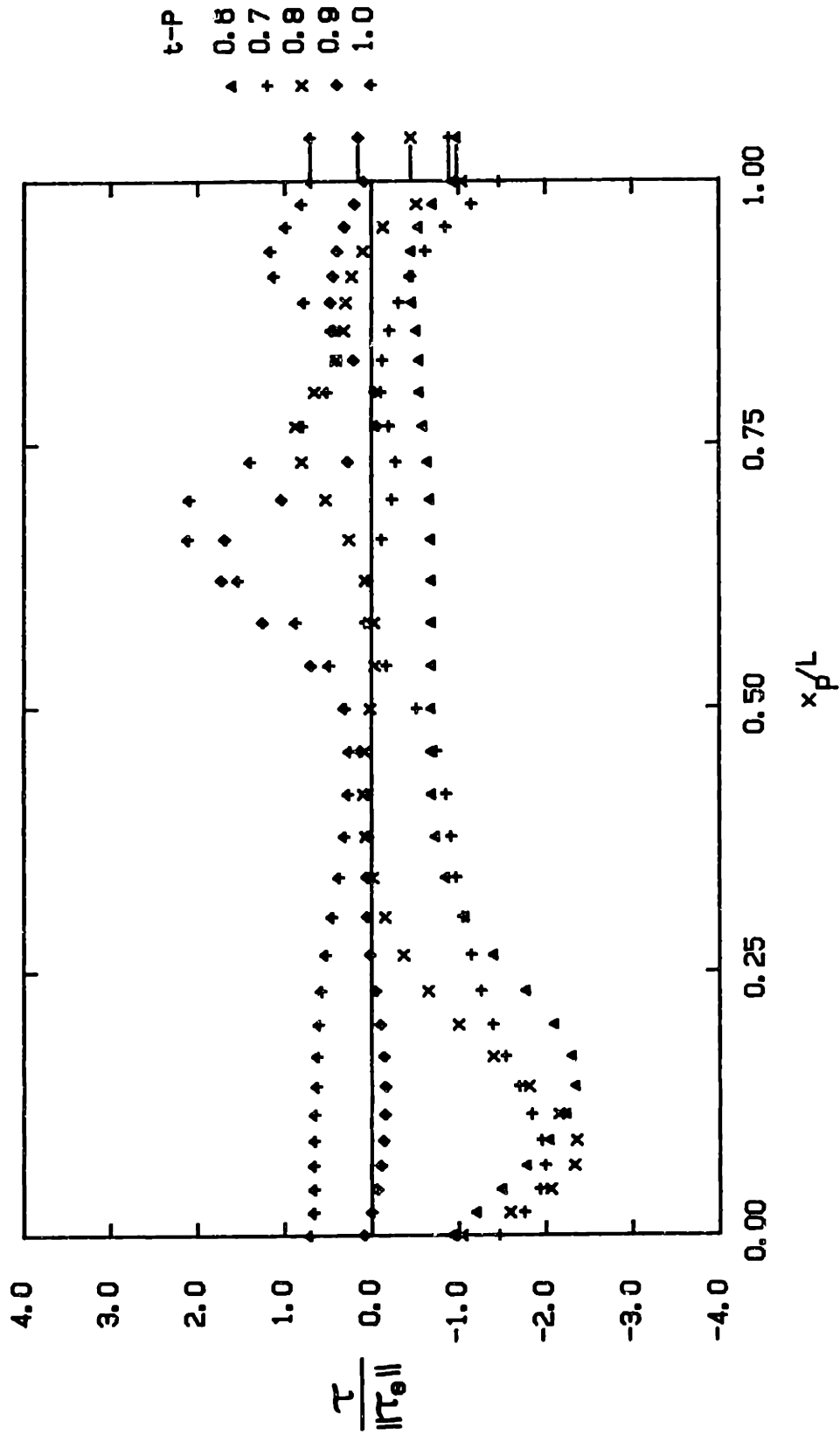
Fig. VII.3.5.ii.   Shear stress on ripple surface

R = 250   K = 4.5   θ = 0.1   M = 32   N = 57   P = 20
dy = (0.0036 , 0.151) y_{max} = 2.08 $\|\tau_e\|$ = 0.0236
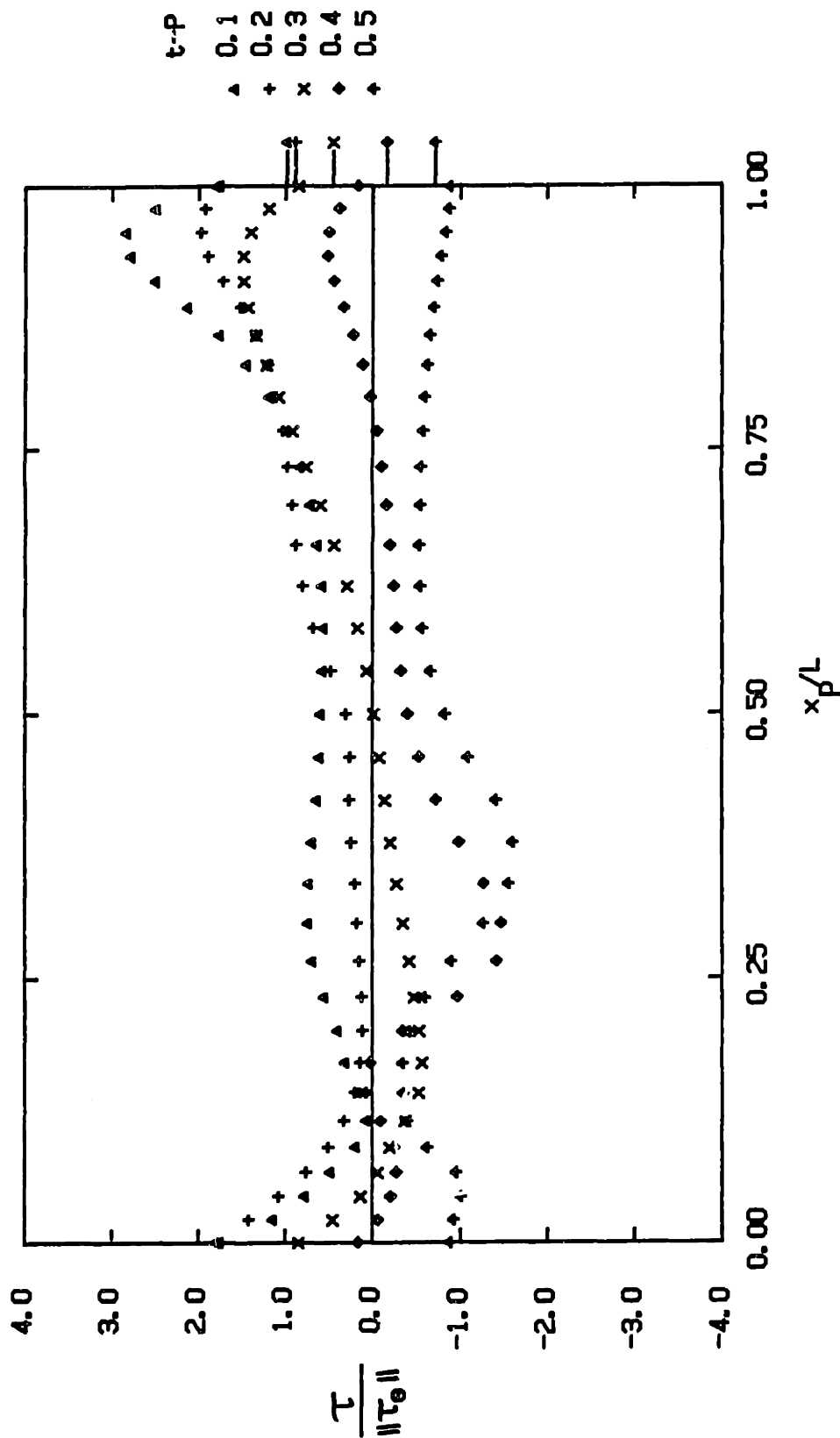
Fig. VII.3.5.iii. Shear stress on ripple surface

R = 250   K = 4.5   s = 0.1   M = 32   N = 57   P = 21

dy = (0.0036, 0.151) y_{max} = 2.08 $\|T_\theta\|$ = 0.0236
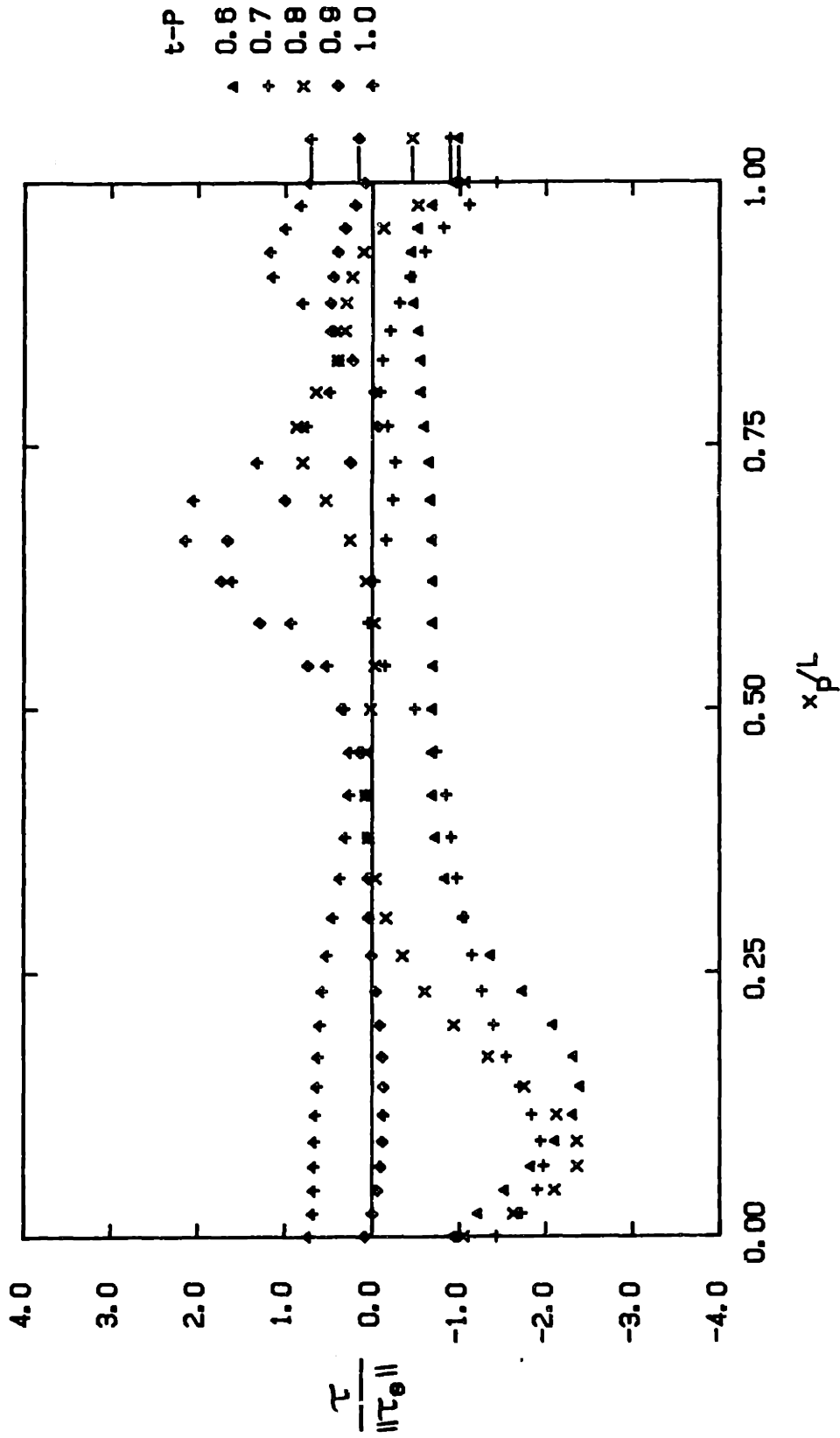
Fig. VII.3.5.1v. Shear stress on ripple surface

R = 250   K = 4.5   θ = 0.1   M = 32   N = 57   P = 21

dy = (0.0036, 0.151) y_{max} = 2.08 $\|\tau_e\|$ = 0.0236
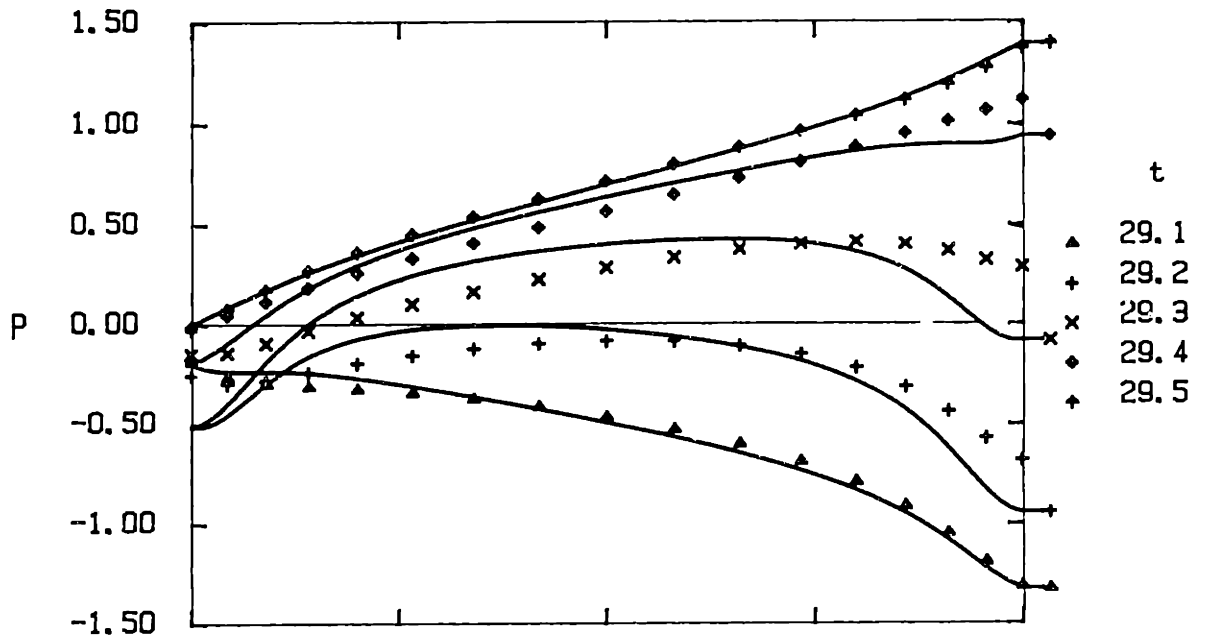
i.   t = 29.1 to t = 29.5
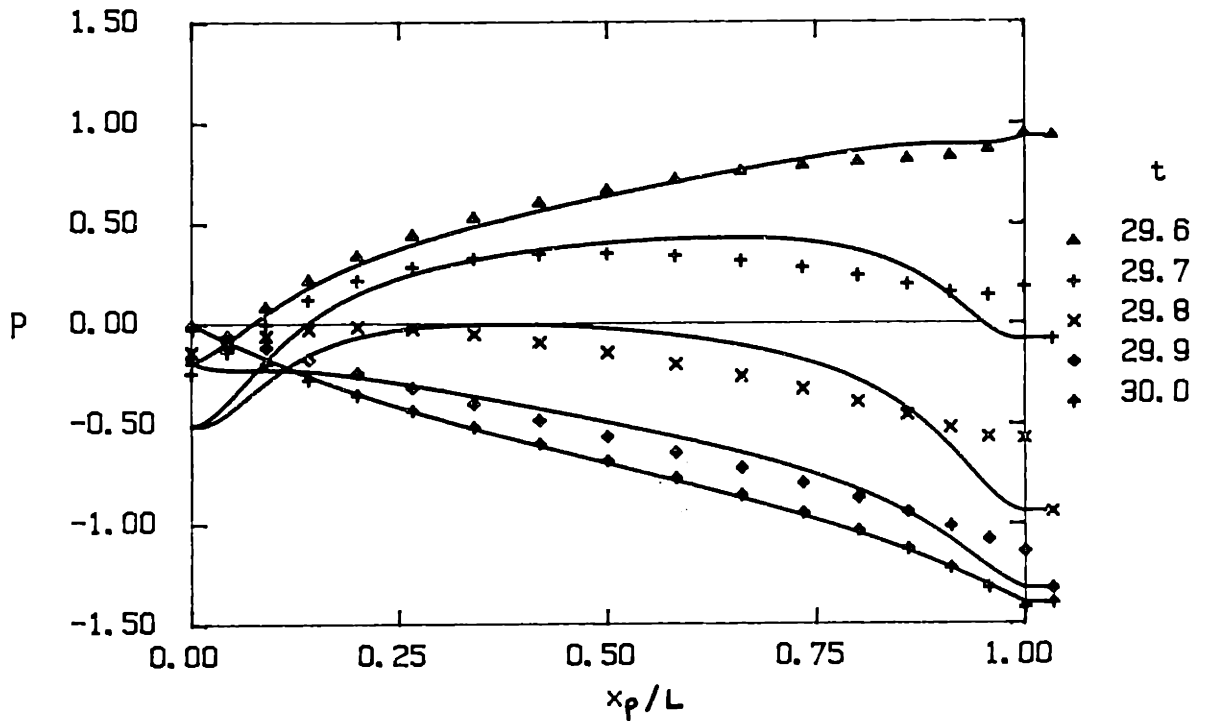
ii.   t = 29.6 to t = 30.0

Fig. VII.4.1.   Pressure on ripple surface
R = 15   K = 4.5   s = 0.1
M = 16   N = 31 y_{max} = 2.05
$\Delta y \in$ (0.0124, 0.254)
────── potential pressure

203

i.   t = 18.1 to t = 18.5

ii.   t = 18.6 to t = 19.0
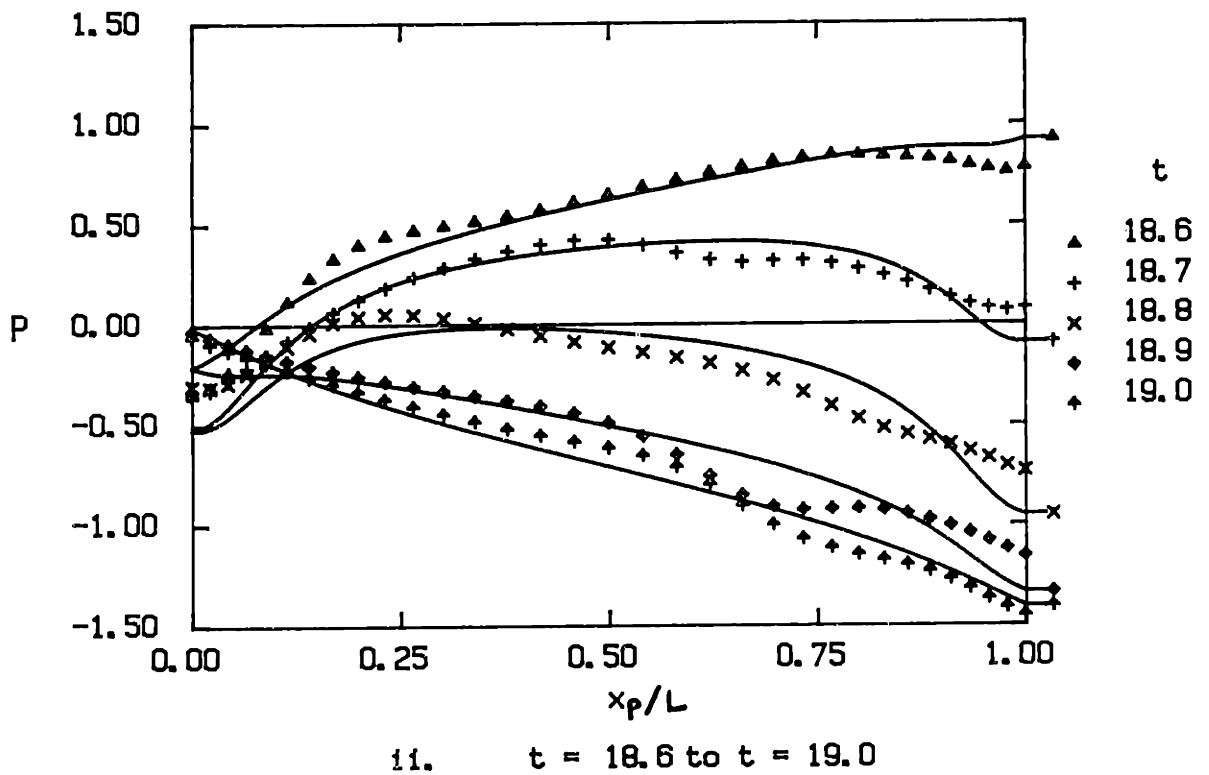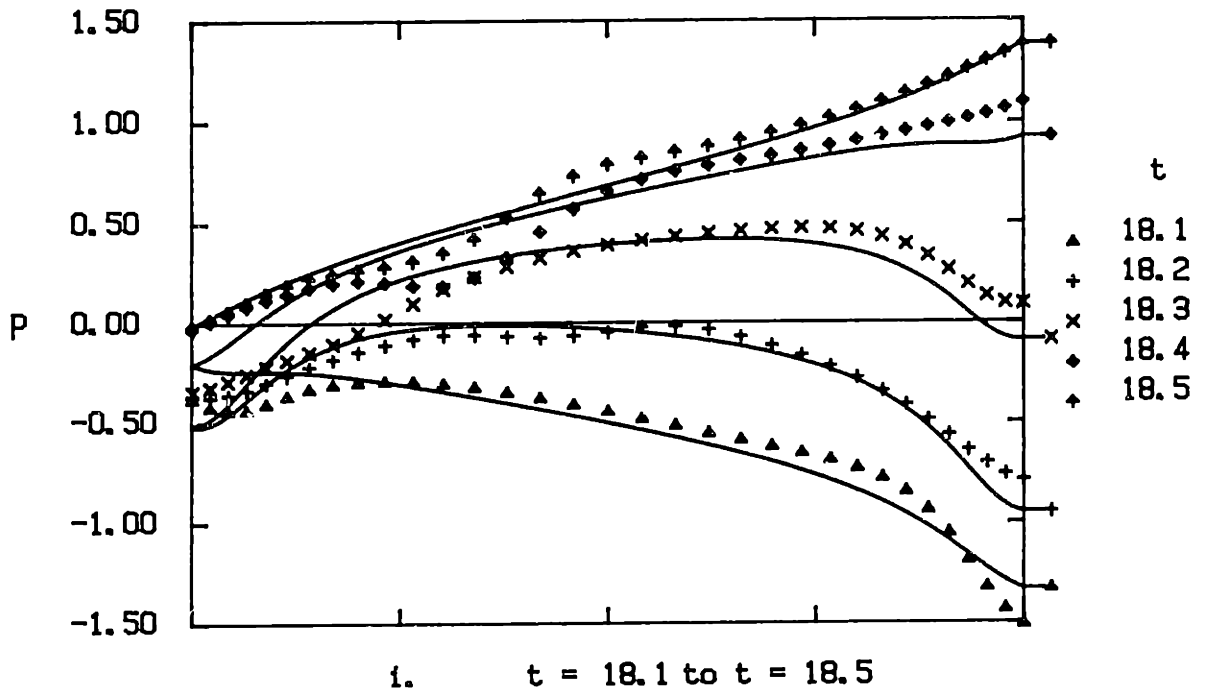
Fig. VII.4.2.   Pressure on ripple surface
R = 175   K = 4.5   e = 0.1
M = 32   N = 38 y_{max} = 1.02
$\Delta y \in$ (0.0044, 0.100)
———— potential pressure

1.   t = 9.1 to t = 9.5

11.   t = 9.6 to t = 10.0
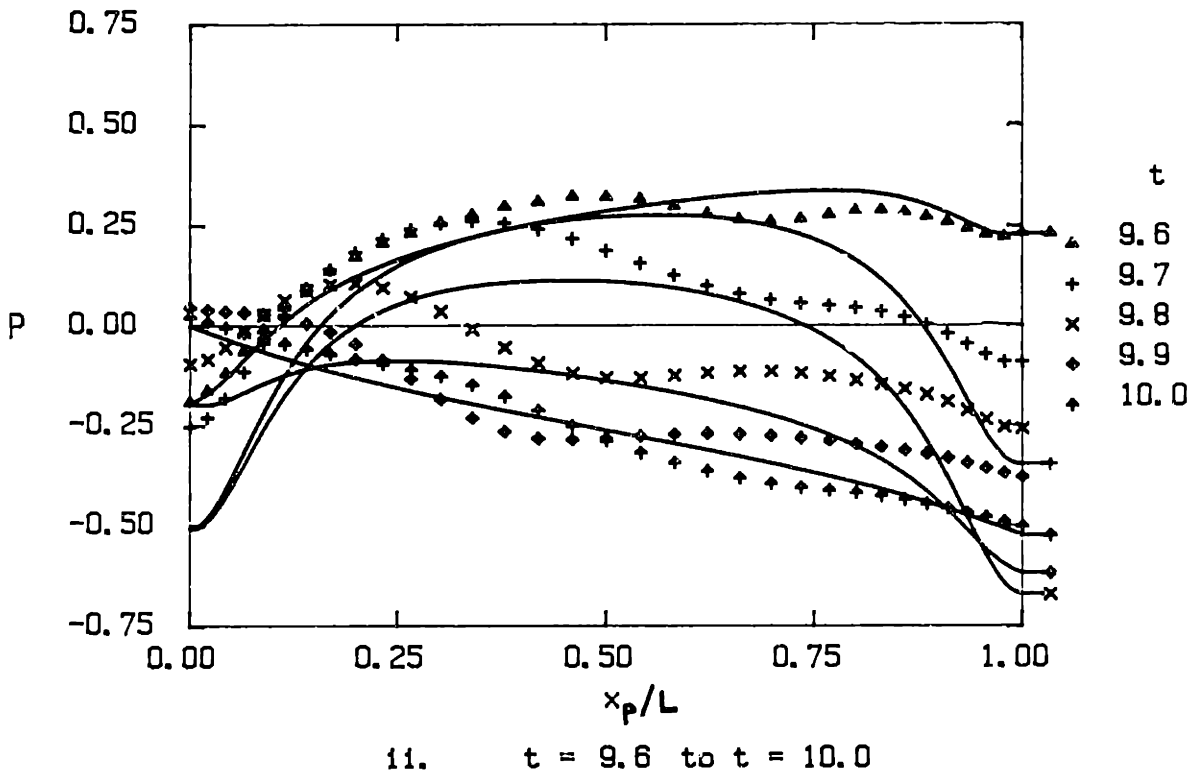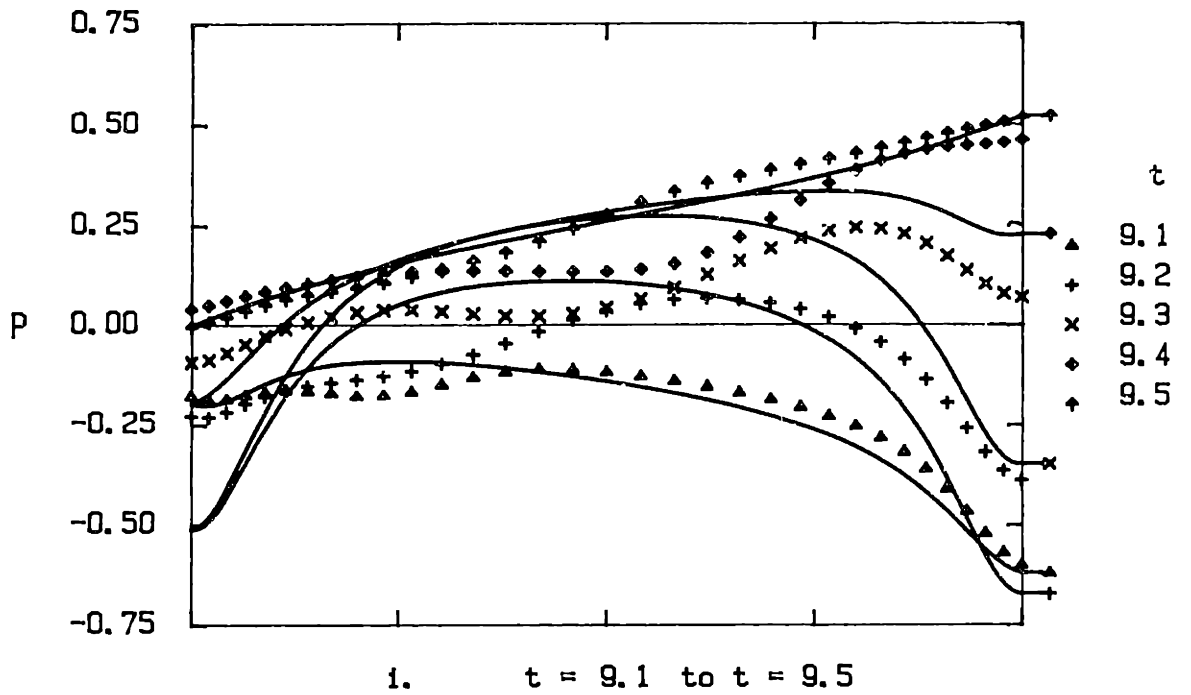
Fig. VII.4.3.   Pressure on ripple surface
                 R = 175   K = 12.0   s = 0.1
                 M = 32   N = 45 y_{max} = 1.33
                 $\Delta y \in$ (0.0071, 0.091)
                 ——— potential pressure

205
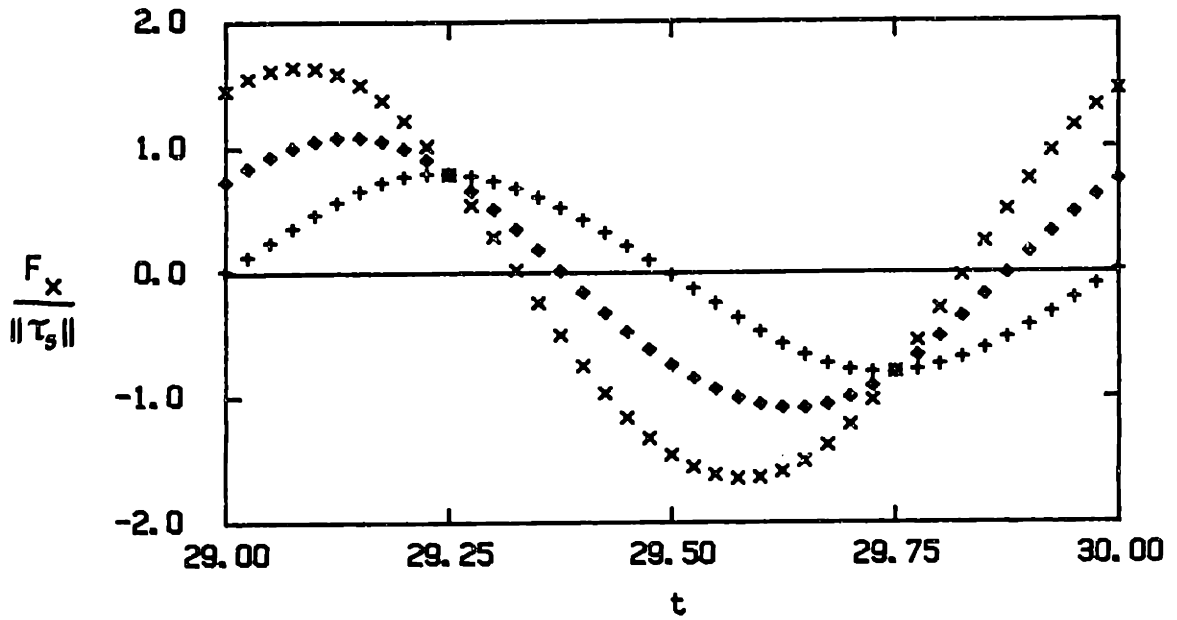
Fig. VII.5.1. Horizontal force on ripple.
R = 15   K = 4.5   e = 0.1
M = 16   N = 31 $\|\tau_e\|$ = 0.0965
dy = (0.0124 , 0.254) y_{max} = 2.05

+ F_c × F_t ♦ F_n
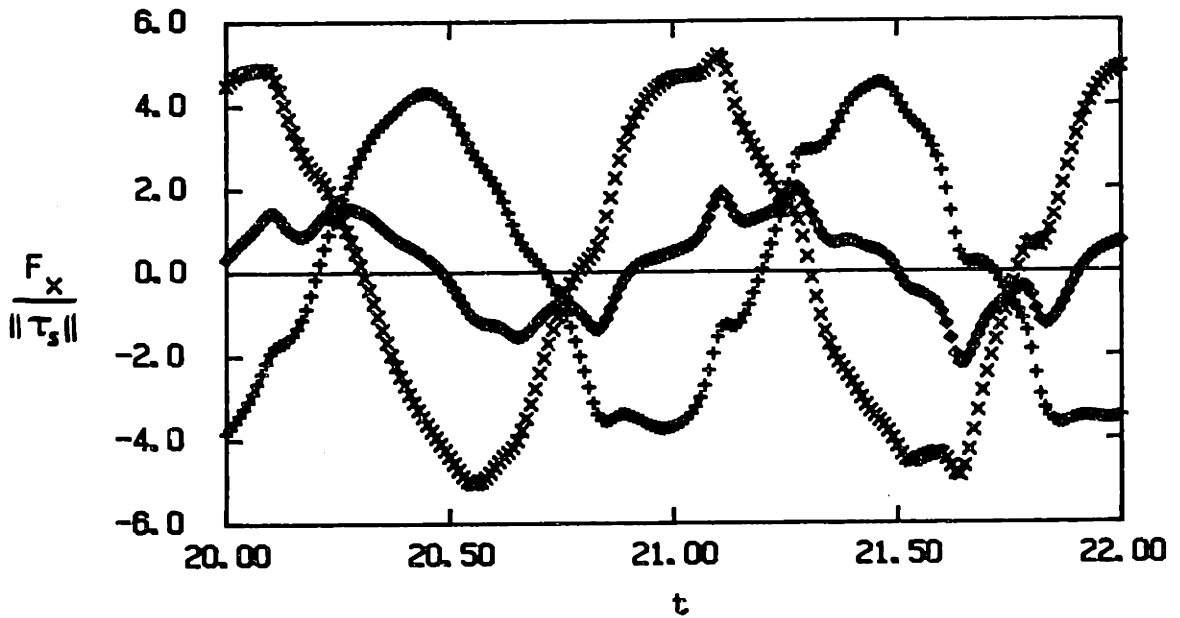
Fig. VII.5.2. Horizontal force on ripple.
R = 500   K = 4.5   e = 0.1
M = 64   N = 72 $\|\tau_e\|$ = 0.0167
dy = (0.0026 , 0.118) y_{max} = 2.03
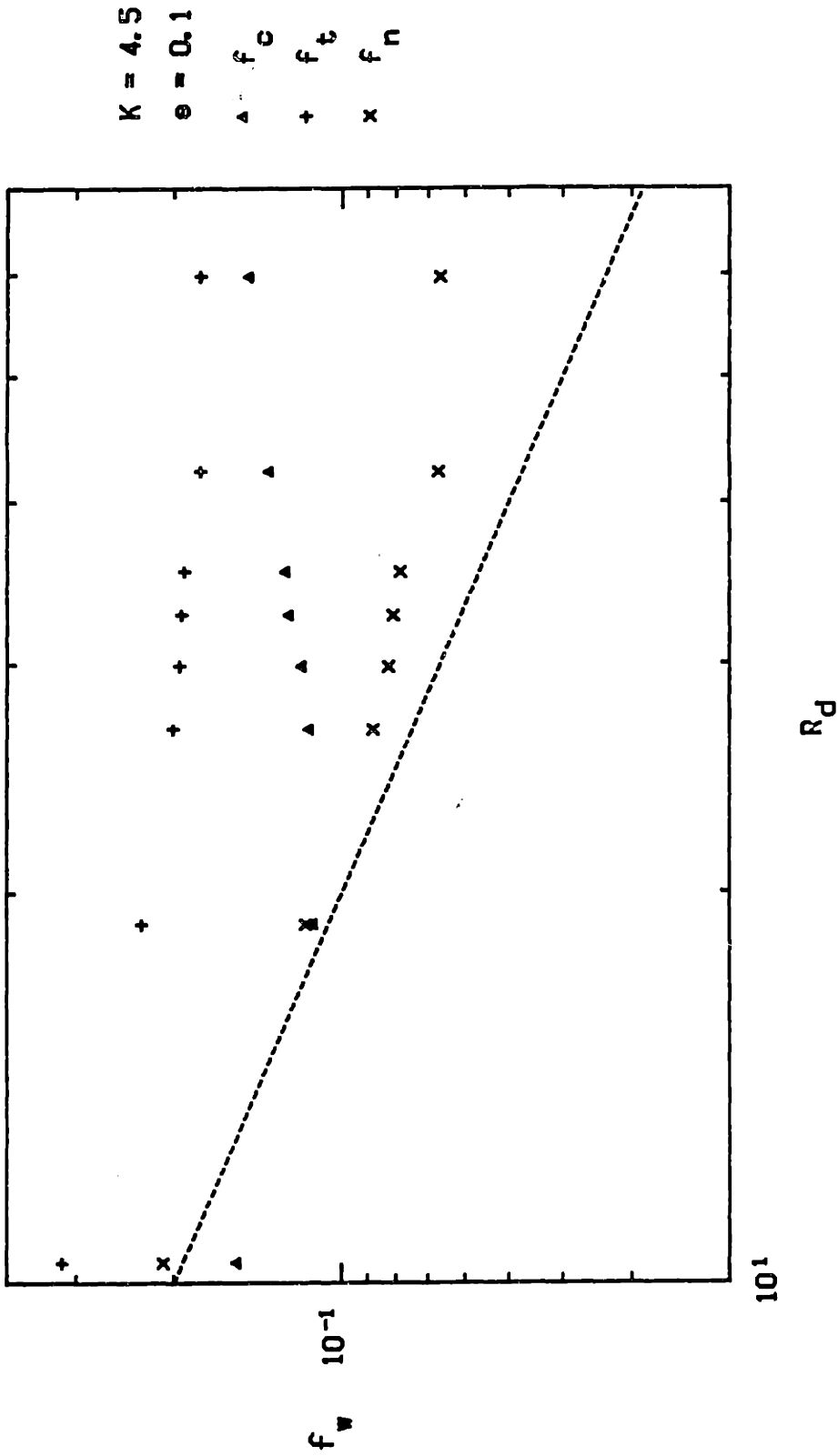
Fig. VII.6.1. Friction factor from the magnitude of horizontal force on a ripple length of the bottom boundary
——— Oscillatory flow over a plane bed
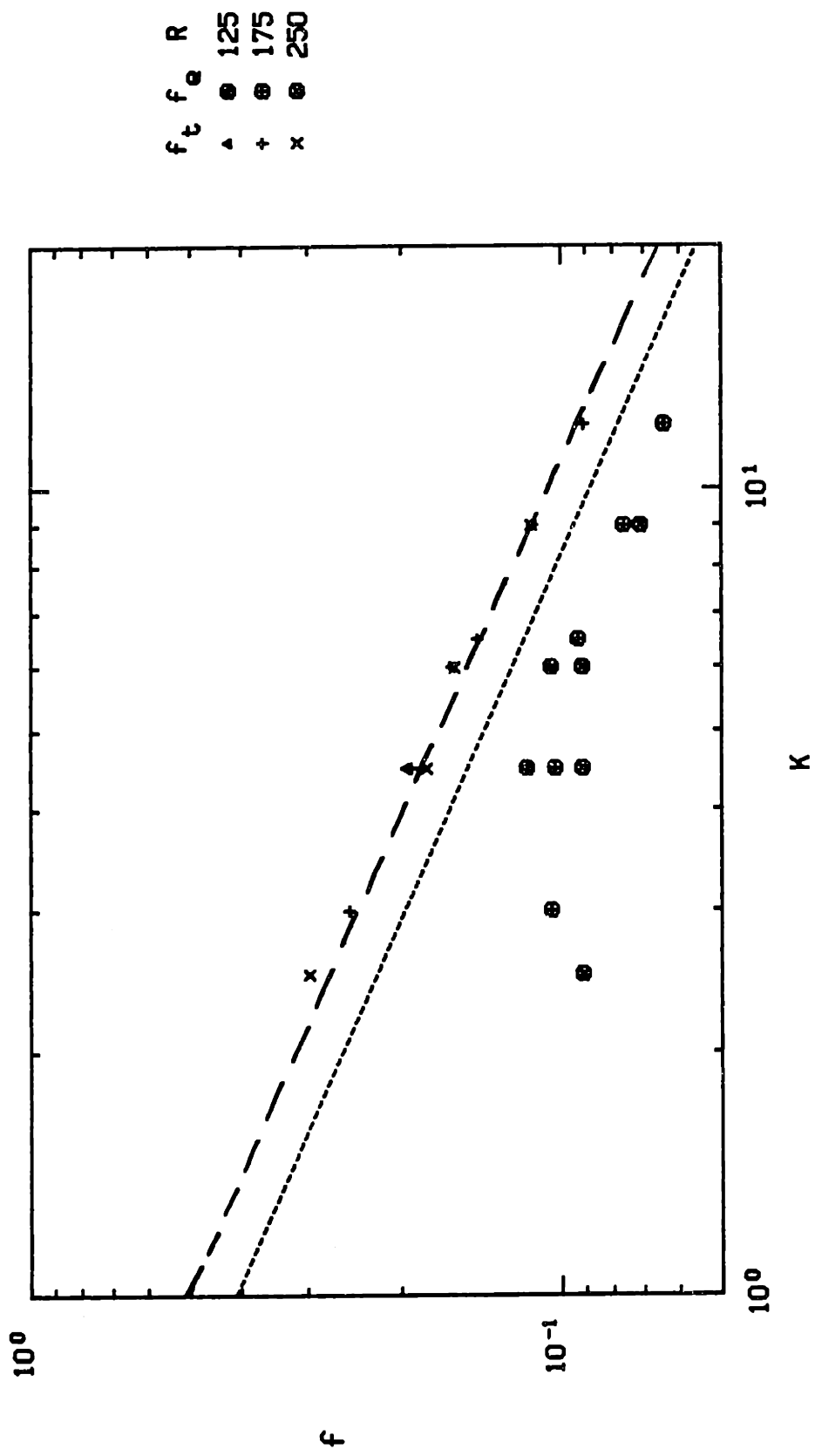
Fig. VII.6.2.   Friction factor deduced from horizontal force on ripple
and from energy dissipation (assuming theta=0) θ = 0.1
——— Theoretical values for rough turbulent flow
(Kajiura, 1968)
——— (7.6.17)
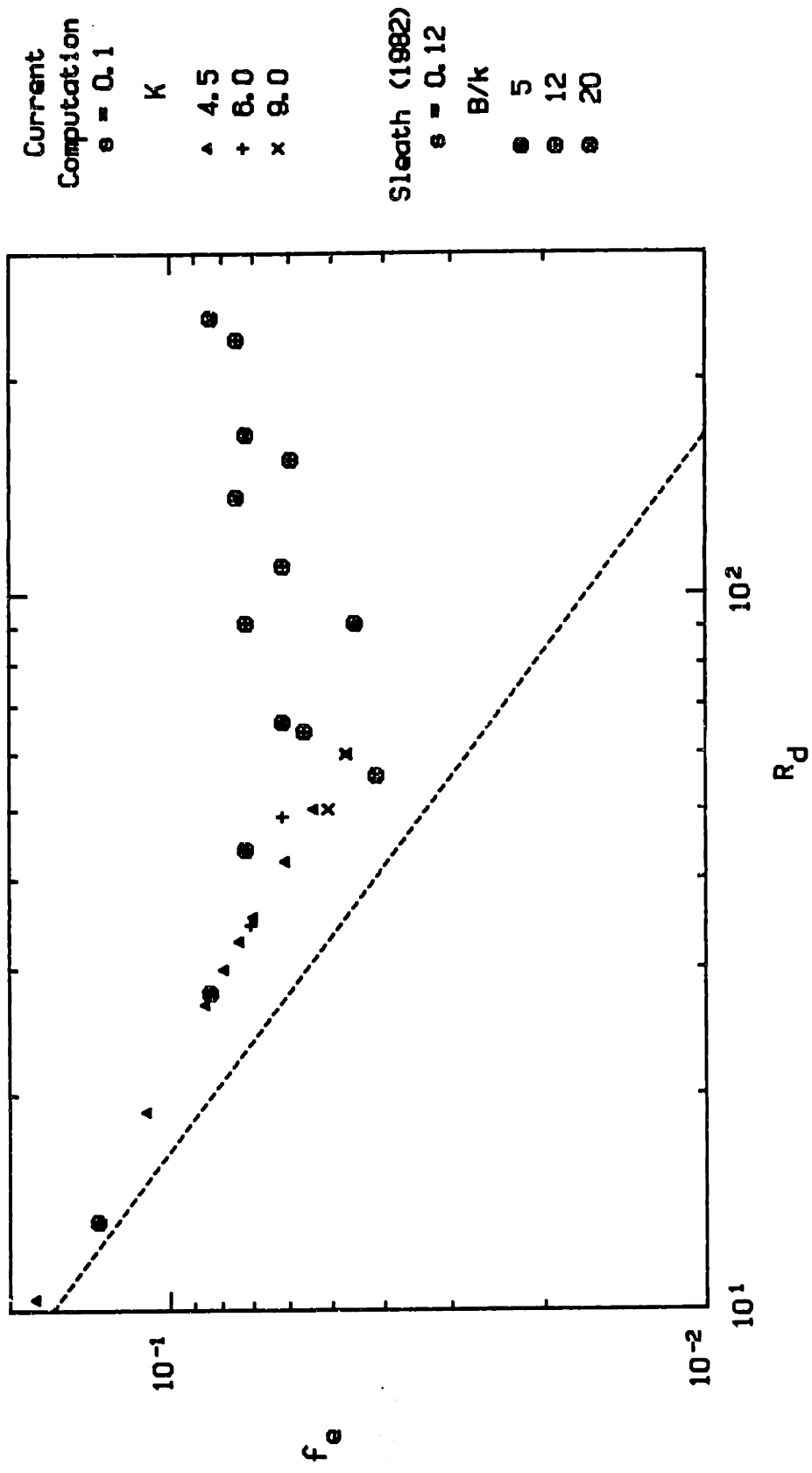
Fig. VII.8.3. Friction factor deduced from energy dissipation assuming theta=0 in (7.6.6). Oscillatory flow over a plane bed
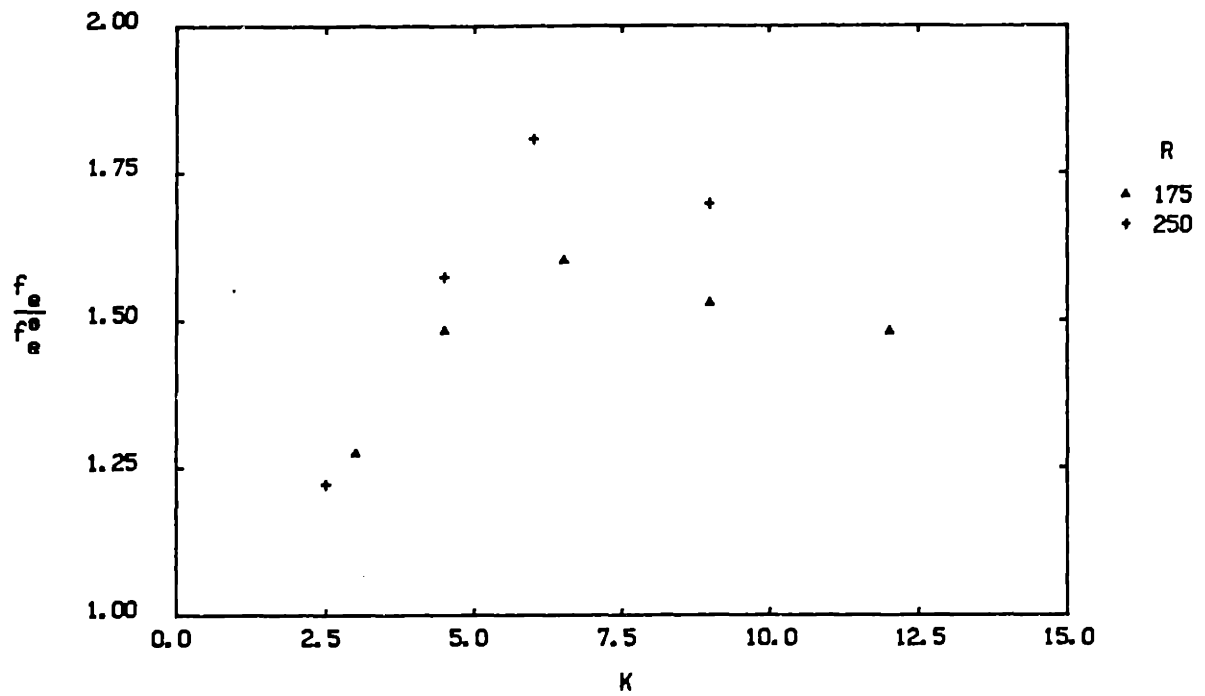
Fig. VII.6.4.   Ratio of friction factors deduced from energy dissipation
assuming theta=0 in (7.6.6).
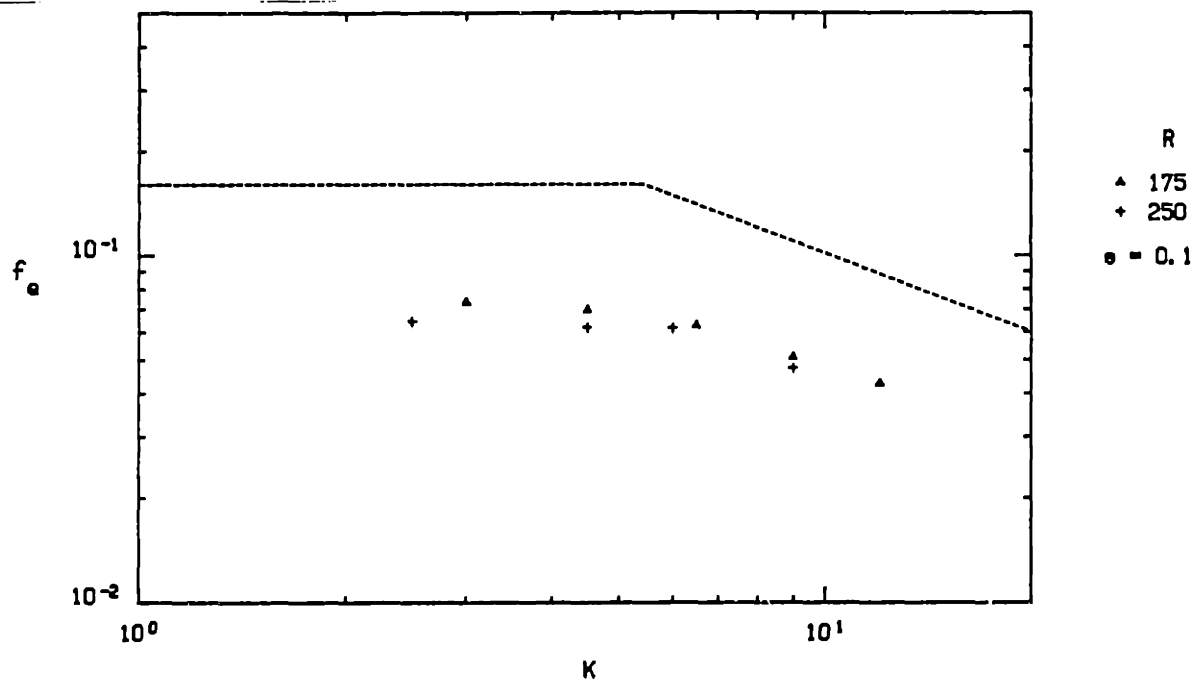
Fig. VII.6.5.   Friction factor deduced from viscous dissipation assuming
theta=0 in (7.6.6).
------   Laboratory measurements for e = 0.15 (Bagnold 1946)
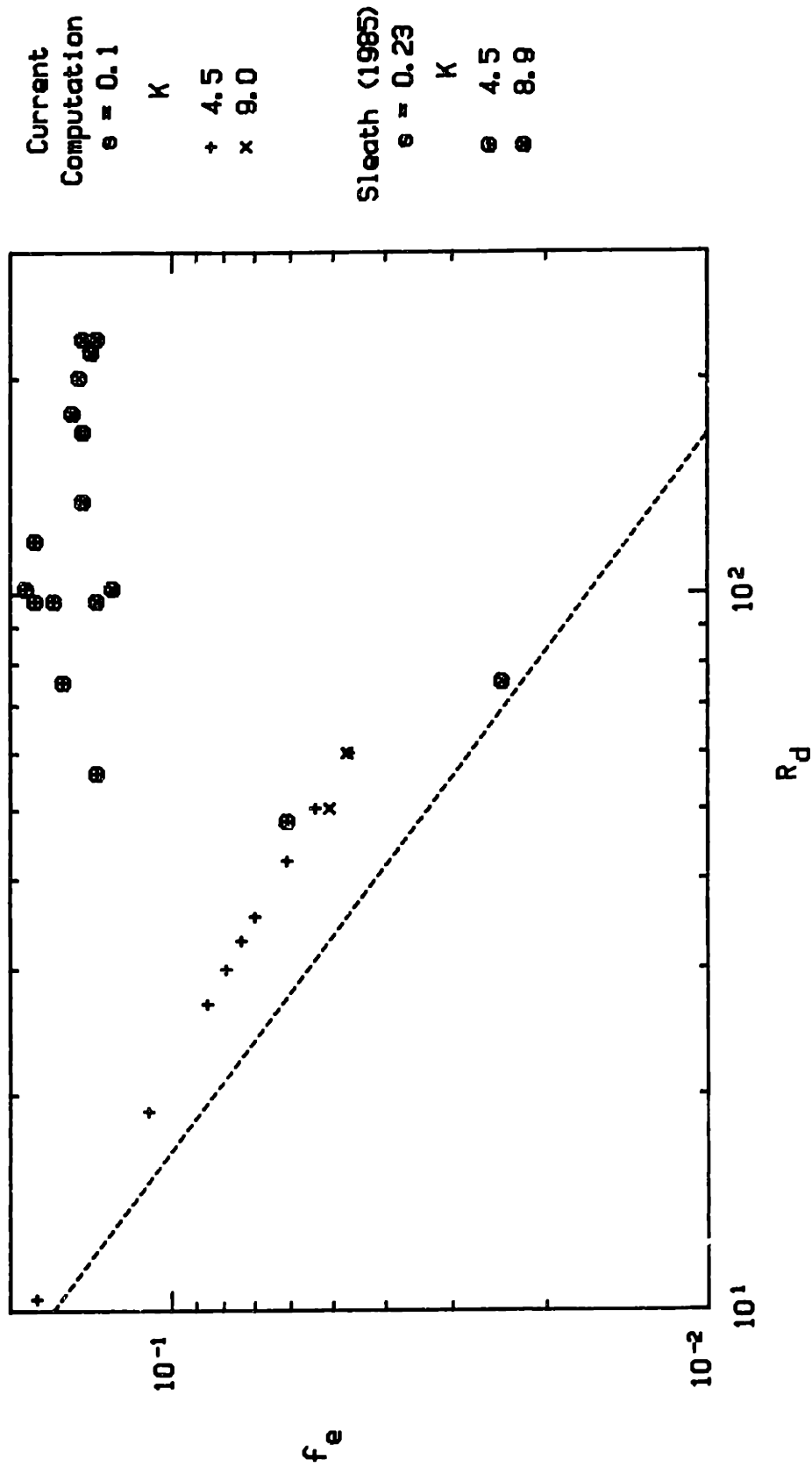
Fig. VII.6.6. Friction factor deduced from energy dissipation
assuming theta=0 in (7.6.6).
------ Oscillatory flow over a plane bed

Chapter VIII. Results for a pure current over ripples

For later comparison with values of the friction factor due to the combined oscillatory and steady ambient flow in Chapter IX, the flow over a ripple bed due to a current only will be discussed in this chapter. The Reynolds numbers and time units used will be denoted with subscript c.

§VIII.1. Formulation and numerical aspects of computation

The formulation and numerical scheme are identical to the case of oscillatory ambient flows except in the definitions of K and the vertical grid. The Reynolds number is defined as in (3.1.8) by replacing U_0 with the magnitude of the current c, such that $R_c = c2a/\nu$.

§VIII.1.1 Definition of the time scale and Keulegan–Carpenter number

There are no intrinsic time scales in the ambient flow, and we choose $T_c = L/c$ as the unit of time such that the Keulegan–Carpenter number cT_c/L equals one in (3.1.8) and (3.1.10). Therefore, when a doubling of the Reynolds number is considered as doubling the ambient flow velocity c, the unit of time T_c is shortened by one-half.

§VIII.1.2. Grid spacing in the vertical direction

In the computation of oscillatory flow over ripples, the grid spacing in the vertical direction is estimated from the boundary layer thickness in the flow of a semi–infinite fluid over a plane bed at steady state (§IV.4). This steady state is defined as after the initial transient behavior becomes negligible, that is, when the integral in (5.1.2) is much smaller than one. A similar criterion for the current

case, however, does not exist since the corresponding boundary layer thickness increases monotonously with time.

The exact solution for the velocity field under an impulsively started current in a semi-infinite fluid is due to G. G. Stokes[1] and takes the form

$$u_p(y_p, t_p) = c\, \text{erf}\left(\frac{y_p}{2\sqrt{\nu t_p}}\right),$$ (8.1.1)

or, in nondimensional variables,

$$u(y,t) = \text{erf}\left(\frac{y}{2\sqrt{t}}\sqrt{\frac{R}{s}}\right),$$ (8.1.2)

in which the error function $\text{erf}(\alpha)$ is defined as

$$\text{erf}(\alpha) = \frac{2}{\sqrt{\pi}}\int_0^\alpha dx\, \exp(-x^2).$$ (8.1.3)

The boundary layer therefore expands as $\sqrt{t}$. For example, if we define a boundary layer thickness y_δ as where $u=0.99$, we have, since $\text{erf}(1.82)=0.99$,

$$y_\delta = 3.64\sqrt{\left(\frac{s}{R}t\right)}.$$ (8.1.4)

Since our computation is for later comparisons with the cases of combined wave and current in Chapter IX, the grid is chosen the same as used in the oscillatory flows. Only one Reynolds number, $R=U_0 2a/\nu=250$ is used in those computations, and both $K=U_0 T/L=4.5$ ($c/U_0=1$, 2, and 4) and $K=9$ ($c/U_0=1$) are studied, in which the grid spacings are determined by considering the boundary layer thickness due to the oscillatory component alone. That is, the vertical grid is given by (4.4.3) with δ defined in (4.4.1), and the one used in $R=250$ and $K=4.5$ is used in the computations in this chapter. From (8.1.4), the boundary layer in the present case will therefore be resolved adequately for all $t > \pi/3.64^2 \approx 0.24$ in the absence of

---

[1] "Some authors refer to this problem as the 'Rayleigh problem'; there is no justification for it, as it can be found fully discussed and solved in" Stokes (1851). (Schlichting, 1968)

213

ripples.

§VIII.1.3. Extent in time of computation

From (8.1.4), the time required for the boundary layer in an infinite fluid to reach a height y_{max} is $0.075y_{max}^2 R/s$ which, for $y_{max} \approx 2$, equals 750 and 3000 for $R_c = 250$ and 1000, respectively. This gives an estimate on the time it takes before the final steady state is reached in our computation with the flow domain truncated at $y = y_{max}$. Since this requires an expenditure of computer time beyond our budget, our computation for flow over ripples are continued only until further changes in various hydrodynamic quantities, for example the rate of energy dissipation and the horizontal force on a ripple, are small. It will be apparent from the results shown in §VIII.2 that this is when their time dependence approaches those in the corresponding flow over a plane bed.

§VIII.1.4. Numerical aspects of computation

We have examined the various requirements described in §VI.1, §VI.2, and §VI.4 that the numerical solution has to meet for a true representation of the exact solution. That is, the components with nonzero wavenumbers in the Fourier spectrum of streamfunction must vanish near the top boundary of the computational domain, the components above the Nyquist frequency in the same spectra must be small compared with those components below, and that the conservation of energy within computational domain has to be satisfied. The details will be omitted here. Note, however, that since the acceleration in the ambient flow after the initial start is zero, a net pressure gradient in the x_p direction does not exist. Energy input into the fluid in the control volume over a ripple (bounded by contour ABCD in Fig. III.1.1) through pressure work is therefore zero, and the rate

of energy dissipation through viscosity equals the rate of decrease in total kinetic energy. This energy balance holds until a velocity gradient appears at the upper boundary of computation due to the vertical expansion of the boundary layer. After this time, the hydrodynamic shear stress at the upper boundary due to the velocity gradient does work on the fluid. Since our computation is terminated before the disturbance reaches y_{max},[2] the final steady state is not reached at the end of the computation.

§VIII.2. Numerical results

Currents with $R_c = 250$ and 1000 over ripples with $s = 0.1$ are studied. This provides the background for Chapter IX, in which an oscillatory flow of amplitude U_0 is superposed on these currents. Specifically, the Reynolds number of the oscillatory flow will be $R = U_0 2a/\nu = 250$ and the currents studied in this chapter correspond to the cases of $c/U_0 = 1$ and 4.

The ambient flow is made to increase gradually to its final value over a time of $\frac{1}{2}r\pi$ according to,

$$c\, U_\infty(t) = \begin{cases} c \sin\left(\frac{1}{r}\frac{c}{L} t_p\right), & 0 < t_p < \frac{1}{2}r\pi \frac{L}{c} \\ \\ c, & \frac{1}{2}r\pi \frac{L}{c} \leq t_p \end{cases} \qquad (8.2.1)$$

or, in nondimensional form,

$$U_\infty(t) = \begin{cases} \sin t/r, & t < \frac{1}{2}r\pi \\ \\ 1, & \frac{1}{2}r\pi \leq t \end{cases}. \qquad (8.2.2)$$

The value of r determines the transition time in the start-up of the far field velocity. It is chosen such that the time it takes the ambient current to reach its

---

[2] This can be infered from the plots of velocity profiles in §VIII.2.3 and the estimate of boundary layer thickness (8.1.4).

215

magnitude is approximately the same as that in the corresponding flow in Chapter IX. Computations are continued to $t=300$ for both $R_c=250$ and 1000.

To ensure that the solution at large time is not dependent on how the magnitude of the current is approached, the flow with $R_c=250$ is computed for two different values of r.

In all computations flow separations are present during the initial start, and no vortices are found at large times. A typical velocity profile at large time increases monotonously from zero on the ripple surface to the ambient velocity in the far field.

§VIII.2.1. Rate of energy dissipation

The rates of energy dissipation $\mathscr{D}$ are plotted as a function of time in Figs. VIII.2.1 to VIII.2.4. As a comparison, the rate of energy dissipation in the impulsively started current over a flat plate (Stokes first problem) is also plotted as a dotted line. From (8.1.1),

$$\frac{\partial u_p}{\partial y_p} = \frac{c}{\sqrt{\pi \nu t_p}} \exp(-\frac{y_p^2}{4\nu t_p}) \tag{8.2.3}$$

which, upon substitution into (3.3.4), gives

$$\mathscr{D}_p = \rho L \int_0^\infty dy_p \, \nu(\frac{\partial u_p}{\partial y_p})^2 = \frac{\rho c^2 L}{\pi t_p} \int_0^\infty dy_p \, \exp(-\frac{y_p^2}{2\nu t_p}) = \rho c^2 L \sqrt{\frac{\nu}{2\pi t_p}}$$

or, in nondimensional variables,

$$\mathscr{D}_s = \frac{\mathscr{D}_p}{\rho c^3 L} = \sqrt{\frac{s}{2\pi R_c}} \frac{1}{\sqrt{t}}. \tag{8.2.4}$$

Since our computation is for an ambient velocity that is approached gradually while (8.2.4) is obtained from an impulsively started flow, the initial values of the rates of

energy dissipation in the two cases are not directly comparable. In Figs. VIII.2.1 to VIII.2.4, the curve (8.2.4) is plotted only after the ambient velocity in our computation has attained its maximum value, that is, for $t > \frac{1}{2}r\pi$.

The rates of viscous dissipation when $R_c = 250$ are plotted in Figs. VIII.2.1 and VIII.2.2, corresponding to $r = 5$ and 10 in (8.2.2). In both cases $\mathcal{D}$ increases to its maximum at about the same time when the far field velocity attains its magnitude, at $t \approx 8$ and 16 respectively, after which it decreases sharply until $t \approx 50$. For $t > 80$ the values of $\mathcal{D}$ in the two cases $r = 5$ and 10 become identical and are indistinguishable from that in the corresponding flow over a plane bed given by (8.2.4).

The maximum value of $\mathcal{D}$, however, is considerably higher when the ambient velocity is approached twice as fast. Furthermore, oscillations (with a period of about 2.5) are found in the flow with $r = 5$ but not when $r = 10$. These oscillations are associated with vortex shedding and will be discussed in detail in §VIII.3.

From §VII.2, $\mathcal{D}$ in a purely oscillatory flow varies between 0.014 to 0.010 as K increases from 2.5 to 9 at $R = 250$. Therefore, the rate of energy dissipation under an ambient current of an equal amplitude is an order of magnitude smaller.

The time history of $\mathcal{D}$ when $R_c = 1000$ is plotted in Fig. VIII.2.3 for $r = 20$. High frequency oscillations with a period of around 1.7 is found, which start long before the ambient current reaches its maximum value. At large t, the decrease in $\mathcal{D}$ is also proportional to $1/\sqrt{t}$, but its magnitude is smaller than that in the flow over a plane bed. At $t = 300$, $\mathcal{D} = 0.192 \times 10^{-3}$ while $\mathcal{D}_s = 0.230 \times 10^{-3} \approx 1.20 \, \mathcal{D}$.

The initial oscillations at $R_c = 1000$ are examined in more detail in Fig. VIII.2.4. The value of r defined in (8.2.2) is one and therefore the far field velocity reaches its magnitude considerably faster. The value of $\mathcal{D}$ increases monotonously with time and does not reach its maximum until after the ambient velocity has reached its final magnitude. As in the case of $R_c = 250$, the maximum in $\mathcal{D}$ is considerably

217

larger when the initial acceleration of the far field velocity is faster. Note also that smaller grid spacings, with M=64 and the minimum of Δy=0.0014, are needed to resolve the increased complexity of the flow field associated with the faster acceleration.

§VIII.2.2. Horizontal force on ripple

Unlike the case of an oscillatory ambient flow, the horizontal force on a ripple under a steady current is independent of the particular choice of ripple profile used in the calculation, since a net pressure gradient due to the acceleration of the ambient flow is absent. The horizontal force computed using any of the three profiles discussed in Appendix IV are therefore identical, that is, $F_c=F_t=F_n=F_x$.

As in the rate of energy dissipation, the corresponding curve for the horizontal force in Stokes first problem is plotted after the ambient velocity has reached its final value in our computation. The horizontal force on a plane bed under an ambient current can be deduced from (8.2.3), that is,

$$F_x^S = \frac{1}{\rho c^2} \tau_p = \frac{1}{\rho c^2} \rho \nu \frac{\partial u_p}{\partial y_p}\Bigg|_{@y_p=0} = \sqrt{\frac{s}{\pi R_c}} \frac{1}{\sqrt{t}}. \qquad (8.2.5)$$

Both F_x and F_x^S for R_c=250 are plotted in Figs. VIII.2.5 and VIII.2.6 for r=5 and 10 defined in (8.2.2). In both cases, F_x is positive at all times and reaches its maximum just after the ambient velocity have reached its magnitude. Large amplitude oscillations are found soon after in the first case with a faster start. For t>50, F_x in both cases varies exactly as F_x^S defined in (8.2.5).

Recall from Chapter VII that, when the ambient flow is oscillatory and of the same magnitude, $\|F_x\|$ decreases from 0.15 to 0.07 as K increases from 2.5 to 6 for R=250. As in the case of energy dissipation, this is an order of magnitude greater than that in the flow under an ambient current.

On the other hand, F_x oscillates between positive maxima and negative minima when $R_c=1000$, both with magnitudes much larger than the positive mean of this horizontal force or F_x^S defined in (8.2.5). This shown in Fig. VIII.2.7 for r=20. The magnitudes of these oscillations decrease with time until at around t=160, it begins to decrease monotonously with time as $1/\sqrt{t}$. The period of oscillation is the same as the periodicity observed in the rate of energy dissipation, and is associated with the shedding frequency of vortices to be discussed in §VIII.3. The horizontal force on the ripple is smaller than that in the flow over a plane bed at large time. At the end of our computation at t=200, $F_x=0.255\times10^{-3}$ while $F_x^S=0.399\times10^{-3}\approx1.6F_x$.

The case of $R_c=1000$ is further examined in Fig. VIII.2.8 with r=1. As in the case of $\mathscr{D}$, oscillations in this case start only after the ambient velocity has reached its peak. The frequency of oscillations is approximately the same as that with r=20, but unlike the other case, the amplitudes remain fairly constant over ten periods.

§VIII.2.3. Velocity profiles

The results in the last two sections suggest that the flow field over ripples may be very similar to that over a plane bed at large time.[3] To investigate this further, the horizontal velocity component averaged over a ripple length,

$$\langle\bar{u}\rangle(y,t) = \frac{1}{M}\sum_{m=1}^{M}\bar{u}(m\Delta x, y; t) \tag{8.2.6}$$

where $\Delta x=1/M$, is plotted as a function of y at various t. This gives the horizontal velocity at a mean distance y away from the ripple surface.[4] The velocity profile

---

[3]On the other hand, vortices generated over ripples at the beginning of motion lead to a very different flow field than that over a plane bed.

[4]The variation of the elevation of this contour along the ripple profile in the physical plane, corresponding to different values of y, has been plotted in Fig. IV.1.1.

(8.1.2) corresponding to the flow over a plane bed is also plotted as a broken line.

The velocity profile for $R_c = 250$ at $60 \leq t \leq 80$ is shown in Fig. VIII.2.9. Despite the significant differences in the two flows (the generation of vortices over ripples but not over a plane bed) in the beginning, the extent of the boundary layer at large time is very nearly the same. Good agreement is found in the two velocities along the entire profile, with $\langle \bar{u} \rangle$ slightly smaller than that over a plane bed near the ripple surface.

The velocity profile for $R_c = 1000$ at $100 \leq t \leq 300$ are plotted in Fig. VIII.2.10. Near the ripple surface, the mean horizontal velocity is considerably smaller than that over a plane bed, but this difference decreases with time. Compared with the previous case, the discrepancy between the two profiles is much larger. If we consider the increase in R_c as due to a four-fold increase in c, the unit of time (defined in §VIII.1.1) is one-fourth that at $R_c = 250$ and therefore t=100 and 300 corresponds to 25 and 75 in the previous case. Recall that the time in Fig. VIII.2.9 is between 60 and 80, the better agreement in that comparison is not unexpected.

§VIII.2.4. Shear stress on ripple surface

As a further comparison with the flow over a plane bed, we shall examine the shear stress over a ripple profile at after the initial transient effects have subsided. In Fig. VIII.2.11 we plot the shear stress at t=50, 75, and 100 for the flow at R=250. The shear profiles at the three time instants are similar, and the maximum shear stress is found immediately upstream of the ripple crest. The shear stress at the trough and over half of the ripple length is much smaller in magnitude and opposite to the direction of current. This suggests the presence of a weak stationary vortex over the trough.

Recall from (8.2.4) that the corresponding shear stress over a plane bed τ_s

decreases from 0.0016 to 0.0011 over the same time interval, the variation of the shear stress across the ripple is therefore between over three times τ_s to less than one-fourth τ_s in the opposite direction. Interestingly, the horizontal component of this shear stress integrated over the ripple length, plus the contribution due to the pressure fluctuations, give a net horizontal force that is the same as that over a plane bed as shown in Fig. VIII.2.6.

The shear stress across the ripple for the flow with R_c=1000 is very similar to that shown in Fig. VIII.2.11. These shear profiles for t=200 and 300 are plotted in Fig. VIII.2.12. It ranges from a minimum of -0.108×10^{-3} near the trough to 0.862×10^{-3} near the crest at t=200, and from -0.105×10^{-3} to 0.841×10^{-3} at t=300. The rate of decrease with time of the amplitude of the shear stress on a ripple is therefore much slower than that on a plane bed, which from (8.2.5) decays as $1/\sqrt{t}$.

§VIII.3. Results during the transient oscillations (vortex shedding)

It is shown in §VIII.2 that both the rate of energy dissipation and the horizontal force on the ripple oscillates in time with large amplitudes during the early part of the computation, despite that the ambient velocity is constant in time. These fluctuations are due to vortex sheddings and will be examined in detail in this section. Specifically, we shall examine the flow at R_c=1000 with the far field velocity defined by (8.2.1) and r=1, during the very beginning of the computation, 0<t<22. The rate of energy dissipation and the horizontal force on the ripple have been plotted in Figs. VIII.2.4 and VIII.2.8.

§VIII.3.1. Flow field during vortex shedding

The velocity field becomes periodic in time after the initial transient effects at the start has decayed significantly, at around t=6. Velocity vectors at the grid

points over a typical period are plotted at a time shortly thereafter in Fig. VIII.3.1 at time intervals of 0.5 between t=17 and 18.5.

At t=17 a single vortex with a clockwise rotation is found downstream of the crest (Fig. VIII.3.1.i). As it moves downstream to past the trough, another smaller vortex with the same circulation develops between the first vortex and the crest (Fig. VIII.3.1.ii). This new vortex grows bigger and moves further downstream as the first vortex now reduced in strength moves over the next ripple crest downstream (at t=18, Fig. VIII.3.1.iii). By t=18.5 only one vortex is found over a ripple length (Fig. VIII.3.1.iv), and the flow is now very much like that at t=17. This indicates the coalescence of a vortex developed over the ripple upstream with the one generated locally. The flow field then evolves in the exact same manner just described. The time the vortex takes to travel a ripple length is the same as that between recurrence of the pressure and shear profiles, and the period of fluctuation of the instantaneous rate of energy dissipation $\mathscr{D}$ already discussed in §VIII.2.1. From the time history of $\mathscr{D}$, the periodicity of the flow field is found to be between 1.56 and 1.86, with a mean of 1.74. The vortices therefore move at about 57% of the speed of the ambient current.

§VIII.3.2. Shear Stress on ripple during vortex shedding

Profiles of the shear stress spanning the same time interval as in the plots of velocity vectors are shown in Fig. VIII.3.2 at time intervals of 0.25. Between t=17 and 17.5, the maximum local shear is found immediately upstream (at a distance of 0.05L to 0.1L) of the crest and its magnitude is nearly constant over this period. The shear stress decreases upstream to a negative minimum below the center of the vortex in the flow field. As this vortex moves downstream and further away from the crest, the local minimum of the shear stress decreases and varies from 80% to

50% of the maximum shear immediately upstream of the crest. At t=17.25, a new negative minimum of a significant amplitude appears at about 0.1L downstream of the crest. This is due to the newly developing vortex which, although smaller in size, is closer to the ripple surface and therefore induces a larger shear (Fig. VIII.3.1.ii). This new vortex induces the highest local shear over the wave period at about t=18.5 and at 0.3L downstream of the crest. Between t=17.75 to 18.25, the shear stress at the ripple crest is in the negative x_p direction when the vortex present in the beginning is now above the downstream crest. When this vortex climbs onto the next ripple and merges with the vortex already there, the shear profile becomes the same as at t=17, and the evolution of the stress profile recurs.

§VIII.3.3. Pressure on ripple surface during vortex shedding

The pressure profiles on the ripple surface are plotted in §VIII.3.3 at the same instants as discussed in the previous two sections. As a comparison, the normalized potential flow pressure increases from a minimum of –0.57 at the crests to a maximum of 0.20 at the troughs, and is constant in time due to the absence of acceleration in the ambient flow.

The pressure profile propagates downstream similar to the shear stress profile. A negative minimum is found slightly upstream of the center of the clockwise rotating vortex. The pressure gradient therefore acts in a way such that, below and to the right of the center of vortex, the flow is accelerated to the left, and, below and to the left of the center of vortex, the flow is accelerated to the right.

The amplitude of the pressure profile is significantly lower than that of the corresponding osillatory ambient flow since the pressure component due to the acceleration in the ambient flow is absent in this case.

High frequency spatial oscillations in the pressure profile are found near the crests at t=17 and 17.25. This is due to inaccuracy in the numerical quadrature of the integral in (3.2.7), an error analogous to that discussed in §VI.4.

§VIII.3.4. Horizontal force on ripple during vortex shedding

The horizontal force on the ripple for $0<t<22$ has been plotted in §VIII.2.8. For $t>6$, F_x oscillates with a period of 1.7 which is consistent with the periodicity observed in the shear stress and pressure profile on the ripple. The amplitude of F_x remains fairly constant in time, and in $20<t<22$, the positive maximum is 0.0254 which is higher than the value of –0.0205 for the negative minimum. The time averaged net horizontal force during the same time is 0.0039, which is in the direction of the ambient flow. By comparing with the plots of the velocity field in §VIII.3.1, the maximum force in the positive x direction is at a time when the vortex is close to and downstream of the ripple crest, and the maximum force in the negative x direction is at a time when the vortex is climbing up the ripple crest downstream. Also, a positive maximum horizontal force occurs at a time when the rate of energy dissipation $\mathscr{D}$ is at a maximum, and a negative minimum force occurs when $\mathscr{D}$ is at its minimum.

Owing to the significantly smaller pressure force acting on the ripple discussed in §VIII.3.3, the amplitude of the horizontal force on a ripple under an ambient current is much smaller than its oscillatory counterpart.

§VIII.4. Summary

Vortex sheddings are prominent over a considerable period of time when the far field velocity over a ripple bed is started from rest. The magnitudes of these initial transient effects increases with the Reynolds number R_c and the initial acceleration,

after which the flow characteristics resemble closely the impulsively started current over a plane bed (Stokes first problem). Both the rate of energy dissipation and the horizontal force on the ripple decreases monotonously. Towards the end of computation, these values are already smaller by an order of magnitude than those of the coresponding oscillatory flow with the same amplitude.
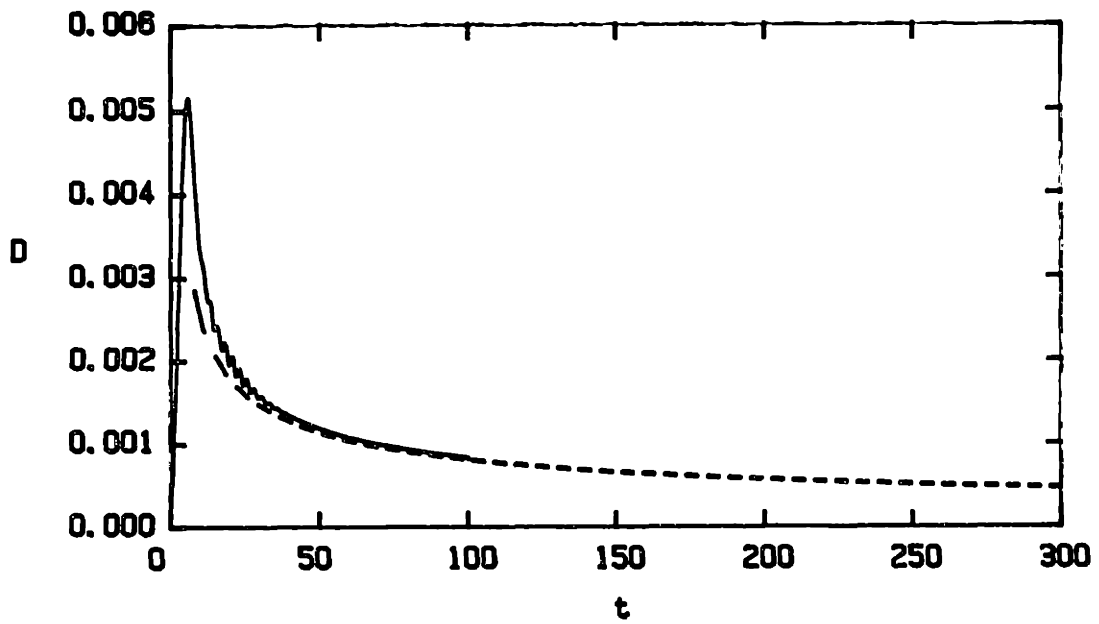
Fig. VIII.2.1.   Rate of viscous dissipation
R = 250   e = 0.1
M = 32   N = 57   r = 5
dy = (0.0036, 0.151) y_{max} = 2.08

——————— over ripples
-------- over plane bed
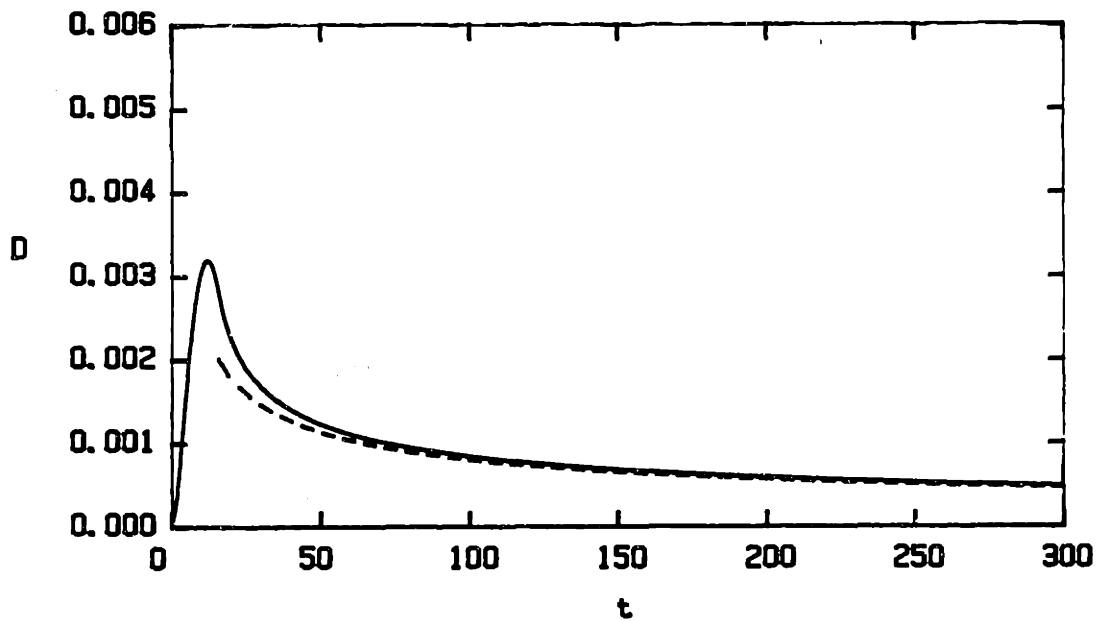
Fig. VIII.2.2.   Rate of viscous dissipation
R = 250   e = 0.1
M = 32   N = 57   r = 10
dy = (0.0036, 0.151) y_{max} = 2.08
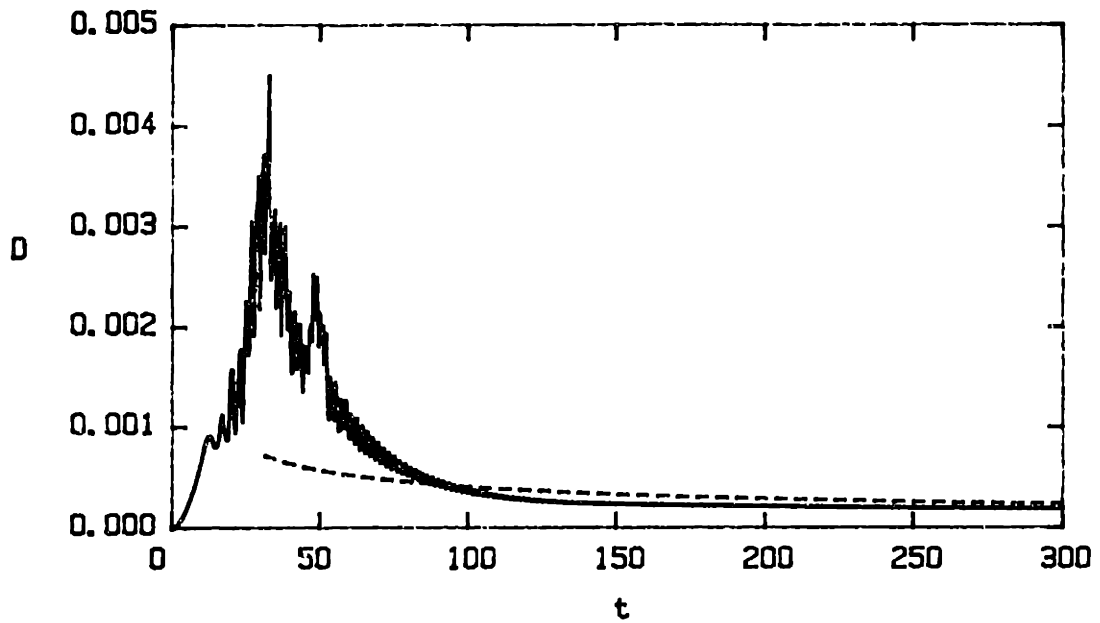
Fig. VIII.2.3. Rate of viscous dissipation
R = 1000   s = 0.1
M = 32   N = 57   r = 20
dy = (0.0036, 0.151) y_{max} = 2.08

——————— over ripples
--------- over plane bed
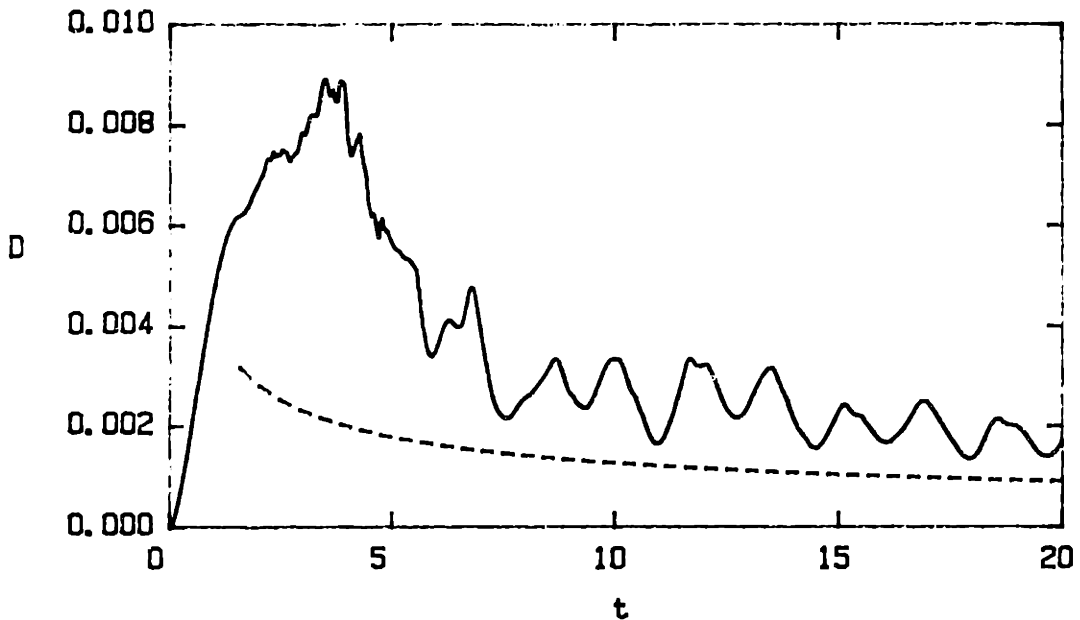
Fig. VIII.2.4. Rate of viscous dissipation
R = 1000   s = 0.1
M = 64   N = 68   r = 1
dy = (0.0014, 0.106) y_{max} = 1.59

227
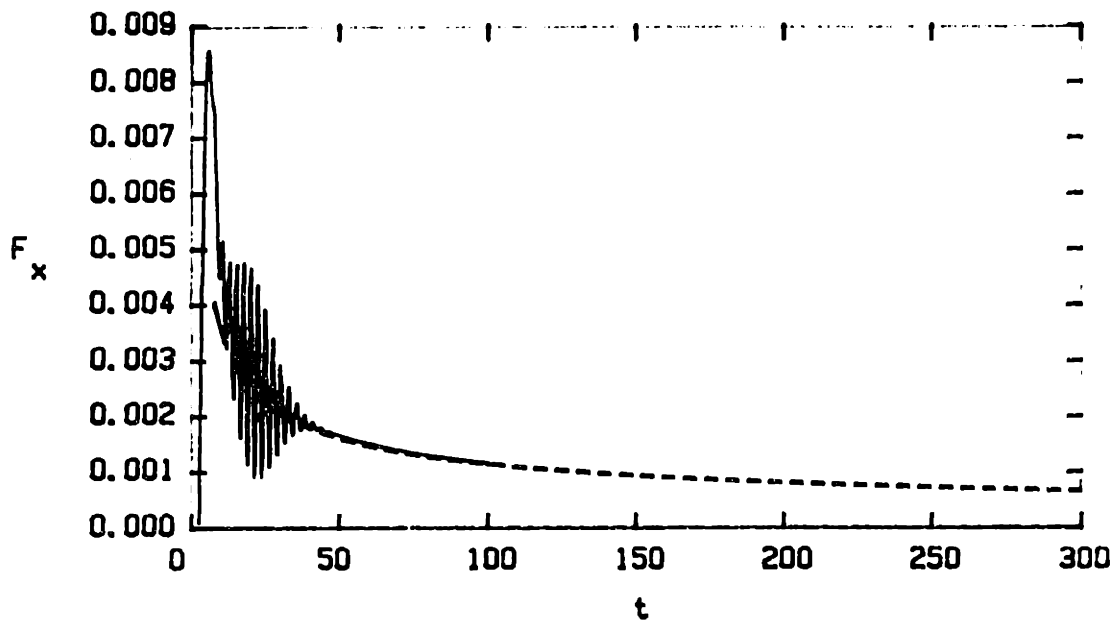
Fig. VIII.2.5. Horizontal force on ripple
R = 250   s = 0.1
M = 32   N = 57   r = 5
dy = (0.0036, 0.151) y_{max} = 2.08

———————— over ripples
-------- over plane bed
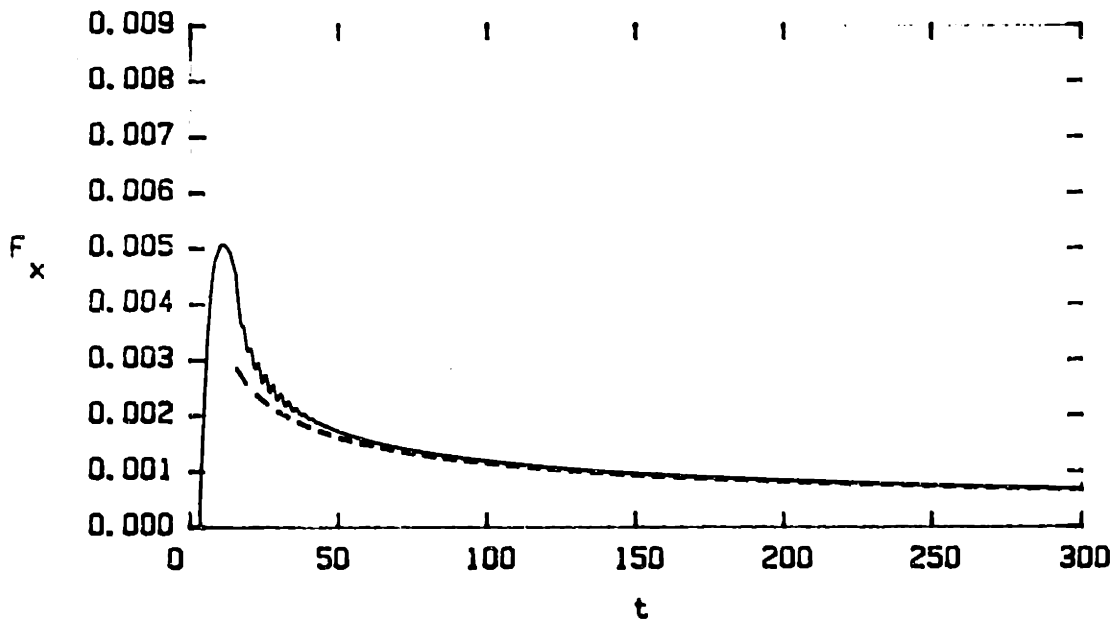
Fig. VIII.2.6. Horizontal force on ripple
R = 250   s = 0.1
M = 32   N = 57   r = 10
dy = (0.0036, 0.151) y_{max} = 2.08

228
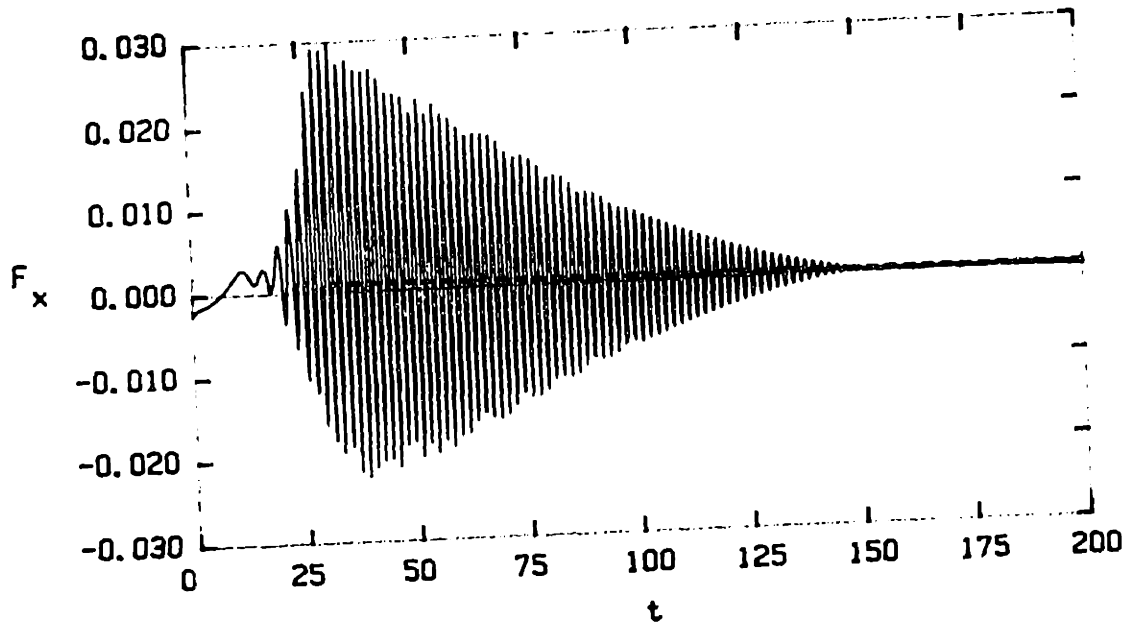
Fig. VIII.2.7. Horizontal force on ripple

R = 1000   s = 0.1

M = 32   N = 57   r = 20

dy = (0.0036, 0.151) y_{max} = 2.08

——————— over ripples
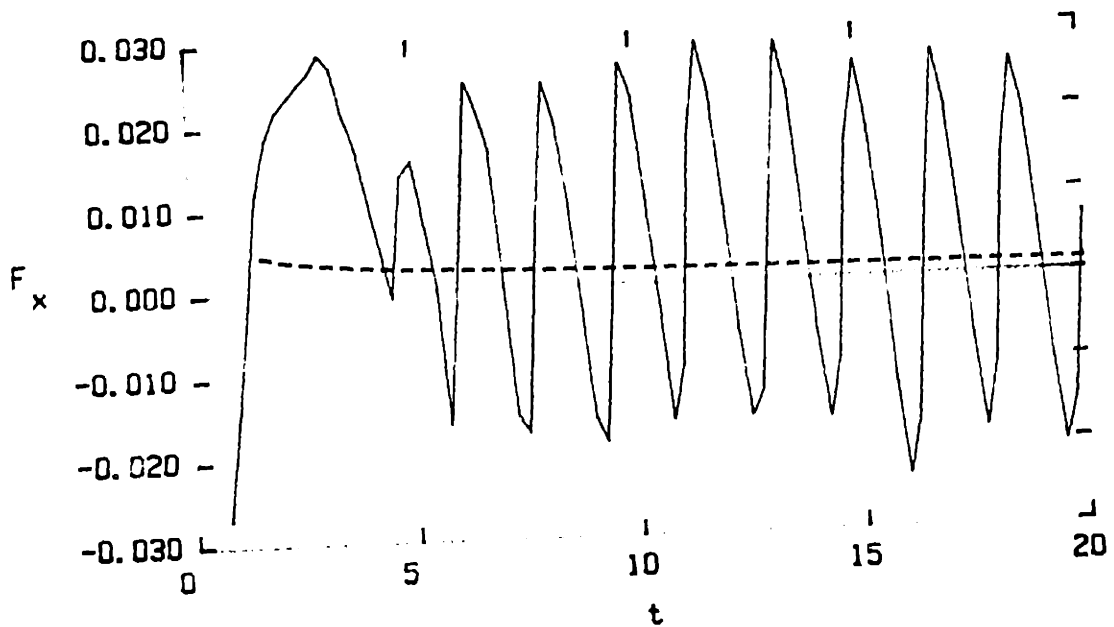
- - - - - - over plane bed

Fig. VIII.2.8. Horizontal force on ripple

R = 1000   s = 0.1

M = 64   N = 68   r = 1

dy = (0.0014, 0.106) y_{max} = 1.59

229
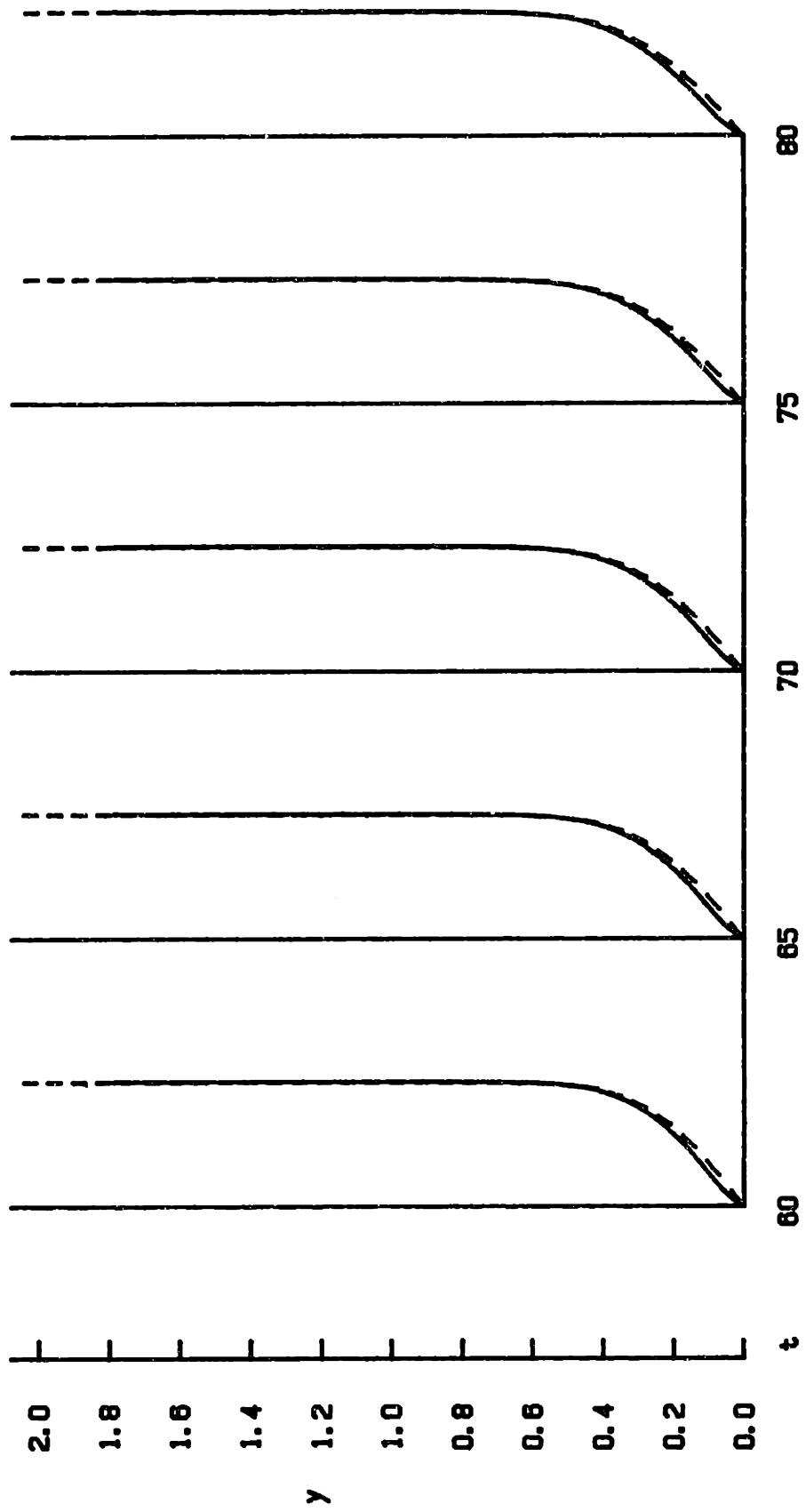
Fig. VIII.2.9.   Mean velocity profiles under an ambient current.
——— over ripples   ------- over a plane bed
R = 250   e = 0.1   M = 32   N = 57   r = 5
dy = (0.0036,   0.151) y_{max} = 2.08
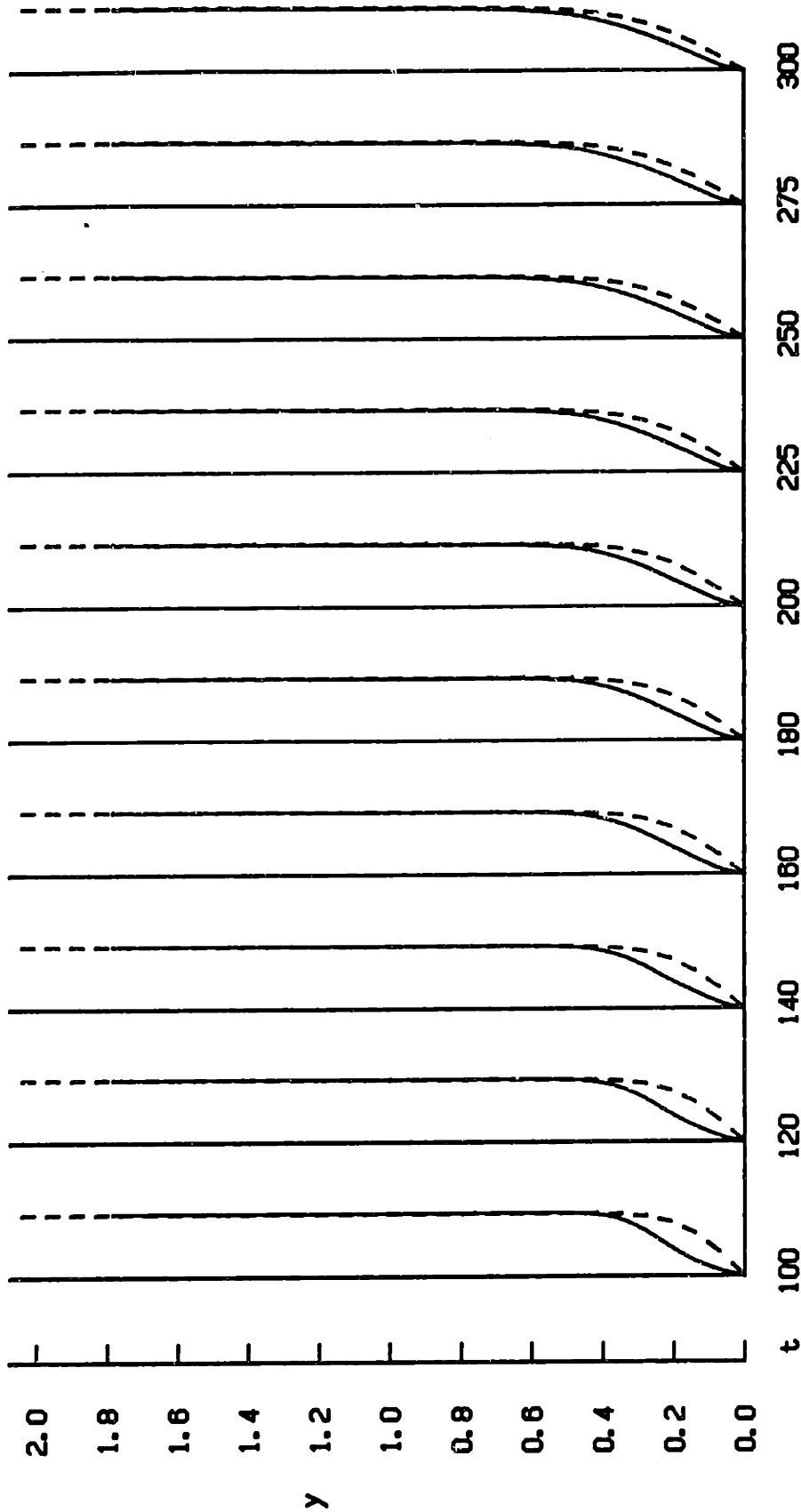
Fig. VIII.2.10.   Mean velocity profiles under an ambient current.
    ———— over ripples   ------ over a plane bed
    R = 1000   s = 0.1   M = 32   N = 57   r = 20
    dy = (0.0036, 0.151) y_{max} = 2.08
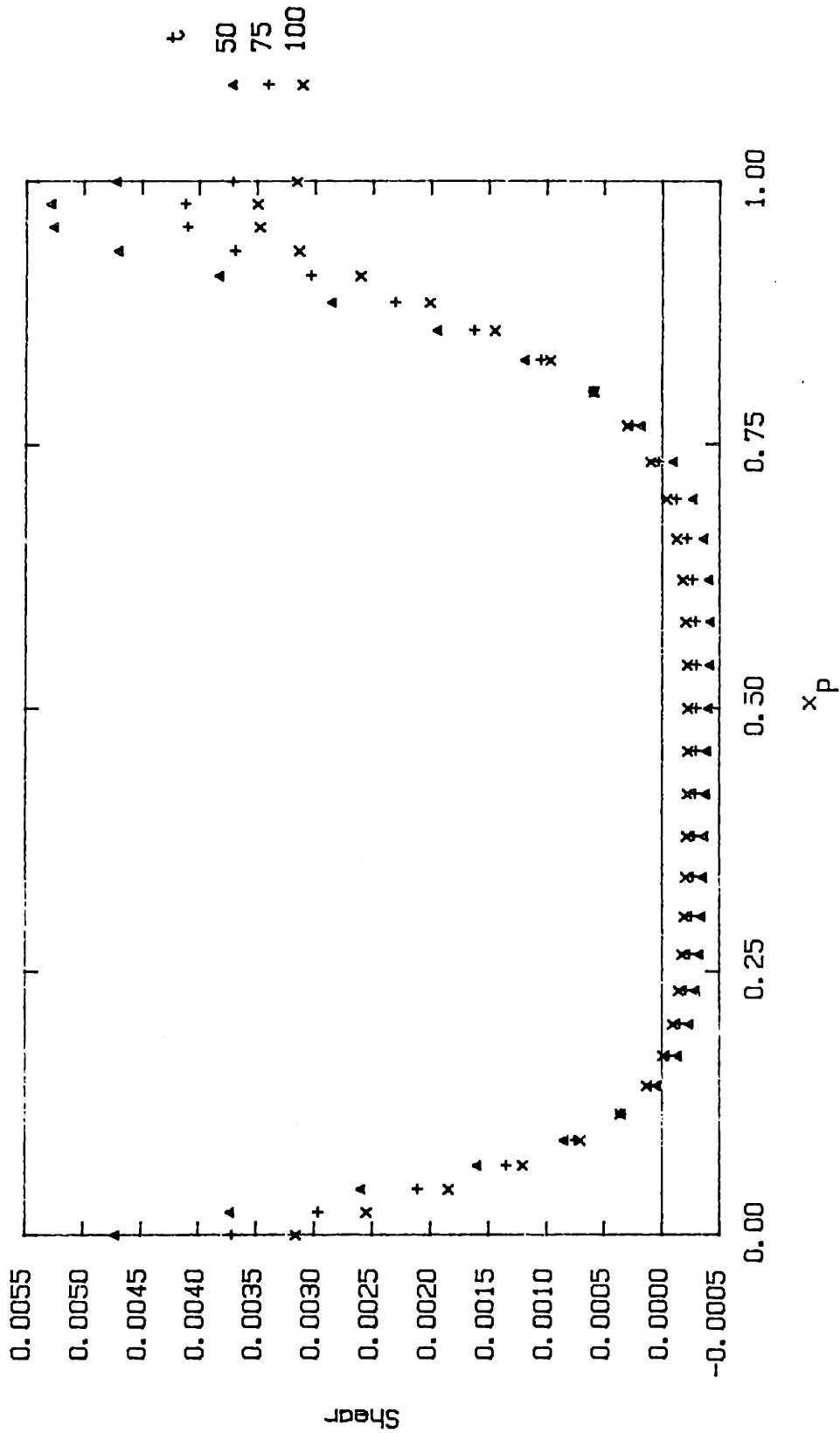
Fig. VIII.2.11.   Shear stress on ripple surface.

R_c = 250   s = 0.1   r = 10   M = 32   N = 57

dy : (0.0036 , 0.151) y_{max} = 2.08
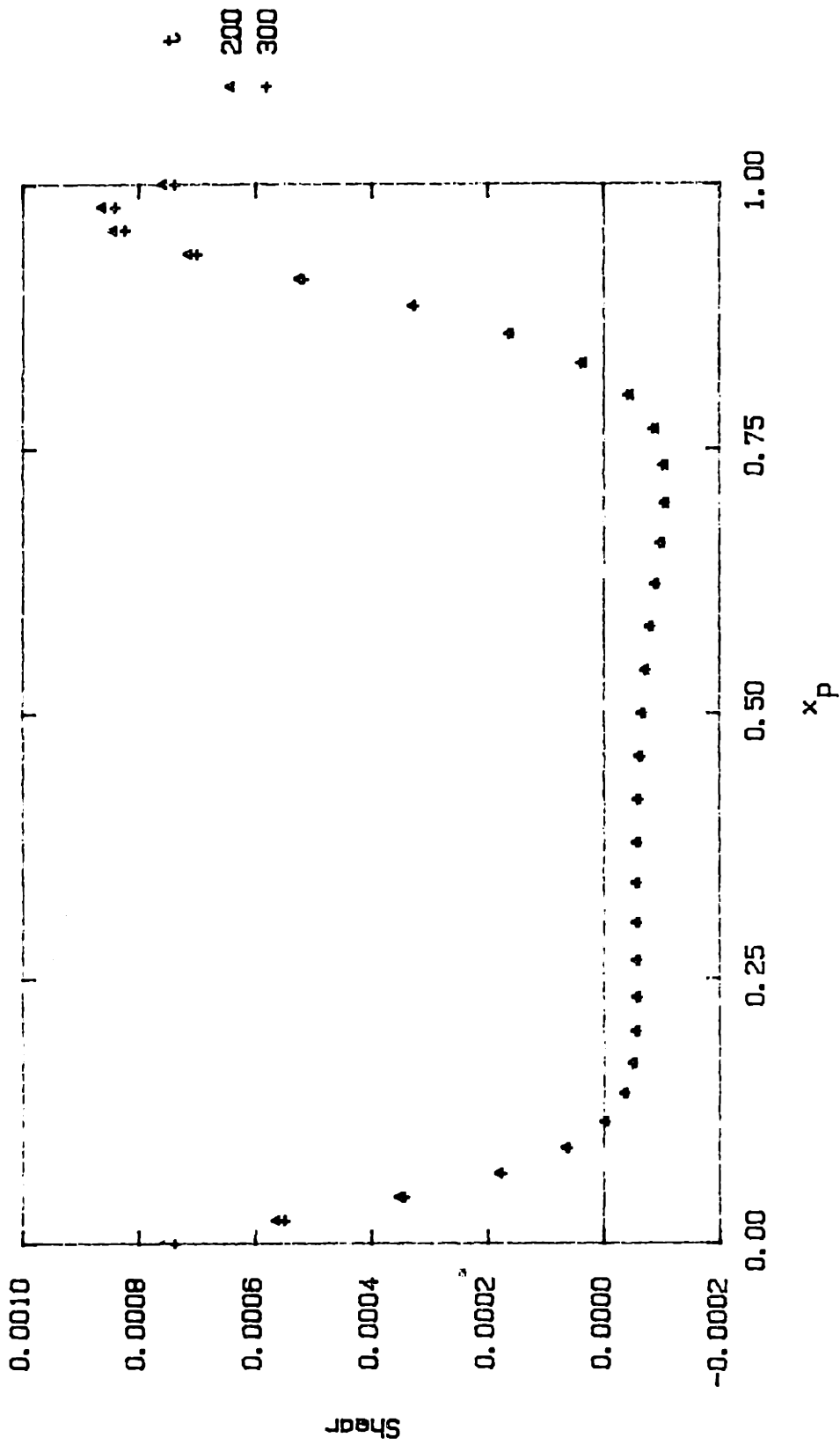
Fig. VIII.2.12.   Shear stress on ripple surface.

$R_c = 1000$ $s = 0.1$ $r = 20$ $M = 32$ $N = 57$

$dy : (0.0036, 0.151)$ $y_{max} = 2.08$
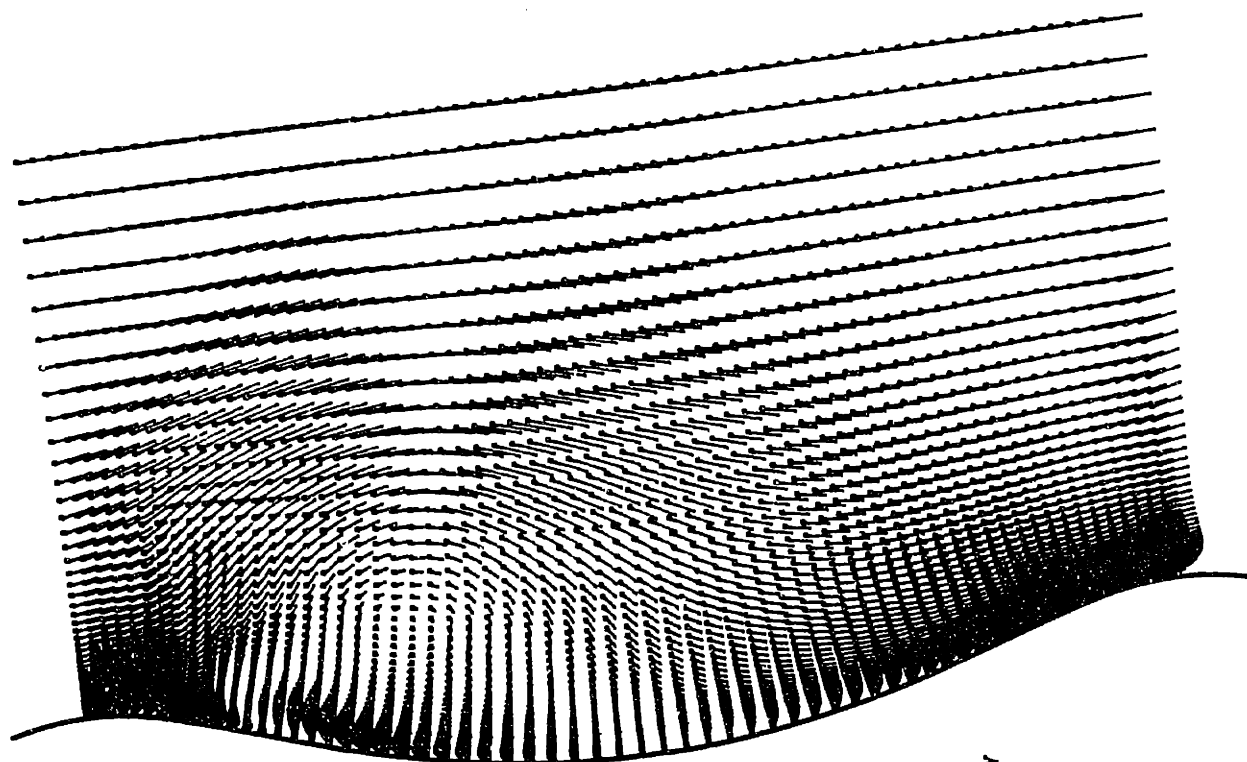
i.   t =   17.00 U_∞:
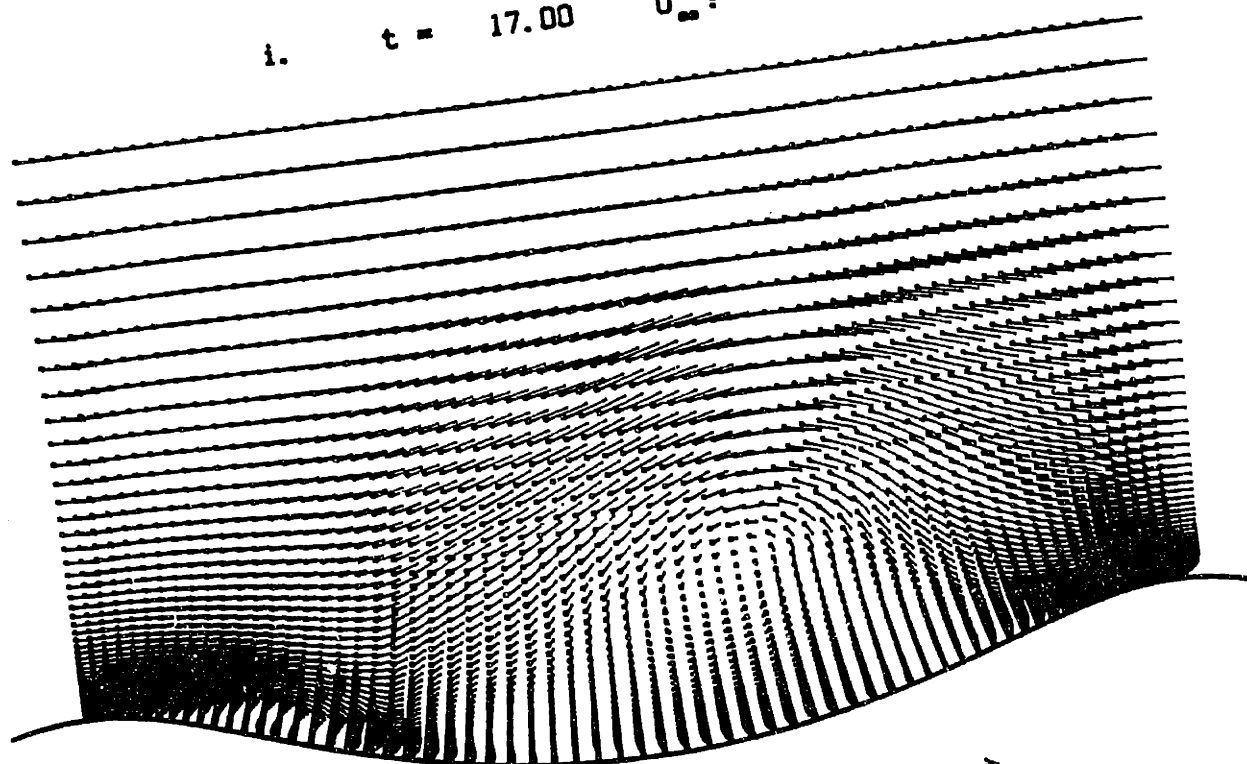
ii.   t =   17.50 U_∞:

Fig. VIII.3.1.   Velocity field

$R_c = 1000$ $s = 0.1$ $M = 64$ $N = 68$

$dy = (0.0014, \; 0.106)$ $y_{max} = 1.59$ $r = 1$
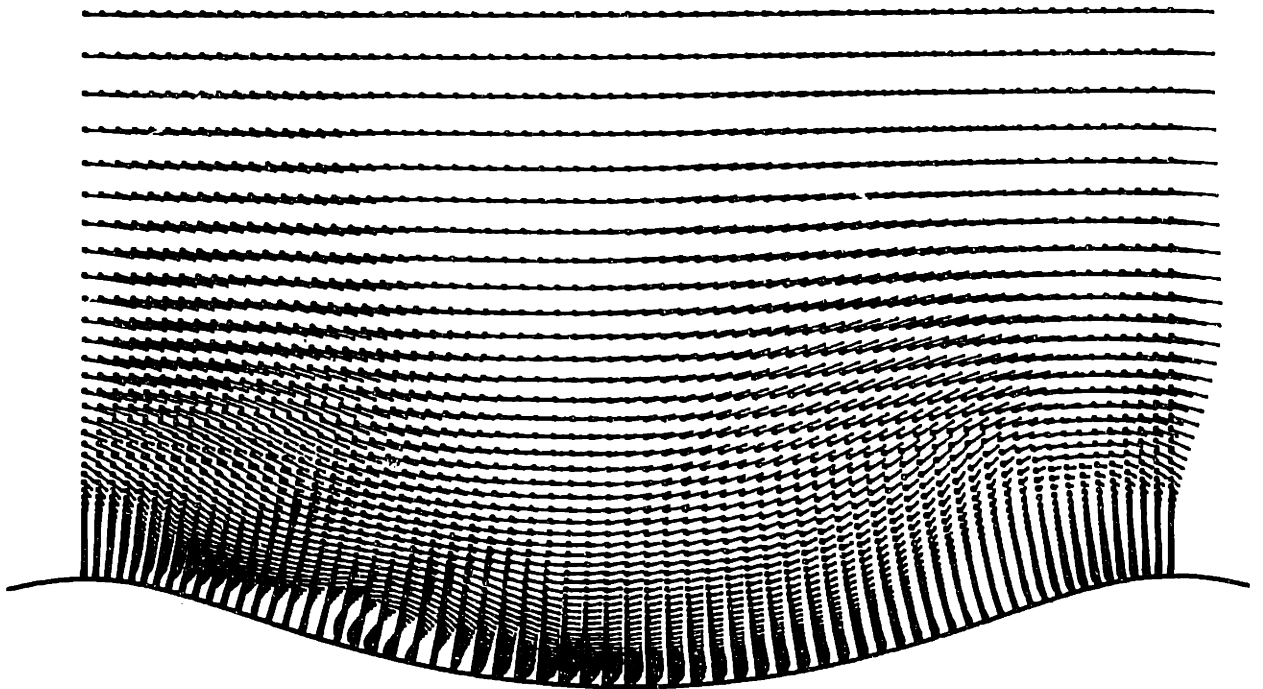
iii.   t =   18.00   U$_{\infty}$:   →
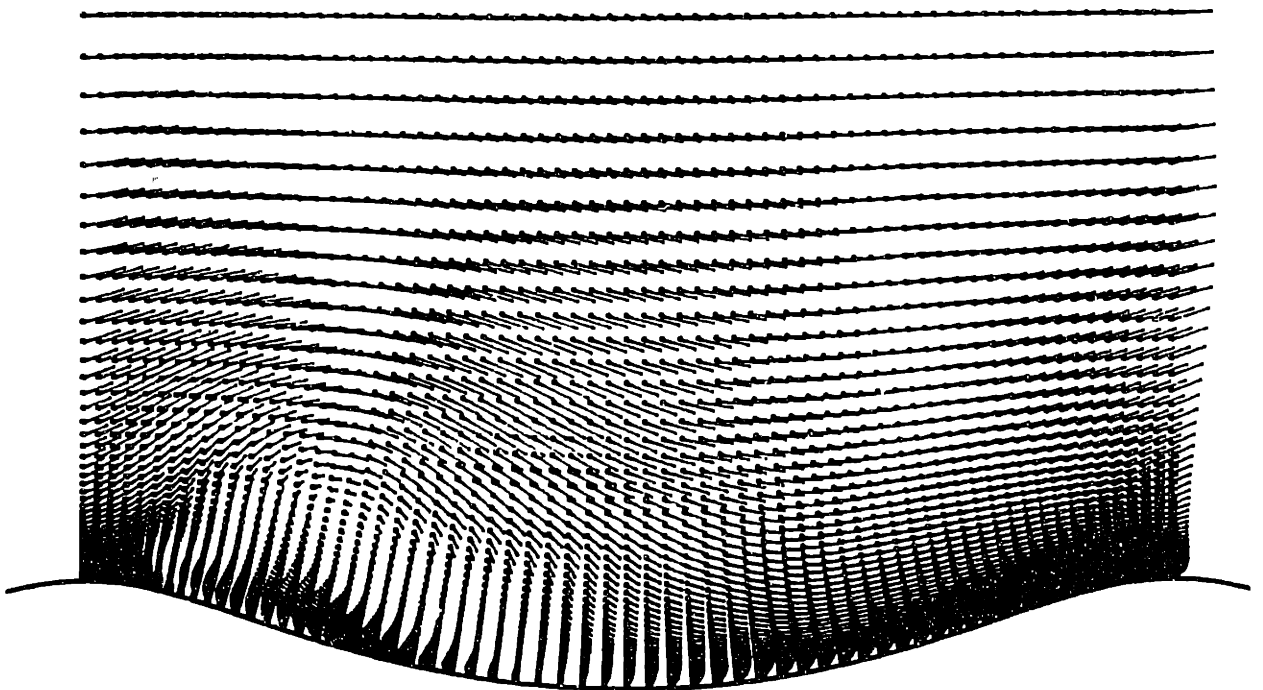
iv.   t =   18.50   U$_{\infty}$:   →

Fig. VIII.3.1.   Velocity field

R_c = 1000   s = 0.1   M = 64   N = 68
dy = (0.0014, 0.106)   y$_{max}$ = 1.59   r = 1

235
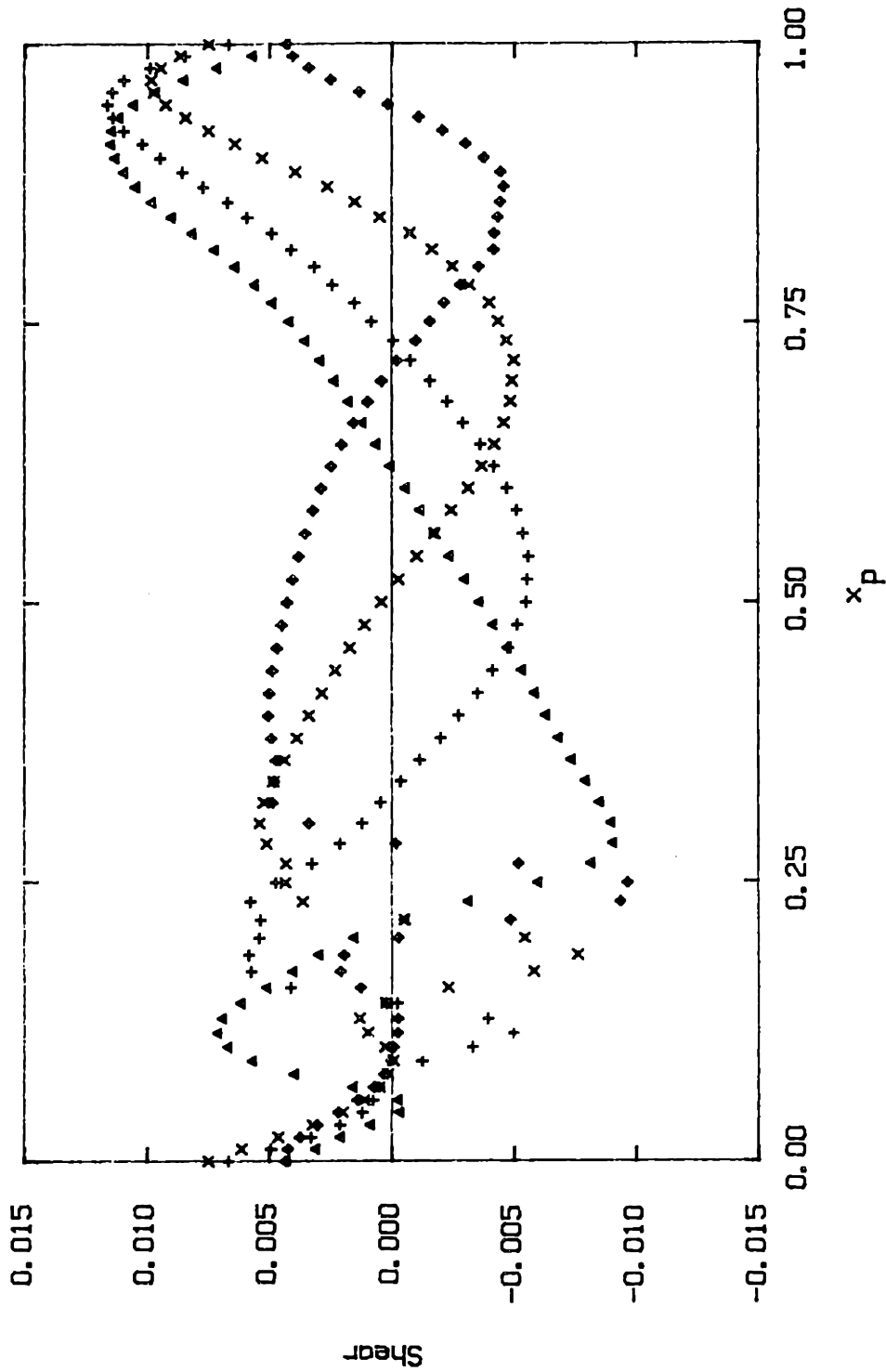
Fig. VIII.3.2.1.   Shear stress on ripple surface

R_c = 1000   s = 0.1   r = 1   M = 64   N = 68

dy : (0.0014 , 0.106) y_{max} = 1.59
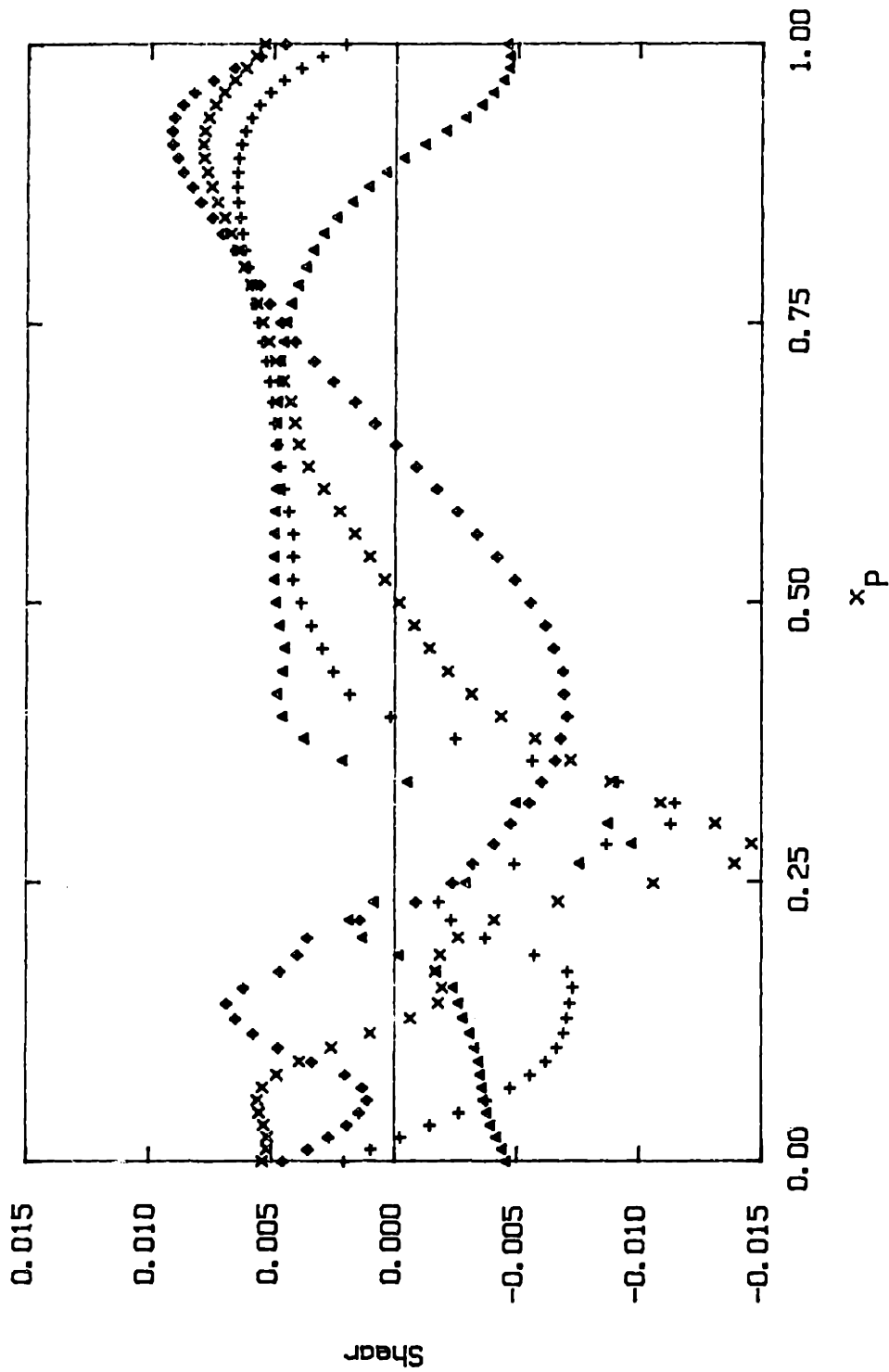
Fig. VIII.3.2.11. Shear stress on ripple surface

$R_c = 1000$ $s = 0.1$ $r = 1$ $M = 64$ $N = 68$

$dy : (0.0014 , 0.106)$ $y_{max} = 1.59$
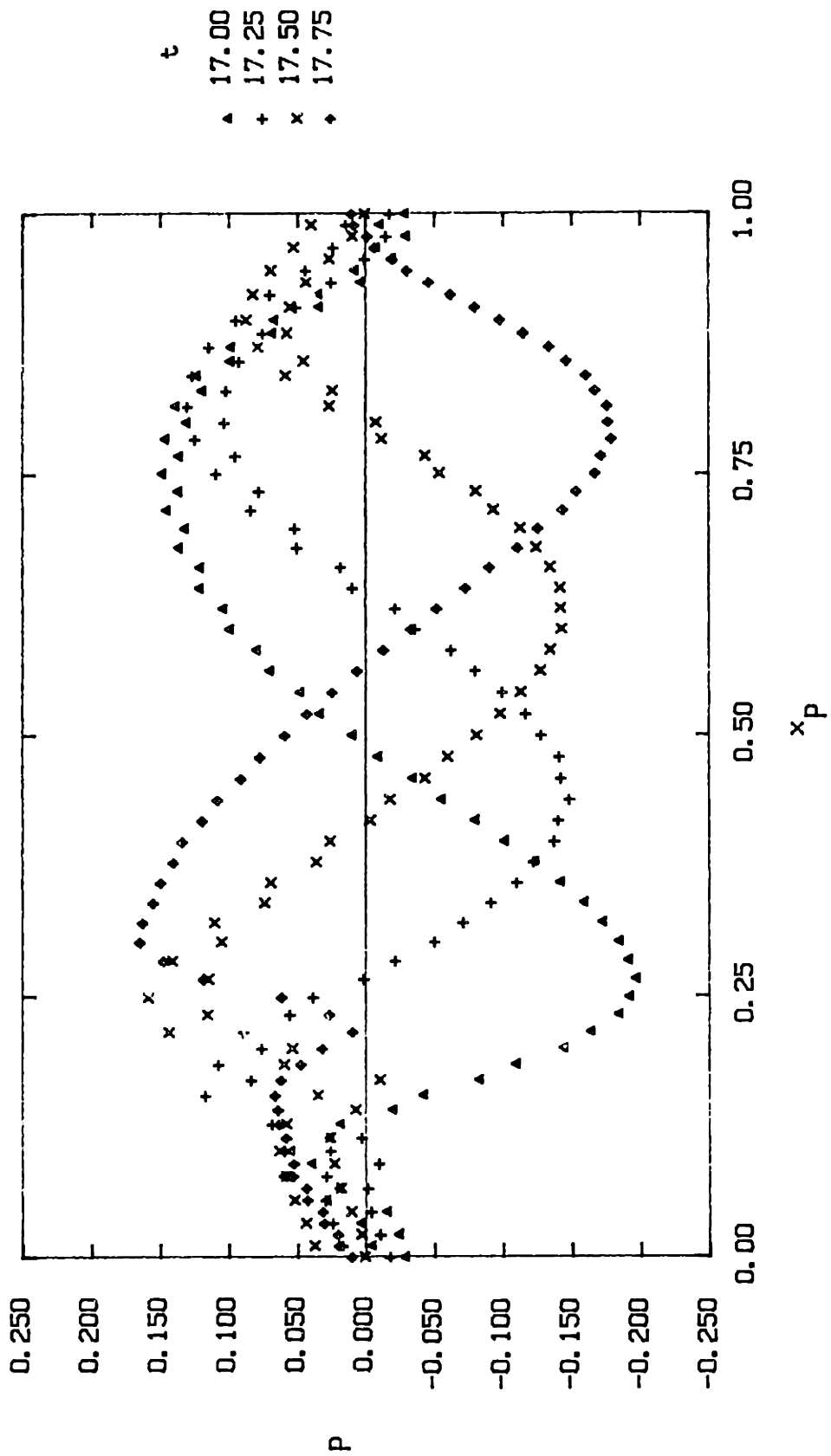
Fig. VIII.3.3.1.   Pressure on ripple surface

$R_c = 1000$ $s = 0.1$ $r = 1$ $M = 64$ $N = 68$

dy : (0.0014 , 0.106) $y_{max} = 1.59$
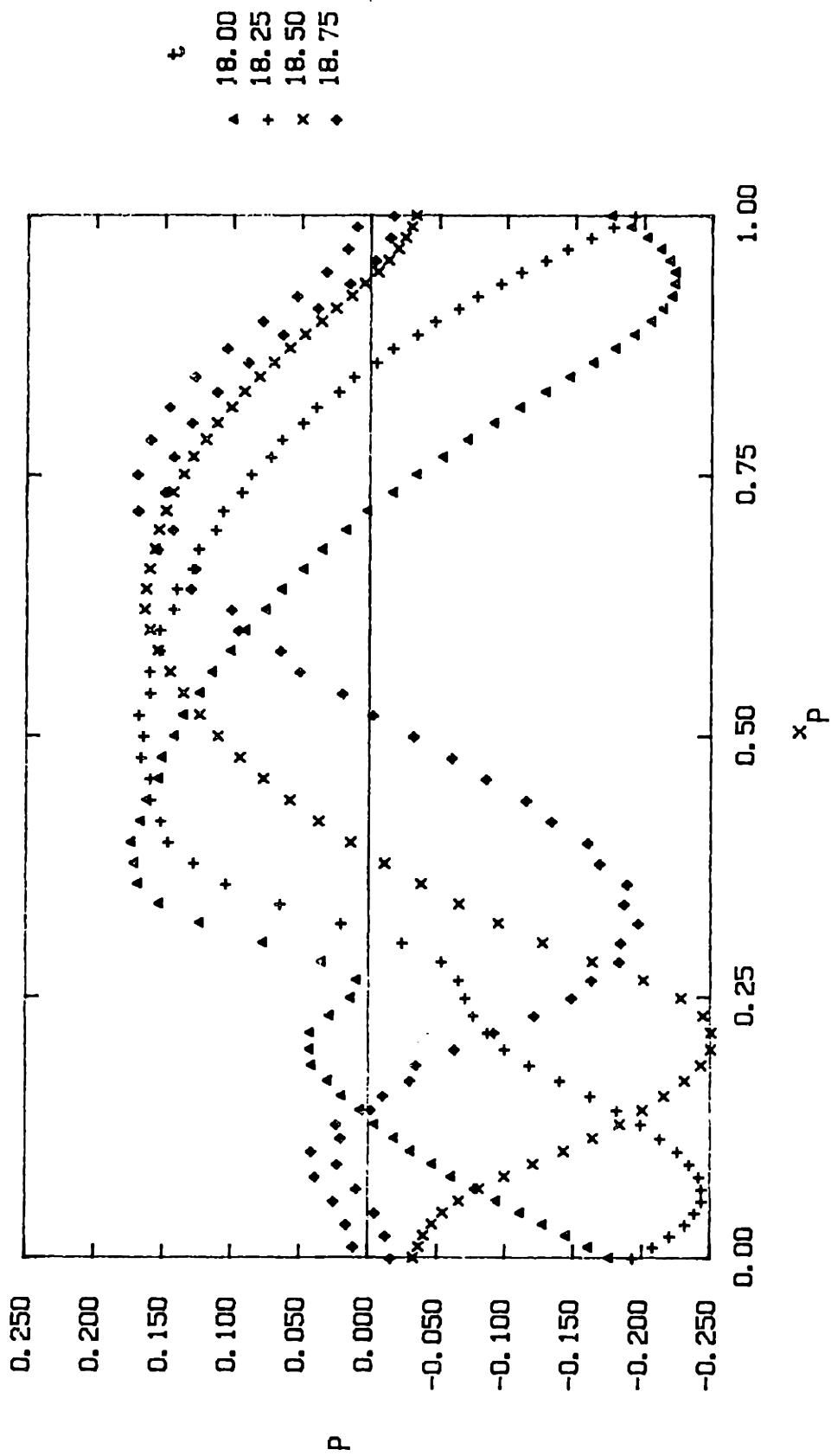
Fig. VIII.3.3.11. Pressure on ripple surface

$R_c = 1000$ $s = 0.1$ $r = 1$ $M = 64$ $N = 68$

$dy : (0.0014, 0.106)$ $y_{max} = 1.59$

Chapter IX. Results for the combined current and oscillatory ambient flow

It has been observed in the last two chapters that, at the same Reynolds number, both the rate of energy dissipation and the hydrodynamic stresses on ripples under waves are considerably higher than those under currents. It may therefore be expected that the addition of an oscillatory component of even a significantly smaller amplitude U_0 to a current of magnitude c will change the original flow field dramatically. We shall show that this indeed is the case.

In this chapter we shall include both a steady and an oscillatory component in the ambient flow over ripples of slope 0.1. Both the nondimensionalization of the physical variables ψ_p, ω_p, t_p, ..., and the dimensionless parameters R and K are the same as defined in (3.1.4) and (3.1.8), that is, they are based on the magnitudes of the oscillatory component. We shall study the flow with R=250, K=4.5, and c/U_0=1, 2, and 4. The corresponding Reynolds numbers based on the current velocity (R_c=c2a/ν) are therefore 250, 500, and 1000. In addition, the flow with R=250, K=9, and c/U_0=1 is compared with the pure oscillatory case.

The ambient current is defined to be in the positive x_p direction and increases from zero at the start of computation to its full amplitude over a time of $\pi/2$. The total ambient flow is therefore defined by

$$U_\infty(t) = \begin{cases} \sin 2\pi t + c/U_0 \sin t , & t < \pi/2 \\ \sin 2\pi t + c/U_0 , & \pi/2 < t \end{cases} . \qquad (9.0.1)$$

After the initial start of the current, the oscillatory part of the ambient flow acts to reinforce the current during the first half of the period P<t<P+0.5 and acts against the current in the second half period P+0.5<t<P+1, where P is the number of complete periods of oscillation from the beginning of computation. The ambient

flow is in the positive x_p direction at all times since $c \geq U_0$ in all cases studied.

It was found in the case of a pure current that considerable time must elapse before the initial oscillations (due to vortex shedding) of the solution subside, after which the changes in the hydrodynamic stresses and the rate of viscous dissipation follow closely those in Stokes first problem. We assume that the time it takes for the vortex shedding to subside is the same when an oscillatory component is superimposed onto the current. Using the results discussed in Chapter VIII, we now show that this time is indeed reached in the present computations. The unit of time in this chapter is defined from the Keulegan–Carpenter number $K=U_0T/L$, which gives $T=KL/U_0 =4.5L/U_0$ or $9L/U_0$, while the unit of time in the previous chapter is defined as $T_c=L/c$. For $K=4.5$, the ratios of the two are therefore $T/T_{c,250}=4.5$ and $T/T_{c,1000}=18$ for $c=U_0$ ($R_c=250$) and $c=4U_0$ ($R_c=1000$), respectively. The ratios for $K=9$ are twice as high. The times it takes for the ambient currents to reach their amplitudes for $R_c=250$ and 1000 in the last chapter are 2.5π and 10π, which are, in physical units, $2.5\pi T_{c,250}=10\pi T_{c,1000}\approx1.75T$. In this chapter this time is $\pi/2\approx1.57T$, and the two are comparable.[1] The time it takes the initial transient effects to diminish in the last chapter is around $60T_{c,250}\approx15T$ for $R_c=250$ and $160T_{c,1000}\approx9T$ for $R_c=1000$. Therefore the solutions discussed in this chapter, taken at $t\geq15$, are free from the initial vortex shedding due to the current.

The results for $c/U_0=1$ and 4 with $R=250$ and $K=4.5$ are presented for time t in the interval (15,16), which corresponds to $(67.5,72)T_{c,250}$ and $(270,288)T_{c,1000}$ respectively. The corresponding flows due to the current alone, that is, for $R_c=250$ and 1000, at these instants have been discussed in the previous chapter. An ambient flow that includes the oscillatory component only has also been presented

---

[1]The flow under an ambient current is, at large time, independent of the initial start of the current. This can be infered by comparing the results for r=5 and 10 for $R_c=250$ in the previous chapter.

in Chapter VII.

In the flow field over ripples due to an ambient current, the vertical profile (that is, as a function of y) of the horizontal velocity averaged over a ripple length follows very closely that of the corresponding flow over a plane bed. This is shown in Figs. VIII.2.9 and VIII.2.10 for a time after the initial vortex shedding has subsided. The extent in y at which the mean horizontal velocity is noticeably different from the magnitude of the current can therefore be estimated from the boundary layer thickness over a plane bed given by (8.1.4). In terms of dimensionless variables in this chapter, (8.1.4) can be written as

$$y_\delta = 3.64 \sqrt{(\frac{K}{R} st)} \qquad (9.0.2)$$

and is less than one in all computations in this chapter. It is therefore expected that the component of velocity due to the current reaches the magnitude c at a height considerable less than $y_{max}=2$ in this case.

There is ambiguity in the definition of the magnitude of the current in relation to that of the oscillatory component due to the time dependence of the thickness of the current boundary layer y_δ defined in (9.0.2). Our computations have not been carried out long enough such that y_δ reaches the upper boundary of computation, and we shall obtain an estimate of the magnitude of the velocity component due to the current, at various heights above the ripples, from the vertical profile of the horizontal velocity of the flow field averaged over a wave period and a ripple length. This will be discussed in detail in the section on the velocity field, §IX.1.

For $c/U_0=1$ with $R=250$ and $K=4.5$, the convergence to a periodic solution follows the same pattern as when the current is absent, which is shown in Fig. VI.3.2. Computation is therefore stopped at $t=16$ when δ_∞ defined in (4.7.2) has decreased to around 0.01. For $c/U_0=2$ the decrease in δ_∞ becomes much more gradual after the initial decline and is shown in Fig. IX.0.1. The value of δ_∞

decreases by a factor of less than 1.5 from t=12 to t=22. As the dimensionless numbers increase further, when c/U_0=4 and in flows with R=250 and K=9, δ_∞ remains at some finite values under 0.1 after twenty periods of computation. This is similar to the case of R=500 and K=4.5 shown in Fig. VI.3.3. We therefore compute to t=22 at which δ_∞ is no longer decreasing in these flows except for c/U_0=4 with R=250 and K=4.5. In this latter case we compute only to t=16 due to computer cost. The decrease in δ_∞ between t=16 and 22 is found to be insignificant in the other computations in this section.

The routine checks on aliasing, vertical extent of computation, and energy balance are also performed with satisfactory results and will not be discussed. There is one significant difference in the rate of pressure work done on the fluid in the control volume, however. In the presence of currents, this rate of pressure work is considerably smaller when the oscillatory motion opposes the current than when the two velocity components are in the same direction. From our results, the ratio of the magnitudes of the two is 0.25 when c/U_0=1, R=250, and K=4.5.

Since the nondimensionlization of all hydrodynamic variables (u_p, v_p, $\mathscr{D}_p$, τ_p, p_p, and F_{x_p}) are based on the corresponding dimensions in the oscillatory flow (U_0 and T), which are of the same magnitude in all cases examined, the magnitudes of their nondimensional counterparts are directy comparable. For example, the ratio of the dimensionless shear stress in two flow cases equals that of their physical counterpart, that is,

$$\frac{\tau_{p_2}}{\tau_{p_1}} = \frac{\tau_2}{\tau_1} . \tag{9.0.3}$$

§IX.1. Velocity field

In the absence of a current, the flow field when R=250 and K=4.5 is very

similar to that of R=175 and K=4.5 shown in Fig. VII.1.2. It is periodic and, though asymmetric, the qualitative features in the two half periods of the wave period are very much the same.[2] During the first half of a wave period starting at t=P, a vortex at the lee of the ripple crest is generated when the magnitude of the ambient flow begins to decrease (at t=P+0.30), and grows to its maximum size and strength just after the ambient flow reverses in direction (at t=P+0.50). The vortex gets embedded soon afterwards (at t=P+0.55) and travels with the ambient flow for the next half period and reappears when the ambient velocity is small again (at t=P+0.95). In the second half period another vortex makes its appearance at t=P+0.80 and develops in the same manner just described.

Before we examine the change in the flow field when a current is superimposed onto the far-field velocity, the magnitude of the current component of the horizontal velocity needs clarification. This ambiguity arises since our calculations are not proceeded to a time when the boundary layer thickness due to the current spans the entire height in our domain of computation, and has been discussed earlier in this chapter.

An estimate of the magnitude of this current velocity as a function of the distance from the ripple bed can be made from the vertical profiles of the horizontal velocity averaged over both a ripple length and a wave period. They are shown in Figs. IX.1.1 and IX.1.2 for the flows with K=4.5 and 9, respectively, at the same times the results corresponding to these flows are discussed later in this chapter. The time below each profile refers to the midpoint of the wave period, for example, t=20.5 denotes the average of t=20 to 21. The profiles are scaled with the magnitude c. The velocity profiles at the same instants due to an ambient current over a plane bed are also plotted as broken curves for comparison. From

---

[2]The periodicity and symmetry of a flow field have been defined in (7.1.1) and (7.1.2), respectively.

Fig. VIII.2.9 and VIII.2.10, they are very nearly the same as those over ripples.

From Figs. IX.1.1 and IX.1.2, the mean velocity immediately above the ripple surface in all cases are considerably smaller than those due to the current alone. For $c/U_0=2$ and 4 with $R=250$ and $K=4.5$, this averaged horizontal velocity reaches the magnitude of the current at a mean distance of about 0.7L from the bed. For $c/U_0=1$ when $R=250$ and $K=4.5$ and 9, this elevation is approximately one ripple length. The profiles for the purely oscillatory flow are also plotted for comparison (scaled with U_0), and the mean velocity is up to 20% of the amplitude of oscillation.

In Fig. IX.1.1 the profile for $c/U_0=1$, $R=250$ and $K=4.5$ is plotted for $t=15.5$, which corresponds to a time of $70T_{c,250}$ in the pure current case with $R_c=250$ discussed in the previous chapter. From Fig. VIII.2.9, the mean velocity profiles averaged over a ripple length are very close to those over a plane bed at the same time, while the profile in Fig. IX.1.1 shows that the mean velocity is significantly reduced when an oscillatory component equal in magnitude is superimposed. Understandably, this reduction is considerably smaller at $c/U_0=4$ when the relative magnitude of the oscillatory component to the current is smaller. The time of $15.5T$ shown in Fig. IX.1.1 corresponds to $280T_{c,1000}$ in Fig. VIII.2.10, and the two profiles are very similar. This is not surprising since the relative magnitude of the oscillatory component to current is much smaller than the previous case of $c/U_0=1$.

§IX.1.i. Flow field when $c/U_0=1$

The velocity field when the magnitude of current is no larger than that of the oscillation in the ambient flow is very much similar to that of pure oscillations and will not be presented here. Vortices generated in the first half period, however, last a little longer after the oscillatory part of the ambient flow reverses.

§IX.1.ii. Flow field when $c/U_0=2$

When the ratio c/U_0 increases to two, the velocity field is significantly different and is plotted from t=20 to 21 in Fig. IX.1.3. Recall that the mean velocity profile at this time (t=20.5 in Fig. IX.1.1) is small within two ripple heights from the ripple surface and reaches the magnitude of the current at 0.7L above the mean bed level. At the cutoff in the plots of the velocity vectors, which is half a ripple length above the ripple bed, this mean velocity is around 0.8c.

In the first half period, the vortex generated is very much similar to the cases with weaker currents or pure oscillatory flow (Fig. IX.1.3.i to v). However, instead of becoming embedded in the ambient flow in the second half period, this vortex remains distinct and rises to about three ripple heights above the bed (Fig. IX.1.3.vi). It extends further in the horizontal direction and develops into an elongated vortex spanning the entire ripple length, dividing the flow domain into two horizontal bands of opposite flow directions (Fig. IX.1.3.vii to x). In the lower region where the mean flow is opposite to the ambient flow, the flow pattern is very similar to flows with a smaller c/U_0, and a vortex of an opposite circulation is generated at the left side of the ripple crest (Fig. IX.1.3.ix).

At the end of the period this new vortex climbs up the ripple crest at which it developed, and the vortex generated in the first half period moves closer to the bed (Fig. IX.1.3.x). Both vortices are overwhelmed by the increasing ambient flow soon afterwards.

§IX.1.iii. Flow field when $c/U_0=4$

When the current increases to four times the amplitude of the oscillatory velocity, the flow picture over a period is completely different from the previous cases. The mean flow is now always in one direction and no vortices are generated in the second half period. The flow field has been examined at time intervals of

0.025 from t=15 to 16, and the velocity vectors over a ripple length at selected time intervals are shown in Fig. IX.1.4. From Fig. IX.1.1 the mean velocity at the top of the velocity plots has reached 0.9c.

At the beginning of the period (t=P, Fig. IX.1.4.i) the flow above the ripple is in one direction only. A tiny vortex appears at about $\frac{1}{4}$L downstream of the crest at t=15.025 (Fig. IX.1.4.ii) and moves towards the trough. This vortex has vanished by t=15.075 and the flow picture resembles the one at t=15. A second vortex (labeled 1 in Fig. IX.1.4) to the right of the ripple crest appears at t=15.10 (Fig. IX.1.4.iii) which grows bigger and moves away from the crest. At t=15.175 (Fig. IX.1.4.iv), another vortex (labeled 2) appears between the crest and vortex 1. At t=15.20 vortex 2 catches up with vortex 1 and the two merge soon thereafter (t=15.225, Fig. IX.1.4.v).

A new vortex appears at t=15.25 between the crest and the merged vortex, and the flow is now similar to that at t=15.175. Both vortices increase in strength and move further downstream until the new vortex catches up and merges with vortex 1 at t=15.30, and the flow at this time is very much like the one at t=15.225. At this same instant yet another vortex (labeled 3) with a clockwise circulation appears between the crest and this merged vortex, and both of them grow and move downstream.

A vortex (labeled 4) of an opposite (counter clockise) circulation develops between vortices 1 and 3 and the ripple surface at t=15.35 (Fig. IX.1.4.vi). While these three vortices move downstream together, another new vortex (labeled 5) appears at t=15.40 and develops, and all four vortices move downstream (Fig. IX.1.4.vii, t=15.425). By t=15.45 vortex 5 has caught up with vortex 3 and the two merge soon thereafter, and at t=15.475 the velocity field is very much like the one at t=15.35 with all three vortices displaced downstream.

At t=15.50 another vortex with a clockwise circulation (labeled 6) develops and

the flow at t=15.50 is very much like that at t=15.425. When the oscillatory part of the ambient velocity accelerates to the left (while the total ambient flow is still towards the right), vortex 1 and 3 merge and develop into being the prominent vortex in the flow field, at the same time rising above the trough (t=15.60, Fig. IX.1.4.viii). This configuration of vortices moves slowly downstream. At t=15.85 vortex 1 is just upstream of the downstream crest (Fig. IX.1.4.ix), and it is now farther apart from vortices 4 and 6. At t=15.875 vortex 1 is directly above the ripple crest and by t=15.90 has caught up and merged with vortex 6 (Fig. IX.1.4.x). At this time vortex 4 is overwhelmed by the ambient flow that is increasing in strength and vortex 1 becomes the only vortex in the flow picture. In between t=15.90 and 15.975 vortex 1 moves further downstream and passes the ripple trough before disappearing into the ambient flow after t=15.975.

Summary

The addition of a current to an oscillatory flow does not change the flow field immediately above the ripple bed qualitatively as long as the magnitude of the current is no greater than the amplitude of the ambient oscillation. Vortices are generated during the two half periods in very much the same manner when the ratio c/U_0 remains not greater than two.

At $c/U_0=2$, the vortex generated in the first half period remains distinct throughout the second half period, its presence above the ripple bed divides the flow domain into two horizontal stripes. The top layer is in the positive x_p direction and approaches the ambient velocity in the far field. The velocity in the bottom layer is predominantly in the negative x_p direction, with vortices generated to the left of the ripple crests just like in pure oscillatory ambient flows.

The fact that vortices are generated on both sides of the ripple crests despite the fact that the far field velocity is always in one direction only suggests that the

acceleration in the ambient flow, and not its magnitude and direction,[3] is the controlling factor in determining separations. Associated with this acceleration is the pressure component with gradient given by (3.2.5),

$$[\frac{\partial p}{\partial x}]_{inertial} = -\frac{1}{K}\frac{dU_\infty}{dt}.$$

The dependence of this term on K only explains why that the Keulegan–Carpenter number is a more critical parameter in separations than the Reynolds number, as is observed in §VII.1.

At $c/U_0=4$ the flow separates earlier in the wave period and the flow field is much more complicated. Six distinguishable vortices are generated during the first half period when the oscillatory part of the ambient flow and the current are in the same direction. No new vortices develop in the second half period. The vortices generated in the first half period remain distinct above the ripple until finally overwhelmed by the increasing ambient flow at the end of the wave period.

The considerable number of vortices generated in the first half period resembles the vortex shedding immediately after the start of a pure current in the ambient flow. As discussed at the beginning of this chapter, the unit of time for the steady current case is given by $T_c=L/c=L/4U_0$ for $c/U_0=4$, compared with that of $T=4.5L/U_0$ in this chapter. The ratio T_c/T is 1/18. It was pointed out in §VIII.2 that, in the case of a steady current only in the ambient flow, a vortex is shed about every $1.7T_c \approx 0.094T$. This would suggest that, over a half wave period, between five to six vortices are generated. As observed above, the same number of vortices are generated in the first half period when an oscillatory component one quarter the magnitude of the current is added onto the ambient flow.

---

[3]Recall that the mean velocity profiles in Fig. IX.1.1 show a gradual increase from zero to c in the far field. Despite that the velocity induced by the current is very small immediately above the ripple surface, this averaged velocity has increased to over the magnitude of the oscillatory component less than half a ripple length above the ripple bed for the cases of $c/U_0=2$ and 4.

§IX.2. Rate of energy dissipation

The nondimensional rate of energy dissipation $\mathscr{D}$ for the cases of $c/U_0=1$ and 4 are plotted in Figs. IX.2.1 and IX.2.2 respectively. The rate of energy dissipation $\mathscr{D}_s$ for the flow over a plane bed due to the oscillatory component alone is also plotted for comparison. Since the wave component in all cases considered are identical, the functions $\mathscr{D}_s$ are the same.

The amplitude of $\mathscr{D}$ when $c/U_0=1$ is very nearly the same as that in the case of the purely oscillatory ambient flow, $c/U_0=0$. Its variation with time, however, is as if the time scale is shifted by half a wave period, such that $\mathscr{D}$ in the first half period when $c/U_0=1$ is almost identical to that in the second half period when $c/U_0=0$, and vice versa. The larger amplitude of $\mathscr{D}$ in the second half period is due to the thicker shear layer of the mean flow, across which the reversed flow in the negative x_p direction near the ripple surface increases to that of the ambient flow in the far field, which is moving to the right.

The variation of $\mathscr{D}$ when $c/U_0=2$ is qualitatively similar to when $c/U_0=1$ except that the maxima in both half periods are around 20% larger.

The time history of $\mathscr{D}$ becomes highly irregular but periodic when the current far exceeds the amplitude of oscillation in the ambient flow ($c/U_0=4$, Fig. IX.2.2). High frequency fluctuations, at approximately five per half period, are found in the first half period and corresponds to the appearance and coalescence of the vortices discussed in §IX.1. The amplitude is also significantly higher in the first half period by approximately 70% due to the stronger presence of vortices.

The energy dissipation over a period for all cases studied are listed in Table IX.6.1. A quantitative comparison with those due to the oscillatory component or the current alone is postponed until §IX.6.

§IX.3. Shear stress on ripple surface

The evolution of the shear profiles over a wave period for $c/U_0=2$ and 4 are shown in Figs. IX.3.1 and IX.3.2 respectively. The shear stress profiles for c/U_0 between zero and two are very similar, and the magnitudes of the shear stress induced by the vortices throughout this range of c/U_0 are almost the same. However, instead of an increase (decrease) in the shear stress when the oscillatory component reinforces (opposes) the current, the reverse is true.

The shear stress over the entire period is considerably higher when $c/U_0=4$ and is shown in Fig. IX.3.2. In §IX.1, the flow field under an ambient current is shown to change dramatically when an oscillatory component one-fourth its magnitude is superimposed onto the far field velocity. The shear stress across the ripple profile is also much different. It reaches a maximum of approximately 0.120 between $t=15.2$ and 15.3, compared with a magnitude of 0.075 in the pure oscillatory flow attained at about $t=P+0.1$ where P is the number of wave periods since the beginning of computation. Despite the fact that the ambient flow is always in the positive x_p direction, shear stress in the negative x_p direction has very nearly the same magnitude as that in the positive x_p direction due to the increased strengths of vortices generated. Unlike the case of $c/U_0=2$, in which the shear stress is positive across the entire ripple in between $t=20$ to 20.2, the shear stress is negative immediately downstream (to the right) of the crests since vortices are generated much earlier in the wave period. As more vortices develop along the ripple into the first half period (Fig. IX.1.4), the shear stress profiles alternate between positive and negative along the ripple.

The magnitude of the shear stress profile is considerably smaller during the second half of the wave period, and since no vortices develops to the left of the crests, the positive shear due to vortices generated at lower values of c/U_0 is not found. As the configuration of vortices (1, 4, and 6 in Fig. IX.1.4) moves

downstream in between t=15.6 and 15.85, the shear profile on the ripple remains qualitatively similar and moves downstream accordingly.

The shear stress profile averaged over one wave period are plotted in Figs. IX.3.3 and IX.3.4 for flows with K=4.5 and 9 and different ratios of c/U_0. To assess the effects of the addition of an oscillatory component to a current, we recall from Fig. VIII.2.11 that the shear stress due to an ambient current alone is in the same direction as the current near the crests. The shear around the troughs are in the opposite direction but only one-tenth in magnitude. The maximum local stress is immediately upstream of the crests and is approximately 0.0042 at time $75T_{c,250}$ = 16.7T. From Fig. IX.3.3, the mean stress profiles for $c/U_0 \leq 2$ are anti-symmetric about the crests (or troughs) such that

$$\overline{\tau}(x_p) \approx -\overline{\tau}(L-x_p) . \qquad (9.3.1)$$

For $c/U_0=1$ in which the current component corresponds to $R_c=250$, the magnitude of the maximum shear is at about the same location as that in the flow due to an ambient current alone, but at approximately $0.5\|\tau_s\| = 0.012$ which is almost three times higher.

A dramatic increase in the shear is found even when the magnitude of the oscillatory component is only a small fraction of the current. From Fig. VIII.2.12, the maximum shear at $300T_{c,1000}=16.7T$ is $0.00085\rho c^2 = 0.014\rho U_0^2$ for $c/U_0=4$. When an oscillatory component one-fourth the magnitude of the current is added, the amplitude of the mean shear is, from Fig. IX.3.4, $1.23\|\tau_s\| = 0.030$ which is more than two times that when the current alone is present in the ambient flow. Furthermore, the mean shear profile is more complicated than that due to a current alone, alternating in directions over the ripple length with a magnitude much higher than the current case especially at the troughs.

§IX.4. Pressure on the surface of ripple

As observed earlier this chapter, various properties of the flows when $c/U_0=0$, 1, and 2 are very much similar, and the same is true in the pressure profile along the ripple over a wave period. The magnitude of variation fluctuates within 10% when the current increases from 0 to $2U_0$. As a comparison, the pressure in an equivalent potential flow increases with the ratio c/U_0, since the component proportional to u^2+v^2 increases with c.

The variation in the nondimensional pressure on the ripple surface is shown in Figs. IX.4.1 and IX.4.2 for $c/U_0=2$ and 4. The amplitude of pressure fluctuation when $c/U_0=4$ is 2.3 and is considerably larger than that of 1.4 when c/U_0 is 2 or smaller. Furthermore, at the highest value of c/U_0 studied, the spatial variation is not as dominated by the pressure component due to the acceleration in the ambient flow, as is found in the the other cases.

At t=P and P+0.1 where P is the number of wave periods from the beginning of computation, the pressure on the ripple decreases monotonously with x_p when c/U_0 is two or lower, while in the case of $c/U_0=4$, it rises to a maximum near the trough. Similarly, the pressure profile monotonously increases or decreases across the ripple at lower ratios of c/U_0 while the profile oscillates much more irregularly at the higher ratio of c/U_0. From the plot of velocity vectors in Fig. IX.1.4, oscillations in the pressure profile nearly coincide with the locations of vortices above the ripple, such that the (spatial) local minima of pressure are found immediately below the centers of vortices with clockwise circulations.

Since positive pressure gradients lead to accelerations in the negative x_p direction, and vice versa, the fluid between the center of vortex with a clockwise rotation and the ripple surface, which moves from right to left, is therefore accelerated to the right of the vortex center and decelerated to the left. The same pattern is observed in the pressure profiles in the second half of the wave period.

§IX.5. Horizontal force on ripple

As would be expected from the previous discussion, the time history of the horizontal force F_x on a ripple for $c/U_0=0$, 1, and 2 are quantitatively very much the same. Therefore only the variations of F_c, F_t, and F_n for $c/U_0=2$ and 4 are plotted in Figs. IX.5.1 and IX.5.2, respectively. The amplitudes of the three forces for all cases studied are listed in Table IX.6.1.

When $c/U_0=2$, the magnitude of the horizontal force in the positive x_p direction (direction of the current) is about 15% higher than that in the other direction. Both F_c and F_t vary nearly sinusoidally over a wave period and approximately $\frac{1}{4}T$ out of phase, and the magnitude of F_t is higher than F_c by about 30%. The function F_n is considerably smaller in amplitude (about 40% of F_c) and has the same sign as the oscillatory part of the ambient velocity (positive during the first half of the wave period).

The magnitude of the forces when $c/U_0=4$ are around twice that when $c/U_0=2$, and F_t varies over a larger range than F_c and F_n. High frequency fluctuations, at about six oscillations per half period and an ampliude up to 70% of the magnitude of the force itself, are found during the first half period. The amplitudes in the direction of current of all three horizontal forces F_c, F_t, and F_n are about 20% higher than those in the opposite direction.

The magnitudes of the horizontal forces will be used to deduce the friction factors f_w in the next section. They will be compared with those in the flows due to the current or the oscillatory component alone on a ripple bed.

§IX.6. Friction factor

It is found in §VII.6.3 and §VIII.3 that the friction factors in flows over a ripple bed due to an oscillatory ambient flow are much higher than those due to an ambient current of the same magnitude. It may therefore be suspected that, when

an oscillatory component with a considerably smaller amplitude is superimposed onto an ambient current, the friction factor based on the magnitude of the current can increase dramatically. On the other hand, when a current of a comparable magnitude is added to an oscillatory ambient flow, the friction factors of the combined flow may remain very close to those when the current is absent if the ambient velocity used in the definitions of the friction factors (7.6.1) are based on the oscillatory component alone. We shall show in the following that this indeed is the case. The friction factors f_w and f_e based on the oscillatory component, the total ambient flow, and the current, will be listed in Tables IX.6.2 to IX.6.4.

The values of the horizontal force and energy dissipation used in deducing the friction factors will be from the same time as those of the velocity profiles shown in Figs. IX.1.1 and IX.1.2. The values due to the current component alone are from Chapter VIII and correspond to the same instants as those in the combined flow cases.

§IX.6.1. Friction factor based on the oscillatory component of ambient flow

As discussed above, it is more appropriate to use the oscillatory component in the definition of friction factors when the magnitude of the current is not much larger than the amplitude in the oscillatiory component. This gives a direct comparison on the effects of increasing the current with the same oscillation. The same equations for f_w and f_e given respectively by (7.6.3) and (7.6.6) with $\theta=0$ apply. The values of the friction factors are listed in Table IX.6.2.

Comparing the values for $c/U_0=0$ and 1 for both $K=4.5$ and 9, the friction factors deduced both from viscous dissipation and from the horizontal force on the ripple are found to remain virtually unchanged when a current of the same magnitude is superimposed onto an oscillatory flow. At $K=4.5$, even the ratios of the friction factors of $c/U_0=2$ to those of $c/U_0=0$ are not much different from one.

The effects of a current on an oscillatory flow not much smaller in amplitude is therefore insignificant.

§IX.6.2. Friction factor based on the total velocity in the ambient flow

The friction factor based on the horizontal force on the ripple is defined as in §VII.6.1.i, only that (7.6.2) is now replaced by

$$\langle \tau_p \rangle_{max} = \frac{1}{2} f_w \rho (U_0 + c)^2 . \tag{9.6.1}$$

Equating this stress with

$$\frac{1}{L} \{F_{x_p}\}_{max} = \rho U_0^2 \{F_x\}_{max} \tag{9.6.2}$$

gives

$$f_w = \frac{2}{(1+r)^2} \{F_x\}_{max} \tag{9.6.3}$$

where $r = c/U_0$.

If we write

$$U_p(t) = c + U_0 \sin 2\pi t \tag{9.6.4}$$

in (7.6.1) and substitute into (7.6.5), the total energy dissipated in a wave period per ripple length is

$$\int_0^T dt_p \, L\langle \tau_p \rangle \, U_p = \int_0^T dt_p \, \frac{f}{2} \rho L \, (c + U_0 \sin 2\pi t)|c + U_0 \sin 2\pi t| \, (c + U_0 \sin 2\pi t)$$

$$= \frac{f}{2} \rho U_0^3 TL \int_0^1 dt \, (r + \sin 2\pi t)^3 = \frac{f}{2} \rho U_0^3 TL \, r \, (1.5 + r^2) \tag{9.6.5}$$

where r is assumed to be greater than unity. Equating this with the integral over a wave period of the rate of energy dissipation computed from (3.3.9), the friction factor can be expressed as

$$f_e = \frac{2}{r \, (1.5 + r^2)} \int_0^1 dt \, \mathscr{D}. \tag{9.6.6}$$

256

The expression for $r < 1$ can be found, for example, in Brevik and Aas (1980). It is not used in the following since $c/U_0 \geq 1$ in all our cases.

The values of f_w and f_e defined by (9.6.3) and (9.6.6) are listed in Table IX.6.3. Except for the values of f_n for $c/U_0 = 2$ and 4, the friction factors decrease considerably when the ratio of the amplitude of oscillation to the magnitude of the total velocity decreases.

§IX.6.3. Friction factor based on the magnitude of current alone

Similarly, if we replace $U_0 + c$ in (9.6.1) and $c + U_0 \sin 2\pi t$ in (9.6.5) by c, (9.6.3) and (9.6.6) are modified to

$$f_w = \frac{2}{r^2} \{F_x\}_{max} \qquad (9.6.7)$$

and

$$f_e = \frac{2}{r^3} \int_0^1 dt \, \mathscr{D}. \qquad (9.6.8)$$

They are listed in Table IX.6.4. The decrease in the friction factors with decreasing U_0/c is even more drastic than those in Table IX.6.3.

§IX.6.4. Turbulence theory of Grant and Madsen (1979)

Our results will be compared with the theoretical values proposed by Grant and Madsen (1979), In their paper, the friction factor for the three dimensional turbulent flow due to the combined wave and current action over a rough bottom is derived based on the linearized momentum equation and an eddy viscosity model. The combined wave and current friction factor f_{cw} is assumed to be constant in time and relates the shear stress τ_b at the bottom to the instantaneous velocity at the boundary.

The water depth is divided into two layers: a wave boundary layer immediately

above the bottom, and further up a current boundary layer which extends over the entire water depth. By making use of Prandtl's mixing length hypothesis, the eddy viscosities in these two layers are related to the two boundary shear stresses. The shear at the wave boundary and current boundary are assumed to be respectively the maximum and the mean of τ_b over a wave period. The ripple height appears in the velocity profile in the wave boundary as a parameter proportional to the Nikuradse roughness.

The logarithmic velocity profiles in the two layers are expressed in terms of three parameters: the wave-current friction factor f_{cw}; an apparent roughness parameter k_{bc} in the velocity profile in the current boundary layer; and the magnitude and direction of the velocity due to the current component at the boundary. The last two quantities are unknown *a priori* since the current boundary layer spans the entire water depth and therefore its velocity varies continuously in the vertical direction. These four unknowns are subjected to four simultaneous equations obtained from the following conditions: the bottom shear stress expressed in terms of the velocity profile is equated to that in terms of the friction factor; the velocity at the interface of the wave and current boundary given by the velocity profiles in the two boundary layers has to be equal; and the magnitude and direction of the current velocity is specified at a certain height above the bottom. The friction factor f_{cw} can then be solved by an iteration procedure.

Note that, even though only the linearized problem is considered, the coupling of wave and current enters through the assumed quadratic dependence of τ_{cw} on the velocity,

$$\tau_{cw} = \frac{1}{2}\rho f_{cw}(U+c)|U+c| . \qquad (9.6.9)$$

One of the main conclusions of their theory is that if oscillations are added to a current, the friction factor is drastically increased.

§IX.6.5. Results

The values of the energy dissipation $\mathscr{D}$ and horizontal force on ripple $\{F_x\}_{max}$ are listed in Table IX.6.1. The values of f_e and f_w based on the oscillatory component, the total velocity, and the current, are listed in Table IX.6.2 to IX.6.4 for $c/U_0 = 0$, 1, 2, and 4. The corresponding pure current cases with $R_c = 250$ and 1000, and the purely oscillatory cases with $K = 4.5$ and 9 and $R = 250$ are also listed.

From Table IX.6.1, the values of $\mathscr{D}$ and $\{F_x\}_{max}$ do not change appreciably when c/U_0 increases from zero to two. This is expected since it has been shown in §IX.1 that the near bed flow field does not change significantly when c/U_0 varies within this range. The values of friction factors based on U_0 therefore remains very nearly the same. The values based on $U_0 + c$ listed in Table IX.6.3, on the other hand, decreases dramatically with increasing c/U_0.

It would be of interest to compare the results from our laminar flow model with those of Grant and Madsen (1979). Their results, however, are formulated in terms of the parameter $|\tilde{u}_a|/|\tilde{u}_b|$ which is the ratio of the current velocity to that due to the wave component at the wave boundary $y_p = \delta_{cw}$. To relate their values of the friction factor to those listed in Table IX.6.4, we need to assume a value of δ_{cw} and deduce $|\tilde{u}_a|$, for example from the mean velocity profiles plotted in Figs. IX.1.1 and IX.1.2. For $\delta_{cw} = o(a)$, a small change in the value of δ_{cw} will lead to a significant change in the mean velocity $|\tilde{u}_a|$, and therefore a quite different value of friction factor. Because of these uncertainties, a quantitative comparison is therefore not made.

When the magnitude of the current is much larger than the amplitude of oscillation, at $c/U_0 = 4$, f_e increases to almost three times that of the pure oscillatory flow, whereas both $\{F_c\}_{max}$ and $\{F_t\}_{max}$ are doubled and $\{F_n\}_{max}$ quadrupled. Since the magnitude of the current is much higher than that of the oscillation, this case is better considered as an addition of a small oscillation to a current and thus

the friction factors based on the magnitude of current is more appropriate. From Table IX.6.4, f_e and f_n listed under $U_0/c=0.25$ are 1.2×10^{-3} and 17×10^{-3}, about three and thirty times those in the absence of the oscillatory component of 0.39×10^{-3} and 0.50×10^{-3} for the case of $R_c=1000$. This is in qualitative agreement with the semi-empirical theory of Grant & Madsen (1979) for a turbulent boundary layer.

Table IX.6.1. Energy dissipation and amplitudes of horizontal force on ripple

R=250

K	c/U_0	$\int_0^1 dt\ \mathscr{D}$	$\{F_c\}_{max}$	$\{F_t\}_{max}$	$\{F_n\}_{max}$
4.5	0	0.0132	0.0675	0.0897	0.0335
	1	0.0133	0.0673	0.0879	0.0315
	2	0.0155	0.0663	0.0916	0.0397
	4	0.0377	0.1412	0.1704	0.1334
9.0	0	0.0100	0.0408	0.0612	0.0322
	1	0.0106	0.0400	0.0638	0.0349

Pure current

R_c	t_p/T_c	$\int_0^1 dt\ \mathscr{D}$	$\{F\}_{max}$
250	70[1]	0.00100	0.00139
	140[2]	0.00069	0.00096
1000	280[3]	0.000196	0.000252

---

[1]Corresponds to the component of current for the flow with $c/U_0=1$, R=250, and K=4.5 at t=15.5.

[2]Corresponds to the component of current for the flow with $c/U_0=1$, R=250, and K=9 at t=15.5.

[3]Corresponds to the component of current for the flow with $c/U_0=4$, R=250, and K=4.5 at t=15.5.

Table IX.6.2. Friction factors based on the oscillatory velocity component U_0

R=250

K	c/U_0	f_e	f_c	f_t	f_n
4.5	0	0.062	0.135	0.179	0.067
	1	0.063	0.135	0.176	0.063
	2	0.073	0.133	0.183	0.079
	4	0.178	0.282	0.341	0.267
9.0	0	0.047	0.082	0.122	0.064
	1	0.050	0.080	0.128	0.070

Table IX.6.3. Friction factors based on the magnitude of ambient velocity U_0+c

R=250

K	c/U_0	f_e	f_c	f_t	f_n
4.5	1	0.011	0.034	0.044	0.016
	2	0.003	0.015	0.020	0.009
	4	0.0011	0.011	0.014	0.011
9.0	1	0.025	0.040	0.064	0.035

Table IX.6.4. Friction factors based on amplitude of current c

Pure current

R_c	t_p/T_c	f_e	f_w
250	70	0.0020	0.0028
	140	0.0014	0.0019
1000	280	0.00039	0.00050

R=250

K	U_0/c	f_e	f_c	f_t	f_n
4.5	1.00	0.027	0.135	0.176	0.063
	0.50	0.004	0.033	0.046	0.020
	0.25	0.0012	0.018	0.021	0.017
9.0	1.00	0.021	0.080	0.124	0.070
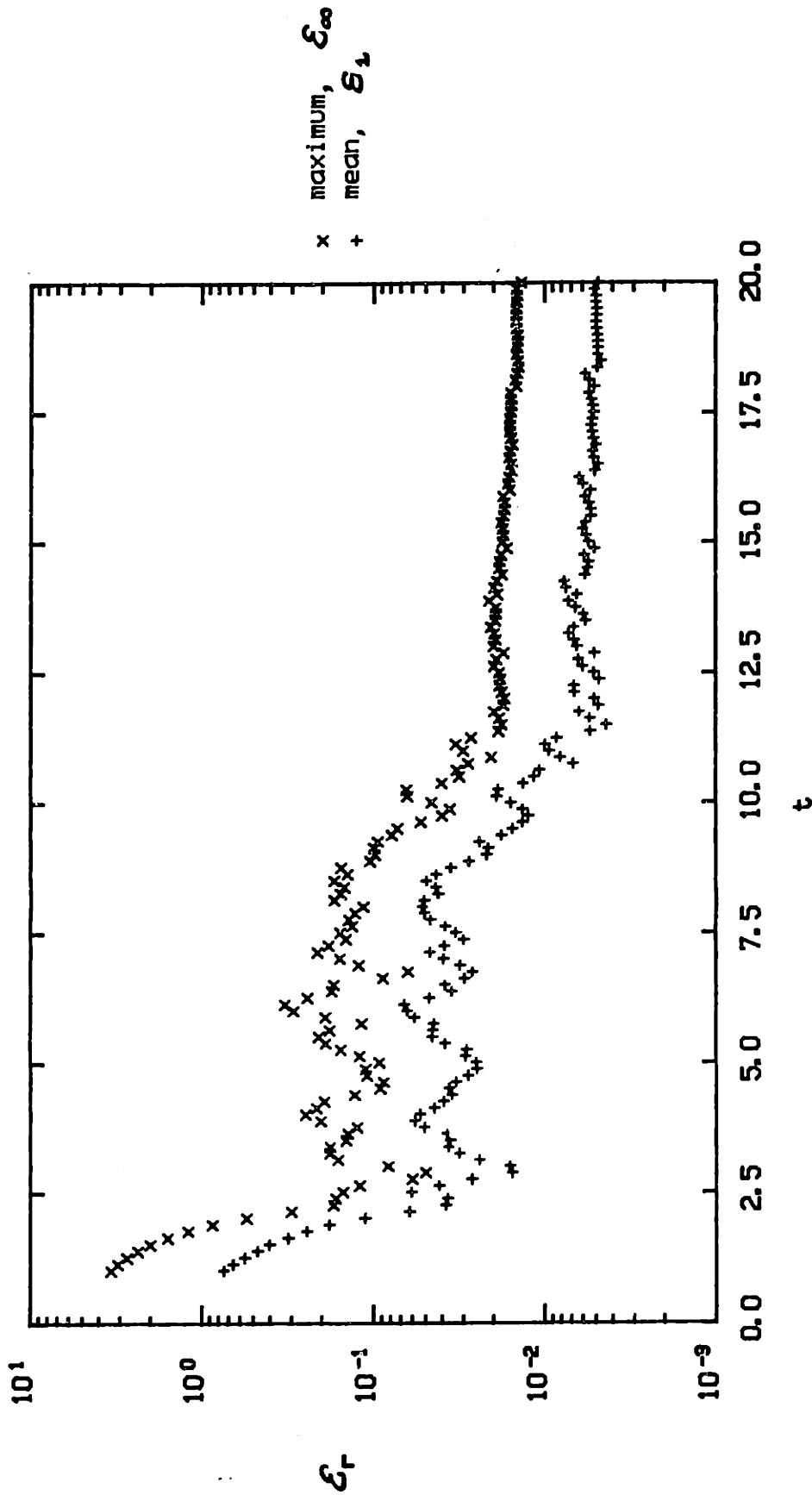
Fig. IX.0.1. Variation of streamfunction values one wave period apart as
defined in (4.7.2)

R = 250   K = 4.5   s = 0.1   M = 32   N = 57
dy = (0.0036 , 0.151) y_{max} = 2.08 c/U_0 = 2

263
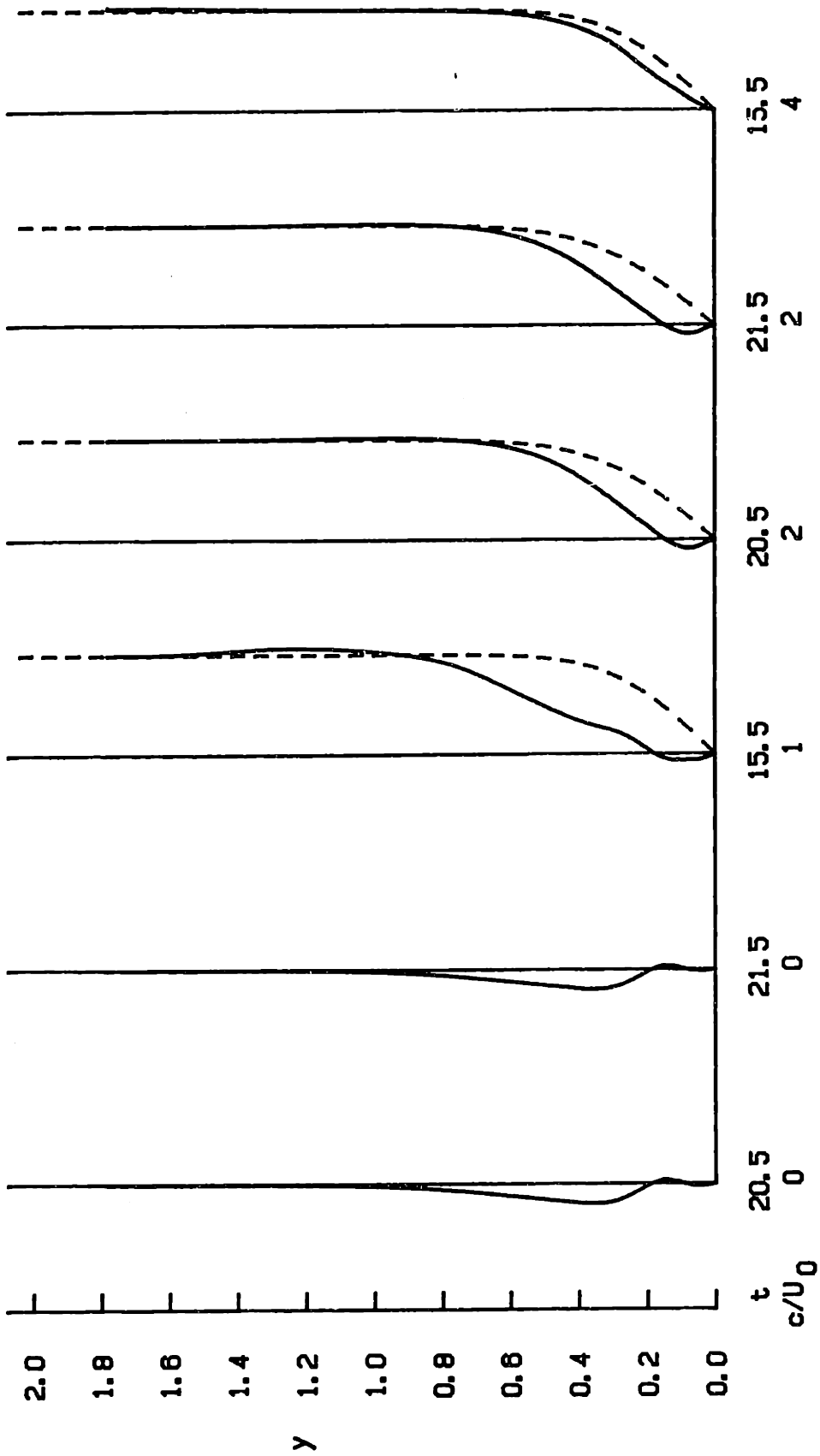
Fig. IX.1.1. Mean velocity profiles over a wave period
—— wave and current over ripples
------ current over a plane bed

R = 250   K = 4.5   s = 0.1   M = 32   N = 57 y_{max} = 2.08
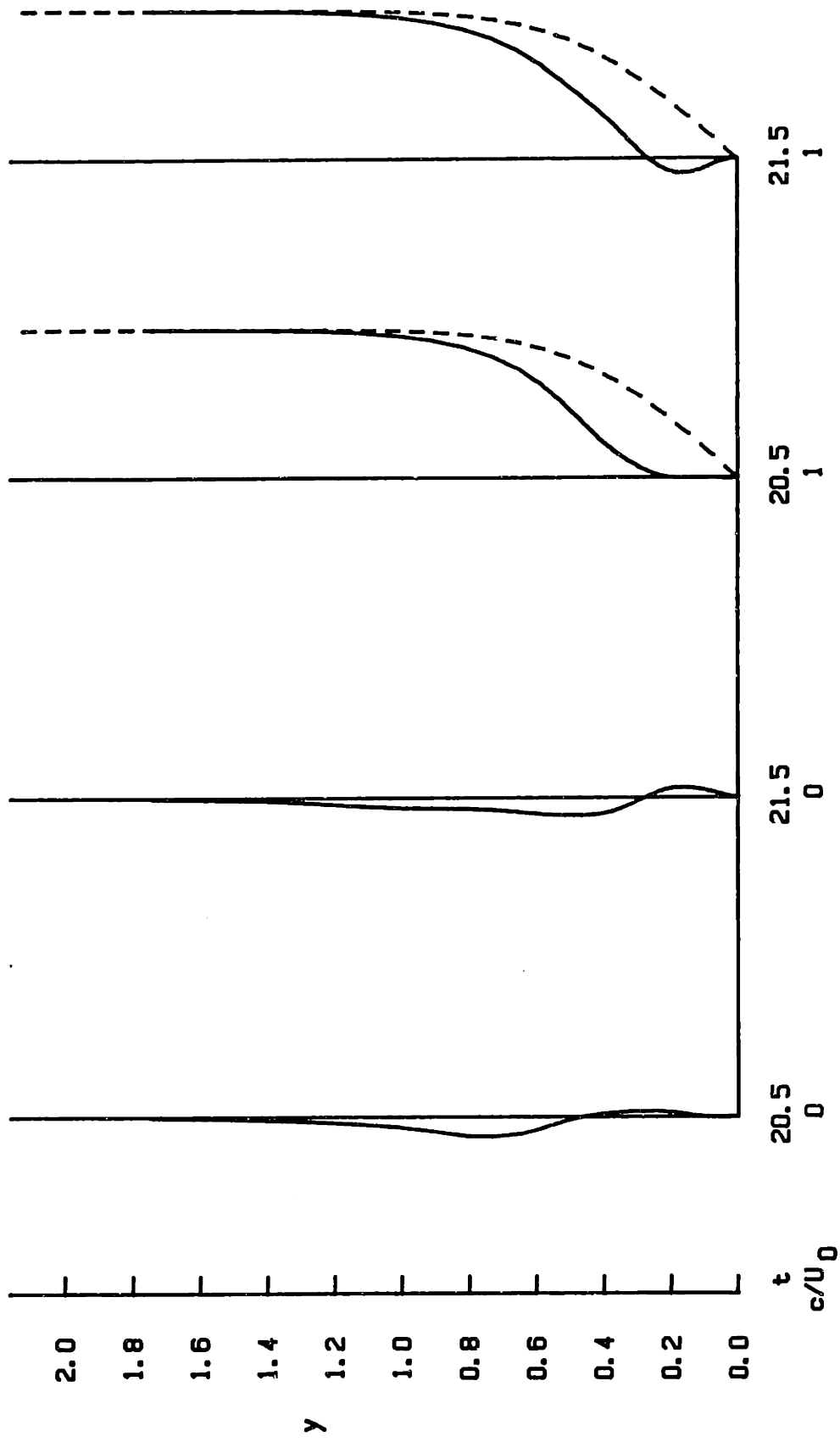
Fig. IX.1.2. Mean velocity profiles over a wave period

——— wave and current over ripples

- - - - current over a plane bed

R = 250   K = 9.0   e = 0.1   M = 32   N = 42

y_{max} = 2.16

265
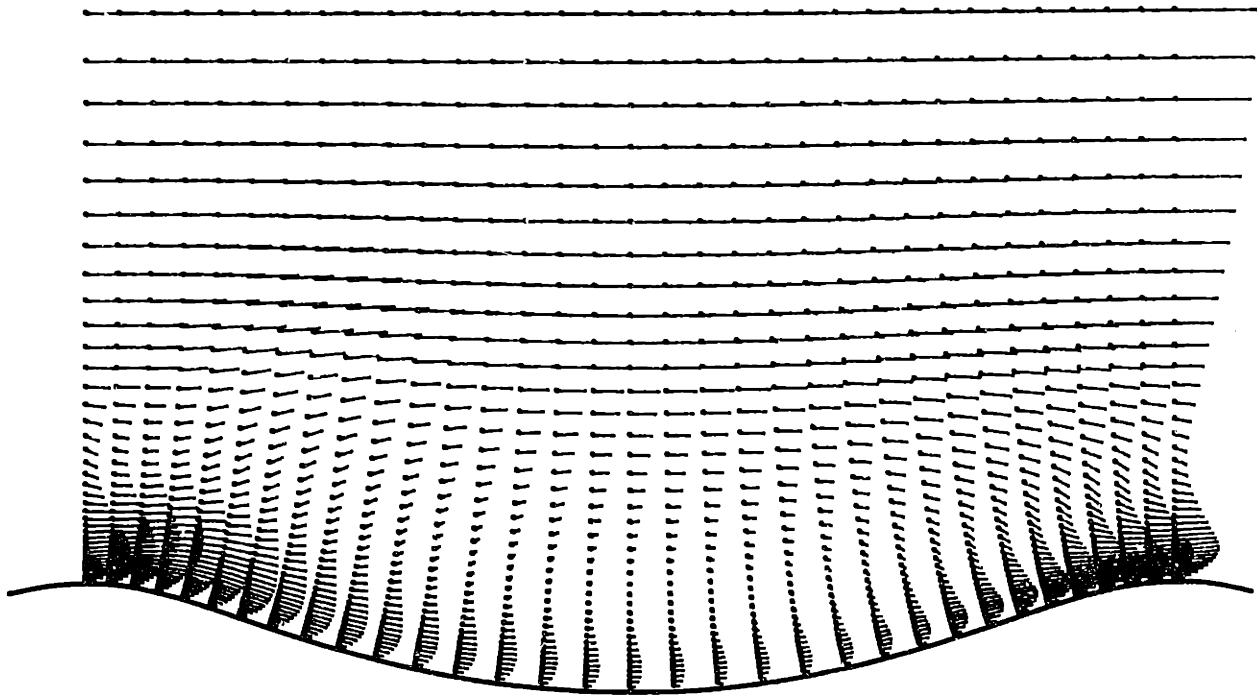
i.   t =   20.050 U_∞ : $\longrightarrow$
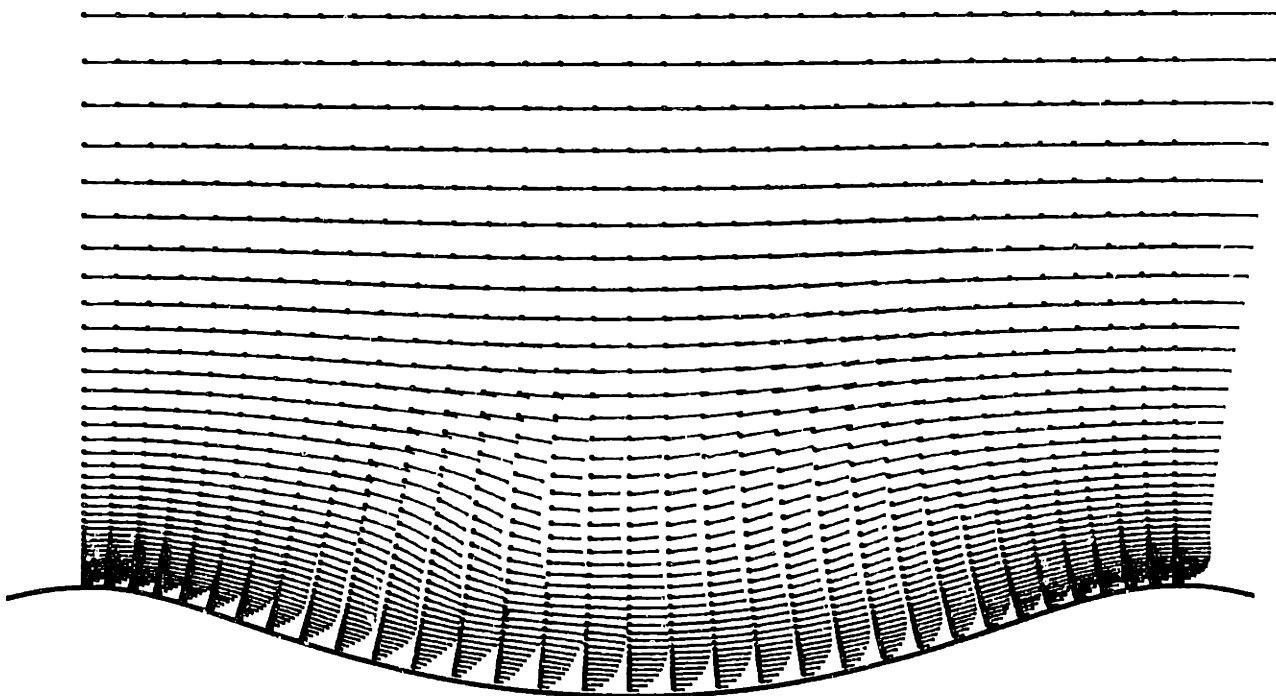
ii.   t =   20.150 U_∞ : $\longrightarrow$

Fig. IX.1.3.   Velocity vectors.
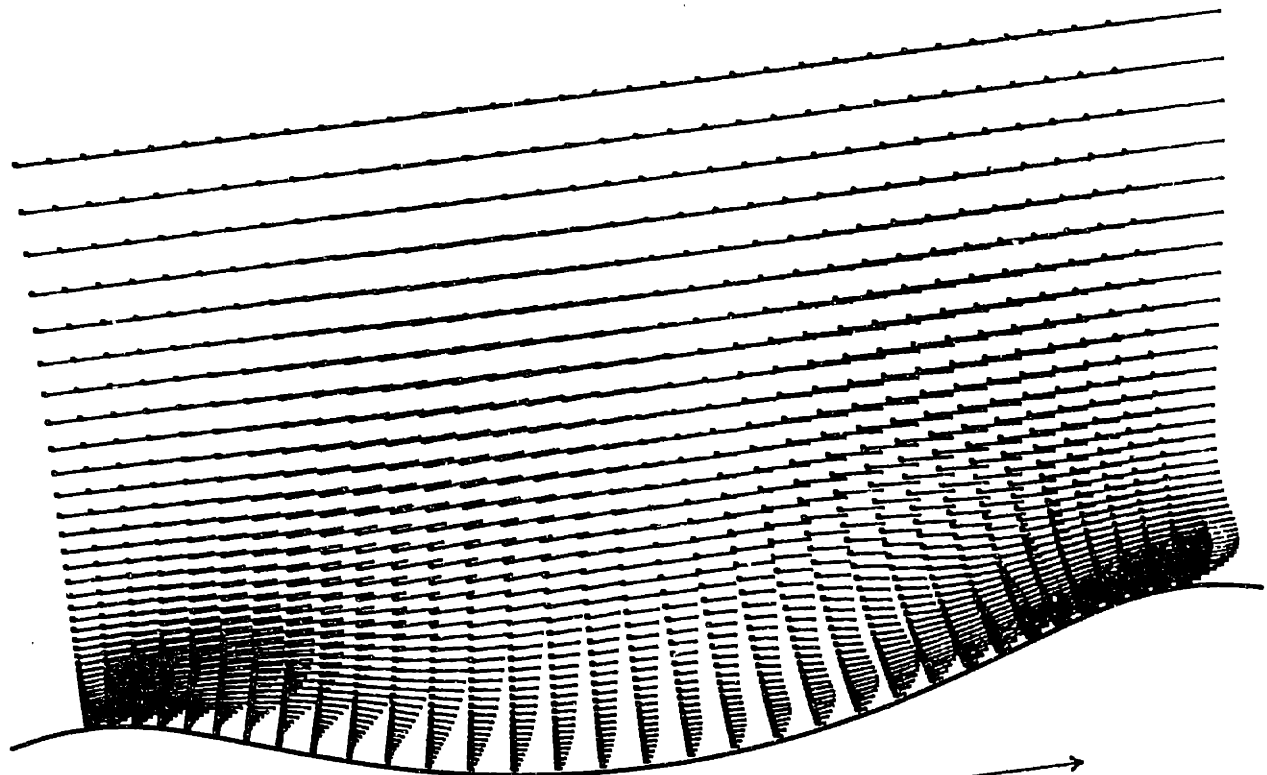
$R = 250$ $K = 4.5$ $s = 0.1$ $M = 32$ $N = 57$

$dy = (\ 0.0036,\ 0.151\ )$ $y_{max} = 2.08$ $c/U_0 = 2$

iii.   t =   20.250 U_∞:
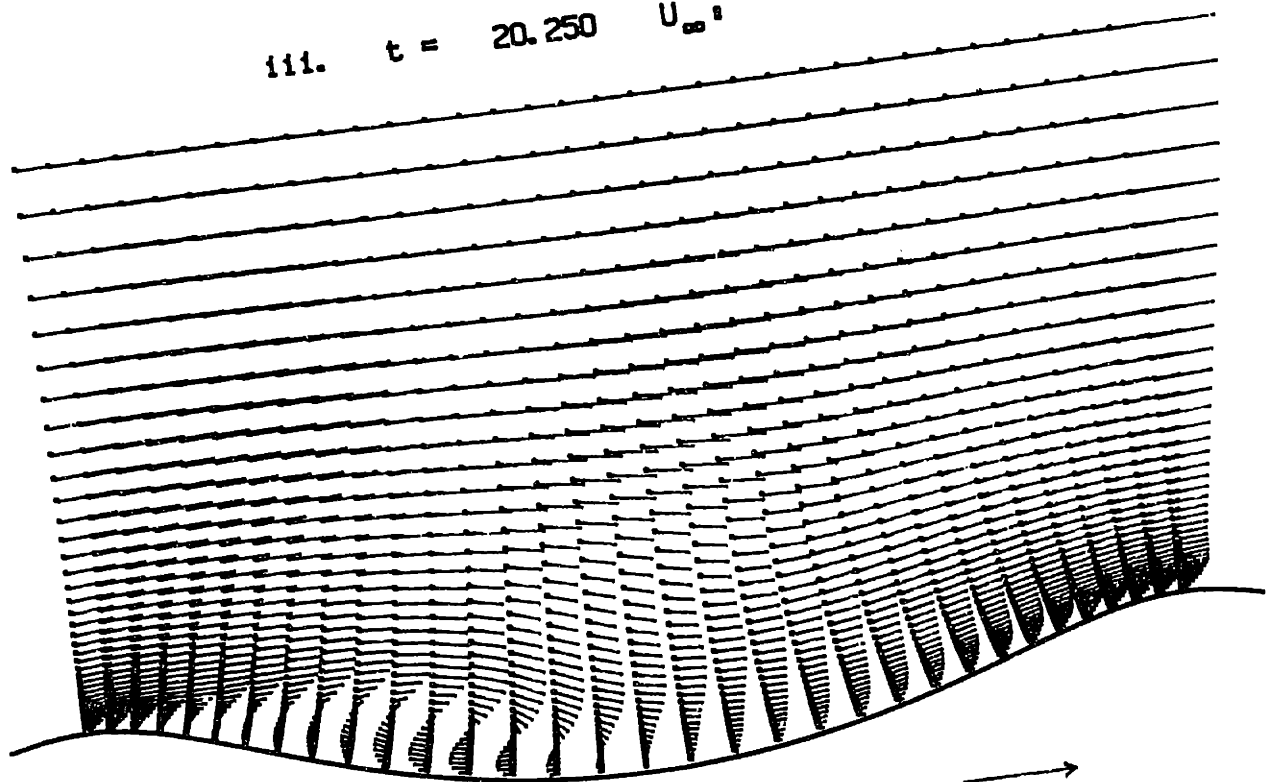
iv.   t =   20.350 U_∞:

Fig. IX.1.3.   Velocity vectors.

R = 250   K = 4.5   e = 0.1   M = 32   N = 57

dy = (0.0036. 0.151) Y_{max} = 2.08 c/U_0 = 2

v.   t =   20.450 U_∞ :
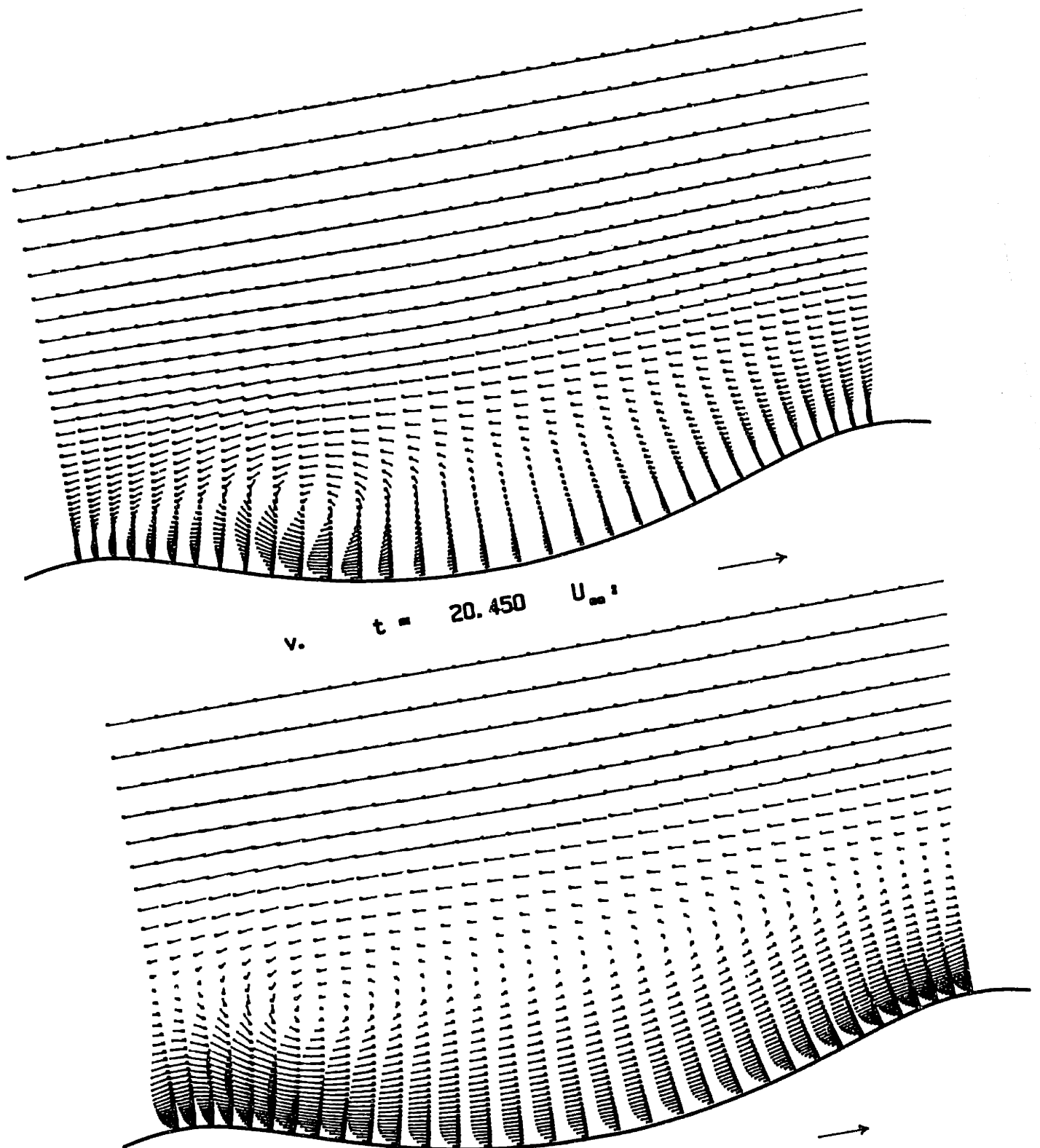
vi.   t =   20.550 U_∞ :

Velocity vectors.

Fig. IX.1.3.

R = 250   K = 4.5   s = 0.1   M = 32   N = 57

dy = (0.0036. 0.151) y_{max} = 2.08 c/U_0 = 2

This is the most complete text of the
thesis available. The following page(s)
were not included in the copy of the
thesis deposited in the Institute Archives
by the author:

Pg 269
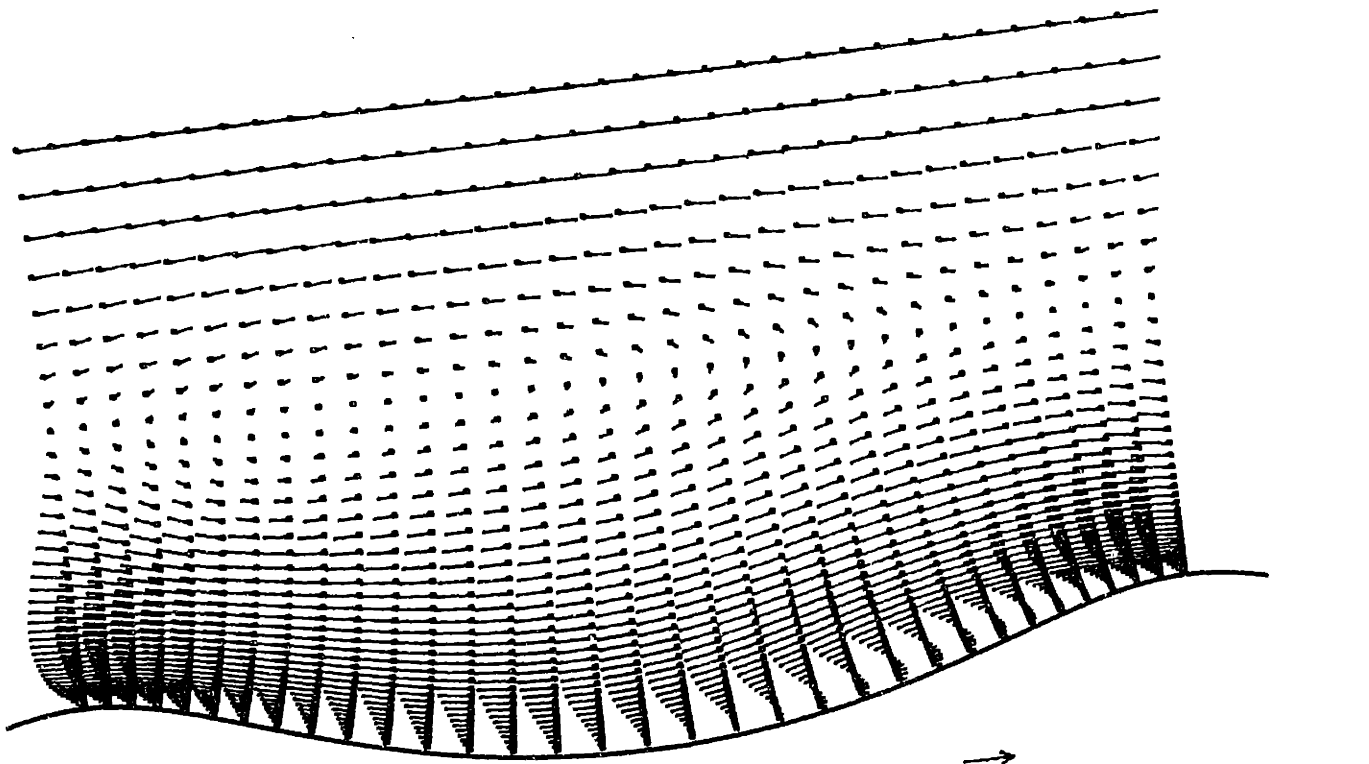
ix.   t =   20.850 U_∞ :
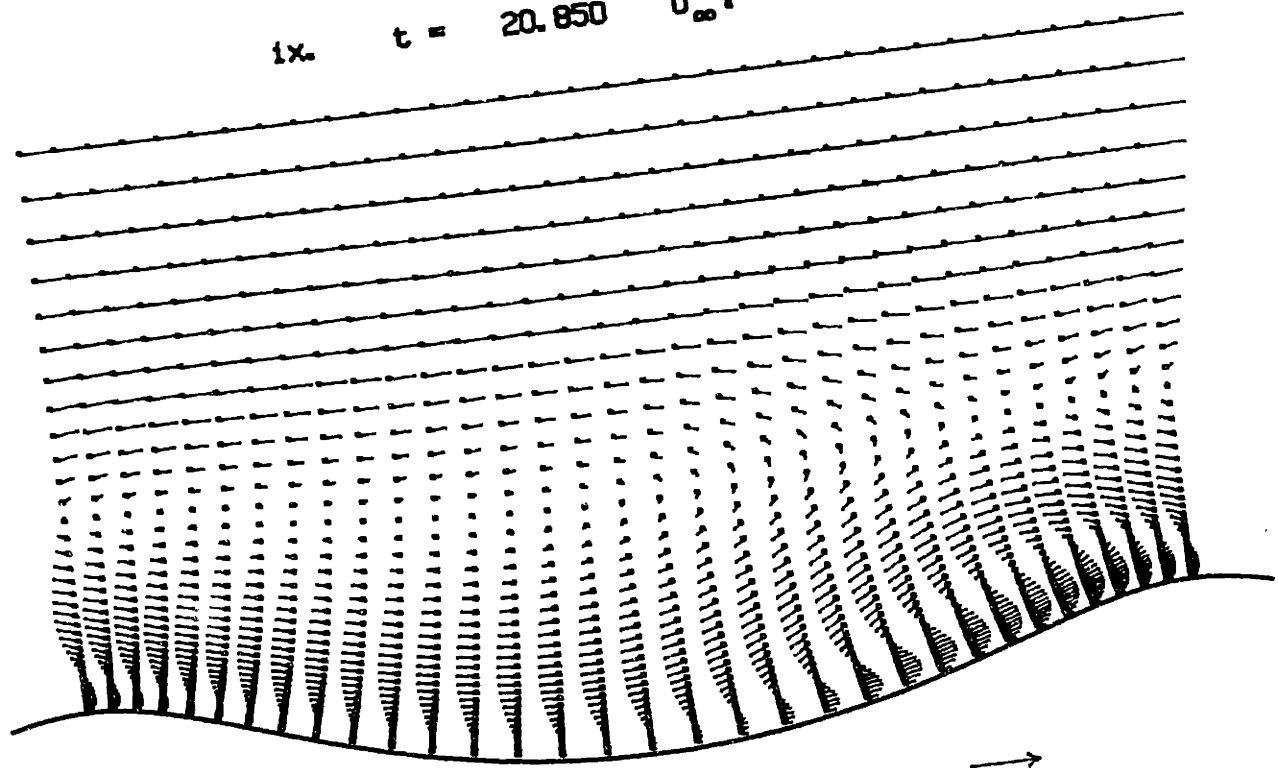
x.   t =   20.950 U_∞ :

Fig. IX.1.3.   Velocity vectors.

R = 250   K = 4.5   s = 0.1   M = 32   N = 57
dy = (0.0036,   0.151) y_{max} = 2.08 c/U_0 = 2
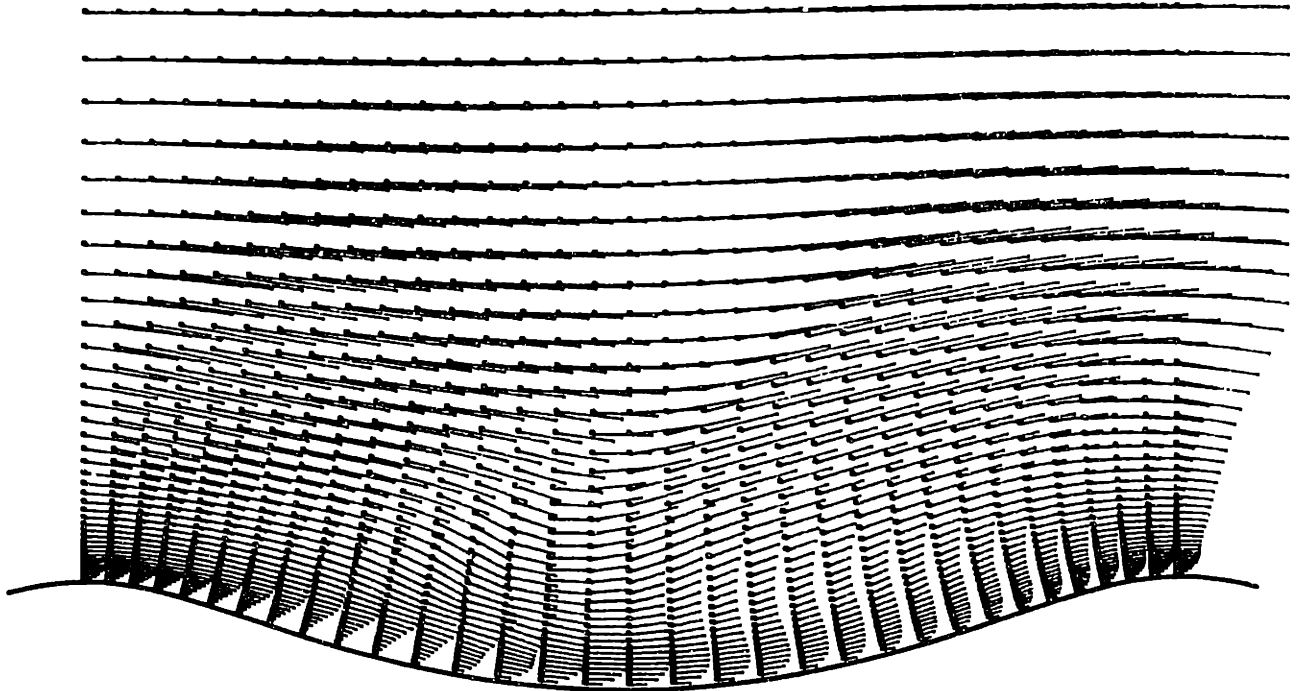
i.　　　t ＝　　15.000　　U∞ :　　　　——————→
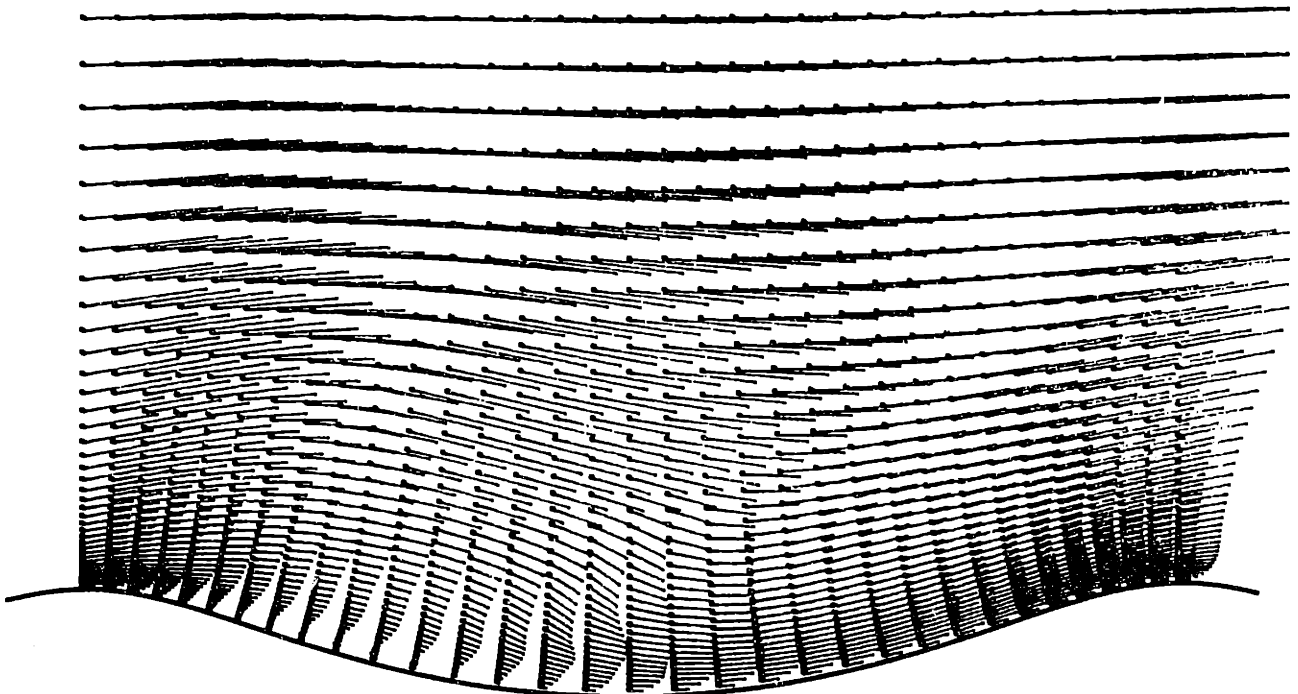
ii.　　　t ＝　　15.025　　U∞ :　　　　——————→

Fig. IX. 1. 4.　　　　Velocity vectors.

R = 250　　K = 4.5　　s = 0.1　　M = 32　　N = 57

dy = (0.0036,　0.151)　　　y_{max} = 2.08　　c/U_0 = 4
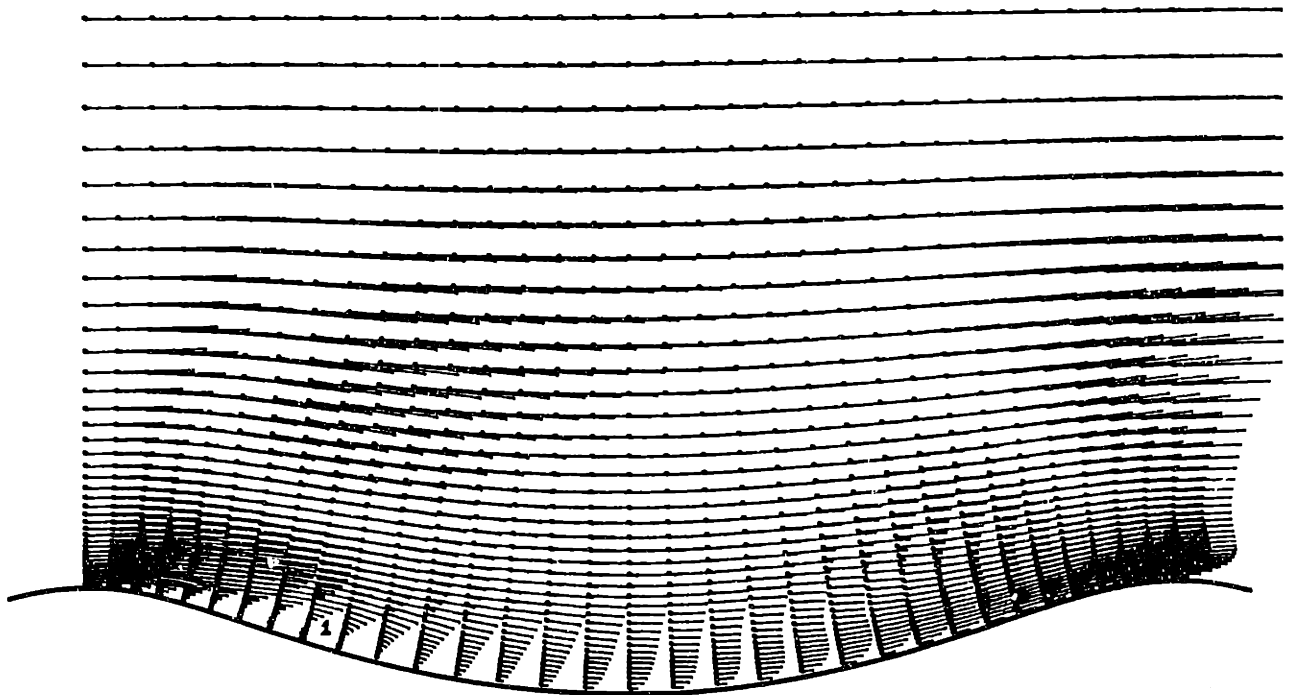
iii.   t =   15.100 U_∞ :   ———————→
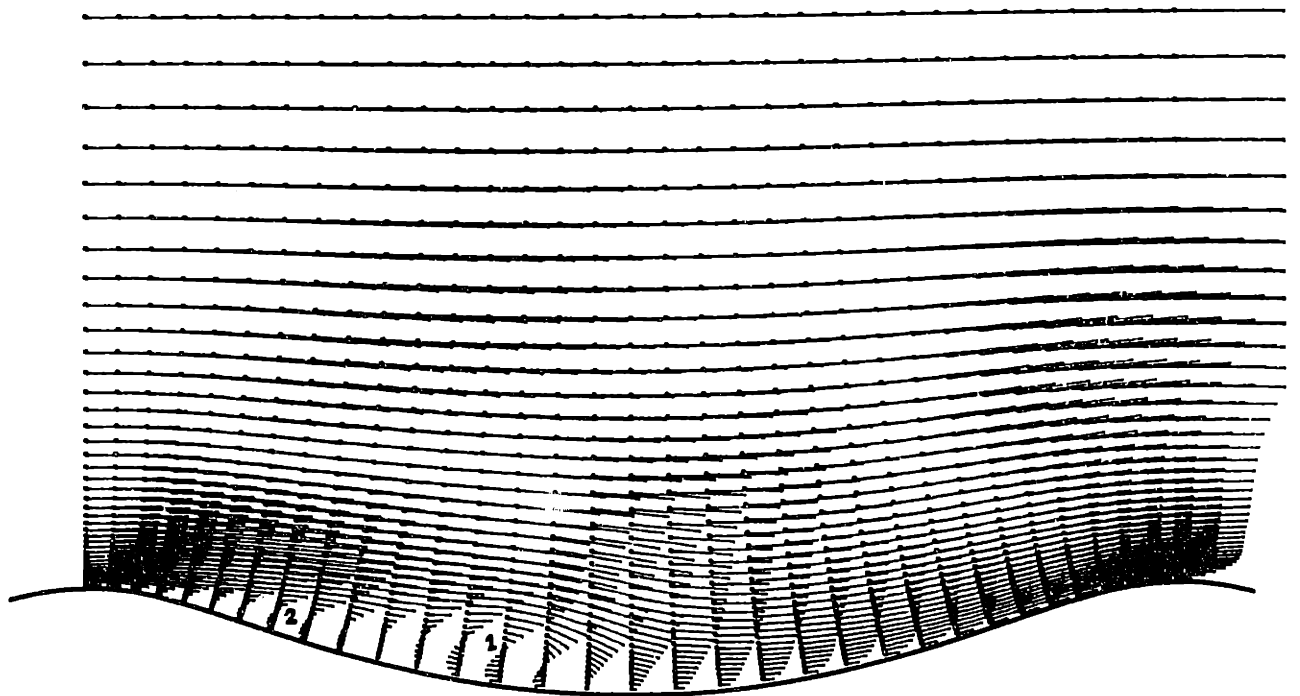
iv.   t =   15.175 U_∞ :   ———————→

Fig. IX.1.4.   Velocity vectors.

R = 250   K = 4.5   s = 0.1   M = 32   N = 57

dy = (0.0036, 0.151) y_{max} = 2.08 c/U_0 = 4
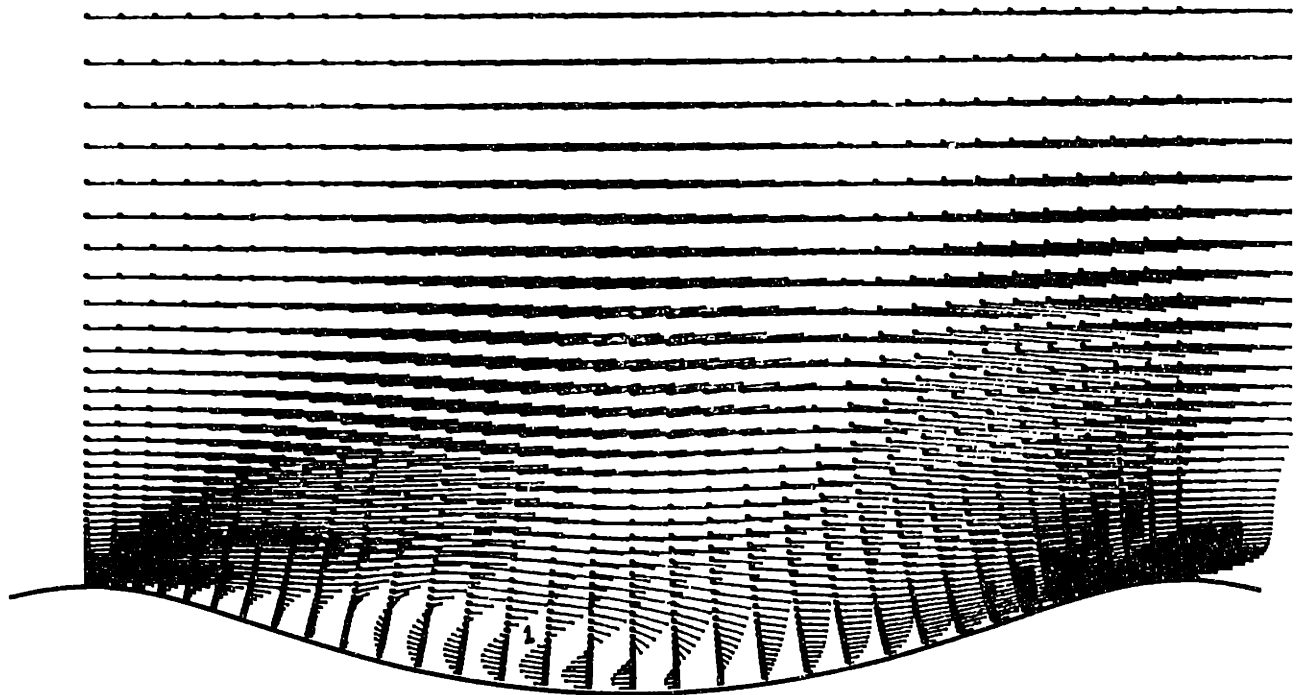
v.   t =   15. 225 U_{∞} :   ⟶
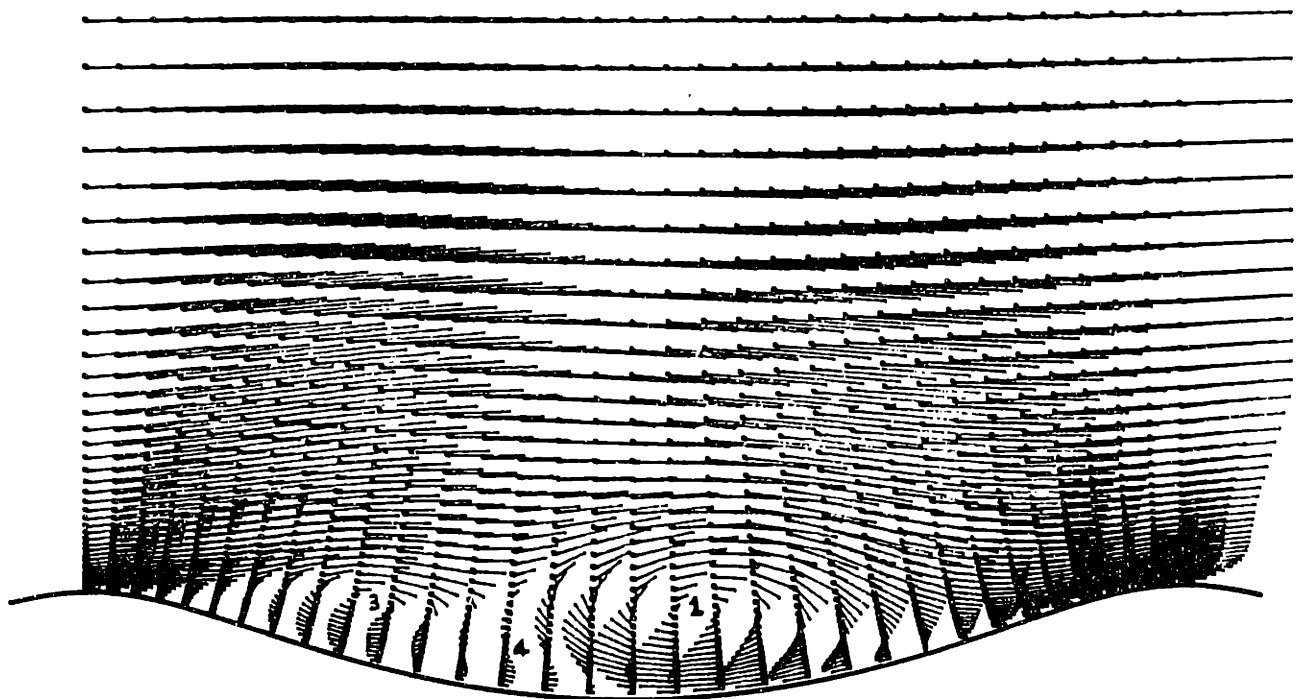
vi.   t =   15. 350 U_{∞} :   ⟶

Fig. IX. 1. 4.   Velocity vectors.

R = 250   K = 4. 5   s = 0. 1   M = 32   N = 57

dy = (0. 0036, 0. 151) y_{max} = 2. 08 c/U_0 = 4
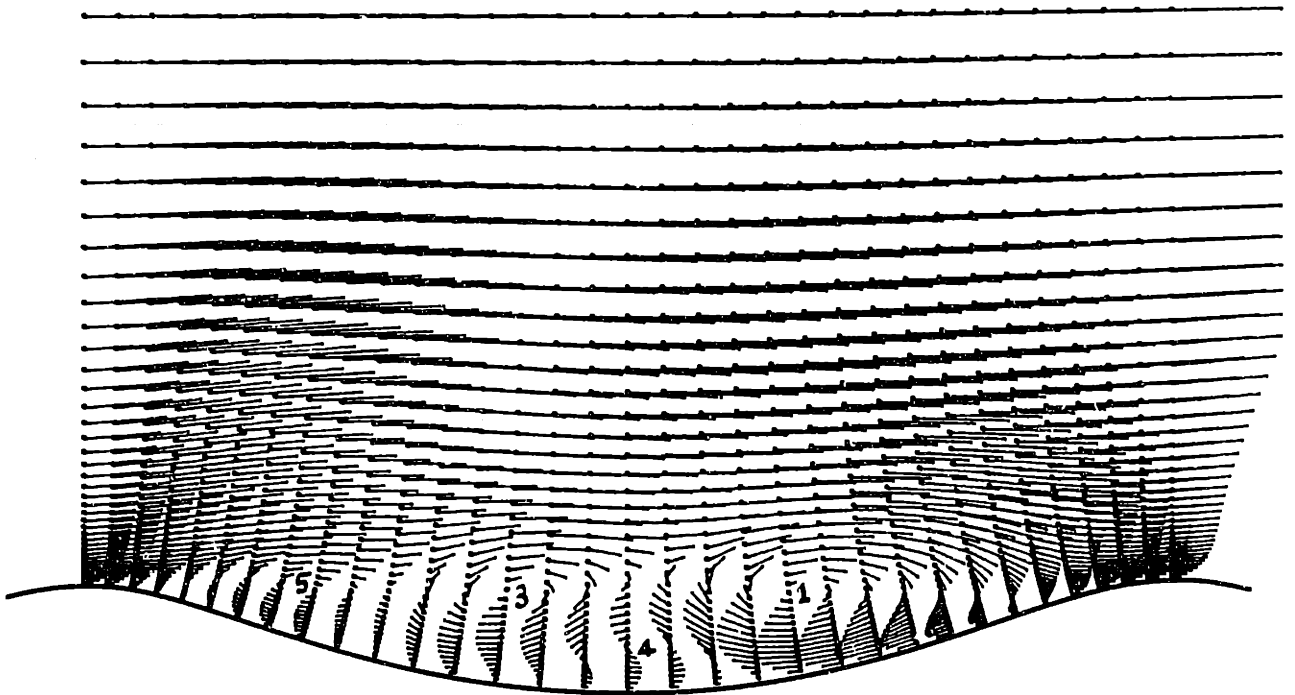
vii. t = 15.425 U∞:
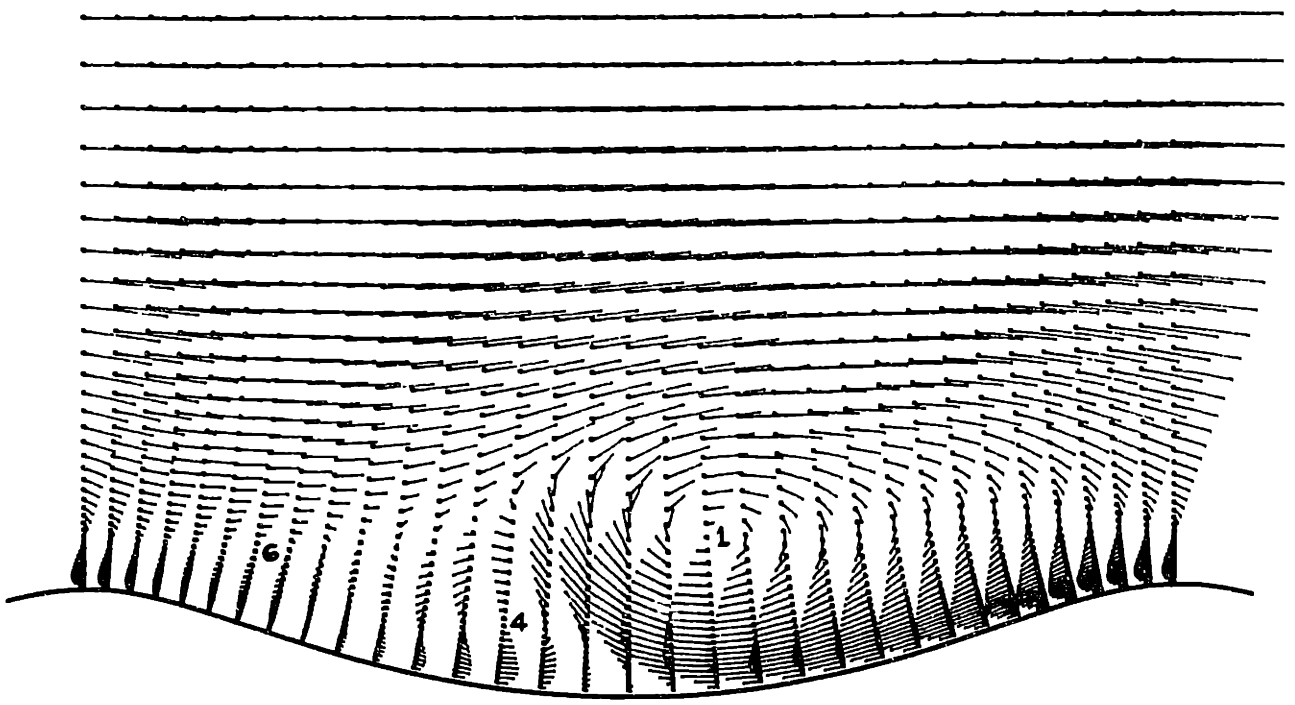
viii. t = 15.600 U∞:

Fig. IX.1.4. Velocity vectors.
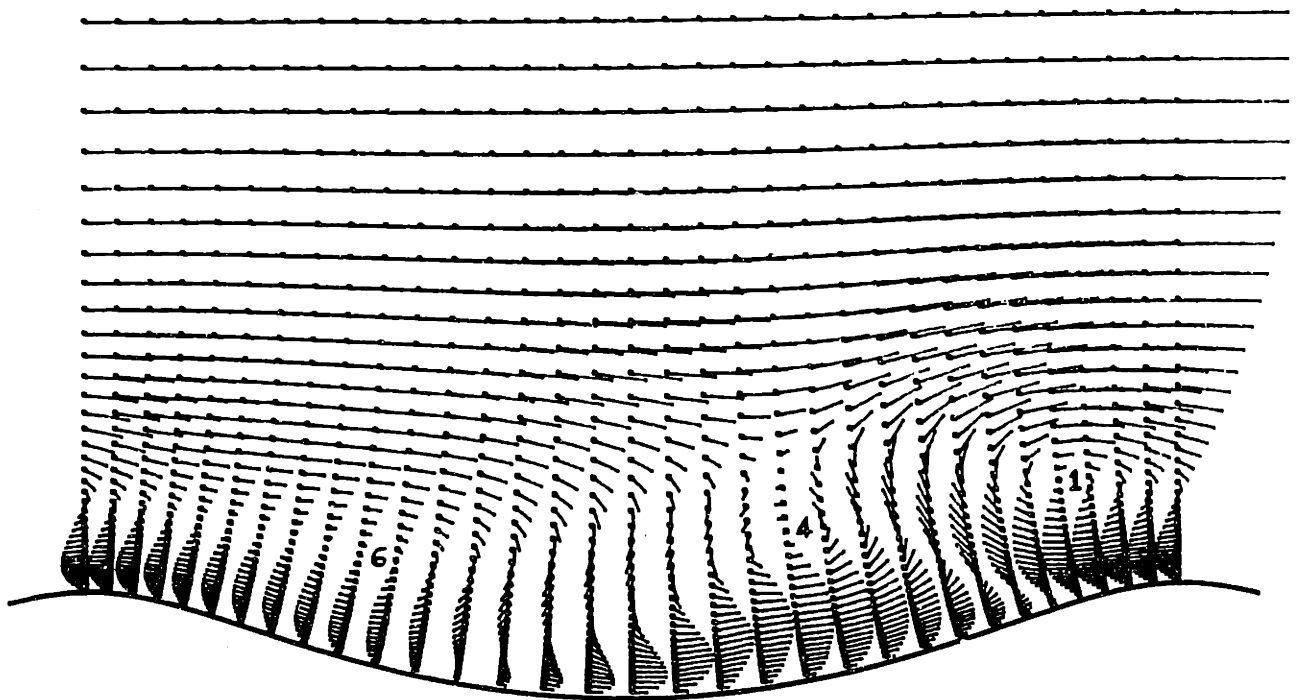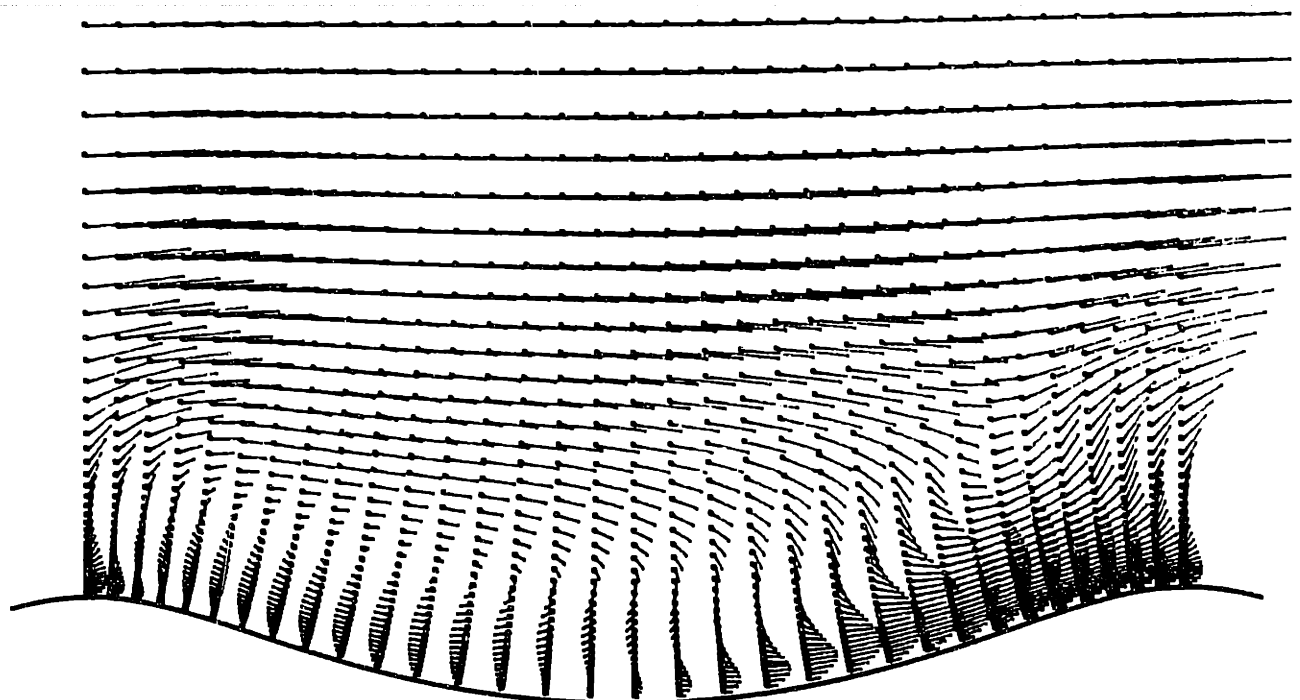
R = 250   K = 4.5   s = 0.1   M = 32   N = 57

dy = (0.0036, 0.151) y_{max} = 2.08 c/U_0 = 4

274

1x.   t ≈   15. 850 U_∞ :   ⟶⟶

x.   t =   15. 900 U_∞ :   ⟶⟶

Fig. IX. 1. 4.   Velocity vectors.

R = 250   K = 4.5   ε = 0.1   M = 32   N = 57
dy = (0.0036. 0.151) y_{max} = 2.08 c/U_0 = 4

275
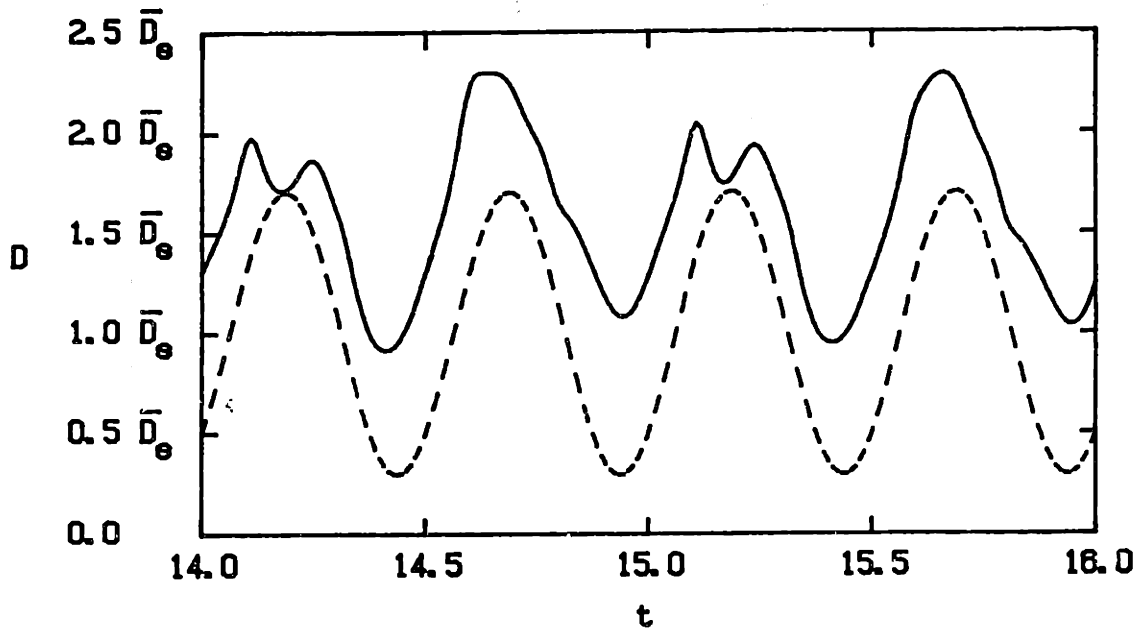
Fig. IX.2.1. Rate of viscous dissipation. $c/U_0 = 1$
R = 250   K = 4.5   e = 0.1
M = 32   N = 57 $\overline{D}_e$ = 0.0084
dy = (0.0036, 0.151) y_{max} = 2.08

———— over ripples, D
- - - - - oscillatory component over plane bed, D_e
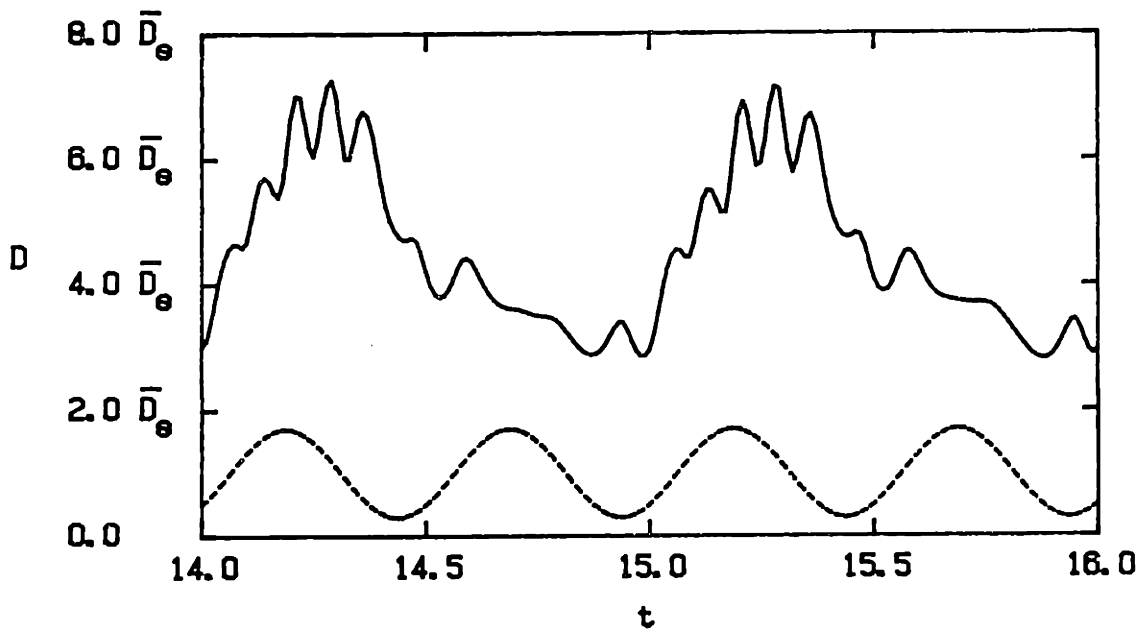
Fig. IX.2.2. Rate of viscous dissipation. $c/U_0 = 4$
R = 250   K = 4.5   e = 0.1
M = 32   N = 57 $\overline{D}_e$ = 0.0084
dy = (0.0036, 0.151) y_{max} = 2.08
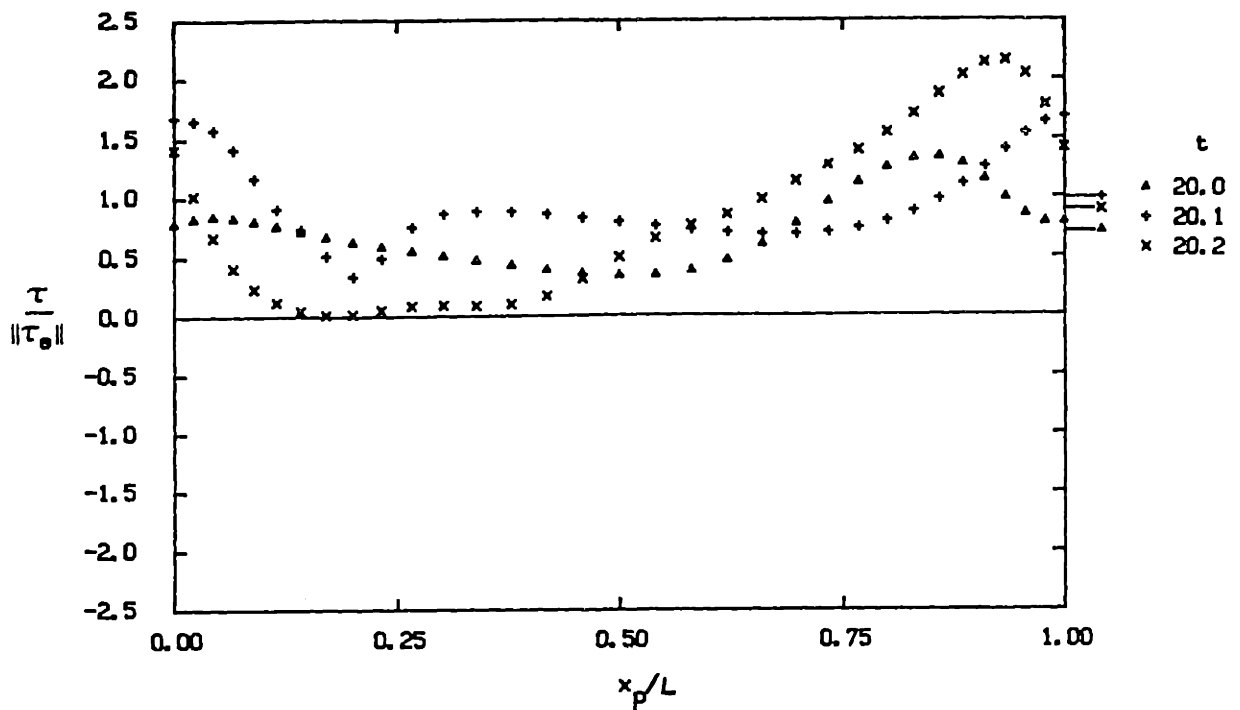
Fig. IX.3.1.1. Shear stress distribution on the ripple surface.

R = 250   K = 4.5   e = 0.1   M = 32   N = 57   c/U_0 = 2
dy = (0.0036 , 0.151)   y_max = 2.08   ‖τ_e‖ = 0.0236

Fig. IX.3.1.11. Shear stress distribution on the ripple surface.

R = 250   K = 4.5   s = 0.1   M = 32   N = 57   c/U_0 = 2
dy = (0.0036 , 0.151)   y_max = 2.08   ‖τ_e‖ = 0.0236

277
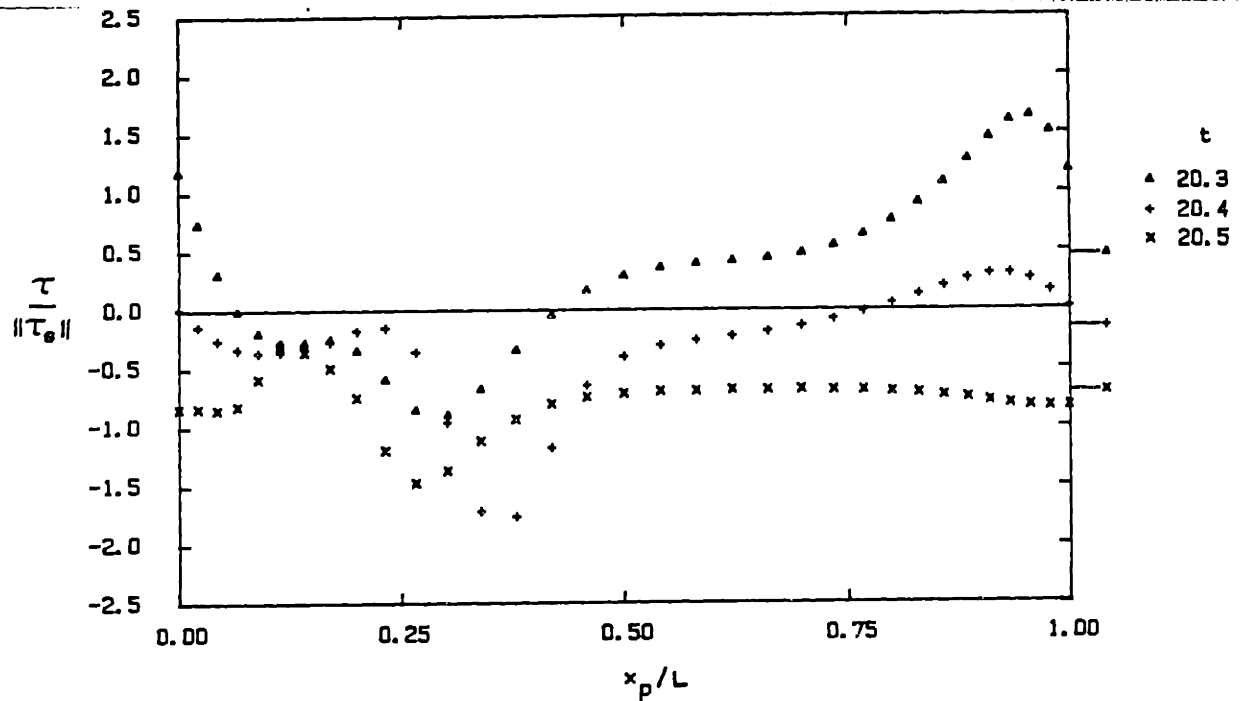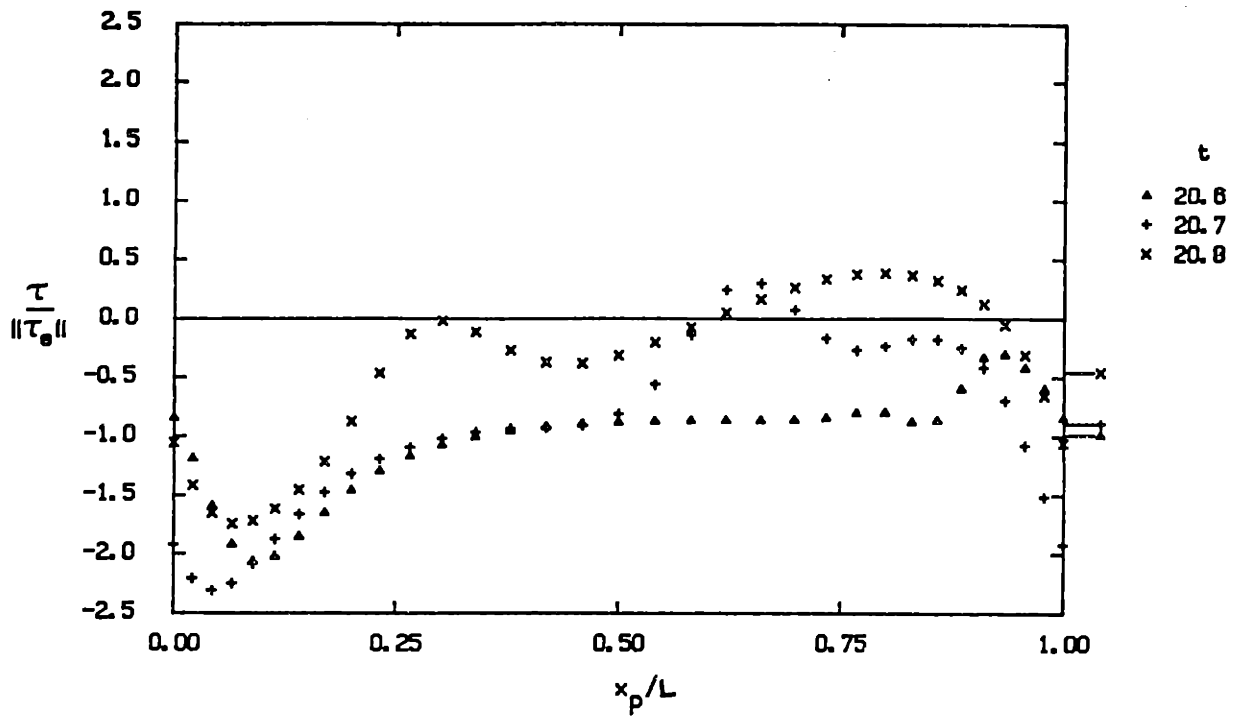
Fig. IX.3.1.iii.   Shear stress distribution on the ripple surface.

R = 250   K = 4.5   e = 0.1   M = 32   N = 57   c/U$_0$ =2
dy = (0.0036 , 0.151)   y$_{max}$ = 2.08 ||τ$_e$||= 0.0236
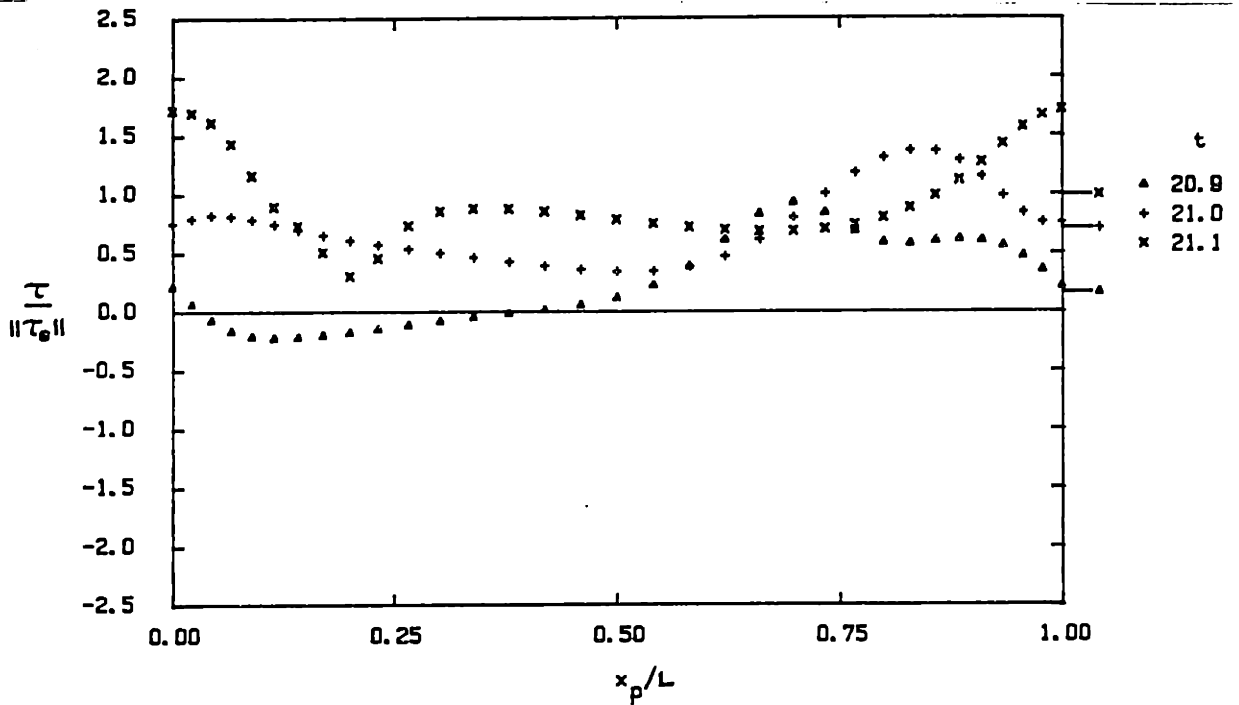
Fig. IX.3.1.iv.   Shear stress distribution on the ripple surface.

R = 250   K = 4.5   s = 0.1   M = 32   N = 57   c/U$_0$ =2
dy = (0.0036 , 0.151)   y$_{max}$ = 2.08 ||τ$_e$|| = 0.0236

278
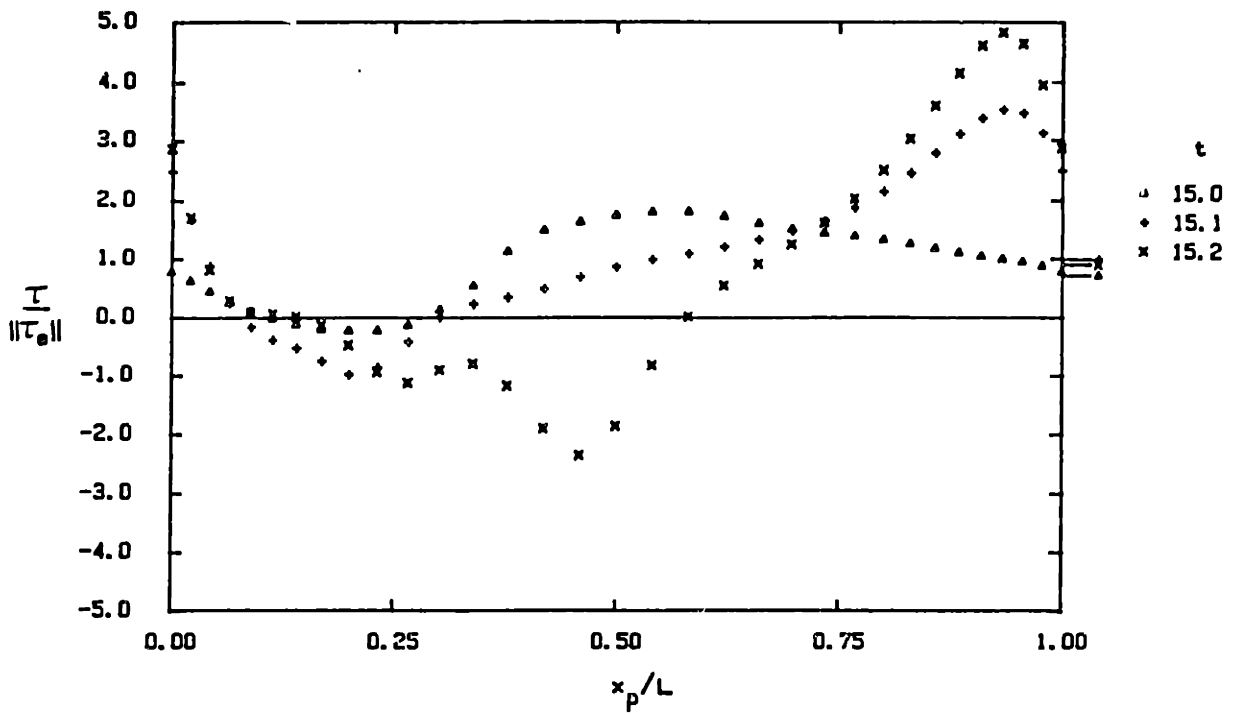
Fig. IX.3.2.i.   Shear stress distribution on the ripple surface.

R = 250   K = 4.5   s = 0.1   M = 32   N = 57   c/U$_0$ = 4

dy = (0.0036 , 0.151)   y$_{max}$ = 2.08 ||τ$_e$|| = 0.0236
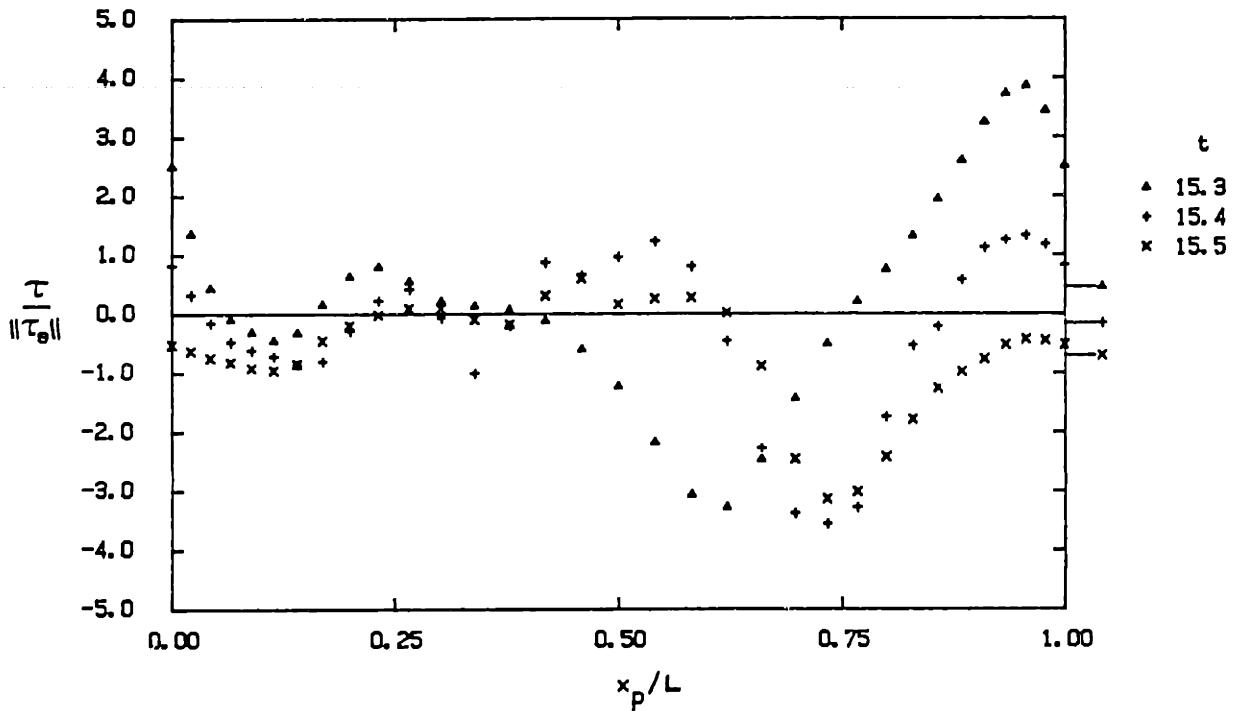
Fig. IX.3.2.ii.   Shear stress distribution on the ripple surface.

R = 250   K = 4.5   s = 0.1   M = 32   N = 57   c/U$_0$ = 4

dy = (0.0036 , 0.151)   y$_{max}$ = 2.08 ||τ$_e$|| = 0.0236

279
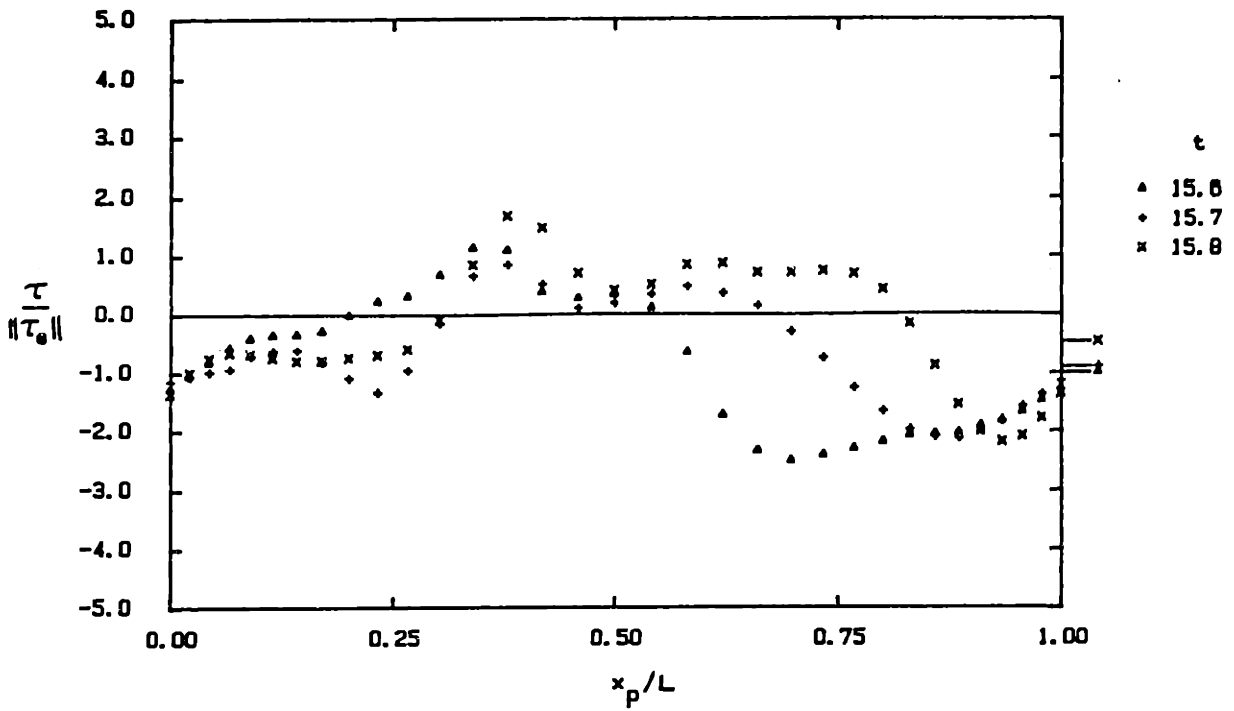
Fig. IX.3.2.iii.   Shear stress distribution on the ripple surface.

R = 250   K = 4.5   ε = 0.1   M = 32   N = 57 c/U_0 = 4
dy = (0.0036 , 0.151) y_{max} = 2.08 $\|\tau_e\|$ = 0.0236
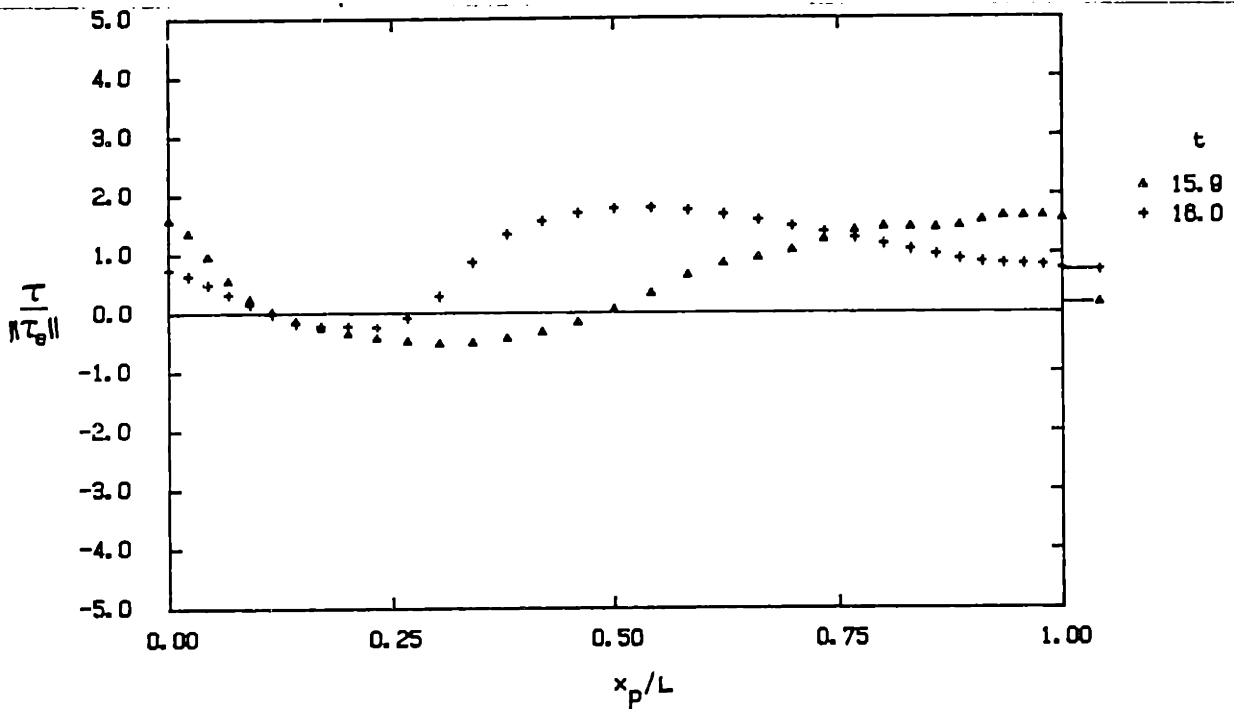
Fig. IX.3.2.iv.   Shear stress distribution on the ripple surface.

R = 250   K = 4.5   ε = 0.1   M = 32   N = 57 c/U_0 = 4
dy = (0.0036 , 0.151) y_{max} = 2.08 $\|\tau_e\|$ = 0.0236
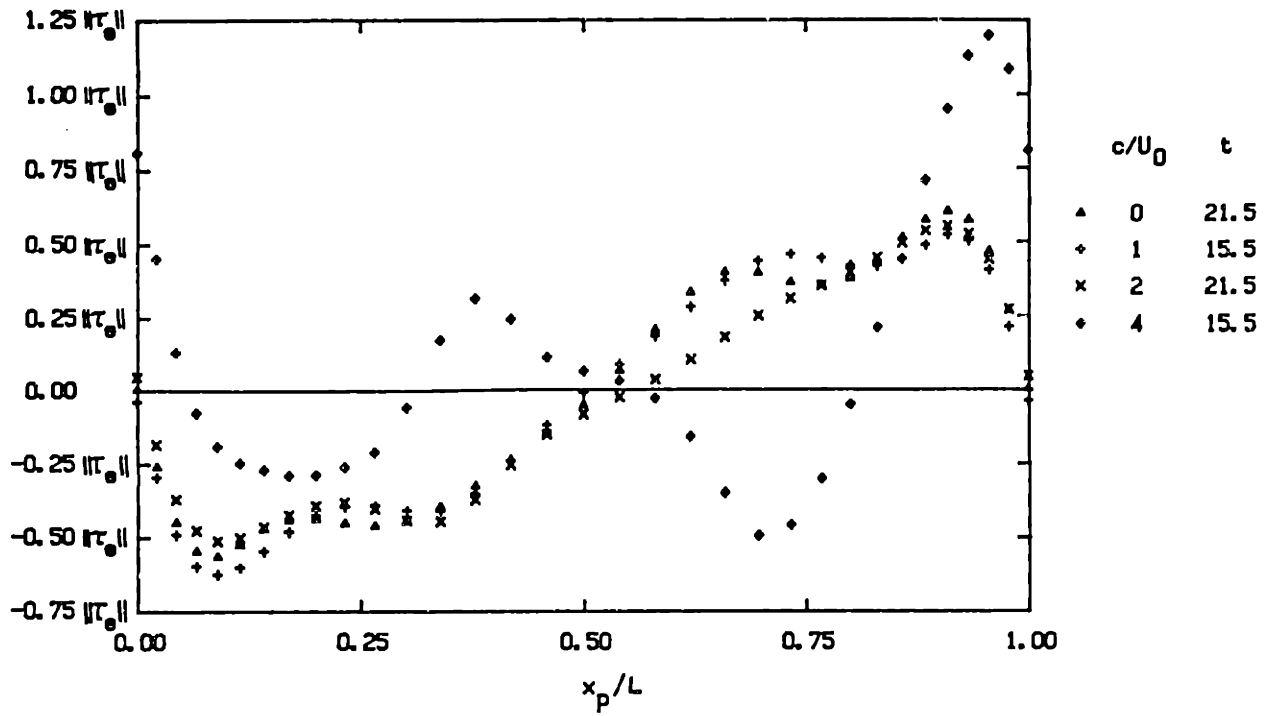
Fig. IX.3.3.   Shear stress on ripple surface averaged over one wave period.

R = 250   K = 4.5   s = 0.1   M = 32   N = 57
dy = (0.0036, 0.151) y_{max} = 2.08 $\|\tau_e\|$ = 0.0236
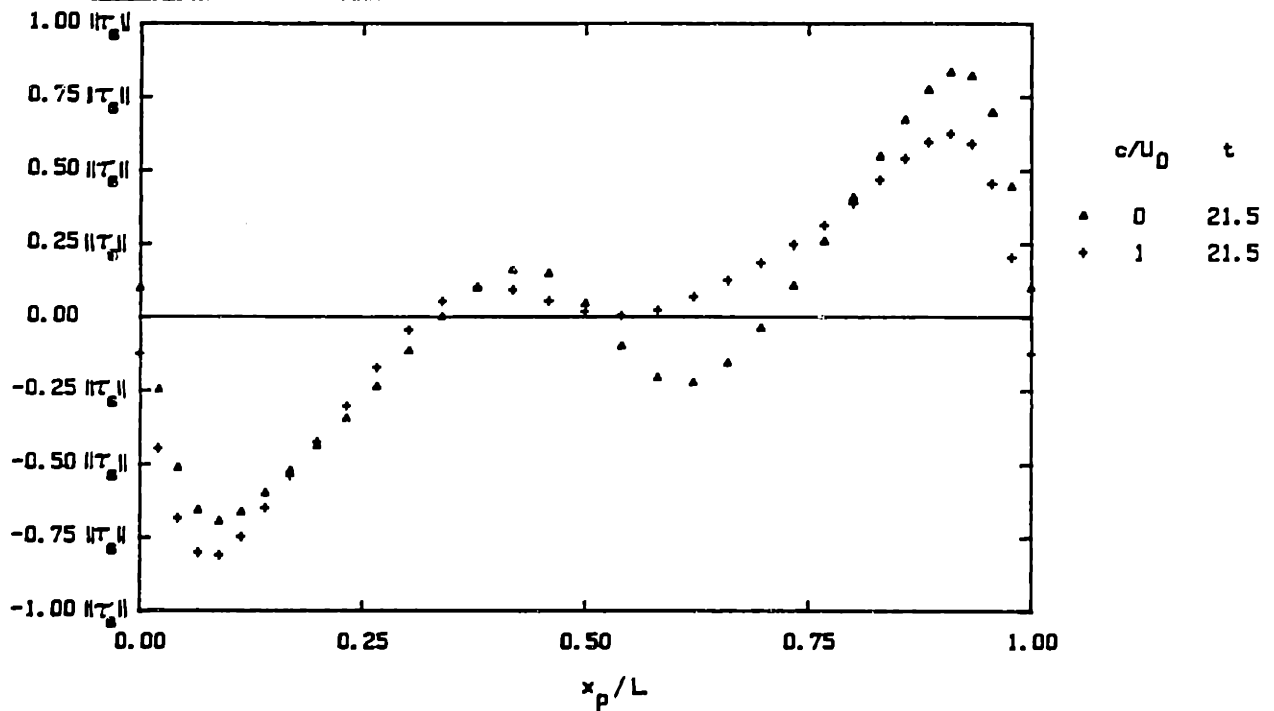
Fig. IX.3.4.   Shear stress on ripple surface averaged over one wave period.

R = 250   K = 9.0   s = 0.1   M = 32   N = 42
dy = (0.0052, 0.223) y_{max} = 2.16 $\|\tau_e\|$ = 0.0167
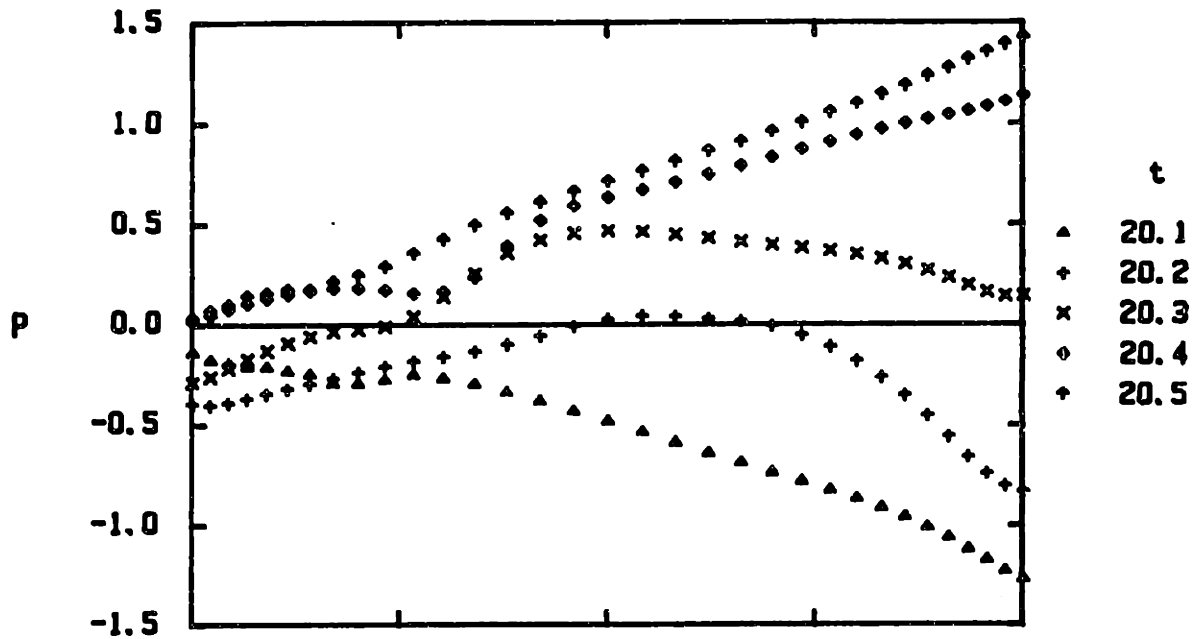
iii.   t = 20.1   to 20.5
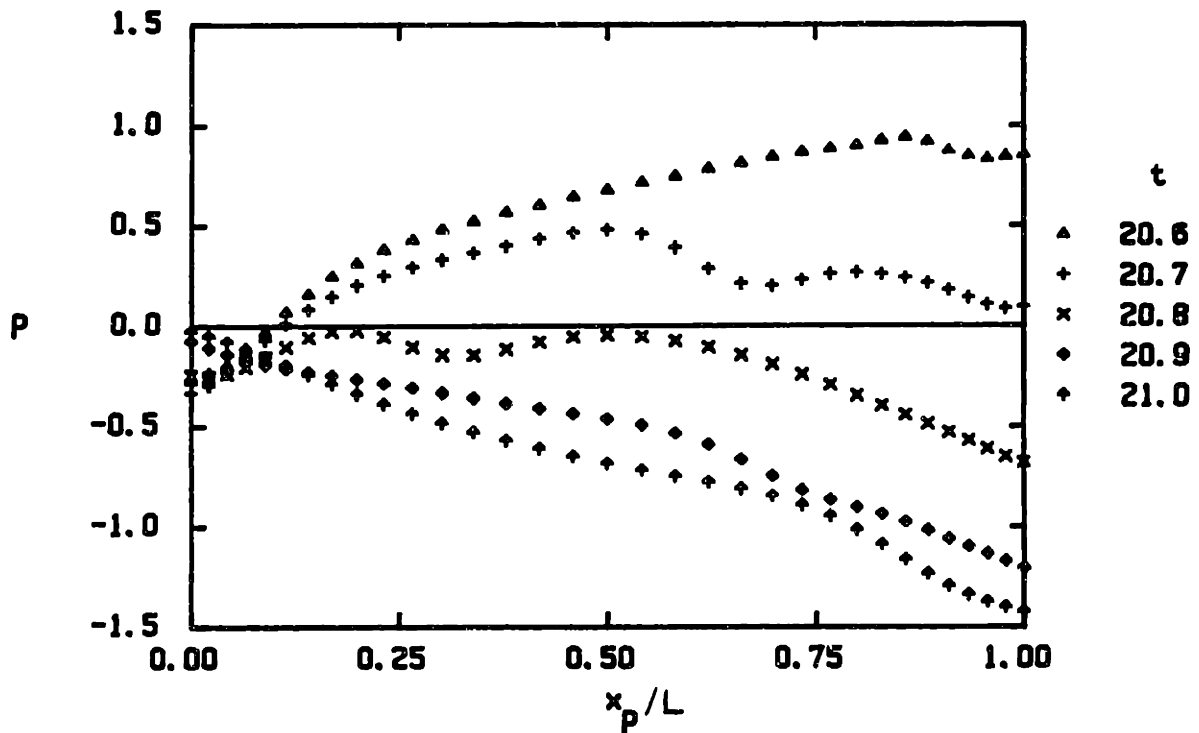
iv.   t = 20.6   to 21.0

Fig. IX.4.1.   Pressure distribution on the ripple surface.
R = 250   K = 4.5   s = 0.1
M = 32   N = 57 c/U_0 = 2
dy = (0.0036, 0.151) y_{max} = 2.08
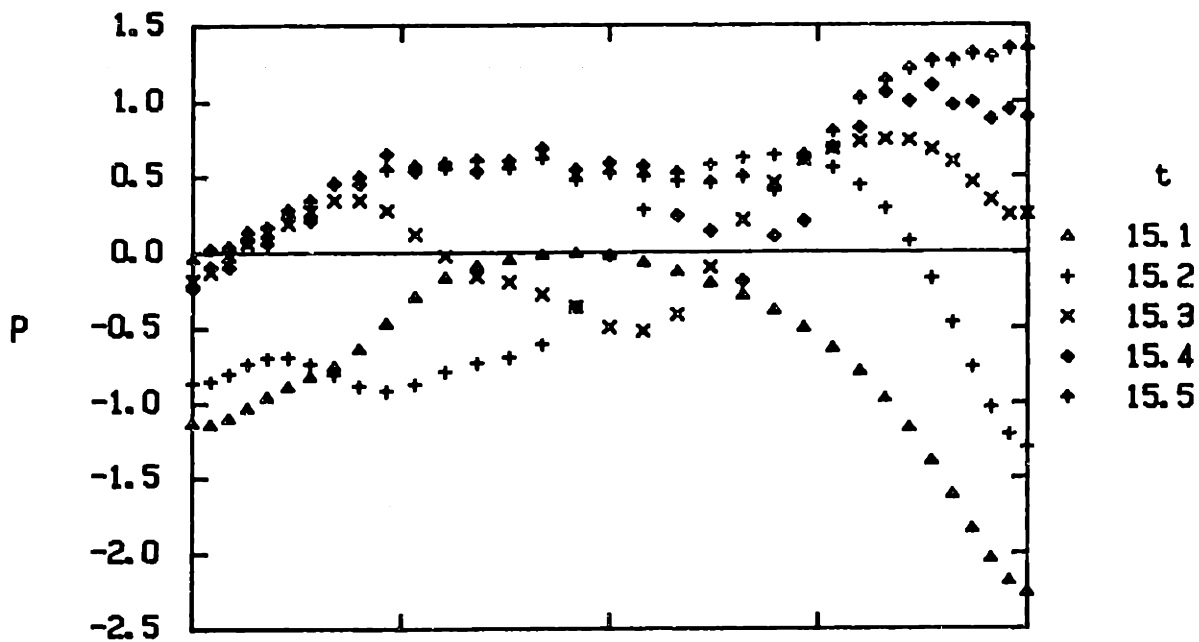
iii.   t = 15.1   to 15.5
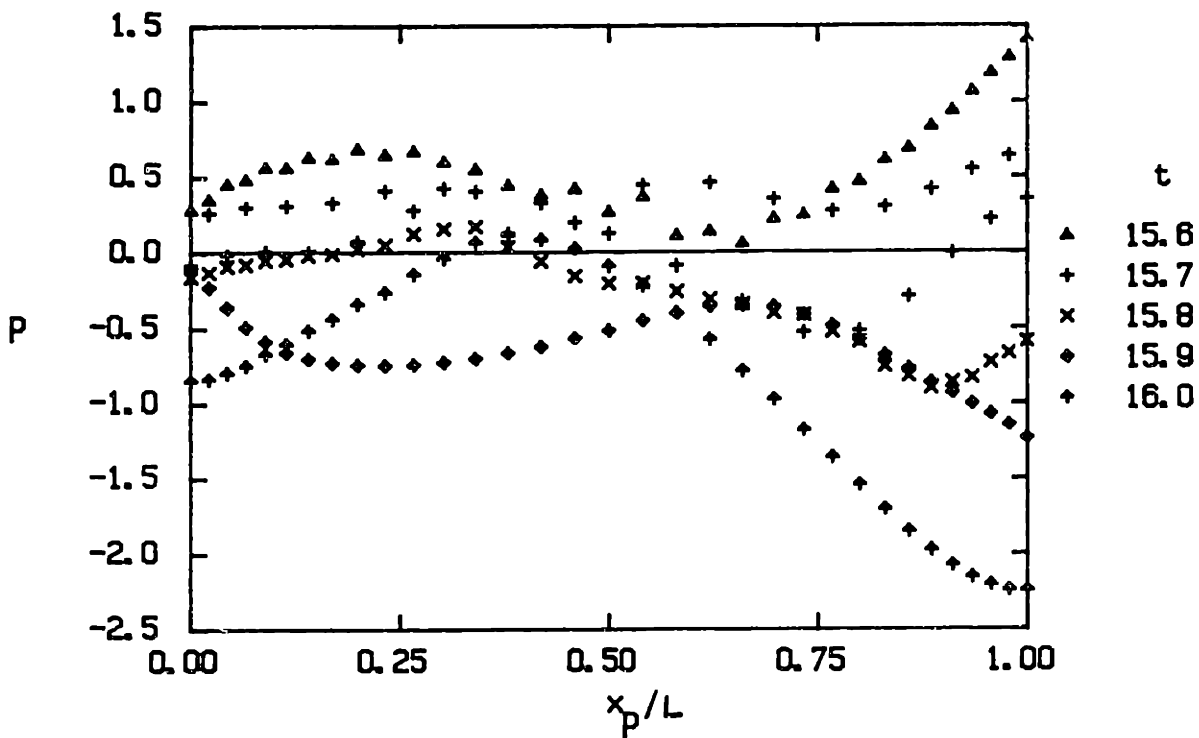
iv.   t = 15.6   to 16.0

Fig. IX. 4. 2.   Pressure distribution on the ripple surface.
R = 250   K = 4.5   e = 0.1
M = 32   N = 57   c/U_0 = 4
dy = (0.0036, 0.151)   y_max = 2.08
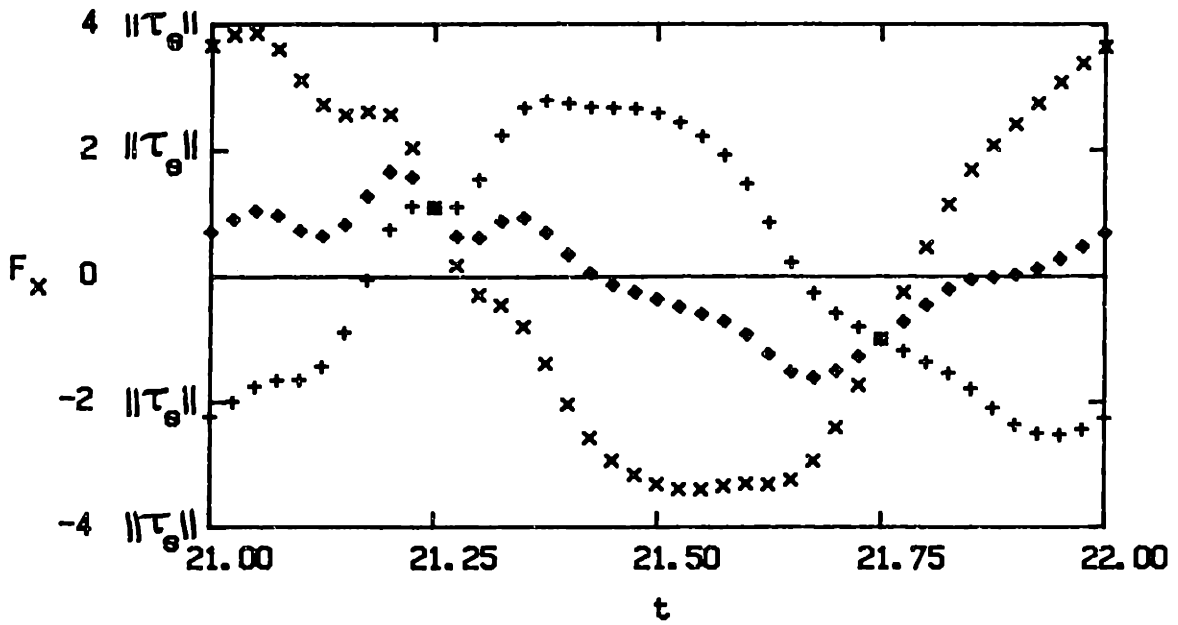
Fig. IX.5.1.   Horizontal force on ripple. $c/U_0 = 2$
R = 250   K = 4.5   e = 0.1
M = 32   N = 57 $\|\tau_e\| = 0.0236$
dy = (0.0036 , 0.151) $y_{max} = 2.08$

    $+$ F_c $\times$ F_t $\bullet$ F_n
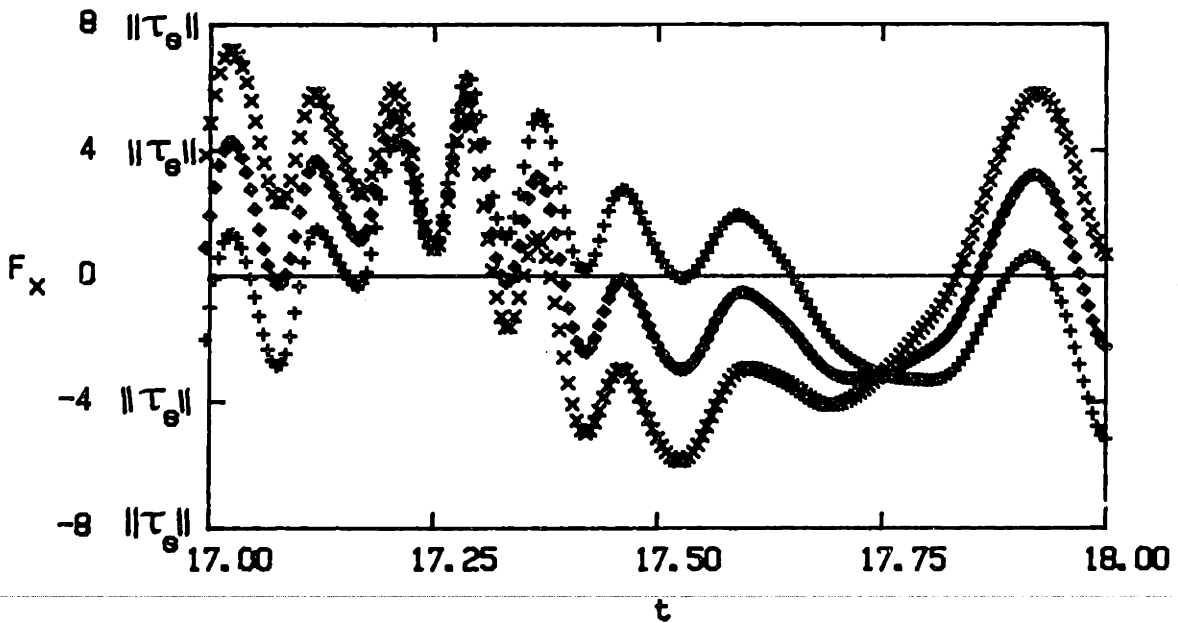
Fig. IX.5.2.   Horizontal force on ripple. $c/U_n = 4$
R = 250   K = 4.5   e = 0.1
M = 32   N = 57 $\|\tau_e\| = 0.0236$
dy = (0.0036 , 0.151) $y_{max} = 2.08$

Chapter X. Summary and Discussion

In this thesis we have examined the separated laminar flow over fixed ripples with an approximately sinusoidal profile. Three cases of far field velocity: purely oscillatory, pure current, and a combintation of the two, are studied over a range of Reynolds number $15 \leq R \leq 500$, $R_c = 250$ and 1000, Keulegan-Carpenter number $2.5 \leq K \leq 12$, and $c/U_0 = 1$, 2, and 4 for a fixed ripple slope of 0.1.

Two-dimensional Navier-Stokes equations are solved numerically in terms of streamfunction and vorticity function. No empirical parameters are required in the formulation. The numerical scheme is tested by comparing with the exact solution to the oscillatory flow over a plane bed, a numerical solution to the impulsively started flow around a circular cylinder using a different scheme, and an asymptotic solution to the flow over ripples. The numerical solutions for flows over ripples are verified with the convergence test and the conservation of energy over the computational domain. Satisfactory results are obtained in all these tests administered except for the flow with $R = 500$ and $K = 4.5$. We stress again that, for this latter case, the results are tentative only, due to lack of complete verification of convergence, which has been discussed in length in Chapter VI.

In all ambient flows consisting of an oscillatory component only, one vortex is generated per half period during the deceleration of the far field velocity. The strengths of these vortices, and the complexity of the flow field, increase with R and K. The hydrodynamic stresses on the ripple bed and the rate of energy dissipation in the domain of computation are found to be only slightly higher than the corresponding flow over a plane bed at low R or K. However, they increase significantly with these dimensionless parameters due to the increased strength of the separated flow. The maximum amplitude of the shear stress across the ripple profile can be up to three times that on a plane bed under an ambient flow of the

same magnitude.

The pressure distribution along the ripple surface is found to be very close to that from the potential flow solution except at the ripple crests and under the vortices, where the amplitudes of the local shear stress are also highest. The horizontal force on a ripple length of the bed depends on the exact ripple profile used in the computation, for example, that calculated from a crest to crest profile F_c or from a trough to trough profile F_t. Both F_c and F_t vary sinusoidally with time at low Reynolds numbers (≤ 50) or Keulegan–Carpenter numbers (≤ 3), and F_t is in phase with the ambient velocity. At higher values of R and K the ambient velocity leads F_c and lags F_t in phase. The amplitudes of these forces are up to over five times those in the corresponding flow over a plane bed.

Values of the friction factor are deduced using two different definitions: from the energy dissipation in the flow domain, and from the magnitude of the horizontal force on a ripple length of the bed. Both friction factors decrease when R or K increases, with the dependence on K appearing to be stronger. Despite that our results are for laminar flows, this dependence on K is very similar to that obtained for turbulent flows. The variation of the computed values of the friction factor based on the horizontal force follows closely that of the theoretical values for rough turbulent flows proposed by Kajiura (1968), while that based on energy dissipation appears to follow the same bilinear relationship deduced from the laboratory data of Bagnold (1946).

When the far field velocity consists of a steady current only, both the velocity profile and the hydrodynamic stresses are very nearly the same as those in the impulsively started current over a plane bed at large time. Both the dissipation and the forces on the ripple are much smaller than those in an oscillatory ambient flow with the same amplitude. The addition of an oscillatory component of even a much smaller magnitude can therefore lead to dramatic increases and is discussed in

Chapter IX.

The upper limit on the dimensionless parameters is determined by the time and storage available on the computer, since both the grid spacing and time step decrease with increasing R and K. With our current budget, this upper limit is decided by the CPU time requirement. The most expensive case using a 64x72 grid requires close to ten Cray-hours for computation up to twenty wave periods.

The effects of changing the ripple slope have not been examined due to the constraint on the computer time for this study. Most ripple slopes found in the laboratory (Lofquist, 1978) and the field (Dingler and Inman, 1976) are above the value s=0.1 we studied. From (4.4.1) and (4.5.8), both the grid spacing and time-step decrease with increasing ripple slope.

The contribution to wave attenuation from a ripple bed can be infered from the computed rate of energy dissipation by substituting U_0 with the magnitude of the velocity of fluid particles at the bottom. Different time dependences of this bottom velocity using nonlinear wave theory can also be used in the computation. The results are applicable to deep water or small amplitude waves in shallow water where the Reynolds numbers are closer to the range studied.

We have assumed a smooth, fixed, two-dimensional, impermeable, periodic ripple bed to the modeling of flow above sand ripples which are considerably more complicated in nature. Some of the justifications and implications of these assumptions have been discussed in Chapter I. We shall now examine some effects they may have on our results.

The surface roughness due to individual sand grains has not been modeled due to the high spatial resolution it requires. From the flow pictures taken over mobile sand ripples, for example by Honji *et al* (1980), small scale separations are hardly visible, and their effects on the flow field are likely to be small.

When the ripple bed is mobile, part of the surface stresses acts to change the

inertia of the sand particles and therefore may reduce the actual forces measured had the ripple been fixed. Seepage through the sand also modifies the pressure along the ripple profile and reduces the magnitudes of the fluctuations that are calculated based on an impermeable boundary.

Despite that our formulation is for periodic bed profiles, considerable variations in the bottom geometry can be made from the generalized conformal mapping defined by (3.4.6) and (3.4.13). For example, the domain of computation can consist of two or more ripples with different geometries, both symmetric or asymmetric. Aside from the initial calculation of the Jacobian function, which is insignificant, the amount of computation is independent of the complexity of the bed profile.

The asymmetry over the two half periods may depend on the choice of initial conditions. Aside from defining a quiescent fluid at the start, a boundary layer solution or the solution in the limit of vanishing Reynolds number may be specified. These latter initial conditions have been used, for example, in Collins and Dennis (1973) and Ta Phuoc Loc and Bouard (1985) in the numerical solutions to the flow around circular cylinders. In addition, our ambient velocity is started as a step function (6.0.1). An alternative is to increase the amplitude of oscillation of the far field velocity to the final magnitude more gradually.

While our formulation does not require empirical parameters and is able to account for the detailed spatial variations of the flow field, its solution is limited by a upper limit in the Reynolds number. It is not uncommon to have Reynolds number of the order of 10^3 or even 10^4 in the field, and computations at such high values of R will be beyond the practical limit of supercomputers in the near future. Furthermore, the application of laminar flow equations to field conditions, which for all practical purposes are turbulent in nature, is inappropriate.

The simplest extension of our numerical scheme to turbulence modeling would

be by introducing an eddy viscosity in the vorticity equation. This can be easily accomplished by incorporating a coefficient that varies in both space and time in place of the Reynolds number in (3.1.10) and (4.1.9). Aside from that used in deducing the eddy viscosity, the amount of computation per time step in this case will be the same as in the laminar model since the vorticity equation is solved in the mapped plane. If we replace R in (4.5.2) with the maximum of the coefficient related to the eddy viscosity, the time step may not be different since the critical time step in the treatment of the convective terms may remain as the criterion for numerical stability. The expressions for the rate of energy dissipation, and the shear stress and pressure on the ripple, however, will have to be modified.

References

Arakawa, A. 1966. Computational design of long-term numerical integration of the equations of fluid motion: I. Two-dimensional incompressible flow. *Journal of Computational Physics* 1 (1): 119-143.

Aydin, I., and N. Shuto. 1985. A flow pattern on sand ripples due to waves and currents. (In Japanese) *Proceedings of the 32nd Japanese Conference on Coastal Engineering, Japan Society of Civil Engineers* 278-282.

Ayrton, H. 1910. The origin and growth of ripple-mark. *Proceedings of the Royal Society of London* A84: 185-310.

Badr, H. M., and S. C. R. Dennis. 1985. Time-dependent viscous flow past an impulsively started rotating and translating circular cylinder. *Journal of Fluid Mechanics* 158: 447-488.

Bagnold, R. A. 1946. Interaction between waves and sand bottoms. *Proceedings of the Royal Society of London* 187: 1-18.

Batchelor, G. K. 1967. *An Introduction to Fluid Dynamics.* Cambridge University Press.

Bayazit, M. 1969. Resistance to reversing flows over movable beds. *Journal of the Hydraulic Division, ASCE Proceedings* 95 (HY 4): 1109-1127.

Bender, C. M., and S. A. Orszag. 1978. *Advanced Mathematical Methods for Scientists and Engineers.* New York: McGraw-Hill.

Benjamin, T. B. 1959. Shearing flow over a wavy boundary. *Journal of Fluid Mechanics* 6: 161-205.

Bouard, R., and M. Coutanceau. 1980. The early stage of development of the wake behind an impulsively started cylinder for $40 < \text{Re} < 10^4$. *Journal of Fluid Mechanics* 101 (3): 583-607.

Brevik, I., and B. Aas. 1980. Flume experiment on waves and currents. I. Rippled bed. *Coastal Engineering* 3: 149-177.

Carslaw, H.S., and J. C. Jaeger. 1963. *Operational Methods in Applied Mathematics.* 2nd ed. New York: Dover.

Carstens, M. R., F. M. Neilson, and H. D. Altinbilek. 1969. Bed forms generated in the laboratory under an oscillatory flow: Analytical and experimental study. *Coastal Engineering Research Center, U.S. Army Corps of Engineers, Technical Memorandum No. 28.*

Collins, W. M., and S. C. R. Dennis. 1973a. Flow past an impulsively started circular cylinder. *Journal of Fluid Mechanics* 60: 105-127.

Collins, W. M., and S. C. R. Dennis. 1973b. The initial flow past an impulsively started circular cylinder. *Quarterly Journal of Mechanics and Applied Mathematics* 26: 53.

Cooley, J. W., and J. W. Tukey. 1966. An algorithm for the machine calculation of complex Fourier series. *Mathematics of Computation* 19: 297.

Coutanceau, M., and R. Bouard. 1977a. Experimental determination of the main features of the viscous flow in the wake of a circular cylinder in uniform translation. Part 1. Steady flow. *Journal of Fluid Mechanics* 79: 231.

Coutanceau, M., and R. Bouard. 1977b. Experimental determination of the main features of the viscous flow in the wake of a circular cylinder in uniform translation. Part 2. Unsteady flow. *Journal of Fluid Mechanics* 79: 257.

Crighton, D. G. 1985. The Kutta condition in unsteady flow. *Annual Review of Fluid Mechanics* 17: 411-445.

Darwin, G. H. 1883. On the formation of ripple-mark in sand. *Proceedings of the Royal Society of London* A36: 18-43.

Dingler, J. R., and D. L. Inman. 1976. Wave-formed ripples in nearshore sands. *Proceedings of the 14th Coastal Engineering Conference, Copenhagen, Denmark,* 2109-2126.

Du Toit, C. G., and Sleath, J. F. A. 1981. Velocity measurements close to the rippled beds in oscillatory flow. *Journal of Fluid Mechanics* 112: 71-96.

DuFort, E. C., and S. P. Frankel. 1953. Stability conditions in the numerical treatment of parabolic differential equations. *Math. of Comp.* 7: 135-152.

Fornberg, B. 1985. Steady viscous flow past a circular cylinder up to Reynolds number 600. *Journal of Computational Physics* 61: 297-320.

Gillani, N. V., and W. M. Swanson. 1976. Time-dependent laminar incompressible flow through a spherical cavity. *Journal of Fluid Mechanics* 78: 99-127.

Ghaddar, N. K., K. Z. Korczak, B. B. Mikic, and A. T. Patera. 1986a. Numerical investigation of incompressible flow in grooved channels. Part 1. Stability and self-sustained oscillations. *Journal of Fluid Mechanics* 163: 99-127.

Ghaddar, N. K., M. Magen, B. B. Mikic, and A. T. Patera. 1986b. Numerical investigation of incompressible flow in grooved channels. Part 2. Resonance and oscillatory heat-transfer enhancement. *Journal of Fluid Mechanics* 168: 541-567.

Grant, W. D. 1977. Bottom friction under waves in the presence of a weak current: It's relationship to coastal sediment transport. *Sc. D. Thesis, Department of Civil Engineering, Massachusetts Institute of Technology.*

Grant, W. D., and O. S. Madsen. 1979. Combined wave and current interaction with a rough bottom. *Journal of Geophysical Research* 84 (C4): 1797-1808.

Grant, W. D., and O. S. Madsen. 1982. Movable bed roughness in unsteady oscillatory flow. *Journal of Geophysical Research* 87 (C1): 469-481.

Hedegaard, I. B. 1985. Wave generated ripples and resulting sediment transport in waves. *Institute of Hydrodynamics and Hydraulic Engineering, Technical University of Denmark, Series Paper 36.*

Honji, H., A. Kaneko, and N. Matsunaga. 1980. Flows above oscillatory ripples. *Sedimentology* 27: 225-229.

Honji, H., and N. Matsunaga. 1979. Note on separation vortices above a wavy wall. (In Japanese) *Bulletin of the Research Institute of Applied Mechanics* 50: 81-86.

Hunt, A. R. 1882. On the formation of ripplemark. *Proceedings of the Royal Society of London* 34: 1-18.

Ikeda, S., and T. Asaeda. 1983. Sediment suspension with rippled bed. *Journal of Hydraulic Engineering, ASCE* 109 (3): 409-423.

Jonsson, I. G. 1963. Measurements in the turbulent wave boundary layer. *Tenth Congress of the International Association for Hydraulic Research*, London 85-92.

Jonsson, I. G. 1966. Wave boundary layers and friction factors. *Proceedings of the 7th ASCE Coastal Engineering Conference*, Tokyo, Japan 127-148.

Jonsson, I. G. 1980. A new approach to oscillatory rough turbulent boundary layers. *Ocean Engineering* 7: 109-152.

Jonsson, I. G., and N. A. Carlsen. 1976. Experimental and theoretical investigations in an oscillatory turbulent boundary layer. *Journal of Hydraulic Research* 14: 45-60.

Kajiura, K. 1968. A model of the bottom boundary layer in water waves. *Bulletin of the Earthquake Research Institute* 46: 75-123.

Kamphuis, J. W. 1975. Friction factor under oscillatory waves. *Journal of the Waterways, Harbors and Coastal Engineering Division, ASCE Proceedings* 101 (WW 2): 135-144.

Kaneko, A., and H. Honji. 1979. Double structures of steady streaming in the oscillatory viscous flow over a wavy wall. *Journal of Fluid Mechanics* 93 (4): 727-736.

von Karman, Th. 1911. Iber den Mechanismus des Widerstandes, den ein bewegter Koper in einer Flussigkeit erfahrt. (in German) Gottinger Nachrichten, math.-phys. K1: 509-517.

Kemp, P. H., and R. R. Simons. The interaction between waves and a turbulent current: Waves propagating with the current. *Journal of Fluid Mechanics* 116: 227-250.

Kennedy, J. F., and M. Falcon. 1965. Wave-generated sediment ripples. *Hydrodynamics Laboratory Report No. 86, Department of Civil Engineering, Massachusetts Institute of Technology.*

Kobayashi, N. 1979. Turbulent flows over a wavy boundary and formation of bed forms in erodible channels. *Ph. D. Thesis, Department of Civil Engineering, Massachusetts Institute of Technology.*

Kobayashi, N., and O. S. Madsen. 1985b. Formation of ripples in erodible

channels. *Journal of Geophysical Research* 90 (C4): 7332-7340.

Lecointe, Y., and J. Piquet. 1965. Compact finite-difference methods for solving incompressible Navier-Stokes equations around oscillating bodies. *Computational Fluid Dynamics, Lecture Series 1985-04, von Karman Institute for Fluid Dynamics* 2: 1-218.

Lofquist, K. E. B. 1978. Sand ripple Growth in an Oscillatory-flow water tunnel. *Coastal Engineering Research Center, U.S. Army Corps of Engineers, Technical Memorandum No. 78-5.*

Longuet-Higgins, M. S. 1981. Oscillating flow over steep sand ripples. *Journal of Fluid Mechanics* 107: 1-35.

Lyne, W. H. 1971. Unsteady viscous flow over a wavy wall. *Journal of Fluid Mechanics* 50 (1): 33-48.

Nakato, T., F. A. Locher, J. R. Glover, and J. F. Kennedy. 1977. Wave entrainment of sediment from rippled beds. *Journal of the waterway, port, coastal and ocean division, ASCE Proceedings* 103 (WW 1): 83-99.

Ralph, M. E. 1986. Oscillatory flows in wavy-walled tubes. *Journal of Fluid Mechanics* 168: 515-540.

Ralston, A., and Rabinowitz, P. 1978. *A First Course in Numerical Analysis.* 2nd ed. New York: McGraw-Hill.

Raudkivi, A. J. 1963. Study of sediment ripple formation. *Journal of the Hydraulic Division, ASCE Proceedings* 89 (Hy 6): 15-33.

Richards, K. J. 1980. The formation of ripples and dunes on an erodible bed. *Journal of Fluid Mechanics* 99 (3): 597-618.

Richtmyer, R. D., and K. W. Morton. 1967. *Difference Methods for Initial-value Problems.* 2nd ed. New York: Interscience Publishers, Wiley.

Rosenhead, L. 1931. The formation of vortices from a surface of discontinuity. *Proceedings of the Royal Society of London* A134: 170-192.

Sato, S., N. Mimura, and A. Watanabe. 1984. Oscillatory boundary layer flow over rippled beds. *Proceedings of the 19th ASCE Coastal Engineering Conference, Houston, TX* 2293-2309.

Schlichting, H. 1968. *Boundary-Layer Theory.* 7th ed. New York: McGraw-Hill.

Sleath, J. F. A. 1970. Velocity measurements close to the bed in a wave tank. *Journal of Fluid Mechanics* 42 (1): 111-123.

Sleath, J. F. A. 1973. A numerical study of the influence of bottom roughness on mass transport. *Proceedings of the International Conference on Numerical Methods in Fluid Dynamics,* University of Southampton, England: 482-493.

Sleath, J. F. A. 1974. Velocities above rough bed in oscillatory flow. *Journal of the Waterways, Harbors and Coastal Engineering Division, ASCE Proceedings* 100

(WW 4): 287-304.

Sleath, J. F. A. 1976. Forces on a rough bed in oscillatory flow. *Journal of Hydraulic Research* 14: 155-164.

Sleath, J. F. A. 1982. Friction coefficients of rippled beds in oscillatory flow. *Continental Shelf Research* 1 (1): 33-47.

Sleath, J. F. A. 1984. *Sea Bed Mechanics*. New York: John Wiley & Sons.

Sleath, J. F. A. 1985. Energy dissipation in oscillatory flow over rippled beds. *Coastal Engineering* 9: 159-170.

Sobey, I. J. 1980. On flow through furrowed channels. Part 1. Calculated flow patterns. *Journal of Fluid Mechanics* 96 (1): 1-26.

Sobey, I. J. 1982. Oscillatory flows at intermediate Strouhal number in asymmetric channels. *Journal of Fluid Mechanics* 125: 359-373.

Sobey, I. J. 1983. The occurence of separation in oscillatory flow. *Journal of Fluid Mechanics* 134: 247-257.

Stokes, G. G. 1851. On the effect of the internal friction of fluids on the motion of pendulums. *Cambridge Philosophical Transactions* IX: 8. Also in *Mathematics and Physics Papers* III: 1-141. Cambridge (1901).

Ta Phuoc Loc. 1980. Numerical analysis of unsteady secondary vortices generated by an impulsively started circular cylinder. *Journal of Fluid Mechanics* 100 (1): 111-128.

Ta Phuoc Loc, and R. Bouard. 1985. Numerical solution of the early stage of the unsteady viscous flow around a circular cylinder: a comparison with experimental visualization and measurements. *Journal of Fluid Mechanics* 160: 93-117.

Ta Phuoc Loc, and O. Daube. 1977. *C. R. Acad. Sc. Paris* 284: A1241.

Tanaka, H., and N. Shuto. 1987. Velocity measurements of wave-current combined motion over an asymmetric rippled bed. *ASCE Conference on Coastal Sediments*, New Orleans, LO 379-392.

Tunstall, E. B., and D. L. Inman. 1975. Vortex generation by oscillatory flow over rippled surfaces. *Journal of Geophysical Research* 80 (24): 3475-3484.

Vitale, P. 1979. Sand bed friction factors for oscillatory flows. *Journal of the Waterway, Port, Coastal and Ocean Division, ASCE Proceedings* 105 (WW 3): 229-245.

Williams, P. B., and P. H. Kemp. 1971. Initiation of ripples on flat sediment beds. *Journal of the Hydraulic Division, ASCE Proceedings* 97 (HY 4): 505-522.

Yalin, M. S. 1964. Geometrical properties of sand waves. *Journal of the Hydraulic Division, ASCE Proceedings* 90 (HY 5): 105-119.

Appendix I. Derivation of Navier–Stokes equations in transformed coordinates

§AI.1. Some basic identitites

Before deriving Navier–Stokes equations in transformed coordinates, we shall first establish a few equalities between derivatives in the original coordinates $(\tilde{x}, \tilde{y})$ and transformed coordinates (x, y). The mapping is assumed to be conformal such that Cauchy–Riemann relations

$$\frac{\partial \tilde{y}}{\partial y} = \frac{\partial \tilde{x}}{\partial x} \quad \text{and} \quad \frac{\partial \tilde{x}}{\partial y} = -\frac{\partial \tilde{y}}{\partial x} \tag{A1.1.1.2}$$

are satisfied. Henceforth all derivatives of $\tilde{x}$ or $\tilde{y}$ with respect to y will be expressed in terms of derivatives in x.

Derivatives for analytic functions f and g defined on $(\tilde{x}, \tilde{y})$,

$$\frac{\partial f}{\partial x} = \frac{\partial \tilde{x}}{\partial x}\frac{\partial f}{\partial \tilde{x}} + \frac{\partial \tilde{y}}{\partial x}\frac{\partial f}{\partial \tilde{y}} \tag{A1.1.3}$$

and

$$\frac{\partial f}{\partial y} = \frac{\partial \tilde{x}}{\partial y}\frac{\partial f}{\partial \tilde{x}} + \frac{\partial \tilde{y}}{\partial y}\frac{\partial f}{\partial \tilde{y}} = -\frac{\partial \tilde{y}}{\partial x}\frac{\partial f}{\partial \tilde{x}} + \frac{\partial \tilde{x}}{\partial x}\frac{\partial f}{\partial \tilde{y}} \tag{A1.1.4}$$

can be inverted to give

$$\frac{\partial f}{\partial \tilde{x}} = \frac{1}{J}\left(\frac{\partial \tilde{x}}{\partial x}\frac{\partial f}{\partial x} - \frac{\partial \tilde{y}}{\partial x}\frac{\partial f}{\partial y}\right) \tag{A1.1.5}$$

and

$$\frac{\partial f}{\partial \tilde{y}} = \frac{1}{J}\left(\frac{\partial \tilde{x}}{\partial x}\frac{\partial f}{\partial y} + \frac{\partial \tilde{y}}{\partial x}\frac{\partial f}{\partial x}\right), \tag{A1.1.6}$$

where J is the Jacobian of transformation,

$$J \equiv \begin{vmatrix} \dfrac{\partial \tilde{x}}{\partial x} & \dfrac{\partial \tilde{x}}{\partial y} \\[2mm] \dfrac{\partial \tilde{y}}{\partial x} & \dfrac{\partial \tilde{y}}{\partial y} \end{vmatrix} = \left(\frac{\partial \tilde{x}}{\partial x}\right)^2 + \left(\frac{\partial \tilde{y}}{\partial x}\right)^2 \tag{A1.1.7}$$

from Cauchy-Riemann conditions (A1.1.1) and (A1.1.2). Derivatives of the Jacobian are

$$\frac{\partial J}{\partial x} = 2\left(\frac{\partial \tilde{x}}{\partial x}\frac{\partial^2 \tilde{x}}{\partial x^2} + \frac{\partial \tilde{y}}{\partial x}\frac{\partial^2 \tilde{y}}{\partial x^2}\right) \tag{A1.1.8}$$

and

$$\frac{\partial J}{\partial y} = 2\left(-\frac{\partial \tilde{x}}{\partial x}\frac{\partial^2 \tilde{y}}{\partial x^2} + \frac{\partial \tilde{y}}{\partial x}\frac{\partial^2 \tilde{x}}{\partial x^2}\right), \tag{A1.1.9}$$

from (A1.1.1) to (A1.1.4).

From (A1.1.1), (A1.1.2), (A1.1.5), (A1.1.7), (A1.1.8), and (A1.1.9), the second-order derivative with respect to $\tilde{x}$ is given by

$$\frac{\partial^2 f}{\partial \tilde{x}^2} = \frac{1}{J}\left(\frac{\partial \tilde{x}}{\partial x}\frac{\partial}{\partial x} - \frac{\partial \tilde{y}}{\partial x}\frac{\partial}{\partial y}\right)\left[\frac{1}{J}\left(\frac{\partial \tilde{x}}{\partial x}\frac{\partial f}{\partial x} - \frac{\partial \tilde{y}}{\partial x}\frac{\partial f}{\partial y}\right)\right]$$

$$= \frac{1}{J^2}\left\{\frac{\partial \tilde{x}}{\partial x}\frac{\partial^2 \tilde{x}}{\partial x^2} + \frac{\partial \tilde{y}}{\partial x}\frac{\partial^2 \tilde{y}}{\partial x^2} - \frac{2}{J}\left[\left(\frac{\partial \tilde{x}}{\partial x}\right)^2\left(\frac{\partial \tilde{x}}{\partial x}\frac{\partial^2 \tilde{x}}{\partial x^2} + \frac{\partial \tilde{y}}{\partial x}\frac{\partial^2 \tilde{y}}{\partial x^2}\right)\right.\right.$$

$$\left.\left. - \frac{\partial \tilde{y}}{\partial x}\frac{\partial \tilde{x}}{\partial x}\frac{\partial \tilde{y}}{\partial x}\left(\frac{\partial \tilde{x}}{\partial x}\frac{\partial^2 \tilde{x}}{\partial x^2} - \frac{\partial \tilde{x}}{\partial x}\frac{\partial^2 \tilde{y}}{\partial x^2}\right)\right]\right\}\frac{\partial f}{\partial x} + \frac{1}{J^2}\left\{-\frac{\partial \tilde{x}}{\partial x}\frac{\partial^2 \tilde{y}}{\partial x^2} + \frac{\partial \tilde{y}}{\partial x}\frac{\partial^2 \tilde{x}}{\partial x^2}\right.$$

$$\left. - \frac{2}{J}\left[\left(\frac{\partial \tilde{y}}{\partial x}\right)^2\left(-\frac{\partial \tilde{x}}{\partial x}\frac{\partial^2 \tilde{y}}{\partial x^2} + \frac{\partial \tilde{y}}{\partial x}\frac{\partial^2 \tilde{x}}{\partial x^2}\right) - \frac{\partial \tilde{y}}{\partial x}\frac{\partial \tilde{x}}{\partial x}\left(\frac{\partial \tilde{x}}{\partial x}\frac{\partial^2 \tilde{x}}{\partial x^2} + \frac{\partial \tilde{y}}{\partial x}\frac{\partial^2 \tilde{y}}{\partial x^2}\right)\right]\right\}\frac{\partial f}{\partial y}$$

$$+ \frac{1}{J^2}\left[\left(\frac{\partial \tilde{x}}{\partial x}\right)^2\frac{\partial^2 f}{\partial x^2} + \left(\frac{\partial \tilde{y}}{\partial x}\right)^2\frac{\partial^2 f}{\partial y^2} - 2\frac{\partial \tilde{y}}{\partial x}\frac{\partial \tilde{x}}{\partial x}\frac{\partial^2 f}{\partial x\,\partial y}\right] \tag{A1.1.10}$$

after some algebra.

The second-order derivative with repect to $\tilde{y}$ can be infered from (A1.1.10) by using symmetry. Rotation through $\pi/2$ of both original and transformed coordinates is equivalent to replacing $(\tilde{x}, \tilde{y}; x, y)$ by $(-\tilde{y}, \tilde{x}; -y, x)$ respectively in (A1.1.10), and gives

$$\frac{\partial^2 f}{\partial \tilde{y}^2} = \frac{1}{J^2}\left\{-\frac{\partial \tilde{x}}{\partial x}\frac{\partial^2 \tilde{y}}{\partial x^2} + \frac{\partial \tilde{y}}{\partial x}\frac{\partial^2 \tilde{x}}{\partial x^2} - \frac{2}{J}\left[\left(\frac{\partial \tilde{x}}{\partial x}\right)^2\left(-\frac{\partial \tilde{x}}{\partial x}\frac{\partial^2 \tilde{y}}{\partial x^2} + \frac{\partial \tilde{y}}{\partial x}\frac{\partial^2 \tilde{x}}{\partial x^2}\right)\right.\right.$$

$$+ \frac{\partial \tilde{y}}{\partial x}\frac{\partial \tilde{x}}{\partial x}\left(\frac{\partial \tilde{y}}{\partial x}\frac{\partial^2 \tilde{y}}{\partial x^2} + \frac{\partial \tilde{x}}{\partial x}\frac{\partial^2 \tilde{x}}{\partial x^2}\right)\}] \frac{\partial f}{\partial y} + \frac{1}{J^2}\{\frac{\partial \tilde{x}}{\partial x}\frac{\partial^2 \tilde{x}}{\partial x^2} + \frac{\partial \tilde{y}}{\partial x}\frac{\partial^2 \tilde{y}}{\partial x^2}$$

$$- \frac{2}{J}\left[\left(\frac{\partial \tilde{y}}{\partial x}\right)^2\left(\frac{\partial \tilde{x}}{\partial x}\frac{\partial^2 \tilde{x}}{\partial x^2} + \frac{\partial \tilde{y}}{\partial x}\frac{\partial^2 \tilde{y}}{\partial x^2}\right) - + 2\frac{\partial \tilde{y}}{\partial x}\frac{\partial \tilde{x}}{\partial x}\left(-\frac{\partial \tilde{x}}{\partial x}\frac{\partial^2 \tilde{y}}{\partial x^2} + \frac{\partial \tilde{y}}{\partial x}\frac{\partial^2 \tilde{x}}{\partial x^2}\right)\}] \frac{\partial f}{\partial x}$$

$$+ \frac{1}{J^2}\left[\left(\frac{\partial \tilde{x}}{\partial x}\right)^2\frac{\partial^2 f}{\partial y^2} + \left(\frac{\partial \tilde{y}}{\partial x}\right)^2\frac{\partial^2 f}{\partial x^2} + 2\frac{\partial \tilde{y}}{\partial x}\frac{\partial \tilde{x}}{\partial x}\frac{\partial^2 f}{\partial x\,\partial y}\right] \tag{A1.1.11}$$

where Cauchy-Riemann relations have been used.

§AI.2. The Jacobian

Equations (A1.1.5) and (A1.1.6) give

$$\frac{\partial f}{\partial \tilde{y}}\frac{\partial g}{\partial \tilde{x}} = \frac{1}{J^2}\left(\frac{\partial \tilde{x}}{\partial x}\frac{\partial f}{\partial y} + \frac{\partial \tilde{y}}{\partial x}\frac{\partial f}{\partial x}\right)\left(\frac{\partial \tilde{x}}{\partial x}\frac{\partial g}{\partial x} - \frac{\partial \tilde{y}}{\partial x}\frac{\partial g}{\partial y}\right) \tag{A1.2.1}$$

and

$$\frac{\partial f}{\partial \tilde{x}}\frac{\partial g}{\partial \tilde{y}} = \frac{1}{J^2}\left(\frac{\partial \tilde{x}}{\partial x}\frac{\partial f}{\partial x} - \frac{\partial \tilde{y}}{\partial x}\frac{\partial f}{\partial y}\right)\left(\frac{\partial \tilde{x}}{\partial x}\frac{\partial g}{\partial y} + \frac{\partial \tilde{y}}{\partial x}\frac{\partial g}{\partial x}\right). \tag{A1.2.2}$$

Subtracting (A1.2.2) from (A1.2.1) gives (3.1.9.a),

$$\frac{\partial f}{\partial \tilde{y}}\frac{\partial g}{\partial \tilde{x}} - \frac{\partial f}{\partial \tilde{x}}\frac{\partial g}{\partial \tilde{y}} = \frac{1}{J^2}\left\{\frac{\partial f}{\partial y}\frac{\partial g}{\partial x}\left[\left(\frac{\partial \tilde{x}}{\partial x}\right)^2 + \left(\frac{\partial \tilde{y}}{\partial x}\right)^2\right] - \frac{\partial f}{\partial x}\frac{\partial g}{\partial y}\left[\left(\frac{\partial \tilde{x}}{\partial x}\right)^2 + \left(\frac{\partial \tilde{y}}{\partial x}\right)^2\right]\right\}$$

$$= \frac{1}{J}\left(\frac{\partial f}{\partial y}\frac{\partial g}{\partial x} - \frac{\partial f}{\partial x}\frac{\partial g}{\partial y}\right), \tag{A1.2.3}$$

using (A1.1.7).

§AI.3. The Laplacian

The sum of (A1.1.10) and (A1.1.11) can be simplified to give (3.1.9.b),

$$\frac{\partial^2 f}{\partial \tilde{x}^2} + \frac{\partial^2 f}{\partial \tilde{y}^2} = \frac{1}{J}\left(\frac{\partial^2 f}{\partial x^2} + \frac{\partial^2 f}{\partial y^2}\right). \tag{A1.3.1}$$

§AI.4. The Wave Operator

The difference of (A1.1.10) and (A1.1.11) can be simplified to give (3.2.13.a),

$$\frac{\partial^2 f}{\partial \tilde{x}^2} - \frac{\partial^2 f}{\partial \tilde{y}^2} = \frac{1}{J^2}\{[(\frac{\partial \tilde{x}}{\partial x})^2 - (\frac{\partial \tilde{y}}{\partial x})^2](\frac{\partial^2 f}{\partial x^2} - \frac{\partial^2 f}{\partial y^2}) - 4\frac{\partial \tilde{x}}{\partial x}\frac{\partial \tilde{y}}{\partial x}\frac{\partial^2 f}{\partial x \partial y}\}$$

$$+ \frac{2}{J^3}\{[\frac{\partial \tilde{x}}{\partial x}\frac{\partial^2 \tilde{x}}{\partial x^2}[3(\frac{\partial \tilde{y}}{\partial x})^2 - (\frac{\partial \tilde{x}}{\partial x})^2] + \frac{\partial \tilde{y}}{\partial x}\frac{\partial^2 \tilde{y}}{\partial x^2}[(\frac{\partial \tilde{y}}{\partial x})^2 - 3(\frac{\partial \tilde{x}}{\partial x})^2]\}\frac{\partial f}{\partial x}$$

$$+ \frac{2}{J^3}\{[-\frac{\partial \tilde{y}}{\partial x}\frac{\partial^2 \tilde{x}}{\partial x^2}[(\frac{\partial \tilde{y}}{\partial x})^2 - 3(\frac{\partial \tilde{x}}{\partial x})^2] - \frac{\partial \tilde{x}}{\partial x}\frac{\partial^2 \tilde{y}}{\partial x^2}[(\frac{\partial \tilde{x}}{\partial x})^2 - 3(\frac{\partial \tilde{y}}{\partial x})^2]\}\frac{\partial f}{\partial y}. \qquad (A1.4.1)$$

§AI.5. The Cross Derivatives

Equations (A1.1.5) and (A1.1.6) give (3.2.13.b),

$$\frac{\partial^2 f}{\partial \tilde{x} \partial \tilde{y}} = \frac{1}{J}(\frac{\partial \tilde{x}}{\partial x}\frac{\partial}{\partial x} - \frac{\partial \tilde{y}}{\partial x}\frac{\partial}{\partial y})[\frac{1}{J}(\frac{\partial \tilde{x}}{\partial x}\frac{\partial f}{\partial y} + \frac{\partial \tilde{y}}{\partial x}\frac{\partial f}{\partial x})]$$

$$= \frac{1}{J^2}\{\frac{\partial \tilde{x}}{\partial x}\frac{\partial \tilde{y}}{\partial x}(\frac{\partial^2 f}{\partial x^2} - \frac{\partial^2 f}{\partial y^2}) + [(\frac{\partial \tilde{x}}{\partial x})^2 - (\frac{\partial \tilde{y}}{\partial x})^2]\frac{\partial^2 f}{\partial x \partial y}\}$$

$$+ \frac{1}{J^3}\{[\frac{\partial \tilde{x}}{\partial x}\frac{\partial^2 \tilde{y}}{\partial x^2}[(\frac{\partial \tilde{x}}{\partial x})^2 - 3(\frac{\partial \tilde{y}}{\partial x})^2] + \frac{\partial \tilde{y}}{\partial x}\frac{\partial^2 \tilde{x}}{\partial x^2}[(\frac{\partial \tilde{y}}{\partial x})^2 - 3(\frac{\partial \tilde{x}}{\partial x})^2]\}\frac{\partial f}{\partial x}$$

$$+ \frac{1}{J^3}\{[\frac{\partial \tilde{y}}{\partial x}\frac{\partial^2 \tilde{y}}{\partial x^2}[(\frac{\partial \tilde{y}}{\partial x})^2 - 3(\frac{\partial \tilde{x}}{\partial x})^2] - \frac{\partial \tilde{x}}{\partial x}\frac{\partial^2 \tilde{x}}{\partial x^2}[(\frac{\partial \tilde{x}}{\partial x})^2 - 3(\frac{\partial \tilde{y}}{\partial x})^2]\}\frac{\partial f}{\partial y}. \qquad (A1.5.1)$$

§AI.6. The Convective Terms

The convective terms in the Navier-Stokes equation in transformed coordinates are

$$\frac{\partial \tilde{x}}{\partial x}[\frac{\partial \psi}{\partial y}\frac{\partial}{\partial x}(\frac{\partial \psi}{\partial \tilde{x}}) - \frac{\partial \psi}{\partial x}\frac{\partial}{\partial y}(\frac{\partial \psi}{\partial \tilde{x}})] + \frac{\partial \tilde{y}}{\partial x}[\frac{\partial \psi}{\partial y}\frac{\partial}{\partial x}(\frac{\partial \psi}{\partial \tilde{y}}) - \frac{\partial \psi}{\partial x}\frac{\partial}{\partial y}(\frac{\partial \psi}{\partial \tilde{y}})]$$

$$= \frac{\partial \tilde{x}}{\partial x}\{\frac{\partial \psi}{\partial y}\frac{\partial}{\partial x}[\frac{1}{J}(\frac{\partial \tilde{x}}{\partial x}\frac{\partial \psi}{\partial x} - \frac{\partial \tilde{y}}{\partial x}\frac{\partial \psi}{\partial y})] - \frac{\partial \psi}{\partial x}\frac{\partial}{\partial y}[\frac{1}{J}(\frac{\partial \tilde{x}}{\partial x}\frac{\partial \psi}{\partial x} - \frac{\partial \tilde{y}}{\partial x}\frac{\partial \psi}{\partial y})]$$

$$+ \frac{\partial \tilde{y}}{\partial x} \{ \frac{\partial \psi}{\partial y} \frac{\partial}{\partial x} \frac{1}{J} [- (\frac{\partial \tilde{x}}{\partial x} \frac{\partial \psi}{\partial y} + \frac{\partial \tilde{y}}{\partial x} \frac{\partial \psi}{\partial x})] - \frac{\partial \psi}{\partial x} \frac{\partial}{\partial y} \frac{1}{J} [- (\frac{\partial \tilde{x}}{\partial x} \frac{\partial \psi}{\partial y} + \frac{\partial \tilde{y}}{\partial x} \frac{\partial \psi}{\partial x})]]\}$$

$$= \frac{\partial \psi}{\partial y} \frac{\partial^2 \psi}{\partial x^2} - \frac{\partial \psi}{\partial x} \frac{\partial^2 \psi}{\partial x \partial y} + \frac{1}{2J} \frac{\partial J}{\partial y} [(\frac{\partial \psi}{\partial x})^2 + (\frac{\partial \psi}{\partial y})^2] \ , \tag{A1.6.1}$$

upon substitution of (A1.1.5) through (A1.1.9), and

$$\frac{\partial \tilde{x}}{\partial x} [\frac{\partial \psi}{\partial x} \frac{\partial}{\partial y} (\frac{\partial \psi}{\partial \tilde{y}}) - \frac{\partial \psi}{\partial y} \frac{\partial}{\partial x} (\frac{\partial \psi}{\partial \tilde{y}})]] + \frac{\partial \tilde{y}}{\partial x} [\frac{\partial \psi}{\partial y} \frac{\partial}{\partial x} (\frac{\partial \psi}{\partial \tilde{x}}) - \frac{\partial \psi}{\partial x} \frac{\partial}{\partial y} (\frac{\partial \psi}{\partial \tilde{x}})]$$

$$= \frac{\partial \tilde{x}}{\partial x} \{ \frac{\partial \psi}{\partial x} \frac{\partial}{\partial y} \frac{1}{J} [- (\frac{\partial \tilde{x}}{\partial x} \frac{\partial \psi}{\partial y} + \frac{\partial \tilde{y}}{\partial x} \frac{\partial \psi}{\partial x})] - \frac{\partial \psi}{\partial y} \frac{\partial}{\partial x} \frac{1}{J} [- (\frac{\partial \tilde{x}}{\partial x} \frac{\partial \psi}{\partial y} + \frac{\partial \tilde{y}}{\partial x} \frac{\partial \psi}{\partial x})]]\}$$

$$+ \frac{\partial \tilde{y}}{\partial x} \{ \frac{\partial \psi}{\partial y} \frac{\partial}{\partial x} \frac{1}{J} [- (\frac{\partial \tilde{x}}{\partial x} \frac{\partial \psi}{\partial x} - \frac{\partial \tilde{y}}{\partial x} \frac{\partial \psi}{\partial y})] - \frac{\partial \psi}{\partial x} \frac{\partial}{\partial y} \frac{1}{J} [- (\frac{\partial \tilde{x}}{\partial x} \frac{\partial \psi}{\partial x} - \frac{\partial \tilde{y}}{\partial x} \frac{\partial \psi}{\partial y})]]$$

$$= \frac{\partial \psi}{\partial x} \frac{\partial^2 \psi}{\partial y^2} - \frac{\partial \psi}{\partial y} \frac{\partial^2 \psi}{\partial x \partial y} + \frac{1}{2J} \frac{\partial J}{\partial x} [(\frac{\partial \psi}{\partial x})^2 + (\frac{\partial \psi}{\partial y})^2] \ . \tag{A1.6.2}$$

§AI.7. The Navier–Stokes equations

In terms of streamfunction and nondimensionalized variables defined in (3.1.3) and (3.1.4), the Navier–Stokes equations can be written as

$$\frac{\partial}{\partial t} (\frac{\partial \psi}{\partial \tilde{y}}) + K [\frac{\partial \psi}{\partial \tilde{y}} \frac{\partial}{\partial \tilde{x}} (\frac{\partial \psi}{\partial \tilde{y}}) - \frac{\partial \psi}{\partial \tilde{x}} \frac{\partial}{\partial \tilde{y}} (\frac{\partial \psi}{\partial \tilde{y}})]$$

$$= - K \frac{\partial p}{\partial \tilde{x}} + s \frac{K}{R} [\frac{\partial^2}{\partial \tilde{x}^2} (\frac{\partial \psi}{\partial \tilde{y}}) + \frac{\partial^2}{\partial \tilde{y}^2} (\frac{\partial \psi}{\partial \tilde{y}})] \tag{A1.7.1}$$

and

$$\frac{\partial}{\partial t} (\frac{\partial \psi}{\partial \tilde{x}}) + K [\frac{\partial \psi}{\partial \tilde{y}} \frac{\partial}{\partial \tilde{x}} (\frac{\partial \psi}{\partial \tilde{x}}) - \frac{\partial \psi}{\partial \tilde{x}} \frac{\partial}{\partial \tilde{y}} (\frac{\partial \psi}{\partial \tilde{x}})]$$

$$= K \frac{\partial p}{\partial \tilde{y}} + s \frac{K}{R} [\frac{\partial^2}{\partial \tilde{x}^2} (\frac{\partial \psi}{\partial \tilde{x}}) + \frac{\partial^2}{\partial \tilde{y}^2} (\frac{\partial \psi}{\partial \tilde{x}})] \tag{A1.7.2}$$

From (A1.1.6),

$$K \frac{\partial p}{\partial y} = K (\frac{\partial \tilde{x}}{\partial x} \frac{\partial p}{\partial \tilde{y}} - \frac{\partial \tilde{y}}{\partial x} \frac{\partial p}{\partial \tilde{x}}) \ . \tag{A1.7.3}$$

Substitution of (A1.7.1) and (A1.7.2) into (A1.7.3) gives

$$K \frac{\partial p}{\partial y} = K \left\{ \frac{\partial \tilde{x}}{\partial x} \left[\frac{\partial \psi}{\partial \tilde{y}} \frac{\partial}{\partial \tilde{x}} \left(\frac{\partial \psi}{\partial \tilde{x}} \right) - \frac{\partial \psi}{\partial \tilde{x}} \frac{\partial}{\partial \tilde{y}} \left(\frac{\partial \psi}{\partial \tilde{x}} \right) \right] + \frac{\partial \tilde{y}}{\partial x} \left[\frac{\partial \psi}{\partial \tilde{y}} \frac{\partial}{\partial \tilde{x}} \left(\frac{\partial \psi}{\partial \tilde{y}} \right) - \frac{\partial \psi}{\partial \tilde{x}} \frac{\partial}{\partial \tilde{y}} \left(\frac{\partial \psi}{\partial \tilde{y}} \right) \right] \right\}$$

$$- s \frac{K}{R} \left\{ \frac{\partial \tilde{x}}{\partial x} \left[\frac{\partial^2}{\partial \tilde{x}^2} \left(\frac{\partial \psi}{\partial \tilde{x}} \right) + \frac{\partial^2}{\partial \tilde{y}^2} \left(\frac{\partial \psi}{\partial \tilde{x}} \right) \right] + \frac{\partial \tilde{y}}{\partial x} \left[\frac{\partial^2}{\partial \tilde{x}^2} \left(\frac{\partial \psi}{\partial \tilde{y}} \right) + \frac{\partial^2}{\partial \tilde{y}^2} \left(\frac{\partial \psi}{\partial \tilde{y}} \right) \right] \right\}$$

$$+ \frac{\partial}{\partial t} \left(\frac{\partial \tilde{x}}{\partial x} \frac{\partial \psi}{\partial \tilde{x}} + \frac{\partial \tilde{y}}{\partial x} \frac{\partial \psi}{\partial \tilde{y}} \right) . \tag{A1.7.4}$$

From (A1.2.3) and (A1.6.1), the convective term (first term on the right hand side of (A1.7.4)) can be rewritten as

$$K \left\{ \frac{\partial \tilde{x}}{\partial x} \left[\frac{\partial \psi}{\partial \tilde{y}} \frac{\partial}{\partial \tilde{x}} \left(\frac{\partial \psi}{\partial \tilde{x}} \right) - \frac{\partial \psi}{\partial \tilde{x}} \frac{\partial}{\partial \tilde{y}} \left(\frac{\partial \psi}{\partial \tilde{x}} \right) \right] + \frac{\partial \tilde{y}}{\partial x} \left[\frac{\partial \psi}{\partial \tilde{y}} \frac{\partial}{\partial \tilde{x}} \left(\frac{\partial \psi}{\partial \tilde{y}} \right) - \frac{\partial \psi}{\partial \tilde{x}} \frac{\partial}{\partial \tilde{y}} \left(\frac{\partial \psi}{\partial \tilde{y}} \right) \right] \right\}$$

$$= K \left\{ \frac{\partial \tilde{x}}{\partial x} \left[\frac{\partial \psi}{\partial y} \frac{\partial}{\partial x} \left(\frac{\partial \psi}{\partial \tilde{x}} \right) - \frac{\partial \psi}{\partial x} \frac{\partial}{\partial y} \left(\frac{\partial \psi}{\partial \tilde{x}} \right) \right] + \frac{\partial \tilde{y}}{\partial x} \left[\frac{\partial \psi}{\partial y} \frac{\partial}{\partial x} \left(\frac{\partial \psi}{\partial \tilde{y}} \right) - \frac{\partial \psi}{\partial x} \frac{\partial}{\partial y} \left(\frac{\partial \psi}{\partial \tilde{y}} \right) \right] \right\}$$

$$= K \left\{ \frac{\partial \psi}{\partial y} \frac{\partial^2 \psi}{\partial x^2} - \frac{\partial \psi}{\partial x} \frac{\partial^2 \psi}{\partial x \, \partial y} + \frac{1}{2J} \frac{\partial J}{\partial y} \left[\left(\frac{\partial \psi}{\partial x} \right)^2 + \left(\frac{\partial \psi}{\partial y} \right)^2 \right] \right\} . \tag{A1.7.5}$$

From (A1.1.4) and (A1.3.1), the viscous term (second term on the right hand side of (A1.7.4)) can be rewritten as

$$- s \frac{K}{R} \left\{ \frac{\partial \tilde{x}}{\partial x} \left[\frac{\partial^2}{\partial \tilde{x}^2} \left(\frac{\partial \psi}{\partial \tilde{x}} \right) + \frac{\partial^2}{\partial \tilde{y}^2} \left(\frac{\partial \psi}{\partial \tilde{x}} \right) \right] + \frac{\partial \tilde{y}}{\partial x} \left[\frac{\partial^2}{\partial \tilde{x}^2} \left(\frac{\partial \psi}{\partial \tilde{y}} \right) + \frac{\partial^2}{\partial \tilde{y}^2} \left(\frac{\partial \psi}{\partial \tilde{y}} \right) \right] \right\}$$

$$= - s \frac{K}{R} \left[\frac{\partial \tilde{x}}{\partial x} \frac{\partial}{\partial \tilde{x}} \left(\frac{\partial^2 \psi}{\partial \tilde{x}^2} + \frac{\partial^2 \psi}{\partial \tilde{y}^2} \right) + \frac{\partial \tilde{y}}{\partial x} \frac{\partial}{\partial \tilde{y}} \left(\frac{\partial^2 \psi}{\partial \tilde{x}^2} + \frac{\partial^2 \psi}{\partial \tilde{y}^2} \right) \right] = - s \frac{K}{R} \frac{\partial}{\partial y} \left[\frac{1}{J} \left(\frac{\partial^2 \psi}{\partial x^2} + \frac{\partial^2 \psi}{\partial y^2} \right) \right] .$$

Substitution of the preceeding results into equation (A1.7.4) gives

$$K \frac{\partial p}{\partial y} = \frac{\partial}{\partial t} \left(\frac{\partial \psi}{\partial x} \right) + K \left\{ \frac{1}{J} \left(\frac{\partial \psi}{\partial y} \frac{\partial^2 \psi}{\partial x^2} - \frac{\partial \psi}{\partial x} \frac{\partial^2 \psi}{\partial x \, \partial y} \right) - \frac{1}{2} \frac{\partial}{\partial y} \left(\frac{1}{J} \right) \left[\left(\frac{\partial \psi}{\partial x} \right)^2 + \left(\frac{\partial \psi}{\partial y} \right)^2 \right] \right\}$$

$$- s \frac{K}{R} \frac{\partial}{\partial x} \left[\frac{1}{J} \left(\frac{\partial^2 \psi}{\partial x^2} + \frac{\partial^2 \psi}{\partial y^2} \right) \right] . \tag{A1.7.6}$$

Similarly,

$$K \frac{\partial p}{\partial x} = K \left(\frac{\partial \tilde{x}}{\partial x} \frac{\partial p}{\partial \tilde{x}} + \frac{\partial \tilde{y}}{\partial x} \frac{\partial p}{\partial \tilde{y}} \right)$$

$$= K \left\{ \frac{\partial \tilde{x}}{\partial x} \left[\frac{\partial \psi}{\partial \tilde{x}} \frac{\partial}{\partial \tilde{y}} \left(\frac{\partial \psi}{\partial \tilde{y}} \right) - \frac{\partial \psi}{\partial \tilde{y}} \frac{\partial}{\partial \tilde{x}} \left(\frac{\partial \psi}{\partial \tilde{y}} \right) \right] + \frac{\partial \tilde{y}}{\partial x} \left[\frac{\partial \psi}{\partial \tilde{y}} \frac{\partial}{\partial \tilde{x}} \left(\frac{\partial \psi}{\partial \tilde{x}} \right) - \frac{\partial \psi}{\partial \tilde{x}} \frac{\partial}{\partial \tilde{y}} \left(\frac{\partial \psi}{\partial \tilde{x}} \right) \right] \right\}$$

$$+ s \frac{K}{R} \left\{ \frac{\partial \tilde{x}}{\partial x} \left[\frac{\partial^2}{\partial \tilde{x}^2} \left(\frac{\partial \psi}{\partial \tilde{y}} \right) + \frac{\partial^2}{\partial \tilde{y}^2} \left(\frac{\partial \psi}{\partial \tilde{y}} \right) \right] - \frac{\partial \tilde{y}}{\partial x} \left[\frac{\partial^2}{\partial \tilde{x}^2} \left(\frac{\partial \psi}{\partial \tilde{x}} \right) + \frac{\partial^2}{\partial \tilde{y}^2} \left(\frac{\partial \psi}{\partial \tilde{x}} \right) \right] \right\} - \frac{\partial}{\partial t} \left(\frac{\partial \tilde{x}}{\partial x} \frac{\partial \psi}{\partial \tilde{y}} - \frac{\partial \tilde{y}}{\partial x} \frac{\partial \psi}{\partial \tilde{x}} \right)$$

$$= K \left\{ \frac{\partial \tilde{x}}{\partial x} \left[\frac{\partial \psi}{\partial x} \frac{\partial}{\partial y} \left(\frac{\partial \psi}{\partial \tilde{y}} \right) - \frac{\partial \psi}{\partial y} \frac{\partial}{\partial x} \left(\frac{\partial \psi}{\partial \tilde{y}} \right) \right] + \frac{\partial \tilde{y}}{\partial x} \left[\frac{\partial \psi}{\partial y} \frac{\partial}{\partial x} \left(\frac{\partial \psi}{\partial \tilde{x}} \right) - \frac{\partial \psi}{\partial x} \frac{\partial}{\partial y} \left(\frac{\partial \psi}{\partial \tilde{x}} \right) \right] \right\}$$

$$+ s \frac{K}{R} \left[\frac{\partial \tilde{x}}{\partial x} \frac{\partial}{\partial \tilde{y}} \left(\frac{\partial^2 \psi}{\partial \tilde{x}^2} + \frac{\partial^2 \psi}{\partial \tilde{y}^2} \right) - \frac{\partial \tilde{y}}{\partial x} \frac{\partial}{\partial \tilde{x}} \left(\frac{\partial^2 \psi}{\partial \tilde{x}^2} + \frac{\partial^2 \psi}{\partial \tilde{y}^2} \right) \right] - \frac{\partial}{\partial t} \left(\frac{\partial \tilde{x}}{\partial x} \frac{\partial \psi}{\partial \tilde{y}} - \frac{\partial \tilde{y}}{\partial x} \frac{\partial \psi}{\partial \tilde{x}} \right)$$

$$= K \left\{ \frac{\partial \psi}{\partial x} \frac{\partial^2 \psi}{\partial y^2} - \frac{\partial \psi}{\partial y} \frac{\partial^2 \psi}{\partial x \partial y} + \frac{1}{2J} \frac{\partial J}{\partial x} \left[\left(\frac{\partial \psi}{\partial x} \right)^2 + \left(\frac{\partial \psi}{\partial y} \right)^2 \right] \right\} - \frac{\partial}{\partial t} \left(\frac{\partial \tilde{x}}{\partial x} \frac{\partial \psi}{\partial \tilde{y}} - \frac{\partial \tilde{y}}{\partial x} \frac{\partial \psi}{\partial \tilde{x}} \right)$$

$$+ s \frac{K}{R} \left\{ \frac{\partial \tilde{x}}{\partial x} \frac{\partial}{\partial \tilde{y}} \left[\frac{1}{J} \left(\frac{\partial^2 \psi}{\partial x^2} + \frac{\partial^2 \psi}{\partial y^2} \right) \right] - \frac{\partial \tilde{y}}{\partial x} \frac{\partial}{\partial \tilde{x}} \left[\frac{1}{J} \left(\frac{\partial^2 \psi}{\partial x^2} + \frac{\partial^2 \psi}{\partial y^2} \right) \right] \right\}$$

$$= - \frac{\partial}{\partial t} \left(\frac{\partial \psi}{\partial y} \right) + K \left\{ \frac{1}{J} \left(\frac{\partial \psi}{\partial x} \frac{\partial^2 \psi}{\partial y^2} - \frac{\partial \psi}{\partial y} \frac{\partial^2 \psi}{\partial x \partial y} \right) - \frac{1}{2} \frac{\partial}{\partial x} \left(\frac{1}{J} \right) \left[\left(\frac{\partial \psi}{\partial x} \right)^2 + \left(\frac{\partial \psi}{\partial y} \right)^2 \right] \right\}$$

$$+ s \frac{K}{R} \frac{\partial}{\partial y} \left[\frac{1}{J} \left(\frac{\partial^2 \psi}{\partial x^2} + \frac{\partial^2 \psi}{\partial y^2} \right) \right] . \tag{A1.7.7}$$

The identities in (A1.1.3), (A1.1.5), (A1.2.3), (A1.3.1), and (A1.6.2) have been used.

Appendix II. Variable grid-spacings : definition and differencing formulas

A mesh of variable size grids in the vertical direction is used in the computation, with grid points defined in (4.4.3) to (4.4.7). Details on the definition of these grid points, differencing formulae for spatial derivatives for non-uniform grids (both inside the domain of computation and at boundaries), compact differencing formula, and their discretization errors, will be presented in this appendix.

§AII.1. Set-up of grids in the y direction

The domain of computation is divided into two regions. The lower region consists of a layer of five to ten fine grids and is required to resolve the velocity profile immediately above the surface of ripple. Its thickness is estimated from that of the corresponding viscous boundary sublayer, δ_p in (4.4.1), due to an oscillatory flow over a plane bed. The h+1 grid points in this layer are then defined as

$$y_1 = 0 \,, \quad y_2 = \frac{\delta}{h} \,, \quad y_3 = \frac{2}{h}\delta \,, \quad \dots \,, \quad y_{h+1} = \delta \,. \tag{A2.1.1}$$

It is shown in §V.1 that five grids (h=5) are sufficient to resolve this velocity profile accurately.

For the upper region, grid spacing increases exponentially with increasing y in $\delta \leq y \leq y_{max}$, where y_{max} is the vertical extent of computation. To define grids in this second domain, we introduce local coordinates

$$\hat{y} = y - \delta \,, \tag{A2.1.2}$$

$$\hat{y}_j = y_{j+h} - \delta \,,$$

and let

$$z = \frac{1}{a}\ln(1 + b\hat{y}) \,, \quad \hat{y} = \frac{1}{b}(e^{az} - 1) \,. \tag{A2.1.3,4}$$

Parameters a, b are to be chosen such that:

(i) the first grid spacing is the same as that inside the viscid sublayer,

$$\hat{y}_2 - \hat{y}_1 = \frac{1}{b}(e^{a\Delta z} - 1) = \frac{\delta}{h} ; \qquad (A2.1.5)$$

(ii) the upper boundary corresponds to z=1,

$$y_{max} - \delta = \frac{1}{b}(e^a - 1) ; \text{ and} \qquad (A2.1.6)$$

(iii) the size of the last (uppermost) grid spacing is H times that of the first (lowest),

$$\frac{1}{b}e^a [1 - e^{-a\Delta z}] = H\frac{\delta}{h}. \qquad (A2.1.7)$$

Equations (A2.1.5) to (A2.1.7) can be solved to give

$$a = \frac{\ln H}{1 - \Delta z}, \quad b = \frac{h}{\delta}[H^{\Delta z/(1-\Delta z)} - 1] , \qquad (A2.1.8,9)$$

and

$$\Delta z = 1 - \frac{\ln H}{\ln H + \ln (1 - \theta) - \ln (1 - H\theta)} ,$$

where

$$\theta = \frac{\delta}{h}\frac{1}{y_{max} - \delta} .$$

The grid points $y_{j+h} = \hat{y}_j + \delta$ are then defined as

$$y_{h+2} = \delta + \frac{1}{b}(e^{a\,\Delta z} - 1) , \quad y_{h+3} = \delta + \frac{1}{b}(e^{a2\Delta z} - 1) , \quad ...,$$

$$y_{h+n} = \delta + \frac{1}{b}[e^{a(n-1)\Delta z} - 1], \quad ..., \quad y_N = \delta + \frac{1}{b}(e^a - 1) = y_{max} .$$

§AII.2. Spatial derivatives over non-uniform grids

Formulae for finite differencing in grids of variable size, and the truncation errors involved, will be presented in this section. These are second order (or pseudo second-order) centered-differencing schemes except when used in boundary

303

conditions, which are one-sided differencing schemes.

Let grid-spacings in the y-ordinate with grid points

$$y_1, \ y_2, \ \ldots, \ y_N$$

be denoted as

$$\Delta_1 = y_2 - y_1, \quad \Delta_2 = y_3 - y_2, \quad \ldots, \quad \Delta_n = y_{n+1} - y_n,$$

$$\ldots, \quad \Delta_{N-1} = y_N - y_{N-1}.$$

Let function ϕ of y be defined as

$$\phi_j = \phi(y_j).$$

The differencing formulae for derivatives at y_j,

$$\frac{\partial \phi}{\partial y} = \frac{1}{\Delta_{j-1}\Delta_j(\Delta_{j-1}+\Delta_j)} [\Delta_{j-1}^2 \phi_{j+1} + (\Delta_j^2 - \Delta_{j-1}^2)\phi_j - \Delta_j^2 \phi_{j-1}]$$

$$- \frac{1}{6} \Delta_{j-1} \Delta_j \frac{\partial^3 \phi}{\partial y^3} + o(\Delta^3) \qquad (A2.2.1)$$

and

$$\frac{\partial^2 \phi}{\partial y^2} = \frac{2}{\Delta_{j-1}\Delta_j(\Delta_{j-1}+\Delta_j)} [\Delta_{j-1} \phi_{j+1} - (\Delta_{j-1}+\Delta_j)\phi_j + \Delta_j \phi_{j-1}]$$

$$- \frac{1}{3} (\Delta_j - \Delta_{j-1}) \frac{\partial^3 \phi}{\partial y^3} + \frac{1}{12} (\Delta_{j-1}^2 - \Delta_{j-1}\Delta_j + \Delta_j^2) \frac{\partial^4 \phi}{\partial y^4} + o(\Delta^3), \qquad (A2.2.2)$$

$j = 2, \ldots, N-1$, can be easily verified from the Taylor series expansions of ϕ_{j+1} and ϕ_{j-1} about y_j.

One-sided derivatives are used in computing the boundary values. At the bottom boundary y=0, boundary conditions $\psi = \partial \psi / \partial y = 0$ allow the estimate of $\partial^2 \psi / \partial y^2$ to second order with only values of ψ at y_2 and y_3:

$$\frac{\partial^2 \psi}{\partial y^2} = 2 \frac{\Delta_1}{\Delta_2} (\Delta_1 + \Delta_2) \left[\frac{\psi_2}{\Delta_1^3} - \frac{\psi_3}{(\Delta_1+\Delta_2)^3} \right] + \frac{\Delta_1}{12} (\Delta_1 + \Delta_2) \frac{\partial^4 \psi}{\partial y^4} + o(\Delta^3).$$

$$(A2.2.3)$$

The expression (4.1.11) for the boundary values of ω then follows from (3.1.11) since $\psi=0$ implies $\partial^2\psi/\partial x^2=0$.

The horizontal velocity at the upper boundary $y_{max}=y_N$ is given by

$$\frac{\partial\psi}{\partial y} = \frac{1}{\Delta_{N-2}\Delta_{N-1}(\Delta_{N-2}+\Delta_{N-1})}\,[(\Delta_{N-2}+2\Delta_{N-1})\Delta_{N-2}\psi_N$$

$$-(\Delta_{N-2}+\Delta_{N-1})^2\psi_{N-1} + \Delta_{N-1}{}^2\psi_{N-2}] + \frac{1}{6}\Delta_{N-1}(\Delta_{N-2}+\Delta_{N-1})\frac{\partial^3\psi}{\partial y^3}$$

$$+ o(\Delta^3) \tag{A2.2.4}$$

and therefore

$$\psi_N = \frac{1}{\Delta_{N-2}+2\Delta_{N-1}}[\,\Delta_{N-1}(\Delta_{N-2}+\Delta_{N-1})\frac{\partial\psi}{\partial y} + \frac{(\Delta_{N-2}+\Delta_{N-1})^2}{\Delta_{N-2}}\psi_{N-1}$$

$$-\frac{\Delta_{N-1}{}^2}{\Delta_{N-2}}\psi_{N-2}] + \frac{1}{6}\Delta_{N-1}{}^2\frac{(\Delta_{N-2}+\Delta_{N-1})^2}{\Delta_{N-2}+2\Delta_{N-1}}\frac{\partial^3\psi}{\partial y^3} + o(\Delta^4)\,, \tag{A2.2.5}$$

in which the derivatives are evaluated at y_N. Substitution of (3.1.16), $\partial\psi_\infty/\partial y=U_\infty$, gives (4.1.13) and its Fourier transform (4.1.14). Furthermore, Taylor expansion of ψ at the upper boundary gives

$$\frac{\partial^2\psi}{\partial y^2} = 2\,\{ -\frac{\Delta_{N-1}}{\Delta_{N-2}(\Delta_{N-2}+\Delta_{N-1})^2}\psi_{N-2} + \frac{\Delta_{N-2}+\Delta_{N-1}}{\Delta_{N-2}\Delta_{N-1}{}^2}\psi_{N-1}$$

$$-\frac{\Delta_{N-2}{}^2+3\Delta_{N-2}\Delta_{N-1}+3\Delta_{N-1}{}^2}{\Delta_{N-1}{}^2(\Delta_{N-2}+\Delta_{N-1})^2}\psi_N\} + \frac{\Delta_{N-2}+2\Delta_{N-1}}{\Delta_{N-1}(\Delta_{N-2}+\Delta_{N-1})}\frac{\partial\psi}{\partial y}$$

$$+\frac{1}{24}\Delta_{N-1}(\Delta_{N-2}+\Delta_{N-1})\frac{\partial^4\psi}{\partial y^4} + o(\Delta^3). \tag{A2.2.6}$$

Boundary condition (4.1.15) then follows from (3.1.11).

§AII.3. Compact differencing in the Poisson equation

The equation for the streamfunction (3.1.11), is solved in the Fourier space and takes the form

$$\frac{\partial^2 \Psi_m}{\partial y^2} - (2\pi m)^2 \Psi_m = -(J\Omega)_m , \qquad (A2.3.1)$$

$m = 0, 1, 2, ..., \frac{1}{2}M$. The functions Ψ_m and $(J\Omega)_m$ are coefficients of the m-th component in the Fourier transform of functions ψ and $J\omega$, and $M\pi$ is the Nyquist frequency. If the derivative $\partial^2 \Psi_m / \partial y$ is to be approximated by a second-order centered-differencing scheme, (A2.3.1) yields $\frac{1}{2}M+1$ independent sets of equations, each composing of N-2 simultaneous equations. The overall accuracy is then second order in Δy.

The truncation error in (A2.3.1) can be improved to fourth-order with a small percentage increase in computational work by introducing compact differencing, as defined in (4.1.10). This is used in all computations and its derivation for the case of variable grid sizes will be outlined in this section.

For simplicity in notation we shall derive the compact differencing for the equation

$$\frac{\partial^2 f}{\partial y^2} - \kappa^2 f = g . \qquad (A2.3.2)$$

As in the last section, we denote

$$f_j \equiv f(y_j) \quad \text{and} \quad g_j \equiv g(y_j) ,$$

$j = 1, ..., N$; and

$$\Delta_j \equiv y_{j+1} - y_j ,$$

$j = 1, ..., N-1.$ We seek coefficients a_j's and b_j's,

$$\left\{ \begin{matrix} a_j \\ b_j \end{matrix} \right\} = \left\{ \begin{matrix} a_{j,0} \\ 0 \end{matrix} \right\} + \left\{ \begin{matrix} a_{j,1} \\ b_{j,1} \end{matrix} \right\} + \left\{ \begin{matrix} a_{j,2} \\ b_{j,2} \end{matrix} \right\} + ... , \qquad (A2.3.3)$$

where

$$\left\{ \begin{array}{c} a_{j,n} \\ b_{j,n} \end{array} \right\} = O(\Delta^{2n-2}),$$

such that (A2.3.2) at y_j,

$$a_{j+1}f_{j+1} + a_j f_j + a_{j-1}f_{j-1} + b_{j+1}g_{j+1} + b_j g_j + b_{j-1}g_{j-1} = 0, \qquad (A2.3.4)$$

can be satisfied for the highest order in Δ.

Since (A2.3.2) can be written as

$$\frac{\partial^{n+2} f}{\partial y^{n+2}} - \kappa^2 \frac{\partial^n f}{\partial y^n} = \frac{\partial^n g}{\partial y^n}, \qquad (A2.3.5)$$

the Taylor expansion of f and g in (A2.3.4) about y_j in orders of Δ is

$$\{(a_{j+1} + a_j + a_{j-1}) f_j\} + \{(a_{j+1}\Delta_j - a_{j-1}\Delta_{j-1}) \frac{\partial f}{\partial y}\}$$

$$+ \{(b_{j+1} + b_j + b_{j-1})[-(\frac{\partial^2 f}{\partial y^2})_j + \kappa^2 f_j] + \frac{1}{2}(a_{j+1}\Delta_j^2 + a_{j-1}\Delta_{j-1}^2) \frac{\partial^2 f}{\partial y^2}\}$$

$$+ \{(b_{j+1}\Delta_j - b_{j-1}\Delta_{j-1})[-(\frac{\partial^3 f}{\partial y^3})_j + \kappa^2 (\frac{\partial f}{\partial y})_j] + \frac{1}{6}(a_{j+1}\Delta_j^3 - a_{j-1}\Delta_{j-1}^3) \frac{\partial^3 f}{\partial y^3}\}$$

$$+ \{ \frac{1}{2}(b_{j+1}\Delta_j^2 + b_{j-1}\Delta_{j-1}^2)[-(\frac{\partial^4 f}{\partial y^4})_j + \kappa^2 (\frac{\partial^2 f}{\partial y^2})_j]$$

$$+ \frac{1}{24}(a_{j+1}\Delta_j^4 + a_{j-1}\Delta_{j-1}^4) \frac{\partial^4 f}{\partial y^4}\}$$

$$+ \{ \frac{1}{6}(b_{j+1}\Delta_j^3 - b_{j-1}\Delta_{j-1}^3)[-(\frac{\partial^5 f}{\partial y^5})_j + \kappa^2 (\frac{\partial^3 f}{\partial y^3})_j]$$

$$+ \frac{1}{120}(a_{j+1}\Delta_j^5 - a_{j-1}\Delta_{j-1}^5) \frac{\partial^5 f}{\partial y^5}\}$$

$$+ \{ \frac{1}{24}(b_{j+1}\Delta_j^4 + b_{j-1}\Delta_{j-1}^4)[-(\frac{\partial^6 f}{\partial y^6})_j + \kappa^2 (\frac{\partial^4 f}{\partial y^4})_j]$$

$$+ \frac{1}{720} (a_{j+1}\Delta_j^{\,6} + a_{j-1}\Delta_{j-1}^{\,6}) \frac{\partial^6 f}{\partial y^6} \} + O(\Delta^5) = 0 \, . \qquad (A2.3.6)$$

By equating terms of like order in Δ and y-derivatives, we get

$$\left\{ \begin{array}{c} a_{j+1,0} \\ a_{j,0} \\ a_{j-1,0} \end{array} \right\} = \frac{2}{\Delta_{j-1}\Delta_j(\Delta_{j-1}+\Delta_j)} \left\{ \begin{array}{c} \Delta_{j-1} \\ -(\Delta_{j-1}+\Delta_j) \\ \Delta_j \end{array} \right\} \, ,$$

and

$$\left\{ \begin{array}{c} a_{j+1,1} \\ a_{j,1} \\ a_{j-1,1} \end{array} \right\} = -\kappa^2 \left\{ \begin{array}{c} b_{j+1,1} \\ b_{j,1} \\ b_{j-1,1} \end{array} \right\}$$

$$= -\frac{1}{6} \frac{\kappa^2}{\Delta_{j-1}\Delta_j(\Delta_{j-1}+\Delta_j)} \left\{ \begin{array}{c} \Delta_{j-1}\,(-\Delta_{j-1}^{\,2} + \Delta_{j-1}\Delta_j + \Delta_j^{\,2}) \\ \Delta_{j-1}^{\,3} + 4\Delta_{j-1}^{\,2}\Delta_j + 4\Delta_{j-1}\Delta_j^{\,2} + \Delta_j^{\,3} \\ \Delta_j\,(\Delta_{j-1}^{\,2} + \Delta_{j-1}\Delta_j - \Delta_j^{\,2}) \end{array} \right\} \, ,$$

.... $\qquad (A2.3.7)$

Substitution of (A2.3.7) into (A2.3.4) gives

$$\frac{2}{\Delta_{j-1}\Delta_j(\Delta_{j-1}+\Delta_j)} \{ [\Delta_{j-1}\,f_{j+1} - (\Delta_{j-1}+\Delta_j)\,f_j + \Delta_j\,f_{j-1}]$$

$$+ \frac{1}{12} [(-\Delta_{j-1}^{\,2} + \Delta_{j-1}\Delta_j + \Delta_j^{\,2})\,\Delta_{j-1}\,(g_{j+1} - \kappa^2 f_{j+1})$$

$$+ (\Delta_{j-1}^{\,3} + 4\Delta_{j-1}^{\,2}\Delta_j + 4\Delta_{j-1}\Delta_j^{\,2} + \Delta_j^{\,3})\,(g_j - \kappa^2 f_j)$$

$$+ (\Delta_{j-1}^{\,2} + \Delta_{j-1}\Delta_j - \Delta_j^{\,2})\,\Delta_j\,(g_{j-1} - \kappa^2 f_{j-1})]\}$$

$$= \frac{1}{180} \frac{\Delta_j - \Delta_{j-1}}{\Delta_j + \Delta_{j-1}} (2\Delta_{j-1}^{\,3} + 7\Delta_{j-1}^{\,2}\Delta_j + 7\Delta_{j-1}\Delta_j^{\,2} + 2\Delta_j^{\,3}) \frac{\partial^5 f}{\partial y^5} +$$

$$\frac{1}{720} \frac{1}{\Delta_j + \Delta_{j-1}} (4\Delta_{j-1}^{\,5} + 5\Delta_{j-1}^{\,4}\Delta_j - 5\Delta_{j-1}^{\,3}\Delta_j^{\,2} - 5\Delta_{j-1}^{\,2}\Delta_j^{\,3} + 5\Delta_{j-1}\Delta_j^{\,4} + 4\Delta_j^{\,5}) \frac{\partial^6 f}{\partial y^6}$$

$$+ O(\Delta^5) \qquad (A2.3.8)$$

which is pseudo fourth-order. Equation (4.1.10) is recovered by rewriting

308

$$f_j \equiv \Psi_{m,j}^{n+1} \quad \text{and} \quad g_j \equiv (J\Omega)_{m,j}^{n+1}.$$

Appendix III. Stability criteria and truncation errors

In the time-stepping of vorticity equation (3.1.10), a third-order Adams-Bashforth scheme (4.1.7) is used for the convective terms and an Euler forward scheme (4.1.8) is used for the viscous terms. The stability criteria and magnitudes of truncation error of these numerical schemes will be derived in this appendix.

§AIII.1. Stability criteria

Stability conditions (4.5.1) and (4.5.2) for the numerical treatment of vorticity equation (3.1.10) will be derived by applying the von Neumann stability criterion separately to the convective part and the viscous part of the vorticity equation.

Let the unknown function $\theta(x, y, t)$ defined in $(0<x<L_x,\ 0<y<L_y,\ 0<t)$ be written in the form

$$\theta^n_{xy} = \theta(x, y, t_n) = \sum_{m,j} a^n_{mj} \exp(im\kappa_x x) \exp(ij\kappa_y y) , \qquad (A3.1.1)$$

with

$$\kappa_x = \frac{2\pi}{L_x}, \quad \kappa_y = \frac{2\pi}{L_y} . \qquad (A3.1.2)$$

We shall assume grid-spacings (Δx and Δy) and time-steps (Δt) to be constant. Stability conditions for the two split-step components, (4.1.7) and (4.1.8) for the convective and viscous terms respectively, will be derived independently.

§AIII.1.i. Third-order Adams-Bashforth scheme

The third order Adams-Bashforth scheme for the linearized convection equation,

$$J \frac{\partial \theta}{\partial t} + K (U \frac{\partial \theta}{\partial x} + V \frac{\partial \theta}{\partial y}) = 0 \qquad (A3.1.3)$$

is given by

$$J \frac{\theta^{n+1} - \theta^n}{\Delta t} + K \left[\frac{23}{12} \left(U \frac{\partial \theta}{\partial x} + V \frac{\partial \theta}{\partial y} \right)^n - \frac{4}{3} \left(U \frac{\partial \theta}{\partial x} + V \frac{\partial \theta}{\partial y} \right)^{n-1} \right.$$

$$\left. + \frac{5}{12} \left(U \frac{\partial \theta}{\partial x} + V \frac{\partial \theta}{\partial y} \right)^{n-2} \right] = 0 , \tag{A3.1.4}$$

where superscripts n-2, n-1, n, and n+1 denote the values at the n-2, ..., (n+1)-th time-step. Substitution of (A3.1.1) into (A3.1.4) gives

$$\sum_{m,j} \exp(im\kappa_x x) \exp(ij\kappa_y y) \left\{ a_{mj}^{n+1} - a_{mj}^n + \frac{i}{J} K \Delta t \left(\frac{23}{12} a_{mj}^{n+1} - \frac{4}{3} a_{mj}^{n+1} \right. \right.$$

$$\left. \left. + \frac{5}{12} a_{mj}^{n+1} \right) \left[m\kappa_x U + \frac{V}{\Delta y} \sin(j\kappa_y \Delta y) \right] \right\} = 0 \tag{A3.1.5}$$

in which the y-derivatives are approximated by second-order centered-differencing and x-derivatives are evaluated in Fourier space.

Assume coefficients a_{mj}^n's to be of the form

$$a_{mj}^n = \lambda^n \tag{A3.1.6}$$

(λ raised to the n-th power). In view of (A3.1.1), it is apparent that

$$|\lambda| \leq 1 \quad (A3.1.7)$$

for function θ to be bounded. Substitution of (A3.1.6) into (A3.1.5) gives

$$\lambda^3 + \left(\frac{23}{12} i\alpha - 1 \right) \lambda^2 - \frac{4}{3} i\alpha \lambda + \frac{5}{12} i\alpha = 0 \tag{A3.1.8}$$

where

$$\alpha = \frac{1}{J} K \Delta t \left[m\kappa_x U + \frac{V}{\Delta y} \sin(j\kappa_y \Delta y) \right] . \tag{A3.1.9}$$

For real values of α in (A3.1.8), inequality (A3.1.7) will be satisfied if

$$0 < \alpha < 0.7236272 . \tag{A3.1.10}$$

At the most unstable wavenumber,

$$m \kappa_x = \frac{\pi}{\Delta x} \quad \text{and} \quad j \kappa_y = \frac{\pi}{2\Delta y} , \tag{A3.1.11}$$

(A3.1.9) and (A3.1.10) imply

$$\alpha = \frac{1}{J} K \, \Delta t \, [\frac{\pi U}{\Delta x} + \frac{V}{\Delta y}] \leq 0.7236272 \,, \qquad\qquad (A3.1.12)$$

which gives the upper bound for time-steps used as given in (4.5.1).

As a comparison, the stability criterion for the hyperbolic convective equation

$$\frac{\partial \theta}{\partial t} + \frac{\partial \theta}{\partial x} = 0 \,,$$

where x-derivatives are evaluated in Fourier space, is given by

$$\alpha = i \, \pi \frac{\Delta t}{\Delta x} \,, \quad \text{and therefore} \quad \frac{\Delta t}{\Delta x} < \frac{0.7236272}{\pi} \,.$$

Similarly, for

$$\frac{\partial \theta}{\partial t} + \frac{\partial \theta}{\partial y} = 0$$

where y-derivatives are computed by finite-differencing, the stability criterion is

$$\alpha = i \frac{\Delta t}{\Delta y} \,, \quad \text{or} \quad \frac{\Delta t}{\Delta y} < 0.7236272 \,.$$

§AIII.1.ii. Euler forward scheme

The stability criterion for the Euler forward scheme applied to the viscous diffusion equation

$$J \frac{\partial \theta}{\partial t} - s \frac{K}{R} (\frac{\partial^2 \theta}{\partial x^2} + \frac{\partial^2 \theta}{\partial y^2}) = 0 \qquad\qquad (A3.1.13)$$

can be obtained the same way as outlined in the last section. By substituting (A3.1.1) into the Euler forward scheme for (A3.1.13),

$$J \frac{\theta^{n+1} - \theta^n}{\Delta t} - s \frac{K}{R} (\frac{\partial^2 \theta}{\partial x^2} + \frac{\partial^2 \theta}{\partial y^2})^n = 0 \,, \qquad\qquad (A3.1.14)$$

where superscripts denote values at the n-th time-step and (n+1)-th time-step, we obtain

$$a_{mj}^{n+1} = \{1 - \frac{s}{J}\frac{K}{R}\Delta t \,[\, m^2\kappa_x^{\,2} + \frac{2}{\Delta y^2}(1 - \cos j\kappa_y\Delta y)]\}\, a_{mj}^n \,. \qquad (A3.1.15)$$

The absolute value of the ratio a_{mj}^{n+1}/a_{mj}^n cannot be greater than unity if θ is to stay bounded. This requires that

$$0 \le \frac{s}{J}\frac{K}{R}\Delta t \,[\, m^2\kappa_x^{\,2} + \frac{2}{\Delta y^2}(1 - \cos j\kappa_y\Delta y)\,] \le 2 \,. \qquad (A3.1.16)$$

At the most unstable wavenumbers defined in (A3.1.11), (A3.1.16) gives

$$0 \le \frac{s}{J}\frac{K}{R}\Delta t \,(\frac{\pi^2}{\Delta x^2} + \frac{4}{\Delta y^2}) \le 2 \,, \qquad (A3.1.17)$$

which can be rearranged to give (4.5.2).

§AIII.2. Truncation errors

Truncation errors due to temporal and spatial (in the vertical direction) discretizations in the numerical solution of vorticity equation can be estimated from the Taylor expansions in terms of Δt and Δy. Discretization error in x has been discussed in §IV.3. Quantitative estimate of this error will not be attempted here.

Refering to (4.1.7) to (4.1.9), temporal discretization of vorticity equation can be written as

$$\frac{1}{\Delta t}[(J\omega)_{kj}^{n+1} - (J\omega)_{kj}^n] + [\frac{23}{12}\varphi_{kj}^n - \frac{4}{3}\varphi_{kj}^{n-1} + \frac{5}{12}\varphi_{kj}^{n-2}] - \vartheta_{kj}^n$$

$$= \frac{\partial}{\partial t}J\omega + \frac{\Delta t}{2}\frac{\partial^2}{\partial t^2}J\omega + \frac{\Delta t^2}{6}\frac{\partial^3}{\partial t^3}J\omega + \frac{\Delta t^3}{24}\frac{\partial^4}{\partial t^4}J\omega + O(\Delta t^4)$$

$$+ [\,\varphi + \frac{\Delta t}{2}\frac{\partial\varphi}{\partial t} + \frac{\Delta t^2}{6}\frac{\partial^2\varphi}{\partial t^2} - \frac{\Delta t^3}{3}\frac{\partial^3\varphi}{\partial t^3} + O(\Delta t^4)\,] - \vartheta \,, \qquad (A3.2.1)$$

where all terms are evaluated at $(x=x_k,\ y=y_j,\ t=t_n)$. The vorticity equation (3.1.10) gives

$$\frac{\partial^{n+1}}{\partial t^{n+1}} J\omega = -\frac{\partial^n \varphi}{\partial t^n} + \frac{\partial^n \vartheta}{\partial t^n}, \qquad (A3.2.2)$$

$n = 1, 2, 3, \dots$. Equation (A3.2.1) can therefore be reduced to

$$\frac{1}{\Delta t}[(J\omega)_{kj}^{n+1} - (J\omega)_{kj}^{n}] + [\frac{23}{12}\varphi_{kj}^{n} - \frac{4}{3}\varphi_{kj}^{n-1} + \frac{5}{12}\varphi_{kj}^{n-2}] - \vartheta_{kj}^{n}$$

$$= [-\frac{3}{8}\Delta t^3 \frac{\partial^3 \varphi}{\partial t^3} + O(\Delta t^4)] + [\frac{1}{2}\Delta t \frac{\partial \vartheta}{\partial t} + O(\Delta t^2)] . \qquad (A3.2.3)$$

From (A2.2.1) and (A2.2.2), spatial discretization errors in y of φ and ϑ are respectively

$$\frac{1}{6} K \Delta_{j-1} \Delta_j (\frac{\partial \omega}{\partial x}\frac{\partial^3 \psi}{\partial y^3} - \frac{\partial \psi}{\partial x}\frac{\partial^3 \omega}{\partial y^3})_{kj}^{n} + O(\Delta^3) \qquad (A3.2.4)$$

and

$$-\frac{s}{12}\frac{K}{R}(\Delta_{j-1}^2 - \Delta_{j-1}\Delta_j + \Delta_j^2)(\frac{\partial^4 \omega}{\partial y^4})_{kj}^{n} , \qquad (A3.2.5)$$

if $\Delta_j \cong \Delta_{j-1}$. Adding (A3.2.4) and (A3.2.5) to (A3.2.3), we arrive at the leading orders in the truncation errors in the numerical treatment of vorticity equation (3.1.10),

$$-\frac{3}{8} K \Delta t^3 [\frac{\partial^3}{\partial t^3}(\frac{\partial \psi}{\partial y}\frac{\partial \omega}{\partial x} - \frac{\partial \psi}{\partial x}\frac{\partial \omega}{\partial y})]_{kj}^{n} + \frac{1}{2}\Delta t \, s \frac{K}{R}[\frac{\partial}{\partial t}(\frac{\partial^2 \omega}{\partial x^2} + \frac{\partial^2 \omega}{\partial y^2})]_{kj}^{n}$$

$$+\frac{K}{6} \Delta_{j-1}\Delta_j (\frac{\partial \omega}{\partial x}\frac{\partial^3 \psi}{\partial y^3} - \frac{\partial \psi}{\partial x}\frac{\partial^3 \omega}{\partial y^3})_{kj}^{n} - \frac{s}{12}\frac{K}{R}(\Delta_{j-1}^2 - \Delta_{j-1}\Delta_j + \Delta_j^2)(\frac{\partial^4 \omega}{\partial y^4})_{kj}^{n} ,$$

$$(A3.2.6)$$

as stated in (4.2.1).

Appendix IV. Choice of ripple profile in the evaluation of horizontal force

It was suggested at the end of §III.2.2 that the net horizontal force acting on a bottom profile of one ripple length depends on the particular section (crest-to-crest, trough-to-trough, ..., etc.) chosen. This is due to the monotonous increase/decrease with x_p of the component of ambient pressure due to the inertial acceleration of the unsteady far field velocity. In this appendix we shall examine this point in more detail.

The expression for p_r in (3.2.7) includes a term linear in x, $-\dfrac{x}{K}\dfrac{dU_\infty}{dt}$, which when multiplied with $\partial \tilde{y}/\partial x$ gives an integral whose value depends on x_0 in (7.5.1). Its contribution to the horizontal force on N ripples is given by

$$-\int_{x_0}^{x_0+N} dx \, \frac{x}{K} \frac{dU_\infty}{dt} \frac{\partial \tilde{y}}{\partial x} = \pi \frac{s}{K} \frac{dU_\infty}{dt} \int_{x_0}^{x_0+N} dx \, x \sin 2\pi x$$

$$= -\frac{s}{2K} \frac{dU_\infty}{dt} N \cos 2\pi x_0 \qquad\qquad (A4.1)$$

with $\partial \tilde{y}/\partial x$ defined in (3.4.4). For example, the choice of $x_0=0$, $N=1$ (a crest-to-crest profile) and $dU_\infty/dt>0$ (ambient velocity accelerating to the right) leads to a net horizontal force component in the negative x_p direction. Physically, this is due to the negative pressure gradient in the x_p direction associated with the inertial acceleration, leading to a larger pressure force acting on the downward sloping ripple surface (0<x<0.5) than that on the upward sloping ripple surface (0.5<x<1). This results in a larger horizontal force in the negative x-direction (acting on 0<x<0.5) than the force in the positive x-direction (acting on 0.5<x<1).

It is apparent from (A4.1) that this arbitrariness cannot be removed by taking the mean over a large number of ripple lengths. For a far field velocity that is sinusoidal in time, this component also varies sinusoidally and lags the ambient flow

in phase by a quarter of a wave period. Its magnitude does not depend on R, and its integral over a wave period, however, is always zero.

In our computation, we shall compare the net horizontal force acting on a crest to crest ripple profile, denoted as F_c. That is, choose $x_0=0$ and $N=1$ in (A4.1) such that

$$F_c = \int_0^1 dx \, \{ \, [-\frac{x}{K}\frac{dU_\infty}{dt} - \int_0^{y\max} dy \, (\frac{1}{K}\frac{\partial}{\partial t}\frac{\partial \psi}{\partial x} + \frac{s}{R}\frac{\partial \omega}{\partial x} - \omega \frac{\partial \psi}{\partial y}) \,] \, \frac{\partial \tilde{y}}{\partial x}$$

$$+ \frac{s}{R} [A(x,0)\frac{\partial \tilde{x}}{\partial x} + 2 B(x,0)\frac{\partial \tilde{y}}{\partial x}] \frac{\partial^2 \psi}{\partial y^2} \} \qquad (A4.2)$$

since $\int_0^1 dx \, \frac{1}{2} U_\infty^2 \frac{\partial \tilde{y}}{\partial x} = 0$ for a symmetric profile. Similarly, the horizontal force on a trough–to–trough ripple profile F_t is defined by choosing $x_0=\frac{1}{2}$,

$$F_t = \int_{\frac{1}{2}}^{1\frac{1}{2}} dx \, \{ \, [-\frac{x}{K}\frac{dU_\infty}{dt} - \int_0^{y\max} dy \, (\frac{1}{K}\frac{\partial}{\partial t}\frac{\partial \psi}{\partial x} + \frac{s}{R}\frac{\partial \omega}{\partial x} - \omega \frac{\partial \psi}{\partial y}) \,] \, \frac{\partial \tilde{y}}{\partial x}$$

$$+ \frac{s}{R} [A(x,0)\frac{\partial \tilde{x}}{\partial x} + 2 B(x,0)\frac{\partial \tilde{y}}{\partial x}] \frac{\partial^2 \psi}{\partial y^2} \} = F_c + \frac{s}{K}\frac{dU_\infty}{dt} \qquad (A4.3)$$

for the mapping defined §III.4. Alternatively, we can take $x_0=\frac{1}{4}$, which amounts to removing the pressure component due to inertial acceleration. That is, we define

$$F_n = \int_0^1 dx \, \{ - \int_0^\infty dy \, (\frac{1}{K}\frac{\partial}{\partial t}\frac{\partial \psi}{\partial x} + \frac{s}{R}\frac{\partial \omega}{\partial x} - \omega \frac{\partial \psi}{\partial y}) \frac{\partial \tilde{y}}{\partial x} + \frac{s}{R} [A(x,0)\frac{\partial \tilde{x}}{\partial x}$$

$$+ 2 B(x,0)\frac{\partial \tilde{y}}{\partial x}] \frac{\partial^2 \psi}{\partial y^2} \} = F_c + \frac{s}{2K}\frac{dU_\infty}{dt} \qquad (A4.4)$$

which also equals

$$F_n = \int_{\frac{1}{4}}^{1\frac{1}{4}} dx \, \{ \, [-\frac{x}{K}\frac{dU_\infty}{dt} - \int_0^{y\max} dy \, (\frac{1}{K}\frac{\partial}{\partial t}\frac{\partial \psi}{\partial x} + \frac{s}{R}\frac{\partial \omega}{\partial x} - \omega \frac{\partial \psi}{\partial y}) \,] \, \frac{\partial \tilde{y}}{\partial x}$$

$$+ \frac{s}{R} [A(x,0)\frac{\partial \tilde{x}}{\partial x} + 2 B(x,0)\frac{\partial \tilde{y}}{\partial x}] \frac{\partial^2 \psi}{\partial y^2} \} \qquad (A4.3)$$

or the horizontal force on a node-to-node ripple profile.

In our discussion of the horizontal force on a ripple length in §VII.5 and the friction factor deduced from its magnitude in §VII.6, we shall examine the variations of all three values F_c, F_t, and F_n over a wave period.

Appendix V. FORTRAN code used in the implementation of numerical scheme described in §IV.1.

```
c
c compute.for
c
c impulsively started oscillatory motion
c spectral decomposition in x, derivatives in Fourier space
c variable grid size in y : centred-differencing
c Euler forward for viscous term / third-order Adams-Bashforth for convective
c   terms ( Euler forward ; second-order Adams-Bashforth to start )
c variable time-step / limit on maximum size of time-step : time-step allowed
c   only to decrease
c
c LU-decomposition / forward/back-solve / compact differencing in Poisson
c   equation for streamfunction
c mapping z = w + i s/2 exp(i 2 pi w)
c semi-implicitness in Poisson equation : old boundary values of vorticity
c   used in compact scheme
c
c set-up of data files
c    fort.10   (input)    parameters in computation
c    fort.11              dimensionless parameters (input in ripple_df.f)
c    fort.12   (output)   streamfunction values
c    fort.13   (output)   functional values at the end of computation
c    fort.14              velocity vectors (output in ripple_fl.f)
c    fort.15   (input)    values of various functions at start of computation
c    fort.16   (output)   time history of rate of pressure work done on the fluid,
c                         rate of change of kinetic energy and energy dissipation
c    fort.17              time history of stresses on ripple surface
c    fort.18   (output)   vorticity function at surface of ripple
c    fort.19              listing of parameters used (output in ripple_pm)
c    fort.20   (output)   time history of size of time-step
c    fort.21   (output)   times at which streamfunction and vorticity values are
c                         recorded
c    fort.22   (output)   location of point of separation determined (where
c                         vorticity vanishes)
c    fort.23   (output)   time history of friction coefficients
c
      real ck,re,slope,x,pl,ps,pi,tpi,cv1,cv2,cp,cs,b2,b4,curren,wave,
     1 vmax1,vmax2,endtme,tratio,time,tmstep,tstart,p,q,r,s,t,wck,
     1 tew,tfw,tpw,tsw,tvw,tcrit,tcheck,test,twrite,terg,tsepar,tts,
     1 tbkint,tssnew,timpul,pretms,tstres,ovmax1,ovmax2,vel,speed,accel,
     1 forcex,forcey,del,deltpi,realnx,bsder,bsv1,bsv2,dedt,dsdt,tback
c
      real rjacob(64,101),wj(64,101),rl(33,101),d(33,101),u(33,101),
     1 w0(101),w1(101),w2(101),bvv2(64),bvv3(64),xaxis(54),yaxis(101),
     1 xarray(65),wk(7493),pint(64,101),bpar(4),coef(100,3),
     1 energy(3),fx(64),fy(64),press(64),z1(64),z2(64),bv(64,4)
c       dimensions of w1 and w2 are the maximum of nx and ny
c
      dimension stream(64,101),vort(64,101),old(65,101),fsch(3,3),
     1 der1(101,3),der2(101,3),cd(101,3),store(2,64,101),y(101),
     1 dy(101),dsdx(64,101),dvdx(64,101),d2vdx2(64,101),ffts(2,33,101),
     1 dert(4,3),dsdxdt(64,101),sha(64),shb(64)
c
      complex factor,d1(64),d2(64),array1(64),array2(64),array3(64)
c
      integer i,j,j1,k,nfft,nx,ny,nxa(33),nxh,nx1,ny1,ny2,n0,n1,
     1 isch,maxim,maxim1,maxim2,nconsw,mconsw,mstrea,iwk(7),
     1 ier,ierx1,ierx2,iery1,iery2,knum,ier1(64),ier2(64)
c
      common /lumat/rl,d,u/lud/ny2,der2,cd,bsv1,bsv2
```

319

```
      1 /current/curren,wave
c

        data fsch/1.,0.,0.,1.5,-0.5,0.,1.91667,-1.3333,0.41667/,
      1 dert/-1.,1.,0.,0.,0.5,-2.,1.5,0.,-0.3333,1.5,-3.,1.8333/,
      1 pi/3.14159265358979323846263/
c

        dert(1,3)=-1./3.
        dert(4,3)=11./6.
        fsch(1,3)=23./12.
        fsch(2,3)=-4./3.
        fsch(3,3)=5./12.
        tpi=2.*pi
c
c       input parameters
        read(15)wck,re,slope,curren
        read(15)x,nfft,ny
        read(15)tstart
        read(15)isch,tmstep
        read(15)(y(j),j=1,ny)
        wave=1.
        ck=wck
        if (wck.ne.0) go to 1
          wave=0.
          ck=1.
      1   nx=2**nfft
        realnx=float(nx)
        nxh=nx/2
        nx1=nxh+1
        ny1=ny-1
        ny2=ny-2
        ps=pi*slope
        cp=slope/re
        cs=cp*ck
        cv1=ck*tmstep
        cv2=cs*tmstep
        read(10,*)timpul,endtme,tratio,tts,tcheck,tsw,tvw,tew,tfw,tpw,
      1 twrite,nconsw,mconsw
        read(10,*)tbkint
c
c       define coefficients in differencing formulae for first and second
c       y-derivatives
        do 10 j=1,ny1
          dy(j)=y(j+1)-y(j)
          yaxis(j)=y(j+1)
     10   continue
        do 20 j=2,ny1
          j1=j-1
          p=dy(j1)+dy(j)
          q=dy(j1)*dy(j)
          der1(j,1)=dy(j1)/dy(j)/p
          der1(j,2)=(dy(j)-dy(j1))/dy(j)/dy(j1)
          der1(j,3)=-dy(j)/dy(j1)/p
          der2(j,1)=2./dy(j)/p
          der2(j,2)=-2./dy(j)/dy(j1)
          der2(j,3)=2./dy(j1)/p
          cd(j,1)=(-dy(j)**2-q+dy(j1)**2)/dy(j)/p/6.
          cd(j,2)=(-dy(j)**3-4.*p*q-dy(j1)**3)/p/q/6.
          cd(j,3)=(dy(j)**2-q-dy(j1)**2)/dy(j1)/p/6.
     20   continue
c
```

```
c        define coefficients in computing boundary values for streamfunction
         p=dy(ny1)+dy(ny2)
         q=p+dy(ny1)
         bsder=p*dy(ny1)/q
         bsv1=p**2/dy(ny2)/q
         bsv2=-dy(ny1)**2/dy(ny2)/q
c
c        differential operator in x and LU decompostion of Laplacian operator
         do 30 i=1,nx1
            d1(i)=cmplx(0.,float(i-1)*tpi/x)
            d2(i)=d1(i)**2
            call lu(i,real(d2(i)))
  30     continue
         do 40 i=2,nxh
            nxa(i)=nx-i+2
            d1(nxa(i))=conjg(d1(i))
            d2(nxa(i))=conjg(d2(i))
  40     continue
c
c        define Jacobian, initialize vorticity and stream function
         del=x/realnx
         deltpi=tpi*del
         do 60 i=1,nx
            xaxis(i)=float(i)*del
            xarray(i)=xaxis(i)-del
            w1(i)=cos(float(i-1)*deltpi)
            z1(i)=1.-ps*w1(i)
            z2(i)=ps*sin(float(i-1)*deltpi)
  60     continue
         xarray(nx+1)=x
         do 70 j=1,ny
            p=ps*exp(-tpi*y(j))
            q=1.+p**2
            r=2.*p
            do 65 i=1,nx
               vort(i,j)=0.
               old(i,j)=0.
               stream(i,j)=0.
               dvdx(i,j)=0.
               d2vdx2(i,j)=0.
               dsdx(i,j)=0.
               dsdxdt(i,j)=0.
               store(1,i,j)=0.
               store(2,i,j)=0.
               wj(i,j)=0.
               rjacob(i,j)=q-r*w1(i)
  65        continue
  70     continue
         tcrit=0.7236272*dy(1)*rjacob(1,1)*tratio/ck
c
c        coefficients in computing values of vorticity and shear stresses at
c        ripple surface and upper boundary
         p1=-2.*(dy(1)+dy(2))/dy(2)/dy(1)**2
         q=2.*dy(1)/dy(2)/(dy(1)+dy(2))**2
         p=dy(ny1)+dy(ny2)
         r=2.*p/dy(ny2)/dy(ny1)**2
         s=-2.*dy(ny1)/dy(ny2)/p**2
         t=-2.*(p**3-dy(ny1)**3)/dy(ny2)/(dy(ny1)*p)**2
         b2=2.*(dy(ny1)+p)/dy(ny1)/p
         do 75 i=1,nx
```

321

```fortran
         bvv2(i)=p1/rjacob(i,1)
         bvv3(i)=q/rjacob(i,1)
         sha(i)=(z2(i)**2-z1(i)**2)/rjacob(i,1)
         shb(i)=2.*z1(i)*z2(i)/rjacob(i,1)
         bv(i,1)=-r/rjacob(i,ny)
         bv(i,2)=-s/rjacob(i,ny)
         bv(i,3)=-t/rjacob(i,ny)
         bv(i,4)=-b2/rjacob(i,ny)
  75     continue
c
c        define coefficients used in cubic spline
         b2=12./(dy(1)+dy(2))/(dy(1)+2.*dy(2))
         b4=12./(dy(ny2)+dy(ny1))/(2.*dy(ny2)+dy(ny1))
c
         do 80 j=1,ny
           do 80 i=1,nx1
             do 80 k=1,2
  80             ffts(k,i,j)=0.
c
         n1=0
         n0=1
         nenerg=1
         dedt=0.
         dsdt=0.
         time=tstart
         test=tstart+tcheck
         terg=twrite
         tstart=twrite
         tsepar=twrite
         tstres=twrite
         tback=time+tbkint
         mstrea=0
         knum=1
c
c        read in initial functional values if it is a continuation of a previous
c        run
         if (time.eq.0.) go to 90
           read(15)((stream(i,j),i=1,nx),j=1,ny)
           read(15)((old(i,j),i=1,nx),j=1,ny)
           read(15)((dsdx(i,j),i=1,nx),j=2,ny1)
           read(15)((dvdx(i,j),i=1,nx),j=2,ny1)
           read(15)((d2vdx2(i,j),i=1,nx),j=2,ny1)
           read(15)((wj(i,j),i=1,nx),j=2,ny1)
           if (isch.gt.1) read(15)((store(2,i,j),i=1,nx),j=2,ny1)
           if (isch.gt.2) read(15)((store(1,i,j),i=1,nx),j=2,ny1)
c
  90     write(12)wck,re,slope,curren
         write(12)x,nx,ny,timpul
         write(12)(y(j),j=1,ny)
         write(16,*)wck,re,slope,curren
         write(16,*)x,y(ny),nx,ny,timpul
         write(16,*)dy(1),dy(ny1)
         write(17,910)wck,re,slope,curren
         write(17,940)nx,ny
         write(17,920)dy(1),dy(ny1),y(ny),x
         write(18,*)wck,re,slope,curren
         write(18,*)y(ny),nfft,ny,timpul,x,dy(1),dy(ny1)
         write(20,*)wck,re,slope,curren
         write(20,*)x,y(ny),nx,ny,timpul,tratio
         write(20,*)dy(1),dy(ny1)
```

322

```
          write(20,*)time,tmstep
          write(22,*)wck,re,slope,curren
          write(22,*)x,y(ny),nx,ny,timpul
          write(22,*)dy(1),dy(ny1)
          write(23,*)wck,re,slope,curren
          write(23,*)x,y(ny),nx,ny,timpul
          write(23,*)dy(1),dy(ny1)
c
c   time-stepping of vorticity equation in physical variables
  100     time=time+tmstep
          speed=vel(timpul,time)
          n1=mod(n1,2)+1
          n0=mod(n0,2)+1
          do 150 j=2,ny1
            do 110 i=1,nx
c     -         convective terms
              wj(i,j)=wj(i,j)+fsch(2,isch)*store(n0,i,j)
     1                +fsch(3,isch)*store(n1,i,j)
              store(n1,i,j)=cv1*(dsdx(i,j)*(der1(j,1)*old(i,j+1)+
     1                       der1(j,2)*old(i,j)+der1(j,3)*old(i,j-1))-
     1                       dvdx(i,j)*(der1(j,1)*stream(i,j+1)+
     1                       der1(j,2)*stream(i,j)+der1(j,3)*stream(i,j-1)))
              wj(i,j)=wj(i,j)+fsch(1,isch)*store(n1,i,j)
c     -         viscous terms
              wj(i,j)=wj(i,j)+cv2*(d2vdx2(i,j)+der2(j,1)*old(i,j+1)+
     1                 der2(j,2)*old(i,j)+der2(j,3)*old(i,j-1))
              array3(i)=cmplx(wj(i,j)/realnx,0.)
              vort(i,j)=wj(i,j)/rjacob(i,j)
              array1(i)=cmplx(vort(i,j)/realnx,0.)
  110       continue
c     -       first- and second- x-derivatives of vorticity function
            call fft2c(array1,nfft,iwk)
            do 120 i=1,nx
              factor=conjg(array1(i))
              array1(i)=d1(i)*factor
              array2(i)=d2(i)*factor
  120       continue
            call fft2c(array1,nfft,iwk)
            call fft2c(array2,nfft,iwk)
            do 130 i=1,nx
              dvdx(i,j)=real(array1(i))
              d2vdx2(i,j)=real(array2(i))
  130       continue
c     -       Fourier transform of product of Jacobian and vorticity function
            call fft2c(array3,nfft,iwk)
            do 140 i=1,nx1
              factor=conjg(array3(i))
              ffts(1,i,j)=real(factor)
              ffts(2,i,j)=aimag(factor)
  140       continue
  150     continue
c
c Fast Fourier Transform of boundary values for vorticity * Jacobian function
          do 160 i=1,nx
            array1(i)=cmplx(rjacob(i,1)*old(i,1)/realnx,0.)
            array2(i)=cmplx(rjacob(i,ny)*old(i,ny)/realnx,0.)
            array3(i)=cmplx(old(i,ny)/realnx,0.)
  160     continue
          call fft2c(array1,nfft,iwk)
          call fft2c(array2,nfft,iwk)
```

323

```fortran
      call fft2c(array3,nfft,iwk)
      do 170 i=1,nx1
        factor=conjg(array1(i))
        ffts(1,i,1)=real(factor)
        ffts(2,i,1)=aimag(factor)
        factor=conjg(array2(i))
        ffts(1,i,ny)=real(factor)
        ffts(2,i,ny)=aimag(factor)
170   continue
      do 180 i=1,nx
180     array3(i)=d1(i)*conjg(array3(i))
      call fft2c(array3,nfft,iwk)
      do 190 i=1,nx
190     dvdx(i,ny)=real(array3(i))
c
c  Poisson equation solved in transformed space
      do 230 i=1,nx1
        do 210 j=2,ny1
          w1(j-1)=ffts(1,i,j+1)*cd(j,1)+ffts(1,i,j)*cd(j,2)+
     1            ffts(1,i,j-1)*cd(j,3)
          w2(j-1)=ffts(2,i,j+1)*cd(j,1)+ffts(2,i,j)*cd(j,2)+
     1            ffts(2,i,j-1)*cd(j,3)
210     continue
        if (i.eq.1) w1(ny2)=w1(ny2)-der2(ny1,1)*bsder*speed
        call solve(i,ny2,w1)
        call solve(i,ny2,w2)
        do 220 j=2,ny1
          ffts(1,i,j)=w1(j-1)
          ffts(2,i,j)=w2(j-1)
220     continue
230   continue
c
c     inverse transform of streamfunction
      do 270 j=2,ny1
        do 240 i=1,nx1
          array1(i)=cmplx(ffts(1,i,j),ffts(2,i,j))
          array2(i)=d1(i)*array1(i)
240     continue
        do 250 i=2,nxh
          array1(nxa(i))=conjg(array1(i))
          array2(nxa(i))=conjg(array2(i))
250     continue
        call fft2c(array1,nfft,iwk)
        call fft2c(array2,nfft,iwk)
        do 260 i=1,nx
          stream(i,j)=real(array1(i))
          dsdx(i,j)=real(array2(i))
260     continue
270   continue
c
c     boundary values of vorticity and streamfunction
      do 280 i=1,nx
        stream(i,ny)=bsv1*stream(i,ny1)+bsv2*stream(i,ny2)
     1               +bsder*speed
        vort(i,1)=bvv2(i)*stream(i,2)+bvv3(i)*stream(i,3)
        vort(i,ny)=bv(i,1)*stream(i,ny1)+bv(i,2)*stream(i,ny2)
     1             +bv(i,3)*stream(i,ny)+bv(i,4)*speed
280   continue
c
c     compute rate of change of kinetic energy in flow domain
```

```
          if (time.lt.terg-float(mconsw)*tmstep) go to 400
          if (nenerg.ne.1.and.tmstep.eq.oldtms) go to 300
            nenerg=1
            oldtms=tmstep
            dsdt=0.
            dedt=0.
 300        do 310 j=1,ny
              do 310 i=1,nx
 310            old(i,j)=rjacob(i,j)*stream(i,j)*vort(i,j)
            do 320 j=1,ny
 320          old(nx+1,j)=old(1,j)
            call dbcqdu (old,65,xarray,nx+1,y,ny,0.,x,y(1),y(ny),
     1      energy(nenerg),wk,ier)
            dsdt=dsdt+dert(nenerg,mconsw)*stream(1,ny)*speed
            dedt=dedt+dert(nenerg,mconsw)*energy(nenerg)
            nenerg=nenerg+1
            if (nenerg.le.mconsw+1) go to 400
 c          compute rate of energy dissipation in flow domain
            do 330 j=1,ny
              do 330 i=1,nx
 330            old(i,j)=rjacob(i,j)*vort(i,j)**2
            do 340 j=1,ny
 340          old(nx+1,j)=old(1,j)
            call dbcqdu (old,65,xarray,nx+1,y,ny,0.,x,y(1),y(ny),dissip,
     1      wk,ier)
            energy(1)=stream(1,ny)*accel(timpul,time)/ck
            energy(2)=(dsdt+dedt/x)/2./ck/tmstep
            energy(3)=cp*dissip/x
            write(16,350)time,energy(3),energy(2),energy(1),
     1      energy(1)-energy(2)-energy(3)
 350        format (5f11.6)
            terg=terg+tew
            nenerg=1
            dedt=0.
            dsdt=0.
 c
 400      do 410 j=1,ny
            do 410 i=1,nx
 410          old(i,j)=vort(i,j)
 c
 c        write streamfunction
          if (time.lt.tstart-tmstep/2.) go to 420
            write(21,*)'streamfunction recorded at ',time
            write(12)time,tmstep,speed,accel(timpul,time)
            write(12)((stream(i,j),i=1,nx),j=2,ny)
            mstrea=mstrea+1
            if (mstrea.lt.nconsw) go to 420
            tstart=tstart+tsw
            mstrea=0
 c
 c        write vorticity on surface of ripple
 420      if (time.lt.twrite-tmstep/2.) go to 430
            write(21,*)'vorticity function recorded at ',time
            write(18,*)time,isch,tmstep
            write(18,930)(vort(i,1),i=1,nx)
            twrite=twrite+tvw
 c
 c        compute stresses on ripple surface
 430      if (time.lt.tstres-float(mconsw)*tmstep) go to 600
          if (knum.ne.1) go to 440
```

```
          do 435 j=2,ny1
            do 435 i=1,nx
   435          dsdxdt(i,j)=dert(1,mconsw)*dsdx(i,j)
          pretms=tmstep
          knum=2
          go to 600
   440    if (tmstep.eq.pretms) go to 460
          knum=1
          go to 600
c         compute time rate-of-change of first x-derivative of streamfunction
   460    do 470 i=1,nx
            do 470 j=2,ny1
   470        dsdxdt(i,j)=dsdxdt(i,j)+dert(knum,mconsw)*dsdx(i,j)
          knum=knum+1
          if (knum.le.mconsw+1) go to 600
c         evaluating integrand in pressure term
          do 480 j=2,ny
            do 480 i=1,nx
   480        pint(i,j)=vort(i,j)*(der1(j,1)*stream(i,j+1)+
     1        der1(j,2)*stream(i,j)+der1(j,3)*stream(i,j-1))
     1        -dsdxdt(i,j)/ck/tmstep-cp*dvdx(i,j)
c         boundary values of integrand (at y=0) in pressure term
          do 500 i=1,nx
   500      array1(i)=cmplx(vort(i,1)/realnx,0.)
          call fft2c(array1,nfft,iwk)
          do 510 i=1,nx
   510      array1(i)=d1(i)*conjg(array1(i))
          call fft2c(array1,nfft,iwk)
          do 520 i=1,nx
            pint(i,1)=-cp*real(array1(i))
   520    continue
c
c         compute integral in pressure term by Cubic Spline Quadrature using
c         IMSL subroutines
          p=dy(2)/dy(1)
          q=dy(ny2)/dy(ny1)
          do 540 i=1,nx
            do 530 j=2,ny1
   530        w0(j-1)=pint(i,j)
            bpar(1)=2.*(dy(2)-dy(1))/(dy(1)+2.*dy(2))
            bpar(2)=b2*(p*(pint(i,1)-pint(i,2))+pint(i,3)-pint(i,2))
            bpar(3)=2.*(dy(ny2)-dy(ny1))/(2.*dy(ny2)+dy(ny1))
            bpar(4)=b4*(q*(pint(i,ny)-pint(i,ny1))+pint(i,ny2)-pint(i,ny1))
            call icsicu(yaxis,w0,ny2,bpar,coef,100,ier1(i))
            call dcsqdu(yaxis,w0,ny2,coef,100,y(1),y(ny),press(i),ier2(i))
   540    continue
          do 550 i=1,nx
   550      press(i)=press(i)-xarray(i)*accel(timpul,time)/ck
     1      +0.5*speed**2
c
c         compute total stress on ripple surface
          do 560 i=1,nx
            fx(i)=cp*vort(i,1)*(sha(i)*z1(i)-shb(i)*z2(i))-press(i)*z2(i)
            fy(i)=cp*vort(i,1)*(z2(i)*sha(i)+z1(i)*shb(i))-z1(i)*press(i)
   560    continue
c
c         compute net force on ripple
          do 570 i=2,nx
            w1(i-1)=fx(i)
            w2(i-1)=fy(i)
```

```
  570     continue
c
c       net force in x-direction
        bpar(1)=0.
        bpar(2)=2.*(fx(3)-2.*fx(2)+fx(1))/del**2
        bpar(3)=0.
        bpar(4)=2.*(fx(1)-2.*fx(nx)+fx(nx-1))/del**2
        call icsicu(xaxis,w1,nx-1,bpar,coef,100,ierx1)
        call dcsqdu(xaxis,w1,nx-1,coef,100,0.,1.,forcex,ierx2)
c       net force in y-direction
        bpar(1)=0.
        bpar(2)=2.*(fy(3)-2.*fy(2)+fy(1))/del**2
        bpar(3)=0.
        bpar(4)=2.*(fy(1)-2.*fy(nx)+fy(nx-1))/del**2
        call icsicu(xaxis,w2,nx-1,bpar,coef,100,iery1)
        call dcsqdu(xaxis,w2,nx-1,coef,100,0.,1.,forcey,iery2)
        write(17,920)time,timpul,tmstep,speed,accel(timpul,time)
        write(17,900)(press(i),i=1,nx)
        write(17,900)(fx(i),i=1,nx)
        write(17,900)(fy(i),i=1,nx)
        write(17,900)forcex,forcey
        frict=speed*abs(speed)/8.
        write(23,920)time,forcex,forcey
        tstres=tstres+tfw
        knum=1
c
c       write separation point
  600   if (time.lt.tsepar-tmstep/2.) go to 800
          old(nx+1,1)=old(1,1)
          write(22,900)time
          do 610 i=1,nx
  610       if (old(i,1)*old(i+1,1).le.0.)
      1     write(22,950)i,old(i,1),old(i+1,1)
          tsepar=tsepar+tpw
c
c       determination of new time-step
  800   if (time.lt.test) go to 850
        vmax1=0.
        vmax2=0.
        maxim=ny
        do 820 i=1,8
          ii=1+nx*(i-1)/8/ifix(x)
          do 810 j=2,ny1
            w1(j-1)=derl(j,1)*stream(ii,j+1)+derl(j,2)*stream(ii,j)
      1             +derl(j,3)*stream(ii,j-1)
            w2(j-1)=dsdx(ii,j)
  810     continue
          call vabmxf(w1(1),ny2,1,maxim1,ovmax1)
          call vabmxf(w2(1),ny2,1,maxim2,ovmax2)
          vmax1=amax1(vmax1,ovmax1)
          vmax2=amax1(vmax2,ovmax2)
          maxim=min0(maxim,maxim1)
          maxim=min0(maxim,maxim2)
  820   continue
        tsnew=tcrit/(pi*vmax1*realnx*dy(maxim)+vmax2)
        if (tsnew.gt.tts) go to 830
          write(20,*)'  computation terminated with time-step = ',tsnew
          write(20,*)'at time = ',time
          go to 1000
  830   if (tsnew.ge.tmstep) go to 840
```

```fortran
        tmstep=tsnew
        isch=0
        cv1=ck*tmstep
        cv2=cs*tmstep
        write(20,*)time,tmstep
  840   test=time+tcheck
  850   if (isch.lt.3) isch=isch+1
        if (time.lt.tback-tmstep/2..and.time.lt.endtme) go to 100
c
  900   format (5f11.6)
  910   format (f7.2,f7.0,f7.4)
  920   format (8f10.6)
  930   format (8f10.3)
  940   format (16i5)
  950   format (i5,2f11.4)
c
 1000   write(20,*)time,tmstep
        write(13)wck,re,slope,curren
        write(13)x,nfft,ny
        write(13)time
        write(13)isch,tmstep
        write(13)(y(j),j=1,ny)
        write(13)((stream(i,j),i=1,nx),j=1,ny)
        write(13)((old(i,j),i=1,nx),j=1,ny)
        write(13)((dsdx(i,j),i=1,nx),j=2,ny1)
        write(13)((dvdx(i,j),i=1,nx),j=2,ny1)
        write(13)((d2vdx2(i,j),i=1,nx),j=2,ny1)
        write(13)((wj(i,j),i=1,nx),j=2,ny1)
        if (isch.gt.1) write(13)((store(n1,i,j),i=1,nx),j=2,ny1)
        if (isch.gt.2) write(13)((store(n0,i,j),i=1,nx),j=2,ny1)
        tback=tback+tbkint
        if (time.lt.endtme.and.tsnew.gt.tts) go to 100
c
        stop
        end
c
c
        real function vel(timpul,time)
        common /current/curren,wave
        pi=3.14159265358979323846263
        if (time.lt.pi) vel=curren*sin(time/2.)
        if (time.lt.0.) vel=0.
        if (time.ge.pi) vel=curren
        if (time.gt.timpul)
      1 vel=vel+wave*cos(2.*pi*(time-timpul))
        return
        end
c
c
        real function accel(timpul,time)
        common /current/curren,wave
        pi=3.14159265358979323846263
        tpi=2.*pi
        accel=0.
        if (time.lt.pi.and.time.ge.0.) accel=curren*0.5*cos(time/2.)
        if (time.gt.timpul)
      1 accel=accel-tpi*wave*sin(tpi*(time-timpul))
        return
        end
c
```

```
c
c   performs a lower-triangular/upper-triangular decomposition of a
c   tridiagonal matrix.
c
      subroutine lu(m,a)
      real rl(33,101),d(33,101),u(33,101),der2(101,3),cd(101,3),
     1 bsv1,bsv2,factor,a
      common /lumat/rl,d,u/lud/ny2,der2,cd,bsv1,bsv2
c
      rl(m,1)=0.
      d(m,1)=-cd(2,2)*a+der2(2,2)
      u(m,1)=der2(2,1)-cd(2,1)*a
      do 2210 i=2,ny2-1
        rl(m,i)=(der2(i+1,3)-cd(i+1,3)*a)/d(m,i-1)
        d(m,i)=der2(i+1,2)-cd(i+1,2)*a-rl(m,i)*u(m,i-1)
        u(m,i)=der2(i+1,1)-cd(i+1,1)*a
 2210 continue
      factor=der2(ny2+1,1)-cd(ny2+1,1)*a
      rl(m,ny2)=(der2(ny2+1,3)-cd(ny2+1,3)*a+factor*bsv2)/d(m,ny2-1)
      d(m,ny2)=der2(ny2+1,2)-cd(ny2+1,2)*a+factor*bsv1
     1          -u(m,ny2-1)*rl(m,ny2)
      u(m,ny2)=0.
c
      return
      end
c
c
      subroutine solve(m,n,e)
      real rl(33,101),d(33,101),u(33,101),e(101)
      common /lumat/rl,d,u
c
      do 3010 i=2,n
        e(i)=e(i)-rl(m,i)*e(i-1)
 3010 continue
      e(n)=e(n)/d(m,n)
      dc 3020 i=n-1,1,-1
        e(i)=(e(i)-u(m,i)*e(i+1))/d(m,i)
 3020 continue
c
      return
      end
c
/EOF
```